Transactions of the ASME®

Transactions of the ASME, Journal of Turbomachinery (ISSN 0889-504X) is published quarterly (Jan., Apr., July, Oct.) by The American Society of Mechanical Engineers, Three Park Avenue, New York, NY 10016. Periodicals postage paid at New York, NY and additional mailing offices. POSTMASTER: Send address changes to Transactions of the ASME, Journal of Turbomachinery, c/o THE AMERICAN SOCIETY OF MECHANICAL ENGINEERS, 22 Law Drive, Box 2300, Fairfield, NJ 07007-2300.
CHANGES OF ADDRESS must be received at Society headquarters seven weeks before they are to be effective. Please send old label and new address.
STATEMENT from By-Laws. The Society shall not be responsible for statements or opinions advanced in papers or ... printed in its publications (B7.1, Par. 3).

INDEXED by Applied Mechanics Reviews and Engineering Information, Inc. Canadian Goods & Services Tax Registration #126148048

Journal of Turbomachinery

Published Quarterly by The American Society of Mechanical Engineers

VOLUME 123 • NUMBER 3 • JULY 2001

TECHNICAL PAPERS

(Contents continued on inside back cover)

This journal is printed on acid-free paper, which exceeds the ANSI Z39.48-1992 specification for permanence of paper and library materials. ∞™
♲ 85% recycled content, including 10% post-consumer fibers.

(**Contents continued**)

Journal of Turbomachinery **Volume 123, Number 3** **JULY 2001**

ANNOUNCEMENTS

2000 Turbomachinery Committee and Structures & Dynamics Committee Best Paper Award

A. F. Storace
D. C. Wisler
H.-W. Shin
B. F. Beacher

GE Aircraft Engines
Cincinnati, OH 45215

F. F. Ehrich
Z. S. Spakovszky
M. Martinez-Sanchez

Massachusetts Institute of Technology,
Cambridge, MA

S. J. Song
Seoul National University,
Seoul, Korea

Unsteady Flow and Whirl-Inducing Forces in Axial-Flow Compressors: Part I—Experiment

An experimental and theoretical investigation has been conducted to evaluate the effects seen in axial-flow compressors when the centerline of the rotor is displaced from the centerline of the static structure of the engine. This creates circumferentially nonuniform rotor-tip clearances, unsteady flow, and potentially increased clearances if the rotating and stationary parts come in contact. The result not only adversely affects compressor stall margin, pressure rise capability, and efficiency, but also generates an unsteady, destabilizing, aerodynamic force, called the Thomas/Alford force, which contributes significantly to rotor whirl instabilities in turbomachinery. Determining both the direction and magnitude of this force in compressors, relative to those in turbines, is especially important for the design of mechanically stable turbomachinery components. Part I of this two-part paper addresses these issues experimentally and Part II presents analyses from relevant computational models. Our results clearly show that the Thomas/Alford force can promote significant backward rotor whirl over much of the operating range of modern compressors, although some regions of zero and forward whirl were found near the design point. This is the first time that definitive measurements, coupled with compelling analyses, have been reported in the literature to resolve the long-standing disparity in findings concerning the direction and magnitude of whirl-inducing forces important in the design of modern axial-flow compressors. [DOI: 10.1115/1.1378299]

1.0 Introduction and the Nature of the Issues

1.1 Introduction. Increases in clearances resulting from rubs between rotating and stationary turbomachinery components operating at tight levels of clearance most frequently result from forces induced by the following situations: rotor unbalance (associated with imperfections in rotor manufacture or assembly), lateral deceleration during a hard landing, lateral forces induced by high-g and high-rate-of turn maneuvers, thermal bowing and/or asymmetric ovalization of the casing, especially for fans.

However, a potentially much more destructive mechanism for inducing rubs is whirl instability. Any radial deflection of the rotor relative to the stator creates circumferentially nonuniform clearances and unsteady aerodynamic forces on the rotor as each blade traverses the varying clearance gap. These unsteady forces are orthogonal to the deflection and therefore are a significant driver of rotor whirl instabilities. The forces increase in magnitude as the deflection increases so that above the onset speed, where destabilizing forces overwhelm the stabilizing damping forces, the deflections are ultimately limited only by damage to the interacting parts or by damping forces. Consequently an accurate determination of their magnitude and direction is of major importance in the design of safe, stable turbomachinery components. Examples of whirl are hysteretic whirl, whirl associated with fluids trapped within cylindrical rotor cavities and plain journal bearings, etc.

1.2 The Nature of the Issues. The unsteady, destabilizing, aerodynamic cross-axis stiffness force that promotes rotor whirl was first postulated by Thomas [1] and Alford [2] to explain rotor whirl instabilities seen in steam turbines and jet engines respectively. Therefore, this force is generally referred to as the Thomas/Alford force.

Whirl in Turbines. For a deflected turbine rotor, it has been shown experimentally that the airfoils in the closure zone are more highly loaded by aerodynamic forces than the airfoils in the open clearance zone because the former are operating more efficiently [3]. This situation is shown schematically in Fig. 1(*a*) for a turbine rotor whose centerline has been displaced upward along the ordinate by an amount $+Y$. This gives minimum clearance at the top of the turbine and maximum clearance at the bottom. The forces at these two locations are the vector sum of the mean blade force, F_m, and the unsteady blade force resulting from the centerline offset, F_u. As suggested by Thomas [1], summing the forces *perpendicular* to the axis of displacement results in a net force, $F_X = F_m + F_u$, due to the difference in airfoil loading. Since F_X acts normal to the axis of displacement, it is called a cross-axis (cross-coupled) stiffness force. As seen in Fig. 1(a), the direction of F_X acts to drive the rotor in orbital (whirling) motion about the nondisplaced centerline in the same direction as rotor rotation, i.e., F_X promotes forward whirl for turbines. Thomas postulated the following model to compute a cross-coupled aerodynamic stiffness coefficient in terms of the acting torque and a β coefficient:

$$K_{XY} = \frac{F_X}{+Y} = \frac{T\beta}{D_P H} \quad (1)$$

Measurements of transverse destabilizing forces in unshrouded turbines give positive β values in the range from 2 to 5 [4–7].

Whirl in Compressors. Alford [2] hypothesized the same phenomenon for compressors, whereby aerodynamic, cross-axis forces caused by asymmetric tip clearance feed energy into the whirling motion of the rotor. Alford reasoned that during rotor whirl, the circumferential variation in radial tip clearance causes a

---

Contributed by the International Gas Turbine Institute and presented at the 45th International Gas Turbine and Aeroengine Congress and Exhibition, Munich, Germany, May 8–11, 2000. Manuscript received by the International Gas Turbine Institute February 2000. Paper No. 2000-GT-565. Review Chair: D. Ballal.

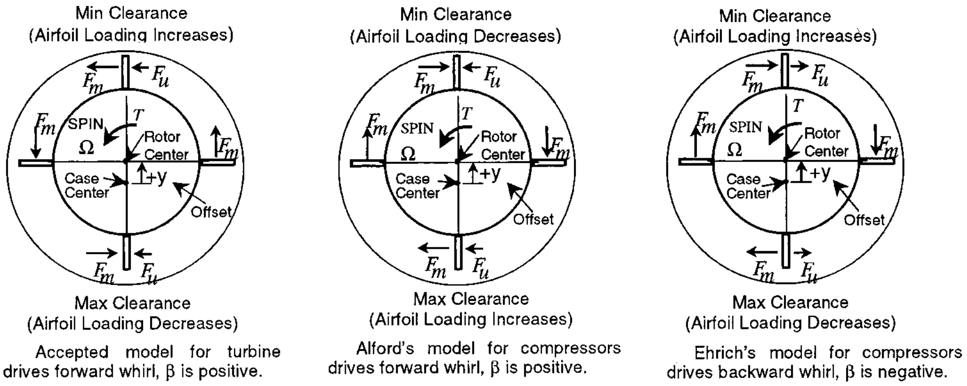

Accepted model for turbine drives forward whirl, β is positive.
(*a*)

Alford's model for compressors drives forward whirl, β is positive.
(*b*)

Ehrich's model for compressors drives backward whirl, β is negative.
(*c*)

Fig. 1 Models of whirl-inducing forces in turbines and compressors. Net force $F_x = F_m + F_u$ acts perpendicular to the axis of displacement and drives rotor whirl; see Appendix B1.

circumferential variation in efficiency so that the blading with the smallest clearance would be the most efficient. Alford further hypothesized that the compressor would pump to a circumferentially uniform exit static pressure and therefore the more efficient blading at tight clearance would have a lower loading than the blading with larger clearance 180 deg away. This situation, illustrated in Fig. 1(*b*), shows that the net force, F_X, tends to cause forward rotor whirl. Thus, Alford concluded that compressors have positive β's so that whirl-inducing forces for both compressors and turbines are in the same direction.

Ehrich [8] hypothesized differently from Alford. He reasoned that compressor airfoils with the smaller clearance would sustain a higher static pressure differential across their tips and would therefore be more highly loaded than the airfoils with larger clearance, 180 deg away. As shown in Fig. 1(*c*), this dictates that the net destabilizing force in compressors, F_x, tends to produce rotor whirl counter to the direction of rotation. Thus Ehrich concluded that compressors tend to have negative β coefficients so that the direction of whirl-inducing forces for compressors would be opposite to those for turbines.

There has been a disparity in the findings in the literature concerning the direction of rotor whirl in compressors. Vance and Laudadio [9] found experimentally that the Thomas/Alford force is rotor-speed dependent and mostly positive, except for some special combinations of rotor speed and stage torque where the direction of the force was reversed. Colding-Jorgensen [10] found the same generality for the shape and slope of the relationship of β coefficient versus flow coefficient as later reported by Ehrich [8], but the Colding-Jorgensen results suggested a more positive level of the parameter than the negative levels reported in Ehrich's work. Ehrich [8] further showed that the experimental data of Vance and Laudadio [9] implied that, for certain values of torque and speed in their low-speed blower tests, the destabilizing forces tend to drive backward whirl. Other evidence was also accumulating in theoretical and experimental results of Yan et al. [11] to indicate negative β coefficients for compressors.

In engine field experience, aerodynamic cross-axis forces were cited by Akin et al. [12] as the destabilizing mechanism in the high-pressure rotor instability of the TF30 P111 + engine when it went into production in mid-1986. Vibration reject rates were as high as 50 percent until the instability was eliminated by using a squeeze-film damper at the high pressure turbine bearing.

In view of the importance of the β coefficient in designing stable turbomachinery components, the disparity between Alford's and Ehrich's conjectures, the mixed findings of researchers on the issues, the need for designers to often use very conservative methods, and the absence of a decisive resolution of rotor whirl issues, we formulated the experimental and analytic program described in Parts I and II.

2.0 Objectives and Definitions

2.1 Objectives. The overall goal of Part I was to provide a definitive resolution of the long-standing disparity in findings concerning the direction and magnitude of rotor whirl in compressors.

There were three major objectives of Part 1. The first was to quantify any changes in compressor performance and airfoil loading produced in compressors when the rotor centerline becomes displaced or offset from that of the stator. The second was to determine which of the two models best describes whirl in compressors, the Alford Model of Fig. 1(*b*) or the Ehrich model of Fig. 1(*c*). The third was to determine the direction and magnitude of rotor whirl-inducing, aerodynamic forces in axial-flow compression systems used in modern turbomachinery, including their design implications.

Comparing the results from analytical and computational models relative to the experimental data will be the subject of Part II.

2.2 Definitions. The following definitions will be helpful.

Rotor whirl instability: Unstable rotor whirl is defined as the self-excited orbital motion of the rotor centerline about its nominal or undisplaced centerline induced by a destabilizing tangential force, which overcomes the stabilizing external damping forces. There are several potential sources of such destabilizing forces. This paper focuses on the Thomas/Alford forces.

Beta coefficient: the ''Thomas/Alford Parameter,'' originally conceived as the change in thermodynamic efficiency per unit change in blade tip clearance, expressed as a fraction of blade height. In practice β, as defined by Eq. (1), is a normalized value of the cross-coupled stiffness.

Forward whirl: whirl whose direction is the same as that of the engine rotor rotation or spin. The β coefficient is positive for forward whirl.

Backward whirl: whirl whose direction is opposite to that of the engine rotor rotation or spin. The β coefficient is negative for backward whirl.

Aerodynamic cross-axis force: the net unbalanced aerodynamic force that acts perpendicular to rotor radial deflection to drive rotor whirl.

3.0 Experimental Test Program

We set up a test program in the GE Low Speed Research Compressor to simulate the eccentricity of a whirling rotor and measure the nonuniform, unsteady flowfield that develops.

3.1 Low Speed Research Compressor (LSRC). The LSRC is an experimental facility that duplicates the relevant aerodynamic features of axial flow compressors in modern gas turbine engines in a large, low-speed machine where very detailed investigations of the flow can be made. Aerodynamic similarity for

Mach number and Reynolds number is used in scaling the high-speed airfoils to their low-speed counterparts. This method of testing has proven reliable for over forty years in understanding and designing HP compression systems provided the phenomena being studied are Reynolds number dependent and not compressibility dependent.

The LSRC, which has a constant casing diameter of 1.524 m (60.0 in.), was set up with four identical stages in order to simulate the repeating stage environment. The third stage was the test stage. The blading was representative of current design practice.

Three different low-speed blading configurations were tested. The first two, called Compressors *A* and *B* respectively, are typical of modern designs and have high hub/tip ratios of 0.85 with low-aspect-ratio, high-solidity blading and shrouded stators. These two compressors are low-speed, aerodynamic models of the middle and rear block of highly loaded, high-reaction (65–70 percent) HP compressors in commercial gas turbine engines currently in service. Compressor *C*, also in commercial engine service, has cantilevered stators and blading with a lower hub/tip ratio of 0.70, lower reaction of 0.55, and higher aspect ratios than the others have. Additional information about the LSRC testing technique and the blading is available in [13–15]. Blading details for all three compressors are given in Table 2 of Appendix A.

A cross section showing the test stage for Compressor *A* is given in Fig. 2. The stators are shrouded so that there is no clearance between the end of the stator airfoil and the hub under the airfoil. The seal tooth inhibits flow leakage from the trailing edge region through the seal cavity upstream to the leading edge region. Consequently, the leakage flowfield across the rotor tip is very different from that in the stator hub.

Only Compressor *A* was tested with the stator centerline offset from that of the rotor, as described below. All three compressors were tested at different axisymmetric clearances without offset to obtain the required input for the models in Part II.

3.2 Offset and Clearance Conditions. The use of large, precision offset rings and offset bearing supports enabled us to assemble the LSRC with the centerline of the stator casing offset (displaced) relative to the centerline of the rotor and its drive mechanism. The offset is shown schematically in Fig. 3. This process of moving the entire stator assembly relative to the rotor to achieve the offset significantly reduced both the cost and complexity of the test program as compared to moving the complex and massive rotor drive mechanisms.

Tests were performed for Configuration A with two displacements of the casing centerline: a larger displacement of 0.1905 cm (0.075 in) and a smaller one of 0.0965 cm (0.038 in). The larger displacement exceeded the baseline rotor tip clearance by 0.0279 cm (0.011 in.). Therefore, to avoid both significant damage to the LSRC test hardware from a rub and the resulting safety issues, we ground the rotor tip and the stator shroud seal to allow both to run at the absolute minimum safe clearance judged to be 0.051 cm (0.020 in.). This permitted the vehicle to enter rotating stall. Although this process increased the magnitude of the average clearances, the levels of centerline offset and clearance magnitudes bounded those of practical field experience where clearances increase in high-time engines.

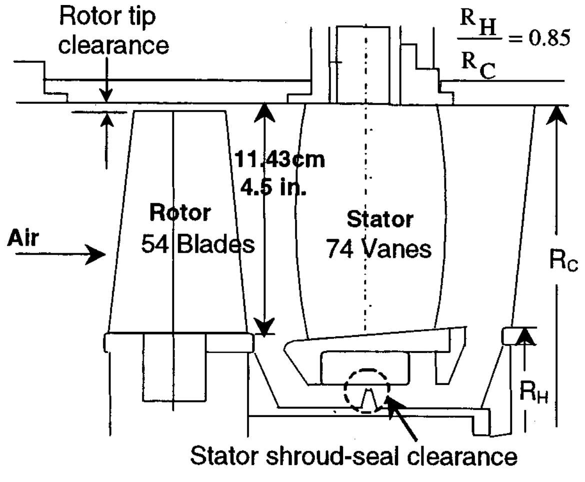

Fig. 2 Schematic showing cross section of compressor A blading

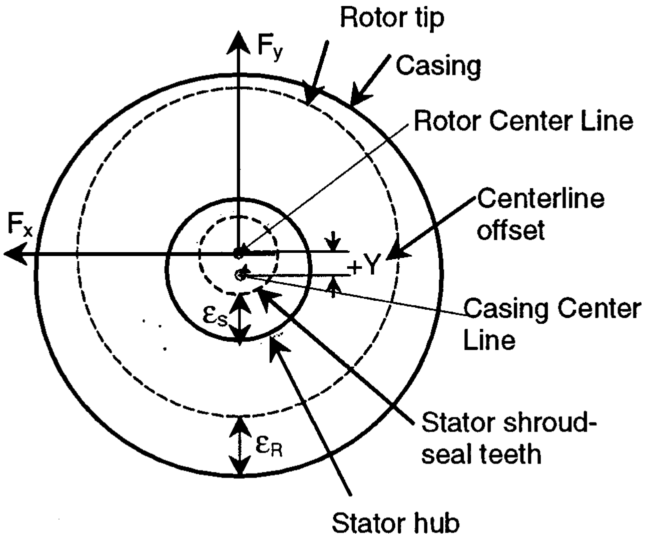

Fig. 3 LSRC configuration for centerline offset tests showing circumferential variation in rotor tip clearance ε_R, and stator shroud seal clearance, ε_s. Looking down on spinning, non-whirling eccentric rotor with casings moved relative to rotor assembly; see Appendix B2.

The offsets gave the corresponding values of minimum and maximum clearance for the rotor-tip and the stator shroud seal-tooth as shown in Table 3 of Appendix A. Precision run-outs gave clearance variations from nominal around the circumference of ±0.0152 cm (0.006 in.). The offset was measured to be accurate to within ±0.0102 cm (0.004 in.).

While the rotor did not actually whirl in these tests, the static shaft offset was intended to approximate the flowfield present in whirling rotor motion to allow evaluation of the dominant aerodynamic forces contributing to rotor whirl. The effects of the additional forces in an actual whirling rotor are analyzed in Part II.

3.3 Instrumentation

Steady-state Instrumentation. High-resolution pressure transducers, accurate to ±0.010 percent of the full-scale values of either 0.068 or 0.136 bar (1 or 2 psi), were used to record steady-state static and total pressures for determining both overall compressor performance and the static pressures on the stator airfoil surfaces. Frequent calibrations were conducted. A strain-gage torque meter, accurate to ±0.07 percent of measured torque, was used to deduce shaft work input to quantify compressor efficiency. Overall measurement accuracy is as follows: Flow coefficient and pressure coefficient are accurate to within ±0.15 percent and efficiency to within ±0.25 points.

Dynamic Instrumentation. A total of 64 ultra-miniature, high-response Kulite model LQ-125 pressure transducers, having a frequency response of 20 kHz, were imbedded inside the rotor airfoil surfaces to measure the unsteady static pressures acting on the suction and pressure surfaces. The locations of the Kulites, shown in Table 4 of Appendix A, were selected to provide resolution of both chordwise and spanwise gradients. Small pressure ports pneumatically connected the sensor to the measurement surface.

The port diameters were sized properly at 0.08128 cm (0.032 in.) and the lengths were small enough at 0.0406 cm (0.016 in.), as defined by Doebelin [16], so as not to attenuate the periodic unsteady pressures.

The transducers were calibrated after installation in the airfoils by using both a pressurized/evacuated chamber and a dynamic frequency-response calibrator. The transducer accuracy was ±1.0 percent. The response was unattenuated with no phase shifting up to 1400 Hz (the limit of the calibrator used) or two times blade passing frequency.

Data Sampling and Signal Processing. The signals from the pressure transducers were digitized and ensemble-averaged. A Kinetic System analog-to-digital converter was used to digitize the data signals using phase locked sampling at constant time increments. The analog data were low-pass filtered at 1 kHz to avoid aliasing. The use of 200 ensemble averages greatly reduced the effects of time-unresolved unsteadiness. A once-per-revolution pulse from an optical encoder in the casing sensed the trigger airfoil on the rotor blade and initiated the sampling for the data windows for each rotor revolution.

3.4 Data Reduction

Calculation of Unsteady Pressures. Since the pressure transducers were mounted in seven different airfoils on the 54-bladed rotor disk, great care was taken in time-shifting and synthesizing these data onto one representative airfoil to construct the unsteady pressure variation experienced by the rotor airfoils during a rotor revolution. The raw pressure data for each transducer were processed using fast Fourier transform (FFT) methodology to give a filtered waveform consisting only of the first harmonic. An example of the raw data is presented in Fig. 4(*a*) and the results from its FFT analysis to obtain the Fourier coefficients are shown in Fig. 4(*b*). The first harmonic is dominant. The 54th and 74th harmonics in the figure are associated with 54 rotors and 74 stators. An example of the circumferential variation of unsteady pressure determined from the first harmonic is shown in Fig. 4(*c*).

The unsteady pressures measured at the discrete locations on the airfoil surfaces were bidirectionally curve-fit along the radial and chordwise directions to obtain continuous pressure distributions on the suction and pressure surfaces. Our confidence levels in being able to integrate the unsteady blade pressures for the given Kulite coverage was about 95 percent. This was assessed by randomly removing data from several kulites from the analysis, re-processing the data, and comparing the forces obtained from the pressure integration. DC-level comparisons were not made because the Kulite transducers were not installed in the centered-rotor configuration.

Calculation of the Thomas/Alford Force. By using the unsteady pressure distributions computed above and the geometric orientation of the airfoil surfaces in the compressor, we integrated over the airfoil surfaces to obtain the unsteady forces acting on the various airfoils around the circumference. We resolved the unsteady forces into their tangential and radial components using the local blade coordinate system shown in Fig. 5; see Appendix B3a.

Next we computed the component of force acting perpendicular to the direction of rotor offset, F_x (the Thomas/Alford force). To do this, we transformed the tangential and radial blade forces in the local blade coordinate system of Fig. 5 to the global coordinate system fixed to the bladed disk, also shown in Fig. 5. We then algebraically summed the individual forces to get the net cross-axis stiffness force F_x, and the net direct positive stiffness force F_Y; see Appendix B3b.

Calculation of the Beta Coefficient. The Beta coefficient is calculated from Eq. (1) using the torque and the slope (cross-axis stiffness, K_{XY}) of the Thomas/Alford force F_X plotted versus rotor offset.

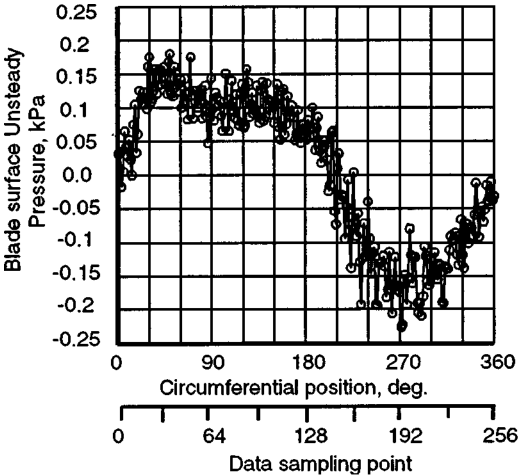

Raw waveform of measured pressure

(*a*)

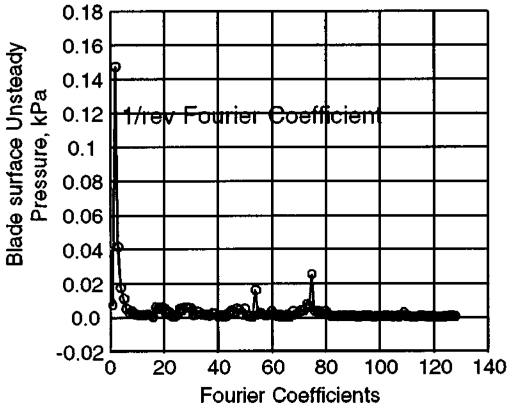

Fast Fourier Transform of raw waveform

(*b*)

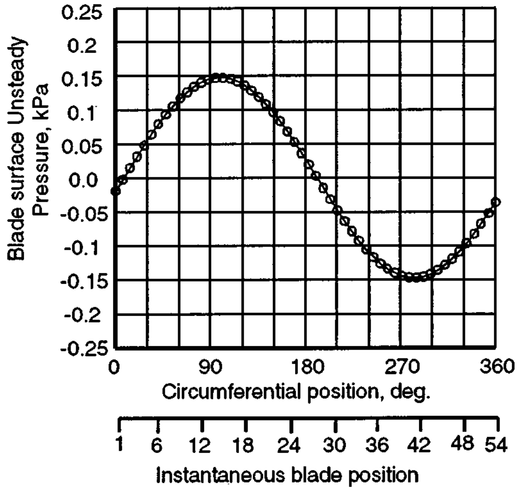

Circumferential variation of unsteady pressure using first Fourier Coefficient.

(*c*)

Fig. 4 Typical example showing the circumferential variation in unsteady static pressure obtained from a Kulite pressure transducer embedded in a rotor airfoil (96 percent span and 50 percent chord for the large rotor offset): (*a*) raw data, (*b*) FFT of raw data, (*c*) filtered signal.

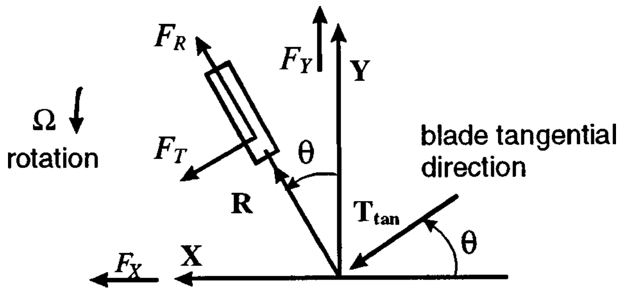

Fig. 5 The two coordinate systems used to resolve blade forces: (1) blade fixed coordinate (T_{tan},R), (blade geometry defined in this system); (2) rotating coordinate (X,Y) (the blade azimuth angle θ is defined in this coordinate system); see Appendix B3

4.0 Effects of Clearance Variation and Centerline Offset on Overall Compressor Performance

Compressor performance is presented in this section as a four-stage average of pressure coefficient and efficiency plotted as a function of flow coefficient. The curve of pressure coefficient versus flow coefficient is called the pressure characteristic. Stall margin is computed for these low-speed tests in terms of throttle margin, TM, as defined in the nomenclature.

Variations in loading levels from high flow (low-loading) to stall were achieved by varying mass flow rate through the compressor using a discharge throttle. Lines of constant throttle setting are shown in the figures to indicate the different loading levels along the pressure characteristic. The tests were run at the design tip speed of 64.0 m/s (210 ft/sec), which required a rotational speed of approximately 804 rpm. This gave a Reynolds number of 3.6×10^5, which is sufficiently above the knee in the Reynolds number-loss curve to be representative of engine conditions.

4.1 Baseline Performance. The baseline performance of Compressor A, shown as Curves A1 in Figs. 6 and 7, was established with no centerline offset and with circumferentially uniform, nominal levels of rotor-tip clearance and stator shroud-seal clearance given in Table 3 of Appendix A. The design point is shown in both figures. The negative slope of the baseline pressure characteristic over all of the flow range from high flow to near peak pressure provides stable operation over this range, after which it begins to roll over. Stall occurs at a flow coefficient of about 0.335, as indicated by the short vertical line at the low-flow end of the pressure characteristic. Baseline Compressor A has high efficiency that peaks at 90.4 percent. It also has a good throttle margin of 30.2 percent, as indicated by the 17.9 percent flow range from the design point to stall. This baseline is the performance standard against which all of the other configurations will be compared.

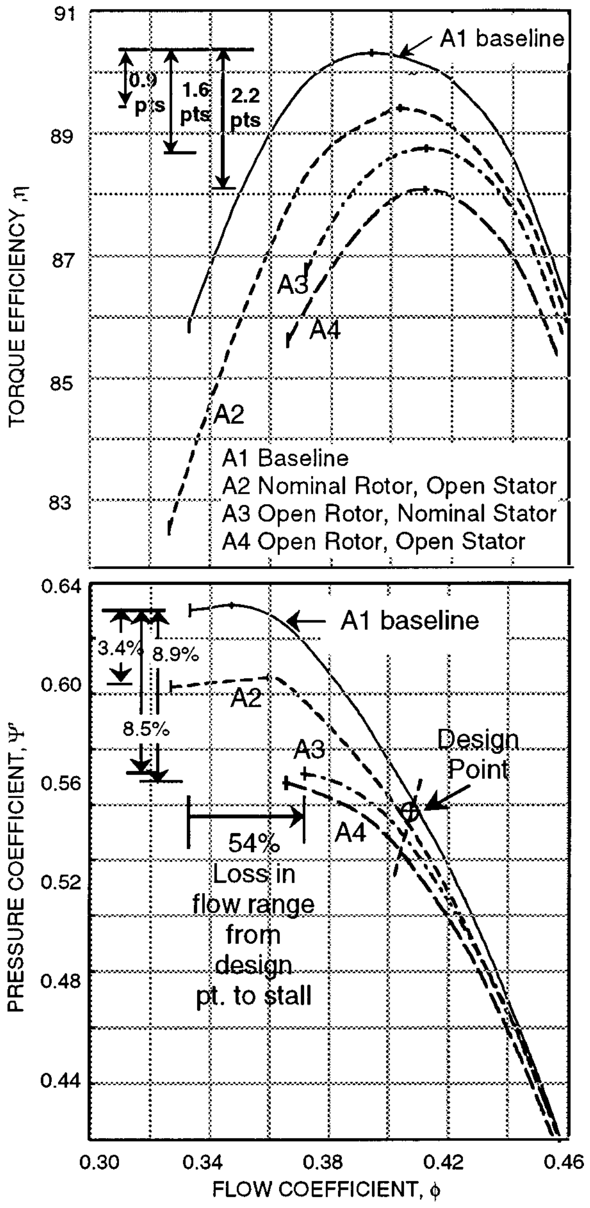

Fig. 6 Overall performance of compressor A showing the effects of variation in axisymmetric clearances relative to baseline performance. Compressors A1–A4 are defined in Table 3 of Appendix A. Data accuracy is identical to that for Fig. 7, therefore data symbols are removed for clarity.

4.2 Effect of Axi-symmetric Clearance Variation on Performance. The effects of varying axisymmetric (circumferentially uniform) clearance on the performance of Compressor A are shown relative to the baseline performance in Fig. 6. The clearance variation was obtained without centerline offset and thus is typical of what occurs in a uniform rotor tip rub. Both rotor tip clearance and stator shroud-seal clearance were varied independently so that we could separate the effects. Detailed surveys of flow properties (not included in this paper) showed that when rotor tip clearance alone was increased, the dominant effect was seen in the outer 25 percent of span. Similarly when the stator seal clearance alone was increased, the dominant effect was seen in the inner 25 percent of span.

Looking first at Curves A2 in Fig. 6 showing the effects of doubling only the stator shroud-seal clearance, we see that peak pressure rise and efficiency are reduced by 3.4 percent and 0.90 points, respectively. However, stalling flow is nearly unaffected because this is tip-sensitive blading with respect to stall onset; thus reasonable changes in hub clearances will not significantly affect the flow level at which stall onset occurs.

Looking next at Curves A3 in Fig. 6, which show the effects of doubling only the rotor tip clearance, we see that all performance quantities are affected significantly. There is a 8.5 percent reduction in peak pressure rise, a 1.6 point loss in efficiency, a 54 percent loss in flow range between the design point and stall, and a throttle margin of 11.1 percent, which is 37 percent of the baseline value. Being a tip-sensitive compressor, changes in rotor tip clearance significantly affect stall onset.

Opening both rotor tip clearance and stator shroud-seal clearance produces the expected results of further loss in pressure rise and efficiency but little further change in stalling flow range, as shown by Curves A4 in Fig. 6.

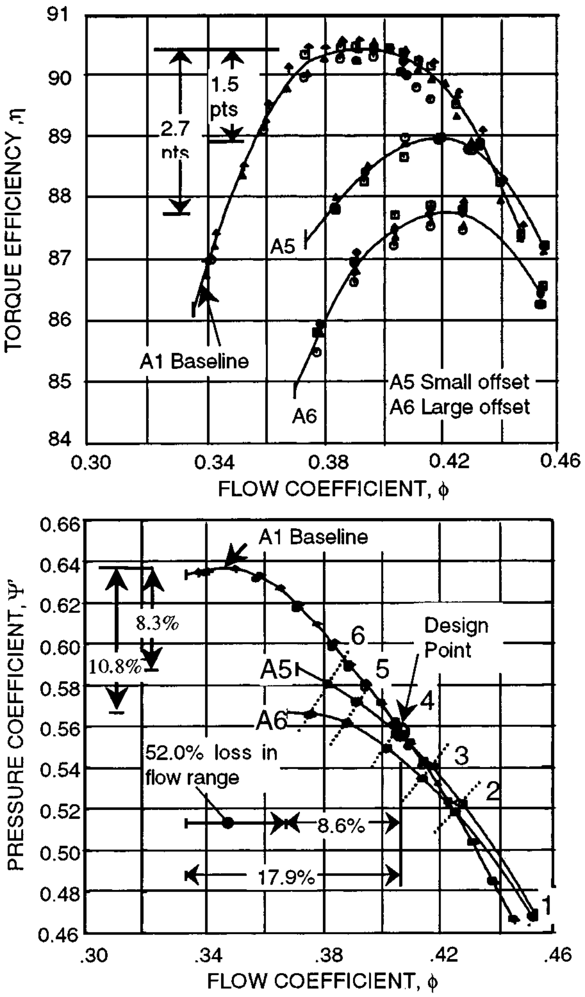

Fig. 7 Overall performance of Compressor A for rotor centerline offset tests relative to baseline performance

4.3 Effect of Centerline Offset Having Increased Average Clearances on Performance. The pressure and efficiency characteristics for the two levels of casing centerline offset are compared in Fig. 7 to those for the baseline configuration. As expected, the offset configurations with their larger average and maximum clearances, shown as Curves A5 and A6, have lower efficiencies and lower peak pressure rise than those for the baseline Curves A1. There is an 8.3 percent, and 10.8 percent loss in peak pressure and 1.5 point and 2.7 point loss in peak efficiency, respectively, for the small and large offsets. Throttle margin is 11.7 percent, which is 39 percent of the baseline value. Thus, stall margin has suffered considerably. Note that there is little change in loss of stalling flow range between small and large offsets.

4.4 Applicability of Parallel Compressor Theory. Two of the models used to compute β coefficients in Part II of this paper rely on the validity of parallel compressor methodology. In addition, Part II will analyze our data by separating it into that for the outer 50 percent span (influenced by rotor tip clearance) and that for the inner 50 percent span (influenced by stator seal clearance), followed by a synthesis of these results. In order to gain confidence in these approaches, we evaluated the Compressor A performance derivatives for the offset tests relative to those for the axisymmetric tests.

Both the change in pressure rise and the change in efficiency were determined for the corresponding change in total average clearance from the baseline clearances as expressed by the following equation:

$$\Delta\overline{\varepsilon}_{r,s} = \left(\frac{\overline{\varepsilon}_r - \overline{\varepsilon}_{r,\mathrm{Baseline}}}{H} + \frac{\overline{\varepsilon}_s - \overline{\varepsilon}_{s,\mathrm{Baseline}}}{H}\right) \times 100 \text{ percent}$$

Note that all clearances are normalized by the blading span of 11.43 cm (4.50 in.). This approach of adding clearances was taken to evaluate the degree of linearity in the performance derivatives. We evaluated derivatives in terms of average clearances since changes in pressure coefficients, efficiency, and loading, which are of primary interest for assessment of Thomas/Alford forces, typically vary systematically with changes in average clearance. Loss in stall margin typically correlates with changes in maximum clearance, but that is of less interest here.

The performance derivatives for axisymmetric Compressors A1–A4 were computed at the peak efficiency and increased loading points in Fig. 6. The results, shown in Fig. 8 as open symbols, describe a linear sensitivity to change in total average clearance within 0.150 variance for the pressure derivative and 0.008 for the efficiency derivative.

The performance derivatives were also computed for both the small and large offset result described previously in Fig. 7. These derivatives, shown as the solid symbols in Fig. 8, have nearly the same linear sensitivity as those for the axisymmetric tests. This provides high confidence that parallel compressor theory and the methodology of Part II are appropriate.

4.5 Performance of Compressors B and C. The pressure and efficiency characteristics for Compressors B and C are presented in Fig. 9. The configurations, labeled Curves B1, B2, B3, C1, and C2, are identified in Table 3 in Appendix A. These results will be used in Part II in Ehrich's methodology for whirl analysis.

5.0 Effects of Centerline Offset on Airfoil Loading for Compressor A

5.1 Unsteady Loading on Rotor Airfoils. Unsteady pressures on the rotor airfoils were measured as the rotor traveled through varying levels of clearances caused by the centerline offset. Suction surface pressures were subtracted from pressure surface pressures to give unsteady pressure difference (loading) on the airfoil. Representative results showing this loading for three clearance levels around the circumference are presented in Fig. 10 as contours of differences in unsteady static pressure. The color red indicates the highest loading and blue indicates the lowest loading. Figure 10(*a*, *b*, *c*) show the rotor at near minimum clearance, nominal clearance, and near maximum clearance respectively. The measured, steady-state, surface static pressure distribution at 80 percent span for the rotor airfoil is shown in Fig. 10(*d*).

It is clear that airfoil unsteady loading across the span increases in the region of minimum clearance (red contours in Fig. 10*a*) and decreases in the region of maximum clearance (blue contours in Fig. 10(*c*)) relative to the mean loading at nominal clearance in Fig. 10(*b*). It is also clear from Fig. 10 that, near the rotor tip in Zone A, the airfoil loading increases at near minimum clearance and decreases at near maximum clearance. This finding confirms the correctness of Ehrich's hypothesis in Fig. 1(*c*) about the nature of rotor whirl-inducing forces in compressors as discussed in Section 1.2.

In trying to explain the driving mechanisms for rotor whirl in turbomachinery, previous investigators have concentrated only on the effects of variation in rotor tip clearance. Our unsteady data in Fig. 10 show an additional feature needing attention in whirl analyses, namely, the effect of clearances in the hub region as an additional driver of rotor whirl. The changes in stator shroud-seal clearance and any radial redistribution of flow produce a change in hub loading on the rotor in Zone B. As seen in Figs. 10(*a*, *c*), the unsteady forces in the hub increase (red contour) at tight clearance and decrease (blue contour) at more open clearance. While it is known that varying stator hub/shroud clearance affects both compressor aerodynamic performance and local hub airfoil/drum

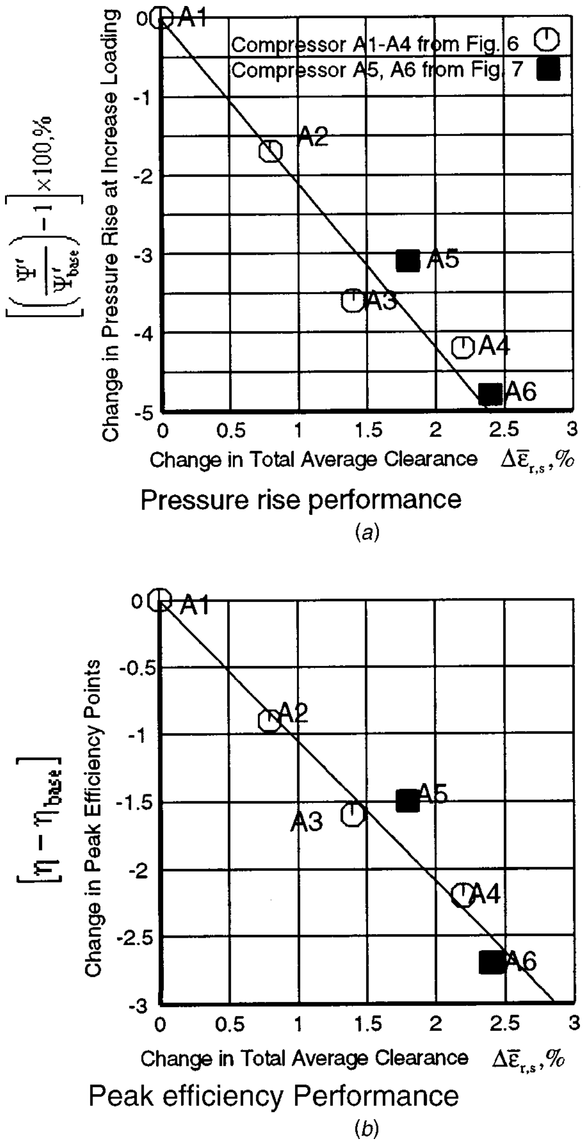

(a)

(b)

Fig. 8 Performance derivatives for compressor A in terms of change in total average clearance from baseline clearance levels

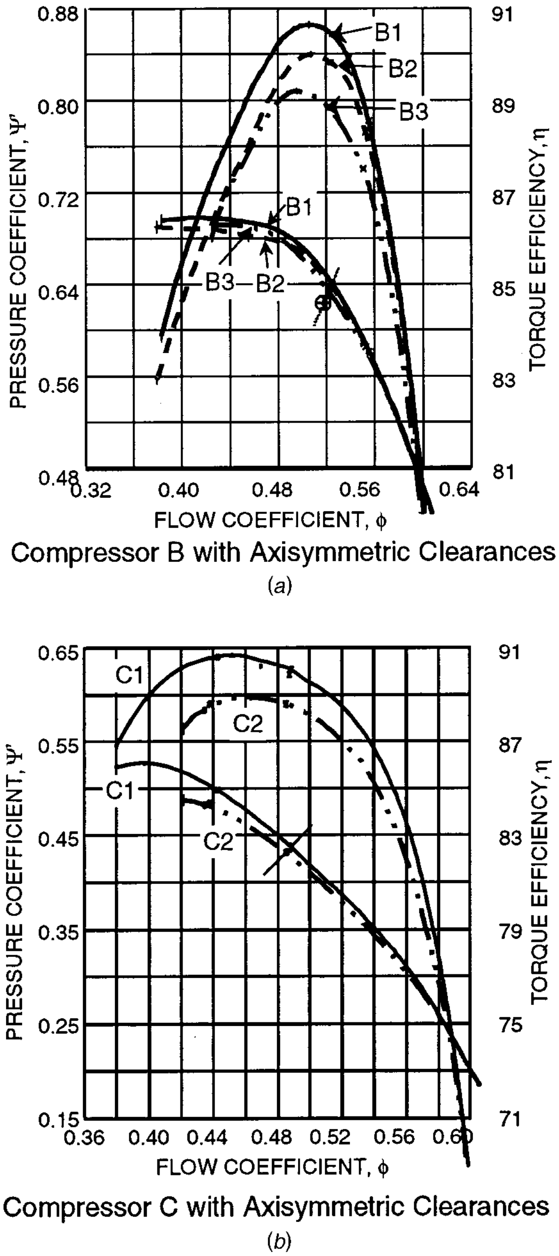

(a)

(b)

Fig. 9 Performance characteristic for compressors *B* and *C*

loading [13,17], until now this effect has not been incorporated into documented rotor-whirl analyses. In that sense, incorporating these findings into the analyses presented in Part II constitutes a new approach to whirl analysis.

5.2 Loading Variation on Stator Airfoils. Stator surface pressures were measured on two instrumented airfoils at locations described in Table 5 of Appendix A. For the large offset conditions of Compressor A, the instrumented vanes were moved to various circumferential positions from minimum to maximum rotor tip clearance to measure the respective stator loading.

The resulting normalized, steady, surface static pressures as a function of percent airfoil chord are presented in Fig. 11(*a–i*). From left to right in the figure, we show the results for compressor low, medium, and high loading, respectively, taken at Test Points 1, 3 and 5 in Fig. 7. From top to bottom, we show the results from near the casing, at midspan and near the hub. In each of the nine parts of the figure, the circumferential variation in stator loading is presented for maximum, nominal, and minimum clearances.

One can identify the magnitudes of the stator incidence angle and leading edge loading in Fig. 11 by the amount of either crossover or separation between the suction and pressure surface curves. For example, the crossover of these surface distributions at about 8 percent chord in Fig. 11(*d*) indicates lower incidence angle and lower leading edge loading compared to the large separation in these distributions near the leading edge for nominal clearance in Fig. 11(*c*).

Near the casing at 90 percent span, we see a progressive increase in the circumferential variation of stator incidence as one moves along the pressure characteristic from low compressor loading, Fig. 11(*a*), to medium loading, Fig. 11(*b*), to high loading, Fig. 11(*c*). Using data from the concentric tests, we computed an incidence angle derivative with respect to changes in leading edge loading. When this derivative was applied to the observed variation in the offset tests shown in Fig. 11, we found variations in incidence angle near the casing of up to 7 degrees around the circumference. Such a large circumferential variation in stator incidence angle and airfoil leading edge loading is clearly seen in Fig. 11(*c*).

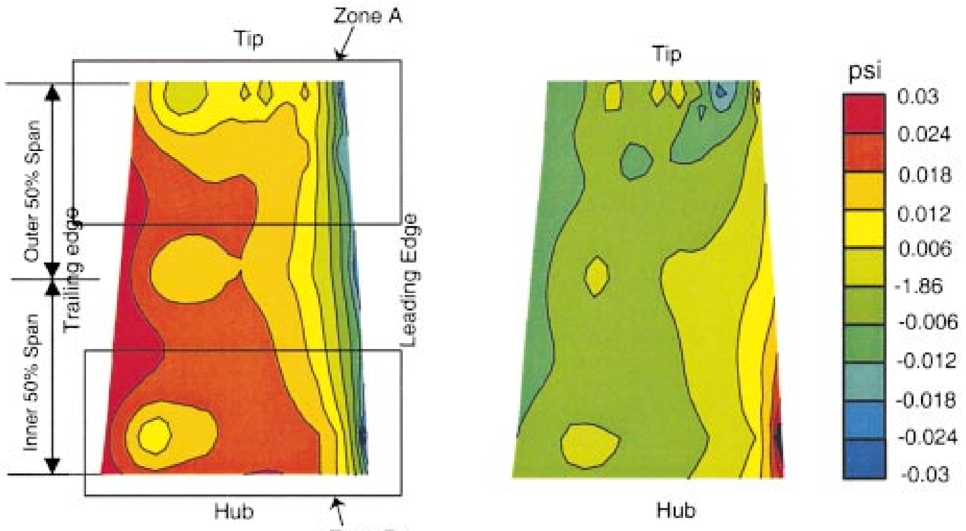

a)Minimum Clearance

b) Nominal Clearance

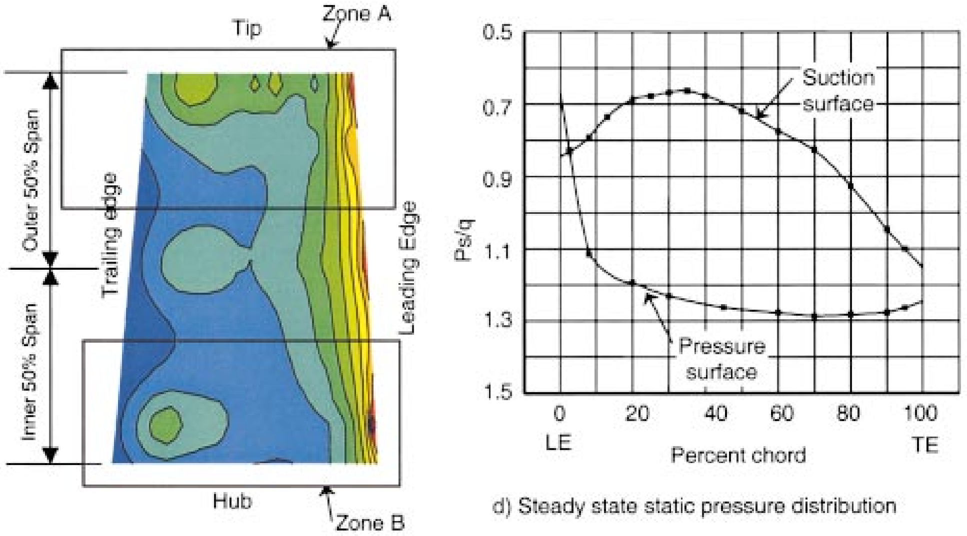

c) Maximum Clearance

d) Steady state static pressure distribution

Fig. 10 **(*a*, *b*, *c*) Contours of unsteady static pressure difference on the rotor airfoils at three clearance levels around the circumference for the large centerline offset. Zone *A* is affected by variation in rotor blade tip clearance and zone *B* is affected by stator shroud seal clearance. Both zones are affected by any radial flow redistribution; (*d*) chordwise distribution of measured, steady-state static pressure on rotor airfoil at 80 percent span.**

At midspan, there is no change in stator incidence around the circumference at low compressor loading, Fig. 11(*d*), with some increase in incidence variation as loading increases from Fig. 11(*e*, *f*). Near the hub, the influence of increased stator seal-tooth clearance makes itself known from Fig. 11(*g*, *h*, *i*).

The circumferential variations in stator loading seen near the hub in Fig. 11 imply circumferential variations in hub spool loading, which constitutes an additional driving mechanism for rotor whirl not previously incorporated into analyses. A discussion of this effect is given in Part II.

6.0 Unsteady Blade Forces and the Thomas/Alford Parameter β Coefficient

In this section we present the unsteady blade forces that drive rotor whirl in compressors and the calculation of the Thomas/Alford parameter, or β coefficient.

6.1 Unsteady Whirl-Inducing Blade Forces. The unsteady pressures presented in Section 5.1 were reduced to unsteady blade forces as described in Section 3.4. A representative result for the large offset configuration running at high compressor loading (Test Point 5 in Fig. 7) is shown in Fig. 12. The tangential and radial components of the unsteady, whirl-inducing blade force are plotted as a function of circumferential position. The circumferential variation of rotor tip clearance is also plotted.

The forces in Fig. 12 need to be understood relative to the sign convention of Fig. 13. The direction of rotation and the direction of the driving torque in Fig. 13 are counterclockwise. The centerline is offset upward, which places the minimum clearance at top-dead-center. Two forces are shown acting on each airfoil: a mean force, F_m, and the tangential component of the unsteady force due to the offset, F_u. The magnitude and direction of the unsteady force will determine the direction of rotor whirl.

In Fig. 12 the radial component of unsteady force is very small

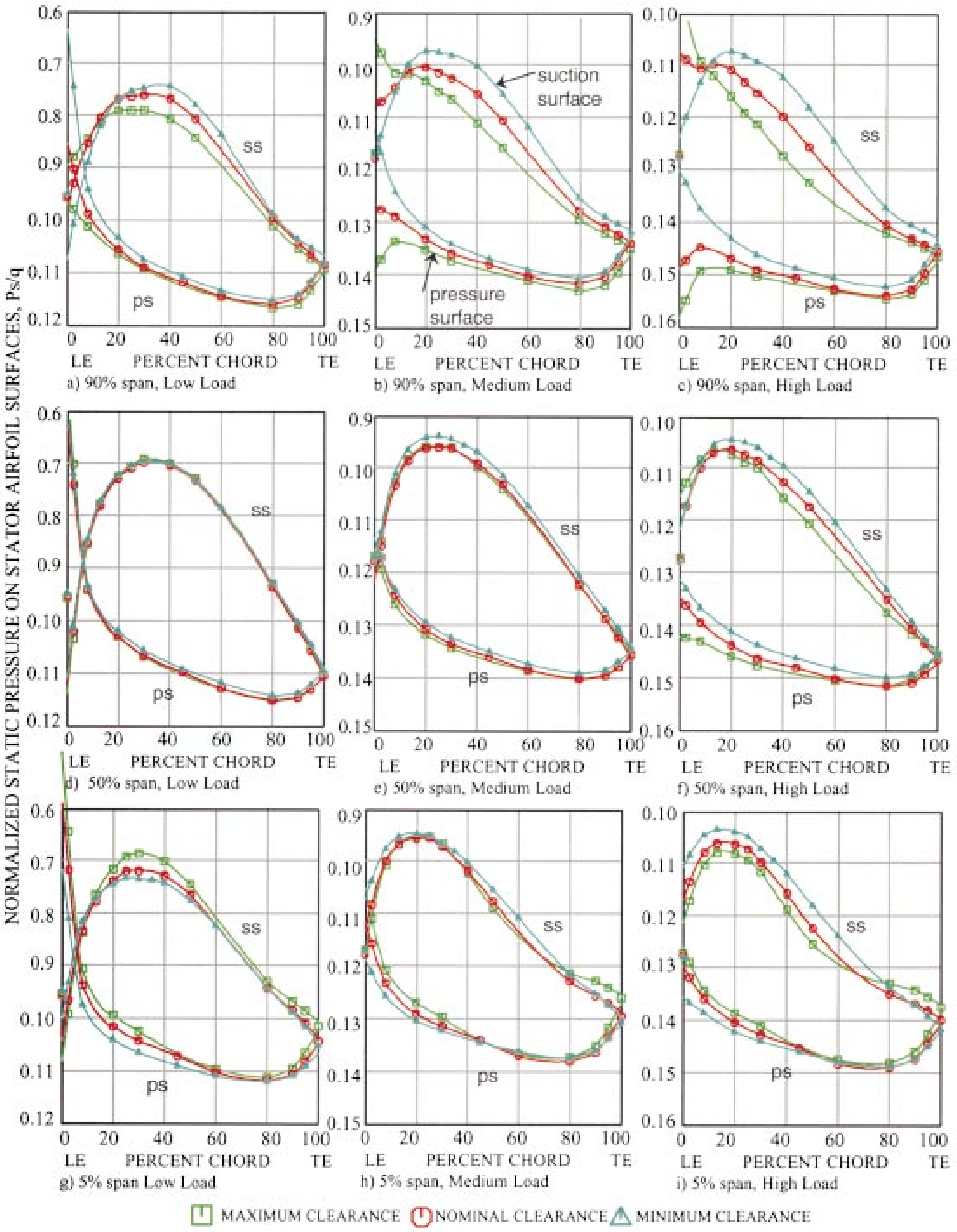

Fig. 11 Circumferential variation of stator airfoil loading for Compressor *A* showing the effects different levels of rotor tip clearance due to centerline offset. (*a–c*) 90 percent span; (*d–f*) 50 percent span; (*g–i*) 5 percent span. Low, medium, and high compressor loading were obtained at test points 1, 3, and 5, respectively, in Fig. 7.

compared to the tangential component. The maximum tangential force occurs near the minimum clearance and the minimum tangential force occurs near the maximum clearance, again confirming the correctness of Ehrich's hypothesis. Careful use of the sign convention in Fig. 13 leads us to conclude that in the region of negative forces shown as Zone 1 in Fig. 12, the net forces acting on the airfoils increase because the unsteady force, F_u, adds vectorially to the mean force, F_m. This occurs around the minimum clearance. In the region of positive forces shown as Zone 2 in Fig. 12, the net forces on the airfoils decrease as the unsteady force, F_u, oppose the mean force, F_m. This occurs around maximum clearance near bottom dead center. The net effect of the force distribution tends to drive the offset rotor shaft counter to the direction of rotation, i.e., it drives backward whirl.

The analysis of the data in Fig. 12 clearly shows that the whirl-inducing forces from centerline offset will tend to drive backward rotor whirl in compressors at this throttle setting.

The unsteady forces do not peak at the minimum clearance, but peak 40 deg from minimum tip clearance in the direction of rotation. This is due to fluid inertia effects as will be discussed in Part II of this paper.

6.2 Stator Vane Tangential Force. Stator surface pressures shown in Fig. 11 were integrated in the chordwise and span-

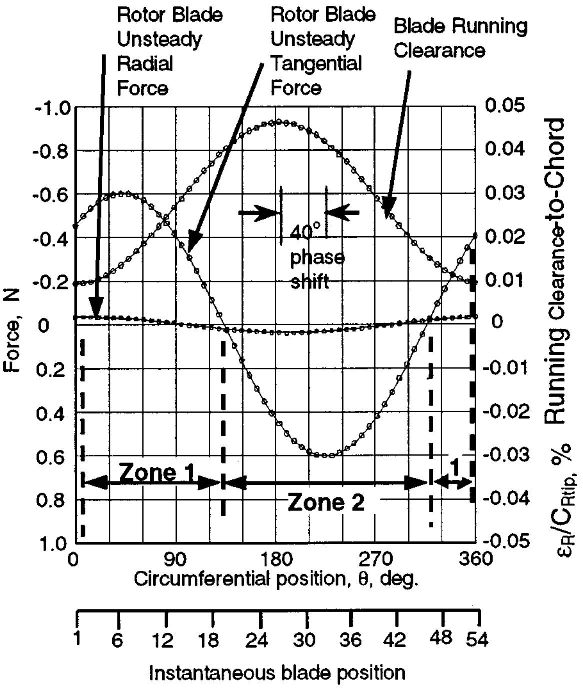

Fig. 12 Circumferential variation of the unsteady whirl inducing force components and running rotor tip clearance for the large centerline offset of LSRC Compressor *A*. Zone 1 is for net force increased and zone 2 for net force decreased. Data shown for Test Point 5 in Fig. 7; see Appendix B3a.

wise directions to obtain the aerodynamic forces. Tangential force component in the direction of rotor rotation was observed to vary around the circumference, in phase with the clearance variation. This force was largest in the region of minimum clearance and was smallest in the region of maximum clearance. This is similar to the force variation measured on the rotor blading.

6.3 The β Coefficient. We computed the cross-axis and direct stiffness forces, F_X and F_Y, for the two centerline offsets and the various values of compressor loading as discussed in Section 3.4. We then computed the cross-axis aerodynamic stiffness coefficient, K_{XY}. An example showing the cross-axis force versus offset is presented in Fig. 14 for Test Point 5 of Compressor A. The slope of this curve, K_{XY}, is linear to within a 0.225 variance. From that and the pertinent geometry and measured torque for the LSRC configuration, we computed the corresponding β coefficient using Eq. (1). The stiffness forces and resulting β coefficients are shown in Table 1. See Appendix B3c.

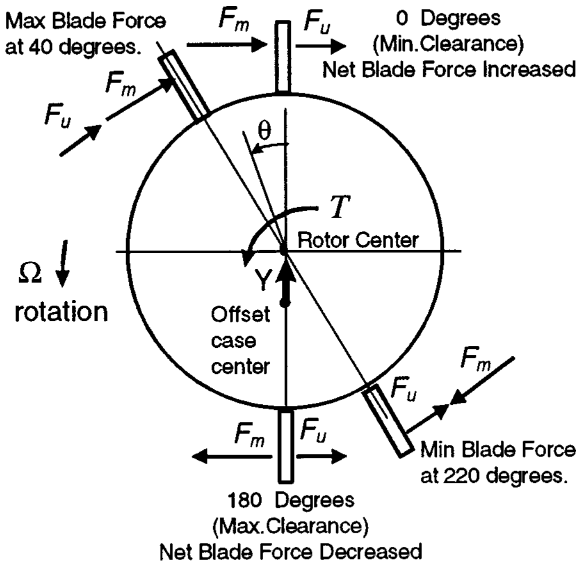

Fig. 13 Distribution of tangential blade force for LSRC Offset Rotor Test showing direction of mean and unsteady forces (F_m and F_u) at various circumferential positions; see Appendices B1 and B3a

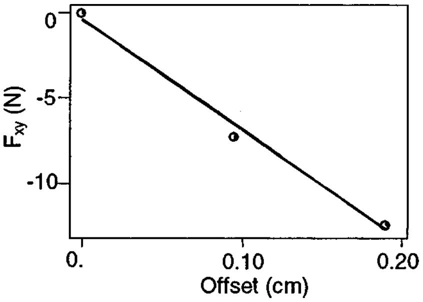

Fig. 14 Regression plot of cross-axis-force for high compressor loading test point 5 in Fig. 7

A curve-fit of the β coefficients from Table 1 is shown in Fig. 15 for Compressor A. Clearly the Thomas/Alford force drives backward rotor whirl over most of the compressor operating range, although some regions of near-zero and positive whirl-inducing forces are observed at high flow coefficients greater than 0.44.

7.0 Discussion

The analysis of the data presented in Part I of this paper clearly shows that the Thomas/Alford forces in axial-flow compressors

Table 1 Stiffness forces and the β coefficients for Compressor *A*: see Appendix B 3c

Operating Condition	Test Pt. In Fig. 7	0.1905 cm offset (0.075 inches)		0.0965 cm offset (0.038 inches)		Beta Coefficient
		F_X N/(lb)	F_Y N/(lb)	F_X N/(lb)	F_Y N/(lb)	
Low Loading	1	0.044 (0.01)	2.27 (0.51)	-0.71 (-0.16)	1.07 (0.24)	0.24
	2	-2.28 (-0.49)	4.36 (0.98)	-1.16 (-0.26)	2.63 (0.59)	-0.82
Peak Efficiency	3	-4.49 (-1.01)	5.87 (1.32)	-2.71 (-0.61)	3.34 (0.75)	-1.64
Design Point	4	-7.48 (-1.68)	7.08 (1.59)	-4.13 (-0.93)	4.36 (0.98)	-2.76
	5	-12.41 (-2.79)	9.65 (2.17)	-7.29 (-1.64)	5.69 (1.28)	-4.63
Peak Pressure - Near Stall	6	-16.51 (-3.71)	17.53 (3.94)	-9.61 (-2.16)	7.88 (1.77)	-6.58

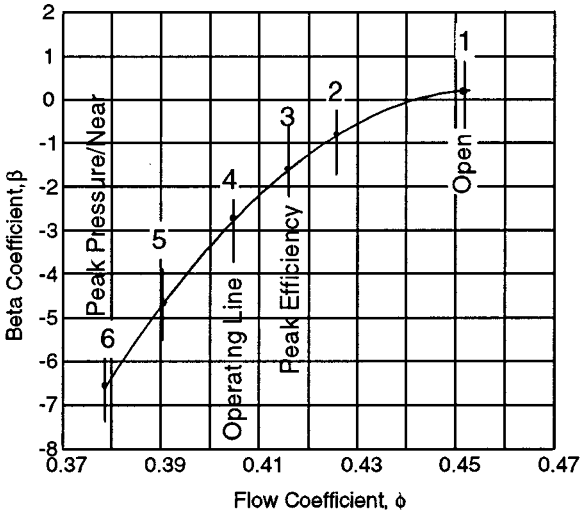

Fig. 15 Computed beta coefficients for the LSRC compressor *A* offset rotor test showing that unsteady forces promote backward whirl over most of the compressor operating range. Test Points 1–6 correspond to those in Fig. 7.

typical of modern design tend to drive backward whirl. In fact, for off-design operation at lower flows and high airfoil loading, the beta coefficients were strongly negative.

However, there are qualifications that go along with our findings. Backward whirl-inducing forces do not occur over all of the operating points of the compressor map, as also clearly shown by our data. At high-flow, low-loading situations, the Thomas/Alford forces were neutral or shown to drive forward whirl, although the magnitudes of the positive β coefficients were small.

In engine operation, the range of β coefficients in Fig. 15 can be encountered during operating line migrations from the steady state design point. Low operating line (high flow coefficient) situations for the HP compressor occur for commercial engine operation primarily during a rapid deceleration from high power. An example of this could be a throttle chop *following* thrust reverser deployment on landing. In this situation fuel flow drops abruptly, causing the pressure in the combustor and rear of the compressor to drop. The operating line then drops but the rotational speed cannot change instantaneously so the pumping (air flow) is high.

High operating line (low flow coefficient) situations for the HP compressor occur primarily during a rapid engine spool-up (acceleration). This can occur during take-off, application of reverse thrust on landing, a go-around on missed approach, and aircraft avoidance maneuvers. Fuel flow to the combustor is increased raising its temperature and back-pressuring the compressor. This causes the operating line to go up before the rotational speed can increase appropriately.

8.0 Conclusions

The following conclusions about whirl-inducing aerodynamic forces in compressors can be drawn from the experimental data of Part I:

The long-standing disparity in findings concerning the direction and magnitude of rotor whirl-inducing, aerodynamic forces in axial-flow compression systems used in modern turbomachinery has been definitively resolved. The Thomas/Alford force drives backward rotor whirl over most of the compressor operating range. This means that the β coefficients are mostly negative with some near-zero and small positive values (forward whirl) at high flow. Consequently, compressor whirl forces tend to promote whirl in the direction opposite to that of turbines over most of the operating range.

When the centerline of the rotor is displaced from the centerline of the casing, the *unsteady* loading on the rotor airfoils in the tighter clearance region increases and the *unsteady* loading on the rotor airfoils in the more-open clearance region decreases relative to the loading for nominal clearance.

The Ehrich model describing compressor whirl resulting from aerodynamic forces, as presented in Fig. 1(*c*), has been validated by the low-speed testing process. This important finding strongly suggests the model's correctness for use in guiding HP compressor designers.

The parallel compressor model has been validated for the offset tests, based on the analysis of the performance derivatives. This finding is important to the applicability of the analytical models in Part II.

The unsteady forces do not peak at the minimum clearance but peak 40 deg from minimum clearance in the direction of rotation for Compressor A. This is due to fluid inertia effects as will be discussed in Part II of this paper.

To date attention has been given only to the effects of rotor tip clearance. A new finding has shown that clearance variations in the hub region can also have a significant effect on the magnitude and direction of rotor whirl. This will be discussed in detail in Part II.

Large performance penalties in efficiency, pressure-rise capability and stall margin can occur if average and maximum clearances increase during rotor centerline displacement. Unsteady incidence angle variations around the circumference of as much as seven degrees were observed.

Acknowledgments

The authors wish to thank technicians Donald Menner and William Groll for building up and running the LSRC, engineers Scott Tripp and David Vu for overseeing the dynamic instrumentation and data gathering, and engineers Robert Maffeo, Steve Schrantz, and Don Beeson for developing the bidirectional curve fit routines used to resolve unsteady blade forces. The authors also thank GE Aircraft Engines for permission to publish this paper.

Appendix A

Tables 2–5 Giving Blading and Configuration Details

Table 2 Blading details for Compressors *A*, *B*, and *C* at midspan

	IGV			ROTOR			STATOR		
	A	B	C	A	B	C	A	B	C
Solidity	1.0	1.0	1.5	1.16	1.11	0.97	1.43	1.32	1.00
Aspect Ratio	1.36	1.36	1.5	1.20	1.25	1.83	1.34	1.45	2.05
Chord, cm	8.38	8.38	15.2	9.55	9.12	12.3	8.53	7.91	11.0
Chord, inch	3.3	3.3	6.0	3.76	3.59	4.86	3.36	3.114	4.33
Stagger, deg.	14.8	3.4	19.9	50.4	49.1	42.0	30.5	20.3	33.4
Camber, deg.	--	--	--	31.8	32.3	32.4	40.5	53.4	40.4
No. of Airfoils	53	53	40	54	54	32	74	74	37

Table 3 Values of clearances and offsets for Compressors *A*, *B*, and *C*

	Rotor Tip Clearance			Stator Shroud-Seal Clearance			Centerline Offset		
	ϵ_r cm	ϵ_r in	$\frac{\epsilon_r}{C_{rTIP}}$ %	ϵ_s cm	ϵ_s in	$\frac{\epsilon_s}{H}$ %	Y cm	Y in	$\frac{Y}{H}$,%
Compressor A									
A1. Baseline	0.155	0.061	1.63	0.089	0.035	0.8	0	0	0
A2. Nom R Open S	0.155	0.061	1.63	0.178	0.070	1.6	0	0	0
A3. Open R Nom S	0.320	0.126	3.35	0.089	0.035	0.8	0	0	0
A4. Open R Open S	0.320	0.126	3.35	0.178	0.070	1.6	0	0	0
A5. Small Offset									
Avg	0.279	0.110	2.92	0.178	0.070	1.6	0.0965	0.038	0.711
Min	0.198	0.078	2.07	0.081	0.032	0.7	0.0965	0.038	0.711
Max	0.351	0.138	3.67	0.274	0.108	2.4	0.0965	0.038	0.711
A6. Large Offset									
Avg	0.251	0.099	2.63	0.284	0.112	2.5	0.191	0.075	1.67
Min	0.056	0.022	0.59	0.094	0.037	0.8	0.191	0.075	1.67
Max	0.437	0.172	4.57	0.475	0.187	4.2	0.191	0.075	1.67
Compressor B									
B1. Baseline	0.160	0.063	1.75	0.089	0.035	0.8	0	0	0
B2. Nom R Open S	0.160	0.063	1.75	0.178	0.070	1.6	0	0	0
B3. Open R Nom S	0.320	0.126	3.51	0.089	0.035	0.8	0	0	0
Compressor C									
C1. Baseline(*)	0.323	0.127	2.61	0.320	0.126	1.40	0	0	0
C2.Open R Nom S(*)	0.625	0.246	5.06	0.320	0.126	1.40	0	0	0

(*) cantilevered stator

Table 4 Rotor blade kulite locations

Percent Chord on Suction Surface										% Span	Percent Chord on Pressure Surface						
4	12	18	24	30	40	50	60	72	87	96.2		12	18	24	30	50	80
	12	18			40					92.2		12	18		40		
	11	18		30				72		82.0		11	18		30		
5	13		21	30	40	55		72	87	51.2	7.5	13		21	30	50	80
5	12			30				72		20.5	6	12					
4	12		21	30	40	50	60	72	87	10.2	5	12		21	30	50	80

Table 5 Stator vane pressure tap locations

Five Rows – at the following percent immersion from casing:
10, 20, 50, 80, and 95

Tap Locations in Each Row													
Percent Chord on Stator Suction Surface													
2.5	8	13	20	25	30	35	40	50	60	70	80	90	96
Percent Chord on Stator Suction Surface													
2.5	8		20		30	45	60	70		80	90	95	

Appendix B

Sign Convention and Coordinate Systems

B1 Direction of the Forces. Regarding F_M and F_U in Figs. 1 and 13, the arrows are drawn with the arrow head pointing in the direction that the forces act in the compressor and the turbine. For example in Fig. 2(*b*) at the top, the arrows show that the unsteady force F_U will reduce the mean force F_M as the arrows oppose each other. But at the top in Fig. 2(*c*), the arrows show that the unsteady force F_U will increase the mean force F_M as the arrows are in the same direction. F_M and F_U must be considered as a vector sum, as stated in the third paragraph of Section 6.1.

B2 The Sign Convention. Following rotordynamic convention, we define forward and backward whirl relative to the direction of rotor rotation. This has a subtle aspect when looking at plus and minus directions in Cartesian coordinates. For engines rotating counterclockwise forward looking aft, positive whirl forces are those which will drive a whirling rotor counterclockwise. In Figs. 3 and 5, we show the force F_X pointing from the origin to the LEFT as a positive force because it will drive the displaced centerline counterclockwise about the undisplaced centerline. To the casual observer, positive in Cartesian coordinates would be from the origin to the RIGHT.

B3 The Coordinate Systems. Two coordinate systems are used, as described by Figs. 3 and 5. All of the forces are defined in the Nomenclature.

a The (local) coordinate system fixed to the blades. The tangential and radial forces that act on the rotor blades, F_T and F_R, are shown schematically in Fig. 5 in a coordinate system fixed to the blades. The measured *unsteady* tangential and radial forces shown in Fig. 12 are in this coordinate system. Note that F_T (rotor blade unsteady tangential force) in Fig. 12 is much larger than F_R (rotor blade unsteady radial force). These unsteady forces, F_T and F_R, are resolved into the total unsteady force, F_U, which is then added vectorially to the mean force, F_M, to get the total force on the airfoil as shown schematically in Fig. 13.

b The (global) coordinate system fixed to the rotor centerline The net unbalanced forces acting perpendicular and parallel to the shaft deflection, F_X and F_Y in Fig. 5, are in a coordinate system fixed to and acting about the rotor centerline as seen in Fig. 3. In this global system, F_X is the cross-axis stiffness force that drives rotor whirl about the undisplaced centerline. F_Y is the direct stiffness force.

The airfoils in the blade-fixed coordinate system rotate about this global coordinate system, with the angle of rotation, theta, shown in Figs. 5 and 13 as positive in the counterclockwise direction.

c Transformation from local to global coordinate system Referring to Fig. 5, the transformation from the local to global coordinate system for the ith rotor blade is:

Global (rotor–disk) coordinate system
Local blade-fixed coordinate system

$$\begin{Bmatrix} F_X \\ F_Y \end{Bmatrix} = \begin{bmatrix} \cos(\theta) & \sin(\theta) \\ -\sin(\theta) & \cos(\theta) \end{bmatrix}_i \begin{Bmatrix} F_T \\ F_R \end{Bmatrix}_i$$

Summing the forces over all of the rotor blades is done as shown below.

$$F_X = \sum_{i=1}^{N_B} F_{Xi} \quad F_Y = \sum_{i=1}^{N_B} F_{Yi}$$

Note that the large unsteady tangential force, F_T, in Fig. 12 will contribute to *both* F_X and F_Y in Table 1 so that the values of F_X and F_Y can be of nearly the same magnitude. The key is that F_X in Table 1 is *negative in sign*, which drives backward whirl over most of the operating range as shown by the negative beta coefficient.

Nomenclature

A = annulus area, m^2
C_{Rtip} = chord length at tip, cm
D_p = mean blade diameter, m
F_T, F_R, F_m = tangential, radial, and mean force on rotor blades, N
F_X = net unbalanced force perpendicular to rotor deflection, N
F_Y = net unbalanced force parallel to rotor deflection N
F_U = unsteady blade force, N
H = blade height cm
K_{XY} = cross-coupled stiffness coefficient, N/m
$k=\Phi/\sqrt{\Psi'}$ = throttle coefficient
$\dot{m}$ = mass flow
P_1, T_1 = compressor inlet pressure and temperature, kPa, °C
P_S = static pressure acting on blade surface, kPa
q = $1/2\rho_{\mathrm{ref}}U_t^2$, dynamic pressure for normalizing pressures, kPa
R_c = casing radius, cm
R_H = hub radius cm
R = radial coordinate
T = stage torque, N-m
$T_{\tan}$ = blade tangential direction
TM = $[(k_D/k_S)-1]\times 100$, throttle margin, percent
U = rotor wheel speed, m/s
X = coordinate orthogonal to Y
Y = vertical coordinate in direction of deflection
$+Y$ = rotor deflection, cm
Z = axial coordinate
β = normalized cross-coupled stiffness coefficient (the ‘‘Thomas/Alford Coefficient’’)
ε_R = rotor tip clearance, cm
ε_S = shroud seal clearance, cm
η = $\Psi'/\Psi\times 100$ percent, torque efficiency, points
$\Phi=\dot{m}/\overline{\rho}AU,_t$ = flow coefficient
$\Psi=T/[(1/2)\overline{\rho}U_t^2\Phi R_t A]$ = work coefficient
$\Psi'=C_pT_1/(1/2)U_t^2[(\Delta P/p_1+1)^{(\gamma-1)/\gamma}-1]$ = pressure coefficient
θ = blade azimuth angle, rad
ρ = density
Ω = spin speed of the rotor, rad/s

Superscripts

$-$ = averaged value

Subscripts

t = rotor tip
D = design point
s = stall point

References

[1] Thomas, H. J., 1958, ‘‘Unstable Natural Vibration of Turbine Rotors Induced by the Clearance Flow in Glands and Blading,’’ Bull. de l’A.I.M., **71**, No. 11/12, pp. 1039–1063.

[2] Alford, J., 1965, ‘‘Protecting Turbomachinery From Self-Excited Rotor Whirl,’’ ASME J. Eng. Power, **8**, pp. 333–344.

[3] Kofskey, M. G., and Nusbaum, W. J., 1968, ‘‘Performance Evaluation of a Two Stage Axial Flow Turbine for Two Values of Tip Clearance,’’ NASA TN D4388.

[4] Urlichs, K., 1975, ‘‘Clearance Flow-Generated Transverse Forces at the Rotors of Thermal Turbomachines,’’ Dissertation, Technical University of Munich (English translation in NASA TM-77292, Oct. 1983).

[5] Urlichs, K., 1977, ‘‘Leakage Flow in Thermal Turbo-Machines as the Origin of Vibration-Exciting Lateral Forces,’’ NASA TT F-17409, Mar.

[6] Wohlrab, R., 1975, ‘‘Experimental Determination of Gap Flow-Conditioned Force at Turbine Stages and Their Effect on Running Stability of Simple Rotors,’’ Dissertation, Technical University of Munich (English translation in NASA TM-77293, Oct. 1983).

[7] Martinez-Sanchez, S., and Jaroux, B., 1991, ‘‘Turbine Blade Tip and Seal Clearance Excitation Forces,’’ M.I.T. Gas Turbine Laboratory, Cambridge, MA (Phase III Report on Contract No. NAS8-35018).

[8] Ehrich, F. F., 1993, ‘‘Rotor Whirl Forces Induced by the Tip Clearance Effect in Axial Flow Compressors,’’ ASME J. Vibr. Acoust., **115**, pp. 509–515.

[9] Vance, J. M., and Laudadio, F. J., 1994, ‘‘Experimental Measurement of Alford’s Force in Axial Flow Turbomachinery,’’ ASME J. Eng. Gas Turbines Power, **106**, p. 585.

[10] Colding-Jorgensen, J., 1992, ‘‘Prediction of Rotordynamic Destabilizing Forces in Axial Flow Compressor,’’ ASME J. Fluids Eng., **114**, p. 621.

[11] Yan, L., Hong, J., Li, Q., Zhu, Z., and Zhao, Z., 1995, ‘‘Blade Tip Destabilizing Force and Instability Analyses for Axial Rotors of Compressor,’’ Beijing, University of Aeronautics and Astronautics, Beijing, China (AIAA Paper No. A95-40315).

[12] Akin, J. T., Fehr, V. S. and Evans, D. L., 1988, ‘‘Analysis and Solution of the Rotor Instability Problem in the Advanced Model P111+ Engine,’’ Paper No. AIAA-88-3166.

[13] Wisler, D. C., 1981, ‘‘Compressor Exit Stage Study Volume IV—Data and Performance Report for the Best Stage,’’ NASA CR-165357.

[14] Wisler, D. C., 1985, ‘‘Loss Reduction in Axial-Flow Compressors Through Low-Speed Model Testing,’’ ASME J. Eng. Gas Turbines Power, **107**, pp. 354–363.

[15] Wisler, D. C., Halstead, D. E., and Beacher, B. F. 1999, ‘‘Improving Compressor and Turbine Performance Through Cost Effective Low-Speed Testing,’’ ISABE99-7073, *Proc. 14th International Symposium on Air Breathing Engines*, Sept., Florence, Italy.

[16] Doebelin, E. O., 1975, *Measurement System*, McGraw-Hill, pp. 398–401.

[17] Wellborn, S., and Okiishi, T., 1999, ‘‘Influence of Shrouded Stator Cavity Flows on Multistage Compressor Performance,’’ ASME J. Turbomach., **121**, pp. 486–498.

2000 Turbomachinery Committee and Structures & Dynamics Committee Best Paper Award

Unsteady Flow and Whirl-Inducing Forces in Axial-Flow Compressors: Part II—Analysis

F. F. Ehrich
Z. S. Spakovszky
M. Martinez-Sanchez
Massachusetts Institute of Technology,
Cambridge, MA 02139

S. J. Song
Seoul National University,
Seoul, Korea

D. C. Wisler
A. F. Storace
H.-W. Shin
B. F. Beacher
GE Aircraft Engines,
Cincinnati, OH 45215

An experimental and theoretical investigation was conducted to evaluate the effects seen in axial-flow compressors when the centerline of the rotor becomes displaced from the centerline of the static structure of the engine, thus creating circumferentially nonuniform rotor-tip clearances. This displacement produces unsteady flow and creates a system of destabilizing forces, which contribute significantly to rotor whirl instability in turbomachinery. These forces were first identified by Thomas (1958. Bull. AIM, **71***, No. 11/12, pp. 1039–1063.) for turbines and by Alford (1965. J. Eng. Power, Oct., pp. 333–334) for jet engines. In Part I, the results from an experimental investigation of these phenomena were presented. In this Part II, three analytic models were used to predict both the magnitude and direction of the Thomas/Alford force in its normalized form, known as the β coefficient, and the unsteady effects for the compressors tested in Part I. In addition, the effects of a whirling shaft were simulated to evaluate differences between a rotor with static offset and an actual whirling eccentric rotor. The models were also used to assess the influence of the nonaxisymmetric static pressure distribution on the rotor spool, which was not measured in the experiment. The models evaluated were (1) the two-sector parallel compressor (2SPC) model, (2) the infinite-segment-parallel-compressor (ISPC) model, and (3) the two-coupled actuator disk (2CAD) model. The results of these analyses were found to be in agreement with the experimental data in both sign and trend. Thus, the validated models provide a general means to predict the aerodynamic destabilizing forces for axial flow compressors in turbine engines. These tools have the potential to improve the design of rotordynamically stable turbomachinery.*
[DOI: 10.1115/1.1370165]

1 Introduction

It is critically important to the operation of high-bypass ratio, turbofan engines and other high-speed, highly loaded turbomachinery that their rotor systems be designed to preclude potentially destructive rotordynamic instability. Instability is engendered when whirl-inducing tangential force systems are induced by radial deflection of the rotor, i.e., cross-coupled forces, with a magnitude that overwhelms stabilizing damping forces. Typical mechanisms for inducing such forces are those associated with internal damping of the rotor (hysteretic whirl); with fluid film bearings; with fluid trapped in internal cylindrical cavities in rotors; and, as addressed in this paper, with the system of aerodynamic forces induced by the nonaxisymmetric rotor and stator tip clearances inherent in rotor displacement. It is therefore of major importance in the design process to be able to determine accurately the magnitude and direction of these whirl-inducing forces.

The aerodynamic forces induced by the nonaxisymmetric rotor and stator tip clearances inherent in rotor displacement were first identified by Thomas [1] for turbines and by Alford [2] for jet engines for both compressors and turbines. Vance and Laudadio [3] found that the Thomas/Alford force is rotor-speed dependent and mostly positive, except for some special combinations of rotor speed and stage torque where the direction of the force was reversed. Colding-Jorgensen [4] found the same generality for the shape and slope of the relationship of β coefficient versus flow coefficient as later reported by Ehrich [5], but the Colding-Jorgensen results suggested a more positive level of the parameter than the negative levels reported in Ehrich's work. Ehrich [5] further showed that the experimental data of Vance and Laudadio [3] implied that, for certain values of torque and speed in their low-speed blower tests, the destabilizing forces tend to drive backward whirl. Other evidence was also accumulating in the theoretical and experimental results of Yan et al. [6] to indicate negative β coefficients for compressors.

A key limitation to the application of the new insights into the destabilizing forces in axial-flow compressors was the lack of accurate, systematic, experimental data that could be used to validate the available analytic procedures. Part I of this two-part paper presents experimental results from several compressor configurations that accurately model compressors in commercial airline service. The tests, conducted in the GE Aircraft Engine's low-speed research compressor (LSRC), used rotor centerline offset to simulate the amplitude of rotor whirl and provide the opportunity to measure the major destabilizing forces that are induced.

2 Objectives

There were two major objectives of this overall work. The first was to compare the available analytic models with the experimental results to validate their potential incorporation into design systems. The second was to assess the relative importance of two effects that were not evaluated in the experimental program—the effects of a whirling shaft, which was not simulated by the static

---

Contributed by the International Gas Turbine Institute and presented at the 45th International Gas Turbine and Aeroengine Congress and Exhibiton, Munich, Germany, May 8–11, 2000. Manuscript received by the the International Gas Turbine Institute February 2000. Paper No. 2000-GT-566. Review Chair: D. Ballal.

offset used in the experiment; and the influence of the nonaxisymmetric static pressure distribution on the rotor spool, which was not measured in the experiment.

3 Description of the Three Analysis Methods

The predictions of three analytic systems were compared in detail to the experimental results that were obtained in Part I. The three methods vary from one another in several ways: (a) in their dependence on experimental characterization of the stage; (b) in their flexibility in dealing with configuration detail like shrouded blade rows; (c) in their accuracy of prediction of the β coefficient compared to the experimental data; and (d) in their capability to accommodate more complex phenomena like the effects of nonaxisymmetric spool surface pressure and of the whirling rotor on the β coefficient.

3.1 Two-Sector-Parallel-Compressor Model. Ehrich [5] developed a procedure, referred to as the two-sector-parallel-compressor model (2SPC), which computes the β coefficient based on parallel compressor theory. The 2SPC model is a one-dimensional system that approximates the continuous circumferential variation of clearance by hypothesizing two compressors operating in parallel, one representing a 180 deg sector with an axisymmetric clearance equal to the minimum local clearance of the deflected rotor; and the other compressor representing the other 180 deg sector with an axisymmetric clearance equal to the maximum local clearance of the deflected rotor. The analysis requires only the stage performance characteristics at two values of axisymmetric tip and/or shroud seal clearance. The model is not able to offer any data or insight on other effects such as actual whirling of the rotor or the effect of nonaxisymmetric pressure distribution on the rotor spool.

3.2 Infinite-Segment-Parallel-Compressor Model. More recently, Spakovszky [7] developed a new procedure, referred to here as the infinite-segment-parallel-compressor model (ISPC), which consists of two parts: (a) an unsteady, two-dimensional, compressor tip clearance model for stall inception, which represents the flow field through the compressor, and (b) a rotordynamic force model. The rotordynamic model uses the unsteady momentum equation, which is applied locally to one blade passage in the circumferential direction. An unsteady control volume analysis is conducted in a frame locked to the rotor and applied locally to each blade passage to obtain the local tangential blade force. The resulting force in the rotor frame, which is obtained by integrating the distributed tangential force, is transformed back to the absolute frame. One advantage of this approach over that of the 2SPC model is that any unsteady flow regime (whirling shaft, rotating stall) can be evaluated. The ISPC approach can be extended to deal with the effects of unshrouded stator tip clearances and stator shroud seal leakage flow, but the results were not available for this paper.

The inputs to the model are the compressor geometry, an axisymmetric compressor characteristic, and the sensitivity of the compressor characteristic to changes in axisymmetric rotor tip clearance, which are matched to data.

3.3 Two-Coupled-Actuator-Disk Model. Song and Cho [8] have developed a procedure, referred to as the two-coupled-actuator-disk model (2CAD) following the same approach used for turbines by Song and Martinez-Sanchez [9]. The 2CAD model is quasi-three-dimensional and consists of two coupled actuator-disk analyses: one at the compressor blade scale and another at the compressor radius scale. The analyses assume inviscid, incompressible flow. They are essentially mean-line analyses, and the blading is assumed to be two dimensional. The blade scale model is an axisymmetric, meridional plane analysis, and thus captures the radial redistribution of the flow due to the existence of rotor and stator tip clearances. Upon passing through a blade row, the initially radial-uniform upstream flow is assumed to split into two streams, one stream associated with the tip clearance and the remainder associated with the blade. Thus, the model can be used to examine radial flow redistribution as well as performance degradation due to rotor and stator tip clearances.

In the radius-scale analysis, the effects of nonaxisymmetric rotor and stator tip clearances can be examined. The continuity equation and the axial and tangential momentum equations are used to analyze upstream and downstream flows, and the results from the blade scale model are used to connect upstream and downstream flows. The nonaxisymmetric flow response or azimuthal flow redistribution effect is obtained through a small perturbation harmonic analysis about the axisymmetric mean, which is provided by the blade scale analysis.

Inputs required for the models are the blade angles, pitch/chord ratio, and mean rotor and stator tip clearances. Thus, no empirical inputs are needed, and the analysis is strictly based on first principles. Outputs from the model include the axisymmetric mean and nonaxisymmetric perturbations in the flow field (i.e., velocity and pressure). The nonuniform rotor blade loading effects and the effects of nonaxisymmetric static pressure on the rotor hub can be examined from the perturbations.

Assessment of the Ability of the Three Models to Compute the β Coefficient

4.1 Identification of the Roles of the Rotor Tip Clearance and the Stator Shroud Seal Effects. The first calculations of the β coefficient were done using Ehrich's 2SPC parallel compressor model in the manner reported previously [5]. The axisymmetric experimental data from Fig. 6 in Part I were used to construct a parallel compressor with one-half of the compressor operating at the nominal rotor blade tip clearance and nominal stator seal clearance, and the other half operating at open rotor blade tip clearance and nominal stator seal clearance. The results from the 2SPC model gave values of the β coefficient that were about one-half of those computed from the experimental data and suggested that a major component of the dynamic force on the rotor blade had not been identified in the analysis.

To help understand this situation, we looked at a key finding from the analysis of the experimental results—a contour map of the dynamic differential pressure across the blade surface as it passed through the point of peak dynamic load for a very highly loaded operating point as shown in Fig. 1. That perspective revealed *two* intense concentrations of dynamic activity: one in the

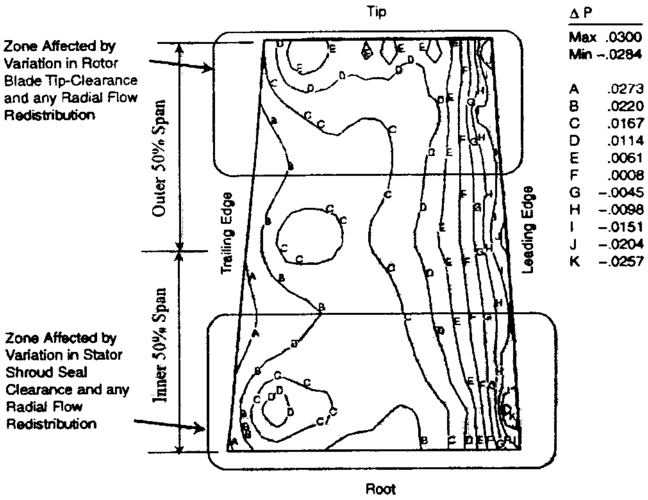

Fig. 1 Measured unsteady static pressure difference (pressure side−suction side) on the surface of the rotor blade at the minimum clearance condition for the maximum centerline offset: LSRC Compressor A

outer one-third span of the blade surface and the other in the *inner* one-third span. It was hypothesized (and ultimately verified in the following analyses) that the activity in the outer one-third span resulted from the variation in *rotor-blade* tip clearance induced by the rotor offset as seen by a typical rotor blade in the course of its rotation. The additional zone of intense activity in the inner one-third span was comparable in magnitude to the activity near the tip and was inferred to result from the variation in flow leakage from the *stator-shroud* seal clearance as seen by the rotating blade. Although the effect of stator shroud-seal leakage on turbomachinery aerodynamic performance has been documented [10,11] the contribution of this phenomenon to rotor whirl instabilities had not been previously recognized in the analysis of experimental data or accommodated in analytic modeling of the problem. It became apparent that the influence of the flow leakage from the seal tooth clearance in the adjacent stator rows (and perhaps radial redistribution of flow) had a substantial impact on the dynamic forces on a rotor.

To identify the relative contributions of each of the two effects, we reduced the experimental unsteady-pressure data in terms of two separate components.

(*a*) A computation of the component of the β coefficient involving integration of the dynamic pressures over the outer 50 percent span of the rotor blade, representative of the cross-coupled forces derived from the variation of rotor-blade tip clearance seen by the rotating blade.

(*b*) A computation of the component of the β coefficient involving integration of the dynamic pressures over the inner 50 percent span of the rotor blade, representative of the cross-coupled forces derived from the variation of stator-shroud seal tooth clearance seen by the rotating blade.

The total value of the experimental β coefficient was then taken as the sum of these two contributions. It represented the cross-coupled forces derived from the variation of both the rotor-blade and stator-shroud seal clearances seen by the rotating blade. The two components of the β coefficient computed above and their sum are presented in Fig. 2.

With this compartmentalization of the individual effects, it was then possible to compare the experimental results with those obtained from three different analytic models.

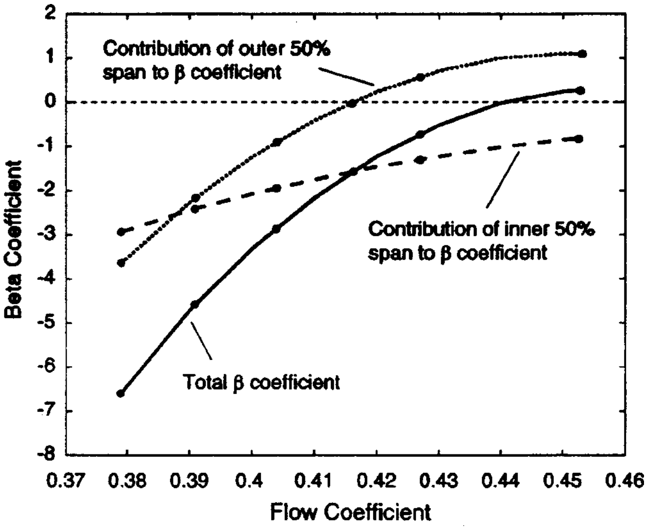

Fig. 2 Relative contributions to the total β coefficient obtained from the experimental data for inner 50 percent and outer 50 percent spans compared to the total β coefficient: LSRC Compressor A

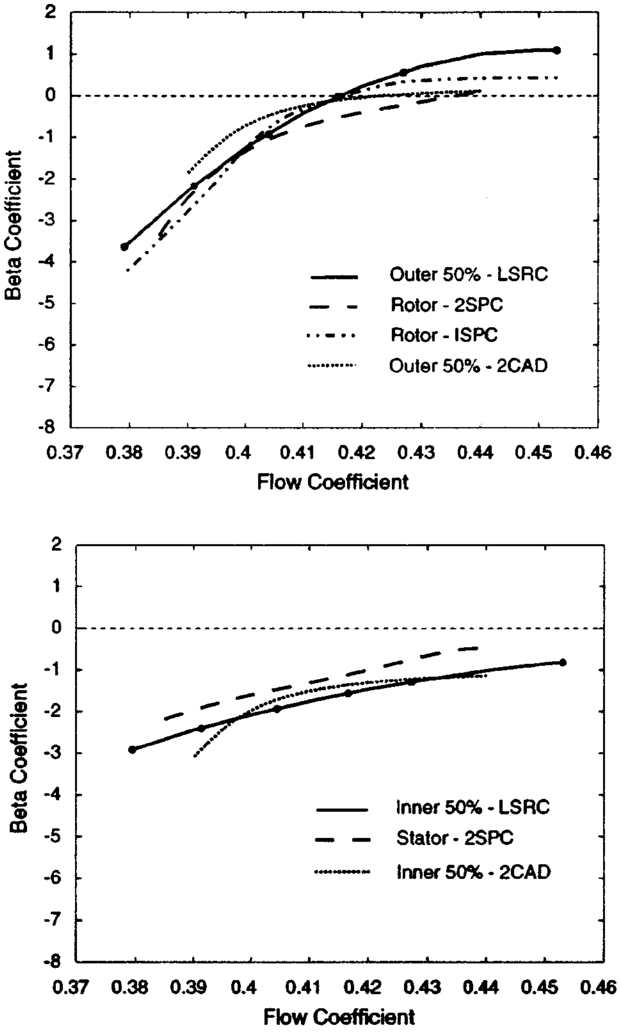

Fig. 3 Alford β coefficient for LSRC centerline offset of Compressor A. (*a*) Pressure integration over outer 50 percent span compared with analytic models of rotor-blade tip clearance effect. (*b*) Pressure integration over inner 50 percent span compared with analytic models of stator-shroud seal clearance effect.

4.2 Calculation of the β Coefficient Using the Three Models

Two-Sector-Parallel-Compressor Model. The 2SPC analytic model was exercised to produce an estimate of the two β coefficients implicit in Compressor A (described in Part I) in the following two-step process.

First, the β coefficient associated with the variation of rotor-blade tip clearance was computed from two of the sets of LSRC data (Fig. 6 of Part I): one set at nominal rotor-blade tip clearance and nominal stator-seal clearance and the other set at open rotor-blade tip clearance and nominal stator-seal clearance. These 2SPC analytic results are compared to offset rotor experimental data integrated over the outer 50 percent span in Fig. 3(*a*). The model predicts the β coefficient to an accuracy of 0.78, with a confidence level of 95 percent.

Secondly, the β coefficient associated with the variation of stator shroud seal clearance was also computed from two of the sets of LSRC data (Fig. 6 of Part I): one set at nominal rotor-blade tip clearance and nominal stator-seal clearance and the other set at nominal rotor-blade tip clearance and open stator-seal clearance. These 2SPC analytic results are compared to offset rotor experimental data integrated over the inner 50 percent span in Fig. 3(*b*). The model predicts the β coefficient to an accuracy of 0.51, with a confidence level of 95 percent.

Figure 4 shows the *sum* of these two effects derived from the 2SPC model compared to the offset rotor experimental data integrated over the entire 100 percent span of the rotor blade. The analytic model results agree precisely in form and yield an accuracy of 0.62 (with a confidence level of 95 percent), thus validating the 2SPC model for this general type of compressor blading.

Infinite-Segment-Parallel-Compressor Model. The ISPC compressor model was used to assess the effect of rotor-blade tip clearance on Compressor A performance. The flow field and compressor performance were computed for a steady shaft offset of 0.9 percent tip clearance to chord and different throttle settings. The performance predictions by the ISPC model and the measured mean operating points are shown in Fig. 5 compared to the experimental data. In addition the locus of operating points around the circumference is marked for one operating point by the lightly dashed line. Although only the sensitivity of the compressor characteristic to changes in axisymmetric rotor tip clearance is used in the model, the average performance predictions match the offset data quite well.

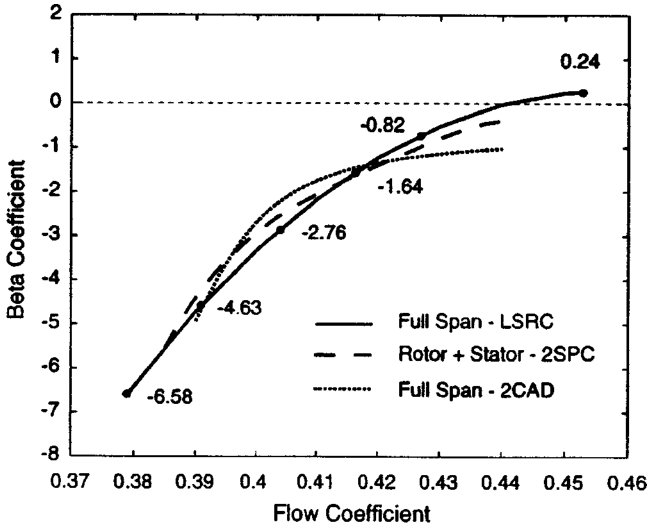

Fig. 4 β coefficient for LSRC centerline offset of Compressor A with pressure integration over entire rotor span compared with analytic models of the sum of rotor-tip and stator-shroud seal clearance effects

These results in Fig. 5 give confidence in using this flow field to predict the forces on the rotor. The estimate of the β coefficient from the ISPC model for the effect of rotor-blade tip clearance is shown in Fig. 3(*a*) compared to the results derived from the LSRC centerline offset experiment for Compressor A. The model predicts the β coefficient to an accuracy of 0.47, with a confidence level of 95 percent.

Two-Coupled-Actuator-Disk Model. The 2CAD model was used to predict the rotor blade loading with both rotor and stator clearances. The resultant β coefficient for the outer 50 percent rotor blade span is plotted versus flow coefficient in Fig. 3(*a*), and the resultant β coefficient for the inner 50 percent rotor blade span is plotted in Fig. 3(*b*). The model predictions yield an accuracy of 1.08 and 0.39 respectively, with a confidence level of 95 percent. Finally, the combined effects are shown in Fig. 4. The results reflect an accuracy of 1.12 with a confidence level of 95 percent. The 2CAD model assumes an unshrouded stator with a tip clearance, when, in fact, the LSRC has a single-tooth labyrinth seal on the shrouded stator tip. Nevertheless, the agreement between the 2CAD prediction and the experimental data is remarkable. Even though it might be fortuitous, the result is quite creditable considering that, as distinct from the 2SPC and ISPC models, no experimental stage characteristics or sensitivities were used in its generation.

4.3 Use of the 2SPC Model to Analyze other Compressor Configurations. With the validation of the 2SPC method by the assessment shown in Sec. 4.2, it appeared to be justified to apply the analysis tool to other axial-flow compressors for which data were available. As shown in Fig. 9 of Part I of this paper, stage performance for Compressor B (typical of modern designs having high hub/tip ratio, low aspect ratio, high-solidity blading, and shrouded stators) and Compressor C (with cantilevered stators and blading with lower hub-tip ratios and higher aspect ratios) was available from LSRC models similar to that shown for Compressor A in Fig. 6 of Part I of this paper. Both axial-flow compressors are in actual commercial airline service. Performance was in the form of overall stage-average pressure characteristics measured at two different values of both axisymmetric rotor tip clearance and stator shroud-seal clearance for Compressor B and two different

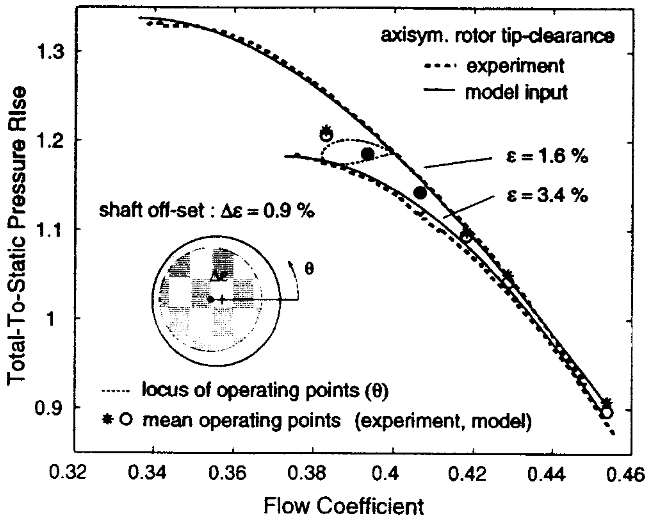

Fig. 5 Compressor A performance predictions by the ISPC model compared with experimental performance data of the LSRC

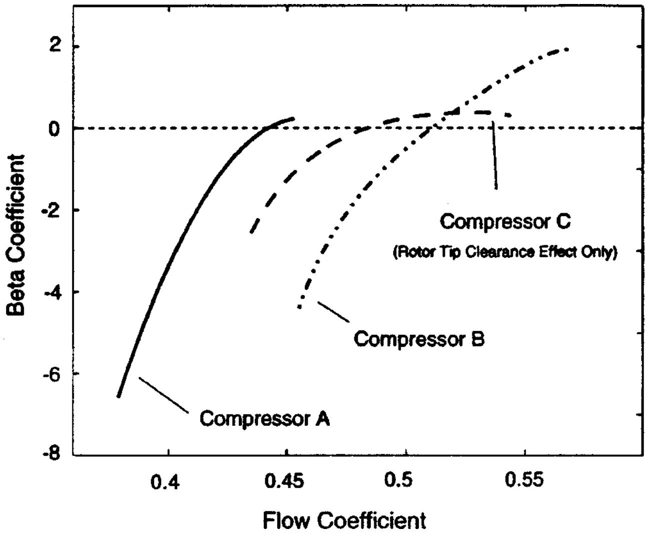

Fig. 6 β coefficient for LSRC Compressors A, B, and C using the 2SPC method, reflecting rotor and stator tip clearance changes values of rotor tip clearance for Compressor C. The results for Compressors B and C are shown in Fig. 6 compared with the results obtained for Compressor A. They suggest that the trends, magnitude, and sign of the predicted values of the β coefficients conform to the generality derived from the experiments for Compressor A but that detailed analysis is required for each compressor to accommodate its specific design features.

5 Discussion of Important Additional Issues

5.1 Phase Shift between the Locations of Minimum Clearance and Maximum Tangential Force. As shown in Fig. 12 of Part I of this paper, experimental LSRC measurements for the maximum centerline offset of Compressor A operating at high loading indicate a significant phase difference of about 40 deg in the peak of the dynamic force variation relative to the vector of the rotor displacement. That is, the peak dynamic force on a given blade was not developed at the same angular location where the blade was experiencing the minimum tip gap. Both the ISPC and the 2CAD models were used to predict the dynamic force distribution for a steady shaft offset. The modeling results showed the same trends in blade loading distribution as observed in the experiment. The ISPC model and the 2CAD model predict a phase lag of 26 and 28 deg, respectively, compared to the experimental value of 40 deg. A detailed analysis using the ISPC model revealed that the flow field lags the clearance distribution due to fluid inertia in the ducts and the blade rows, which gives a shift in the tangential blade loading distribution with respect to the tip-clearance asymmetry. The reasons for this are discussed briefly using the ISPC model.

First let us assume that the family of axisymmetric tip clearance compressor characteristics has no curvature and that unsteady losses and flow inertia effects in the blade rows and ducts are neglected. In this case the flow instantaneously responds to the distortion induced by the asymmetric tip clearance. The pressure rise and flow coefficient variations are then purely sinusoidal and 180 deg out of phase with respect to the tip clearance distribution. Regions with tight tip clearance yield high pressure rise, less blockage, and therefore a higher flow coefficient. The opposite holds for regions of large tip clearance.

Now let us consider the family of compressor characteristics shown in Fig. 5 and assume that unsteady losses and unsteady flow inertia effects are present. The compressor pressure rise distribution around the annulus is now distorted due to curvature of the compressor characteristics (see lightly dashed line in Fig. 5). Part of the compressor pressure rise is now devoted to accelerating the fluid in the blade row passages. The flow coefficient variation lags the tip clearance distribution due to the fluid inertia. The combination of a simplified tangential momentum analysis and kinematic relations reveals that, to first order, the variation in tangential blade loading is proportional to the variation in flow coefficient. Hence the tangential blade loading is predicted to lag the tip clearance distribution as is observed in the experiment and shown in Fig. 12 of Part I of this paper. A more detailed discussion is given in [7].

In other words, there is a finite amount of time necessary for the circulation around the rotor tip to be completely reestablished in response to the change in clearance. This time is associated with that necessary for the fluid to transverse the axial length of the rotor. However, since the tip clearance is continually changing, this is a dynamic process.

Unlike the ISPC model, the fluid inertia in the blade passage is not explicitly modeled in the 2CAD approach. Instead, the 2CAD model looks at the global flow behavior as it approaches the compressor with nonaxisymmetric flow redistribution. The phase lag of the blade loading nonuniformity relative to the tip clearance variation is mainly due to the higher mass flux near the smaller gap region. In summary the effect of flow redistribution due to inertial flow effects induces a significant phase shift (on the order of 40 deg) of the dynamic blade loading distribution.

5.2 Effect of Spool Pressure Loading. Nonaxisymmetric pressure distribution was first identified as a separate forcing source by Martinez-Sanchez et al. [12], and its effects on turbines were analyzed by Song and Martinez-Sanchez [9]. In order to assess the nature and magnitude of the nonaxisymmetric pressure effects in compressors as well, Spakovszky [7] investigated the effects of flow inertia on the destabilizing forces in a detailed analysis. The ISPC modeling results showed that the flow field lags the clearance distribution due to the fluid inertia. It is deduced that, due to this phase shift, the static pressure distribution acting on the rotor hub spool results in a net force that is not parallel to the deflection direction. The pressure force therefore has a component acting tangential to the rotor deflection and hence contributes to the cross-coupled stiffness and ultimately to the value of the β coefficient.

The static pressures acting on the spool were not measured in the experiment and a definitive comparison of the modeling results to experimental data cannot be made. However the average static pressure in the blade passage at mid-span was deduced from the blade surface measurements to obtain a rough estimate of the magnitude of the pressure nonuniformity.

The nondimensional circumferential spool pressure distribution obtained from the ISPC and 2CAD models at mid-span and the rough experimental estimate of the passage pressure nonuniformity are depicted in Fig. 7 for a compressor operating point close to stall. To be consistent with the scheme used in LSRC data reduction described in Part I, only the first spatial harmonic of the pressure distribution is considered here.

The ISPC model predicts a phase shift of 16 deg between the nonuniform spool pressure distribution and the tip clearance distribution. Regions with tight tip clearance yield less blockage and therefore a higher flow coefficient. Conserving total pressure in the upstream duct (potential flow) yields lower static pressure in the tight clearance region at the compressor face. Assuming that the flow angle from the last set of stator vanes is uniform and that the downstream duct has constant area implies a uniform static pressure distribution at the compressor exit. Hence the average of the upstream and downstream static pressure will be minimal in the tight clearance region as it is shown in Fig. 7.

The 2CAD approach predicts the same trend. Essentially higher mass flux toward the tight clearance region lowers the pressure in this region at the rotor inlet, and this nonuniform pattern persists through the stage. Thus, the average pressure acting on the rotor hub has a phase shift of 32 deg relative to the clearance distribu-

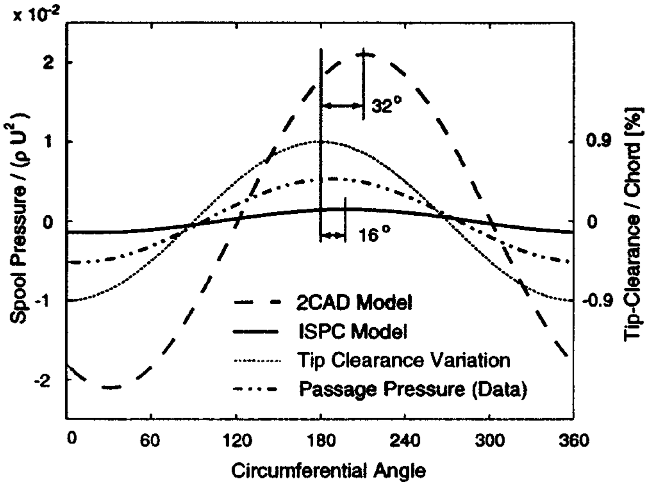

Fig. 7 The circumferential static pressure distribution obtained from the ISPC and 2CAD models at mid-span compared to experimental data

tion. The ISPC and the 2CAD modeling results differ in the prediction of the magnitude of the pressure nonuniformity but show similar trends.

A spool loading coefficient β_{spool} equivalent in form to the β coefficient was introduced to assess the relative impact of the pressure nonuniformity. It is assumed in the calculation of the β_{spool} coefficient that the spool pressure distribution acts on the hub surface of the rotor and the adjacent upstream and downstream interblade row gaps.

The β_{spool} coefficients predicted by the ISPC and 2CAD methods are compared in Fig. 8. Both models' results show the same forward whirling trend due to the nonuniform spool pressure loading. The estimated β_{spool} coefficient acts in a direction tending to counteract the backward whirl induced by the net unbalanced tangential blade loading (see Figs. 3 and 4). The β_{spool} coefficient estimated by the 2CAD model is larger in magnitude than the ISPC prediction, which is associated with the larger magnitude and phase of the static pressure distribution in Fig. 7.

5.3 Effects of Actual Forced Rotor Whirl. The LSRC experiment was performed with a *static* offset of the rotor. In the actual situation that is being modeled, the unstable rotor would be whirling at the offset radius at the natural frequency of the system. It has been suggested that this whirling, which was not simulated in the experiment might have some significant effect on the value of the β coefficients.

Forced shaft whirl was simulated by the ISPC model to assess the effects of shaft motion on the destabilizing rotor forces (for details see [7]). (The 2CAD model can also be extended to include unsteady whirl effects as has previously been done for turbines—but that analysis was not available for this paper.) The forced whirl frequency was varied from synchronous backward whirl to synchronous forward whirl. Figure 9 provides an estimate of the impact of this effect on the β coefficient and the spool loading coefficient β_{spool}. A detailed analysis shows that an enhanced distortion of the flow field, due to shaft motion, induces an amplification of the β coefficient near a whirl frequency close to the frequency of rotating stall. The ISPC model predicts this frequency to be in the range of 22 percent to 46 percent of rotor speed for Compressor A. It should be noted that, due to the flow distortion that is generated by the shaft whirl, the rotating stall frequency varies slightly with the forced whirl frequency.

By the same token, the phase shift of the spool static pressure distribution relative to the clearance distribution varies as a function of the forced whirl frequency. The direction of induced whirl changes from forward whirl for negative frequencies to backward whirl for forced whirl frequencies above 0.1 times rotor frequency.

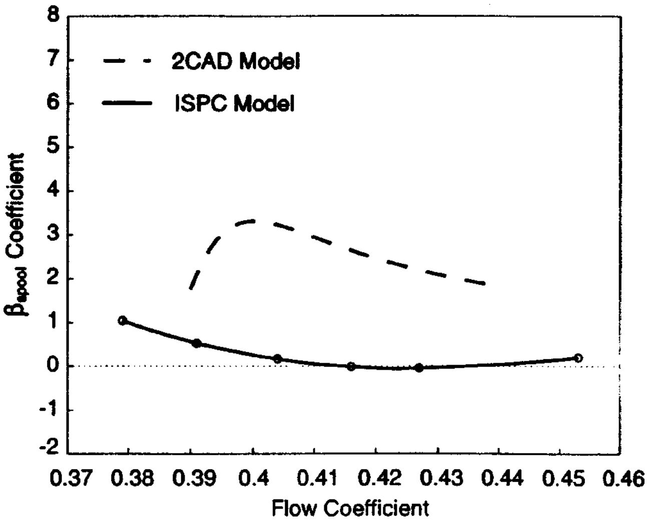

Fig. 8 Computed β coefficient attributable to the compressor spool pressure effect estimated by the ISPC and 2CAD models

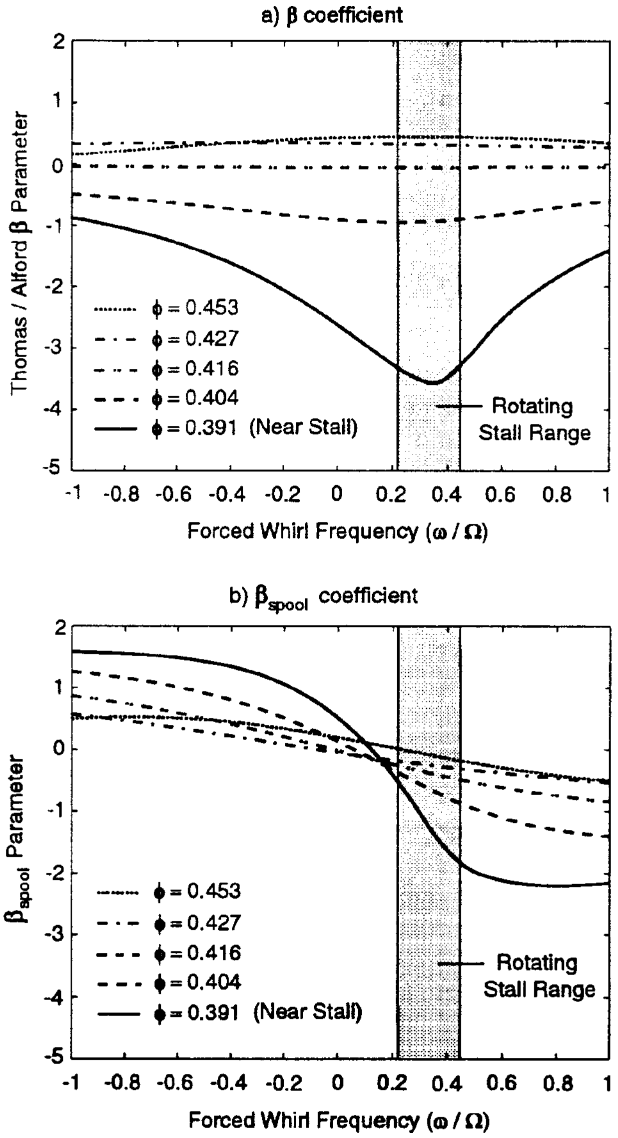

Fig. 9 β coefficient (*a*) and β_{spool} coefficient (*b*) attributable to the compressor rotor whirl effect as estimated by the ISPC model

It is important to note that the spool pressure-induced whirling force dampens the whirl tendency when backward whirl occurs due to the net unbalanced tangential blade loading, that is, the spool loading coefficient β_{spool} increases when the whirl frequency grows in the negative direction (see Fig. 9). The whirl speed at which the β coefficient is most affected by whirl and the angular speed of rotating stall are nearly equal. This suggests that, in an engine where the rotordynamics and compressor aerodynamics form one dynamic system, shaft whirl might interact and resonate with flow instability patterns such as rotating stall.

In summary, the simulation results from the ISPC model for actual forced rotor whirl suggest the following two important effects, which are present in actual rotor whirl but absent in our tests simulating whirl with a static offset.

1 For low flow coefficients (i.e., those near stall), shaft whirl close to rotating stall frequency enhances backward whirl, which implies a more negative β coefficient, as seen in Fig. 9(*a*). At the

other flow coefficients shown in Fig. 9(*a*), the additional contributions to the β coefficient of actual rotor whirl are relatively small and constant.

2 As forced whirl frequency changes from synchronous backward whirl (negative frequencies in Fig. 9(*b*)) to synchronous forward whirl (positive frequencies in Fig. 9(*b*)), the sign of the β_{spool} coefficient changes from positive to negative. This implies that the spool pressure effect dampens the whirling motion.

An additional finding for a statically deflected rotor is the existence of a relatively small contribution (compared to the total β coefficient) originating from the action of asymmetric pressure forces on the spool; this contribution tends to oppose that of the blading itself.

6 Capability of the Three Models

- The 2SPC method [5] gave predictions of the basic β coefficient for both the unshrouded rotor and the shrouded stator and the combined effect of the two that were accurate enough to justify their use in design calculation where the effects of nonaxisymmetric static pressure distribution on the rotor spool and the effects of rotor whirl might not be important. The method is applicable to any axial-flow compressor where an experimental definition of the stage characteristics at two levels of axisymmetric clearance is available.
- The ISPC method [7] provides a much better prediction than the 2SPC method of the basic β coefficient due to rotor tip clearances. The ISPC method is not limited to evaluation of the effect of rotor tip clearance. It can also be extended to analyze stator hub clearance and seal leakage flow effects but the results were not available for this paper. The rotor force model is not limited to the particular compressor model used here: any prediction of the compressor flow field (i.e., CFD analysis, experimental data, etc.) can be used to predict the aerodynamically induced rotor forces. The ISPC method provides a means for estimating the effects of the static pressure distribution on the rotor spool and of the effects of rotor whirl and can be easily integrated in existing engine design tools, particularly where the effects of nonaxisymmetric static pressure distribution on the rotor spool and the effects of rotor whirl may be important.
- The 2CAD method [8] does not require any prior experimental definition of stage characteristics and so is capable of carrying out systematic studies of the effects of stage design parameters to ascertain their influence on rotordynamic instability without requiring extensive experimental stage performance data. In addition to the blade loading variation, the model can predict nonaxisymmetric static pressure distribution on the rotor spool. Although not included in this paper the 2CAD method can be extended to accommodate rotor and stator shrouds (i.e., seals) and unsteady whirl effects.

7 Conclusions

This is the first time that definitive measurements, coupled with compelling analyses, have been reported in the literature to resolve whirl instability issues important in the design of modern, axial-flow compressors.

1 The computation of the β coefficient from all three models assessed in this paper showed agreement when compared to the experimental data in both form and direction, thus validating their use to understand whirl effects in compressors. In addition, the validation provides confidence for designers to use the models in the assessment of rotordynamically stable turbomachinery.

2 All three analysis methods conclude that the Thomas/Alford forces generally promote *backward* rotor whirl (associated with negative β coefficient) except for operation at higher flows where the results were mixed, with some compressors having strongly negative β and others having β's near zero or slightly positive. At lower-flow conditions, the β's were generally strongly negative.

3 It was established that the effects of rotor tip clearance explain only about one-half of the total value of the β coefficient. It is necessary to recognize the influence of the flow leakage around the stator-shroud seal-tooth clearance to understand and account for the full effect.

4 The ISPC model gave additional insight into the effects of an actual forced rotor whirl, which were not modeled in the experiment. For low flow coefficients (i.e., those near stall), shaft whirl close to rotating stall frequency enhances backward whirl, which implies a more negative β coefficient. At the other flow coefficients the additional contributions of actual rotor whirl to the β coefficient are relatively small and constant.

5 The modeling results are not definitive for the effect of nonaxisymmetric spool pressure distribution on the β coefficient. The ISPC model suggests that, for static shaft deflections, β_{spool} is quite small at flow coefficients typical of the operating regime of this class of compressors. The 2CAD model suggests that the effect of nonaxisymmetric spool pressure distribution may be more significant than predicted by the ISPC model. For forced shaft whirl β_{spool} is of comparable magnitude to the β coefficient (rotor effect only). It opposes the effects of the β coefficient for two cases: for negative whirl frequencies and low flow coefficients and for positive whirl frequencies and high flow coefficients.

6 The validated computational capability described above provides the general means to predict the aerodynamic destabilizing forces for axial-flow compressors in gas turbine engines (subject to the limitations that might result from the approximations implicit in the analytic models where the effects of compressibility and variations in radius ratio were not addressed). This capability permits improved accuracy in predicting the rotordynamic instability thresholds for existing, derivative, and new turbomachinery designs that will operate at higher speeds and higher energy-density levels in the future.

References

[1] Thomas, H. J., 1958, ''Unstable Natural Vibration of Turbine Rotors Induced by the Clearance Flow in Glands and Blading,'' Bull. AIM, **71**, No. 11/12, pp. 1039–1063.

[2] Alford, J., 1965, ''Protecting Turbomachinery From Self-Excited Rotor Whirl,'' J. Eng. Power, Oct., pp. 333–334.

[3] Vance, J. M., and Laudadio, F. J., 1984, ''Experimental Measurement of Alford's Force in Axial Flow Turbomachinery,'' ASME J. Eng. Gas Turbines Power, **106**, No. 3, pp. 585–590.

[4] Colding-Jorgensen, J., 1992, ''Prediction of Rotordynamic Destabilizing Forces in Axial Flow Compressors,'' J. Fluids Eng., **114**, No. 4, pp. 621–625.

[5] Ehrich, F. F., 1993, ''Rotor Whirl Forces Induced by the Tip Clearance Effect in Axial Flow Compressors,'' J. Vibr. Acoust., **115**, pp. 509–515.

[6] Yan, L., Hong, J., Li, Q., Zhu, Z., and Zhao, Z., 1995, ''Blade Tip Destabilizing Force and Instability Analyses for Axial Rotors of Compressor,'' AIAA Paper No. A95-40315, Beijing University of Aeronautics and Astronautics, Beijing, China.

[7] Spakovszky, Z. S., 2000, ''Analysis of Aerodynamically Induced Whirling Forces in Axial Flow Compressors,'' ASME J. Turbomach., **122**, No. 4, pp. 761–768.

[8] Song, S. J., and Cho, S. H., 2000, ''Non-uniform Flow in a Compressor D Asymmetric Tip Clearance,'' ASME J. Turbomach., **122**, pp. 751–760.

[9] Song, S. J., and Martinez-Sanchez, M., 1997, ''Rotordynamic Forces Due to Turbine Rip Leakage,'' ASME J. Turbomach., **119**, No. 3, pp. 695–713.

[10] Wisler, D. C., 1985, ''Loss Reduction in Axial-Flow Compressors Through Low-Speed Model Testing,'' ASME J. Eng. Gas Turbines Power, **107**, pp. 354–363.

[11] Wellborn, S. R., and Okiishi, T. H., 1999, ''Influence of Shrouded Stator Cavity Flows on Multistage Compressor Performance,'' ASME J. Turbomach., **121**, No. 3, pp. 486–498.

[12] Martinez-Sanchez, M., Jaroux, B., Song, S. J., and Yoo, S. M., 1995, ''Measurement of Tip Blade–Tip Rotordynamic Excitation Forces,'' ASME J. Turbomach., **117**, No. 3, pp. 384–392.

Rotating Instabilities in an Axial Compressor Originating From the Fluctuating Blade Tip Vortex

R. Mailach

I. Lehmann

K. Vogeler

Dresden University of Technology,
01062 Dresden, Germany

Rotating instabilities (RIs) have been observed in axial flow fans and centrifugal compressors as well as in low-speed and high-speed axial compressors. They are responsible for the excitation of high amplitude rotor blade vibrations and noise generation. This flow phenomenon moves relative to the rotor blades and causes periodic vortex separations at the blade tips and an axial reversed flow through the tip clearance of the rotor blades. The paper describes experimental investigations of RIs in the Dresden Low-Speed Research Compressor (LSRC). The objective is to show that the fluctuation of the blade tip vortex is responsible for the origination of this flow phenomenon. RIs have been found at operating points near the stability limit of the compressor with relatively large tip clearance of the rotor blades. The application of time-resolving sensors in both fixed and rotating frame of reference enables a detailed description of the circumferential structure and the spatial development of this unsteady flow phenomenon, which is limited to the blade tip region. Laser-Doppler-anemometry (LDA) within the rotor blade passages and within the tip clearance as well as unsteady pressure measurements on the rotor blades show the structure of the blade tip vortex. It will be shown that the periodical interaction of the blade tip vortex of one blade with the flow at the adjacent blade is responsible for the generation of a rotating structure with high mode orders, termed a rotating instability.
[DOI: 10.1115/1.1370160]

1 Introduction

Extensive investigations of aerodynamic instabilities in axial compressors have been carried out in the last years. The main objective of this research is to avoid critical flow conditions and to extend the stable operating range of compressors.

There are two major different stall inception patterns. The first one is a short length scale disturbance, which is known as ''spike.'' It is a small rotating stall cell which is in its initial phase limited to the blade tip region of only one or a few blade passages. It grows within a few rotor revolutions to a fully developed rotating stall cell.

The second pattern is the modal wave stall inception. In this case a long length scale wavelike disturbance rotates around the annulus. Often it occurs only a short time before exceeding the stability limit. The breakdown of the flow field is initiated in a velocity minima of the modal wave. Camp and Day [1] give a detailed overview on the recent work on these two stall inception patterns.

Another aerodynamic instability, which is quite different to the phenomena described above, can be found already in the stable range of compressors. The disturbance can be described by a group of superimposed modes or a part-span stall with fluctuating cell numbers. This phenomenon is known as rotating instability (RI). It does not necessarily lead to full-span rotating stall inception, but it is responsible for an intensification of the tip clearance noise and for the excitation of rotor blade vibrations.

The first description of this unsteady flow phenomenon is given by Mathioudakis and Breugelmans [2]. They described a group of rotating stall cells with different cell numbers in a single-stage axial compressor. Mongeau [3] and Bent et al. [4] found this instability in centrifugal compressors. Mongeau and Quinlan [5], Kameier [6], Krane et al. [7], Kameier and Neise [8], and März et al. [9] observed this aerodynamic instability in different axial fans. In high-pressure compressors RIs were investigated by Baumgartner et al. [10] and Witte and Ziegenhagen [11].

In pressure or velocity frequency spectra RIs are to be found as a significant amplitude increase within a frequency band below the BPF, usually superimposed by peaks with constant frequency spacing. This pattern is related to a group of consecutively numbered modes. The frequencies of RIs are not harmonically related to the rotor frequency.

The main parameters of RIs in axial machines vary over a wide range. Mode orders of RIs of about 1/3 up to the double rotor blade number have been observed. Thus the circumferential wavelength of this disturbance is only about 0.5–3.0 times the rotor blade pitch. The rotation velocity of RIs in different machines varies between 25 percent and 90 percent of rotor velocity.

Major influence parameters on the origination of RIs axial compressors are the tip clearance of the rotor blades, the pressure difference across the rotor blade row and the axial component of velocity depending on the operating point.

März et al. [9] presumed the periodical interaction of the blade tip vortex with the tip flow of the neighboring blade to be the reason for the origination of RIs. However, recent numerical investigations of Hoying et al. [12] and experiments of Inoue et al. [13] showed the influence of the blade tip vortex on short length scale disturbances and rotating stall inception.

This paper describes experimental investigations of the flow field at the casing, on the rotor blades and within the rotor blade passages respectively the tip clearance. The objective is to show how the blade tip vortex influences the origination of RIs.

2 Experimental Facility

The experiments have been carried out in the Dresden LSRC. The compressor consists of four stages, which are preceded by an inlet guide vane, Fig. 1. Detailed descriptions of the construction of the compressor are given by Boos et al. [14] Table 1 gives a summary of the main design parameters.

It was assumed that RIs are a local phenomenon, restricted to the blade tip region of the rotor blade row. At the nominal tip clearance ratio $s^* = 1.3$ percent (tip clearance/chord length at

---

Contributed by the International Gas Turbine Institute and presented at the 45th International Gas Turbine and Aeroengine Congress and Exhibition, Munich, Germany, May 8–11, 2000. Manuscript received by the International Gas Turbine Institue February 2000. Paper No. 2000-GT-506. Review Chair: D. Ballal.

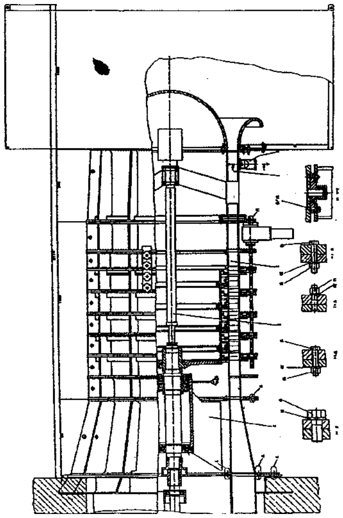

Fig. 1 Sectional drawing of Dresden LSRC

blade tip) it could not be observed. To induce it, the tip clearance of the third stage was enlarged step by step from the nominal size to 2.0 percent, 3.0 percent, and finally 4.3 percent. This stage was chosen for the investigations because the behavior of it is typical for a middle stage of a high-speed compressor. Detailed results of conventional flow measurements were also available there.

Different measurement techniques were used to investigate the flow field of the compressor. A 2D-LDA system was applied to determine the axial and circumferential velocity components of the flow field within the rotor blade passage. Measurements within the tip clearance were only possible for a tip clearance ratio of 4.3 percent. The measuring volume was 0.06 mm×0.06 mm×0.63 mm.

For postprocessing the data were ensemble averaged. Time-resolved results of these measurements are not available because of a low tracer particle rate. Detailed descriptions of the LDA system are given by Müller et al. [15].

Due to the large scale of the compressor, many time resolving pressure sensors could be used.

Kulite LQ47 sensors were applied to acquire unsteady pressures on the rotor blade surfaces, Fig. 2. They were mounted at both pressure and suction sides of two adjacent rotor blades of the third stage. By this arrangement correlations between the signals of both sides of the blade as well as between different blades are possible. The signals were transmitted via rotating amplifiers and slip rings into the stationary system. All signals were acquired simultaneously.

One-quarter-inch capacity microphones (Microtech MK301) were used to measure the pressure fluctuations at the casing wall in two measuring configurations.

Table 1 Design parameters of Dresden LSRC

Hub diameter	1260 mm
Hub to tip ratio	0.84
Design speed	1000 rpm
Reynolds number at inlet of rotor, midspan	$5.7 \cdot 10^5$
Mach number at inlet of rotor, midspan	0.22
Mass flow at design point	25.35 kg/s
Number of rotor blades	63
Chord length of rotor blades, midspan	110 mm
Chord length of rotor blades, tip	116 mm
Nominal tip clearance of rotor blades	1.5 mm
Solidity of rotor blades, tip	1.55
Stagger angle of rotor blades, tip	40.5°
Number of stator blades	83
Chord length of stator blades, midspan	89 mm

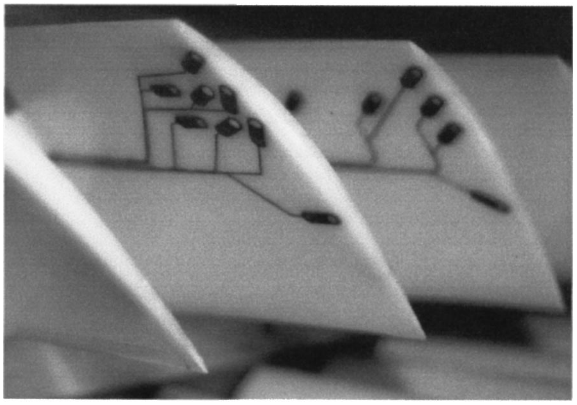

Fig. 2 Time-resolving pressure transducers on the PS of rotor blades

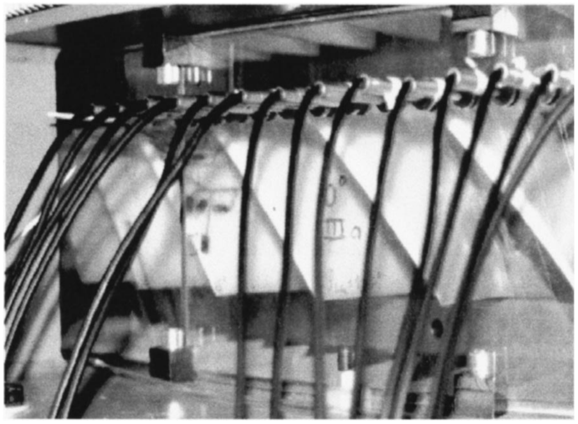

Fig. 3 Configuration C1 of microphones at the casing

An array of microphones, distributed over the circumference at constant axial position, was installed to determine the expected high mode orders of RIs, Fig. 3 (configuration C1). The microphones were mounted at the casing wall at the leading edge position of the rotor blades. An equal spacing of 1.5° enables the acquisition of mode orders up to 120. The 30 available microphones allow to observe the pressure fluctuations over a 45° section of the circumference simultaneously. To determine the mode orders one of the sensors always remained at a fixed position as a reference, while the others were moved stepwise over the whole circumference.

A second measuring configuration C2 consists of an array of microphones, covering the area of one rotor blade passage at the casing at different axial and circumferential positions. They were arranged in different traces following the rotor blade contour. This configuration was used for determining the propagation velocity and direction of the perturbation in the fixed frame of reference.

3 Influence of Tip Clearance and Operating Point on RIs

First signs of RIs have been found at a tip clearance ratio of 3.0 percent. At a larger tip clearance ratio of 4.3 percent it was fully developed. It has been found at all investigated rotor speeds (50 percent, 80 percent, and 100 percent design speed) [16,17]. The results shown in this section are referred to the measurements with the largest tip clearance and design speed only.

The formation of RIs is limited to a narrow operating range near the stability limit. At design speed this includes the range of dimensionless mass flow rates of about $\xi = 0.87 - 0.81$, Fig. 4. At the operating point $\xi = 0.87$ a narrow band increase of the ampli-

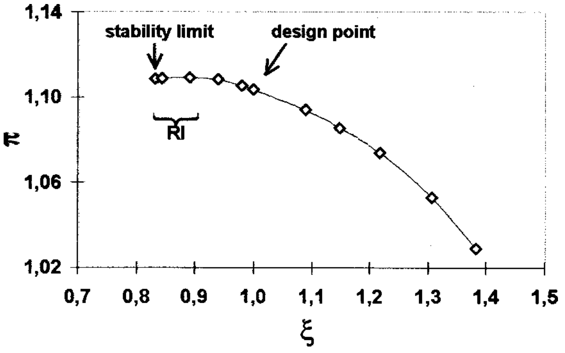

Fig. 4 Compressor characteristic for design speed

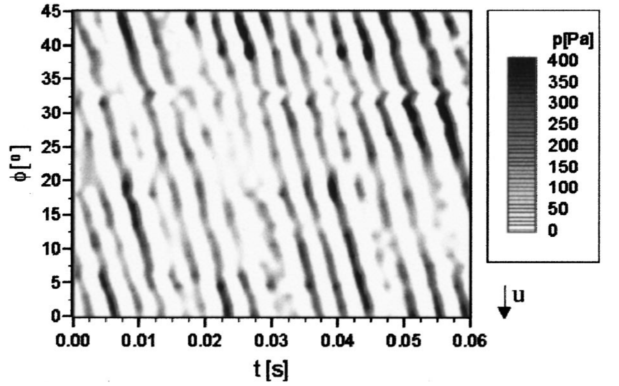

Fig. 6 Propagation of RIs in circumferential direction at the casing wall, axial position at the leading edge of the rotor blades, design speed, $\xi = 0.82$

tudes in the frequency spectrum at about 30 percent of blade passing frequency (BPF) can be observed. Approaching the stability limit by throttling the compressor, the RI shifts to slightly lower frequencies while the amplitude of the perturbation grows. Figure 5 shows a typical frequency spectrum measured at the casing wall for an operating point near the stability limit. The largest amplitudes of RIs can be found at a frequency of 265 Hz. This is 25 percent of 1. BPF of rotor blades. Furthermore a modulation of 1. BPF and RI frequencies can be seen. Referred to the rotating system RIs can be detected within about the same frequency range.

At the same time two different modal waves (first and second order) can be observed in the whole compressor. They are represented as discrete peaks at much lower frequencies than RIs (about 1 percent of BPF respectively 50 percent of rotor frequency). An interaction of these long-length disturbances with the short-length RIs could not be detected.

Measurements on the rotor blades show that RIs are limited to the blade tip region. Maximum amplitudes appear at the positions of the upper measuring traces at 92 percent of the blade height and 20–30 percent of chord length. The disturbance is more pronounced on the pressure side (PS) than on the suction side (SS). At the casing highest amplitudes occurs at the same axial position. A second maximum can be observed in the axial gap downstream the rotor blade row at the casing.

The mode orders and the rotating velocity of RIs were determined using the C1 configuration of microphones. Figure 6 shows the pressure fluctuations at the casing over a 45° section of the circumference (≈8 rotor blade pitches) for about one rotor revolution. The signals were band-pass filtered (finite impulse response filter) to suppress higher frequency parts (for instance rotor wakes), low-frequency parts of the signal (like modal waves) and stochastic disturbances. It can be seen that RIs propagate in rotor direction with 50–60 percent of rotor velocity. The estimated mean wavelength in circumferential direction is only about two rotor blade pitches. Hence the mean mode order of RIs is about 30. This is nearly half the rotor blade number (63). Strong fluctuations of the amplitude, frequency and wavelength of the disturbance can be observed.

For an exact determination of the mode orders the microphones were moved stepwise over the whole circumference. One sensor always remains at a fixed position as a reference. In that way evenly distributed signals were achieved. The phase angle of the cross power spectra of each sensor referring to the fixed reference sensor permits the detailed evaluation of the mode order depending on the frequency. A detailed description of this method and the results for different operating points are given by Mailach [16,17].

As an example Fig. 7 shows the mode orders for an operating point at design speed near the stability limit. It complements Figs. 5 and 6, which show results for the same operating point. Figure 7 indicates that RIs can be described by a group of superimposed modes. This is the reason why RIs can be identified as an amplitude increase in a frequency band. The mode orders of RIs rise with frequency; they are consecutively numbered. Mode orders of about 10–40 can be attributed to the disturbance. The highest amplitude of RIs given for a mode order of 28. This agrees very well with the observations in the time domain, Fig. 6.

The strong fluctuation of RIs shown above is the reason for the appearance of RIs as an amplitude increase in a frequency band in the spectrum, Fig. 5. These fluctuations are averaged in the frequency spectrum over a certain time period.

Contrary to that modal waves or rotating stall are flow phenomena with constant mode order respectively cell number. This is the reason for their appearance as a discrete peak in the spectrum, Fig. 5.

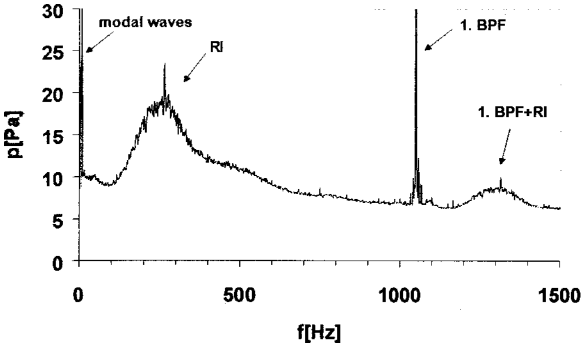

Fig. 5 Frequency spectrum at the casing, design speed, $\xi = 0.82$, $s^* = 4.3$ percent

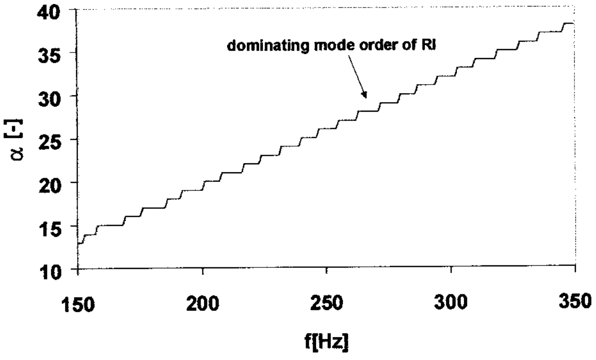

Fig. 7 Mode orders of RIs, design speed, $\xi = 0.82$

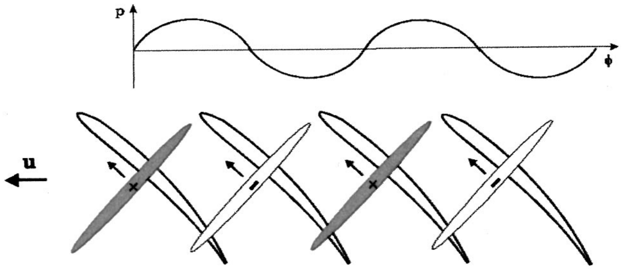

Fig. 8 Propagation of RIs at the casing wall and circumferential pressure distribution at profile leading edge, $t=\text{const}$ (fixed frame of reference)

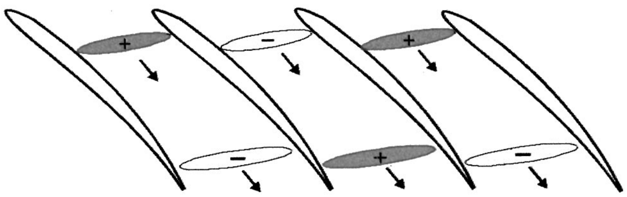

Fig. 9 Propagation of RIs in the blade tip region, $t=\text{const}$ (relative frame of reference)

Up to now only the circumferential distribution and propagation of RIs was described. Using statistical evaluation methods Mailach [16,17] could show that RIs propagate in the blade tip region and at the casing wall like wavefronts. The measurements (C2) reveal a periodic reversed axial flow component at the casing, Fig. 8. This corresponds to the findings of Kameier [6] who showed reversed flow due to RIs with hot-wire measurements within the tip clearance. März et al. [9] also confirm this, using measuring data of an array of time-resolving pressure sensors at the casing.

As the dominating mode order is about half the rotor blade number that means, the same process repeats simultaneously at every other blade. This is schematically shown in Fig. 8 (+ and − marks the pressure maxima and minima of RIs.

The propagation direction in the blade tip region is determined by correlating the signals of pressure transducers on PS and SS of two adjacent rotor blades, Fig. 9. With respect to the rotating frame of reference the circumferential propagation takes place against rotor turning direction. Contrary to the propagation at the casing wall respectively within the tip clearance the axial component of RIs in the blade tip region is directed downstream.

Both in the blade tip region and at the casing wall the phase difference between leading and trailing edge of the profile is about 180° for constant circumferential position. That means if at the leading edge a pressure maximum appears at the trailing edge a pressure minimum can be found, etc.

To use a consistent frame of reference the observations made in the fixed frame at the casing wall have been transformed into the rotating system. With respect to the relative frame the flow within the tip clearance of the rotor can be described by a reversed axial component and a counterrotating circumferential component of RIs. The periodical flow due to RIs in the blade tip region also counterrotates, but propagates downstream. Thus a spiral propagation of the rotating instability modes against the rotor direction takes place, whereby the disturbance propagates like wavefronts, Fig. 10.

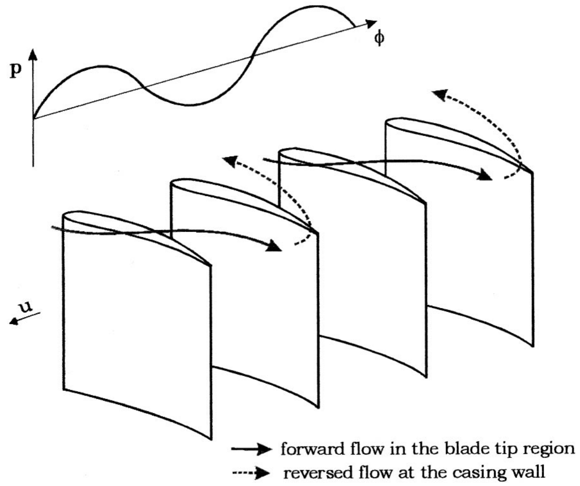

Fig. 10 Propagation direction of RIs in the blade tip region, rotating system

4 Influence of the Rotor Blade Tip Vortex on the Formation of RIs

The flow field in the blade tip region of the rotor blades is dominantly influenced by the blade tip vortex. While the blade tip vortex occurs at each rotor blade, these investigations show dominating mode orders of RIs of only half the rotor blade, *i.e.* the disturbance occurs at the same time at each other blade.

The tip vortex is induced by the pressure difference between PS and SS of the rotor blades. The maximum vortex intensity can be expected in the region of the maximum pressure difference between PS and SS, Inoue et al. [18]. The rollup of the vortex can be located there.

The main influence parameter on the blade tip vortex is the tip clearance height. Other parameters are the thickness of casing wall boundary layer, Reynolds number, Mach number, blade thickness, blade loading, and speed.

4.1 Nominal Tip Clearance, $s^*=1.3$ percent. First evidence on the location of the maximum tip vortex strength is given by the time-averaged pressure differences between positions at PS and SS of a rotor blade, Fig. 11. Measuring positions on a line at $r^*=92$ percent were used for this. Only signals of sensors at comparable chordwise positions will be compared.

The largest pressure difference between PS and SS at design point can be seen close to the leading edge of the blade. Approaching the stability limit this difference grows. Thus the vortex intensity increases in this region, while it is decreases in the rear part of the blade.

The results of the LDA measurements are in accordance with these observations. For nominal tip clearance at design point Fig. 12 shows the distributions of the relative flow angle in a measuring plane at $r^*=95$ percent.

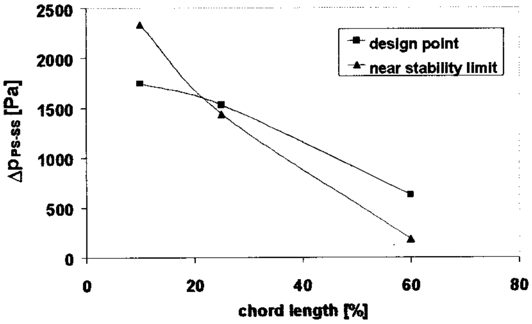

Fig. 11 Pressure difference between PS and SS of a rotor blade vs chord length, $s^*=1.3$ percent, $r^*=92$ percent, design speed

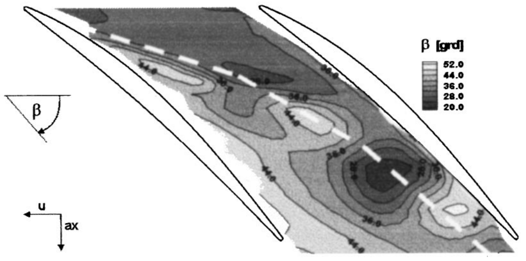

Fig. 12 Relative flow angle in the blade tip region of the rotor blades, nominal tip clearance ($s^*=1.3$ percent), $r^*=95$ percent, design speed, design point ($\xi=1.0$). Dashed line: expected vortex trajectory

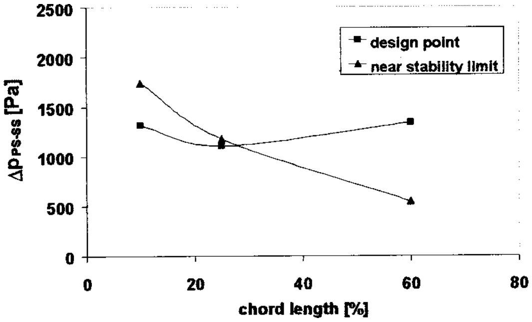

Fig. 14 Pressure difference between PS and SS of a rotor blade vs chord length, $s^*=4.3$ percent, $r^*=92$ percent, design speed

The relative flow angle distribution indicates a spiral blade tip vortex. Three areas of large flow angles and two areas of small flow angles clearly illustrate this. These regions of local under- and overturning show the intersection points of the vortex with the measuring plane. The axial velocity distribution shows the blade tip vortex as a region of low velocities between the front part of the SS of one blade and the rear part of the PS of the adjacent blade, Müller et al. [15]. Extremely low axial velocity components are to be found in the regions of underturned flow.

If the flow rate is reduced the vortex is displaced upstream with a slightly stronger inclination toward the circumferential direction, Fig. 13. This coincides with the results of the experiments of Saathoff and Stark [19] and the numerical investigations of Hoying et al. [12]. The reason for this is the reduced axial velocity component. The distances between the intersection points of the vortex with the measuring plane are also clearly smaller.

An interaction of the blade tip vortex and the flow along the PS of the adjacent blade seems to be possible in the rear part of the blade at both operating points. The only evident periodical influence on the pressure difference between PS and SS can be attributed to the stator wakes (compare Fig. 20 for large tip clearance).

4.2 Large Tip Clearance, $s^*=4.3$ percent. At design point the pressure difference between PS and SS is nearly constant along the chord, Fig. 14. Thus the time-averaged tip vortex intensity is not depending on the axial position. However, at an operating point near the stability limit again an increase of this driving pressure difference at the leading edge can be observed, which indicates that an increase of the vortex intensity can be expected.

The results of LDA measurements show significant changes in the nature of the blade tip vortex for large tip clearance.

Already at design point in the measuring plane through the tip clearance large regions of reversed flow can be observed. This seems to be due to the rolling-up of the blade tip vortex. The positive pressure gradient across the rotor blade row intensifies this reversed flow in the plane inside the tip clearance.

Figure 15 shows this region with low axial velocity or even axial reversed flow for design point. In the front part of the blades a zone of low axial velocity which means an underturning of the flow can be seen in the middle of the blade passage. The relative flow angle remains positive. The reversed flow region within the tip clearance is limited to the rear part of the blades and extends over the whole circumference. Minimum axial velocities and relative flow angles can be observed between the middle of the blade passage and the PS. This can be explained by the existence of a large tip vortex. This corresponds to the observations of Inoue and Kuroumaru [18], who also observed the center of the reversed flow region away from the SS at a comparable tip clearance ratio.

In the measuring plane near the blade tips at $r^*=92$ percent a low velocity area is visible in the rear part of the blades towards the PS, Fig. 16. This is caused by the reversed flow due to the tip vortex which radially moves away from the casing. This results in a blockage of the flow in the rear part of the rotor blades, Fig. 19. This blockage region causes a turning of the flow towards the hub and the SS of the blades. Near the SS an overturning of the flow can be seen, Fig. 16.

The reversed flow region within the tip clearance is shifted upstream when approaching the stability limit, Fig. 17. This is due to the reduced axial velocity component and the increase of the pressure difference between PS and SS at the leading edge. In operating points near the stability limit the blade tip vortex can be

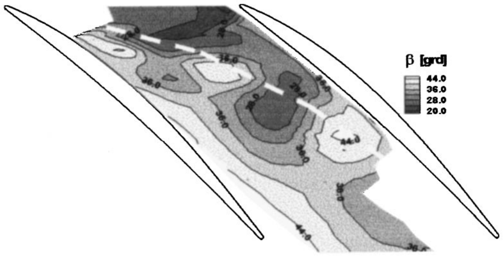

Fig. 13 Relative flow angle in the blade tip region of the rotor blades, nominal tip clearance ($s^*=1.3$ percent), $r^*=95$ percent, design speed, operating point near stability limit ($\xi=0.85$). Dashed line: expected vortex trajectory

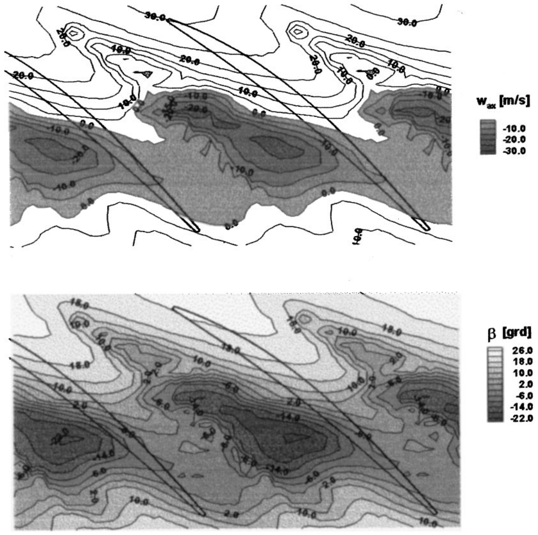

Fig. 15 Axial component of velocity and relative flow angle within the rotor blade tip clearance, large tip clearance ($s^*=4.3$ percent), $r^*=97.9$ percent, design speed, design point ($\xi=1.0$)

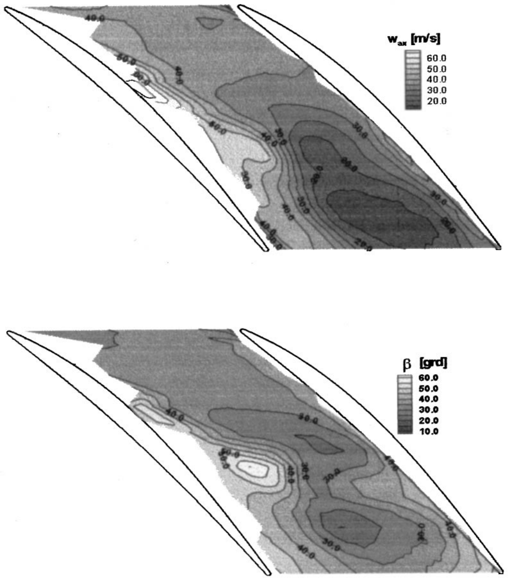

Fig. 16 Axial component of velocity and relative flow angle in the blade tip region of the rotor blades, large tip clearance ($s^*=4.3$ percent), $r^*=92.0$ percent, design speed, design point ($\xi=1.0$)

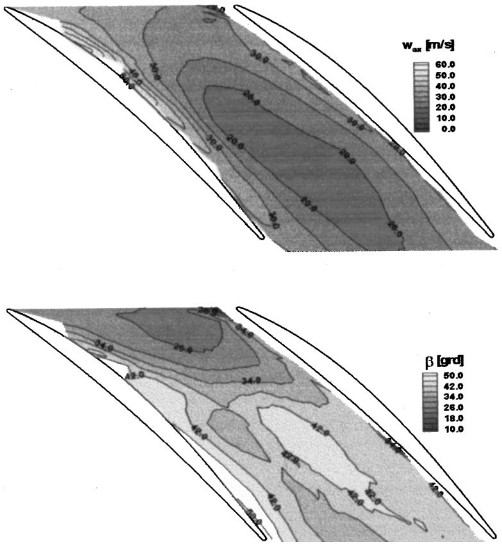

Fig. 18 Axial component of velocity and relative flow angle in the blade tip region of the rotor blades, large tip clearance ($s^*=4.3$ percent), $r^*=92.0$ percent, design speed, operating point near stability limit ($\xi=0.85$)

located in the front part of the blade, Fig. 18. A strong underturning of the flow occurs near the leading edge within the blade passage. Thus an interaction of the tip vortex of one blade and the flow at the tip of the PS of the adjacent blade is likely. According to the shifted reversed flow region the area of low velocity in the blade tip region also moves upstream. Minimum velocities can be located in the middle of the blade passage at about 50 percent of chord length. This low velocity region is restricted to about the upper quarter of the blade height.

One should remind that the results of LDA measurements are ensemble-averaged. It will be shown that the flow field shown for the operating point close to the stability limit is strongly influenced by periodic fluctuations. These parts of the signal disappear due to the averaging of the results explained above.

The time dependence of the blade tip vortex can be described using once more the data of the unsteady pressure measurements on the rotor blade surface. At design point, where no signs of RI have been found, the pressure difference between PS and SS is strongly periodically influenced by the stator wakes, Fig. 20.

At an operating point near the stability limit a totally different behavior can be seen. In addition to the stator wakes another much stronger influence appears, Fig. 21. Especially in the tip region of the front part of the blade strong pressure decreases can be seen for short time periods. This seems to be caused by the reversed flow of the blade tip vortex through the tip clearance. These pressure drops, which are stronger at the PS, strongly diminishes the pressure difference between PS and SS. For short moments the pressure on the SS is larger than on the PS, which means that the tip clearance flow is stopped or even a reversed flow trough the tip clearance from the SS to the PS, Fig. 21. The strongest influence can be observed at positions where also maximum amplitudes of RIs have been found.

Contrary to the design point the reversed flow affects the flow in a region where the maximum pressure difference between PS and SS is to be found. Thus the consequences of the reversed flow of one blade tip vortex on the formation of the tip vortex of the adjacent blade are much stronger.

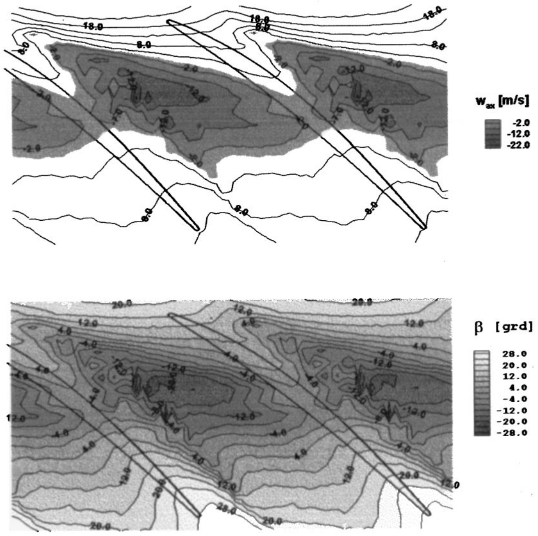

Fig. 17 Axial component of velocity and relative flow angle within the rotor blade tip clearance, large tip clearance ($s^*=4.3$ percent), $r^*=97.9$ percent, design speed, operating point near stability limit ($\xi=0.85$)

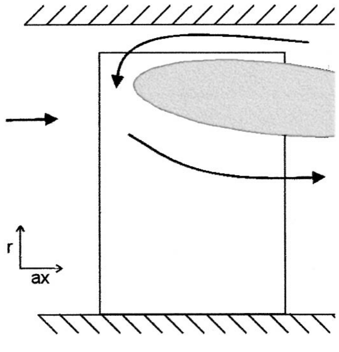

Fig. 19 Blockage in the blade tip region induced by the blade tip vortex, large tip clearance ($s^*=4.3$ percent)

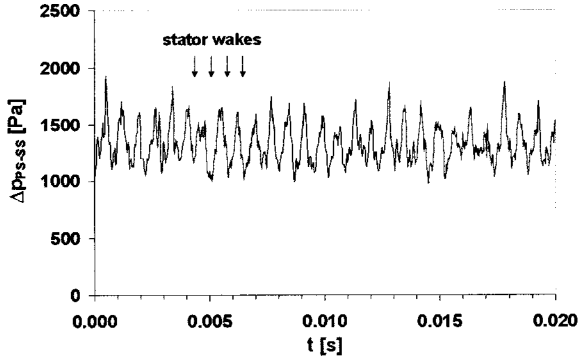

Fig. 20 Periodical influence of stator wakes on the pressure difference between PS and SS of a rotor blade ($s^*=4.3$ percent), $r^*=92$ percent, 10 percent chord, design speed, design point

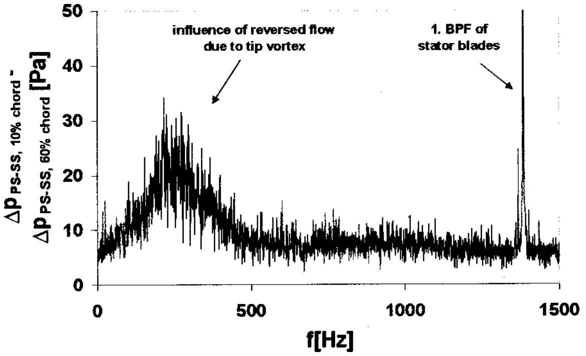

Fig. 22 Fluctuation of tip vortex along the blade chord, frequency spectrum of the difference of the pressure differences between PS and SS near the leading edge (10 percent chord) and the rear part (60 percent chord) of a rotor blade, $r^*=92$ percent), $s^*=4.3$ percent, design speed, operating point near stability limit ($\xi=0.83$)

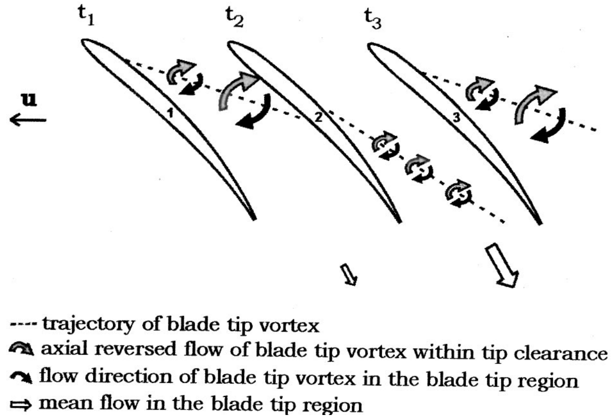

Fig. 23 Time-dependent development of blade tip vortex, rotating system

The vortex intensity in the front part of the blade strongly fluctuates. As a result of this the location of the strongest vortex intensity periodically moves along the blade chord. This can clearly be seen in the time trace of the difference of the pressure differences between PS and SS near the leading edge (10 percent chord) and in the rear part (60 percent chord) of the blade. A frequency spectrum of this time trace is shown in Fig. 22. It shows the periodical fluctuation of the maximum pressure difference between PS and SS along the blade chord, caused by the periodic characteristic of the tip clearance flow. This can be seen as a hump in the spectrum, which agrees very well with the typical pattern of RIs shown in Fig. 5. This periodical fluctuation along the blade chord is also according to the results for the propagation of RIs in the blade tip region, Fig. 9. The discrete peak at 1383 Hz in Fig. 22 shows ones more the periodical influence caused by the stator wakes.

This fluctuation of the blade tip vortex presumably propagates into circumferential direction [17]. At the time t_1 a blade tip vortex with strong intensity near the leading edge occurs at blade 1, Fig. 23. The large reversed flow region of this vortex affects the flow in the front region of the neighboring blade 2 at the time t_2. At this time the pressure difference in this region of blade 2 is diminished and the maximum pressure difference is shifted downstream to the rear part of the blade. However, the pressure difference in this region is considerably smaller than at the leading edge without the influence of the reversed flow. This means the blade tip vortex at time t_2 at blade 2 is weaker than that at time t_1 at blade 1 and can be localized to the rear part of the blade. The vortex presumably leaves the passage and does not affect the flow at time t_3 at blade 3, which again produces a strong tip vortex, etc.

Thus the fluctuating blade tip vortices propagate in circumferential direction against the rotor turning direction along the rotor blade row (referred to the relative frame). At the same time a

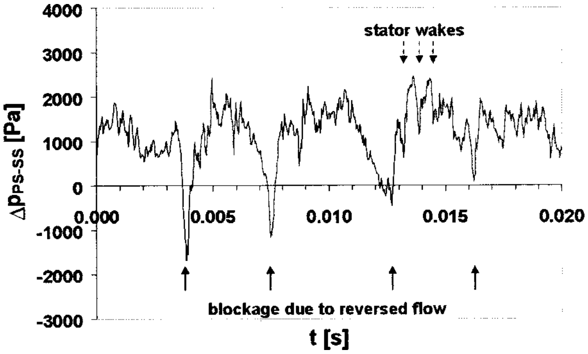

Fig. 21 Pressure difference between PS and SS of a rotor blade, $s^*=4.3$ percent, $r^*=92$ percent, design speed, operating point near stability limit ($\xi=0.83$), sensors at nearly the same axial position: 20 percent chord at PS, 30 percent chord at SS

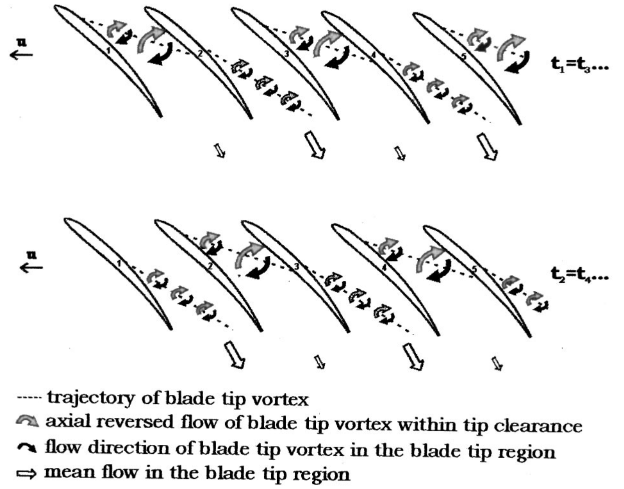

Fig. 24 Blade tip vortices at different times, rotating system

strong blade tip vortex can be found at every second blade, Fig. 24. At this time the other blades can only develop a weak tip vortex. Thus the mode order of the disturbance is about half the rotor blade number. This rotating structure in the blade tip region is the rotating instability (RIs) which was to be investigated.

The propagation direction of the periodically reversed flow due to the strong tip vortices fluctuates, Mailach [17]. This seems to be the reason for the fluctuation of the circumferential wavelength of the disturbance respectively the excitation of different mode orders. The time-dependent fluctuations are averaged in the spectrum. This is the reason why RIs are spread over a certain frequency range in a spectrum.

At design point and large tip clearance RIs have not been found because only the rear part of the blade is affected by the tip clearance flow of the neighboring blade. Stronger fluctuations at measuring positions on the PS near the trailing edge and the blade tip give evidence for that. Because the pressure difference between PS and SS near the blade tip is relatively constant along the chord the effect on the formation of the tip vortex seems to be small and does not result in a rotating structure.

5 Conclusions

Rotating instabilities have been observed near the stability limit of the compressor provided a relatively large rotor blade tip clearance. This phenomenon can be responsible for the intensification of clearance noise and the excitation of large amplitude blade vibrations.

Measurements both in stationary and rotating system reveal that this phenomenon is limited to the blade tip region within a rotor blade row and the axial gaps upstream and downstream of it. The largest pressure fluctuations of the disturbance could be observed at measuring positions next to the blade tip within the area of the largest blade thickness, whereby the disturbance on the PS is more pronounced than on the SS. The circumferential structure and the spatial development of this unsteady flow phenomenon has been described. RIs comprise a group of modes of much higher order than those of rotating stall. The dominating mode order of RIs is nearly half the rotor blade number. The circumferential velocity is 50–60 percent of rotor velocity.

The results of LDA measurements within the rotor blade passages and the tip clearance show the structure of the blade tip vortex. For a large tip clearance at operating points with RIs a strong blade tip vortex with a reversed flow region within the tip clearance and a blockage in the tip region of the rotor blades has been observed.

Unsteady pressure measurements in the blade tip region of the rotor blades reveal a strong fluctuation of the blade tip vortices. It is caused by periodical interactions of the tip clearance flow of one blade and the flow at the adjacent blade. The fluctuating blade tip vortices propagate in circumferential direction along the rotor blade row and yield a rotating structure with high mode orders, which is the investigated rotating instability.

Acknowledgments

The project underlying to this publication was supported by the German Bundesministerium für Bildung, Wissenschaft, Forschung und Technologie. This work has been carried out within the project group AG Turbo (Arbeitsgemeinschaft Hochtemperatur-Gasturbine). The responsibility for the contents of this publication is entirely with the authors. The authors thank BMW Rolls-Royce Dahlewitz, DLR Berlin and MTU München for the co-operation and their support of the work.

Nomenclature

f = frequency
p = pressure
r^* = dimensionless passage height
s^* = dimensionless tip clearance
t = time
u = rotor velocity
w = relative velocity
α = mode order
β = relative flow angle (from circumferential direction)
ϕ = circumferential position
π = total pressure ratio
ξ = mass flow/design mass flow

Abbreviations

ax = axial
BPF = blade passing frequency
C1/C2 = measuring configurations
LDA = laser doppler anemometry
LSRC = Low Speed Research Compressor
PS = pressure side
SS = suction side
RI = rotating instabilities

References

[1] Camp, T. R. and Day, I. J., 1998, ''A Study of Spike and Modal Stall Phenomena in a Low-Speed Axial Compressor,'' ASME J. Turbomach., **120**, pp. 393–401.
[2] Mathioudakis, K., and Breugelmans, F. A. E., 1985, ''Development of Small Rotating Stall in a Single Stage Axial Compressor,'' ASME paper 85-GT-227.
[3] Mongeau, L., 1991, ''Experimental Study of the Mechanism of Sound Generation by Rotating Stall in Centrifugal Turbomachines,'' Ph.D. dissertation, Pennsylvania State University.
[4] Bent, P. H., McLaughlin, D. K., and Thompson, D. E., 1992, ''The Influence of Discharge Configuration on the Generation of Broadband Noise in Centrifugal Turbomachinery,'' 14th Aeroacoustics Conference, May 11–14, 1992, Aachen, Germany, DGLR/AIAA 92-02-099.
[5] Mongeau, L., and Quinlan, D. A., 1992, ''An Experimental Study of Broadband Noise Sources in Small Axial Fans,'' International Symposium on Fan Noise INCE, Senlis, France, Sept. 1–3, 1992.
[6] Kameier, F., 1994, ''Experimentelle Untersuchung zur Entstehung und Minderung des Blattspitzen-Wirbelárms axialer Strömungsmaschinen,'' Fortschritt-Berichte VDI Reihe 7 Nr. 243 Düsseldorf, Germany.
[7] Krane, M. H., Bent, B. H., and Quinlan, D. A., 1995, ''Rotating Instability Waves as a Noise Source in a Ducted Axial Fan,'' ASME Winter Annual Meeting, Turbomachinery Noise Symposium, San Francisco.
[8] Kameier, F., and Neise, W., 1997, ''Experimental Study of Tip Clearance Losses and Noise Generation in Axial Turbomachines and Their Reduction,'' ASME J. Turbomach., **119**, pp. 460–471.
[9] März, J., Neuhaus, L., Neise, W., and Gui, X., 1998, ''Circumferential Structure of Rotating Instability under Variation of Flow Rate and Solidity,'' VDI-Tagung: Turbokompressoren im industriellen Einsatz, Oct. 6–7, Hannover, Germany.
[10] Baumgartner, M., Kameier, F., and Hourmouziadis, J., 1995, ''Non-Engine Order Blade Vibration in a High Pressure Compressor,'' 12th International Symposium on Airbreathing Engines, Sept. 10–15, Melbourne, Australia.
[11] Witte, H., and Ziegenhagen, S., 1998, ''Beurteilung von strömungserregten Schaufelschwingungen eines Flugtriebwerks-Axialverdichters mittels statistischer Analysemethoden,'' VDI-Tagung: Turbokompressoren im industriellen Einsatz, Oct. 6–7, Hannover, Germany.
[12] Hoying, D. A., Tan, C. S., Huu Duc Vo, and Greitzer, E. M., 1998, ''Role of Blade Passage Flow Structures in Axial Compressor Rotating Stall Inception,'' ASME paper 98-GT-588.
[13] Inoue, M., Kuroumaru, M., Tanino, T., and Furukawa, M., 1999, ''Propagation of Multiple Short Length-Scale Stall Cells in an Axial Compressor Rotor.'' ASME paper 99-GT-97.
[14] Boos, P., Möckel, H., Henne, J. M., and Selmeier, R., 1996, ''Flow Measurement in a Multistage Large Scale Low Speed Axial Flow Research Compressor,'' Proceedings of the 43rd Gasturbine & Aeroengine Technical Congress, Exposition and Users Symposium, June 2–5, Stockholm, Sweden.
[15] Müller, R., Mailach, R., Lehmann, I., and Sauer, H., 1999, ''Flow Phenomena Inside the Rotor Blade Passages of Axial Compressors,'' AIAA99-IS-084, 14th International Symposium on Airbreathing Engines, Sept. 6–10, Florence, Italy.
[16] Mailach, R., 1999, ''Experimental Investigation of Rotating Instabilities in a Low-Speed Research Compressor,'' 3rd European Conference on Turbomachinery—Fluid Dynamics and Thermodynamics, March 2–5, London, GB.
[17] Mailach, R., 1999, ''Früherkennung rotierender Instabilitäten,'' Abschlußbericht zum BMBF-Vorhaben 0327041L, July 1999, Dresden, Germany.
[18] Inoue, M., Kuroumaru, M., 1989, ''The Structure of Tip Clearance Flow in an Isolated Axial Compressor Rotor,'' ASME J. Turbomach., **111**, pp. 250–256.
[19] Saathoff, H., and Stark, U., 1998, ''Endwall Boundary Layer Separation in a High-Stagger Compressor Cascade and a Single-Stage Axial-Flow Low-Speed Compressor,'' 11. DGLR-Fach-Symposium, Strömungen mit Ablösung, Nov. 10–12, Berlin, Germany.

Discussion: ''Rotating Instabilities in an Axial Compressor Originating From the Fluctuating Blade Tip Vortex'' (Mailach, R., Lehmann, I., and Vogeler, K., 2001, ASME J. Turbomach., 123, No. 3, pp. 453–460)

N. A. Cumpsty
Rolls-Royce plc, P.O. Box 31, Derby DE24 8BJ, United Kingdom

It is very welcome to see papers appearing with results obtained on the superb compressor facility in the Technical University of Dresden. One feels confident that these have been obtained to the highest standards in a machine that models the flow in high-performance compressors.

I am less happy about some aspects of the paper. I believe that the phenomenon that is the basis of this paper, which the authors call ''rotating instability,'' is part-span rotating stall. This phenomenon is very common in high-speed multistage axial compressors in which the front stages quite normally go into a multicell, part-scan rotating stall when the machine is operating at speeds below the design value. This phenomenon was described in some detail in the famous NACA report ''The Aerodynamic Design of Axial Flow Compressors,'' first published in 1956 [1]. The present authors are quite mistaken to say that this unsteady flow phenomenon was first described by Mathiodakis and Breugelmans in 1985 [2]; indeed these authors referred to the phenomena they saw as rotating stall, either small stall or big stall.

The particular flow that the authors have investigated is the mismatched stage in a multistage compressor. It seems probable to me that over a narrow range of flow coefficients their third stage stalls, since the tip clearance for this stage is larger than the others, but the other three stages maintain the whole machine stable. What results is a part-span rotating stall in the third stage. A very similar flow was investigated by Silkowski [3], who increased the tip clearance of the first stage, so for his tests it was the first stage that was entered into part-span rotating stall. There are particular reasons why the stall of a single stage in a multistage compressor is likely to be both multicell and part span. By having a relatively large number of stall cells, there can be rapid decay in the axial direction, which is necessary since the adjoining stages are unstalled. The part-span nature of the stall allows some axial flow through the blades that are stalled at the tip so that the stages upstream and downstream can be unstalled at the same circumferential position. This makes possible the close proximity of stalled and unstalled stages at the same circumferential position. To be more definite about what was going on when operating in the condition the authors refer to as ''rotating instability,'' one needs to see the raw data (i.e., signals showing, as a function of time, the wall static pressure signals, or the upstream and downstream velocities). The processing to give Figs. 5, 6, and 7 in the paper necessarily gets rid of important information that might clarify what the phenomenon.

The authors make a number of definite statements and conclusions regarding the role of the tip vortex and its part in the ''rotating instability.'' I would prefer that these were seen as highly tentative hypotheses for the behavior, since they are based on inference rather than direct observation. It is well known that increasing rotor tip clearance increases the flow across the tip and (beyond a very small minimum clearance) reduces pressure rise and efficiency. It is less clear that the clearance flow forms a well-defined vortex; what appears to matter most is the formation of flow blockage, with the consequent reduction in static pressure rise. The existence of flow close to the wall flowing in the reverse direction over the rotor tips is a real effect and the first published example that I know was by Koch [4].

One of the most confusing features of the paper, including its title, is the term ''rotating instability,'' which appears to have been coined relatively recently by Kameier [5]. I am confident that what has been investigated is fully developed (i.e., steady) rotating stall with multiple part-span cells. One of the features of rotating stall, whether it is part span or full span, is its stability; indeed sometimes it can be hard to get a compressor out of rotating stall. A compressor operating in stall can be stable, but on opening the throttle the compressor will become eventually become unstable in the stalled condition and it will then change to become unstalled. The use of the words ''rotating instability'' to denote ''rotating stall'' is unfortunate and its use can only lead to confusion where none is necessary. (It may also be added that the term itself is without meaning; it is applied to a nominally steady process, yet the word ''instability'' implies that it is in the process of change from one state to another.)

The paper refers back to the original work by Kameier, which was performed on a single stage fan. Single-stage compressors have a tendency to go into part-span, multicell stall; see Day [6]. At design speed the well-matched multistage machine tends to go into full-span stall with a very small number of stall cells, most often only a single cell, extending the whole length of the compressor. Only when the multistage machine is mismatched (either because its speed is below design or because of geometric changes) does a multicell, part-span stall occur.

References

[1] NACA, 1956, ''The Aerodynamic Design of Axial Flow Compressors,'' NACA TN 3662.
[2] Mathioudakis and Breugelmans, 1985.
[3] Silkowski, 1995.
[4] Koch, C. C., 1975.
[5] Kameier, 1994.
[6] Day, I. J., 1976, ''Axial Compressor Stall,'' PhD Dissertation, University of Cambridge, United Kingdom.

Closure to ''Discussion of 'Rotating Instabilities in an Axial Compressor Originating from the Fluctuating Blade Tip Vortex' (2000-GT-506)'' (2001, ASME J. Turbomach., 123, p. 461)

Konrad Vogeler, Ronald Mailach, and Ingolf Lehmann
Dresden University of Technology,
Institute for Fluid Mechanics, 01062 Dresden, Germany

The authors thank Prof. Cumpsty for his critical comments. After the discussion in Munich (ASME Turbo Expo 2000), it is disappointing that a major part of this comment still focuses on the chosen term ''rotating instability'' (RI). It is understood that a common term for a certain effect is needed in order to ensure efficient communication. This is the reason the authors used the questioned term, as it was already in use (''coined'') by several investigators to name the observed characteristic flow unsteadiness.

The authors agree that there might be better names for this effect. They do not agree that the term ''rotating instability'' is

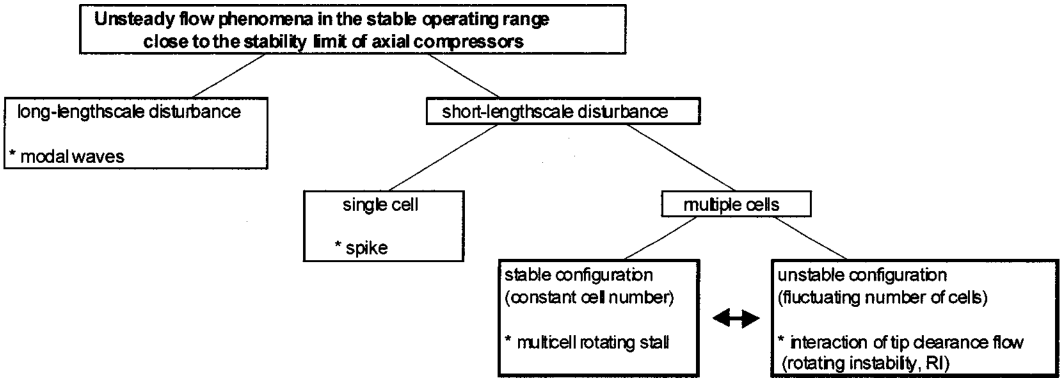

Fig. 1 Overview of the main unsteady flow phenomena in the stable operating range close to the stability limit of axial compressors

totally wrong. They are still convinced that the physics of the observed flow unsteadiness is different from the typical part-span rotating stall caused by overloaded blades.

Figure 1 shows the classification of different flow effects that can be observed close to the stability limit of a compressor. In addition to modal waves and spikes, multicell disturbances can appear. It is well known that part-span multicell disturbances occur in the front stages of multistage compressors at speeds below the design speed while the compressor works well. In multistage low-speed compressors, this normally does not take place as all stages are loaded nearly equally. In this case, multicell disturbances can be found only in mismatched stages. This could be a single mis-staggered blade row or a single blade row with larger tip clearance. Increasing the tip clearance of one rotor blade row was our way to excite a part-span multicell disturbance in the four-stage low-speed research compressor of Dresden (Dresden LSRC). The reason for this was the assumption that the observed unsteady characteristic of the RI has its driving force in the physics of the tip vortex.

Nevertheless, the authors propose to distinguish between stable and unstable multicell configurations. Although this classification cannot be found in the literature, it is thought to be necessary because of the different behavior of the cells and presumably different origination mechanisms of the disturbances.

A stable configuration is characterized by a constant number and a nearly constant size of the rotating cells. This stable multicell configuration is commonly known as multicell rotating stall. It was reported by Day et al. [1] and Inoue et al. [2]. In a pressure or velocity signal versus time, one can observe nearly equal time intervals between consecutive passing cells (e.g., Day et al. [1], Fig. 14). In the frequency spectrum of this signal the disturbance is reflected by a discrete peak.

The multicell configurations are truly unstable if their numbers and size of cells are strongly fluctuating. The phenomenon observed in the Dresden LSRC has this unstable characteristic. The term ''rotating instability'' was taken from an ongoing discussion in the literature to avoid confusion with stable unsteady stall phenomena. To the knowledge of the authors, the first description of this unstable, unsteady behavior of a multicell disturbance is reported by Mathioudakis and Breugelmans [3] in a single-stage compressor. However, at that time they used another term for it (''small rotating stall''). Unstable behavior in multistage compressors is also reported by Longley and Hynes [4], who used the name ''rough running'' and Baumgartner et al. [5], who termed it ''rotating instability.''

Professor Cumpsty claims that information is lost due to the postprocessing used. The authors do not believe that this is the case. Figure 2 shows raw data from a sensor positioned close to the tip. Very strong nonperiodic fluctuations of the pressure signals due to RI occur. Some periodicity can be observed but is not dominating. This is where the observed flow shows its unstable behavior.

Much additional information can be obtained when the analysis of the raw signals is coupled with filtering of the time-dependent signals and statistical evaluation methods like autopower and cross-power spectra. This allows us to isolate the information on the disturbance in which we are interested from the influence of wake passages and from other disturbances like modal waves.

The time-dependent fluctuations of the amplitudes, frequency,

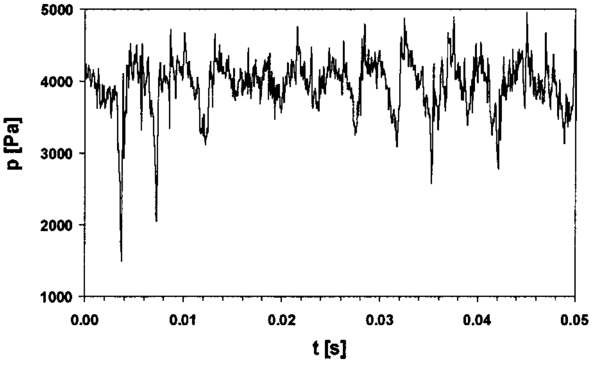

Fig. 2 Signal of a pressure sensor on a rotor blade, sensor near blade tip (92 percent of channel height) and leading edge (10 percent of chord length), operating point near stability limit (design speed, $\xi=0.82$), tip clearance ratio $s^*=4.3$ percent

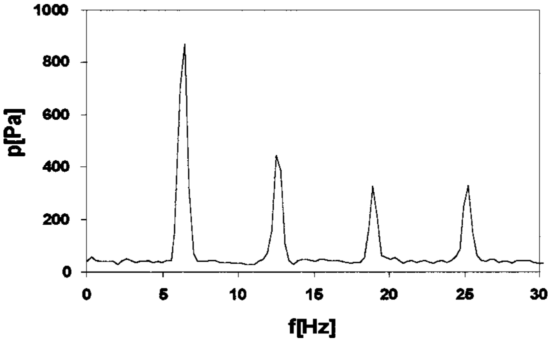

Fig. 3 Frequency spectrum with typical sign of a single-cell full-span rotating stall in Dresden LSRC (measured at the casing)

and wavelength of the disturbance can clearly be seen in Fig. 6 of the paper. These signals are bandpass-filtered to get rid of the influence of modal waves and passing wakes.

The time-averaged results of the statistical evaluation methods confirm the unstable behavior. It can be seen that many frequencies as well as mode orders (respectively cell numbers) of the disturbance are present (Figs. 5 and 7 in the paper). This typical behavior was also shown by other authors (e.g., Kameier [6]). Contrary to that a stable single-cell or multicell rotating stall, with its stable number of cells and constant circumferential velocity, would be recognized by a dominating discrete peak and possibly its harmonics in the frequency spectrum (Fig. 3).

From Fig. 7 of the discussed paper it follows, that the wavelength, that is, the distance between adjacent cells, varies from 1.5 to 5.0 pitches of the rotor blades (63 rotor blades). (In the model presented in Fig. 24 in the paper only the dominating wavelength of 2.0 pitches is considered.) Hence the disturbance is far from being stable. It is not a frozen rotating pattern but changes permanently. Because of this, the term ‘‘rotating instability’’ is absolutely correct for this disturbance. However, Prof. Cumpsty is correct in this point, the compressor unit is running stable.

Additional remark: The strong fluctuations of the disturbance, which were investigated in the third stage of the Dresden LSRC, are not caused by the passing blade wakes and the high turbulence of the flow. This is shown in the recent investigations of Mailach et al. [7] in a plane cascade. Even in a plane cascade, this disturbance propagates along the tip region of the blade row. In spite of the low turbulence intensity of the incoming flow and without passing wakes, the wavelength of the short-length-scale disturbance is strongly fluctuating. Of course we cannot talk about a ‘‘rotating’’ instability in the plane cascade anymore. But the mechanism of the disturbance, which propagates along a blade row, is the same.

It is the tip clearance flow that is responsible for the characteristic of this kind of disturbance. There is no doubt that it results in a strong tip vortex. This can clearly be seen from the results of LDA measurements for the design tip clearance ratio of 1.3 percent (Figs. 12 and 13 in the paper). As shown in the discussed paper, for larger tip clearance ratios, the tip vortex fluctuates strongly. Due to the ensemble-averaging, its structure is less pronounced in the results of the LDA measurements (Figs. 15–18 in the paper).

Both for the stable multicell configuration (Inoue et al. [2]) and—as shown in this paper—for the unstable multicell configuration, the tip clearance flow is responsible for the resulting disturbance. As shown in this paper, the axial reversed flow only occurs within the tip clearance and causes a reduction or a blockage of the incoming flow in the blade tip region. It is the opinion of the authors that this is definitely not a classical stall, even if we observe reversed flow within the tip clearance with influence into the outer blade passage.

It is agreed by the authors that the term ‘‘rotating instabilities’’ could be substituted by a more precise one. We did agree on that already in Munich. But considering the above said, it is definitely not wrong. However, in order to avoid confusion with stalled blades due to separated flow on the profiles, one can discuss whether the expression ‘‘stall’’ should be used in the eventually improved term at all. In the opinion of the authors a term like ‘‘propagating tip vortex instability’’ (‘‘rotating tip vortex instability,’’ ‘‘interaction of tip clearance flow’’ . . .) would be more suitable, since it applies more specifically to the physical mechanism of the disturbance, described in the discussed paper.

References

[1] Day, I. J., Breuer, T., Escuret, J., Cherett, M., and Wilson, A., 1999, ‘‘Stall Inception and the Prospects for Active Control in Four High-Speed Compressors,’’ ASME J. Turbomach., **121**, pp. 18–27.

[2] Inoue, M., Kuroumaru, M., Tanino, T., and Furukawa, M., 2000, ‘‘Propagation of Multiple Short Length-Scale Stall Cells in an Axial Compressor Rotor,’’ ASME J. Turbomach., **122**, pp. 45–53.

[3] Mathioudakis, K., and Breugelmans, F. A. E., 1985, ‘‘Development of Small Rotating Stall in a Single Stage Axial Compressor,’’ ASME Paper No. 85-GT-227.

[4] Longley, J. P., and Hynes, T. P., 1990, ‘‘Stability of Flow Through Multistage Axial Compressors,’’ ASME J. Turbomach., **112**, pp. 126–132.

[5] Baumgartner, M., Kameier, F., and Hourmouziadis, J., 1995, ‘‘Non-Engine Order Blade Vibration in a High Pressure Compressor,’’ Proc. 12th International Symposium on Airbreathing Engines, Sept. 10–15, Melbourne, Australia.

[6] Kameier, F., 1994, ‘‘Experimentelle Untersuchung zur Entstehung und Minderung des Blattspitzen-Wirbellärms axialer Strömungsmaschinen,’’ Fortschritt-Berichte VDI Reihe 7 No. 243, Düsseldorf, Germany.

[7] Mailach, R., Sauer, H., and Vogeler, K., 2001, ‘‘The Periodical Interaction of the Tip Clearance Flow in the Blade Rows of Axial Compressors,’’ ASME Paper No. 2001-GT-0299.

Tip Clearance Actuation With Magnetic Bearings for High-Speed Compressor Stall Control

Z. S. Spakovszky

J. D. Paduano

Gas Turbine Laboratory,
Department of Aeronautics and Astronautics,
Massachusetts Institute of Technology,
Cambridge, MA 02139

R. Larsonneur

A. Traxler

MECOS Traxler AG,
Winterthur, CH 8404,
Switzerland

M. M. Bright

NASA Glenn Research Center,
Cleveland, OH 44135

Magnetic bearings are widely used as active suspension devices in rotating machinery, mainly for active vibration control purposes. The concept of active tip-clearance control suggests a new application of magnetic bearings as servo-actuators to stabilize rotating stall in axial compressors. This paper presents a first-of-a-kind feasibility study of an active stall control experiment with a magnetic bearing servo-actuator in the NASA Glenn high-speed single-stage compressor test facility. Together with CFD and experimental data a two-dimensional, incompressible compressor stability model was used in a stochastic estimation and control analysis to determine the required magnetic bearing performance for compressor stall control. The resulting requirements introduced new challenges to the magnetic bearing actuator design. A magnetic bearing servo-actuator was designed that fulfilled the performance specifications. Control laws were then developed to stabilize the compressor shaft. In a second control loop, a constant gain controller was implemented to stabilize rotating stall. A detailed closed loop simulation at 100 percent corrected design speed resulted in a 2.3 percent reduction of stalling mass flow, which is comparable to results obtained in the same compressor by Weigl et al. (1998. ASME J. Turbomach. ***120****, 625–636) using unsteady air injection. The design and simulation results presented here establish the viability of magnetic bearings for stall control in aeroengine high-speed compressors. Furthermore, the paper outlines a general design procedure to develop magnetic bearing servo-actuators for high-speed turbomachinery.*

[DOI: 10.1115/1.1370163]

1 Introduction

The stable operation of axial flow compressors, as they are encountered in modern jet engines and gas turbines, is often limited by two flow breakdown processes known as surge and rotating stall. Surge is a circumferentially uniform pulsation of the mass flow through the machine, while rotating stall appears as a reduced flow region in part of the circumference, which travels around the compressor annulus at a fraction of rotor speed. Active control of rotating stall was first proposed by Epstein et al. [1] and since then a significant amount of further research has been done. In particular, theoretical and experimental investigations have been conducted at the NASA Glenn Research Center on a single-stage transonic core compressor inlet stage. Active stabilization of rotating stall and surge using unsteady air injection was first presented by Weigl et al. [2] in the NASA high-speed stage. The experiments showed a significant benefit in stable operating range.

Blade tip clearance in axial flow compressors is known to have a strong impact on compressor performance and stability; it also plays a major role in the interaction between rotordynamic shaft deflections and the aerodynamic behavior of the compressor. Graf et al. [3] report an experimental and analytical investigation of circumferentially nonuniform tip-clearance effects on axial compressor stability and performance. The study reveals that the compressor prestall dynamics are very sensitive to the blade tip clearance. Based on this conceptual framework Gordon [4] extended this approach to analyze the influence of rotating clearance asymmetries. The work presented here uses a modified version of this compressor model and introduces the concept of tip-clearance actuation for compressor stall control.

Magnetic bearings are widely used as active suspension devices in rotating machinery, mainly for active vibration control purposes. The concept of active tip-clearance control suggests a new application of magnetic bearings as servo-actuators to stabilize rotating stall in axial compressors. The magnetic bearing servo-actuator is used to *actively* whirl the shaft, inducing an unsteady variation of the rotor blade tip-clearance distribution as shown in Fig. 1.

This paper presents a feasibility study and the design of a stall control experiment on a transonic compressor stage. The following research questions are of interest and are addressed in this paper.

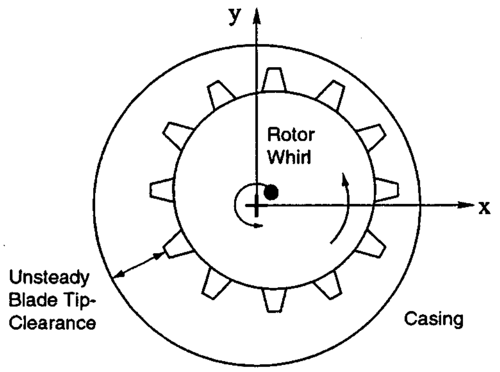

Fig. 1 Active tip-clearance stall control concept

Contributed by the International Gas Turbine Institute and presented at the 45th Internataional Gas Turbine and Aeroengine Congress and Exhibition, Munich, Germany, May 8–11, 2000. Manuscript received by the International Gas Turbine Institute February 2000. Paper No. 2000-GT-528. Review Chair: D. Ballal.

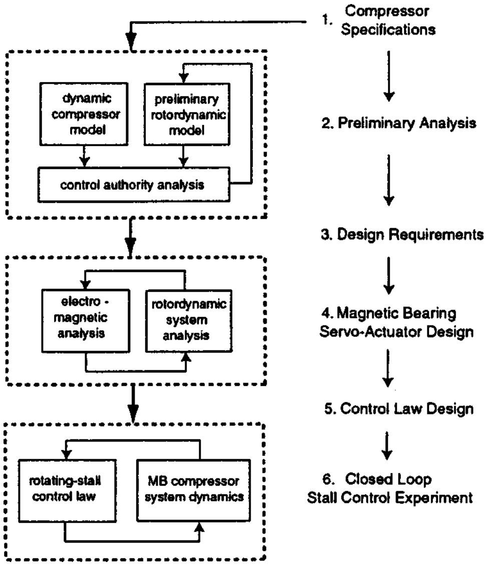

Fig. 2 Design process for an axial compressor magnetic bearing system

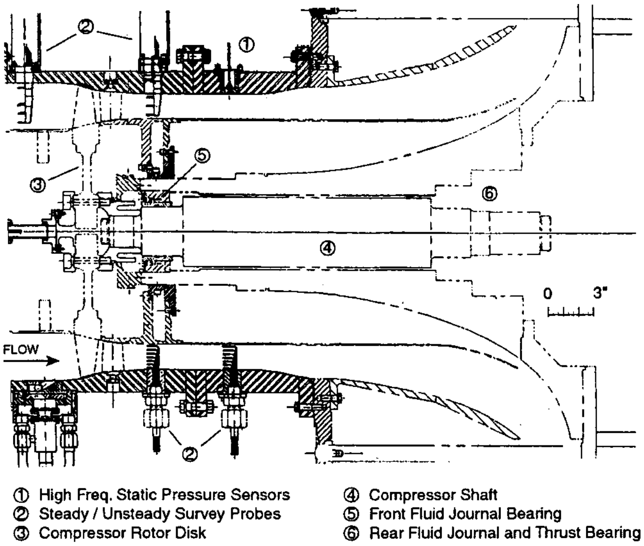

Fig. 3 NASA Glenn high-speed single-stage compressor test facility

- How does a magnetic bearing servo-actuator for stall control differ from conventional magnetic levitation devices?
- How much control authority and shaft motion is required to stabilize rotating stall?
- How beneficial is tip-clearance actuation compared to unsteady air injection and other actuation schemes?
- What analytical process has to be conducted in order to design a stall control experiment with magnetic bearings?

The organization of the paper is briefly outlined to guide the reader through the design process. The general sequence of steps involved in the analysis and design of an axial compressor magnetic bearing system is depicted in Fig. 2. First, in Sec. 2, the axial flow compressor specifications and the test facility envelope are discussed. Then in Sec. 3 an unsteady compressor tip-clearance model and a simple, first-cut rotordynamic model of the compressor system are implemented in a preliminary analysis to determine the control authority and the design requirements, which are discussed in Sec. 4. The detailed design of the magnetic bearing servo-actuator and rotor system is outlined in Sec. 5, and the final closed loop system simulation results are presented in Sec. 6.

The above design process is implemented in an example analysis for the NASA Glenn high-speed single-stage axial flow compressor and results specific to this compressor are reported in this paper.

2 Axial Compressor Rig Specifications

The NASA Stage 37 test compressor, originally designed as an inlet stage of an eight-stage 20:1 pressure ratio core compressor [5], has a total pressure ratio of 2.05, a mass flow of 20.2 kg/s, a rotor tip speed of 454 m/s, and a rotation frequency of 286 Hz at design conditions. Rotor 37 consists of 36 blades with an aspect ratio of 1.19, a hub-to-tip radius ratio of 0.7, and a blade tip diameter of approximately 50 cm. The mean-line rotor chord length is 56 mm. Detailed performance descriptions are given by Reid and Moore [6].

Atmospheric air is drawn into the test facility through an orifice plate and a plenum chamber upstream of the test section. Downstream of the compressor the flow is regulated with a sleeve-type throttle valve and the compressor shaft is coupled over a drive train to a 2.2 MW DC drive motor. The shaft setup of the test compressor is an overhung rotor with radial fluid film bearings at the front (near the rotor disk) and at the back of the compressor (near the motor drive coupling) as well as a fluid film thrust bearing on the motor coupling side. A schematic of the test section and the compressor shaft is shown in Fig. 3.

In this specific case it is desired to limit modifications to the compressor test rig as much as possible. The rear fluid film journal and thrust bearings must be kept the same to mate with the existing motor drive train. The front fluid film journal bearing is to be replaced by the magnetic bearing servo-actuator. Fail-safe operation of the magnetic bearing is compulsory and a special catcher bearing system is to be designed. Also the compressor gas path must remain the same to yield an unchanged aerodynamic compressor performance.

3 Preliminary Analysis

The effect of tip-clearance asymmetries due to shaft deflections on compressor performance and stability is addressed next. The objective of the preliminary analysis is to determine the magnetic bearing force bandwidth and the stall control authority required to conduct rotating stall control with tip-clearance actuation. The specific question is: how much shaft motion and magnetic bearing force is required to stabilize rotating stall? To answer this question a simplified rotordynamic design analysis and a unique stochastic estimation and control analysis are conducted.

3.1 Simplified Rotordynamic Design and Analysis. A preliminary design of the magnetic bearing rotor is suggested in Fig. 4. The solid shaft in Fig. 3 is replaced by a hollow shaft including the magnetic bearing rotor laminations. The shaft is pinned at the rear (journal and thrust fluid film bearings) and coupled to the motor drive train. Typical catcher bearing designs do not contact the shaft during magnetic bearing suspension. However for the proposed stall experiments in the NASA high-speed test facility, a fail-safe suspension system is mandatory. In particular, the compressor blades must be protected from possible blade-tip rubs; destructive impacts must also be avoided in the case of a loss of magnetic levitation. A possible failsafe solution is to use a spring loaded catcher bearing that is always in contact with the shaft. This is the approach adopted for the design analysis.

In the general case of free-free magnetic suspension a simple, single lumped mass analysis is sufficient to obtain a first-cut estimate of the required magnetic force. Since in this magnetic bearing application shaft motion is constrained at both ends (soft

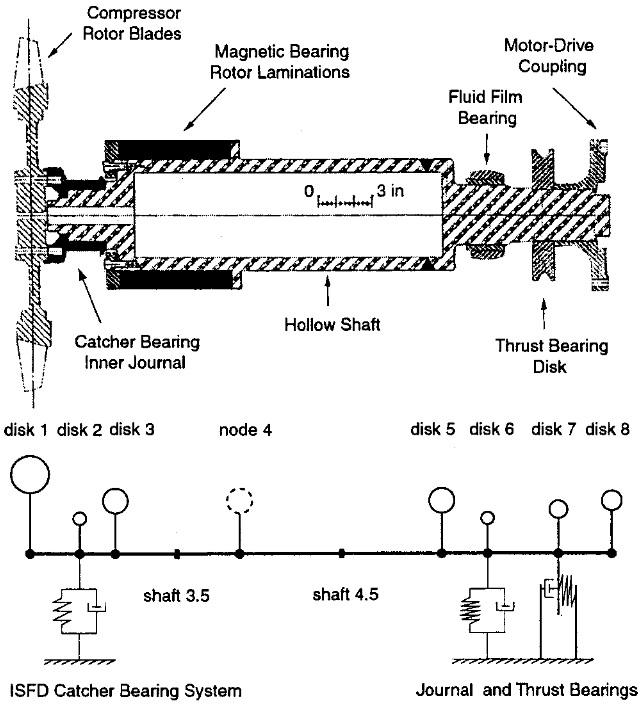

Fig. 4 Preliminary magnetic bearing compressor rotor and corresponding lumped parameter model

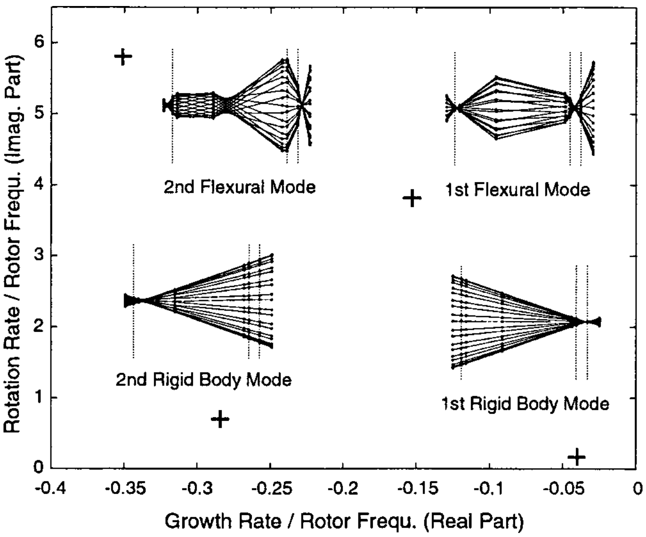

Fig. 5 Preliminary open loop rotor model eigenvalues and mode shapes

spring loaded catcher bearing support at the front and conventional fluid film bearings at the rear) the rotordynamic analysis needs to be more detailed.

Therefore in this preliminary design analysis a simple, direct stiffness lumped parameter method (described in [7]) is conducted. The rotor model consists of thin rigid disk elements (lumped masses) connected either by massless flexible beam elements or by flexible uniform shaft elements (distributed mass) as depicted in Fig. 4. The overall mass of the shaft is 128.5 kg. Each disk element has four degrees of freedom: two displacement directions normal to the axis of rotation and small angle rotations about the spin axis (precession and nutation). Axial motion is neglected but the fluid film thrust bearing constrains the shaft in angular deflections at the rear and is modeled as an angular spring and an angular damper. The rear journal bearing and the soft spring loaded catcher bearing are modeled as spring and damper elements. For a closed loop analysis[1] the magnetic bearing force can be introduced at node points 3 and 4.

The catcher bearing system for this nonstandard high-speed application is suggested to consist of a fluid film journal bearing embedded in a soft spring loaded support. This allows for shaft deflections but still yields a hard stop in case of an emergency. To ensure safe transient operation without large vibrations when critical frequencies are crossed during an emergency shut down, damping must be added in parallel to the soft spring loaded support. One possible, compact solution is an integral squeeze film damper (ISFD) setup as reported by Santiago et al. [8]. ISFD's are comprised of arcuate squeeze film pads rendering viscoelastic support and wire-electrical discharge machined webs acting like a squirrel cage.

The open loop whirl speeds, natural frequencies and mode shapes are obtained from an eigenvalue problem resulting from the equations of motion. Assuming that the rotor is spinning at design speed (286 Hz) the first four eigenvalues are plotted in Fig. 5 and the mode shapes are reconstructed from the corresponding eigenvectors. The forward whirling modes are marked with pluses and the bearing locations (nodes 2, 6, and 7 in Fig. 4) are indicated by the dotted lines. The preliminary hollow shaft design yields two conical modes, denoted as the first and second rigid body modes, which rotate at 0.16 and 0.7 times the rotor frequency, and two flexural modes. The rotation rates of the flexural modes are well above the operating range but note that the first flexural mode is less damped than the second rigid body mode.

This preliminary shaft setup conforms well with the design issues for active tip-clearance control. The magnetic bearing rotor is rigid with a dominant conical rigid body mode at a natural frequency of 0.16 times rotor frequency. The low rotation rate of this first rigid body mode is due to the softly supported catcher bearing system (ISFD). None of the open loop rotordynamic modes are in the vicinity of flow field resonances such as rotating stall, which for this compressor rotates at 0.4 times the rotor frequency. This is a crucial constraint on the rotordynamic design to avoid direct interaction between the compressor prestall dynamics and the structural dynamics. Note that the suggested magnetic bearing rotor yields supercritical operation with respect to the rigid body modes.

In order to obtain an estimate of the required force (introduced by the magnetic bearing) for a certain blade tip deflection, the open loop transfer function from magnetic bearing force input to blade tip deflection is computed and shown in Fig. 6. However, the necessary blade tip deflection for rotating stall control still needs to be determined. This is the key analysis in the preliminary design process and is discussed next.

3.2 Analysis of Tip-Clearance Control Authority. In order to determine the effective shaft motion (i.e., blade tip deflection) for rotating stall control the closed loop system depicted in Fig. 7 is considered. The compressor prestall dynamics are denoted by the transfer function $\mathbf{G}(s)$. The outputs of $\mathbf{G}(s)$ are the prestall pressure perturbations sensed upstream of the rotor $\delta p(t)$, which are fed back to the rotating stall feedback controller $\mathbf{K}(s)$. The controller outputs are the actuator commands $\delta c(t)$, which are modified by the magnetic bearing servo-actuator dynamics $\mathbf{A}_{\mathrm{MB}}(s)$ to yield the actual shaft position and the corresponding tip-clearance distribution $\delta\epsilon(t)$. The open loop stable magnetic bearing servo-actuator dynamics $\mathbf{A}_{\mathrm{MB}}(s)$ consist of the shaft rotordynamics and the magnetic bearing servo control loop. The inputs to the compressor prestall transfer function $\mathbf{G}(s)$ are the tip-clearance distribution $\delta\epsilon(t)$ and background noise modeled by unsteady velocity fluctuations $\delta w(t)$. The actuator dynamics

---

[1] Note that the rotor system is open loop stable and that the magnetic bearing is primarily used as a servo-actuator.

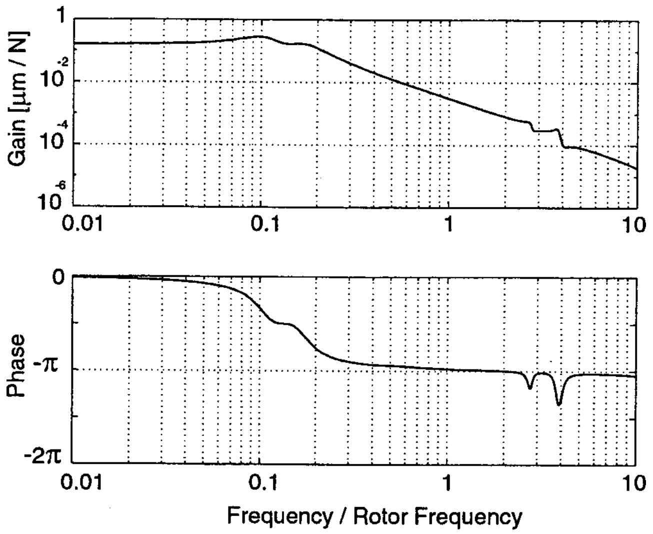

Fig. 6 Transfer function from magnetic bearing force input [N] to blade tip deflection [μm]

$\mathbf{A}_{\mathrm{MB}}(s)$ and the compressor tip-clearance transfer function $\mathbf{G}(s)$ form the plant $\mathbf{P}(s)$, which will be considered in the rotating stall control law design process. Note that this feedback control system is a *regulator* system since the error signal $\delta e(t)$ is composed only of the sensed pressure perturbations. The purpose of the regulator is to drive the pressure perturbations to zero, even if the plant is unstable.

The objective of this analysis is to determine the required closed loop shaft motion $\delta\epsilon(t)$ to stabilize rotating stall. Since the feedback system is highly resonant and in a noisy environment, the compressor dynamics must be included in the analysis. A stochastic estimation approach is then applied.

Compressor Dynamics With Tip-Clearance Effect. To investigate the effect of blade tip deflection on compressor stability, the compressor prestall dynamics $\mathbf{G}(s)$ need to be modeled. Based on the conceptual framework developed by Hynes and Greitzer [9], Graf et al. [3], and Gordon [4] (see Sec. 1) a two-dimensional, incompressible, state-space compressor model actuated by rotor tip clearance was created. The derivation of the compressor model equations (see [4]) is omitted here and a short model description is given instead.

The overall modeling approach [10] consists of incompressible models of the inlet and exit ducts, the blade rows, the downstream plenum, and the throttle. The hub-to-tip ratio is assumed high so that the model is two-dimensional with axial and circumferential unsteady flow field variations. The rotor and stator blade rows are modeled as semiactuator disks with unsteady inertia, unsteady deviation, and loss terms. The model assumes that the background flow is steady in the reference frame locked to the (rotating) tip-clearance asymmetry so that any tip-clearance distribution (unsteady in the absolute frame) can be prescribed. In a first step the steady, fully nonlinear flow field equations are solved in the asymmetry frame to obtain the nonuniform background flow [9]. In a second step a linearized version of the model equations is solved to obtain the behavior of unsteady, small amplitude perturbations to the known steady state nonuniform flow field. Assigning control inputs and outputs to the model and identifying states in the resulting dynamic equations yields a state-space formulation of the compressor model [4].

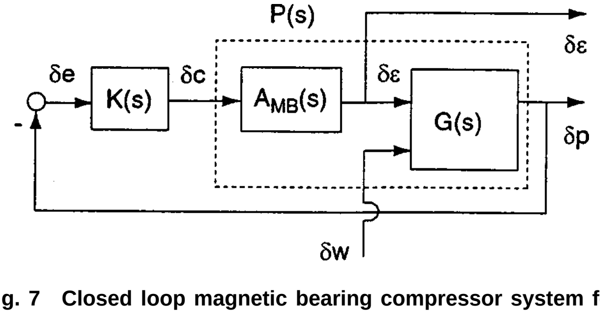

Fig. 7 Closed loop magnetic bearing compressor system for stall control

The compressor model by Gordon [4] was modified to include unsteady air injection in addition to tip-clearance actuation. Air injection was used in stall control experiments by Weigl et al. [2] in the same compressor. This modified compressor model will be useful to match the modeled compressor dynamics to the experimental data by Weigl et al. [2] and to verify the control authority analysis in a test case for jet injection.

The inputs to the model are the compressor geometry, an axisymmetric tip clearance compressor characteristic, and the sensitivity of the compressor characteristic to changes in axisymmetric tip clearance. These inputs were based on CFD calculations of the NASA Stage 37 compressor performance. The APNASA blade passage code by Adamczyk et al. [11] was used to calculate the three-dimensional, viscous flow through the stage for different levels of axisymmetric tip clearance. In addition, the modeled compressor dynamics were compared to the experimentally obtained system identification results by Weigl et al. [2]. The dynamic model parameters, i.e., loss time lags and system reduced frequency, were adjusted to match the open loop and closed loop compression system poles to the measured eigenvalues. This gives confidence in using the tip-clearance actuated compressor model in the stochastic estimation analysis.

Stochastic Estimation of Closed Loop Shaft Motion. The system input noise $\delta w(t)$ is modeled as white noise of intensity W, which is determined by comparing the spectrum $\Phi_{pp}(\omega)$ of the sensed prestall pressure perturbations $\delta p(t)$ obtained from the experiment [2] to the spectrum of the open loop model transfer function $\mathbf{G}(j\omega)$:

$$\Phi_{pp}(\omega)=\mathbf{G}(j\omega)\mathbf{G}^{T}(j\omega)W. \tag{1}$$

The white noise intensity W is adjusted to match both the peak and the RMS values of the measured and modeled spectra for a compressor operating point that is close to stall. This is shown in Fig. 8. Note that the compression system is highly resonant and exhibits a sharp peak in the spectrum at a frequency of about 0.4 times the rotor frequency. This resonance of the flow field corresponds to a rotating stall precursor.

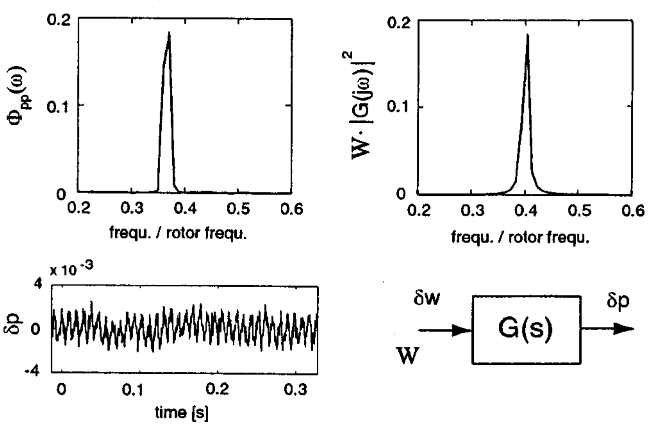

Fig. 8 Spectral analysis of open loop prestall pressure perturbations (experiment by Weigl et al. [2]) and of open loop compressor model

A closed loop analysis is conducted next. The circumferentially sensed pressure perturbations are decomposed into circumferential spatial Fourier harmonics. The prestall mode with first-harmonic circumferential structure is linearly controllable with tip-clearance actuation (if the rotor is offset from its casing a first-harmonic tip-clearance distribution is induced) and all other harmonics are linearly uncontrollable. To simplify the analysis only first-harmonic linear control with tip-clearance actuation is considered here. Additional unsteady injection is implemented in this case to stabilize the zeroth-harmonic (surgelike) mode. In general nonlinear control laws can be used to stabilize the zeroth- and second-harmonic modes with tip-clearance actuation as discussed in [12]. Such control schemes, however, will yield further bandwidth and magnetic force requirements.

A simple constant gain control strategy is implemented for $\mathbf{K}(s)$ to stabilize the compressor dynamics. The idea behind constant gain control is as follows. The sensed spatial harmonic waves of the pressure perturbations $\delta p(t)$ are rotated by an optimized angle and multiplied by a constant gain to form the spatial harmonics of the control signal. The commanded shaft position $\delta c(t)$ is modified by the magnetic bearing servo-actuator dynamics $\mathbf{A}_{\mathrm{MB}}(s)$ to yield the effective shaft position and tip-clearance distribution $\delta\epsilon(t)$. In this analysis a simple PI-lead network is used in the inner servo control loop of the magnetic bearing actuator. The constant gain stall controller was tuned to stabilize the zeroth-harmonic mode with unsteady air injection and the first-harmonic mode with tip-clearance actuation. The mass flow through the compressor is gradually decreased in the simulation until the second-harmonic mode becomes unstable. This is shown in Fig. 9. Note that it is this mode that determines the overall compressor stability and the compressor operating range.

Defining the state-space matrices $\mathbf{A}_c$, $\mathbf{B}_c$, and $\mathbf{C}_c$ the time invariant closed loop system in Fig. 7 is cast into state-space form,

$$\begin{aligned}\dot{\mathbf{x}}(t)&=\mathbf{A}_c\cdot\mathbf{x}(t)+\mathbf{B}_c\cdot\delta w(t),\\ \delta\epsilon(t)&=\mathbf{C}_c\cdot\mathbf{x}(t),\end{aligned} \tag{2}$$

where the same system input noise $\delta w(t)$ of intensity W is assumed during stall control. The system output of interest is $\delta\epsilon(t)$. The RMS of *effective* shaft motion, which is required to stabilize the compression system, can be estimated from the steady state output covariance $\Sigma_\epsilon = E\{\delta\epsilon(t)^2\}$, where the expected mean of $\delta\epsilon(t)$ is zero $(E\{\delta\epsilon(t)\}=0)$ and $E\{\ \}$ denotes the time average of an ergodic process. Assuming steady state, the state covariance Σ_x is obtained from the Lyapunov equation

$$\mathbf{0}=\mathbf{A}_c\Sigma_x+\Sigma_x\mathbf{A}_c^T+\mathbf{B}_c\mathbf{W}\mathbf{B}_c^T, \tag{3}$$

where $\mathbf{W}$ is the white noise intensity matrix. The output covariance and the RMS of $\delta\epsilon(t)$ then yield

$$\mathrm{RMS}(\delta\epsilon)=\sqrt{\Sigma_\epsilon}=\sqrt{\mathbf{C}_c\Sigma_x\mathbf{C}_c^T}. \tag{4}$$

This procedure is applicable to any actuation scheme and is implemented in a test case for unsteady air injection. The estimated RMS of injector valve motion of 0.141 (±0.005) compares well to the RMS of the measured actual valve motion of 0.121 in the NASA Glenn stall control experiment, where the valve command ranges from 0 (valve half open) to 1 (valve fully open). This gives confidence in using the presented technique to estimate the effective shaft motion for tip-clearance actuation. The analysis predicts

$$\mathrm{RMS}(\delta\epsilon)=207.5\pm 5.0\quad \mu\mathrm{m}.$$

The indicated uncertainty in the prediction is due to the uncertainty in the data matched white noise intensity W.

The constant gain control law commands shaft whirl at a frequency of 0.4 times the rotor frequency. This corresponds to the rotation rate of the first-harmonic rotating stall precursor. To guarantee a robust magnetic bearing design the required force bandwidth is determined for a shaft displacement of 250 μm for frequencies up to 0.5 times rotor frequency. Using Fig. 6 the required magnetic bearing force yields 25 kN for frequencies up to 0.5 times rotor frequency (143 Hz). This high load capacity is due to the large mass of the shaft (128.5 kg), the high whirl speed (143 Hz) and radius (250 μm), and the rotordynamic constraints of the shaft at the front end (catcher bearing) and at the rear end (motor drive coupling). Analyzing a typical five-axis magnetic bearing would result in different requirements, but could use the exact procedure described here.

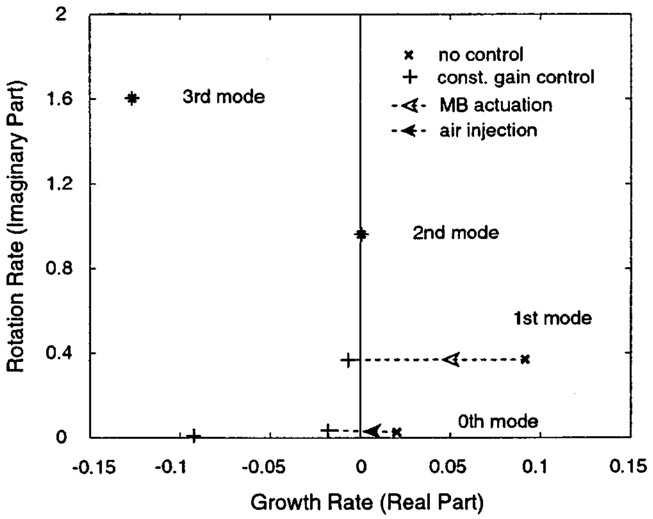

Fig. 9 Open loop compressor dynamics (×) and closed loop poles with constant gain control (+)

4 Design Requirements

The magnetic bearing servo-actuator design requirements from the preliminary analysis are summarized here. The concept of rotating stall control with tip-clearance actuation requires a magnetic bearing servo-actuator design with state of the art performance and very high load capacities. The desired design and performance requirements include the following:

- Rotordynamically stable shaft operation over the entire compressor speed range (0 to 286 Hz).
- Maximum shaft deflection of 250 μm to avoid blade tip rubs.
- 250 μm whirl radius between 0 and 143 Hz excitation frequency.
- Desired minimum whirl radius of 75 μm at the maximum excitation frequency of 286 Hz.
- Maximum bearing diameter of 0.356 m to fit into the compressor hub housing (see Fig. 3) without modification of the compressor gas path.

The next section discusses these design issues and presents the detailed design of the magnetic bearing servo-actuator.

5 Magnetic Bearing Servo-Actuator Design

Standard magnetic bearing suspension devices usually only yield large forces during static shaft levitation. The magnetic bearing servo-actuator for active stall control, however, must deliver a large *dynamic* load capacity and high magnetic forces must be generated over an air gap substantially larger than the nominal gap, since the rotor is whirling offset from its centerline. In addition, the outer bearing diameter and the space within the compressor hub housing are limited in this application. Hence a special magnetic pole configuration and a new soft magnetic material with relatively small magnetic losses and very high saturation flux densities were considered. Apart from the magnetic bearing actuator itself, the above issues will also strongly influence the actuator

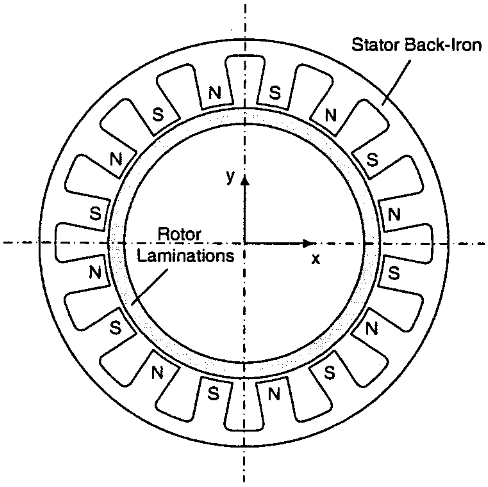

Fig. 10 Pole configuration and rotor lamination of magnetic bearing servo-actuator

Table 1 Optimized magnetic bearing servo-actuator design parameters

Actuator dimensions	
Number of poles	16
Inner actuator dia.	220 mm
Outer actuator dia.	320 mm
Actuator length	175 mm
Pole width	24.4 mm
Nominal air gap	600 μm
Electromagnetic properties	
Saturation flux density (Co iron)	2.4 T
Max. force (at nom. air gap)	31.6 kN
Flux density (at max. force)	2.28 T
Current stiffness (K_i)	1.021 kN/A
Position stiffness (K_x)	93.149 kN/mm
Max. current (saturation)	100 A
Max. voltage (saturation)	300 V
Electric resistance	37 mΩ
Coil inductance	6.9 mH

power electronics design. It has to be mentioned that, since the magnetic bearing actuator system design is a highly iterative process, only the final results are discussed here.

5.1 Electro-Magnetic Actuator Analysis

Pole Configuration. In order to achieve as much dynamic load capacity as possible within the given compressor housing envelope a nonstandard 16-pole configuration is considered. This allows one to pack the required amount of copper wiring within the narrow space between the inner and outer stator diameter. Also, a rather unconventional alternating N-S-N-S pole configuration is used here with the advantage that the magnetic flux through the rotor laminations and the stator back iron is half the value of a standard N-S-S-N pole configuration.[2] Therefore to obtain the same magnetic flux density as delivered by a standard configuration, the stator back iron and rotor lamination radial width can be reduced by a factor of 2. This yields a lighter weight magnetic rotor with beneficial influence on the overall rotordynamics, bending mode frequencies, and achievable whirl radii. However, the eddy current and hysteresis losses will be higher than in the standard case since the magnetic flux reversal frequency is doubled. It is clear that in general a trade-off between overall rotor weight and size and rotor heat loss must be made. In the presented application higher priority is attributed to the achievable whirl radii. Figure 10 illustrates the 16-pole N-S-N-S pole configuration and the rotor lamination of the magnetic bearing servo-actuator. The stator and rotor dimensions are given in Table 1.

Servo-Actuator Load Capacity Calculation. The load capacity calculation is based on a full 16-pole flux network model which includes all magnetic interactions and nonlinearities resulting from the magnetization curve of the soft magnetic material. Individual rotor and stator magnetic path geometries are also taken into account but the stray flux between the magnetic poles is neglected. One major advantage of the flux network model compared to finite element modeling techniques is its numerical effectiveness while yielding about the same accuracy [13]. The load capacity calculation mainly depends on the geometry, the air gap, and the maximum flux density of the soft magnetic iron. Furthermore, a very important and sometimes limiting factor in the design is the ability of the magnetic bearing servo-actuator to dissipate the heat that is generated from coil, eddy current, and hysteresis losses. Therefore an optimal actuator design yields a well balanced trade-off between available copper volume, pole width, and actuator surface area that is necessary to conduct the generated heat loss to a heat sink. The final results of the iterative design process are shown in Table 1. Note that the maximum achievable force at the nominal air gap (zero shaft offset) is approximately 20 percent higher than the estimated requirement of 25 kN. This is due to the fact that *in the case of a whirling shaft the air gap is increased and a larger force is needed for the same shaft displacement.*

5.2 Overall Dynamic System Analysis—Achievable Whirl Radii.

In order to compute the achievable whirl radii the magnetic bearing servo-actuator model must be combined with a rotordynamic model of the compressor shaft. Since large forces are generated at high frequencies, nonlinear current effects and voltage saturation of the electric power amplifier must also be taken into account. These models are briefly outlined here.

Rotordynamic Model. A standard finite element modeling approach is carried out to obtain a system of differential equations describing the rotor motion. This approach accounts for shear force influence, gyroscopic effects and additional lumped mass and rotational inertia effects:

$$\mathbf{M}\ddot{\mathbf{z}}+(\mathbf{G}+\mathbf{D})\dot{\mathbf{z}}+\mathbf{K}\mathbf{z}=\mathbf{B}_{\mathrm{act}}\mathbf{f}_{\mathrm{act}}, \tag{5}$$

where $\mathbf{z}$ is the rotor position vector, containing both the horizontal and the vertical displacements x and y of the elements. $\mathbf{M}$ denotes the mass matrix and includes all inertia properties (mass, radial moments of inertia). The $\mathbf{G}$ matrix contains the gyroscopic terms (polar and radial moments of inertia, rotational speed). The radial and axial fluid film bearings at the motor coupling end and the ISFD catcher bearing system at the compressor wheel end are modeled as spring damper elements and are included in the stiffness matrix $\mathbf{K}$ and the damping matrix $\mathbf{D}$. The actuator force $\mathbf{f}_{\mathrm{act}}$ is coupled into the rotordynamic system by the influence matrix $\mathbf{B}_{\mathrm{act}}$ which defines the geometric point of action of the magnetic force. The homogeneous solution of Eq. (5) can be analyzed in terms of a Campbell diagram which is shown in Fig. 11. The two rigid body forward and backward whirling modes are crossed by the one-per-rev line (1-E) at about 30, 180, and 200 Hz. Note that none of the flexural modes are crossed despite the strong gyroscopic effects and that the rigid body mode frequencies compare well to the preliminary results (see Fig. 5) obtained from the simple lumped parameter model. The frequencies of the two rigid body modes mostly depend on the stiffness of the fluid film and catcher bearings, the mass properties of the compressor shaft, and the actuator feedback control. In order to limit the vibration level when the rigid body critical frequencies are crossed, either the

---

[2] Usually N-S-S-N pole configurations are considered when high magnetic force capacities are required.

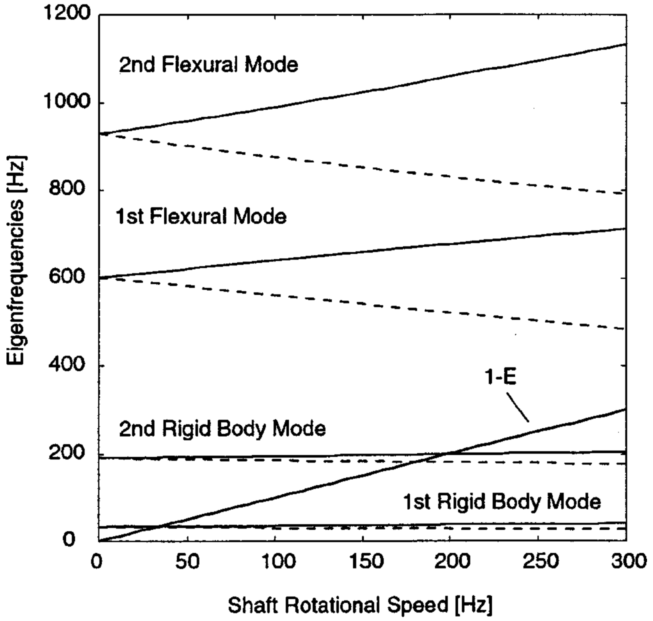

Fig. 11 Campbell diagram of magnetic bearing servo-actuator (forward and backward whirling modes are marked solid and dashed, respectively)

rotor must be well balanced or the bearings, especially the magnetic actuator, must dissipate a substantial amount of energy, i.e., provide a sufficient amount of external damping to the system.

Actuator and Power Amplifier Model. A linearized model of the magnetic bearing servo-actuator is used to keep the computation times at an affordable level. Nonlinear effects are included in the voltage and current saturation characteristics of the power amplifier. The linearized actuator force can be written as

$$\mathbf{f}_{\mathrm{act}}=\mathbf{K}_x\mathbf{z}_b+\mathbf{K}_i\mathbf{i}, \tag{6}$$

where the matrix $\mathbf{K}_x$ contains the two identical position stiffnesses in the x and y directions and $\mathbf{K}_i$ contains the corresponding current stiffnesses of the magnetic bearing servo-actuator. Vectors $\mathbf{z}_b$ and $\mathbf{i}$ denote the rotor position within the magnetic actuator and the control current input, respectively. In order to combine Eqs. (5) and (6) $\mathbf{z}_b$ must be transformed into $\mathbf{z}$ assuming rigid body relations between the shaft locations. The amplifier dynamics contain the influence of the actuator inductance and resistance $\mathbf{L}$ and $\mathbf{R}$ and the back-EMF term due to rotor motion (for details see [14]):

$$\mathbf{u}=\mathbf{R}\mathbf{i}+\mathbf{L}\frac{d\mathbf{i}}{dt}+\frac{1}{2}\mathbf{K}_i^T\dot{\mathbf{z}}_b, \tag{7}$$

where the vector $\mathbf{u}$ contains the coil voltages. The achievable whirl radii can now be determined by solving Eqs. (5), (6), and (7) for position vector $\mathbf{z}$.

The resulting high-order system of nonlinear differential equations must be solved numerically and the solution procedure is quite involved and time consuming. Instead a much faster iterative solution procedure was developed. First let us consider the following thought experiment. If the whirling rotor is a single lumped mass then it is kept in orbit by a single radial force of constant amplitude with a phase of 180 deg relative to the displacement vector. Therefore in the iterative solution procedure the excitation force is assumed to be 180 deg out of phase despite gyroscopic effects of the rotor and external stiffnesses and damping properties of the fluid film journal bearings.[3] It has to be mentioned that in the experiment the same effect can be achieved by introducing a synchronous signal rejection scheme in the magnetic bearing feedback controller (for details see [15]). This yields a completely force-free rotation about the principal axis of the rotor and eliminates the transmission of synchronous unbalance forces to the machine housing. Also, since the steady state whirl orbits are of interest all transient parts of the solution are neglected and Eqs. (5), (6), and (7) are solved in the frequency domain.

The results of the iterative solution procedure are shown in Fig. 12 for the shaft spinning at design speed (286 Hz). The plot on the

---

[3] It can be shown that this assumption yields a maximum error in the phase of about 20 deg for frequencies above 50 Hz.

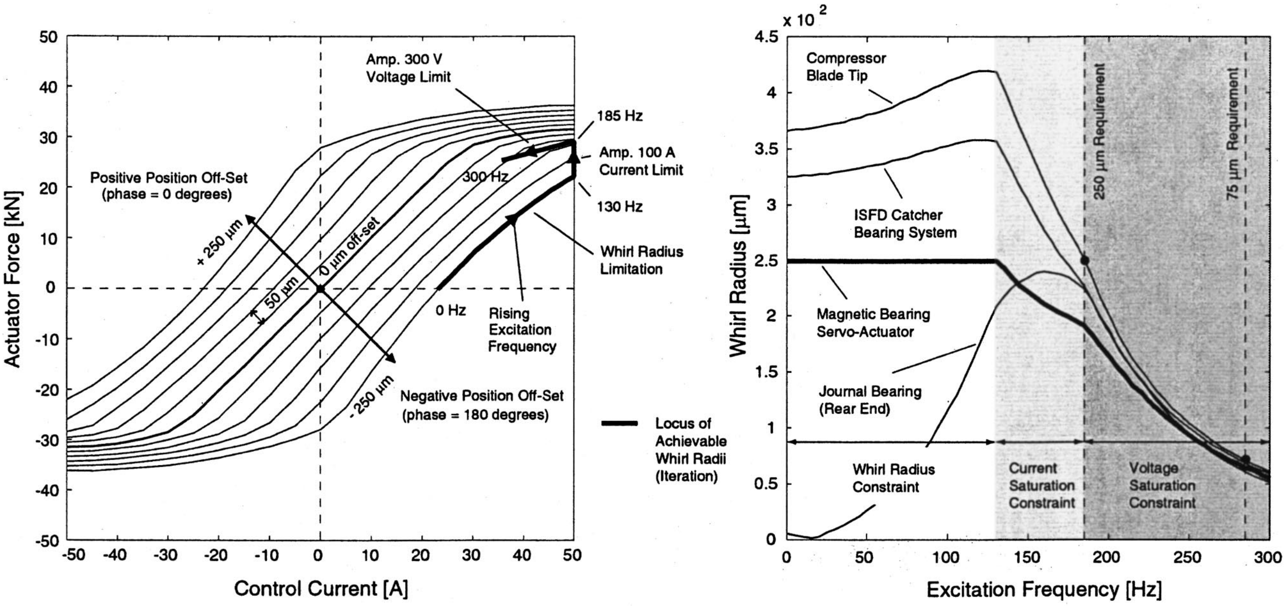

Fig. 12 Current-force characteristic of magnetic bearing servo-actuator and operating locus (left); achievable whirl radii at several shaft locations and amplifier operation limits (right)

left hand side depicts the family of nonlinear current-force characteristics of the magnetic bearing servo-actuator and the locus of operating points ranging from 0 to 300 Hz excitation frequency at maximum available power (thick solid line). Note that the effect of a varying air gap is included in the calculation. The achievable whirl radii at several shaft locations are plotted on the right hand side together with the operational constraints of the amplifier (300 V saturation voltage, 100 A saturation current split into 50 A bias and 50 A maximum control current) and the whirl radius limitation at the magnetic bearing location (250 μm). The results show that the design requirements stated in Sec. 4 are fulfilled: 250 μm compressor blade tip deflection is achieved up to 185 Hz (the blade tip displacement in this frequency band is even higher than the requirement since the actuator is operating at maximum available power) and a minimum of 75 μm is obtained at the synchronous excitation frequency of 286 Hz. The nonlinear current and voltage saturation effects of the amplifier are well visible in these performance characteristics.

Table 2 Total mechanical, electro-magnetic, and aerodynamic losses at design speed (286 Hz)

	Loss [W]	Frequency [Hz]
Stator losses		
Coil resistance	560	115
Eddy current and hysteresis	180	190
Rotor losses		
Windage loss	2500	286
Eddy current and hysteresis	5060	286
Bearing dissipation		
ISFD catcher bearing	864	120
Fluid journal bearing	2729	185

5.3 Heat Loss and Cooling Analysis. As mentioned earlier, a trade-off between achievable whirl radii and magnetic bearing heat loss had to be considered in this design. Since the required shaft displacements and excitation frequencies are rather high compared to standard magnetic bearing applications the heat loss is expected to be substantial. Therefore a detailed heat loss and cooling analysis described in [16] was carried out. The analysis involved the modeling of magnetic bearing stator losses (coil resistance, magnetic reversal (hysteresis), and eddy current loss), magnetic bearing rotor lamination losses (hysteresis and eddy current loss), aerodynamic windage loss in the magnetic bearing gap, and dissipation in the fluid film journal and catcher bearing systems due to high-frequency rotor whirl. All magnetic bearing stator loss and the dissipation in the fluid film journal bearings must be supplied by the power amplifiers. The lamination and aerodynamic losses in the magnetic bearing rotor however must be supplied by the motor drive. The results of the heat loss analysis are summarized in Table 2. It should be mentioned that these values correspond to a worst-case situation since all losses are taken at their peak values (different frequencies in Table 2) and the shaft is assumed to be spinning at design speed (286 Hz).

The cooling concept for the NASA Stage 37 magnetic bearing axial flow compressor includes three different cooling systems and a preliminary cooling analysis was also conducted. Water cooling through a cooling jacket around the stator is estimated to provide a cooling power of 950 W which covers the stator losses plus a part of the aerodynamic losses. Cooling oil is run through and around the fluid film bearings at the front and rear shaft end and is expected to exchange a total of 8650 W power due to the bearing dissipation and rotor lamination loss. In addition cold high-pressure air is run around the shaft with an estimated cooling power of 2280 W to cover most of the aerodynamic losses. Clearly this analysis indicates that heat dissipation significantly complicates this particular magnetic bearing design.

6 Closed Loop Stall Control Simulation

The final design of the magnetic bearing servo-actuator was then used to simulate the closed loop stall control experiment. The final magnetic bearing system dynamics $\mathbf{A}_{\mathrm{MB}}$ were included in the closed loop system shown in Fig. 7. As mentioned earlier, a simple PI-lead network was implemented in the inner servo control loop of the magnetic bearing actuator. Again a constant gain stall controller was used in the outer loop to stabilize the zeroth-harmonic mode with unsteady air injection and the first-harmonic mode with tip-clearance actuation. The compressor was throttled into stall and a 2.3 percent reduction of stalling mass flow was obtained.

The stable operating range extension with tip-clearance actuation is comparable to the results obtained in the same compressor by Weigl et al. [2] using unsteady air injection. These results show that tip-clearance actuation with magnetic bearings is an effective actuation scheme and establish the viability of magnetic bearings for stall control in high-speed compressors.

7 Summary and Concluding Remarks

This paper presents a general design procedure to develop magnetic bearing servo-actuators for high-speed compressor stall control. The design procedure is carried out in an example analysis for the NASA Glenn high-speed single-stage axial flow compressor and results specific to this compressor are reported in this paper. It has to be pointed out that this specific application introduced special design constraints and unusual complexities due to the existing test rig setup and environment. For example, the constraint of a two-axis magnetic bearing with a contacting catcher bearing system and an existing fluid film journal bearing setup at the motor drive coupling end are not encountered in a general design problem. If a compressor with magnetic bearings were developed from scratch, many of the design constraints would be relaxed. Therefore the design process is emphasized here rather than the presented numbers.

The key analysis in the design process is to determine the control authority of tip-clearance actuation and the design requirements of the magnetic bearing. A unique stochastic estimation and control analysis is presented and applied first to unsteady air injection actuation as a test case. The obtained results compare well to experimental data and give confidence in using this procedure for tip-clearance actuation.

Next the magnetic bearing servo-actuator design requirements are determined by combining the stochastic estimation and control approach with a preliminary rotordynamic analysis and a dynamic compressor tip-clearance model that utilizes both CFD and experimental data. Although the results are for a specific experimental rig, they indicate that in general the concept of rotating stall control with tip-clearance actuation requires a magnetic bearing servo-actuator design with state of the art performance and very high dynamic load capacities.

A detailed electromagnetic and mechanical analysis of the magnetic bearing servo-actuator is conducted and the design fulfills the requirements. The magnetic bearing servo-actuator yields a remarkably high dynamic force level and bandwidth which are necessary for this application due to the large mass and the high excitation frequencies. The design considers a trade-off between the achievable whirl radii and the generated heat loss. The heat loss calculation reveals rather high values due to the special constraints and in addition a cooling analysis is conducted. Active water, oil, and air cooling are considered necessary to provide sufficient cooling power.

Stall control laws are then developed and the final magnetic bearing servo-actuator design is implemented in a closed loop stall control simulation to determine the benefit in stable compressor operating range. The simulation results yield a 2.3 percent reduction in stalling mass flow which is comparable to results with unsteady air injection. The design and simulation results presented in this paper establish the viability of magnetic bearings for stall control in aero-engine high-speed compressors.

Acknowledgments

This research was conducted under collaboration between the Gas Turbine Laboratory at MIT, the NASA Glenn Research Center, and MECOS Traxler AG. The authors would like to thank Dr. A. Strazisar, Dr. G. Brown, and Dr. A. Kascak at the NASA Glenn Research Center, Dr. K. Gordon and Dr. F. Ehrich at MIT, and Dr. L. San Andrés and Dr. A. Palazzolo at Texas A&M University for their support and insightful discussions. This project was conducted under NASA grant NAG3-1457.

References

[1] Epstein, A., Williams, J., and Greitzer, E., 1989, ''Active Suppression of Aerodynamic Instabilities in Turbomachines,'' J. Propul., **5**, No. 2, pp. 204–211.

[2] Weigl, H., Paduano, J., Fréchette, L., Epstein, A., Greitzer, E., Bright, M., and Strazisar, A., 1998, ''Active Stabilization of Rotating Stall and Surge in a Transonic Single Stage Axial Compressor,'' ASME J. Turbomach., **120**, pp. 625–636.

[3] Graf, M., Wong, T., Greitzer, E., Marble, F., Tan, C., Shin, H. W., and Wisler, D., 1997, ''Effects of Non-Axisymmetric Tip Clearance on Axial Compressor Performance and Stability,'' ASME Paper No. 97-GT-406.

[4] Gordon, K., 1999, ''Three-Dimensional Rotating Stall Inception and Effects of Rotating Tip Clearance Asymmetry in Axial Compressors,'' Ph.D. thesis, Department of Aeronautics and Astronautics, MIT.

[5] Reid, L., and Moore, D., 1978, ''Design and Overall Performance of Four Highly Loaded, High Speed Inlet Stages for an Advanced High Pressure Ratio Core Compressor,'' Technical Report TP-1337, NASA.

[6] Reid, L., and Moore, D., 1978, ''Performance of a Single-Stage Axial-Flow Transonic Compressor with Rotor and Stator Aspect Ratios of 1.19 and 1.26, Respectively, and With Design Pressure Ratio 1.82,'' Technical Report TP-1338, NASA.

[7] Ehrich, F., 1992, *Handbook of Rotordynamics*, McGraw-Hill, New York.

[8] Santiago, O., San Andrés, L., and Olivera, J., 1998, ''Imbalance Response of a Rotor Supported on Open-End Integral Squeeze Film Dampers,'' ASME Paper No. 98-GT-6.

[9] Hynes, T., and Greitzer, E., 1987, ''A method for Assessing Effects of Circumferential Flow Distortion on Compressor Stability,'' ASME J. Turbomach., **109**, pp. 371–379.

[10] Moore, F., and Greitzer, E., 1986, ''A Theory of Post-Stall Transients in Axial Compressors: Part I—Development of the Equations,'' ASME J. Eng. Gas Turbines Power, **108**, pp. 68–76.

[11] Adamczyk, J., Celestina, M., Beach, T., and Barnett, M., 1990, ''Simulation of Three-Dimensional Viscous Flow Within a Multistage Turbine,'' ASME J. Turbomach., **112**, pp. 370–376.

[12] Wang, Y., Paduano, J., and Murray, R., 1999, ''Nonlinear Control Design for Rotating Stall and Surge With Tip Clearance Actuation,'' *Proc. IEEE International Conference on Control Applications.*

[13] Schmidt, E., Platter, T., and Springer, H., 1996, ''Force and Stiffness Calculations in Magnetic Bearings—Comparison Between Finite Element Method and Network Theory,'' *Proc. 5th International Symposium on Magnetic Bearings*, Kanazawa, Japan, pp. 259–264.

[14] Vischer, D., and Bleuler, H., 1990, ''A New Approach to Sensorless and Voltage Controlled AMB's Based on Network Theory Concepts,'' *Proc. 2nd International Symposium on Magnetic Bearings*, T. Higuchi, ed., University of Tokyo.

[15] Herzog, R., Bühler, P., Gähler, C., and Larsonneur, R., 1996, ''Unbalance Compensation Using Generalized Notch Filters in the Multivariable Feedback of Magnetic Bearings,'' IEEE Trans. Control Syst. Technol., **4**, pp. 580–586.

[16] Traxler, A., 1985, ''Eigenschaften und Auslegung von berührungsfreien elektromagnetischen Lagern,'' Ph.D. thesis, Swiss Federal Institute of Technology, ETH Zürich, ETH thesis no. 7851.

Gianmario L. Arnulfi
Pietro Giannattasio
University of Udine,
Dipartimento di Energetica e Macchine,
Udine, Italy

Diego Micheli
University of Trieste,
Dipartimento di Energetica,
Trieste, Italy

Piero Pinamonti
University of Udine,
Dipartimento di Energetica e Macchine,
Udine, Italy

An Innovative Device for Passive Control of Surge in Industrial Compression Systems

The present paper reports a numerical–experimental study on the dynamic behavior of a compression system based on a multistage centrifugal blower and fitted with an innovative device for the dynamic suppression of surge instability. The control device is of passive type and is based on the aeroelastic coupling of the basic compression system with a hydraulic oscillator. The controlled system is modeled at first by using a nonlinear lumped parameter approach. The simulated system dynamics within a wide range of operating conditions allows a parametric analysis to be performed and the optimal values of the control parameters to be singled out. Such optimal values are then used to design the hydraulic oscillator, which results in a technically feasible and very simple configuration. Finally, experimental tests are carried out on the compression plant with and without the passive control device, which demonstrate the effectiveness of the proposed control system in suppressing surge instabilities, at least within the limits predicted by the numerical simulation. [DOI: 10.1115/1.1348021]

Introduction

Dynamic suppression of surge, based on the use of active or passive control devices, appears to be a very promising approach, since it allows normally unstable regions of the compressor map to be made accessible. The control of surge is based on the coupling of the compression plant with a dynamic system capable of absorbing and dissipating the unsteady energy associated with the surge instability. Epstein et al. [1] proposed that surge can be inhibited by actively damping the small disturbances associated with the early stages of instability, so that the unsteady perturbations are directly affected, while the average flow parameters are virtually unaltered. For the active suppression of surge, a classic feedback control system is used, i.e., a sensor/actuator pair and a suitable control law. Ffowcs Williams and Huang [2] and Pinsley et al. [3] proved the concept of active stabilization by means of experimental tests carried out on small centrifugal compressors. A detailed linear stability analysis of compression systems fitted with different active control devices was performed by Simon et al. [4], who pointed out the impact of the choice of the sensor/actuator pair on the control effectiveness.

An alternative concept of surge suppression was suggested by Gysling et al. [5], who proposed the aeroelastic coupling of the compression system with a mass-spring-damper device through the action of a movable plenum wall. In this way, the external control law required by an active device is replaced by the structural feedback of the movable wall, resulting in a passive-type control. Giannattasio and Giusto [6] carried out a theoretical analysis of the effectiveness of the passive device when applied to an industrial compression system, such as the one described by Arnulfi et al. [7]. The numerical results of a nonlinear model of the controlled system showed that surge suppression is very difficult to obtain over the whole operating range of the compressor, because of the abrupt stall, which affects the compressor characteristics. Furthermore, a parametric analysis allowed the optimum values of the control parameters to be singled out.

The present paper further develops the concept of passive suppression of surge. A first attempt of using the optimal control parameters provided by Giannattasio and Giusto [6] showed severe difficulties in the design of a practical control device for an industrial compression system, mainly due to the very low natural frequency required to the movable wall. In fact, it turned out that the control device requires, to be effective, a very large mass of the movable wall and a very large auxiliary volume (typically, an order of magnitude greater than the plenum volume). As an attempt to overcome such difficulties, the present study proposes the aeroelastic coupling of an industrial compression system with an innovative, very simple and compact device, based on an oscillating water column. The idea arose from the observation that a hydraulic oscillator has an intrinsically low natural frequency.

A nonlinear lumped parameter model of the compression system fitted with the new passive control device is presented at first. It was used to obtain the optimal values of the control parameters, which allowed the hydraulic device to be correctly designed. The results of an extensive experimental study are then reported. Measurements of various flow parameters in both steady and unsteady operating conditions have been carried out, in order to test the effectiveness of the control device when varying compressor speed, mass flow rate, and control parameters.

Passive Control of Surge

The device proposed by Gysling et al. [5] for the passive suppression of surge is schematically shown in Fig. 1. The basic compression system (compressor, plenum, throttle valve) is coupled to a mass-spring-damper device, where the inertial element is a movable plenum wall, the gas in an auxiliary plenum acts as an aerodynamic spring, and a viscous dashpot is used for the damping. The main plenum and the auxiliary one are connected by a pressure equilization tube, such that the pressure in the auxiliary chamber can be made equal to the steady equilibrium pressure in the main plenum, while only the unsteady pressure fluctuations can act on the movable wall. The control device is based on the concept that the aeroelastic coupling of the compression system with a proper mechanical oscillator should produce the effect of absorbing and dissipating the unsteady energy introduced by the compressor in the early stages of its unstable operation, so inhibiting the surge development. Such a concept has been demonstrated both theoretically and experimentally by Gysling et al. [5], who performed a linear stability analysis of the controlled system and a comprehensive set of measurements on a small centrifugal compressor for turbocharging application.

Contributed by the International Gas Turbine Institute and presented at the 45th International Gas Turbine and Aeroengine Congress and Exhibition, Munich, Germany, May 8–11, 2000. Manuscript received by the International Gas Turbine Institute February 2000. Paper No. 2000-GT-352. Review Chair: D. Ballal.

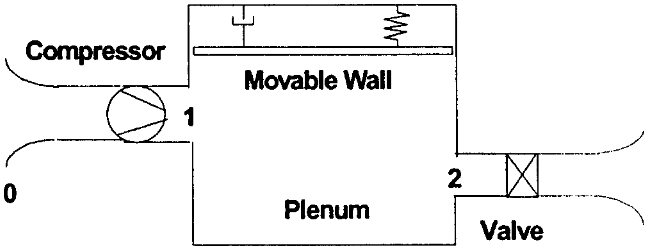

Fig. 1 Compression system with movable plenum wall

The dynamics of a compression system under unstable operating conditions is usually and effectually modeled by using a lumped parameter approach [8,3,5,4,9]. In particular, the controlled system in Fig. 1 can be described by the following set of dimensionless equations [5,6]:

$$\frac{d\varphi_c}{d\tau}=B(\psi_c-\psi_p) \tag{1}$$

$$\frac{d\psi_p}{d\tau}=\frac{1}{B}(\varphi_c-\varphi_t)-2\frac{\overline{\rho_p}}{\rho_0}\frac{1}{\mathrm{M}^2}v \tag{2}$$

$$\frac{d\psi_c}{d\tau}=\frac{1}{\tau_c}(\psi_{c,ss}-\psi_c) \tag{3}$$

$$\psi_p=(A_c/A_t)^2\varphi_t^2 \tag{4}$$

$$\frac{d\eta}{d\tau}=v \tag{5}$$

$$\frac{dv}{d\tau}=2WB^2(\psi_p-\overline{\psi_p})-2\zeta Q\sqrt{\frac{p_0}{\overline{p_p}}\frac{\overline{\rho_p}}{\rho_0}}v-Q^2\frac{\overline{\rho_p}}{\rho_0}\eta \tag{6}$$

where the variables are defined as:

$$\varphi=\frac{\dot{m}}{\rho_0UA_c},\quad \psi=\frac{\Delta p}{\rho_0U^2/2},\quad \tau=\omega_Ht=\overline{a}_\rho\sqrt{\frac{A_c}{V_pL_c}}t,$$

$$\eta=\frac{A_w}{V_p}q,$$

and the following dimensionless parameters are introduced:

$$B=\frac{U}{2\omega_HL_c}=\frac{U}{2\overline{a}_p}\sqrt{\frac{V_p}{A_cL_c}}\quad \text{(stability or Greitzer parameter)}$$

$$\mathrm{M}=\frac{U}{\overline{a}_p}\quad \text{(tip Mach number)}$$

$$W=\frac{\rho_0A_w^2L_c^2}{m_wV_p}\quad \text{(aeroelastic coupling parameter)}$$

$$Q=\frac{\omega_{w,0}}{\omega_{H,0}}=\frac{\omega_w}{\omega_H}\sqrt{\frac{\rho_0}{\overline{\rho_p}}}\quad \text{(frequency parameter)}$$

$$\zeta=\frac{c}{2m_w\omega_{w,0}}=\frac{c}{2m_w\omega_w}\sqrt{\overline{p_p}p_0}\quad \text{(damping parameter)}.$$

Equation (1) expresses the momentum conservation in the compressor duct of equivalent length L_c [8], while Eq. (2) is the mass conservation equation in the plenum, which, in the present case, includes the effect of the plenum volume variation due to the moving wall (see the term containing v on the right-hand side). A time constant, τ_c, is introduced in Eq. (3), which represents a first-order model of the transient response of the compressor. This time constant can be related to the time needed for the complete development of a stall cell [8,9] Equation (4) represents the steady-state characteristic of the throttle valve. Finally, Eqs. (5) and (6) describe the movable wall dynamics, being equivalent to the classical second-order linear equation of motion of a single-degree of freedom elastic system.

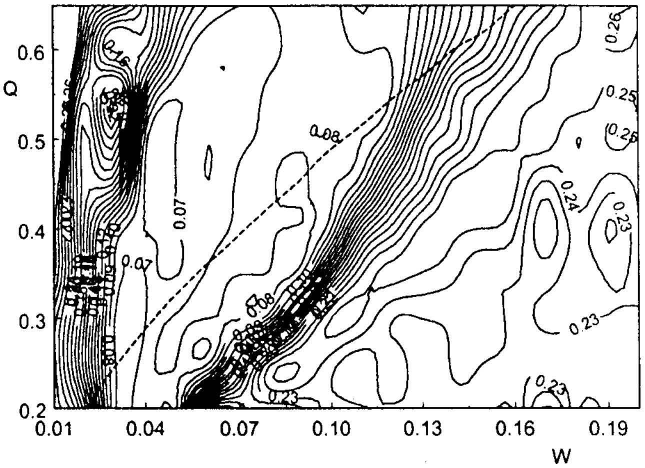

Fig. 2 Contour lines of ⟨RMS⟩ in *W*–*Q* plane for a compression system with movable plenum wall (n=2000 rpm, V_p =3.132 m^2, ξ=2)

Equations (1)–(6) have been employed by Giannattasio and Giusto [6] to perform a nonlinear stability analysis of the industrial compressor system described by Arnulfi et al. [7], fitted with the passive control device proposed by Gysling et al. [5]. The compression system is based on a four-stage centrifugal blower and includes a plenum of large capacity. The compressor characteristic curves exhibit abrupt stall, compelling one to employ a nonlinear approach to predict correctly the dynamic behavior of the system. In fact, as pointed out by Giannattasio and Giusto [6], the finite pressure jump associated with the abrupt stall introduces a large amount of unsteady energy into the system when the stall limit is crossed, which can cause instability even in linearly stable operating points. Indeed, both experimental and numerical (nonlinear) results obtained by Arnulfi et al. [7,9] for the uncontrolled compression system show that all the operating points on the left of the stall limit are unstable, even at the lowest compressor speed of 2000 rpm, while a linear stability analysis predicts that, still at 2000 rpm, over 40 percent of such points should exhibit a stable behavior.

The nonlinear analysis carried out by Giannattasio and Giusto [6] results in a number of plots of a proper stability index, ⟨RMS⟩, in the plane of control variables W and Q, for fixed values of damping parameter ζ and compressor speed. Stability index ⟨RMS⟩ is defined as the mean, over flow coefficient interval $0<\varphi<\varphi_{\text{stall}}$, of the RMS values of signal $\psi_p(\tau)$. Obviously, a stable operating point implies $\text{RMS}(\psi_p(\tau))=0$, so that small values of ⟨RMS⟩ denote wide stable intervals of flow coefficient and vice-versa. Figure 2 shows the contour lines of ⟨RMS⟩ in $W-Q$ plane, as obtained by Giannattasio and Giusto [6] for $\zeta=2$ and $n=2000$ rpm. The broken line in the diagram represents contour line $\eta_{\max}=0.03$, which was assumed to be the maximum acceptable wall displacement; points with $\eta_{\max}<0.03$ are located on the left-upper side of this curve.

The parametric analysis in Fig. 2 allows one to select values of W and Q that correspond to the lowest values of ⟨RMS⟩, maximizing the effectiveness of the passive control device. As an example, values $W=0.06$ and $Q=0.45$ appear to be a good choice, since the corresponding point in $W-Q$ plane lies in the middle of the region of low ⟨RMS⟩ values. Since the natural frequency of the movable wall can be expressed as

$$\omega_w=A_w\sqrt{\frac{\gamma\overline{p_p}}{V_{\text{aux}}m_w}} \tag{7}$$

from the definitions of W and Q one easily obtains:

$$V_{\mathrm{aux}}=\left(\frac{V_p^2}{A_c L_c}\right)\frac{W}{Q^2} \tag{8}$$

Equation (8) can be used to evaluate the required volume of the auxiliary plenum as a function of control parameters and plant geometry. The compression system considered by Arnulfi et al. [7] includes a plenum of volume $V_p=3.132\ \mathrm{m}^3$ and a compressor duct of area $A_c=122.7\ \mathrm{cm}^2$ and equivalent length $L_c=13.5\ \mathrm{m}$. By substituting such values in Eq. (8), together with the selected values of W and Q, a volume of $17.5\ \mathrm{m}^3$ is found for the auxiliary plenum. Furthermore, the required mass of the movable wall can be easily obtained from the definition of W:

$$m_w=\frac{\rho_0 A_w^2 L_c^2}{W V_p}\cong 1200\ \ \mathrm{kg} \tag{9}$$

if, for example, $A_w=1\ \mathrm{m}^2$ is assumed for the wall surface area. The estimated values of V_{aux} and m_w appear to be too large for a reasonable technical application of the movable wall device to the present compression system. On the other hand, if an attempt is made to reduce V_{aux} and m_w by chosing different values of W, Q, and A_w within their acceptable variation ranges, an unsatisfactory practical solution is still obtained. This is mainly due to the opposite effects of a W variation on V_{aux} and m_w and to the requirement of a sufficiently large wall area to guarantee an effective interaction between the gas in the main plenum and the control device. The real reason for the aforementioned difficulties is that an effective control device should have a very low natural frequency, comparable to the Helmoltz frequency of the compression system. This explains the high values required for the auxiliary plenum volume and the movable wall mass (see Eq. (7)). Therefore, an effort was undertaken aimed at finding a dynamic system that combined an intrinsically low natural frequency with reduced mass and dimensions, and thus is suitable to be used as a passive control device in industrial-size compression systems. Such an effort resulted in the conception of the innovative control device described in the following section.

Hydraulic Oscillator

If a liquid column contained in a constant-area ''*U*'' tube is perturbed, it begins to oscillate at undamped angular frequency $\omega=\sqrt{2g/l}$. It is easily noticed that small values of l are sufficient to produce low natural frequencies of the liquid column. This simple observation suggested the idea of using a hydraulic oscillator as a device for passive control of surge. The concept is schematically shown in Fig. 3 (patent pending). Surface A_1 of a liquid filling two communicating vessels is in contact with the gas contained in the plenum, while the second liquid surface, of area A_2, communicates with the atmosphere. The hydraulic device includes a dissipative component (D), such as an orifice, a throttle valve, etc. If proper length, surface areas, and loss characteristic of the liquid column are selected, the dynamic response of the hydraulic oscillator to the pressure fluctuations in the plenum can result in an effective absorption and dissipation of the unsteady energy associated with surge.

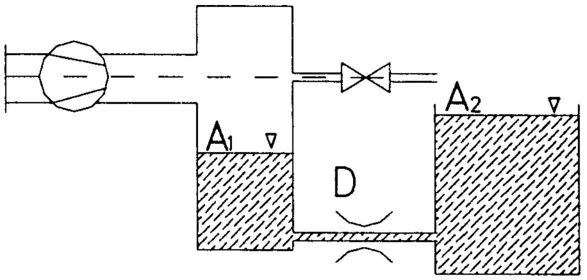

Fig. 3 Compression system with hydraulic oscillator

As shown in the appendix, the dynamics of the hydraulic device is described by the following nonlinear second-order differential equation:

$$(l_{eq}+\alpha x)\ddot{x}+\frac{1}{2}\left(\alpha+\frac{|\dot{x}|}{\dot{x}}C\right)\dot{x}^2+Kx=\frac{p_p(t)-p_{p,ss}}{\rho_l} \tag{10}$$

where $x(t)$ is the displacement of surface A_1 with respect to the equilibrium position corresponding to steady-state plenum pressure $\rho_{p,ss}$. Although Eq. (10) is formally an energy equation, it allows all the dynamic parameters of the system to be singled out. The inertial effect is represented by the coefficient of $\ddot{x}$ and is associated to the length of the liquid column, which can vary with displacement x if $A_1\neq A_2$ ($\alpha\neq 0$). The coefficient of $\dot{x}^2$ in the second term accounts for losses (C) and for the changes in the kinetic energy of the liquid column (α) that occur during the oscillations if $A_1\neq A_2$. Coefficient $K=g(1+A_1/A_2)$ can be interpreted as the ''stiffness'' of the elastic system; it grows linearly with area ratio A_1/A_2 and tends to the gravitational acceleration as $A_1/A_2\rightarrow 0$, i.e., when $A_1\ll A_2$. Finally, the pressure difference term on the right-hand side of Eq. (10) represents the action of an external force on the hydraulic oscillator.

Equation (10) is nondimensionalized by using the same reference quantities as in Eqs. (1)–(6), obtaining:

$$\begin{aligned}(1+R\eta)\frac{dv}{d\tau}+\frac{1}{2}\left(R+\frac{|v|}{v}\zeta\right)v^2+Q^2\left(\frac{\overline{\rho_p}}{\rho_0}\frac{p_0}{\overline{p_p}}\right)\eta\\=2WB^2(\psi_p-\psi_{p,ss})\end{aligned} \tag{11}$$

When compared to Eq. (6), Eq. (11) contains an additional dimensionless parameter, namely,

$$R=\alpha\frac{V_p}{l_{eq}A_1}=\left[\left(\frac{A_1}{A_2}\right)^2-1\right]\frac{V_p}{l_{eq}A_1},$$

while parameters W, Q, and ζ are now defined as:

$$W=\frac{\rho_0 A_1 L_c^2}{\rho_1 l_{eq} V_p},\qquad Q=\frac{\sqrt{K/l_{eq}}}{\omega_{H,0}}=\frac{\sqrt{g(1+A_1/A_2)/l_{eq}}}{\omega_{H,0}},$$

$$\zeta=C\frac{V_p}{l_{eq}A_1}.$$

where $\omega_{H,0}=a_0\sqrt{A_c/V_pL_c}$ is the Helmholtz frequency referred to ambient conditions.

By coupling Eq. (11) with Eqs. (1)–(5), the mathematical model is obtained of the compression system including the novel device for the passive control of surge. Such a model has been employed preliminarily to test the effectiveness of the control device and to perform its optimized design.

The compression system considered here is described by Arnulfi et al. [7,9] and the interested reader is referred to their papers for details. The initial conditions for the present computations are prescribed by simulating a valve throttling process from a steady equilibrium point on the stable branch of the compressor characteristic (for example, $\varphi_{ss}=0.25$) up to the desired steady operating condition. In fact, differently from a linear stability analysis where an arbitrary initial perturbation can be imposed, the present nonlinear model produces results that are normally affected by the dynamic system trajectory required to reach a given operating point. Consequently, the real initial evolution has to be simulated as accurately as possible.

The numerical simulation of the controlled system dynamics typically produces time histories of φ_c, ψ_p, and η at a given compressor speed and for a single steady equilibrium flow coefficient, φ_{ss} (see, for example, Fig. 11). Such data can also be employed to represent the system dynamics in plane $\varphi_c-\psi_p$ (see, for example, Figs. 8–10), where surge cycles are eventually dis-

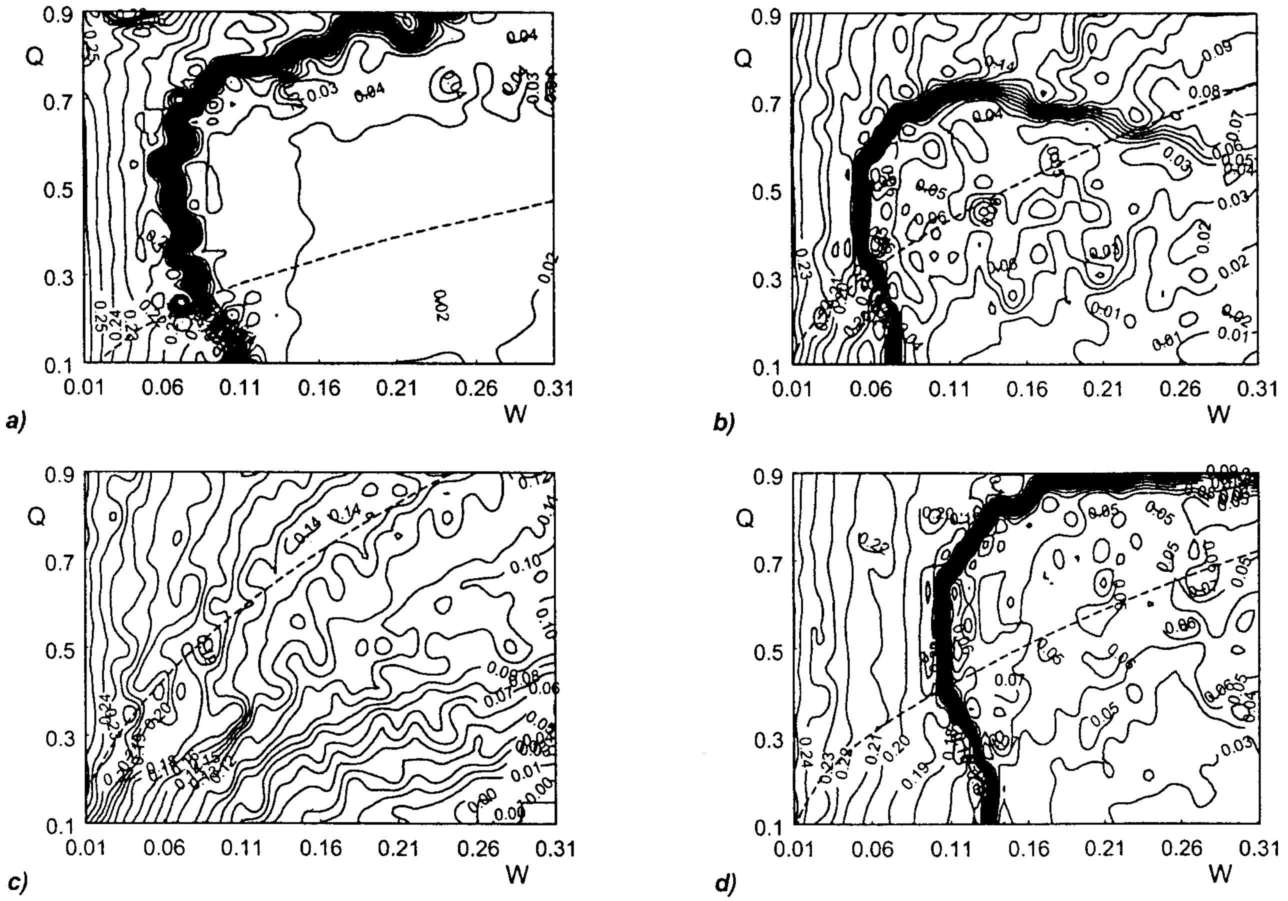

Fig. 4 Contour plots of $\langle E\rangle$ in $W-Q$ plane for the compression system controlled by means of a hydraulic oscillator: (*a*) $B_0=0.2$, $\zeta=4000$; (*b*) $B_0=0.3$, $\zeta=4000$; (*c*) $B_0=0.4$, $\zeta=4000$; (*d*) $B_0=0.3$, $\zeta=8000$

played. In order to quantify the control effectiveness in a given operating condition, a new dimensionless parameter is here introduced, namely:

$$E=\int_{\bar{t}}^{\bar{t}+\bar{T}}(\psi_c-\psi_p)\frac{d\varphi_c}{d\tau}d\tau$$

$$=B\int_{\bar{t}}^{\bar{t}+\bar{T}}(\psi_c-\psi_p)^2 d\tau=\frac{1}{B}\int_{\bar{t}}^{\bar{t}+\bar{T}}\left(\frac{d\varphi_c}{d\tau}\right)^2 d\tau \qquad (12)$$

where the integrals are computed over period $\bar{T}$ of a surge oscillation and the second and third equalities descend from Eq. (1). Parameter E can be interpreted as the unsteady energy associated with the surge cycle, being defined as the integral over the cycle period of perturbing ''force'' $(\psi_c-\psi_p)$ multiplied by ''displacement'' $d\varphi_c$ [8]. Furthermore, it can be immediately shown that, in the case of transient response of the compressor with no delay time $(\tau_c=0\Rightarrow\psi_c=\psi_{c,ss})$, E is equal to the area of the limit cycle in plane $\varphi_c-\psi_p$. It is clear that $E=0$ in a stable operating point, while high values of this parameter indicate an ineffective stabilization. A useful representation of the control effectiveness can be obtained by plotting the values of E in all the operating points on the unstable branch of the compressor characteristic curve, i.e., within interval $0<\varphi_{ss}<\varphi_{\text{stall}}$. This is done, for example, in Fig. 7 with reference to the compression system with and without the control device.

The model of Eqs. (1)–(5), (11) has been employed to perform a sensitivity analysis to the variations of control parameters R, W, Q, and ξ, aimed at selecting their optimal values for a control device of maximum effectiveness. Preliminary simulations showed that the most favorable conditions for the design of a practical control device are obtained when $A_1 \ll A_2$, i.e., $\alpha\cong-1$. Consequently, the parametric analysis has been carried out by setting:

$$R=-\frac{V_p}{l_{eq}A_1}=-\left(\frac{\rho_0 a_0^4 A_c^2}{\rho_1 g^2 V_p^2}\right)\frac{Q^4}{W} \qquad (13)$$

where l_{eq} and A_1 have been eliminated by using the definitions of W and Q. Position (13) simplifies the parametric analysis, since the number of independent variables is now reduced to three, namely, W, Q and ζ. The sensitivity analysis has been carried out by computing, for each set of control parameters, the mean value of E over the whole unstable branch of the compressor characteristic curve, i.e.:

$$\langle E\rangle=\frac{1}{\varphi_{\text{stall}}}\int_0^{\text{stall}}E\,d\varphi.$$

The results of the parametric analysis are a number of contour plots of $\langle E\rangle$ in plane $W-Q$ at fixed ζ, the most representative of which are shown in Fig. 4. Plots 4 (a,b,c) refer to $\zeta=4000$ and to different values of stability parameter B_0, i.e., 0.2, 0.3, and 0.4, respectively, while plot 4 (d) refers to the case $\zeta=8000$ and $B_0=0.3$. These diagrams have been obtained by using the compressor characteristic at 3000 rpm, but only slight deviations can be expected at different speeds within the compressor operating range $(2000<n<4000\,\text{rpm})$, due to the closeness of the blower characteristic curves [7]. However, it is noted that, if the compressor speed is changed, the same value of B_0 corresponds to different plenum volumes (at 3000 rpm, values $B_0=0.2$, 0.3, 0.4 correspond to $V_p=0.62$, 1.4, 2.5 m^3, respectively).

For each set of parameter values, the maximum displacement of the liquid column, $\eta_{\max}$ can also be computed and reported as contour plots similar to the ones in Fig. 4 [6]. Such information is helpful to the designer, since excessive liquid column displacements have to be avoided. For reference, one of such $\eta_{\max}$ contour lines ($\eta_{\max}=0.05$) is reported as a broken curve in each plot of Fig. 4. Lower values of $\eta_{\max}$ are reached on the upper side of such a curve, while the region below the reported contour line refers to $\eta_{\max}$ values greater than 0.05.

Figures 4(*a,b,c*) show that, when the stability parameter is increased, the region of maximum control effectiveness, i.e., with minimum values of $\langle E \rangle$, shrinks and moves towards lower values of Q and higher values of W. It means that high compressor speeds and/or large plenum volumes require long liquid columns with large surface area A_1 (see the definitions of W and Q), while large displacements of the liquid surface must be accepted. In practice, it is difficult to obtain an acceptable configuration of the control device for the present compression system at $B_0=0.4$, which can be thus considered as the upper limit of the present investigation. By comparing Figs. 4(*b*) and 4(*d*) the effect of the damping coefficient can be singled out. It appears that an increase in ζ causes the shift of the low $\langle E \rangle$ region toward higher values of W, which results in a larger surface area, A_1, of the liquid column. All these results have been used to address the design of an effective control device based on the concept of hydraulic oscillator.

Design of the Control Device

The compression system considered by Arnulfi et al. [7] included a plenum volume of 3.132 m^3 and was operated with values of B_0 varying from 0.304 to 0.608 by modifying the compressor speed from 2000 to 4000 rpm. Since the results of the parametric analysis reported in the previous section showed that the hydraulic oscillator can be effective at B_0 values smaller than 0.4, the possibility of an experimental evaluation of the control effectiveness by varying the operating conditions of the original system appeared to be too limited. Therefore, the plant was modified by using a plenum with a smaller volume, namely, $V_p=0.78\,\mathrm{m}^3$. This way, B_0 values ranging from 0.153 to 0.305 can be obtained by varying the compressor speed, if the increase in the system volume due to the introduction of the control device is neglected.

As already mentioned, low values of area ratio A_1/A_2 were considered, so as to reduce l_{eq} to the height of the liquid column of area A_1 and to obtain sufficiently high values of parameter W. The availability of a water pool of large surface area (40 m^2) allowed such a requirement to be fulfilled: The oscillator was designed as a box of proper cross-sectional area, A_1, submerged in the pool, thus resulting in an area ratio, A_1/A_2, of order 10^{-2}.

The design of the prototype was carried out so as to obtain a highly flexible device and a wide possibility of system adjustment (Fig. 5). The box height was made large enough to allow the system to be operated within a wide range of pressure, i.e., of compressor speed, without the need to modify the box submersion, l_s. Value $A_1=0.36\,\mathrm{m}^2$ was chosen as a compromise between the requirements of high W values and of limited air volume variations due to changes of the water level inside the control device. In addition, area A_1 was selected so as to reduce the amplitude of the water column oscillations during the unsteady operation of the system. An adjustable gate is employed as the dissipative component of the control device. It is placed at the bottom of the box and allows different damping values to be obtained by changing the flow area. It is also possible to vary the equilibrium length of the water column, l_{eq}, independently of pressure conditions, by simply modifying the submersion of the box in the pool. The control device is connected to the plenum by means of a PVC pipe of large diameter, so that negligible pressure differences between plenum and oscillator are obtained also in unsteady conditions.

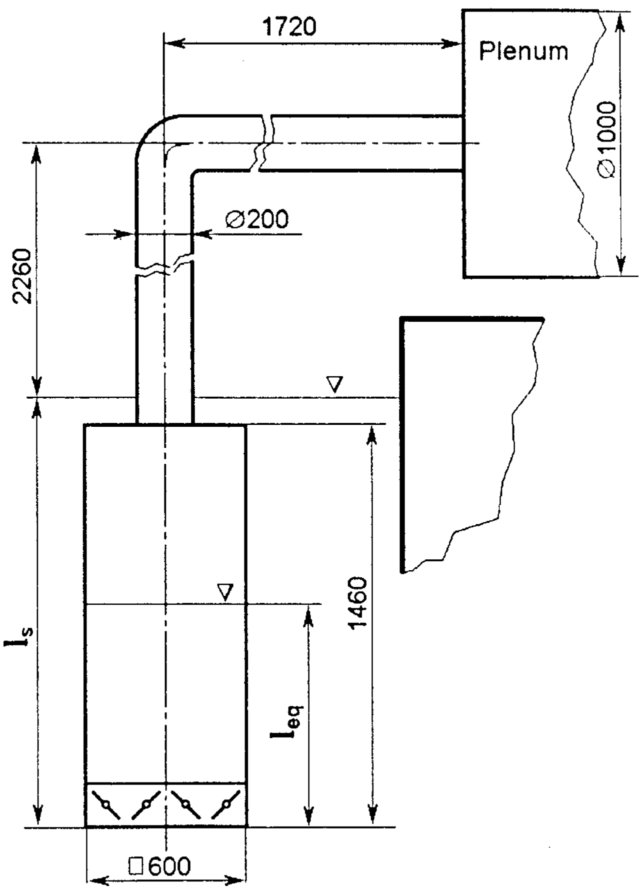

Fig. 5 Schematic of the hydraulic oscillator

The performance of the control device is shown in Fig. 6, as plots of parameters W and Q versus l_{eq}. The figure also shows the effective air volume of the system, which is the sum of the plenum volume and the air volume inside the control device. The values of B_0, which can be obtained when the compression system is coupled with the present hydraulic oscillator, range from 0.171, at 2000 rpm and maximum submersion l_s (minimum effective air volume), to 0.391, at 4000 rpm and minimum submersion level (maximum effective air volume).

The comparison of the curves in Fig. 6 with the contour plots at $B_0=0.3$ in Fig. 4 allows a significant prediction of the device effectiveness to be obtained. With reference to the case $\xi=4000$ (Fig. 4(*b*)), it is observed that the system can be stabilized for any value of l_{eq} with limited values of η (the maximum displacement of the water column is about 200 mm). At $\zeta=8000$ (Fig. 4(*d*))

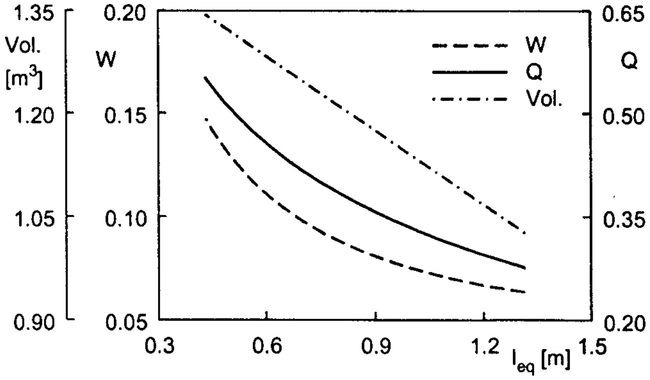

Fig. 6 Performance of the hydraulic oscillator

stabilization can be achieved only for low values of l_{eq}, so that it is possible to operate the system also in conditions of progressive failure of the control effectiveness.

Experimental Validation

A test plant was suitably equipped for the experimental evaluation of the control effectiveness. The instrumentation system, described by Arnulfi et al. [7] and previously used for testing the compression system without control devices, was completed with a capacitive transducer (injected-charge type) of the water level in the hydraulic oscillator. Measurements of plenum pressure, compressor delivery pressure, pressure difference at the orifice flow meter, and water level in the oscillator were performed during 32 Helmoltz periods at a sampling rate of 512 readings per Helmoltz period. The pressure in the oscillator was not measured, because preliminary tests showed that it is very close to the plenum pressure also in unsteady conditions.

Tests were carried out at compressor speeds of 2000, 2500, and 3000 rpm, with an oscillator submersion of 1.836 m. The aim of these tests was to verify the control device capability of operating in different conditions without varying l_s. Tests were performed also at 3500 rpm by using a greater box submersion, namely, 2.436 m, with the aim of approaching the predicted limits of the device effectiveness. For comparison, measurements on the compression system without the control device were also performed at the same rotational speeds. The measurements were carried out for different settings of the valve at the plenum exit, obtained by gradually decreasing the throttle area. The transient behavior of the system during processes of valve throttling and re-opening was also recorded at all the compressor speeds.

The experimental investigation demonstrates the effectiveness of the present control device, at least within the limits predicted by the numerical simulation. This is shown in the diagrams of Fig. 7, which report, for all the compressor speeds, the values of dimensionless unsteady energy E evaluated at different equilibrium flow coefficients. For convenience, E values are divided by T/T_H. These results have been obtained with gate settings corresponding to damping values $\zeta=8000$ at 2000, 2500 and 3000 rpm, and $\zeta=4000$ at 3500 rpm. Each plot shows the experimental and the numerical results in both cases of controlled and uncontrolled compression system.

The effectiveness of the hydraulic oscillator is evident in all the operating conditions. At 2000 rpm, where the uncontrolled compression system turns out to be stable at flow rates significantly lower than the stall limit, the stability range is widened further on, while at the higher rotational speeds the suppression of surge instability is obtained in a large flow range. At very low flow rates ($\varphi_{ss}<0.05$) the system remains unstable, but the associated unsteady energy is reduced by about 50 percent, in very good agreement with the theoretical prediction. Another region of residual instability is observed near the stall limit, as predicted by the nonlinear stability analysis. In this zone, nonperiodic flow oscillations sometimes occur, as found under similar conditions by Arnulfi et al. [7,9]. It must be observed that, in such conditions, parameter E cannot provide a reliable measure of the unsteady energy associated with the system instability. The differences between experimental and theoretical results, which can be observed under uncontrolled conditions, can be explained by considering the rough modelization of the transient compressor response associated with the stall development, Eq. (3), which implies an inaccurate prediction of the compressor delivery pressure, i.e., of the ψ_c values to be used in Eq. (12). On the contrary, the numerical results concerning the controlled compression system appear to be very accurate at low and medium compressor speeds. Only at 3500 rpm the suppression of surge instability, which is found experimentally in a large flow range, is not predicted by the model. This can be justified by considering that such a compressor speed condition is close to the effectiveness limit of the hydraulic oscillator, so that both the theoretical analysis and the experimental results are extremely sensitive to small errors in the setting of the control parameters, such as ζ and l_{eq}. This is also the reason

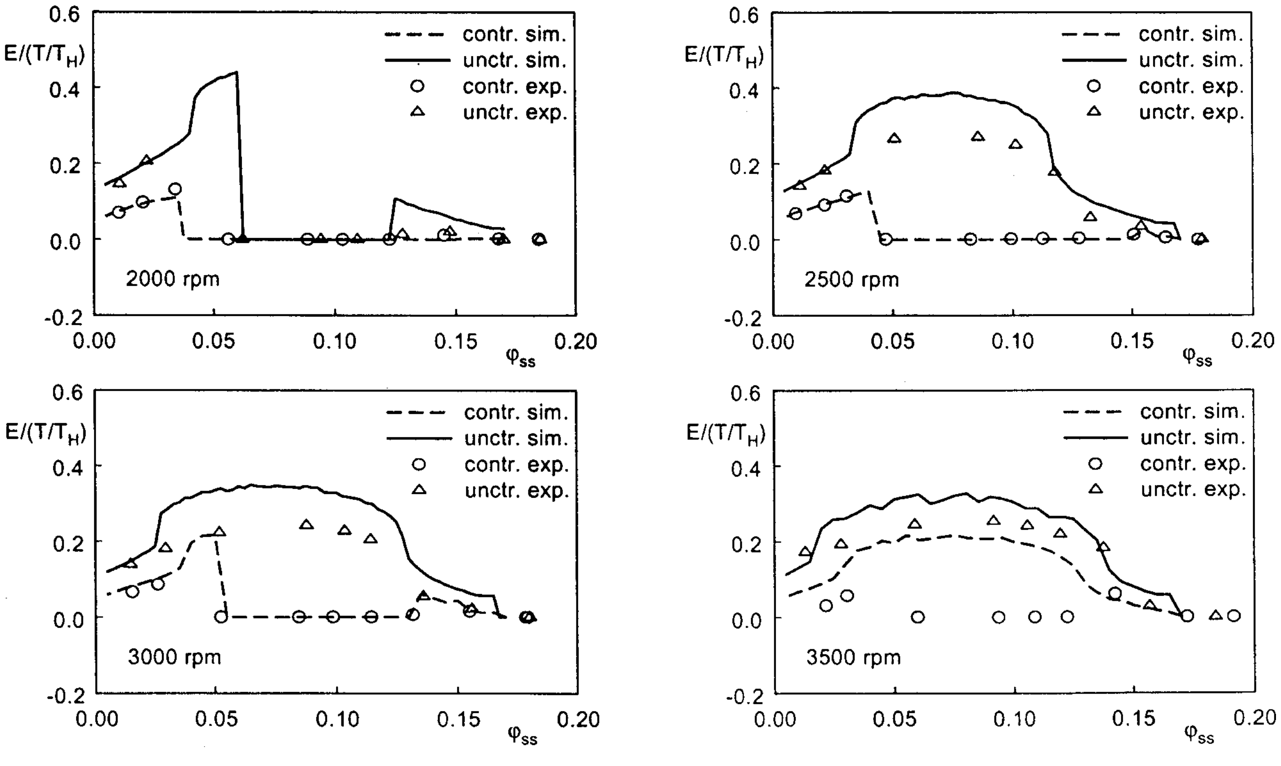

Fig. 7 **Stability index $E/(T/T_H)$ versus flow coefficient for controlled and uncontrolled system at different compressor speeds**

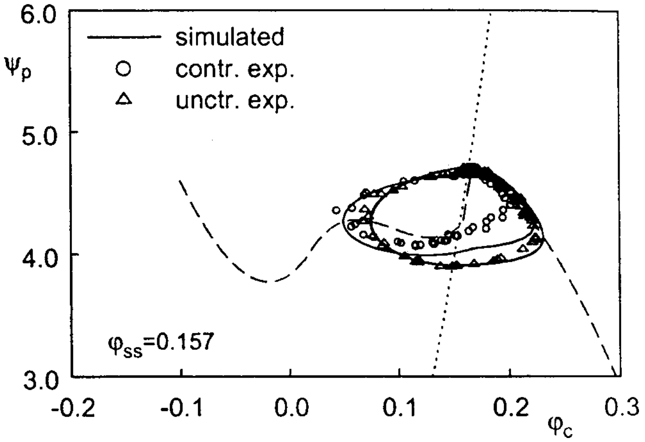

Fig. 8 Surge cycles at 3000 rpm and $\varphi_{ss}=0.157$

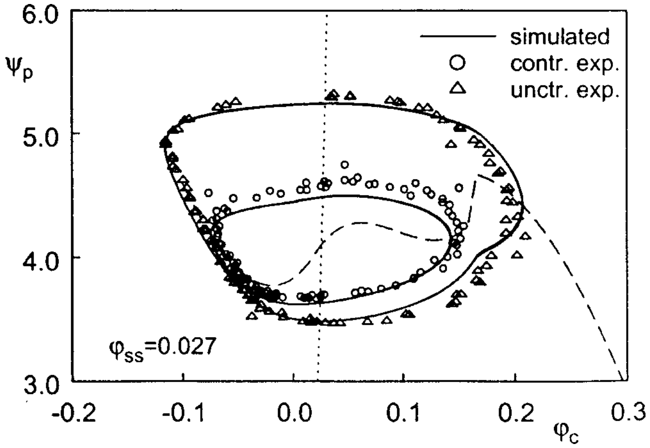

Fig. 10 Surge cycles at 3000 rpm and $\varphi_{ss}=0.027$

why the investigation at the highest values of B, which are reached at 4000 rpm, will be carried out in a future stage of the research.

The effect of the control device in some significant operating conditions is illustrated in detail in Figs. 8–10. These figures show the surge cycles in plane $\varphi_c-\psi_p$ at 3000 rpm and for the steady equilibrium flow coefficients of 0.157, 0.100, and 0.027. For reference, the steady characteristic curves of the compressor (broken line) and of the throttle valve (dotted line) are also plotted in the figures. At $\varphi_{ss}=0.157$ (Fig. 8), corresponding to a flow rate little lower than the stall one, it turns out that the control device is only able to slightly reduce the surge oscillations, as already shown in Fig. 7. At $\varphi_{ss}=0.100$ (Fig. 9), surge is completely suppressed and the limit cycle is reduced to a stable equilibrium point. When the compressor is operated at a very low flow rate, $\varphi_{ss}=0.027$, the control device is not capable of stabilizing the system (Fig. 10). However, it is worth noting that also in such a severe condition the hydraulic oscillator produces a strong reduction of the amplitude of the surge cycle. The agreement between numerical and experimental results appears to be very good for the uncontrolled system, while some acceptable differences can be observed when the oscillator is coupled to the compression system.

Figure 11 shows the time histories of φ_c, ψ_p, and η obtained in the operating condition of Fig. 10 ($n=3000$ rpm, $\varphi_{ss}=0.027$), for the only case of controlled system. The oscillations of all the variables appear to be correctly predicted, as amplitude, frequency, and phase are concerned. It can be observed that the curve of water level in the oscillator exhibits a phase shift of about a quarter of a period when referred to the pressure oscillation. The negative values of η are due to the fact that, in the present operating condition, the mean plenum pressure is smaller than the steady equilibrium pressure.

The overall effectiveness of the control device can be evaluated by computing, at every compressor speed, the mean value of parameter $E/(T/T_H)$ over the instability region, $0<\varphi_{ss}<\varphi_{\text{stall}}$. Plots of mean stability index $\langle E/(T/T_H)\rangle$ versus parameter B are shown in Fig. 12 for the cases of controlled and uncontrolled system. Such plots are only based on experimental data, while the values of B in controlled conditions are computed on the basis of the effective air volume (plenum + oscillator) evaluated at a flow rate slightly higher than the stall limit one. It turns out that, at the same value of B, the mean unsteady energy is reduced by about 90 percent when the control device is introduced. This result appears to be even better considering that, at the same compressor speed, the presence of the oscillator implies an increase in B (due to a larger air volume) and hence a greater tendency of the system to instability. This effect could be limited by selecting a proper value of the box height for each given pressure range.

To complete the present analysis, the results of two experimental tests carried out at 3000 rpm on the controlled system during throttle valve operation are shown in Figs. 13(*a*) and 13(*b*). The former refers to a gate setting which determines a ζ value of about 8000, while the latter corresponds to a damping parameter of about 4000. The valve was closed from a given stable operating point to a final position, corresponding to a flow rate close to zero,

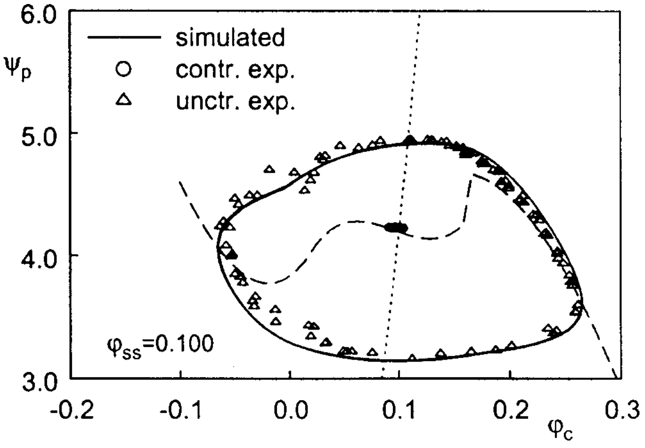

Fig. 9 Surge cycles at 3000 rpm and $\varphi_{ss}=0.100$

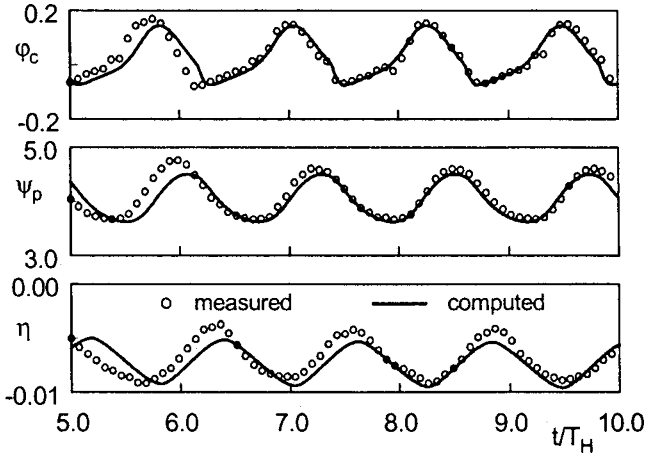

Fig. 11 Time histories of φ_c, ψ_p, and η for the controlled compression system ($n=3000$ rpm, $\varphi_{ss}=0.027$)

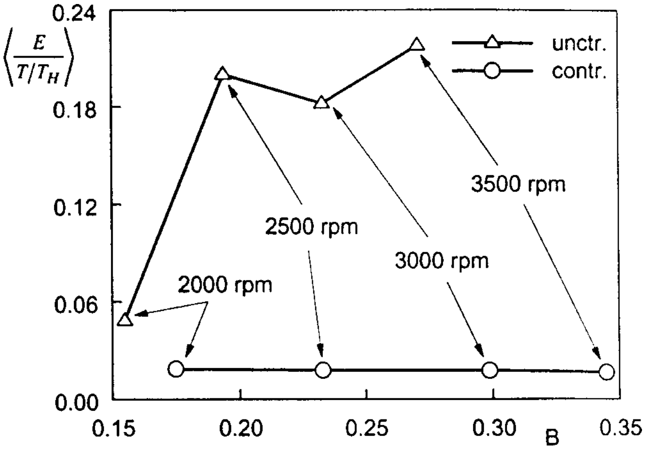

Fig. 12 Experimental values of mean stability index $\langle E/(T/T_H)\rangle$ versus parameter B

and then it was re-opened until the initial stable point was recovered. The figures show that during the closing stage the system is stabilized, as previously discussed, and that the value of ζ has no significant influence on the stabilization process. On the contrary, during the opening period the system turns out to be quite unstable, which means that, in the present condition, the hydraulic oscillator is not able to damp fully developed perturbations. In this latter case, the possibility of stabilizing the system at flow parameters smaller than the stall limit one strongly depends on the value of the damping parameter.

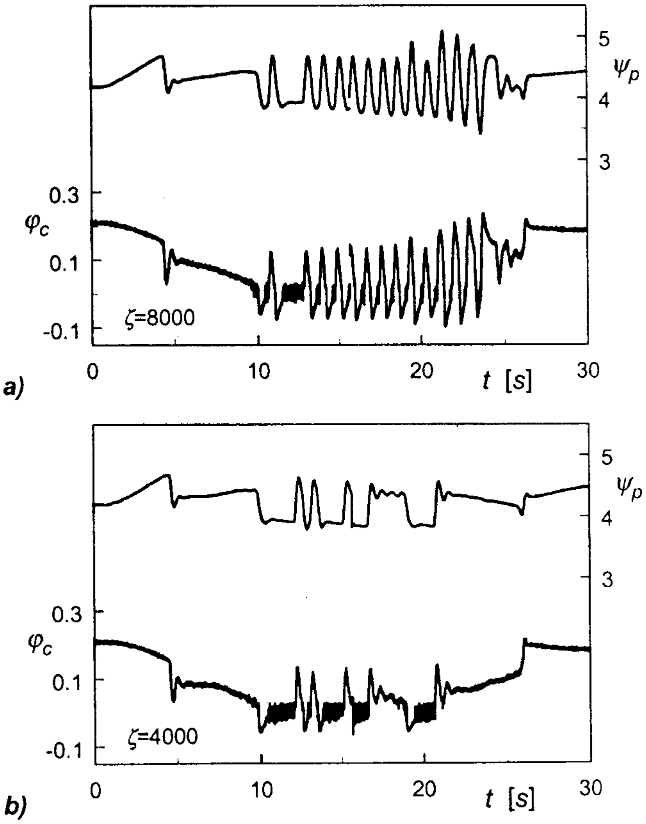

Fig. 13 Time histories of φ_c and ψ_p during throttle valve operation for different damping values (n=3000 rpm)

Conclusions

A detailed theoretical analysis of devices for the passive control of compressor surge has been carried out. The controlled system has been modeled by using a nonlinear lumped parameter approach. It was demonstrated that a mass-spring-damper controller, based on a movable plenum wall, is not suitable for the application to industrial compression plants, due to intrinsic technical limitations (overly large values of wall mass and of auxiliary plenum volume). To remove such a limitation, an innovative control device has been developed, namely, a hydraulic oscillator (patent pending). The new device was analyzed theoretically and a parametric study was performed in order to single out the optimal values of the control parameters. A prototype was then designed, built, and coupled to the low pressure, industrial size compression system described by Arnulfi et al. [7].

Experimental tests carried out at various operating conditions demonstrated the effectiveness of the proposed control device: The compression system was stabilized, within significantly wide ranges of flow rate, for values of stability parameter B up to 0.3 or slightly larger. The reliability of the theoretical model and the accuracy of the numerical results were also proven.

Future developments of the present research include a deeper insight into the behavior of the controlled system when (i) the limits of the hydraulic oscillator effectiveness are approached (B values close to 0.4, with reference to the features of the present compression system) and (ii) the system is moved from a deep surge condition to an operating point where stability is normally achieved when starting from a steady condition. In both situations, preliminary tests, partially reported in the present paper, showed that the system can be stabilized only if a very accurate selection of the control parameters is performed.

The main limit of the present configuration of the control device appears to be the large hydraulic head caused by high plenum pressures, which prevents the hydraulic oscillator from being coupled with high pressure systems. Therefore, a study will be undertaken to overcome such a limitation by considering technical solutions such as the equalization of the mean pressure on the two liquid surfaces of the oscillator or the use of a pressure converter.

Acknowledgments

The present research has been supported by the National Council of Research (CNR).

Nomenclature

A = area
a = speed of sound
B = stability parameter
C = loss coefficient
E = surge unsteady energy
f = friction factor
g = gravitational acceleration
L = equivalent length
l = liquid column length
l_s = oscillator submersion
m = mass
$\dot{m}$ = mass flow rate
M = Mach number
p = pressure
Q = frequency parameter
q = wall displacement
t = time
T = period
$\tilde{T}$ = dimensionless period $=T\omega_H$
U = impeller peripheral velocity
u = flow velocity
V = volume
W = aeroelastic coupling parameter

y = volume flow rate
z = liquid level
γ = ratio of specific heats
φ = flow coefficient
η = dimensionless displacement
ρ = density
τ = dimensionless time
υ = dimensionless velocity
ω = rotational frequency
ψ = pressure coefficient
ζ = damping parameter
θ = angle

Subscripts

0 = ambient
aux = auxiliary
c = compressor
eq = equilibrium
H = Helmholtz
l = liquid
p = plenum
ss = steady state
t = throttle valve
w = wall

Appendix

Equation of Motion of an Oscillating Liquid Column. Let's consider a liquid filling a ''U'' tube with a general distribution of cross-sectional area $A(s)$, s being the curvilinear coordinate along the tube axis; see Fig. 14. Liquid surfaces A_1 and A_2 are subjected to pressures p_1 and p_2, respectively, which, in general, can vary with time. If a one-dimensional unsteady flow of the liquid column is assumed, the force balance over an elemental portion of fluid, such as the one shown in Fig. 14, leads to the following momentum equation:

$$\frac{\partial u}{\partial t}+\frac{\partial}{\partial s}\left(\frac{u^2}{2}\right)+\frac{1}{\rho_l}\frac{\partial p}{\partial s}+\frac{1}{2}f\frac{c}{A}|u|u-g\cos\theta=0 \qquad (A1)$$

where flow velocity and pressure are functions of both space s and time t, f is the wall friction factor ($\tau_w=1/2\rho_l f|u|u$) and $c(s)$ is the tube perimeter at location s.

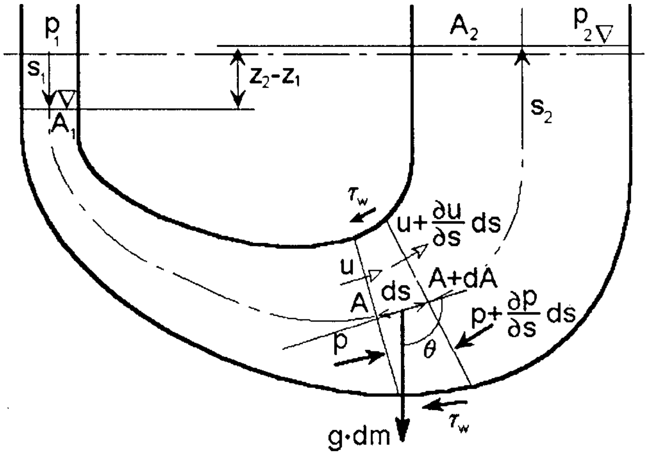

Fig. 14 Oscillating liquid column

If the assumption of incompressible flow is made, the continuity equation provides:

$$u(s,t)A(s)=y(t) \qquad (A2)$$

i.e., volume flow rate y is independent of s, as well as its time derivative $\dot y$. By substituting Eq. ($A2$) into Eq. ($A1$), the following equation is obtained:

$$\frac{\dot y}{A}+\frac{y^2}{2}\frac{d}{ds}\left(\frac{1}{A^2}\right)+\frac{1}{\rho_1}\frac{\partial p}{\partial s}+\frac{f}{2}\frac{c}{A^3}|y|y-g\cos\theta=0 \qquad (A3)$$

Equation ($A3$) can be integrated along the instantaneous liquid column length, i.e., from s_1 to s_2, so obtaining:

$$\dot y\int_{s_1}^{s_2}\frac{ds}{A}+\frac{y^2}{2}\left[\left(\frac{1}{A_2^2}-\frac{1}{A_1^2}\right)+\frac{|y|}{y}\int_{s_1}^{s_2}\frac{fc}{A^3}ds\right]+g(z_2-z_1)=\frac{p_1-p_2}{\rho_1} \qquad (A4)$$

since $ds\cos\theta=-dz$.

A simpler form of Eq. ($A4$) can be obtained by assuming that the two liquid surfaces oscillate in vertical constant-area portions of the ''U'' tube. In this case, if the liquid column oscillates around an equilibrium position corresponding to constant value $(p_1-p_2)_{eq}$, one can write:

$$\int_{s_1}^{s_2}\frac{ds}{A}=\int_{s_{1,eq}}^{s_{2,eq}}\frac{ds}{A}-\frac{s_1-s_{1,eq}}{A_1}+\frac{s_2-s_{2,eq}}{A_2} \qquad (A5)$$

By setting $l_{eq}=A_1\int_{s_{1,eq}}^{s_{2,eq}}ds/A$, $x=s_1-s_{1,eq}$, and by observing that mass conservation requires $A_1(s_1-s_{1,eq})=A_2(s_2-s_{2,eq})$, Eq. ($A5$) reduces to:

$$\int_{s_1}^{s_2}\frac{ds}{A}=\frac{1}{A_1}\left\{l_{eq}+\left[\left(\frac{A_1}{A_2}\right)^2-1\right]x\right\}=\frac{1}{A_1}(l_{eq}+\alpha x) \qquad (A6)$$

Similarly, the gravitational term in Eq. ($A4$) can be expressed as:

$$g(z_2-z_1)=g\left[(z_2-z_1)_{eq}+x+\frac{A_1}{A_2}x\right]=\frac{(p_1-p_2)_{eq}}{\rho_1}+g\left(1+\frac{A_1}{A_2}\right)x \qquad (A7)$$

Furthermore, the approximation is made:

$$C=A_1^2\int_{s_1}^{s_2}\frac{fc}{A^3}ds\cong\text{const} \qquad (A8)$$

i.e., friction losses are assumed to be independent of time.

By substituting Eqs. ($A6$), ($A7$), and ($A8$) into Eq. ($A4$) and by observing that $y=uA=\dot s_1A_1=\dot xA_1$, the final equation is obtained:

$$(l_{eq}+\alpha x)\ddot x+\frac{1}{2}\left(\alpha+\frac{|\dot x|}{x}C\right)\dot x^2+Kx=\frac{(p_1-p_2)-(p_1-p_2)_{eq}}{\rho_l} \qquad (A9)$$

where $K=g(1+A_1/A_2)$.

For the application of Eq. ($A9$) to the present case of hydraulic oscillator, it is assumed that coefficient C accounts also for losses due to obstructions (valves, orifices, elbows, etc.), besides friction losses. Furthermore, the present application requires $p_2=p_{2,eq}=p_0$, so that the term on the right-hand side of Eq. ($A9$) assumes the simpler form $(p_1-p_{1,eq})/\rho_l$.

References

[1] Epstein, A. H., Ffowcs Williams, J. E., and Greitzer, E. M., 1989, ''Active Suppression of Compressor Instabilities,'' J. Propul. Power, **5**, p. 204.
[2] Ffowcs Williams, F. E., and Huang, X., 1989, ''Active Stabilization of Compressor Surge,'' J. Fluid Mech., **204**, p. 245.
[3] Pinsley, J. E., Guenette, G. R., Epstein, A. H., and Greitzer, E. M., 1991, ''Active Stabilization of Centrifugal Compressor Surge,'' ASME J. Turbomach., **113**, p. 723.
[4] Simon, J. S., Valavani, L., Epstein, A. H., and Greitzer, E. M., 1993, ''Evaluation of Approaches to Active Compressor Surge Stabilization,'' ASME J. Turbomach., **115**, p. 57.
[5] Gysling, D. L., Dugundji, J., Greitzer, E. M., and Epstein, A. H., 1991, ''Dynamic Control of Centrifugal Compressor Surge Using Tailored Structures,'' ASME J. Turbomach., **113**, p. 710.
[6] Giannattasio, P., and Giusto, C., 1998, ''Modellizzazione e analisi parametrica

di un sistema di controllo passivo del pompaggio,'' *Proc. LIII Congresso Nazionale ATI*, Firenze, Italy, p. 1179.

[7] Arnulfi, G. L., Giannattasio, P., Giusto, C., Massardo, A. F., Micheli, D., and Pinamonti, P., 1999, ''Multistage Centrifugal Compressor Surge Analysis—Part I: Experimental Investigation,'' ASME J. Turbomach., **121**, p. 305.

[8] Greitzer, E. M., 1976, ''Surge and Rotating Stall in Axial Flow Compressors—Part I: Theoretical Compression System Model,'' ASME J. Eng. Power, **98**, p. 190.

[9] Arnulfi, G. L., Giannattasio, P., Giusto, C., Massardo, A. F., Micheli, D., and Pinamonti, P., 1999, ''Multistage Centrifugal Compressor Surge Analysis—Part II: Numerical Simulation and Dynamic Control Parameters Evaluation,'' ASME J. Turbomach., **121**, p. 312.

Jens Friedrichs
Pfleiderer-Institute,
TU Braunschweig,
Braunschweig, Germany

Sven Baumgarten
Research Department,
KSB AG,
Frankenthal, Germany

Günter Kosyna
Pfleiderer-Institute,
TU Braunschweig,
Braunschweig, Germany

Udo Stark
Fluid Mechanics Institute,
TU Braunschweig,
Braunschweig, Germany

Effect of Stator Design on Stator Boundary Layer Flow in a Highly Loaded Single-Stage Axial-Flow Low-Speed Compressor

The paper describes an experimental investigation of the stator hub and blade flow in two different stators of a highly loaded single-stage axial-flow low-speed compressor. The first stator (A) is a conventional design with blades of rectangular planform. The second stator (K) is an unconventional, more advanced design with blades of a special planform, characterized by an aft-swept leading edge with increasing sweep angle toward hub and casing. The experimental results show that stator K exhibits a much better hub performance than stator A, finally leading to a better overall performance of stage K compared to stage A. The better hub performance of stator K is, primarily, the result of a planform effect of the newly introduced blades with an aft-swept leading edge and the aerodynamics of an aft-swept wing. [DOI: 10.1115/1.1370168]

Introduction

In highly loaded single-stage low-speed compressors of low hub/tip ratio the hub degree of reaction (*R*) may be less than 0.5. Accordingly, the stator hub de Haller number may be quite low and the diffusion factor quite high so that hub boundary layer separation and corner stall are likely to occur. The present paper is concerned with the aerodynamics of two different stators of a highly loaded single-stage low-speed compressor ($\varphi=0.45$, $\psi=0.6$, $\nu=0.55$). The design point diffusion factor (*D*) and the de Haller number (*DH*) of the critical stator hub section are $D=0.62$ and $DH=0.56$ at 5 percent span of both stators. While the diffusion factor is close to the limit (0.6), the de Haller number is far beyond the limit, usually taken as 0.75.

The first stator (A) is a conventional design with blades of rectangular planform and standard (A10) NACA 65-series blade sections. The second stator (K) is a more advanced design with blades of special planform, characterized by an aft-swept leading edge with increasing sweep angle toward the hub (30 deg) and casing (10 deg), combined with an unswept trailing edge, again with NACA 65-series blade sections, but this time with circular arc mean camber lines. For blades of this type a three-dimensional relief of the endwall sections could be expected, following swept wing theory [1,2], together with a reduction in cross-passage flow, endwall boundary layer separation, and losses. For the same reasons the shape of the mean camber line has been changed from A10 to circular arc.

The data to be presented for each of the two stators are (*i*) the stage characteristics, (*ii*) the stator hub and blade pressure distributions, (*iii*) the stator hub and blade oil flow pictures, and (*iv*) the stator exit contour plots of the axial velocity. The two data sets will be compared and discussed. Special attention will be paid to the development of the boundary layers on hub and blades, including boundary layer separations. These separations will be shown to be highly different in stators A and K, especially at part load conditions.

There is little information in the available literature for the use of sweep for subsonic core compressor blading [3,4]; more information is available for the use of sweep for transsonic compressor blading [5–7]. With one exception, all the aforementioned papers deal with the flow in rotors; only Tweedt et al. [4] investigate the flow in stators.

Stage Design and Test Facility

Performance tests and flow field investigations were carried out on a low-speed single-stage axial compressor (Fig. 1) at the Pfleiderer-Institute, Technical University of Braunschweig. The compressor has an outer diameter $D_o=0.4$ m and a hub to tip ratio $\nu=0.55$. The rotor comprises 16 blades of standard (A10) NACA 65-series blade sections and the aerodynamic design is such as to

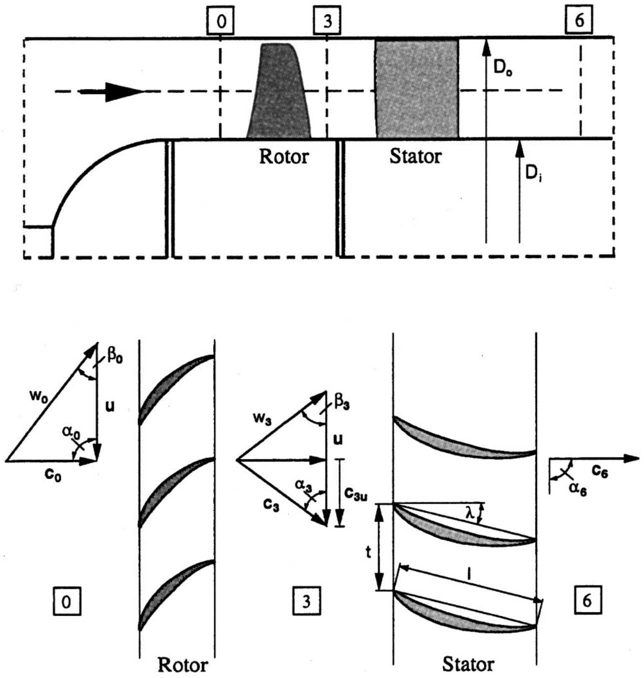

Fig. 1 Single-stage axial-flow compressor and midspan section

---

Contributed by the International Gas Turbine Institute and presented at the 45th International Gas Turbine and Aeroengine Congress and Exhibition, Munich, Germany, May 8–11, 2000. Manuscript received by the International Gas Turbine Institute February 2000. Paper No. 2000-GT-616. Review Chair: D. Ballal.

Table 1 Stage design parameters

Flow coefficient	$\varphi=c_0/u_o$	0.45
Pressure rise coefficient	$\psi=2\Delta p/(\rho u_o^2)$	0.60
Hub/tip ratio	$\nu=D_i/D_o$	0.55
Casing diameter	D_i	0.4 m
Rotational speed	n	75 1/s

give a free vortex flow for the design parameters in Table 1. The rotor tip clearance to chord ratio is $s/l=0.0067$ with a tip clearance $s=0.4$ mm and a chord $l=60$ mm.

To complete the stage, two different stators were designed using a smoothed rotor exit angle distribution—a distribution without the ''kickups'' at hub and casing—as a design input [8]. The stator blades are shown in Fig. 2 and some of the geometric and aerodynamic parameters are summarized in Table 2. The first stator (A) is a conventional design with 19 blades of rectangular planform and standard (A10) NACA 65-series blade sections of constant chord. The second stator (K) is a new design with blades of special planform, characterized by an aft-swept leading edge between hub and casing. At hub and tip, this planform creates geometric and aerodynamic similarities to the center section of hypothetical swept-back wings with similar sweep angle distributions. Accordingly, the blade hub and casing sections were expected to reduce the leading edge loading and, as a consequence, to initiate less secondary flow [9,10]. A stator of this type was designed by using circular arc mean camber lines of constant curvature at all radii resulting in an increasing chord length toward the hub and, to a much lesser extent, toward the casing. The mean camber lines were combined with NACA 65-series thickness distributions (constant $d=5.4$ mm, variable d/l) and the resulting profiles were radially stacked in such a way as to give a straight trailing edge and a backward swept leading edge. The usage of circular arc mean camber lines, instead of standard A10 camber lines, leads to a basic reduction in leading edge loading, which is reinforced by the planform produced loading reduction.

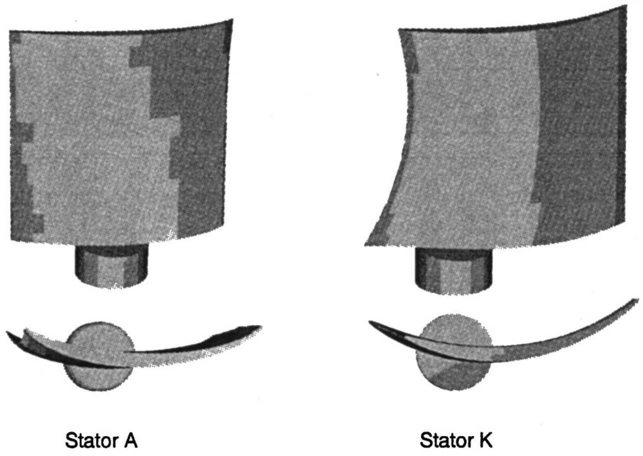

Fig. 2 Stator blades

The stage was run at a constant speed (4500 rpm) and the air flow rate adjusted by means of a throttle and an auxiliary fan until a prescribed flow coefficient φ was obtained. The velocities encountered in the stage were such that the flow may be regarded as incompressible. The Reynolds number (Re) based on chord and relative inlet velocity at the rotor tips is $\mathrm{Re}=4.1\times10^5$ for the design flow conditions. The rotor/stator distance is $a=80$ mm from rotor trailing edge to stator leading edge at midspan height. This is comparatively large and leads to a reduced unsteadiness of the stator flow.

Results and Discussion

Overall Performance. The unstalled static pressure rise (ψ) and efficiency (η) characteristics for compressors A and K are shown in Fig. 3. As expected, the stage with the aft-swept stator K, and the flow physics of an aft-swept aircraft wing, has a higher pressure rise and a higher efficiency than the stage with the conventional unswept stator A. For $\varphi=0.35$ (part load), 0.45 (design flow rate), and 0.55 (overload), the increase in efficiency is about 8, 1, and 3 efficiency points. The flow field investigations, which are described below, were carried out for $\varphi=0.37$ and 0.45, specially marked in Fig. 3.

Pressure Distributions. Surface pressure distributions may be used to analyze the flow next to the surface under consideration. Figures 4 and 5, for example, show measured and calculated pressure distributions $\Delta p_{\mathrm{H}}^{*}=[p(z)-p_0]/[p_6-p_0]$ for the blade hub sections in stators A and K, respectively, at design flow rate $\varphi=0.45$. The experimental distributions were measured on the hub along the blades with pressure taps close to the blade surfaces. The theoretical distributions were calculated using the Martensen [11] method developed for two-dimensional (2D) inviscid flow. The inlet angle α_3 was assumed 6.5 deg above the measured hub endwall angle ($\alpha_3=28$ deg, both stators, taken from the oil flow pictures at a position far in front of the stators) in an attempt to allow, at least approximately, for the 3D relief discovered by Wadia and Beacher [8]. This relief, which is not a topic of the present paper, consists of an unloading of the leading edge region in 3D Euler results compared to 2D cascade results using measured inlet flow angle distributions.

A comparison of Figs. 4 and 5 is not an easy task because more than one parameter was changed when stator K was designed on the basis of stator A. Nevertheless, the results expected can be seen immediately. (i) A basic reduction of the leading edge loading is achieved by using circular arc mean camber lines instead of standard A10 camber lines. This may be seen by comparing the

Table 2 Stator blades and design geometry

		Stator	
		A	K
Chord	$l_{h=50\%}$	90 mm	90 mm
Pitch	$t_{h=50\%}$	51.3 mm	64.8 mm
Span	h	90 mm	90 mm
Aspect ratio	$h/l_{h=50\%}$	1.0	1.0
Blade number	Z	19	15
Solidity	$l/t_{h=5\%/50\%/95\%}$	2.38/1.75/1.39	2.13/1.39/1.11
Stagger angle	$\lambda_{h=5\%/50\%/95\%}$	21.2/17.4/19.1 deg	23.1/18.5/19.2 deg
Camber line		A10	circular arc
Camber	$\vartheta_{\mathrm{eq}}/\vartheta$	62.4/49.8/60.3 deg	71.8/62.6/64.0 deg
Blade section		NACA 65-006	NACA 65-006
Rel. thickness	$d/l_{h=50\%}$	0.06	0.06
Diffusion factor	$D_{h=5\%/50\%/95\%}$	0.62/0.45/0.56	0.62/0.50/0.63
de Haller number	$c_6/c_3\ _{h=5\%/95\%}$	0.56/ /0.69	0.56/ /0.69

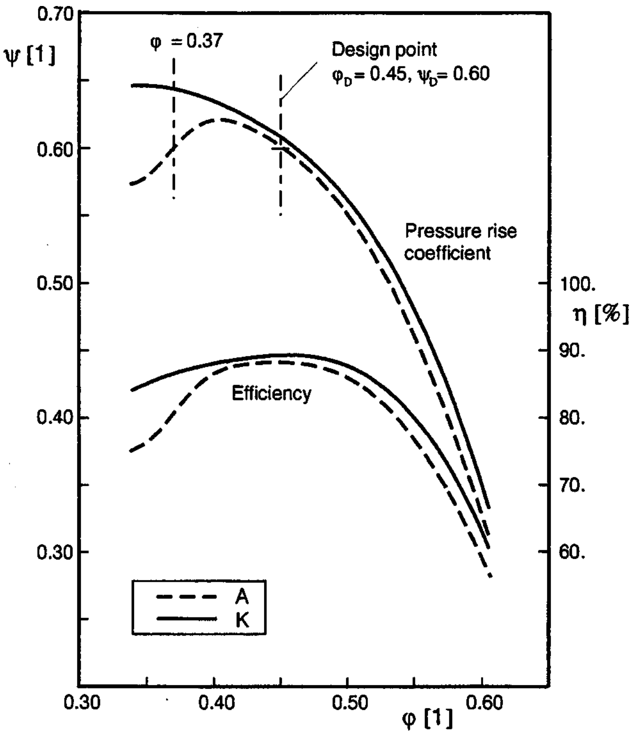

Fig. 3 Compressor performance characteristics

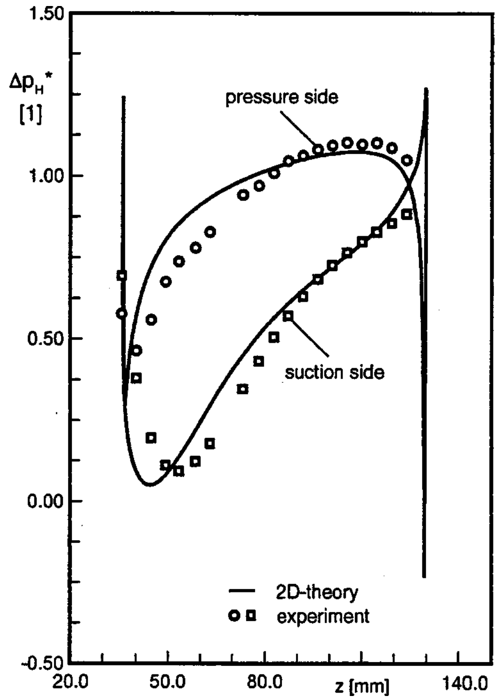

Fig. 5 Experimental and 2D calculated pressure distribution at blade hub section stator K at design point (φ=0.45)

theoretical results in Figs. 4 and 5. (ii) In addition, a three-dimensional reduction of the leading edge loading is obtained by the introduction of new blades with a special planform, characterized by an aft-swept leading edge between hub and casing. This can be verified by comparing the theoretical and experimental results in Fig. 5. Together with a slight increase of the trailing

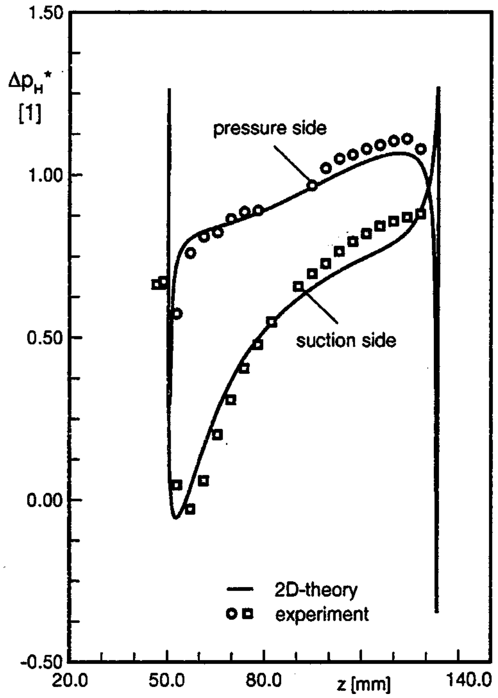

Fig. 4 Experimental and 2D calculated pressure distribution at blade hub section stator A at design point (φ=0.45)

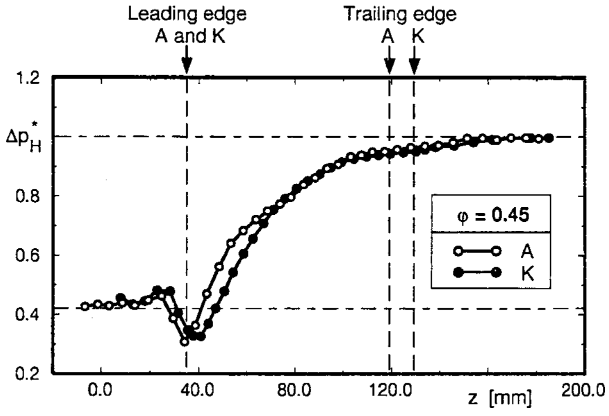

Fig. 6 Comparison of the hub pressure distributions on passage center lines at design flow rate (φ=0.45)

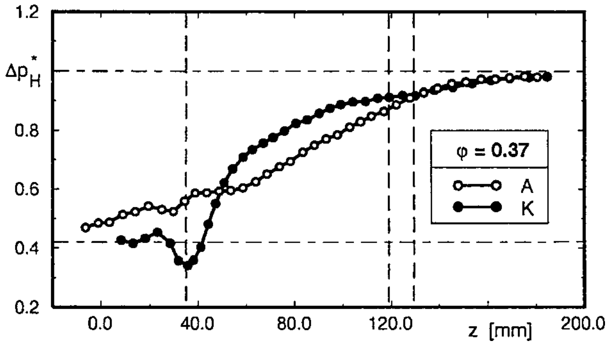

Fig. 7 Comparison of the hub pressure distributions on passage center lines at part load (φ=0.37)

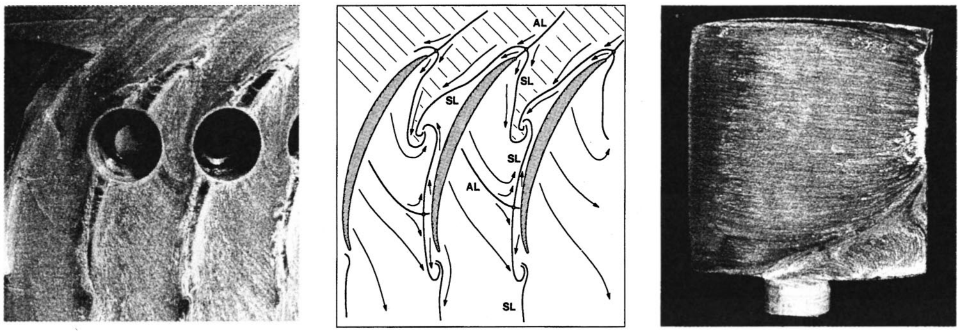

Fig. 8 Oil flow picture of stator A at design point ($\varphi=0.45$) on stator hub and suction surface

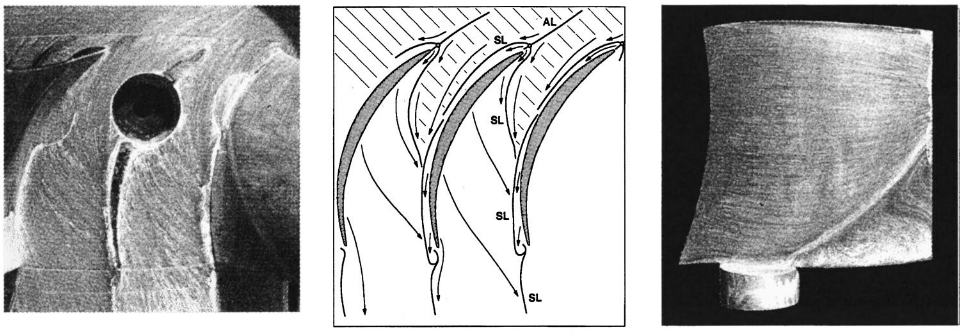

Fig. 9 Oil flow picture of stator K at design point ($\varphi=0.45$) on stator hub and suction surface

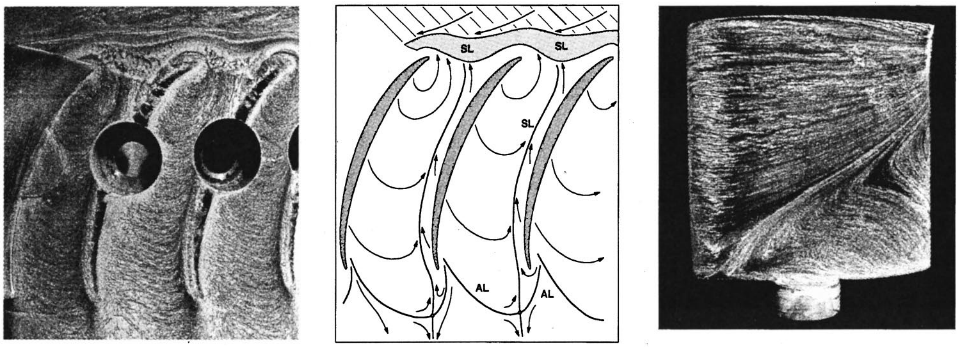

Fig. 10 Oil flow picture of stator A at part load ($\varphi=0.37$) on stator hub and suction surface

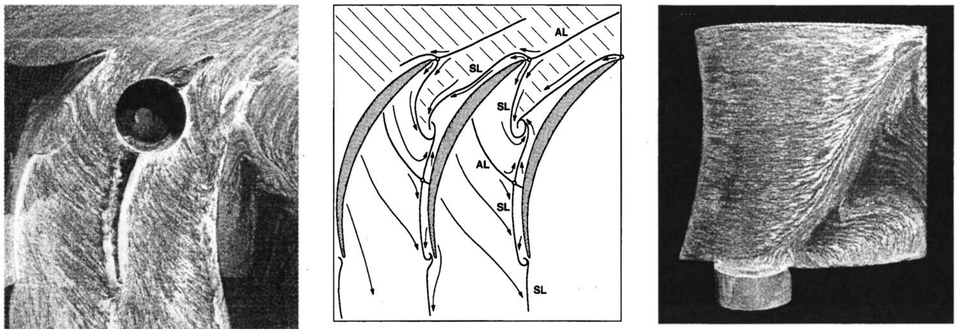

Fig. 11 Oil flow picture of stator K at part load ($\varphi=0.37$) on stator hub and suction surface

edge loading, this is in agreement with aircraft wing theory. The integrated section loading is nearly the same in both cases (i.e., in experiment and theory).

Figures 6 and 7 are leading edge to leading edge comparisons of the hub pressure distributions for stators A and K measured along the passage center line between inlet and outlet for the flow rates $\varphi=0.45$ (design flow rate) and 0.37, respectively. The pressure coefficient $\Delta p_{\mathrm{H}}^{*}$ in Figs. 6 and 7 is defined as before and plotted against the axial direction z. Figure 6 shows that the deceleration of the flow starts directly at the beginning of the passage for stator A, which is a camber line (A10) effect, and at some point further downstream in the passage for stator K, which is a planform effect. For stator K the pressure distributions for $\varphi=0.45$ (Fig. 6) and 0.37 (Fig. 7) are quite similar in shape, indicating a hub boundary layer development without dramatic changes. This is different in the case of stator A with a completely changed pressure distribution for $\varphi=0.37$ compared to $\varphi=0.45$. For $\varphi=0.37$, Fig. 7 shows a long-drawn-out pressure rise, indicating severe hub boundary layer separation.

Flow Visualizations. Because of the high stator hub loading, expressed by the low de Haller number ($DH=0.56$ at 5 percent span), severe hub boundary layer separation could be expected in stator A. Stator K can be assumed to show a much better hub performance as a result of a reduced cross-passage pressure gradient with smaller secondary flow, hub boundary layer separations, and losses. From the surface pressure measurements, described and discussed before, a reduced cross-passage pressure gradient is known to exist. The corresponding reaction of the endwall flow, including separations, was investigated with an oil flow technique.

Oil flow pictures showing the hub endwall and blade suction surface flow in stator A and K are presented in Figs. 8 and 9 for $\varphi=0.45$ (design point) and in Figs. 10 and 11 for $\varphi=0.37$ (part load). In addition rough sketches of the endwall characteristics are included.

Oil flow pictures are photographs of specially prepared surfaces showing the surface pattern of the shear stress lines. The directions of these lines are nearly identical with the flow directions of the fluid particles next to the surface.

Following the criteria described by Tobak and Peak [12], the characteristic features of the surface flow may be identified, for example, as (*i*) three-dimensional separation lines (SL, convergence of the shear stress lines), (*ii*) three-dimensional (re)attachment lines (AL, divergence of the shear stress lines), and (*iii*) so-called singular points (saddle and nodal points, foci). With the help of these features, a first idea of the flow field next to the surface under consideration may be developed.

An analysis of the hub endwall flow starts best with Figs. 8 and 9 for $\varphi=0.45$. By comparison it may be seen that both configurations develop a classical secondary flow superimposed on a primary flow. At about the end of the entrance region, the endwall boundary layer is separated in stator A, as well as in configuration K, with the important difference, however, that in A a vortex—with a spiral point at the hub—is established, which is not so in K. The vortex in A has a strong influence on the downstream flow, which is, due to the vortex induced velocities, partly reversed between the cross-passage attachment line and the spiral point. In K, without a vortex in the passage, there is no backward flow but forward flow only throughout the passage.

With decreasing flow rate, the hub endwall flow deteriorates in stator A as well as in stator K, in K, however, to a much smaller extent than in A, which follows from Figs. 10 and 11 for the special flow rate 0.37 and from Fig. 3 for all flow rates between design and stall. Figure 10 shows backward flow in stator A throughout the passage between outlet and inlet while Fig. 11 for stator K indicates backflow in a small region only, similar to stator A at $\varphi=0.45$ in Fig. 8.

Figures 8 to 11 show the experimental results, which are in close agreement with the expectations at the beginning of the present investigation. At high stator hub loadings, when wall stall of the hub is likely to occur very soon, the use of aft-swept stator blades turns out to be a possibility to delay wall stall to higher loadings or lower de Haller numbers. It should be recalled that stator K represents a very simple design. Still better results may be expected with an optimized design.

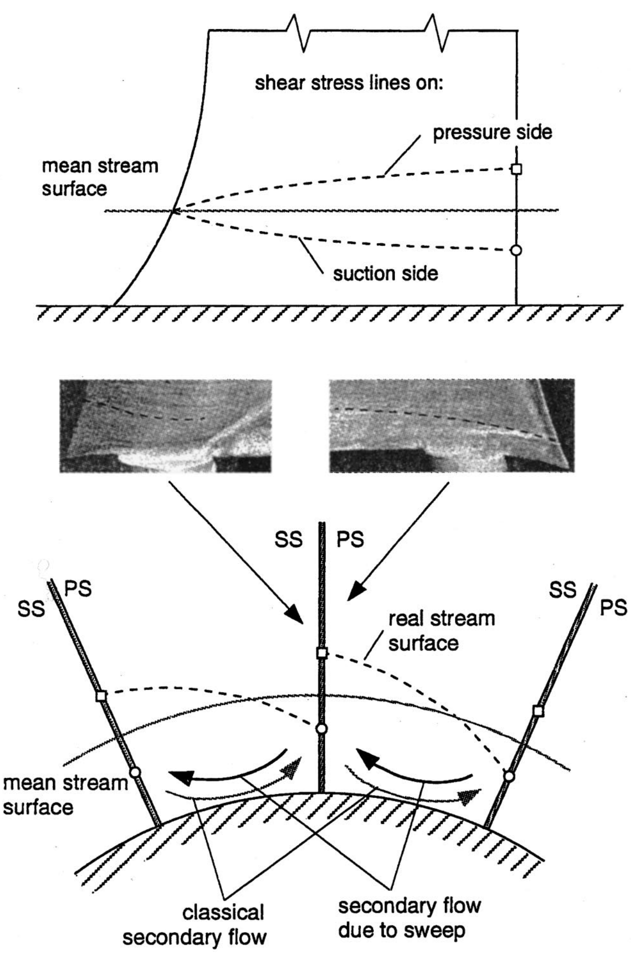

Fig. 12 Combination of classical and new secondary flow

The tendency of stator K blades to produce less secondary flow than stator A blades has been mentioned and explained as a planform effect of the aft-swept blades (plus a contribution due to the mean-line change). Now, by inspection of the right side pictures in Figs. 9 and 11, nonaxisymmetric stream surfaces may be seen to exist in stator K [13], thus indicating a new secondary flow, similar to the classical secondary flow, but opposite in direction. The new secondary flow is again a planform effect and has a strong influence on the net amount of secondary flow in stator K.

A good description of the new secondary flow has been given by Place and Cumpsty [14] in a discussion on Sasaki and Breugelmanns [14]: ''Over the forward part of the blades, the backward sweep induces flow near the suction surface toward the endwall, (which can be seen nicely in Fig. 9 of the present paper) and induces flow near the pressure surface away from the endwall. These changes to the spanwise flow oppose the classical secondary flow created by turning the increasing endwall boundary layer within the blade passage, and therefore reduce the cross-passage flow of endwall fluid toward the suction surface.''

A corresponding sketch with a shear stress line on the suction and pressure side of an aft-swept blade, with a real and a mean stream surface, showing the classical and the sweep induced secondary flow is presented in Fig. 12.

Further inspection of the right side pictures in Figs. 8–11

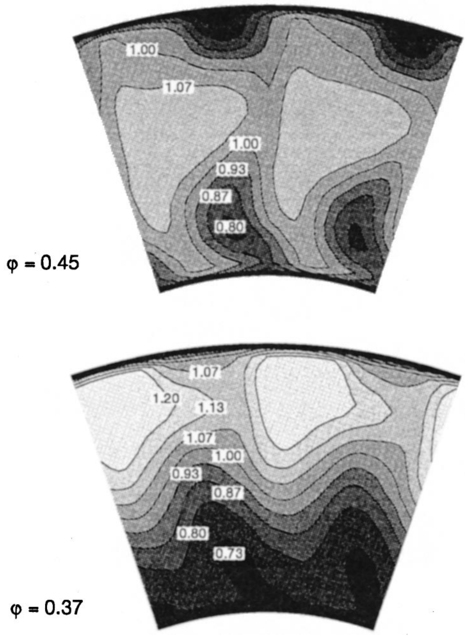

Fig. 13 Axial-velocity ratio behind stator A

shows hub corner stall for stators A and K, growing dramatically with decreasing flow rate. This happens in stator A with a forward (against axial flow direction) moving stall point and a following separation line, which remains roughly parallel to itself, and in stator K with a fixed beginning of the corner stall and a following separation line, which becomes increasingly inclined toward the blade axis. The resulting stall zones are different in shape but have nearly the same size. The flow direction in the stall zones is from radial to axial reverse and vice versa and has its origin on the hub or on the pressure side of the blades, respectively.

All in all there seems to be much less effect of sweep on corner stall than on hub endwall flow and stall.

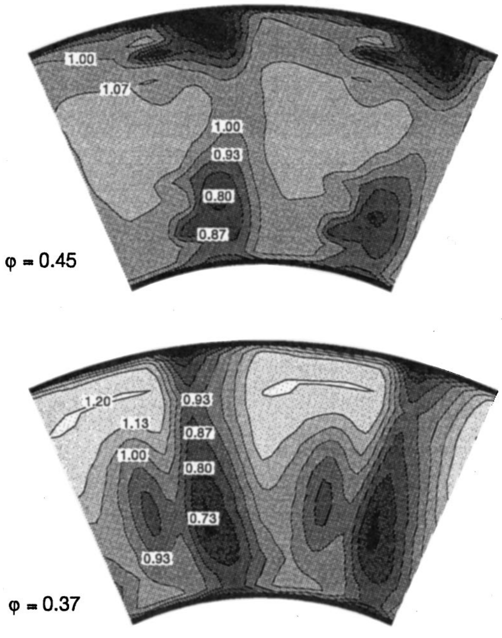

Fig. 14 Axial-velocity ratio behind stator K

Wake Measurements. Detailed radial-circumferential measurements of the dynamic and static pressure and the flow direction (yaw and pitch) were made at the stator inlet plane ''3'' (60 mm ahead of the stator leading edge at midspan height) and at the stator exit plane ''6'' (90 mm aft of the stator trailing edge). The measured velocities were resolved into components in axial (z), radial (r), and circumferential (Θ) directions. Contour plots of the normalized axial velocity $(c_{6z}/\overline{c_{6z}})$ at the stator exit plane are shown for stators A and K in Figs. 13 and 14, respectively. Contour plots of the axial velocity may be used to identify possible regions of high blockage and losses.

A passage vortex and a moderate corner stall are the important phenomena of stator A and K exit flow for $\varphi=0.45$ in Figs. 8 and 9. Downstream of the stator these phenomena combine to a single one as indicated in Figs. 13 and 14, that is, to a single vortex with an axial velocity distribution as shown in the contour plots. The hub boundary layer is extremely thin, in stator A as well as in K. Lowering the flow rate to $\varphi=0.37$ results in a similar growth of the hub corner stall in stators A and K (see Figs. 10 and 11). On the other hand the simultaneous development of the hub endwall flow is known to be different in stators A and K. While stator A (with a conventional blading) develops a severe wall stall, stator K (with a new blading) shows little change of the endwall flow, apart from a small amount of reverse flow (see again Figs. 10 and 11). In stator A, the wall and corner stall generates a substantial amount of endwall blockage (Fig. 13), which is completely missing in stator K (Fig. 14), although the endwall loading is as high, and the de Haller number as low as in stator A. On the other hand, there is also blockage in stator K, caused by the passage vortex and the corner stall, which do not combine to a single feature. All in all there is less blockage in stator K than in stator A and this leads to an increasingly better performance with decreasing flow rate of stage K compared to stage A (see Fig. 3).

Summary and Conclusions

An experimental investigation, with theoretical support, has been carried out to analyze the blade and hub endwall flow in two different stators of a highly loaded single-stage axial-flow low-speed compressor ($\varphi=0.45$, $\psi=0.6$, $\nu=0.55$). Design point diffusion factor (D) and de Haller number (DH) of the critical hub section are $D=0.6$ and $DH=0.56$ for both stators. The first stator (A) is a conventional design with blades of rectangular planform and NACA 65-series thickness distribution on A10 mean camber lines. The second stator (K) is an unconventional, more advanced design with blades of special planform, characterized by an aft-swept leading edge with increasing sweep angle toward the hub and casing combined with an unswept trailing edge, again with NACA 65-series thickness distribution, this time on circular arc mean camber lines.

An analysis of the experimental results, that is, the stage characteristics, hub and blade pressure distributions, oil flow pictures, and contour plots of the axial velocity at the stator exit shows an increasingly stalled hub (covered with reverse flow) in stator A and an unstalled hub (with negligible reverse flow) in stator K with decreasing flow rate. This result is partly due to the successful implementation of sweep into the blade design and partly due to the reduced curvature of the mean camber lines. Further analysis shows increasing hub corner stall with decreasing flow rate for both stators A and K. In stator A, wall and corner stall together generate a substantial endwall blockage, which is completely missing in stator K, although the endwall loading is as high and the de Haller number as low as in stator A.

With less blockage overall in stator K than in A, stage K shows an increasingly better performance than stage A with decreasing flow rate.

Nomenclature

See definitions in Fig. 1 and Tables 1 and 2.

References

[1] Multhopp, H., 1950, ‘‘Methods for Calculating the Lift Distribution of Wings (Subsonic Lifting-Surface Theory),’’ Aeronautical Research Council, Reports and Memoranda, No. 2884.

[2] Küchemann, D., 1952, ‘‘A Simple Method for Calculating the Span and Chordwise Loading on Straight and Swept Wings of Any Given Aspect Ratio at Subsonic Speeds,’’ Aeronautical Research Council, Reports and Memoranda, No. 2935.

[3] Mohammed, K. P., and Prithviraj, D., 1977, ‘‘Investigation on Axial Flow Fan Impellers With Forward Swept Blades,’’ ASME J. Turbomach., **99**, pp. 543–547.

[4] Tweedt, D. W., Okiishi, T. H., and Hathaway, M. D., 1986, ‘‘Stator Endwall Leading-Edge Sweep and Hub Shroud Influence on Compressor Performance,’’ ASME J. Turbomach., **108**, pp. 224–232.

[5] Wennerstrom, A. J., and Puterbaugh, S. W., 1984, ‘‘A Three-Dimensional Model for the Prediction of Shock Losses in Compressor Blade Rows,’’ ASME J. Eng. Gas Turbines Power, **106**, pp. 295–299.

[6] Wadia, A. R., Szucs, P. N., and Crall, D. W., 1998, ‘‘Inner Workings of Aerodynamic Sweep,’’ ASME J. Turbomach., **120**, pp. 671–682.

[7] Hah, C., Puterbaugh, S. W., and Wadia, A. R., 1998, ‘‘Control of Shock Structure and Secondary Flow Field Inside Transonic Compressor Rotors Through Aerodynamic Sweep,’’ ASME Paper No. 98-GT-561.

[8] Wadia, A. R., and Beacher, B. F., 1990, ‘‘Three-Dimensional Relief in Turbomachinery Blading,’’ ASME J. Turbomach., **112**, pp. 587–597.

[9] Place, J. M. M., 1997, ‘‘Three-Dimensional Flow in Core Compressors,’’ Ph.D. dissertation, University of Cambridge, Cambridge, United Kingdom.

[10] Friedrichs, J., Baumgarten, S., and Stark, U., 1999, ‘‘Effect of Stator Design on Stator Hub Boundary Layer Separation in a Highly Loaded Single-Stage Axial-Flow Low-Speed Compressor,’’ IMechE Conf. Trans., **1B**, pp. 573–582.

[11] Martensen, E., 1954, ‘‘Die Berechnung der Druckverteilung an dicken Gitterprofilen mit Hilfe von Fredholmschen Integralgleichungen zweiter Art,’’ *Mitteilungen aus dem Max-Planck-Institut für Strömungsforschung und der Aerodynamischen Versuchsanstalt*, No. 23.

[12] Tobak, M. T., and Peake, D. J., 1982, ‘‘Topology of Three-Dimensional Separated Flows,’’ Annu. Rev. Fluid Mech., **14**, pp. 61–85.

[13] Smith, L. H., and Yeh, H., 1963, ‘‘Sweep and Dihedral Effects in Axial-Flow Turbomachinery,’’ ASME J. Basic Eng., **85**, pp. 401–416.

[14] Place, J. M. M., and Cumpsty, N. A., 1998, Discussion to ‘‘Comparison of Sweep and Dihedral Effects on Compressor Cascade Performance,’’ by Sasaki, T., and Breugelmanns, F., ASME J. Turbomach., **120**, pp. 454–464.

Kinematic Analysis of 3-D Swept Shock Surfaces in Axial Flow Compressors

Peng Shan
Associate Professor,
Department of Jet Propulsion,
Beijing University of Aeronautics
and Astronautics,
Beijing 100083, P. R. China
e-mail: PShan@buaa.edu.cn

This paper is part II of a comprehensive study on the blade leading edge sweep/bend of supersonic and transonic axial compressors. The paper explores and analyzes the kinematic characteristic variables of three-dimensional (3-D) swept shock surfaces. In the research field studying the sweep aerodynamics of axial flow compressors and fans, many types of high loading swept blades are under intensive study. So, in both direct and inverse design methods and experimental validations, an accurate grasp of the sweep characteristic of the blade's 3-D swept shock surface becomes of more concern than before. Associated with relevant blading variables, this paper studies the forward and zero and backward sweeps of shock surfaces, defines and resolves every kind of useful sweep angle, obtains dimensionless sweep similarity factors, suggests a kind of method for the quantitative classification of 3-D shock structures, and proposes the principle of 3-D shock structure measurements. Two rotor blade leading edge shock surfaces from two high loading single stage fans are analyzed and contrasted. This study is the foundation of the kinematic design of swept shock surfaces. [DOI: 10.1115/1.1370159]

Introduction

Since the 1980s, the design strategy of swept blades or sweep aerodynamics has been an important technique for the development of modern high loading axial compressors and fans. Wennerstrom [1] stated that ''a variety of attempts were made to exploit this concept within the 1950s and 1960s. None met with notable success. One problem was that a number of attempts simply swept a leading edge in a linear manner.'' Nowadays, many types of supersonic forward or backward sweep blades and vanes, which employed a variety of leading edge spatial curves and achieved much higher performances, have been designed or tested [2,3]. Even so, it has been difficult up to now to indicate certainly for what purpose what kind and extent of leading edge sweep should be used. The mechanisms of sweep on the supersonic flow field should be further investigated, and the application scheme formulated. It is thought reasonable to divide the issue into kinematic and aerodynamic analyses, and develop the associated and progressive studies [4]. Part I concerning the helical surface model (HSM) was offered by Shan and Zhou [5].

Features of Turbomachine Sweep Shocks

The swept leading edge of a blade is mainly used to reduce the Mach number component normal to an oblique leading edge shock surface (LESS), in addition to its boundary layer controlling effects in subsonic flow fields. The appearance of shock is not a profitless thing, since a shock offers a strong gain in loading and pressure. A double-shock system consisting of a LESS and a downstream passage shock also naturally offers a stall margin. In fact the swept leading edge directly controls the structure of every shock surface. However, in this kinematic analysis attention is paid first to an arbitrary single shock surface, and the result is not subject to the patterns of shock systems.

The sweep aerodynamics of turbomachinery is not the same as that of an airplane. First, the task of the compressor cascade is to load and compress, so the pressure difference between the up and downstream of the cascade is great, while that of the wing is small. Second, due to rotation, the spanwise velocity distribution is strongly inhomogeneous in front of and behind a three-dimensional (3-D) cascade shock, so it generates a direct shock penetrating loss and many kinds of indirect viscous losses. Third, the controlling principle of the aftershock flow is no longer a wedge deflecting flow but a radial-equilibrium flow. So, in addition to the reduction of a direct loss, an optimum 3-D shock surface should suppress every kind of mixing loss generated in the downstream primary flow due to the shock-induced intensive inhomogeneous velocity and pressure. Minimizing the total sum of shock losses is this paper's intention in 3-D swept shock studies.

Noting the following ideas is helpful for one to grasp the kinematic analysis. A forward/zero/backward sweep of a shock surface should be judged from the viewpoint of a relative motion between a flow and a shock, because a resultant physical flux vector penetrating a shock with its distribution is substantially determined by the relative angle of the shock surface's normal vector to the relative incident flow [6]. Quoting the original use of ''the aerodynamic sweep angle'' [7], we call this kind of 3-D shock surface sweep an aerodynamic sweep. Consequently, the sweep of a leading edge spatial curve onto the meridional plane is called a meridional sweep, or a formal sweep of the leading edge, because it serves only as an influencing factor of the aerodynamic sweep. Though, by taking into account the flow's relative motion toward a leading edge, a concept of the leading edge curve aerodynamic sweep has been analytically defined [8], to the idea and analytical purpose of the aerodynamic sweep of a shock surface, this leading edge curve sweep should also serve only as a kind of formal sweep.

Definitions of Shock Surface Sweep Angles

Taking a model compressor with a steady, axisymmetric upstream flow and a shock system, one obtains the undisturbed upstream velocity distribution and two kinds of its non-complete forms:

$$\mathbf{w}_1(r)=w_{1r}(r)\mathbf{e}_r+w_{1c}(r)\mathbf{e}_c+w_{1z}(r)\mathbf{e}_z$$
$$=c_{1r}(r)\mathbf{e}_r+[c_{1c}(r)-r\omega]\mathbf{e}_c+c_{1z}(r)\mathbf{e}_z \qquad (1)$$

$$\mathbf{w}_1(r)=w_{1c}(r)\mathbf{e}_c+w_{1z}(r)\mathbf{e}_z \qquad (2)$$

$$\mathbf{c}_{1m}(r)=c_{1r}(r)\mathbf{e}_r+c_{1z}(r)\mathbf{e}_z \qquad (3)$$

Contributed by the International Gas Turbine Institute and presented at the 45th International Gas Turbine and Aeroengine Congress and Exhibition, Munich, Germany, May 8–11, 2000. Manuscript received by the International Gas Turbine Institute February 2000. Paper No. 2000-GT-492. Review Chair: D. Ballal.

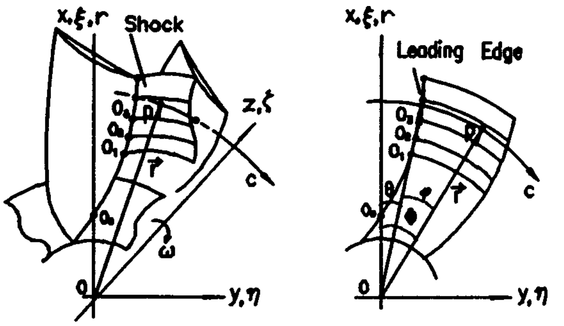

a. Isometric projection b. Axial projection

Fig. 1 The leading edge spatial curve and helical surface model (HSM) generated on it

With a single parameter r, the leading edge curve's parametric equations in the relative cylinder frame are defined as (Fig. 1)

$$r=r, \quad \theta=\theta(r), \quad z=z(r) \tag{4}$$

Concepts of Ten Kinds of Important 3-D Shock Sweep Angles. The definitions below are for a right-running shock specified by Shan and Zhou [8] unless otherwise stated.

γ_{3r} is the angle included between the normal vector of a 3-D shock surface on its point P and the negative relative velocity $-\mathbf{w}_1$ (Fig. 2). The subscript $3r$ means that complete 3-D relative velocity $\mathbf{w}_1$ of Eq. (1) is used here. γ_{3r} is the real and largest sweep angle at point P of a shock surface, and determines the direct shock loss at P. Alternatively, when adopting a 2-D $\mathbf{w}_1$ in Eq. (2), an approximate spatial relative sweep angle γ_r, together with it two easily comprehensible projection sweep angles γ_{cr} on a 2-D cylinder surface, and γ_{rr} on a 2-D meridional plane, are three kinds of frequently used relative sweep angles. Here the subscripts cr and rr denote circumferential relatively and radial relatively respectively.

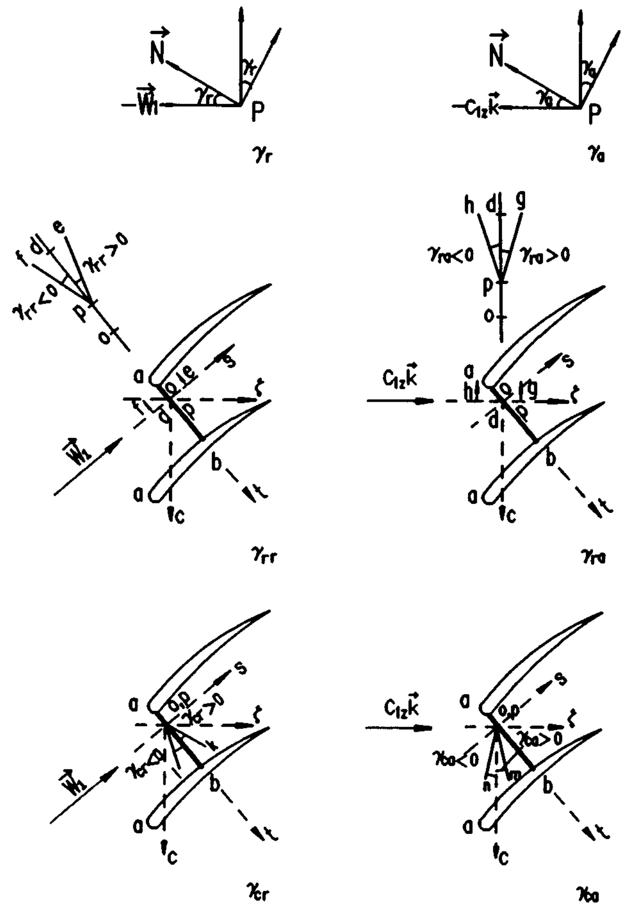

Fig. 2 Definitions of six kinds of frequently used shock sweep angles

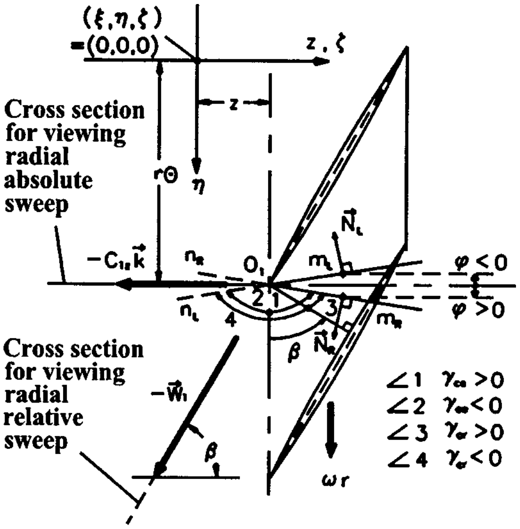

Fig. 3 The jump of a shock's N, the left-running shock's appellation

Analogously, γ_{3a} is the angle included between the 3-D shock's normal vector on point P and the meridional component of the negative absolute velocity $-\mathbf{c}_{1m}$. The subscript a denotes using an absolute velocity. γ_{3a} is very helpful for judging the orientation of a shock surface in the rotating cylinder frame $(r\mathbf{e}_r, \Phi\mathbf{e}_c, \zeta\mathbf{e}_z)$. Alternatively, when adopting a 1-D $\mathbf{c}_{1m}$ by omitting the radial component in Eq. (3), an approximate spatial absolute sweep angle γ_a, together with its two projection sweep angles γ_{ca} on a 2-D cylinder surface and γ_{ra} on a 2-D meridional plane, are three kinds of frequently used absolute sweep angles. When, e.g., point P is on a leading edge, γ_{ra} is approximately the meridional sweep angle of the leading edge's meridional projection $z(r)$, the most familiar sweep angle.

Among the above eight kinds of sweep angles, six of them, γ_r, γ_{cr}, γ_{rr}, γ_a, γ_{ca}, and γ_{ra}, are frequently used in design processes. Why are only the projections of the approximate spatial sweep angles γ_r and γ_a used more? The reason is that employing a projected sweep angle is useful both for obtaining a simplified expression of the shock's sweep head and magnitude in three orthogonal coordinate surfaces and for approximately calculating a direct shock loss. This paper also derived two projected circumferential sweep angles γ_{3cr} and γ_{3ca} from the above two accurate spatial sweep angles γ_{3r} and γ_{3a}, for they are more useful.

Domains of Sweep Angles and Sweep Angles of a Left-Running Shock. As a cross product of two tangent vectors, $\mathbf{N}$ always points from the downstream to the upstream of a shock surface, in terms of the upstream/downstream of an absolute component $c_{1z}\mathbf{k}$. When a right-running shock turns to a left-running shock at the angle $\gamma_{ca}=\pi/2$ (Fig. 3), an upwind surface alternation of the shock must be encountered, together with a direction-jump of $\mathbf{N}$ and, if using a HSM, a sign jump of the ascendent function $f(r)$. Considering this one can derive the domains of sweep angles as

$$\begin{array}{ll} \gamma_a, \gamma_{3a} \in [0, \pi/2] & (\textit{Having an angle jump} \\ \gamma_{ca}, \gamma_{3ca}, \gamma_{ra}, \gamma_{rr} \in [-\pi/2, \pi/2] & \textit{for } \mathbf{N} \textit{ jumping} \\ \gamma_{cr}, \gamma_{3cr}, \gamma_r, \gamma_{3r} \in [-\pi, \pi/2] & \textit{within the domains}) \end{array} \tag{5}$$

Among these, there are half domains which are beyond $\pm\pi/2$, because β itself occupies a domain of $\pi/2$.

According to the direction of **N**, we now analyze the reasonable and convenient appellation of a left-running shock's sweep head. Take γ_{ca} as an example. A left-running shock $\overline{n_L O_1}$, belonging to the circumferential absolute "forward sweep" shock $\overline{nO}$ in Fig. 2, is assumed in Fig. 3. We call another left-running shock $\overline{O_1 m_L}$ an absolute "backward sweep" shock, though it has the negative value of the absolute sweep angle in $\gamma_{ca}\in[-\pi/2,0]$, because this shock is obtained by odd jumps of the shock's **N**. With γ_{ca} increasing further and going into the positive domain $[0,\pi/2]$ as the shock $\overline{n_R O_1}$, we still call it an absolute "forward sweep" shock. Finally, by even jumps of **N**, it returns to a circumferential absolute "forward sweep" shock $\overline{n_L O_1}$.

Direct Solution of the Exact Spatial Relative Sweep Angle

From Eq. (1) for the cylinder frame, the parametric equation of $\mathbf{w}_1$ in a Cartesian frame is

$$\mathbf{w}_1(r)=w_{1\xi}(r,\varphi)\mathbf{i}+w_{1\eta}(r,\varphi)\mathbf{j}+w_{1\zeta}(r,\varphi)\mathbf{k} \tag{6}$$

$$\begin{cases} w_{1\xi}(r,\varphi)=w_{1r}(r)\cos[\theta(r)+\varphi]-w_{1c}(r)\sin[\theta(r)+\varphi] \\ w_{1\eta}(r,\varphi)=w_{1r}(r)\sin[\theta(r)+\varphi]+w_{1c}(r)\cos[\theta(r)+\varphi] \\ w_{1\zeta}(r,\varphi)=w_{1z}(r) \end{cases} \tag{7}$$

so the spatial incident angle γ_{3r} of a relative flow to **N** is

$$\begin{aligned}\cos\gamma_{3r}&=\frac{-\mathbf{w}_1\cdot\mathbf{N}}{|-\mathbf{w}_1||\mathbf{N}|}=-\frac{w_{1\xi}h_\xi+w_{1\eta}h_\eta+w_{1\zeta}h_\zeta}{\sqrt{w_{1r}^2+w_{1c}^2+w_{1z}^2}\sqrt{h_\xi^2+h_\eta^2+h_\zeta^2}} \\ &=\frac{-\tan\sigma(r)h_r+\tan\beta(r)h_c-h_\zeta}{\sqrt{\tan^2\sigma(r)+\tan^2\beta(r)+1}\sqrt{h_r^2+h_c^2+h_\zeta^2}}\end{aligned} \tag{8}$$

where

$$\beta(r)=\mathrm{Tan}^{-1}[-w_{1c}(r)/w_{1z}(r)]\geqslant 0 \tag{9}$$

$$\sigma(r)=\mathrm{Tan}^{-1}[w_{1r}(r)/w_{1z}(r)]=\mathrm{Tan}^{-1}[c_{1r}(r)/c_{1z}(r)] \tag{10}$$

γ_{3r} is laid in a plane having a normal direction $\mathbf{N}\times(-\mathbf{w}_1)$. For clarity and uniformity, this plane will be solved later by a linear transformation method.

A General Formal Solution of Sweep Angles

By developing a linear transformation method (Appendix A), first, related to the absolute velocity component $c_{1z}\mathbf{k}$ and to the $w_{1r}(r)$-omitted relative velocity in Eq. (2), we obtain six kinds of frequently used sweep angles with their situated planes (Appendix B). Second, related to more spacial velocities in Eqs. (3) and (1), two more sweep angles and planes are solved (Appendix B). All results are expressed in terms of coordinates and components of the shock's normal vector.

Review of the Helical Surface Model

The above general formal solutions of sweep angles can be embodied in any kind of analytical 3-D shock surface model such as the HSM. The HSM [5] assumes a 3-D shock surface to be composed of a set of cylinder helixes which originate from continuous points $O_1(r,\theta(r),z(r)),O_2,O_3,\ldots$ on the leading edge, and stretch out rotationwise or oppositely (Fig. 1). With the double parameters r and φ, the finite parametric equations and the differential form of the HSM are written as

$$r=r$$

$$\Phi=\theta(r)+\varphi \tag{11}$$

$$\begin{aligned}\zeta&=z(r)\pm\varphi\cdot f(r)[-w_{1c}(r)/w_{1z}(r)] \\ &=z(r)+\varphi\cdot[\pm f(r)]\tan\beta(r)\end{aligned}$$

$$\begin{aligned}h_r&=h_\xi\cos[\theta(r)+\varphi]+h_\eta\sin[\theta(r)+\varphi] \\ &=r\{z'-[f(r)\tan\beta(r)]\theta'+[f(r)\tan\beta(r)]'\varphi\}\end{aligned} \tag{12}$$

$$\begin{aligned}h_c&=-h_\xi\sin[\theta(r)+\varphi]+h_\eta\cos[\theta(r)+\varphi] \\ &=f(r)\tan\beta(r)\end{aligned} \tag{13}$$

$$h_\zeta=-r \tag{14}$$

Physically, $f(r)$ is a 1-D control function for the 2-D sweep characteristic of a 3-D shock surface $\mathbf{r}(r,\varphi)$.

Similarity Factors and Dimensionless Sweep Vector of the 3-D Shock Structure

HSM Solutions of Sweep Angles. Introducing the normal vector of the HSM surface in Eqs. (12)–(14) into those formal solutions in Appendix B, one obtains the concrete sweep angles which are associated with some relevant flow and blading variables. Two dimensionless factors

$$S_r(r,\varphi)=z'-[f(r)\tan\beta(r)]\theta'+[f(r)\tan\beta(r)]'\varphi \tag{15}$$

$$S_c(r)=f(r)/r\cdot\tan\beta(r) \tag{16}$$

are found to control all the sweep angles. Six frequently used sweep angles are

$$\gamma_{ra}=\mathrm{Tan}^{-1}S_r(r,\varphi)\qquad\gamma_{ra}\in[-\pi/2,\pi/2] \tag{17}$$

$$\gamma_{ca}=\mathrm{Tan}^{-1}S_c(r)\qquad\gamma_{ca}\in[-\pi/2,\pi/2] \tag{18}$$

$$\gamma_a=\mathrm{Tan}^{-1}\sqrt{S_r^2(r,\varphi)+S_c^2(r)}\qquad\gamma_a\in[0,\pi/2] \tag{19}$$

The plane containing γ_a is

$$F=\left(\bar{\bar{g}}_c=\mathrm{const}\,\middle|\,\bar{\bar{g}}_c=\begin{cases}\tan^{-1}[S_c(r)/S_r(r,\varphi)] & (S_r\neq 0) \\ \mathrm{Sign}\,S_c(r)\cdot\pi/2 & (S_r=0)\end{cases}\right)$$

$$\bar{\bar{g}}_c\in[-\pi,\pi] \tag{20}$$

$$\gamma_{rr}=\begin{cases}\mathrm{Tan}^{-1}\dfrac{S_r(r,\varphi)}{S_c(r)\sin\beta(r)+\cos\beta(r)} & (S_c\tan\beta\neq -1) \\ \mathrm{Sign}\,S_r(r,\varphi)\cdot\pi/2 & (S_c\tan\beta=-1)\end{cases}$$

$$\gamma_{rr}\in[-\pi/2,\pi/2] \tag{21}$$

$$\gamma_{cr}=\mathrm{Tan}^{-1}S_c(r)-\beta(r)\qquad\gamma_{cr}\in[-\pi,\pi/2] \tag{22}$$

$$\cos\gamma_r=\frac{\tan\beta(r)S_c(r)+1}{\sqrt{\tan^2\beta(r)+1}\sqrt{S_r^2(r,\varphi)+S_c^2(r)+1}}\qquad\gamma_r\in[-\pi,\pi/2] \tag{23}$$

The plane containing γ_r is

$$F=\left(\bar{\bar{g}}_c=\mathrm{const}\,\middle|\,\bar{\bar{g}}_c=\begin{cases}\tan^{-1}\dfrac{S_c(r)\cos\beta(r)-\sin\beta(r)}{S_r(r,\varphi)} & (S_r\neq 0) \\ \mathrm{Sign}[S_c(r)-\tan\beta(r)]\cdot\pi/2 & (S_r=0)\end{cases}\right)$$

$$\bar{\bar{g}}_c\in[-\pi,\pi] \tag{24}$$

Sweep angles related to more spatial velocities in Eqs. (3) and (1) are

$$\gamma_{3ca}=\begin{cases}\operatorname{Tan}^{-1}\dfrac{S_c(r)}{-S_r(r,\varphi)\sin\sigma(r)+\cos\sigma(r)} & (S_r\tan\sigma\neq 1)\\ \quad\gamma_{3ca}\in[-\pi/2,\pi/2] & \\ \operatorname{Sign}S_c(r)\cdot\pi/2 & (S_r\tan\sigma=1)\end{cases}\tag{25}$$

$$\gamma_{3cr}=\begin{cases}\operatorname{Tan}^{-1}\dfrac{S_c(r)}{-S_r(r,\varphi)\sin\sigma(r)+\cos\sigma(r)}-\beta_m(r) & (S_r\tan\sigma\neq 1)\\ \quad\gamma_{3cr}\in[-\pi,\pi/2] & \\ \operatorname{Sign}S_c(r)\cdot\pi/2-\beta_m(r) \quad (S_r\tan\sigma=1) & \end{cases}\tag{26}$$

$$\cos\gamma_{3r}=\frac{1}{\sqrt{\tan^2\sigma(r)+\tan^2\beta(r)+1}}\,\frac{-\tan\sigma(r)S_r(r,\varphi)+\tan\beta(r)S_c(r)+1}{\sqrt{S_r^2(r,\varphi)+S_c^2(r)+1}}\quad\gamma_{3r}\in[-\pi,\pi/2]\tag{27}$$

The plane containing γ_{3r} is

$$F=\left(\bar{\bar{g_c}}=\text{const}\middle|\bar{\bar{g_c}}=\begin{cases}\tan^{-1}\dfrac{-[-S_r(r,\varphi)\sin\sigma(r)+\cos\sigma(r)]\sin\beta_m(r)+S_c(r)\cos\beta_m(r)}{S_r(r,\varphi)\cos\sigma(r)+\sin\sigma(r)} & (S_r+\tan\sigma\neq 0)\\ \operatorname{Sign}[S_c(r)-\tan\beta(r)]\cdot\pi/2 & (S_r+\tan\sigma=0)\end{cases}\right)$$

$$\bar{\bar{g_c}}\in[-\pi,\pi]\tag{28}$$

where

$$\begin{aligned}\beta_m(r)&=\operatorname{Tan}^{-1}\left[-w_{1c}(r)/\sqrt{w_{1r}^2(r)+w_{1z}^2(r)}\right]\\&=\operatorname{Tan}^{-1}[\tan\beta(r)\cos\sigma(r)]\geqslant 0\end{aligned}\tag{29}$$

and $\beta(r)$ and $\sigma(r)$ are given by Eqs. (9) and (10). Equations (15)–(28) may be called analyzing equations for the shock's spatial sweep angles and their projections.

Derivation of Sweep Similarity Factors. The fact that all analytical results for shock sweep angles are only functions of S_r, S_c, β, and σ should be very meaningful. Combining Eqs. (12)–(14) yields

$$h_r/(-h_\zeta)=S_r(r,\varphi)\tag{30}$$

$$h_c/(-h_\zeta)=S_c(r)\tag{31}$$

In fact the two equations have revealed the original kinematic definitions of S_r and S_c. So, to a certainty, in sweep aerodynamics, for a general 3-D shock structure independent of models, there exist a dimensionless radial sweep similarity factor

$$S_r(r,\Phi)=h_r/(-h_\zeta)=(h_\xi\cos\Phi+h_\eta\sin\Phi)/(-h_\zeta)\tag{32}$$

and a dimensionless circumferential sweep similarity factor

$$S_c(r,\Phi)=h_c/(-h_\zeta)=(-h_\xi\sin\Phi+h_\eta\cos\Phi)/(-h_\zeta)\tag{33}$$

Here S means sweep. Equations (15) and (16) are therefore special forms of S_r and S_c in the HSM. Equations (17)–(28) also suit a general shock when only substituting $S_r(r,\varphi)$ and $S_c(r)$ with S_r and S_c.

Essence of Sweep Similarity of Factors and Sweep Vector. On the axial plane $\zeta(r,\Phi)=\text{const}$ a turbomachine, any projection of a shock's normal vector on a differential element $d\mathbf{1}$ of a planar curve can be written as

$$\begin{aligned}\mathbf{N}\cdot d\mathbf{1}&=(h_r\mathbf{e}_r+h_c\mathbf{e}_c+h_\zeta\mathbf{e}_z)\cdot(\mathbf{e}_r dr+\mathbf{e}_c r d\Phi+\mathbf{e}_z\times 0)\\&=h_r dr+h_c r d\Phi\\&=(-h_\zeta)S_r dr+(-h_\zeta)S_c r d\Phi\\&=(-h_\zeta)(S_r,S_c)(dr,rd\Phi)^T\\&=-h_\zeta\mathbf{N}_{rc}\cdot d\mathbf{1}\end{aligned}\tag{34}$$

where we define a vector

$$\mathbf{N}_{rc}=(S_r,S_c)^T\tag{35}$$

Noting that there is a component ratio $S_r/S_c=h_r/h_c$, we can designate S_r and S_c along directions $\mathbf{e}_r$ and $\mathbf{e}_c$ respectively. This makes the definition of $\mathbf{N}_{rc}$ reasonable. So $\mathbf{N}_{rc}$ lies within a plane $\zeta=\text{const}$ (Fig. 4), and is a dimensionless vector normed by the $\mathbf{N}$'s negative axial component $-h_\zeta$ [Eq. (34)]. $\mathbf{N}_{rc}$ may be called the dimensionless axial normed sweep similarity vector of a general 3-D shock surface, or briefly, the sweep vector. The direction or the component values of $\mathbf{N}_{rc}$ subject only to the relative magnitudes of the $\mathbf{N}$'s components h_ξ,h_η,h_ζ, i.e., to the orientation of a frame. This is consistent with the fact that sweep magnitudes reflects only the relative orientation of a shock surface to coordinates coincident with the incoming flow. Consequently, in essence, we know $\mathbf{N}_{rc}$, with S_r and S_c, to be ''observed variables'' which are not identical to the first or second category variables of a curved surface.

Converting Between Sweep Vector and Normal Vector. Substituting a unit normal vector $\mathbf{n}=(h_\xi\mathbf{i}+h_\eta\mathbf{j}+h_\zeta\mathbf{k})/|\mathbf{N}|$ into Eqs. (32) and (33), one obtains the same S_r and S_c. This means that a sweep vector is subject only to the direction and not to the norm of the normal vector. Equations (32) and (33) convert a normal vector into the sweep vector. Reversing them one obtains

$$h_\xi/(-h_\zeta)=S_r\cos\Phi-S_c\sin\Phi\tag{36}$$

$$h_\eta/(-h_\zeta)=S_r\sin\Phi+S_c\cos\Phi\tag{37}$$

$$-h_\zeta=|\mathbf{N}|/\sqrt{S_r^2+S_c^2+1}\tag{38}$$

Significance of Sweep Similarity Variables

Decomposed radially and circumferentially from a sweep vector, S_r and S_c are the ratios of h_r,h_c,h_ζ, which are along the gradient directions of the independent variables r and Φ and all

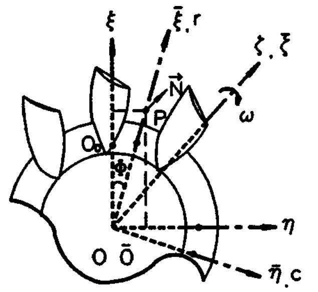

a. Point P on shock surface and turbomachine frame oξηζ,ōξ̄η̄ζ̄,orΦζ

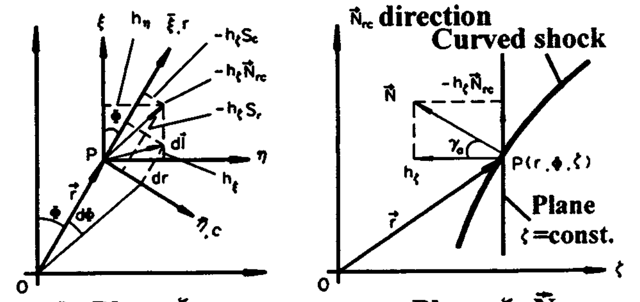

b. Plane ξ−η

c. Plane ζ−N̄rc

Fig. 4 The meaning of the sweep vector $\mathbf{N}_{rc}$ with its components S_r and S_c of a 3-D shock surface and the relation of the sweep vector to the normal vector

the flow's aerodynamic variables. This indicates that as in turbomachine through-flow theories, for the shock's kinematic and aerodynamic variables, taking their meridional orthogonal component resolutions is also the most advantageous method.

$\mathbf{N}_{rc}$, S_r, and S_c afford a decisive control on a shock's sweep characteristic. With different blading methods or leading edge curve shapes, the sweep characteristics of two points on different shock surfaces must be the same under the condition that S_r and S_c and the flow directions β and σ are the same. Further, they must not be the same when S_r and S_c are not the same. So, $\mathbf{N}_{rc}$ is a controlling vector of the sweep characteristic including the effect of leading edge sweeps.

Further comprehension can be gained by taking the HSM as an example. Equations (15) and (16) reveal that for a certain distribution rule of S_r and S_c, infinite kinds of leading edge curves $\theta(r)$ and $z(r)$ can be chosen. This implies that only the distribution of S_r and S_c is important for the classification of 3-D shock surfaces, though many kinds of slightly different leading edge curves can be employed. To some extent, what is being pursued is an optimum shock category, and the concrete leading edge curve can be released from an intensive study and design. For example, two nearly equivalent S_r and S_c distributions of the LESS can be afforded by a slightly meridional forward swept blade or a nearly meridional zero sweep blade. But the latter is better for solving the blade's strength problem. In modern high loading fans with a strong shock system, this kind of problem is often encountered. Of course, the only consideration here is shock control.

For a 3-D shock structure measurement, when any two angles in Eqs. (17)–(28) are measured, all angles and structure variables, especially the important γ_{3r}, can be calculated in terms of S_r, S_c.

Sweep Characteristic and Shock Structure Classification

The sweep characteristic is a joint appellation for the sweep heads and sweep magnitudes of a shock surface. To obtain a sweep characteristic, two necessary conditions, a right- or left-running shock and a sort of sweep angle, must be prescribed. Following is a classification of all 3-D shock surfaces according to their sweep heads. This classification is performed first on the right-running, then on the left-running shocks. The classification is found generally identical with that according to the sign (or value) of S_r and S_c or the quadrant of $\mathbf{N}_{rc}$. It makes the analysis or design of a 3-D shock surface a clear and operable task.

Classification Based on Radial or Circumferential Sweep Head. In Eqs. (39) and (40), S_r is the controller of the radial sweep head.

$$\gamma_{ra}\begin{cases}<0 & (S_r<0) \quad \textit{Radial absolute forward sweep shock}\\ =0 & (S_r=0) \quad \textit{Radial absolute zero sweep shock}\\ >0 & (S_r>0) \quad \textit{Radial absolute backward sweep shock}\end{cases}\tag{39}$$

$$\gamma_{rr}\begin{cases}<0 & (S_r<0) \quad \textit{Radial relative forward sweep shock}\\ =0 & (S_r=0) \quad \textit{Radial relative zero sweep shock}\\ >0 & (S_r>0) \quad \textit{Radial relative backward sweep shock}\end{cases}\tag{40}$$

Likewise, S_c is the controller of the circumferential sweep head:

$$\gamma_{ca}\begin{cases}<0 & (S_c<0) \quad \textit{Circum. abso. forward sweep shock}\\ =0 & (S_c=0) \quad \textit{Circum. abso. zero sweep shock}\\ >0 & (S_c>0) \quad \textit{Circum. abso. backward sweep shock}\end{cases}\tag{41}$$

$$\gamma_{cr}\begin{cases}<0 & (S_c<tg\beta) \quad \textit{Circum. rela. forward sweep shock}\\ =0 & (S_c=tg\beta) \quad \textit{Circum. rela. zero sweep shock}\\ >0 & (S_c>tg\beta) \quad \textit{Circum. rela. backward sweep shock}\end{cases}\tag{42}$$

Classification Based on Spatial Sweep Head. On point P, the $\mathbf{N}$ and the incident velocity crossed the situated plane F of angle γ_a or γ_r. Within F we can define a forward or backward swept shock [see, e.g., Fig. 4(c)], while F itself is located at the angle $\bar{\bar{g}}_c$ on the plane normal to the incident velocity. But by the magnitude of $\bar{\bar{g}}_c$ it is not convenient for us to image the 3-D deflection of an after shock velocity. Alternatively, as the controlling factors of $\bar{\bar{g}}_c$ in absolute spatial sweeps [Eq. (20)], S_r and S_c are two straightforward pointers for this deflection. Also, $\mathbf{N}_{rc}$ is helpful for us to directly image the orientation of a complete or local shock surface in turbomachine coordinates.

$$(S_r,S_c)^T\rightarrow\begin{cases}(+,+)^T & (\mathbf{N}_{rc}\ \textit{Locates at quadrant I})\\ & \textit{Radial absolute backward sweep}\\ & \textit{circum. absolute backward sweep}\\ (-,+)^T & (\mathbf{N}_{rc}\ \textit{Locates at quadrant II})\\ & \textit{Radial absolute forward sweep}\\ & \textit{circum. absolute backward sweep}\\ (-,-)^T & (\mathbf{N}_{rc}\ \textit{Locates at quadrant III})\\ & \textit{Radial absolute forward sweep}\\ & \textit{circum. absolute forward sweep}\\ (+,-)^T & (\mathbf{N}_{rc}\ \textit{Locates at quadrant IV})\\ & \textit{Radial absolute backward sweep}\\ & \textit{circum. absolute forward sweep}\end{cases}\tag{43}$$

when S_r or S_c or $\mathbf{N}_{rc}$ equals zero, we have a radial or circumferential absolute zero swept shock or a local $\zeta=\text{const}$ shock plane, respectively. As to relative spacial sweeps, γ_{rr} and γ_{cr} serve most concisely as the two pointers:

$$(\gamma_{rr},\gamma_{cr})^T \rightarrow \begin{cases} (+,+)^T & \textit{Radial relative backward sweep} \\ & \textit{circum. relative backward sweep} \\ (-,+)^T & \textit{Radial relative forward sweep} \\ & \textit{cirum. relative backward sweep} \\ (-,-)^T & \textit{Radial relative forward sweep} \\ & \textit{circum. relative forward sweep} \\ (+,-)^T & \textit{Radial relative backward sweep} \\ & \textit{circum. relative forward sweep} \end{cases} \quad (44)$$

The relative spanwise sweeps are considered in here.

For 3-D incident velocities [Eqs. (1) and (3)], shock classifications can not be as simple as that stated by radial and circumferential sweeps. But expressions like Eq. (44) are also useful.

Classification for a Left-running Shock Surface. Simply, in Eqs. (39)–(44) substituting all the statements ''circumferential forward/backward'' by the statements ''circumferential backward/forward,'' we obtain a new set of equations (39)–(44) as the classification system of a left-running shock surface.

Experiment Scheme of 3-D Shock Structure

The 3-D shock structure measurement might be carried out according to the relations described in Eqs. (17)–(28). This measurement is independent of whether a shock model is added or not. The task is obtaining sweep characteristics $\mathbf{N}_{rc}$ on the shock surface points, then transferring to all interesting variables. The laser techniques such as holography (Benser et al. [9]) and particle image velocimetry are thought suitable for the measurement.

One-Point–Two-Directions Scheme. $\mathbf{N}_{rc}$ on point $P(r,\Phi)$ of a shock surface can be calculated under the condition that two absolute sweep angles on any two profiles passing through point P is measured out. Referring to Figs. 4 and 5, here we take an absolute frame $Prc\zeta$, then cut the shock surface at P along any two directions $\mathbf{L}_1^0$ and $\mathbf{L}_2^0$ within the plane Prc, then on the two cut planes perpendicular to this paper, we photograph two sweep angles γ_{1a} and γ_{2a} included between plane *Prc* and the shock surface. γ_{1a} and γ_{2a} are in fact two projections of γ_a. Thus the projected equations of γ_a and its solution are

$$\begin{aligned} \cos(\mathbf{L}_1^0,r)\cdot S_r+\sin(\mathbf{L}_1^0,r)\cdot S_c&=\tan\gamma_{1a} \\ \cos(\mathbf{L}_2^0,r)\cdot S_r+\sin(\mathbf{L}_2^0,r)\cdot S_c&=\tan\gamma_{2a} \end{aligned} \quad (45)$$

$$\begin{aligned} S_r&=[\sin(\mathbf{L}_2^0,r)\tan\gamma_{1a}-\sin(\mathbf{L}_1^0,r)\tan\gamma_{2a}]/s_{12} \\ S_c&=[-\cos(\mathbf{L}_2^0,r)\tan\gamma_{1a}+\cos(\mathbf{L}_1^0,r)\tan\gamma_{2a}]/s_{12} \quad (46) \\ s_{12}&=\sin[(\mathbf{L}_2^0,r)-(\mathbf{L}_1^0,r)] \quad (\mathbf{L}_1^0\times\mathbf{L}_2^0\neq 0) \end{aligned}$$

Four angles $\angle(\mathbf{L}_1^0,r)$, γ_{1a}, $\angle(\mathbf{L}_2^0,r)$, and γ_{2a} need measuring in this scheme. One plan is illustrated in Fig. 5.

Two-Points–One-Direction Scheme. This scheme makes use of the circumferential direction and employs the HSM. Much like the above scheme, on point $P_1(r_1,\varphi_1)$ (Fig. 6), we take $\mathbf{L}_1^0$ along the circumferential direction and photograph the absolute sweep angle γ_{1ca}; then do the same on point $P_2(r_2,\varphi_2)$ for γ_{2ca}. Thus the projected equations are

$$\mathbf{N}_{rc1}\cdot\mathbf{L}_1^0=(S_{r1},S_{c1})[\cos(\pi/2),\sin(\pi/2)]^T=S_{c1}=\tan\gamma_{1ca} \quad (47)$$

$$\mathbf{N}_{rc2}\cdot\mathbf{L}_2^0=(S_{r2},S_{c2})[\cos(\pi/2),\sin(\pi/2)]^T=S_{c2}=\tan\gamma_{2ca} \quad (48)$$

On the other hand, from Eqs. (15) and (16) we have

$$S_r(r,\varphi)=z'-[rS_c(r)]\theta'+[rS_c(r)]'\varphi \quad (49)$$

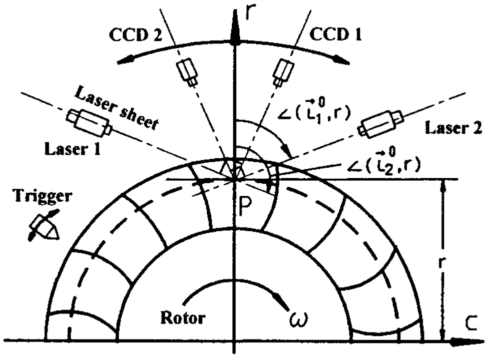

Fig. 5 One plan to use a one-point–two-directions scheme of shock structure measurement

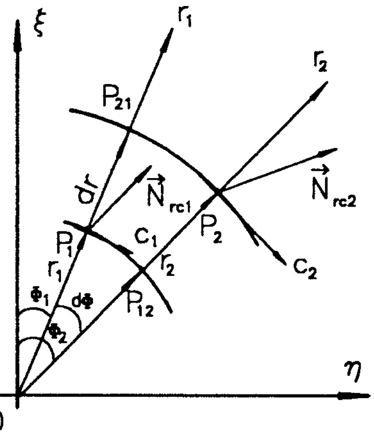

Fig. 6 Principle of a two-points–one-direction scheme of shock structure measurement

$$\partial S_r(r,\varphi)/\partial\varphi=[f(r)\tan\beta(r)]'=[rS_c(r)]' \quad (50)$$

$$\partial S_c(r)/\partial\varphi=0 \quad (51)$$

So from S_{c1} and S_{c2}, four more variables can be calculated:

$$S_r(r_1,\Phi_1)=S_{r1} \approx \frac{(z_2-z_1)-r_1S_{c1}(\theta_2-\theta_1)+(r_2S_{c2}-r_1S_{c1})(\Phi_1-\theta_1)}{r_2-r_1} \quad (52)$$

$$\begin{aligned} S_r(r_1,\Phi_2)&=S_{r12}=S_{r1}+\partial S_r(r,\varphi)/\partial\varphi d\varphi=S_{r1}+[rS_c(r)]'d\Phi \\ &\approx S_{r1}+(r_2S_{c2}-r_1S_{c1})(\Phi_2-\Phi_1)/(r_2-r_1) \end{aligned} \quad (53)$$

$$\begin{aligned} S_c(r_1,\Phi)&=S_c[r_1,\theta(r_1)+\varphi]=S_c(r_1)=S_{c1} \\ &=\tan\gamma_{1ca} \quad (\text{any } \Phi) \end{aligned} \quad (54)$$

$$S_c(r_2,\Phi)=S_{c2}=\tan\gamma_{2ca} \quad (\text{any } \Phi) \quad (55)$$

The relative ascendents for embodying this HSM [Eq. (11)] are

$$[f(r)\tan\beta(r)]_{r=r_i}=r_iS_{ci}=r_i\tan\gamma_{ica} \quad (i=1,2) \quad (56)$$

It is noted that by using the HSM, measuring on two points at different radii, we can obtain two complete sweep vectors on points P_1 and P_{12} of the same radius. The precision drops a little, but the test efficiency increases when compared with the first scheme. In practice this can be used as a $(n+1)$-points–one-direction scheme to obtain $2n$ complete sweep vectors with no error accumulation but a precision rise of S_r. It is a pity that the leading edge curve $z(r), \theta(r)$ must be given.

Two Engineering Examples for a Leading Edge Shock Surface

The structures of two sweep leading edge shock surfaces are analyzed here using the HSM. Example 1 is a single stage high loading fan ATS-2 with backward swept rotor blades (Fig. 7). The fan, as a research stage with a zero preswirl inlet flow, was designed in 1994–1995 by the Department of Jet Propulsion, Beijing University of Aeronautics and Astronautics. Now it is under experiment. Detailed information about the modeling of its LESS was placed by Shan and Zhou [8]. In Fig. 8, on the planes ξ-ζ, η-ζ, and ξ-η, it shows the shock's approximate meridional, approximate radial and exact axial projections respectively. The axial projection is held by two radial lines to show an increasing backward sweep of the shock points that are gradually farther from the leading edge. On the axial projection it can also be seen that, originating from the leading edge *ab*, the shock surface is right-running at the lower half shock span and, by passing through the intersecting point *c* of the leading edge curve with the shock impingement loci on the suction surface, turns left running at the higher half shock span.

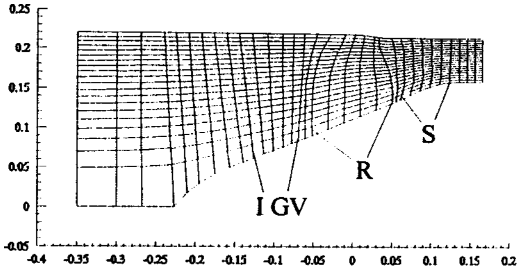

Fig. 7 Through flow calculating station, streamline, overall design data of ATS-2 single stage backward swept fan

Rotation speed	**21500**	**rpm**
Unit mass flow (By CFD)	**173.08**	**kg/m^2/s**
Unit annular mass flow	**208.66**	**kg/m^2/s**
Mass flow	**26.32**	**kg/s**
Pressure ratio	**2.252**	
Adiabatic efficiency	**0.8855**	
Diameter	**0.44**	**m**

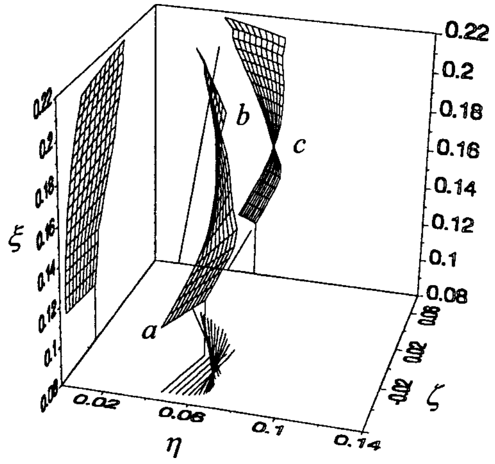

Fig. 8 Leading edge shock surface and three of its planar projections of ATS-2 fan's rotor

Tip speed of leading edge	**495.32 m/s, *M*1.661, positive η**
Blade numbers	**14**
Leading edge total span *r*	**0.09080~0.22 *m***
Leading edge shock span *r*	***a*: 0.1216~*b*: 0.22 *m***
Shock running	**root right~tip left**

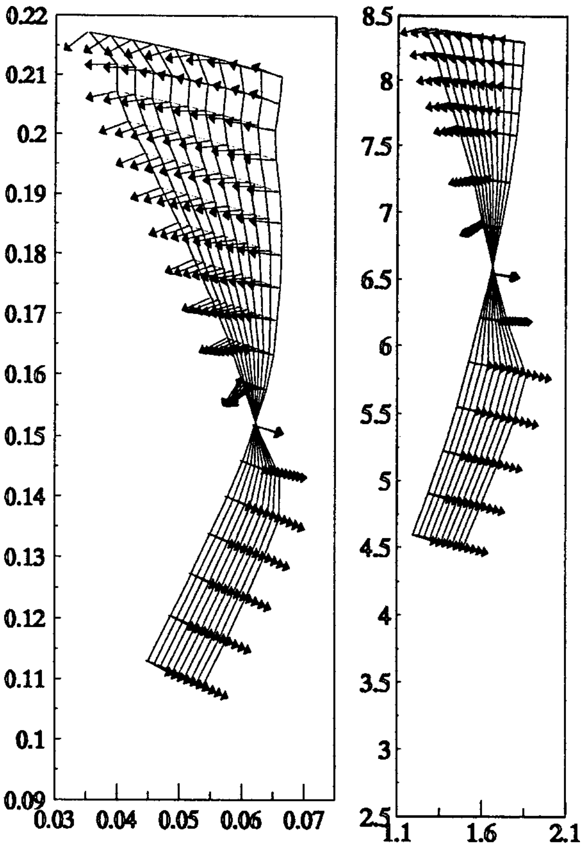

a. Fan ATS-2 b. HTFC

Fig. 9 Distributions of the sweep vector $\mathbf{N}_{rc}$ of two rotors' leading edge shock surfaces

The distribution of the sweep vector $\mathbf{N}_{rc}$ is showed in Fig. 9(a) by arrows. In Fig. 9(a) the absolute velocities penetrate into this paper. With different incident angles, the relative velocities also penetrate into this paper at the right-running shock while they penetrate out of at the left-running shock. First, cutting the shock surface along an arrow can expose the spatial absolute sweep angle γ_a at this point. From this angle and by the regular varying of the $\mathbf{N}_{rc}$ direction, one can easily grasp the shock's orientation in a turbomachine frame. Second, displayed by the radial and circumferential components of $\mathbf{N}_{rc}$ [Eq. (43), Table 1], the right-running shock surface takes the absolute sweeps backward in circumference, forward at the left-lower corner in radius, and backward at the right-upper corner in radius. The left-running shock takes also the absolute sweeps backward in circumference and mainly forward in radius. Third, because beyond the 80 percent span the blade's weight center is deflected $+\zeta$-wise purposely, with the result that the leading edge tip point *b* is drawn into the passage, a local radial absolute backward-swept shock is formed above 19th stream surface, as seen by $\mathbf{N}_{rc}$ directions there.

The concept of the absolute sweeps helps one lay or form a shock surface imaginarily in space, while the relative sweep concept is associated with direct and indirect shock losses. Figure 10 shows the distributions of three radial relative sweep variables S_r, γ_{rr}, and γ_{3r}. First the left-running shock takes mainly a radial

Table 1 Distributions of S_r and S_c of ATS-2 fan's leading edge shock surface

Stream	1 ($\varphi=0$)	2	3	4	5	6	7	8	9	10	$S_c(r)$
21	0.170	−0.076	−0.322	−0.568	−0.814	−1.06	−1.31	−1.55	−1.80	−2.04	−1.86
20	0.217	0.139	0.061	−0.017	−0.095	−0.173	−0.251	−0.329	−0.407	−0.485	−2.22
19	−0.287	−0.380	−0.472	−0.565	−0.658	−0.751	−0.843	−0.936	−1.03	−1.12	−2.39
18	−0.711	−0.820	−0.929	−1.04	−1.15	−1.26	−1.36	−1.47	−1.58	−1.69	−2.60
17	−0.767	−0.898	−1.03	−1.16	−1.29	−1.42	−1.55	−1.68	−1.81	−1.94	−2.85
16	−0.784	−0.948	−1.11	−1.28	−1.44	−1.61	−1.77	−1.94	−2.10	−2.26	−3.19
15	−0.886	−1.10	−1.31	−1.52	−1.74	−1.95	−2.16	−2.37	−2.59	−2.80	−3.64
14	−1.02	−1.32	−1.63	−1.93	−2.23	−2.53	−2.84	−3.14	−3.44	−3.75	−4.33
13	−1.29	−1.70	−2.11	−2.52	−2.92	−3.33	−3.74	−4.15	−4.56	−4.97	−5.50
12	−1.20	−1.98	−2.76	−3.54	−4.32	−5.10	−5.88	−6.66	−7.44	−8.22	−7.52
11	−0.794	−6.75	−12.7	−18.7	−24.6	−30.6	−36.5	−42.5	−48.4	−54.4	−13.06
10	12.1	13.0	13.9	14.8	15.7	16.5	17.4	18.3	19.2	20.1	152.89
9	0.105	0.421	0.738	1.05	1.37	1.69	2.00	2.32	2.64	2.95	7.48
8	−0.060	−0.005	0.050	0.105	0.160	0.214	0.269	0.324	0.379	0.434	4.78
7	−0.175	−0.114	−0.053	0.008	0.069	0.130	0.191	0.252	0.313	0.374	4.62
6	−0.250	−0.188	−0.126	−0.065	−0.003	0.059	0.121	0.182	0.244	0.306	4.42
5	−0.32	−0.259	−0.203	−0.148	−0.092	−0.036	0.020	0.076	0.132	0.187	4.21
4	−0.447	−0.400	−0.353	−0.305	−0.258	−0.211	−0.164	−0.117	−0.070	−0.023	4.04

relative backward sweep with a large area of negative S_r and positive γ_{rr}. As for the right-running shock, in the upper right corner it also takes a radial relative backward sweep with positive S_r and γ_{rr}, and in the lower left corner a radial relative forward sweep with negative S_r and γ_{rr}. Second, on a large part of the left-running shock span, the gradients of the three variables point in the circumferential direction. Because in formulas the sweep similarity factor S_c and the incident flows β and σ are all functions of r and independent of φ, these gradients provide strong evidence that, by varying S_r, the circumferential independent φ exerts a decisive influence on the radial sweep characteristic and finally on the spatial sweep characteristic. The small aspect ratio compressors efficiently share this pattern of employing a large interblade angle to generate a significant radial backward swept shock naturally. From the viewpoint of suppressing the indirect shock losses, whether this circumferential distribution of an increasing radial sweep is advantageous remains an unsolved aerodynamic issue. Third, also because the inward tip point b drawn by the tip weight center deflexion, there appears a significant change in that those gradients near the tip shock span become radial pointing. Associated with this stronger change, in the near leading edge region that forms a local radial relative forward swept shock surface with $\gamma_{rr}=0°--5.1°$. This fact again explains that the relative sweep head of a shock surface is not subject only to the leading edge meridional sweep head. The sweep characteristic of a shock surface braced by a leading edge curve is subjected to four groups of variables: the position on the shock surface, the spatial formation of the leading edge curve, the direction of the relative incoming flow, and the shape of the element airfoil suction surface entrance region curve.

An infinite discontinuity point of $f(r)$ is encountered due to the right- to left-running jump of the shock, with jumps of the absolute sweep variables [Eqs. (11), (15), and (16)]. This will not disturb the solution when introducing any suitable treatment for the transition of the derivative $(f\tan\beta)'$.

Example 2 is the HTFC rotor [10,11], with a small aspect ratio and a not emphasized, only 5.6°, leading edge curve relative backward sweep. The rotor tip Mach numbers of HTFC and ATS-2 are mostly the same [Figs. 8 and 11]. As seen from Figs. 9(*b*) and 12, a smooth sweepless leading edge curve and a smooth flow field design of the HTFC afford a LESS with smooth distributed sweep vectors and sweep angles. Above point *c*, the left-running LESS takes the absolute sweeps backward in circumference and forward in radius, and simultaneously takes the relative sweeps backward in circumference and backward in radius. Below point *c*, the right-

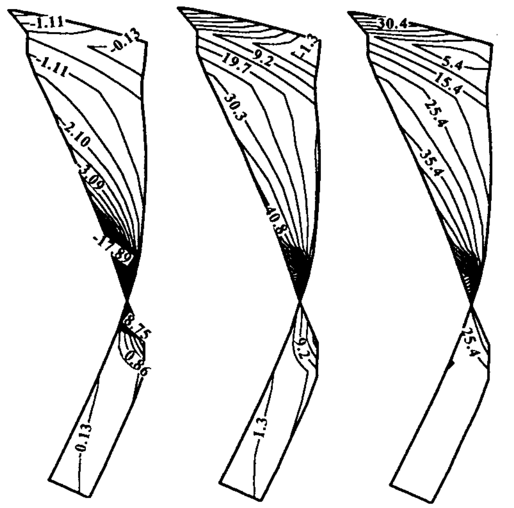

Radial sweep similarity factor S_r Radial relative sweep angle γ_{rr} Spacial relative sweep angle γ_{3r}

Fig. 10 Distributions of three major sweep variables of ATS-2 fan's leading edge shock surface

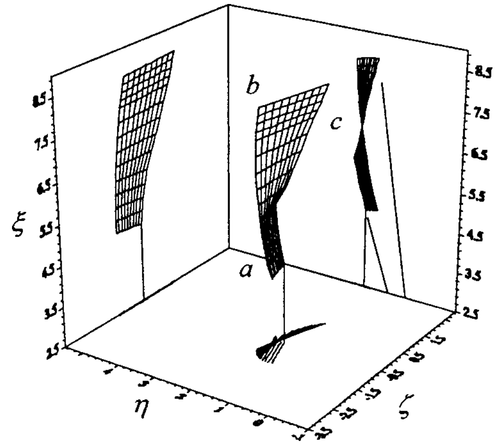

Fig. 11 Leading edge shock surface and three of its planar projections of the HTFC's rotor

Tip speed of leading edge	**457.2 *m/s*, *M*1.658, positive η**
Blade numbers	**20**
Leading edge total span *r*	**2.65∼8.50 *inch***
Leading edge shock span *r*	***a*: 4.75∼*b*:8.50 *inch***
Shock running (Defined by frame in Fig. 1)	**root right∼tip left**

Radial sweep similarity factor S_r Radial relative sweep angle γ_{rr} Spacial relative sweep angle γ_{3r}

Fig. 12 Distributions of three major sweep variables of the HTFC's leading edge shock surface

running shock takes the absolute sweeps backward in circumference, the upper region backward in radius, and the lower region forward in radius. Simultaneously it takes the relative sweeps backward in circumference, the upper region backward in radius, and the lower region forward in radius. The aerodynamic issues of these examples will be discussed in the successive papers.

Concluding Remarks

(1) The radial/circumferential/spatial absolute/relative forward/zero/backward sweeps of a general shock surface can be quantitatively investigated in uniformity. The sweep vector $\mathbf{N}_{rc}$ is formed by its radial component S_r and circumferential component S_c, with S_r and S_c respectively reflecting the shock's radial and circumferential sweep characteristic. $\mathbf{N}_{rc}$ or S_r and S_c exist independently of shock models, and have a decisive control effect on the 3-D shock surface's local/integral structure and the resultant shock interrupted main flow field, so are also called dimensionless sweep similarity factors. The spatial relative sweep angle γ_{3r} is called the aerodynamic sweep angle.

(2) The shock classification can be performed according to the signs or values of the sweep similarity factors. The blading in a supersonic or transonic compressor should pursue an advantageous shock category and release the concrete leading edge curve from an intensive study. A leading edge curve can be moved without varying the distribution rule of the sweep similarity factors.

(3) By the linear transformation method, a set of general formal solutions of sweep angles is obtained. With the help of the helical surface model, a set of concrete sweep angles, which include the influence of a swept leading edge on the leading edge shock's structure, is also obtained. Based on these, a real 3-D shock structure can be measured from a sheet-laser-beamed model experiment or a CFD yielded flow field.

(4) Many examples indicate that the commonly used blading techniques and a smooth forward/zero/backward swept leading edge curve result in circumferentially pointing gradients of all the shock's radial relative sweep variables, except for special treatments of a leading edge curve.

(5) Concerning the use of sweep, an excess and not pertinent leading edge sweep tends to lead to a highly curved 3-D leading edge shock surface, with a suppressed direct shock loss, but an increased indirect shock loss due to shock induced mixing and radial-non-equilibrium. This requires a reasonable pursuit of a minimum total shock loss shock design. The first step of this might be the kinematic analysis and design of a general shock surface. The aerodynamic analysis of the near shock flow field will be discussed in part III of this study.

Acknowledgment

The study was financed by China National Natural Science Foundation and China Aviation Science Foundation.

Appendix A: Linear Transformation Method for a General Sweep Angle

The solving of every kind of sweep angle can be concluded as an issue "the projection angle γ_F of the angle γ included between two planes onto the third plane F." F is the projection plane, while γ_F means the angle within F and included between two intersecting lines of F with the two planes. Since an intersecting line is perpendicular to both planes' normal vectors, we can use two cross products to obtain two intersecting lines, and then their including angle:

$$\mathbf{N}_F=\mathbf{N}\times\mathbf{n}_F=(h_\xi\mathbf{i}+h_\eta\mathbf{j}+h_\zeta\mathbf{k})\times\mathbf{n}_F \tag{A1}$$

$$-\mathbf{w}_{1F}=-\mathbf{w}_1\times\mathbf{n}_F=-(\mathbf{w}_{1\xi}\mathbf{i}+\mathbf{w}_{1\eta}\mathbf{j}+\mathbf{w}_{1\xi}\mathbf{k})\times\mathbf{n}_F \tag{A2}$$

$$\cos\gamma_F=\mathbf{N}_F\cdot(-\mathbf{w}_{1F})/(|\mathbf{N}_F||-\mathbf{w}_{1F}|) \tag{A3}$$

Thus here we take a local shock plane and a negative relative flow's normal plane as two example planes, and F is any plane. Note that γ is also the angle included between two planes' normal vectors, and γ_F the angle included between two normally projected vectors of two planes' normal vectors onto F (Fig. 13). By the rule of the cross product, $\mathbf{N}_F, -\mathbf{w}_{1F}$ are all within F. The solving of γ_F is simplified in uniformity below.

As a first step, we establish a first new Cartesian frame $\overline{O}(\overline{\mathbf{i}},\overline{\mathbf{j}},\overline{\mathbf{k}})$, where $\mathbf{n}_F$ is one of its basis vector, e.g., $\mathbf{n}_F=\overline{\mathbf{i}}$. Thus the two normally projected vectors onto F and γ_F can be expanded as

$$\mathbf{N}_F=(\mathbf{N}\times\mathbf{n}_F)|_O=(\mathbf{N}\times\overline{\mathbf{i}})|_{\overline{O}}=\begin{bmatrix}\overline{\mathbf{i}} & \overline{\mathbf{j}} & \overline{\mathbf{k}}\\ \overline{h_\zeta} & \overline{h_\eta} & \overline{h_\zeta}\\ 1 & 0 & 0\end{bmatrix}=(\overline{h_\zeta}\overline{\mathbf{j}}-\overline{h_\eta}\overline{\mathbf{k}})=\mathbf{N}_{\overline{jk}} \tag{A4}$$

$$-\mathbf{w}_{1F}=(-\mathbf{w}_1\times\mathbf{n}_F)|_O=(-\mathbf{w}_1\times\overline{\mathbf{i}})|_{\overline{O}}=-(\overline{\mathbf{w}_{1\zeta}}\overline{\mathbf{j}}-\overline{\mathbf{w}_{1\eta}}\overline{\mathbf{k}})=-\mathbf{w}_{1\overline{jk}} \tag{A5}$$

$$\cos\gamma_F=-(\overline{h_\zeta}\overline{\mathbf{j}}-\overline{h_\eta}\overline{\mathbf{k}})\cdot(\overline{\mathbf{w}_{1\zeta}}\overline{\mathbf{j}}-\overline{\mathbf{w}_{1\eta}}\overline{\mathbf{k}})/(|\mathbf{N}_{\overline{jk}}||-\mathbf{w}_{1\overline{jk}}|) \tag{A6}$$

$-\overline{h_\eta}$ is the coordinate of $\mathbf{N}$ on the $\overline{\eta}$ axis of $\overline{O}$, etc. As a second step, traversing the $\overline{\mathbf{jOk}}$ plane around the $\overline{\mathbf{i}}$ axis, we have, e.g., $\overline{\mathbf{k}}$ coincide with $-\mathbf{w}_{1\overline{jk}}$, and we take $\overline{\overline{\mathbf{k}}}=-\mathbf{w}_{1\overline{jk}}/|-\mathbf{w}_{1\overline{jk}}|$ as a basis vector of a second new Cartesian frame $\overline{\overline{O}}(\overline{\overline{\mathbf{i}}},\overline{\overline{\mathbf{j}}},\overline{\overline{\mathbf{k}}})$; thus we can further express γ_F in

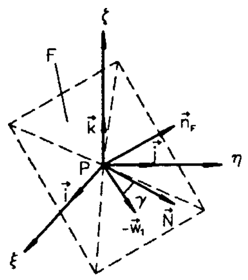

Fig. 13 The projection angle γ_F of the angle γ (included between two planes) onto the third plane F

$$\mathbf{N}_F=(\overline{\overline{h}}_\eta\mathbf{j}+\overline{\overline{h}}_\zeta\mathbf{k})=\mathbf{N}_{\overline{\overline{jk}}} \tag{A7}$$

$$-\mathbf{w}_{1F}=|-\mathbf{w}_{1\overline{jk}}|\bar{\mathbf{k}}=|-\mathbf{w}_{1\overline{\overline{jk}}}|\bar{\bar{\mathbf{k}}}=-\mathbf{w}_{1\overline{\overline{jk}}} \tag{A8}$$

$$\cos\gamma_F=\frac{(\overline{\overline{h}}_\eta\mathbf{j}+\overline{\overline{h}}_\zeta\mathbf{k})\cdot|-\mathbf{w}_{1\overline{\overline{jk}}}|\bar{\bar{\mathbf{k}}}}{|\mathbf{N}_{\overline{\overline{jk}}}||-\mathbf{w}_{1\overline{\overline{jk}}}|}=\frac{\overline{\overline{h}}_\zeta}{\sqrt{\overline{\overline{h}}_\eta^{\,2}+\overline{\overline{h}}_\zeta^{\,2}}} \tag{A9}$$

or, in another form,

$$\gamma_F=\mathrm{Tan}^{-1}(\overline{\overline{h}}_\eta/\overline{\overline{h}}_\zeta) \tag{A10}$$

Obviously, the issue of ‘‘the projection angle γ_F’’ has been converted in unity into another issue, ‘‘a transformation between two sets of coordinates (h_ξ,h_η,h_ζ) and $(\overline{\overline{h}}_\xi,\overline{\overline{h}}_\eta,\overline{\overline{h}}_\zeta)$ of the same $\mathbf{N}$ in two Cartesian frames $O(\mathbf{i},\mathbf{j},\mathbf{k})$ and $\bar{\bar{O}}(\bar{\bar{\mathbf{i}}},\bar{\bar{\mathbf{j}}},\bar{\bar{\mathbf{k}}})$. ’’ This new issue is a question of linear transformation in a linear space, as

$$T\mathbf{N}(h_\xi,h_\eta,h_\zeta)=\mathbf{N}(\overline{\overline{h}}_\xi,\overline{\overline{h}}_\eta,\overline{\overline{h}}_\zeta) \tag{A11}$$

According to the linear transformation theory, if the transforming between two sets of basis vector is

$$(\bar{\bar{\mathbf{i}}},\bar{\bar{\mathbf{j}}},\bar{\bar{\mathbf{k}}})=T(\mathbf{i},\mathbf{j},\mathbf{k})=(T\mathbf{i},T\mathbf{j},T\mathbf{k})=(\mathbf{i},\mathbf{j},\mathbf{k})A \tag{A12}$$

where A is the matrix of a linear transformation T about the basis vector $(\mathbf{i},\mathbf{j},\mathbf{k})$, and the elements of A can be determined in a concrete transforming or frame traversing, then the transforming between two sets of coordinates of a normal vector is

$$(\overline{\overline{h}}_\xi,\overline{\overline{h}}_\eta,\overline{\overline{h}}_\zeta)^T=A^{-1}(h_\xi,h_\eta,h_\zeta)^T \tag{A13}$$

Appendix B: A General Formal Solution of Sweep Angles

For the absolute sweep angles γ_{ra}, γ_{ca}, and γ_a, we first note $(\mathbf{n}_F|\text{ for }\gamma_{ra})=\mathbf{k}\times\vec{op}^\circ$ (Fig. 2). The first step is letting $\bar{\bar{\mathbf{i}}}$ pass through P by traversing O around $\mathbf{k}$ up to the angle $\theta+\varphi$ to make $\mathbf{n}_F=\bar{\bar{\mathbf{j}}}$. No second step is needed. The transformation matrix is

$$A=\begin{bmatrix}\cos(\theta+\varphi) & -\sin(\theta+\varphi) & 0\\ \sin(\theta+\varphi) & \cos(\theta+\varphi) & 0\\ 0 & 0 & 1\end{bmatrix} \tag{B1a}$$

$$A^{-1}=\begin{bmatrix}\cos(\theta+\varphi) & \sin(\theta+\varphi) & 0\\ -\sin(\theta+\varphi) & \cos(\theta+\varphi) & 0\\ 0 & 0 & 1\end{bmatrix} \tag{B1b}$$

Using Eq. (A13) one obtains

$$\gamma_{ra}=\gamma_F=\mathrm{Tan}^{-1}(\overline{\overline{h}}_\xi/-\overline{\overline{h}}_\zeta) \tag{B2}$$

$$\gamma_{ca}=\gamma_F=\mathrm{Tan}^{-1}(\overline{\overline{h}}_\eta/-\overline{\overline{h}}_\zeta) \tag{B3}$$

$$\gamma_a=\mathrm{Tan}^{-1}(\overline{\overline{g}}_r/-\overline{\overline{g}}_\zeta) \tag{B4}$$

$$(F|\text{ for }\gamma_a)=(\overline{\overline{g}}_c=\text{const}) \tag{B5}$$

respectively, here

$$\overline{\overline{g}}_r=\sqrt{\overline{\overline{h}}_\xi^{\,2}+\overline{\overline{h}}_\eta^{\,2}},\quad \overline{\overline{g}}_c=\tan^{-1}(\overline{\overline{h}}_\eta/\overline{\overline{h}}_\xi),\quad \overline{\overline{g}}_\zeta=\overline{\overline{h}}_\zeta \tag{B6}$$

For the relative sweep angles γ_{rr}, γ_{cr}, and γ_r, where $(\mathbf{n}_F|\text{ for }\gamma_{rr})=\vec{os}^\circ\times\vec{op}^\circ$, the matrix is

$$B=\begin{bmatrix}\cos(\theta+\varphi) & -\sin(\theta+\varphi) & 0\\ \sin(\theta+\varphi) & \cos(\theta+\varphi) & 0\\ 0 & 0 & 1\end{bmatrix}\begin{bmatrix}1 & 0 & 0\\ 0 & \cos\beta & -\sin\beta\\ 0 & \sin\beta & \cos\beta\end{bmatrix} \tag{B7a}$$

$$B^{-1}=\begin{bmatrix}\cos(\theta+\varphi) & \sin(\theta+\varphi) & 0\\ -\sin(\theta+\varphi)\cos\beta & \cos(\theta+\varphi)\cos\beta & \sin\beta\\ \sin(\theta+\varphi)\sin\beta & -\cos(\theta+\varphi)\sin\beta & \cos\beta\end{bmatrix} \tag{B7b}$$

Also using Eq. (A13) one obtains

$$\gamma_{rr}=\gamma_F=\mathrm{Tan}^{-1}(\overline{\overline{h}}_\xi/-\overline{\overline{h}}_\zeta) \tag{B8}$$

$$\begin{aligned}\gamma_{cr}&=\gamma_F=\mathrm{Tan}^{-1}(\overline{\overline{h}}_\eta/-\overline{\overline{h}}_\zeta)\\ &=\mathrm{Tan}^{-1}\frac{[-h_\xi\sin(\theta+\varphi)+h_\eta\cos(\theta+\varphi)]\cos\beta+h_\zeta\sin\beta}{[-h_\xi\sin(\theta+\varphi)+h_\eta\cos(\theta+\varphi)]\sin\beta-h_\zeta\cos\beta}\\ &=\mathrm{Tan}^{-1}\frac{h_c/(-h_\zeta)-\tan\beta}{h_c/(-h_\zeta)\cdot\tan\beta+1}\end{aligned} \tag{B9}$$

$$\cos\gamma_r=\overline{\overline{g}}_\zeta/\sqrt{\overline{\overline{g}}_\zeta^{\,2}+\overline{\overline{g}}_r^{\,2}} \tag{B10}$$

$$(F|\text{ for }\gamma_r)=(\overline{\overline{g}}_c=\text{const}) \tag{B11}$$

respectively; here, to obtain $\overline{\overline{g}}_r$, $\overline{\overline{g}}_c$, $\overline{\overline{g}}_\zeta$, Eq. ($B$6) is also used.

For sweep angles related to more spatial velocities in Eqs. (3) and (1), by traversing the frames, we must arrive at in fact a meridional streamline Cartesian frame for γ_{3ca}, and a complete streamlined Cartesian frame for γ_{3cr}, for the γ_{3r}’s situated plane F, etc. The matrix for γ_{3ca} and γ_{3ca} yielded by Eq. (A13) are

$$C=\begin{bmatrix}\cos(\theta+\varphi) & -\sin(\theta+\varphi) & 0\\ \sin(\theta+\varphi) & \cos(\theta+\varphi) & 0\\ 0 & 0 & 1\end{bmatrix}\begin{bmatrix}\cos\sigma & 0 & \sin\sigma\\ 0 & 1 & 0\\ -\sin\sigma & 0 & \cos\sigma\end{bmatrix} \tag{B12a}$$

$$C^{-1}=\begin{bmatrix}\cos(\theta+\varphi)\cos\sigma & \sin(\theta+\varphi)\cos\sigma & -\sin\sigma\\ -\sin(\theta+\varphi) & \cos(\theta+\varphi) & 0\\ \cos(\theta+\varphi)\sin\sigma & \sin(\theta+\varphi)\sin\sigma & \cos\sigma\end{bmatrix} \tag{B12b}$$

$$\gamma_{3ca}=\mathrm{Tan}^{-1}(\overline{\overline{h}}_\eta/-\overline{\overline{h}}_\zeta) \tag{B13}$$

The matrix for γ_{3cr} and γ_{3cr} yielded by Eq. (A13) are

$$D=\begin{bmatrix}\cos(\theta+\varphi) & -\sin(\theta+\varphi) & 0\\ \sin(\theta+\varphi) & \cos(\theta+\varphi) & 0\\ 0 & 0 & 1\end{bmatrix}\begin{bmatrix}\cos\sigma & 0 & \sin\sigma\\ 0 & 1 & 0\\ -\sin\sigma & 0 & \cos\sigma\end{bmatrix}\begin{bmatrix}1 & 0 & 0\\ 0 & \cos\beta_m & -\sin\beta_m\\ 0 & \sin\beta_m & \cos\beta_m\end{bmatrix} \tag{B14a}$$

$$D^{-1}=\begin{bmatrix} \cos(\theta+\varphi)\cos\sigma & \sin(\theta+\varphi)\cos\sigma & -\sin\sigma \\ \cos(\theta+\varphi)\sin\sigma\sin\beta_m & \sin(\theta+\varphi)\sin\sigma\sin\beta_m & \cos\sigma\sin\beta_m \\ -\sin(\theta+\sigma)\cos\beta_m & +\cos(\theta+\varphi)\cos\beta_m & \\ \cos(\theta+\varphi)\sin\sigma\cos\beta_m & \sin(\theta+\varphi)\sin\sigma\cos\beta_m & \cos\sigma\cos\beta_m \\ +\sin(\theta+\varphi)\sin\beta_m & -\cos(\theta+\varphi)\sin\beta_m & \end{bmatrix} \tag{B14b}$$

$$\begin{aligned}\gamma_{3cr}&=\mathrm{Tan}^{-1}(\overline{\overline{h}}_{\eta}/-\overline{\overline{h}}_{\zeta})\\ &=\mathrm{Tan}^{-1}-\frac{h_r\sin\sigma\sin\beta_m+h_c\cos\beta_m+h_\zeta\cos\sigma\sin\beta_m}{h_r\sin\sigma\cos\beta_m-h_c\sin\beta_m+h_\zeta\cos\sigma\cos\beta_m}\\ &=\mathrm{Tan}^{-1}\frac{h_c}{-h_r\sin\sigma-h_\zeta\cos\sigma}-\beta_m\end{aligned} \tag{B15}$$

where β_m is the meridional relative flow angle [Eq. (29)]. Equation (B15) is an universal formula for calculating every kind of circumferential sweep angle. Using also matrix D, Eqs. (A13) and (B6), one obtains the universal formula for the γ_{3r}'s situated plane F:

$$F=(\overline{\overline{g}}_c=\mathrm{const}) \tag{B16}$$

$$\begin{aligned}\overline{\overline{g}}_c&=\tan^{-1}(\overline{\overline{h}}_{\eta}/\overline{\overline{h}}_{\xi})\\ &=\tan^{-1}\frac{(h_r\sin\sigma+h_\zeta\cos\sigma)\sin\beta_m+h_c\cos\beta_m}{h_r\cos-h_\zeta\sin\sigma}\end{aligned} \tag{B17}$$

Nomenclature

$\mathbf{c}_1$ = absolute velocity of the undisturbed upstream flow
c_{1r}, c_{1c}, c_{1z} = radial, circumferential, and axial components of $\mathbf{e}_1$
$\mathbf{e}_r, \mathbf{e}_c, \mathbf{e}_z$ = unit vector of cylinder frame and orthogonal frame of curves
f, F = ascendent function of shock surface, projection plane
g_r, g_c, g_ζ = cylinder coordinates of **N**
h_r, h_c, h_ζ = cylinder components of **N**
h_ξ, h_η, h_ζ = Cartesian coordinates of **N**
$\mathbf{i}, \mathbf{j}, \mathbf{k}$ = unit vector of the Cartesian frame
$\mathbf{l}, \mathbf{l}^{\circ}$ = a direction within a plane
M = Mach number
$\mathbf{N}, \mathbf{n}$ = shock surface normal vector, unit normal vector
$\mathbf{n}_F$ = unit normal vector of a projection plane
$\mathbf{N}_{rc}$ = dimensionless sweep vector
S_r = dimensionless radial sweep similarity factor
S_c = dimensionless circumferential sweep similarity factor
P = a point on a shock surface
$\mathbf{r}$ = radius vector of a blade leading edge curve or a shock surface
r, θ, c, z = radius, circumferential angle, circumferential arc length, and axial coordinate
$\theta(r), z(r)$ = axial and meridional projection of a leading edge curve
Sign = function of the algebraic sign
T = linear transformation
$\tan^{-1}, \mathrm{Tan}^{-1}$ = inverse tangent, value domain $[-\pi,\pi]$, $[-\pi/2,\pi/2]$
$\mathbf{w}_1$ = undisturbed relative velocity
w_{1r}, w_{1c}, w_{1z} = radial, circumferential, and axial components of $\mathbf{w}_1$
x, y, z = relative Cartesian frame, and the blade's streamsurface Cartesian or manufacturing coordinates
α, β = absolute flow angle and relative flow angle
γ_a = spatial absolute sweep angle
γ_{ca}, γ_{ra} = circumferential and radial absolute sweep angles
γ_{3a} = spacial absolute sweep angle
γ_{3ca} = circumferential absolute sweep angle
γ_r = spacial relative sweep angle
γ_{cr}, γ_{rr} = circumferential and radial relative sweep angles
γ_{3r} = spacial relative sweep angle
γ_{3cr} = circumferential relative sweep angle
ξ, η, ζ = relative Cartesian frame, shock surface Cartesian coordinates
σ = meridional streamline slope angle
φ = circumferential angular coordinate measured from a leading edge curve
$\Phi=\theta(r)+\varphi$ = circumferential angular coordinate of the relative cylinder frame
ω = angular velocity of turbomachinery

Superscripts and Subscripts

$a', \overrightarrow{ab}^{\circ}$ = first derivative of a to r, unit vector ab
$-, =$ = the first and second new Cartesian frames
$m, 1$ = meridional streamline, undisturbed upstream flow

References

[1] Wennerstrom, A. J., 1990, ''Highly Loaded Axial Flow Compressors: History and Current Developments,'' ISABE 89-7002; ASME J. Turbomach., **112**, pp. 567–578.
[2] Hah, C., Puterbaugh, S. L., and Wadia, A. R., 1998, ''Control of Shock Structure and Secondary Flow Field Inside Transonic Compressor Rotors Through Aerodynamic Sweep,'' ASME Paper No. 98-GT-561.
[3] Kandebo, S. W., 1996, ''General Electric Tests Forward Swept Fan Technology,'' Aviation Week and Space Technol.
[4] Peng Shan, 1996, ''Kinematic Problems of Leaning Edge Supersonic Sweep-Bend in Supersonic and Transonic Axial Compressors,'' Ph.D. Thesis of Beijing University of Aeronautics and Astronautics.
[5] Peng Shan and Sheng Zhou, 1999, ''A Helical Surface Model for 3-D Shock Structure Analysis,'' ASME Paper No. 99-GT-226.
[6] Prince, Jr., D. C., 1980, ''Three-Dimensional Shock Structures for Transonic/Supersonic Compressor Rotors,'' J. Aircraft, **17**, pp. 28–37.
[7] Puterbaugh, S. L., and Wennerstrom, A. J., 1982, ''Revision of the Shock Loss Re-Estimation Procedure of Program UD0300 Utilizing a Three-Dimensional Shock Model,'' AFWAL-TR-82-2079, AD A124928.
[8] Peng Shan and Sheng Zhou, 1997, ''Kinematic Analysis and Design of Blade Leading Edge Sweep and Bend,'' Research Report BH-B4874, Beijing University of Aeronautics and Astronautics.
[9] Benser, W. A., Bailey, E. E., and Gelder, T. F., 1974, ''Holographic Studies of Shock Waves Within Transonic Fan Rotors,'' ASME Paper No. 74-GT-46.
[10] Wennerstrom, A. J., and Frost, G. R., 1976, ''Design of a 1500 ft/sec, Transonic, High-Through-Flow, Single-Stage Axial-Flow Compressor with Low Hub/Tip Ratio,'' Aerospace Research Laboratories, Wright-Patterson Air Force Base, AD B016386.
[11] Wennerstrom, A. J., Derose, R. D., and Law, C. H., 1976, ''Investigation of a 1500 ft/sec, Transonic, High-Through-Flow, Single-Stage Axial-Flow Compressor With Low Hub/Tip Ratio,'' Aerospace Research Laboratories, Wright-Patterson Air Force Base, AD B016506.

On Flowfield Periodicity in the NASA Transonic Flutter Cascade

J. Lepicovsky
QSS Group, Inc.,
Cleveland, OH 44135

R. V. Chima

E. R. McFarland

J. R. Wood

NASA Glenn Research Center,
Cleveland, OH 44135

A combined experimental and numerical program was carried out to improve the flow uniformity and periodicity in the NASA transonic flutter cascade. The objectives of the program were to improve the periodicity of the cascade and to resolve discrepancies between measured and computed flow incidence angles and exit pressures. Previous experimental data and some of the discrepancies with computations are discussed. In the present work surface pressure taps, boundary layer probes, shadowgraphs, and pressure-sensitive paints were used to measure the effects of boundary layer bleed and tailboard settings on flowfield periodicity. These measurements are described in detail. Two numerical methods were used to analyze the cascade. A multibody panel code was used to analyze the entire cascade and a quasi-three-dimensional viscous code was used to analyze the isolated blades. The codes are described and the results are compared to the measurements. The measurements and computations both showed that the operation of the cascade was heavily dependent on the endwall configuration. The endwalls were redesigned to approximate the midpassage streamlines predicted using the viscous code, and the measurements were repeated. The results of the program were that: (1) Boundary layer bleed does not improve the cascade flow periodicity. (2) Tunnel endwalls must be shaped like predicted cascade streamlines. (3) The actual flow incidence must be measured for each cascade configuration rather than using the tunnel geometry. (4) The redesigned cascade exhibits excellent periodicity over six of the nine blades.
[DOI: 10.1115/1.1378300]

Introduction

Many modern turbofan engines employ a highly loaded, low-aspect-ratio fan with transonic flow at the tip. The tip section airfoils have sharp leading edge and may have concave curvature on the suction surface for precompression. Due to flight envelope requirements, the engines are sometimes operated near the stall flutter boundary of the fan, which occurs at high incidence angles and high subsonic or transonic relative Mach numbers. Blade flutter and associated high cycle fatigue problems are very detrimental to the engine health and must be avoided. Codes for predicting stall-flutter and blade life are not yet fully reliable, and their verification is hampered by a lack of unsteady loading data, particularly for transonic airfoils. Therefore, there is currently great interest in fan blade stall-flutter research.

The transonic flutter cascade facility at NASA Glenn Research Center (GRC) is one of a very few test facilities dedicated to the unsteady aerodynamics of oscillating airfoils. The facility combines a linear cascade wind tunnel with a high-speed drive system that imparts pitching oscillations to cascade blades. It is used to provide data for modeling aerodynamics of blade stall flutter.

The facility was previously used to study a cascade of modern, low-aspect-ratio fan blades operating at high incidence angles and high subsonic and transonic Mach numbers. Results were published by Buffum et al. [1,2]. Measurements were taken at subsonic Mach numbers and at two incidence angles. Acceptable periodicity was found over three blades, which was sufficient for measurements of the unsteady pressures at interblade phase angles of 180 deg. For smaller interblade phase angles, periodicity was needed over more blades. Adjustments to the boundary layer bleed system improved periodicity for some flow conditions, but not sufficiently for all cases of interest.

Comparisons with various computational fluid dynamic (CFD) predictions have suggested that the flow incidence angle ahead of the blades was less than the geometric incidence angle between the headboards and the blades [1,2]. The present work also suggested that the incidence angle might vary across the face of the cascade. Measured downstream pressures were generally inconsistent with CFD predictions.

A combined experimental and numerical study of the facility was carried out to improve the periodicity of the tunnel, and to quantify better the inlet and exit conditions needed for accurate CFD predictions. This paper describes the facility in detail and describes a variety of experimental data taken in the facility. The data include blade and sidewall static pressure data, upstream boundary layer data, and flow visualization measurements made using shadowgraphs and pressure sensitive paints. The paper also describes two CFD codes used to understand the behavior of the original facility and to devise improvements to the facility. A panel code was used to analyze the complete tunnel including the endwalls and nine blades. A quasi-three-dimensional Navier–Stokes code was used to analyze isolated blades under periodic flow conditions.

Four configurations of the tunnel endwalls were analyzed computationally and tested experimentally. The original and final configurations are described here. Intermediate configurations were described by Lepicovsky et al. [3] and Chima et al. [4]. The analyses and tests showed that the endwall configuration had a large impact on the periodicity of the cascade, and that no amount of bleed could correct for poorly configured endwalls. It was also found that the periodic Navier–Stokes code could be used to determine an endwall configuration that maximized the periodicity of the cascade.

Facility Description

A schematic diagram of the NASA transonic flutter cascade facility is shown in Fig. 1. The facility consists of an inlet section, a test section with blades, and an exit section connected to a

---

Contributed by the International Gas Turbine Institute and presented at the 45th International Gas Turbine and Aeroengine Congress and Exhibition, Munich, Germany, May 8–11, 2000. Manuscript received by the International Gas Turbine Institute February 2000. Paper No. 2000-GT-572. Review Chair: D. Ballal.

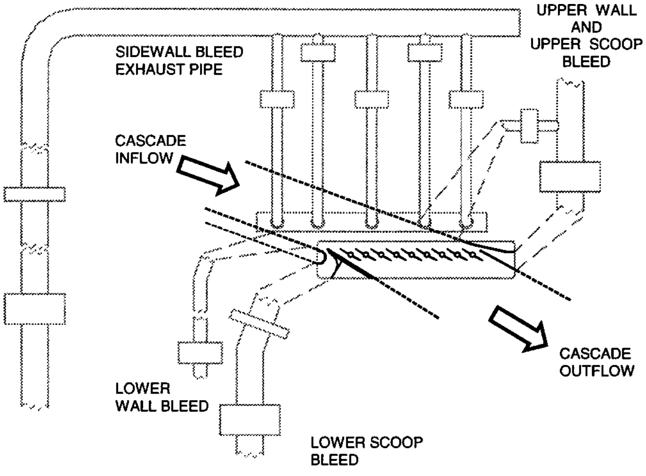

Fig. 1 Boundary layer bleed system of the NASA transonic flutter cascade facility

central air exhaust system. Room air enters the inlet section through a honeycomb in a bellmouth inlet (not shown in Fig. 1). The headboards upstream of the cascade are adjustable to control the incidence to the cascade. As seen in Fig. 1, the facility has a complex bleed system that can be used to remove the boundary layers through endwall scoops and perforations in both the headboards and the sidewalls.

A photograph of the test section is shown in Fig. 2. The test section has a rectangular cross section 586 mm wide × 96 mm along the span. Nine blades designed and fabricated by Pratt and Whitney are located in the test section. Blade geometric parameters are given in Table 1. The blades have a constant cross section except near the endwalls where they have large, diamond-shaped fillets that attach the blades to the drive shafts. All the blades or any single blade can be oscillated at realistic reduced frequencies (Strouhal numbers). Interblade phase angles can be varied in increments of 15 deg. The facility has been described in detail in the work of Boldman and Buggele [5], Shaw et al. [6], and Buffum et al. [1,2,7,8]. Since the present work concentrated on improving the steady behavior of the cascade, no unsteady measurements are described here.

The exit section has adjustable tailboards to control the exit flow angle. The tailboards start just ahead of the leading edge of the cascade and can be moved to form scoops that remove the endwall boundary layers. Downstream of the exit section air is expanded through a diffuser into an exhaust header connected to the GRC central air facility.

Unresolved Problems With Flutter Cascade Data

Buffum et al. reported initial unsteady data for the blades studied here [1,2]. These data were acquired with all nine blades oscillating. Earlier work by Buffum and Fleeter [7] indicated that at some interblade phase angles, the oscillating blades produced waves that reflected off the wind tunnel walls and back into the cascade, interfering with the unsteady measurements. Later the tunnel walls were perforated and backed with acoustic treatment. The effectiveness of this treatment has not been proven. Ott et al. [9] recommended just the opposite for their facility—replacement of slotted walls with solid ones.

Experimental blade surface pressure measurements were presented in [1,2] at Mach numbers between 0.5 and 0.8, and geometric incidence angles, i_{GM}, of 0 and 10 deg. Experimental pressure distributions for steady flow at inlet Mach numbers of up to 0.5 were compared with various CFD predictions, but good agreement was found only up to 85 percent chord and only for 0 deg incidence. The cascade flow periodicity was measured only for the three middle blades and was found to be sufficient for unsteady surface pressure measurements at an interblade phase angle of 180 deg and reduced frequencies of 0.4 and 0.8.

Buffum et al. reported that comparisons between various CFD predictions and their data suggested that the flow incidence angle was between 0.5 and 1.5 deg less than the geometric incidence angle between the headboards and the blades [1,2]. Similar results were found in the present work. Figure 3 compares the measured surface pressure distribution at $M=0.8$ with distributions calculated using the RVCQ3D code (described later) at three incidence angles. The best agreement with the data is for i_{GM} between 8 and 9 deg, which is consistent with the results in [1,2]. Other calcula-

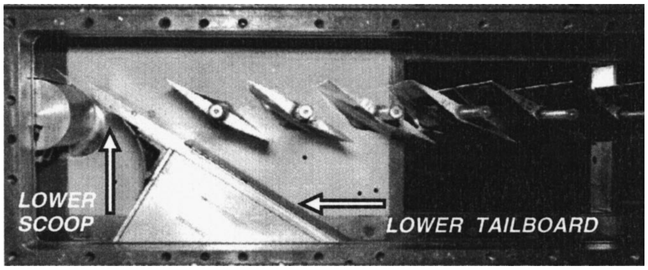

Fig. 2 View of cascade test section

Table 1 Airfoil and cascade parameters

Blade chord,	C	*89.2 mm*
Leading edge camber angle,	θ	*−9.5 dg*
Maximum thickness,	t_{max}	*0.048 C*
Location of maximum thickness,	ξ_{max}	*0.625 C*
Stagger angle,	γ	*60.0 dg*
Number of blades in the cascade,		*9*
Blade pitch,	S	*58.4 mm*
Cascade solidity,	C/S	*1.53*
Pitching axis,	ξ_{ax}	*0.5 C*
Blade height,	h	*95.9 mm*

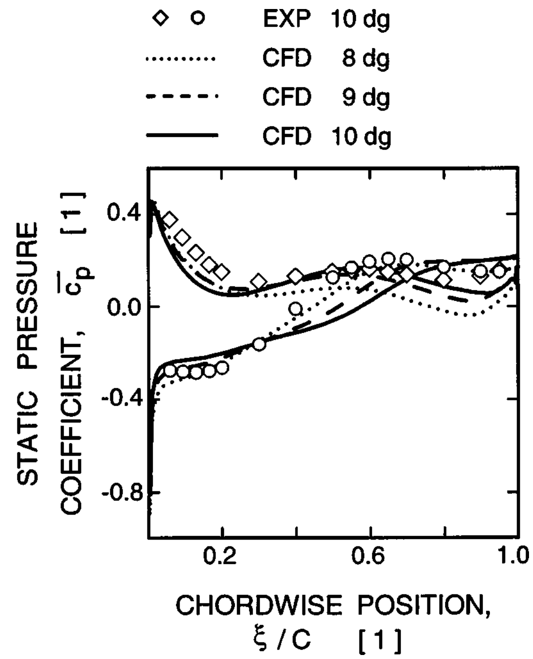

Fig. 3 Effect of incidence angle on pressure coefficient compute with RVCQ3D

tions suggested that the incidence angle might also vary across the face of the cascade. Furthermore, calculated static pressure ratios across the cascade have shown very poor agreement with experimental measurements.

To simplify data acquisition, an influence coefficient technique will be used for future unsteady work in this cascade. With this technique, only one blade in the cascade is oscillated at a time and the resulting unsteady pressures are measured on the remaining (nonmoving) blades. The unsteady aerodynamics of an equivalent cascade with all blades oscillating at a specified interblade phase angle are then determined through a vector summation of unsteady data from individual blades [8]. Although the use of the influence coefficient technique has only been demonstrated for attached flow, this facility has the unique capability of demonstrating this technique for separated flow. Since this technique requires a high degree of flow periodicity over many blades, it was necessary to increase flow periodicity beyond the three middle blades.

Approach to Improving Cascade Periodicity

The initial attempts to improve the cascade periodicity used experimental measurements to study the effects of inlet bleed settings and exit tailboard angles. Several types of measurement were used to assess periodicity: (1) Measurements of surface pressures on all blades gave a rigorous assessment of periodicity. (2) Measurements of sidewall pressure distributions at three axial locations parallel to the face of the cascade gave a quick indication of uniformity. (3) Cobra probe measurements were used to assess the effects of bleed on inlet Mach number and flow angle profiles. (4) Shadowgraphs and pressure sensitive paint (PSP) techniques were used to visualize the flowfield.

Measurement of surface pressures on all blades was usually impractical since only two blades were fully instrumented, with 15 static taps at midspan. One blade was instrumented on the suction side and the other was instrumented on the pressure side. The instrumented blades were marched along the cascade to measure pressures in all locations, which was a time-consuming procedure. In practice, measurements of sidewall pressures along the face of the cascade were most useful for a quick assessment of periodicity.

The various measurements showed that no combination of bleed and tailboard setting significantly improved the periodicity of the cascade. The measurements and concurrent CFD simulations made it clear that there was a fundamental mismatch between the tunnel endwall turning and the flow turning imposed by the blades.

Four different endwall configurations were investigated in order to improve the periodicity of the cascade. The last three configurations were designed using CFD analyses of the complete tunnel made by McFarland, and analyses of isolated blades made by Chima. The CFD codes are described briefly below and in detail by Chima et al. [4].

Only two endwall configurations are discussed here. The configurations are referred to by two angles, the headboard angle followed by the tailboard angle, both measured with respect to the

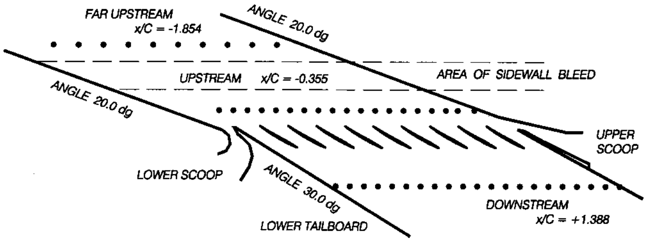

Fig. 4 Cascade configuration *C_20.0/30.0*

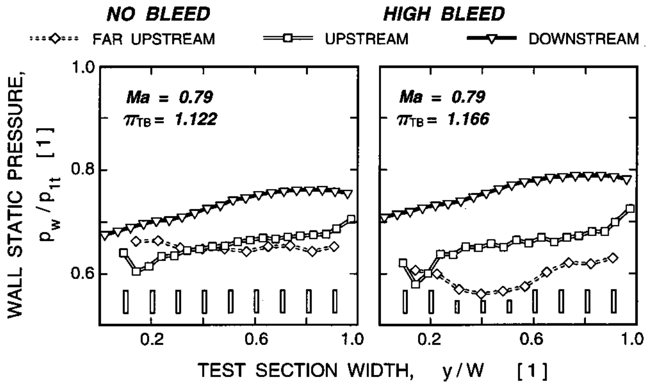

Fig. 5 Effects of sidewall boundary layer bleed rate

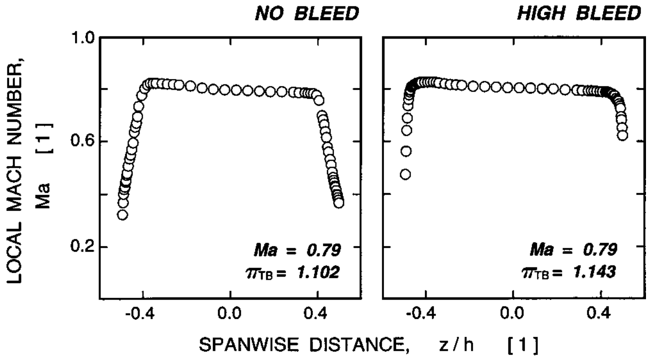

Fig. 6 Effects of sidewall bleed on spanwise Mach number distribution at *y/W*=0.388 and *x/C*=−0.254

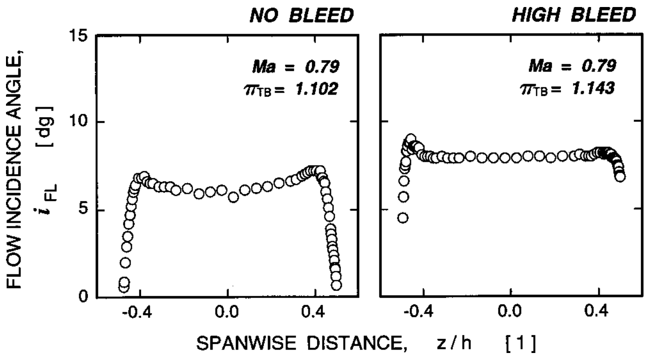

Fig. 7 Effects of sidewall bleed on spanwise distribution of flow incidence angles at y/W=0.388 and *x/C*=−0.254

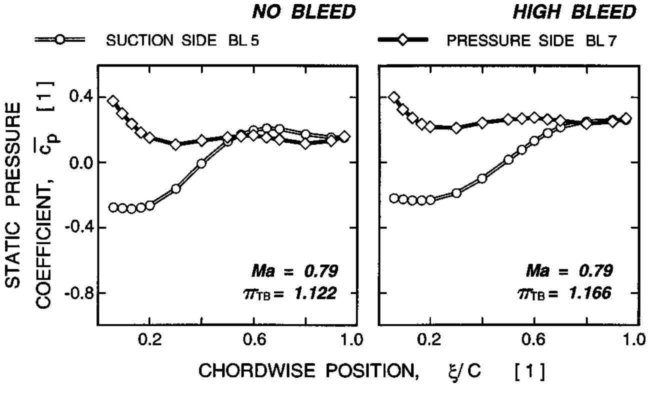

Fig. 8 Effects of sidewall bleed on blade loading

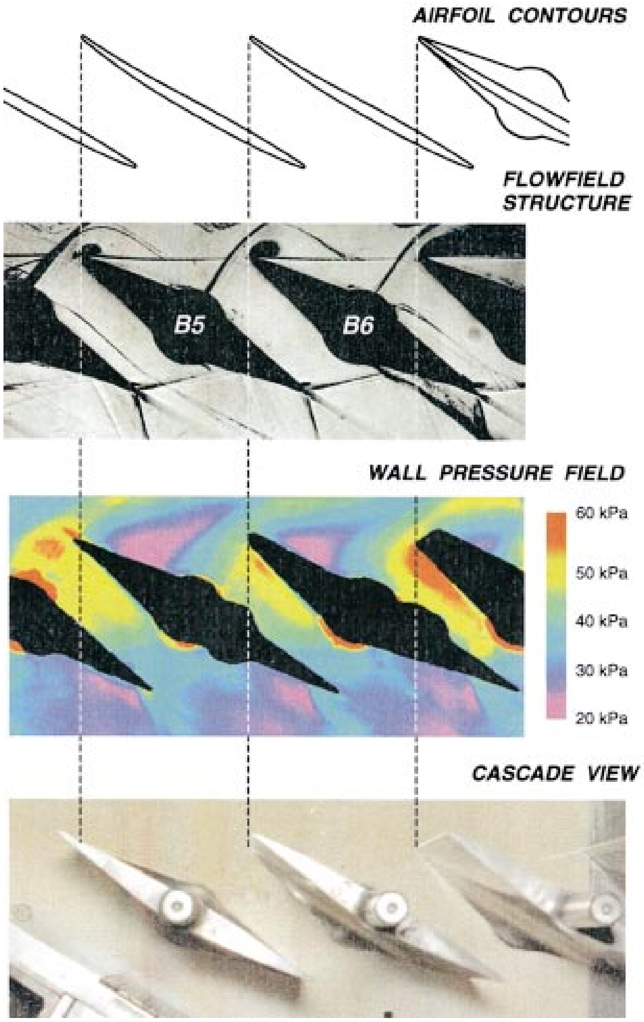

Fig. 9 Cascade flowfield for Mach number 1.35

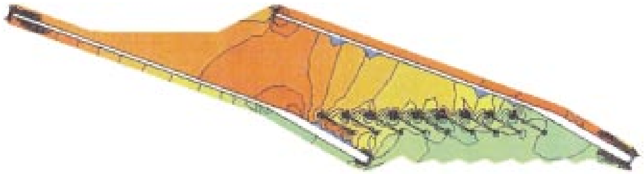

Fig. 10 Mach contours computed with PCSTAGE for original configuration *C_20.0/30.0*

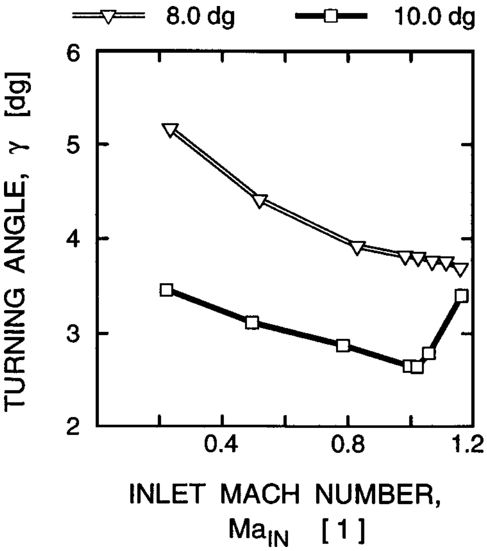

Fig. 11 Cascade turning angle versus inlet Mach number computed with RVCQ3D

horizontal. In the original configuration the headboard was set at 20 deg and the tailboard was set at the blade setting angle. This is the configuration reported by Buffum et al. [5,6] and is referred to here as ***C_20.0/30.0***. In the final configuration the headboard was set at 20 deg and the tailboard was set at 24 deg, so the configuration is referred to as ***C_20.0/24.0***. In both cases the blades were set at 30 deg, i.e., staggered 60 deg, giving a geometric incidence angle of $i_{FL}=10$ deg.

Cascade Configuration *C_20.0/30.0*

A schematic diagram of the original cascade configuration ***C_20.0/30.0*** is shown in Fig. 4. The three rows of static pressure taps on the sidewalls are shown. One row was located far upstream at $x/C=-1.854$, one was near upstream at $x/C=-0.355$, and one was downstream of the blades at $x/C=1.388$. The two rows of static taps upstream of the cascade were on the back sidewall, while the downstream row was on the front sidewall. The inlet Mach number was determined using inlet total pressure and the average static pressure upstream of the cascade at $x/C=-0.355$ (using static taps in the range $0.2<y/W<0.8$).

Effect of Sidewall Bleed. The effect of bleed on the sidewall pressure distributions is shown in Fig. 5 for M=0.79. With no bleed, the far-upstream pressures were fairly uniform; however, the near-upstream pressures varied significantly across the face of the cascade, corresponding to a variation in Mach number from 0.86 at the left to 0.73 on the right. A high sidewall bleed flow (about 15 percent of the total flow) made the far upstream pressure distribution worse and did not improve the pressure distributions elsewhere.

Figure 6 shows the effect of sidewall bleed on spanwise profiles of the upstream Mach number made using a traversing cobra probe. Since the test conditions were always set for a specific upstream Mach number regardless of the bleed rate, the effects of bleed are only seen as changes in the thickness of the wall boundary layer. However, the static pressure ratio across the cascade varied from $\pi_{TB}=1.102$ without bleed to $\pi_{TB}=1.143$ with high bleed.

Figure 7 shows the effect of sidewall bleed on spanwise profiles of the upstream flow angle. Although the geometric incidence angle was 10 deg, the measured flow angle at midspan was 6.2 deg without bleed and 8.1 deg at high bleed. Measurements at other pitchwise locations showed that the flow incidence varied by 2 to 3 deg across the center blade passages and was always 1.5 to 2.5 deg smaller with no bleed than it was with high bleed. Buffum et al. published surface pressures on the three middle blades (4–6) at a specified geometric incidence angle [1,2]. The bleed rate was not reported but there are indications that it was low; consequently, it is assumed that the actual flow incidence angle for Buffum's data was between 7.5 to 9.0 deg. This is consistent with the CFD results shown in Fig. 3. Figure 8 compares blade surface pressure distributions made with and without sidewall bleed and shows that that bleed had a large effect on the measured pressures.

Figure 9 shows two flow visualization images also used to investigate the periodicity of the cascade. The images were made at an inlet Mach number of 1.35 with high bleed. The shadowgraph image shown at the top of the figure was made using a dedicated double-pass Schlieren system described by Boldman and Buggele [10]. The shock structure is fairly periodic across the cascade. The pressure-sensitive paint image at the bottom was made using a technique described by Bencic [11] and Lepicovsky et al. [12]. Here it is evident that the low-pressure region above the suction surface leading edges varies significantly from passage to passage.

The previous results showed that sidewall boundary layer bleed had a large impact on the performance of the cascade but did not significantly improve the uniformity of the flow. Furthermore, the large number of bleed valves (see Fig. 1) made it difficult to quantify bleed flow rates and to repeat previous measurements made with bleed. Consequently, a decision was made not to use the bleed system in further experiments.

Effects of Lower Tailboard Setting. Several researchers had suggested that the exit tailboards should be moved independently to improve the periodicity of the cascade. The lower tailboard was first reset to $\lambda_T=32$ deg angle (diverging exit channel). This setting led to larger upstream flow nonuniformity, particularly on the left side of the cascade. Then the tailboard was then reset to $\lambda_T=24$ deg (converging exit channel). This setting caused a peak in the static pressure distribution on the left side upstream of the cascade. The peak was probably caused by the protrusion of the lip of the lower scoop into the flow (see Fig. 2). Away from this peak the pressure distributions were more uniform than before, although there was still a gradient across the cascade. This suggested that the exit flow angle from the cascade might be closer to 24 deg than the original tailboard setting of $\lambda_T=30$ deg.

In summary, neither boundary layer bleed nor tailboard setting angle substantially improved the uniformity of the original cascade. At this point two CFD codes were used to analyze the complete facility and the isolated blade row.

CFD Codes

PCSTAGE. The PCSTAGE turbomachinery analysis panel code developed by McFarland [13,14] was used to model the complete tunnel configuration. The code uses an integral equation solution method to solve the two-dimensional, inviscid flow equations for multiple bodies. Compressibility effects are approximated in the solution. The method is most accurate for low Mach number flows, but can be applied to flows where Mach numbers remain less than one.

The complete tunnel configuration was modeled, including all nine blades and the endwalls. The endwalls were modeled as a tenth body with one surface shaped like the left wall of the tunnel and the other surface shaped like the right wall. Details such as wall bleed slots and boundary layer scoops were neglected. The endwall body was placed on one side of the cascade, and a periodic boundary condition was used to map the second endwall to the other side of the cascade.

Calculations were made at M=0.5 to minimize compressibility effects. Kutta condition constraints were used on each of the ten bodies rather than assigning a circulation to each. This resulted in an iterative solution, but allowed the solution to determine the flow split around each of cascade bodies.

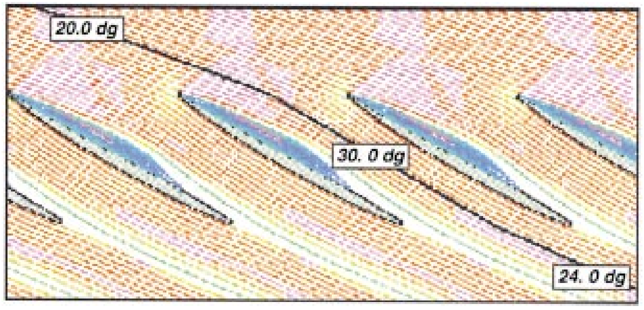

Fig. 12 Particle traces computed with RVCQ3D

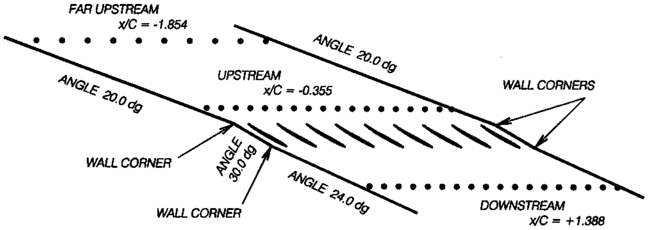

Fig. 13 Cascade configuration *C_20.0/24.0*

The endwall body was modeled with 98 panels, and the cascade blades were modeled with 70 panels each. This resulted in a solution matrix of 748 equations with 748 unknowns. The solution of this matrix provides the surface flow conditions at the center of each body panel. The flow conditions were also calculated at 3147 points in the flow field. These field points plus the surface points were combined using the random points feature of the TecPlot© graphics software to produce contour plots of the flow field. The PCSTAGE calculation took about 4 minutes on an SGI Indigo 2 workstation.

Figure 10 shows Mach contours of the original configuration calculated with PCSTAGE. The calculations show a large variation in Mach number across the entire face of the cascade. Only three passages near the center of the cascade see the nominal Mach number shown by light orange contours. The largest variation in Mach number occurs at the bend in the left endwall, where the measured pressure was lowest.

RVCQ3D. The quasi-three-dimensional (Q-3-D) turbomachinery analysis code RVCQ3D developed by Chima [15,16] was also used to analyze the blades. The code solves the thin-layer Navier–Stokes equations in finite-difference form. Blockage effects can be modeled by specifying a stream sheet thickness that can vary with streamwise distance. Turbulence effects were modeled using the Baldwin–Lomax model, including the original transition model. The flow equations were solved using an explicit Runge–Kutta scheme. A spatially varying time step and implicit residual smoothing were used to accelerate convergence.

A C-type grid was used. The grid had 225 points around the blade and 45 points from the blade to midpitch, for a total of 10,125 points. The spacing at the wall gave $y^+ \sim 3$ at the first grid point. The upstream boundary of the grid was placed at the same location as the near-upstream measurement station used in the experiment at $x/C = -0.355$. The cascade was assumed to be periodic blade-to-blade, so that only one isolated blade was analyzed.

Sidewall boundary layer blockage was neglected after early RVCQ3D calculations with 5 to 10 percent blockage added failed to improve agreement with experimental results. Later three-

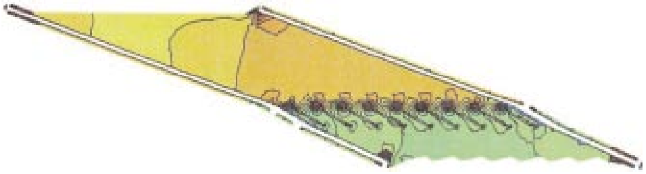

Fig. 14 Mach contours computed with PCSTAGE for final configuration *C_20.0/24.0*

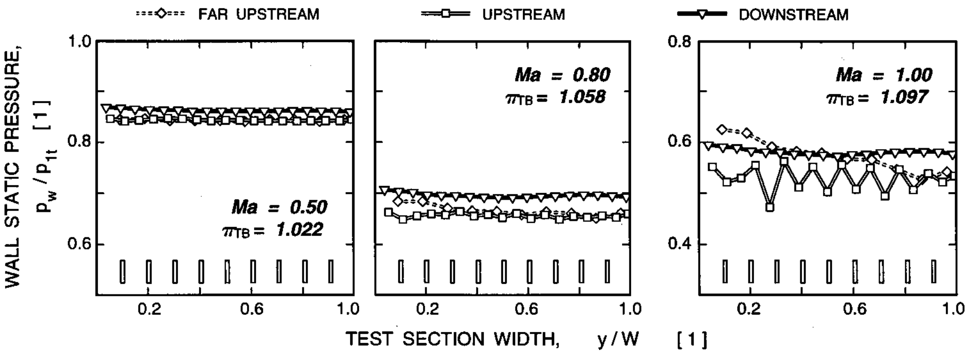

Fig. 15 Wall static distributions for cascade configuration *C_20.0/24.0*

dimensional calculations also showed that blockage effects were negligible.

Most calculations were run for 1500 iterations, which took about 3.5 minutes on an SGI Indigo 2 workstation. This ensured that exit total pressure was converged to four significant digits.

To improve the periodicity of the cascade, the endwall turning was adjusted to match the turning of a perfectly periodic cascade modeled by RVCQ3D. The blades were analyzed over a range of Mach numbers for incidence angles of 8 and 10 deg. The calculated turning angle is plotted versus inlet Mach number in Fig. 11. For 10 deg incidence, the turning varies continuously from about 5 deg at low speeds to 4 deg at M=1.2. At this higher incidence the flow separates at the leading edge for all Mach numbers.

Figure 12 shows computed particle traces for a solution at M=0.8 and $i_{FL}=10$ deg. The particle traces show that the streamlines near the center of a blade passage can be approximated with three line segments: one upstream at the nominal inflow angle, one downstream at the calculated turning angle, and a third within the passage at the blade setting angle. Thus, for the final design the headboard angle was left at 20 deg, the tailboard angle was set to 24 deg to match the turning predicted by RVCQ3D for 10 deg of incidence, and a straight, 30 deg insert was fabricated to connect the two. The endwalls were spaced one-half pitch from their neighboring blade.

A schematic diagram of the final cascade configuration ***C_20.0/24.0*** is shown in Fig. 13. Figure 14 shows Mach number contours calculated for this configuration using PCSTAGE. The contours show very uniform flow ahead of the cascade.

Cascade Configuration *C_20.0/24.0*

Wall Static Pressure Distributions. Figure 15 shows the wall static pressures distributions measured in the final configuration for inlet Mach numbers of 0.5, 0.8, and 1.0. At subsonic speeds the pressure distributions are very uniform, as predicted by PCSTAGE. The uniformity of wall static pressures in the pitchwise direction was an excellent indicator of improved blade periodicity for this configuration. At M=1.0 shock waves from the blades create the sawtooth pattern in the upstream pressures.

Blade Loading and Periodicity. Figure 16 shows blade surface pressure distributions measured on blade B5 at inlet Mach numbers of 0.5, 0.8, and 1.0. Pressure distributions computed with RVCQ3D are also shown for the two higher Mach numbers. Computed static pressure ratios across the cascade matched measured values closely, confirming that the endwall interference had been minimized.

Blade loading periodicity was verified by measuring surface pressures for all nine blade positions by marching the two instrumented blades through the cascade. The tunnel operating conditions were repeatable to within 1 percent of the inlet Mach number for each blade position.

To visualize the differences in loading diagrams between blades, the center blade (B5) was taken as a reference and compared to the other blades. The pressure distribution on blade B5 is shown in Fig. 16 for M=0.8. The differences between this reference pressure distribution and the pressure distributions on the other blades were computed, and are plotted in Fig. 17. The sketch at the top of the figure identifies individual blades with color-coded numbers. The four plots below show the measured differences in pressure coefficients, with the left and right sides of the cascade shown in the left and right plots, and the suction and pressure surfaces shown in the upper and lower plots. Blade B5 is represented by a straight, black, broken line. The deviation curves for the remaining blades are color-coded in accordance with the blade numbers in the sketch. For a perfectly periodic flow, all deviation curves would collapse to the broken straight line of blade B5. Positive values of deviation indicate that a particular blade has a higher pressure coefficient than blade B5 at the same chordwise station. Negative values indicate a lower value than blade B5.

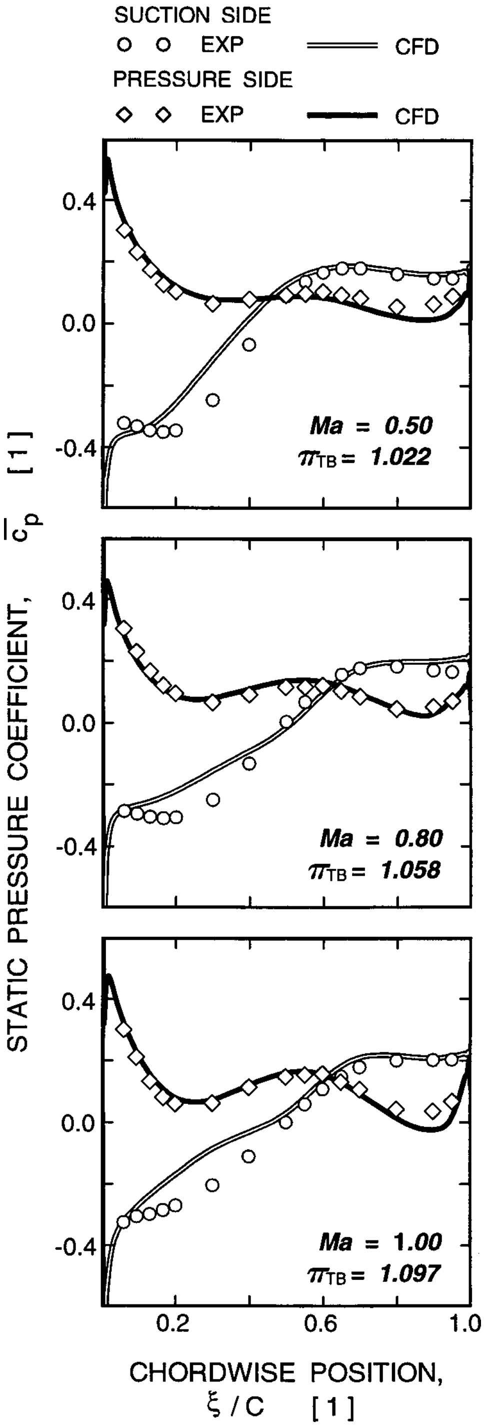

Fig. 16 Blade loading diagrams for middle blade (B5) for cascade configuration *C_20.0/24.0*

All pressures in the cascade were measured using absolute pressure transducers with a range of 100 kPa (15 psia), and accuracy better than ±0.4 percent. This translates to an accuracy of ±0.02 for the value of pressure coefficient. Therefore, deviations of pressure coefficient less than ±0.04 are considered to be insignificant.

The plots of pressure coefficient deviations in Fig. 17 show significant improvements in the flow periodicity for the final cascade configuration. Blades 2–5 in the left half of the cascade show

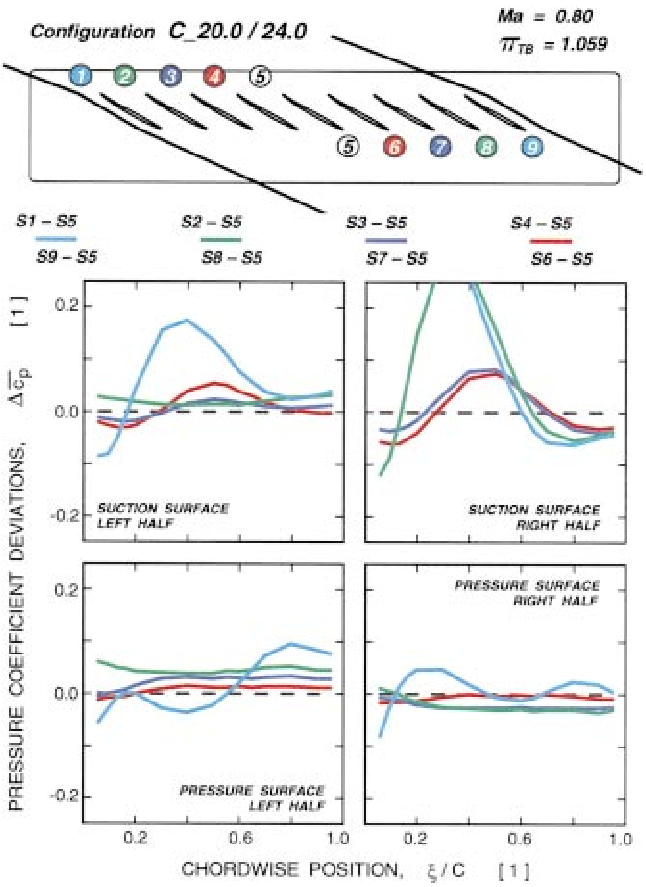

Fig. 17 Blade loading periodicity for configuration *C_20.0/24.0*

excellent agreement of pressure distributions on the suction surface. Blades 5–7 in the right half show acceptable agreement in their suction side pressure distributions. On the pressure side, the agreement is excellent for blades 2–8. Overall the cascade shows excellent periodicity over six blades, numbers 2–7.

Conclusions

A combined experimental and numerical study was carried out to improve the flow periodicity in the NASA transonic flutter cascade facility. Several experimental techniques were used to investigate the effects of boundary layer bleed and tailboard setting angles on flow uniformity. The techniques included measurements of static pressures on the sidewalls and blades, cobra probe measurements of inlet velocity profiles, and shadowgraph and pressure-sensitive paint flow visualization. Several discrepancies in older data were explained, including questions of actual flow incidence angles and exit pressure levels.

Two CFD codes were used to analyze the facility. The PC-STAGE panel code was used to analyze the entire facility, including the endwalls and all nine blades. PCSTAGE results showed that the flow nonuniformity was caused by the endwall configuration, and was extremely useful for evaluating proposed changes to the endwalls. The RVCQ3D quasi-three-dimensional viscous code was used to analyze the isolated blades. These results were used to redesign the endwalls to minimize interference.

The following conclusions were reached concerning design and operation of the facility:

1 Boundary layer bleed did not improve the flowfield periodicity. High bleed flows affected pitchwise distribution of flow incidence angles along the cascade and thus contributed to blade load variations.

2 Sidewall boundary layer blockage is relatively small for this blade row. For future experiments it is recommended that the boundary layer bleed system not be used.

3 The tailboard setting angle strongly affects the pitchwise uniformity of wall static pressures. Tailboards should be set to match the expected exit flow angle for a perfectly periodic cascade. Tailboards must be parallel to each other to produce a periodic flow.

4 Shaping the endwalls like the midpassage streamlines predicted with a viscous analysis code can minimize endwall interference. Endwalls should probably be located at midpassage since midpassage streamlines are smoother than the stagnation streamlines and have less influence on the blade loading.

5 Geometric incidence angles do not always represent the true flow incidence. Actual flow incidence angles should be measured for each new configuration of the facility.

6 The final configuration of the facility shows excellent periodicity over six blades, numbers 2–7. Future work will focus on taking unsteady measurements on these blades.

Acknowledgments

The authors would like to acknowledge the invaluable engineering and technical support provided by Mr. T. A. Jett and Mr. R. Torres of NASA GRC. The help of Mr. K. E. Weiland with flow visualization and Mr. T. J. Bencic with PSP data acquisition is also particularly appreciated. The program was supported by NASA GRC under the Smart Green Engine program managed by Mr. K. C. Civinskas. The continued support of Mrs. L. M. Shaw, the Chief of the GRC Compressor branch, is also particularly acknowledged.

Nomenclature

C = airfoil chord, mm
c_p = pressure coefficient
$\overline{c}_p$ = pressure coefficient: $\overline{c}_p = (p - \overline{p}_1)/(0.5 \cdot \overline{\rho}_1 \overline{v}_1^2)$
i_{FL} = flow incidence angle, deg
i_{GM} = geometric incidence angle, deg
M = Mach number
v = cascade inlet velocity, $\mathrm{m \cdot s^{-1}}$
W = cascade test section width at $x/C = -0.355$, mm
x = axial distance (cascade), mm
y = pitchwise distance (cascade), mm
y^+ = law-of-the-wall distance
z = spanwise distance (cascade), mm
Δc_p = pressure coefficient deviation from blade B5
λ_T = lower tailboard angle (from horizontal direction), deg
π_{TB} = cascade static pressure ratio: $\pi_{TB} = \overline{p}_2/\overline{p}_1$
ρ = density, $\mathrm{kg \cdot m^{-3}}$

Subscripts

0 = far upstream
1 = upstream
2 = downstream
– = average value over the range $0.2 < y/W < 0.8$

References

[1] Buffum, D. H., Capece, V. R., King, A. J., and El-Aini, Y. M., 1998, ''Oscillating Cascade Aerodynamics at Large Mean Incidence,'' ASME J. Turbomach., **120**, pp. 122–130; also NASA TM-107247.

[2] Buffum, D. H., Capece, V. R., King, A. J., and El-Aini, Y. M., 1996, ''Experimental Investigation of Unsteady Flows at Large Incidence Angles in a Linear Oscillating Cascade,'' AIAA Paper No. 96-2823; also NASA TM-107283.

[3] Lepicovsky, J., McFarland, E. R., Chima, R. V., and Wood, J. R., ''On Flowfield Periodicity in the NASA Transonic Flutter Cascade: Part I—Experimental Study,'' ASME Paper No. 2000-GT-572.

[4] Chima, R. V., McFarland, E. R., Wood, J. R., and Lepicovsky, J., 2000, ''On Flowfield Periodicity in the NASA Transonic Flutter Cascade: Part II—Numerical Study,'' ASME Paper No. 2000-GT-573.

[5] Boldman, D. R., and Buggele, A. E., 1978, ''Wind Tunnel Tests of a Blade Subjected to Midchord Torsional Oscillations at High Subsonic Stall Flutter Conditions,'' NASA TM-78998.

[6] Shaw, L. M., Boldman, D. R., Buggele, A. E., and Buffum, D. H., 1986, ''Unsteady Pressure Measurements on a Biconvex Airfoil in a Transonic Oscillating Cascade,'' ASME J. Eng. Gas Turbines Power, **108**, pp. 53–59.

[7] Buffum, D. H., and Fleeter, S., 1991, ''Wind Tunnel Wall Effects in a Linear Oscillating Cascade,'' NASA TM-103690.

[8] Buffum, D. H., and Fleeter, S., 1988, ''Investigation of Oscillating Cascade Aerodynamics by an Experimental Influence Coefficient Technique,'' NASA TM-101313.

[9] Ott, P., Norryd, M., and Bölcs, A., 1998, ''The Influence of Tailboards on Unsteady Measurements in a Linear Cascade,'' ASME Paper No. 98-GT-572.

[10] Boldman, D. R., and Buggele, A. E., 1983, ''Experimental Evaluation of Shockless Supercritical Airfoils in Cascade,'' AIAA Paper No. 83-0003.

[11] Bencic, T. J., 1995, ''Experience Using Pressure Sensitive Paint in NASA Lewis Research Center Propulsion Test Facilities,'' AIAA Paper No. 95-2831.

[12] Lepicovsky, J., Bencic, T. C., and Bruckner, R. J., 1997, ''Application of Pressure Sensitive Paint to Confined Flow at Mach Number 2.5,'' AIAA Paper No. 97-3214.

[13] McFarland, E. R., 1993, ''An Integral Equation Solution for Multistage Turbomachinery Design Calculations,'' ASME Paper No. 93-GT-41.

[14] McFarland, E. R., 1994, ''Use of Preliminary Design Methods in the Analysis of Multi-Stage Turbomachinery,'' NASA CP 3282, Vol. 2.

[15] Chima, R. V., 1987, ''Explicit Multigrid Algorithm for Quasi-Three-Dimensional Viscous Flows in Turbomachinery,'' J. Propul. Power, **3**, No. 5, pp. 397–405.

[16] Chima, R. V., 1995, ''A $k-\omega$ Turbulence Model for Quasi-Three-Dimensional Turbomachinery Flows,'' AIAA Paper No. 96-0248; also NASA TM-107051.

D. B. M. Jouini

S. A. Sjolander

Department of Mechanical &
Aerospace Engineering,
Carleton University,
Ottawa, Ontario, Canada

S. H. Moustapha

Pratt & Whitney Canada Inc.,
Longueuil, Quebec, Canada

Aerodynamic Performance of a Transonic Turbine Cascade at Off-Design Conditions

The paper presents detailed measurements of the midspan aerodynamic performance of a transonic turbine cascade at off-design conditions. The measurements were conducted for exit Mach numbers ranging from 0.5 to 1.2, and for Reynolds numbers from 4×10^5 to 10^6. The profile losses were measured for incidence values of +14.5 deg, +10 deg, +4.5 deg, 0 deg, and −10 deg relative to design. To aid in understanding the loss behavior and to provide other insights into the flow physics, measurements of blade loading, exit flow angles, trailing-edge base pressures, and the axial velocity density ratio (AVDR) were also made. It was found that the profile losses at transonic Mach numbers can be closely related to the base pressure behavior. The losses were also affected by the AVDR.

[DOI: 10.1115/1.1370157]

Introduction

Market requirements for compact, low cost, and fuel-efficient engines generally lead to small size turbomachines. Typical features in the compressor turbine of these engines are a single stage turbine with high-pressure ratio and stage loading, combined with blade passages of small aspect ratio, high turning, transonic Mach numbers, and very low Reynolds numbers. These turbines need to operate at maximum efficiency at the design cruise speed and altitude as well as with a minimum efficiency penalty at off-design conditions arising from changes in the pressure ratio, speed, and altitude. The resulting three-dimensional flow field within the turbine passages, combined with the stringent structural requirements to achieve the desired target life, pose a real challenge for the turbine designer to meet the design and off-design performance requirements.

A number of low speed experimental studies have been carried out to investigate the effect of incidence on the performance of turbine cascades [1–3]. Profile and secondary loss correlations have been derived and improved over the years to include the induced incidence and leading edge geometry and to reflect recent trends in turbine design [4–7]. The effect of the axial velocity density ratio (AVDR) has been investigated experimentally at low speed [3,2], and computationally at high speed [8]. The effects of compressibility on both profile and secondary losses, and the flow physics more generally, have also investigated by a number of researchers: see, e.g., Refs. [9–12].

All of the above investigations have resulted in a better understanding of the flow field in transonic turbine passages. However, there is still a lack of data on the performance of turbine blades of small aspect ratio (0.6–1.0) and high turning (100 deg to 130 deg) operating at variable incidences (±30 deg), transonic Mach numbers (0.8–1.4) and down to very low Reynolds numbers (as low as 50 000).

The present work is part of a collaborative project between Pratt & Whitney Canada and Carleton University to address this lack of data. The ultimate objective is to develop improved design rules for small, low cost and efficient turbines. Krieger et al. [13] tested a realistic turbine stage in a cold flow rotating rig at various pressure ratios, speeds and Reynolds numbers. The mean section of the same turbine blade was tested in a linear cascade in the Carleton University High Speed Wind Tunnel for various values of incidence angle and exit Mach number. The results of these latter tests are presented here.

Experimental Apparatus and Procedures

High Speed Wind Tunnel. All measurements were obtained using the Carleton University High Speed Wind Tunnel shown in Fig. 1 [14]. The wind tunnel is of blow-down type, and is used mainly for transonic turbine cascade research. The wind tunnel exhausts to the laboratory. It is equipped with an ejector-diffuser system to allow the cascade outlet pressure to be controlled independently of the blowing pressure. However, the ejector-diffuser system was not used in the present measurements. Typical wind tunnel runtimes range from 15 to 30 sec, depending on the blowing pressure and the Mach number level, and up to four runs per hour are possible. Typical blowing pressures are 2–3 bars, and cascade exit Mach numbers as high as 1.5 can be achieved. The turbulence intensity in the test section is about 4 percent [15]. A more detailed description of the wind tunnel is given in Jeffries [16].

Cascade Test Section and Test Cascade. A schematic diagram of the cascade test section is shown in Fig. 2. The cascade is mounted on a turntable which allows variations in incidence of about ±20 deg. The blade span is fixed at 61 mm. The geometry of the cascade used in this investigation is summarized in Figs. 3 and 4. The blade geometry represents the midspan section of a high pressure turbine from a Pratt & Whitney Canada engine of recent design. The cascade consists of seven blades and eight complete passages. Two of the blades in the middle of the cascade were instrumented with static taps at midspan. One blade has 19 taps on the pressure surface, and the adjacent blade has 22 taps on the suction surface. In addition, the blade with suction surface taps has a base-pressure tap on the trailing edge. The base pressure static tap diameter-to-trailing edge thickness ratio is equal to 0.203.

The cascade was tested for exit Mach numbers from 0.5 to 1.2. The corresponding Reynolds numbers varied from approximately 4×10^5 to 10^6. Incidence values of +14.5 deg, +10 deg, +4.5 deg, 0 deg, and −10 deg relative to the design were examined.

Instrumentation and Experimental Procedures. All flow field measurements were obtained using a three hole pressure probe. The probe tip has a width of 1.37 mm (0.054 in.) which is roughly 4.7 percent of the blade pitch, and a thickness of 0.46 mm (0.018 in.). Static pressures downstream of the cascade were also

---

Contributed by the International Gas Turbine Institute and presented at the 45th International Gas Turbine and Aeroengine Congress and Exhibition, Munich, Germany, May 8-11, 2000. Manuscript received by the International Gas Turbine Institute February 2000. Paper No. 2000-GT-482. Review Chair: D. Ballal.

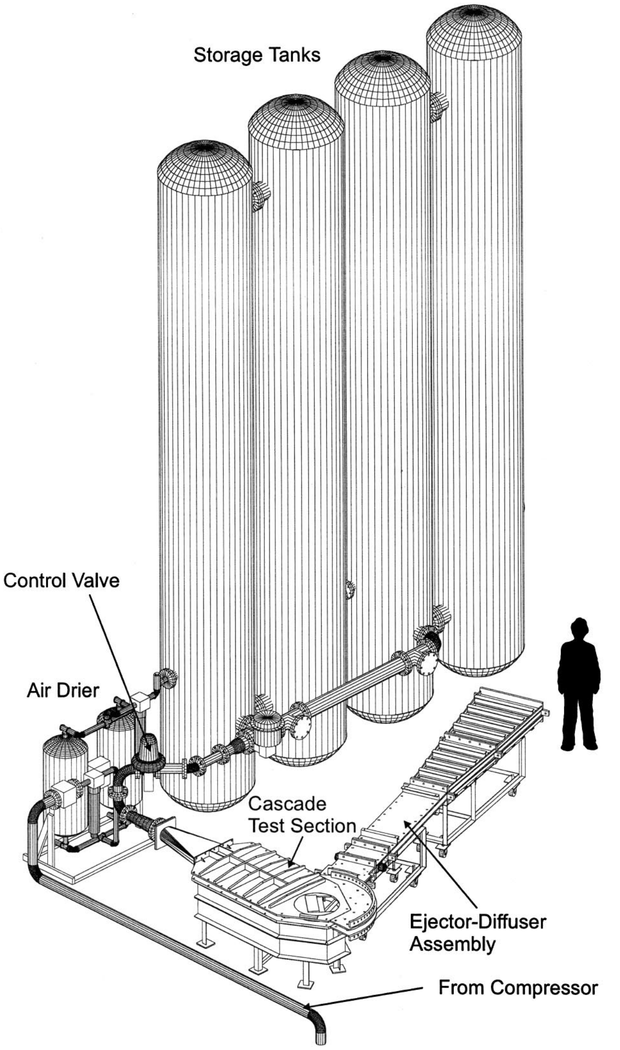

Fig. 1 Carleton University blowdown wind tunnel [14].

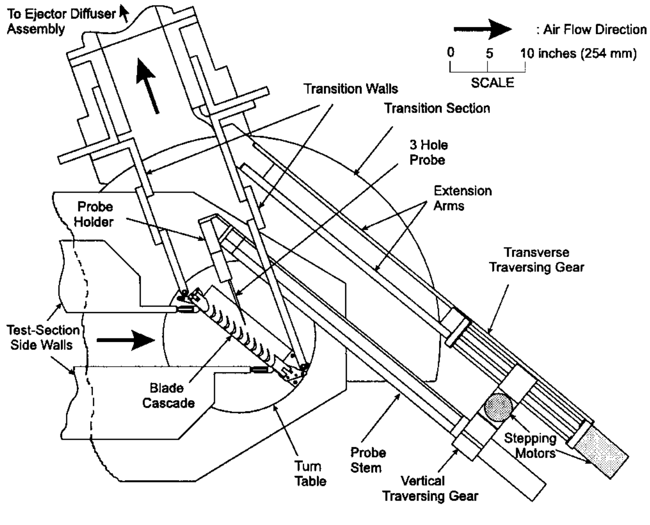

Fig. 2 Plan view of the cascade test section

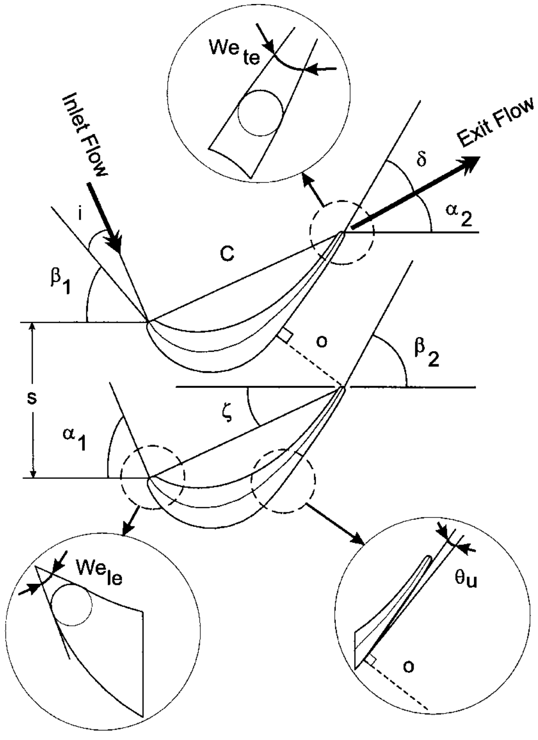

Cascade Parameters	
Chord Length, C	40.0 mm
Axial Chord, Cx	36.98 mm
Blade Span, H	61.0 mm
Blade Spacing, s	29.14 mm
Trailing Edge Thickness, t	1.25 mm
Aspect Ratio, H/C	1.525
Leading Metal Angle, β_1	50.5°
Trailing Metal Angle, β_2	59.0°
Leading Edge Wedge Angle, We_{le}	38.0°
Trailing Edge Wedge Angle, We_{te}	6.0°
Design Incidence, i_{des}	-4.5°
Stagger Angle, ζ	25.1°
Throat Opening, o	15.3 mm
Unguided Turning, θ_u	11.5°

Fig. 3 Summary of the blade geometry and nomenclature

measured directly using a cylindrical static pressure probe. The probe tip has a cone angle of 15 deg, and two static taps are located 180 deg apart at about 12 diameters from the tip. The static probe has a tip outer diameter of 1.02 mm (0.04 in.) which is approximately 3.5 percent of the blade pitch. Both probes were designed by Islam [17]. For loss calculations, the static pressures obtained with the static probe were combined with total pressures and exit flow angles obtained from the three hole probe. The losses quoted are the fully mixed-out values calculated using the procedures of Amecke & Šafařík [18]. Also, mixed-out values were used where downstream parameters, such as the static or dynamic pressure, were needed in quantities such as the base pressure coefficient.

All pressures were measured using a 48-port Scanivalve system and a miniature, fast-response Kulite pressure transducer which is mounted in the Scanivalve housing. The outputs from the pressure transducer were recorded using a Hewlett-Packard high-speed data acquisition system which was controlled by a microcomputer. Pressures were sampled for 0.1 sec at a frequency of 2000 Hz based on investigations by Jeffries et al. [14].

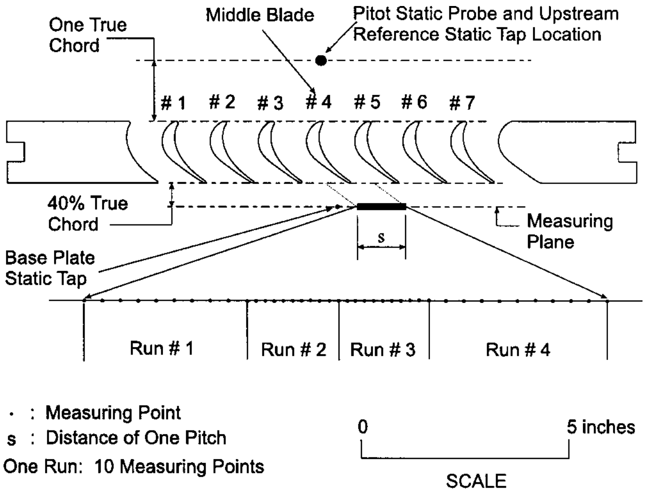

Fig. 4 Cascade blade row measurement locations

The temperature in the storage tanks, and thus the total temperature T_{01} in the test section, typically starts at 13–20°C. The total temperature drops as the air in the tanks expands during a run. Therefore, T_{01} was measured upstream of the cascade during each run. Table I summarizes the temperature changes which were measured for several typical operating points. Also shown are the corresponding average Reynolds numbers and the variation in Reynolds number, which corresponds to the variation in the total temperature. Finally, the estimated variations in the profile loss coefficients due to the Reynolds number variations are also given. These estimates are based on data for the variation in loss coefficient with Reynolds numbers, which are presented later. As seen, the variation in the loss coefficient during the run is quite small compared with the mean value. The variation is also less than the estimated uncertainty in the loss coefficients due to all sources. It should also be mentioned that, for the loss calculations, the total temperature was assumed to be equal at the inlet and outlet planes of the cascade, even though a small amount of heat transfer would be occurring during a run. Jouini [19] estimated in detail the total temperature variations which could occur across the cascade for different operating points. He also calculated the corresponding changes in the loss coefficients. The resulting uncertainty this introduces into the loss coefficients is less than the overall estimated uncertainty, and is considered to be included in that overall value. Finally, it should be mentioned that several runs of the wind tunnel are made before a series of data runs are begun. These preruns are used to cool the cascade blades and the walls of the test section, and thus reduce the heat transfer during the data runs.

Table 1 Typical variations in total temperature and Reynolds number during a run at design incidence

M_2	ΔT_{ol} (°C)	Average Re	$\pm\Delta$ Re	$Y_t \pm \Delta Y_t$
0.55	7	500,000	5,500	0.0729±0.0014
0.71	12	660,000	13,000	0.0666±0.0002
1.14	19	1,040,000	97,000	0.0997±0.0011

The locations of the upstream and downstream traverse planes are indicated in Fig. 4. Downstream of the cascade, four runs are normally used to traverse the flow over one blade pitch. Measurements are made at a total 40 points, with the spacing being halved for the 20 points which span the blade wake. Figures 5(*a*) and 5(*b*) show sample total pressure and flow angle distributions behind the

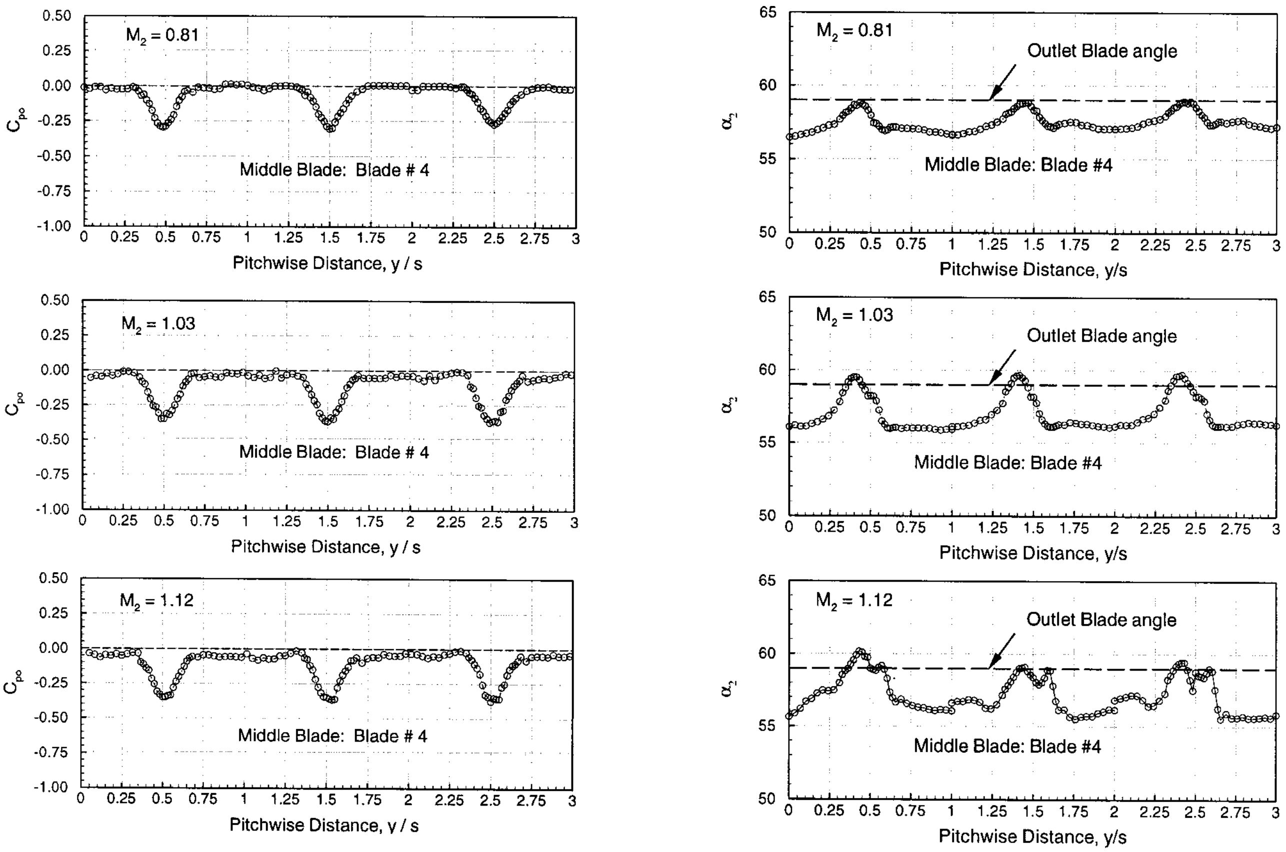

Fig. 5 (*a*) Cascade downstream total pressure at off-design incidence, $i-i_{des}=4.5$ deg; (*b*) cascade downstream flow angle at off-design incidence, $i-i_{des}=4.5$ deg

three middle blades in the cascade at an incidence of +4.5 deg and for three Mach numbers. As shown, the wake profiles were very similar, indicating that there is good periodicity in the cascade flow. The periodicity is somewhat poorer at high values of both positive and negative incidence at Mach numbers above 1.1.

The measured flow quantities are estimated to have the following uncertainties: static pressures, ±2 percent of the local dynamic pressure; flow angles, ±0.5 deg; and exit Mach numbers, ±0.02. The estimated uncertainty for the mixed-out total pressure loss coefficients is ±0.005 for exit Mach numbers less than 0.5, ±0.003 for Mach numbers from 0.5 to 0.85, ±0.004 for Mach numbers between 0.85 and 1.1, and ±0.005 for Mach numbers greater than 1.1. The estimated uncertainties are based on observed variations from blade to blade, as well as repeatability runs made at a given operating point.

Results and Discussion

Axial Velocity Density Ratio (AVDR). Results are presented first for the axial velocity density ratio (AVDR) since the value of the AVDR probably has an influence on most of the other results to be presented.

The value of the AVDR is an indication of the two dimensionality of the flow through the cascade. Some cascade facilities use endwall suction or blowoff to control the thickness of the endwall boundary layers and therefore the AVDR. Blowoff is not currently being used in the present facility, although provision for blowoff exists on the endwalls ahead of the cascade. In the absence of blowoff, Sieverding [20] recommended using an aspect ratio (H/C) of about 1.6 or larger for two-dimensional cascade testing in the transonic range. The aspect ratio of 1.525 for the present cascade, which was chosen to maximize the blade chord, is thus at the lower end of the range recommended by Sieverding.

Figure 6 shows the measured AVDR's for all tested flow conditions. The estimated uncertainty in the value of the AVDR is about ±0.02. The AVDR's are seen to be close to the desired value of 1.0 over the full Mach number range for moderate values of the incidence. However, the AVDR increased with large positive incidence, and decreased slightly with negative values of incidence. This should be borne in mind when interpreting the present results for larger values of off-design incidence.

Unfortunately, the precise influence of the AVDR on the performance of turbine blade rows has not been documented particularly well. The effects of the axial velocity ratio (AVR) in incompressible flow conditions was examined experimentally by Rodger et al. [2] and Whitehouse et al. [3]. They found that the losses decreased with an increasing AVR. This behavior was observed for all off-design values of incidence. At transonic flow conditions, Kiock et al. [21] found that the exit flow angle and the blade losses were essentially independent of the AVDR value, particularly in the Mach number range of 0.9–1.0. Kiock et al.'s results are for design incidence only. Saroch conducted a computational study of the effects of the AVDR in a turbine cascade at transonic

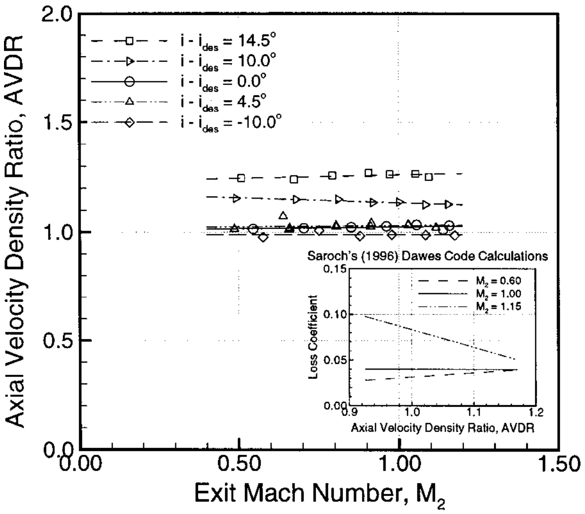

Fig. 6 Effects of incidence and Mach number on the axial velocity density ratio (AVDR)

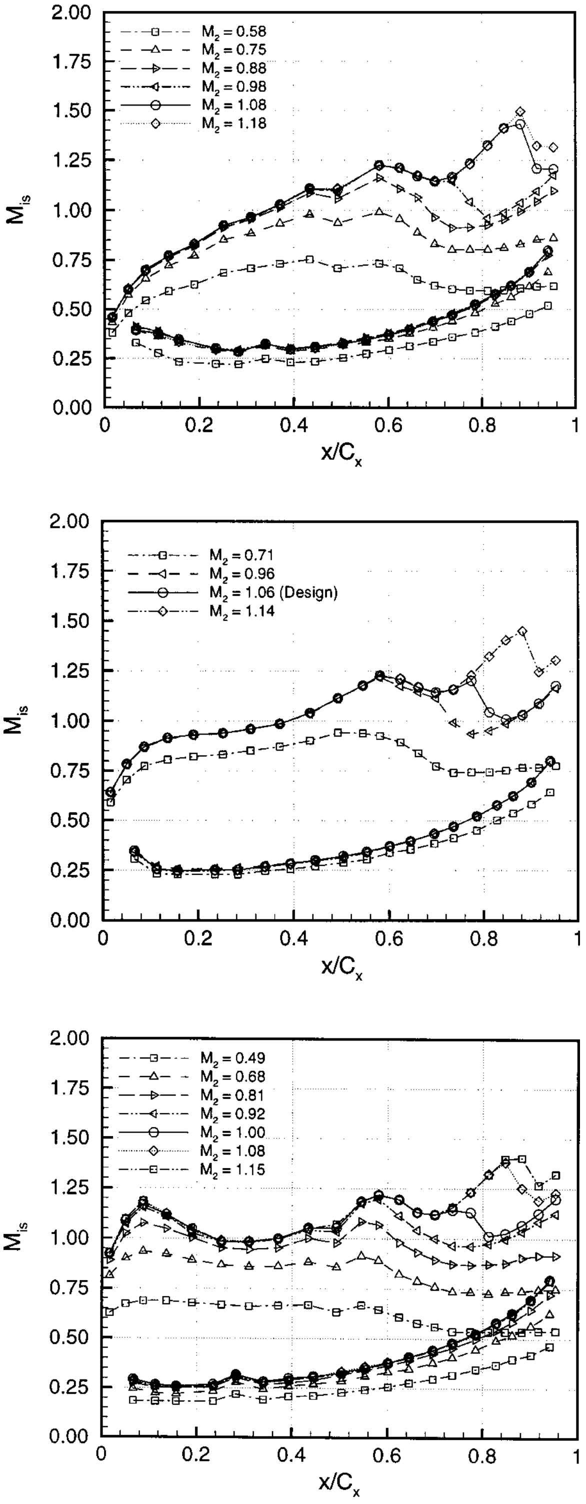

Fig. 7 (*a*)Effects of the Mach number on blade loading at −10.0 deg off-design incidence; (*b*) effects of Mach number on blade loading at design incidence; (*c*) effects of Mach number on blade loading at +10.0 deg off-design incidence

flow conditions, but again just for the design incidence. Saroch used the Navier-Stokes code of Dawes [22] to predict the effects of the AVDR on the loss coefficient and deviation in a linear turbine cascade for outlet Mach numbers from 0.6 to 1.2. The loss coefficients predicted by Saroch are shown in the inset in Fig. 6. For Mach numbers from 0.6 to 0.9, the losses were found to increase slightly with an increasing AVDR. For Mach numbers from 0.9 to 1.0 the predicted losses were essentially independent of the AVDR, as also observed experimentally by Kiock et al. As the Mach number increased beyond unity, Saroch [8] found that the losses decreased with an increasing AVDR. Although the authors are unfortunately not aware of any experimental data that confirm Saroch's findings, his results have been used qualitatively in the interpretation of the present loss results where the AVDR differed significantly from 1.0.

Blade Loadings and Base Pressures. Blade loading measurements were performed for all test conditions. Figs. 7(*a*), 7(*b*), and 7(*c*) show the effects of the exit Mach number on the surface Mach number distributions at incidence values of −10.0 deg, 0.0 deg, and +10.0 deg. The surface isentropic Mach number is calculated from the ratio of the measured surface static pressure to the upstream total pressure. Repeatability measurements showed that the uncertainty in the surface Mach numbers is about ±0.01. At low exit Mach numbers, the loading distributions [e.g., Fig. 7(*a*)] show a region of nearly constant pressure on the suction side beginning at about $x/C_x = 0.75$ and following a region of diffusion. This might be interpreted as the presence of trailing edge separation. This would be consistent with the somewhat higher losses observed at the same conditions. However, trailing edge separation should be associated with a reduced outlet flow angle. As shown below, the outlet angle was in fact very similar at all Mach numbers. This suggests that little if any separation was present at the low Mach numbers. Once the outlet Mach number reaches about 0.95, the passage chokes, and the loading remains constantly forward of about 60 percent of the axial chord for any further increases in M_2. At $M_2 = 0.96$, a nearly normal shock also impinges on the suction side at about 75 percent axial distance. With a further increase in the Mach number, the shock becomes more oblique and the impingement point migrates towards the trailing edge.

Figure 8 shows the effects of incidence on the loading at exit Mach numbers close to the design value of 1.05. The variation in the Mach numbers reflects the difficulties in setting precise wind tunnel operating points. Aft of the throat (which is at about 60 percent C_x) the variation in the loading distributions appears to be mainly the result of the variations in the exit Mach number rather than the incidence. At the high positive values of incidence there may be some influence of the AVDR although this does not appear to be very strong. On the other hand, major changes in the loading distribution occur with incidence in the vicinity of the leading edge. With increasingly positive incidence, a strong suction peak develops on the suction side close to the leading edge. At +14.5 deg the local Mach number reaches a peak value of about 1.30 at only 10 percent of the axial chord. The flow is subsequently decelerated to close to sonic conditions without the apparent presence of a shock and without any signs of boundary layer separation. At −10 deg incidence, a region of diffusion develops on the pressure surface after the initial acceleration aft of the stagnation point. A disturbance in the pressure distribution near 30 percent C_x may be a sign of the presence of a separation bubble here.

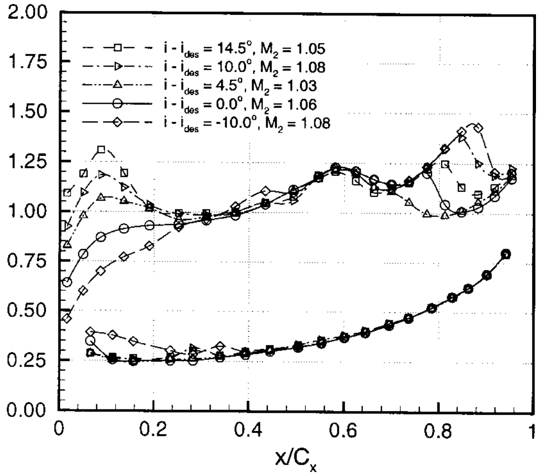

Fig. 8 Effects of incidence on blade loading near the design Mach number

Based on both experimental and computational investigations at low-speed conditions, Benner et al. [4] concluded that turbine blades would be more sensitive to off-design incidence if there were large discontinuities in surface curvature at the leading-edge blend points. A similar effect was identified by Walraevens and Cumpsty [23] for compressor blades. The present blade has a leading-edge circle and consequently such curvature discontinuities must be present. Unfortunately, the distribution of blade-surface static taps on the present cascade was too sparse to resolve the pressure disturbances which would have originated from such curvature discontinuities. Therefore, it is not possible from the present measurements to confirm a similar sensitivity to incidence due to surface-curvature discontinuities for transonic conditions.

The influence of the base pressure on the profile losses in transonic turbines is well recognized (e.g., [24]). Using a simple control volume analysis, Denton [25] showed that the main base-pressure contribution to the total-pressure loss coefficient is given approximately by

$$\Delta Y_{t,te} = -C_b\left(\frac{t}{o}\right), \tag{1}$$

where C_b is the trailing-edge base pressure coefficient, t is the trailing edge thickness, and o is the throat opening. However, the behavior of the base pressure coefficient is not well documented at off-design incidence. Therefore, one of the present blades was instrumented with a base pressure tap, and base pressure measurements were made for all of the operating points examined.

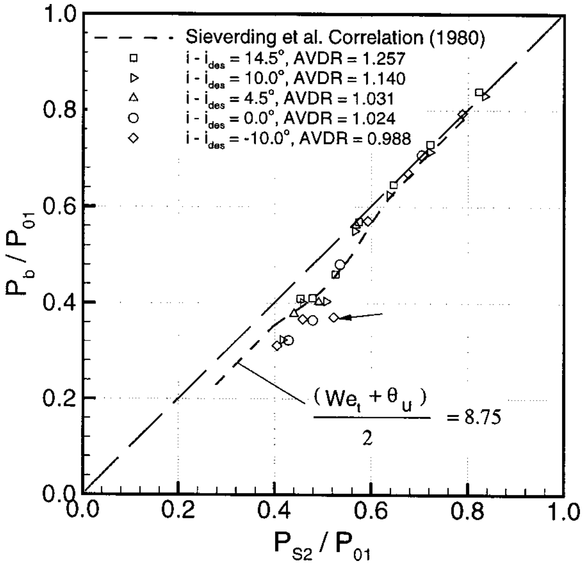

Fig. 9 Comparison between measured base pressures and the correlation of Sieverding et al.

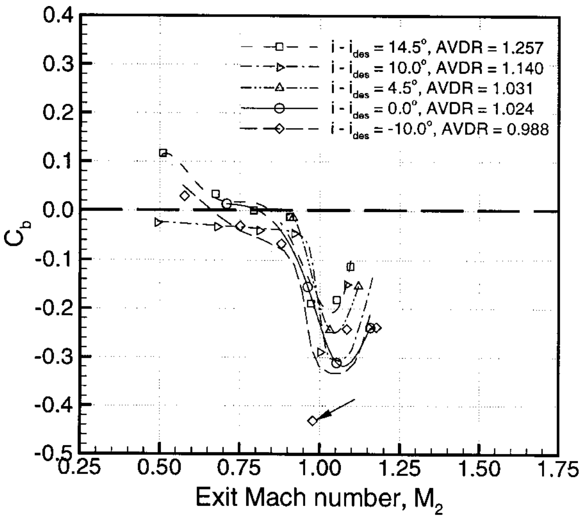

Fig. 10 Variation of the base pressure coefficient

Perhaps the most widely used correlation for the base pressure behavior on turbine blades is that due to Sieverding et al. [26]. Sieverding et al. correlated the base pressure with the trailing edge wedge angle, the unguided turning, and the downstream static pressure. They also provided an explanation for the trend in the base pressures in terms of the appearance of shock waves in the trailing-edge region of the blades. Figure 9 compares the measured base pressures for the present cascade with the Sieverding et al. correlation. The measurements show good agreement with the correlation for pressure ratios $P_{S2}P_{01}$ larger than about 0.55 (which corresponds to outlet isentropic Mach numbers of less than about 0.95). At lower values of the pressure ratio shock waves are present near the trailing edge. As seen from the figure, the correlation predicts somewhat higher base pressures than were observed for these conditions. These discrepancies do not appear to be strongly related to the incidence. Nor do they appear to be primarily due to the effects of the AVDR, since comparable discrepancies were obtained at significantly different values of the AVDR. Similar discrepancies have been observed at design incidence by other investigators (e.g., Xu and Denton, [27] and Denton and Xu, [28], Denton [25]) who attributed these differences to the effects of trailing-edge blockage, which is not included as a correlating parameter in Sieverding et al.'s correlation. It is not possible to confirm Denton's explanation from the present measurements. However, they do seem to support the suggestion that one or more important geometric parameters is missing from the correlation of Sieverding et al. It should also be noted that at high Mach numbers the base pressure varies considerably with location on the trailing edge, and the present single tap gives a somewhat limited picture of the base pressure behavior.

Figure 10 presents the base pressure results in terms of the variation of base pressure coefficient with exit Mach number and incidence. The corresponding values of the AVDR are also indicated on the figure. These results will be used along with Eq. (1) in interpreting the profile loss data which will be presented next. As also found in other investigations, C_b is generally negative and has a strong minimum near $M_2=1.0$. A few positive values of C_b are seen at low Mach numbers. The highest value occurs for an incidence value of +14.5 deg. For this operating point, the Reynolds number was about 450 000. The lowest value of C_b occurs for an incidence of −10 deg and $M_2=0.98$; the point is indicated by a small arrow. However, this point appears somewhat out of keeping with the other results for the same incidence. The same point, again indicated with an arrow, is also the most anomalous point in Fig. 9. As a result, the curve for −10 deg has not been forced to pass close to this point. The minimum C_b is seen to vary somewhat with incidence and the AVDR. In broad terms, the weakest minima were obtained at high positive incidence and a high AVDR. However, as with Fig. 9, the pattern is not completely consistent. Pending further investigations, the effect of AVDR seems to be the most likely reason for the variation in the minimum value of C_b.

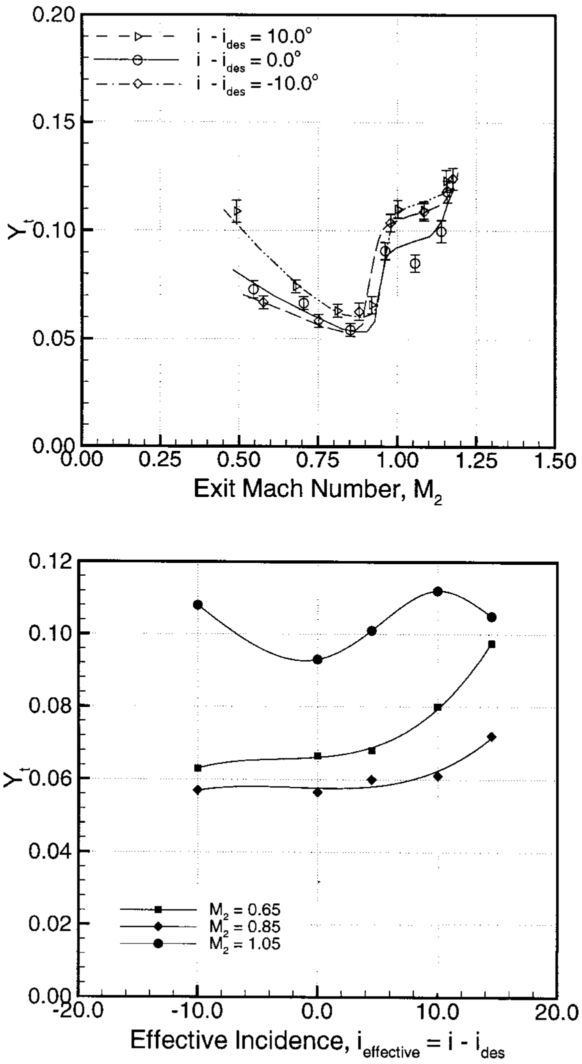

Fig. 11 (*a*) Effects of Mach number and incidence on losses; (*b*) effects of off-design incidence on losses at different Mach numbers

Profile Losses. Figures 11(*a*) and 11(*b*) show the measured results for the profile losses. Results are presented primarily for an incidence range from −10 deg to +10 deg. As seen earlier, for measurements at +14.5 deg the AVDR reached about 1.25, and the results probably cannot be considered even approximately two-dimensional.

Figure 11(*a*) shows the variation of the total pressure loss coefficient Y_t with an exit Mach number for three values of incidence. The trend is similar for all three curves, and is generally consistent with the variation with Mach number found by Mee et al. [24] at design incidence. In all cases, the loss coefficient reached a minimum at about $M_2=0.85$, after which the losses rose sharply through an exit Mach number of unity. From Fig. 10, it appears that the minimum losses occur at the point were the base pressure coefficient starts to decrease. For the present blade row the value of (t/o) is 0.08 and thus, from Eq. (1) and Fig. 10, just above $M_2=1.0$ the base pressure effect contributes about 0.025 to

Y_t. This accounts for roughly half of the rise in losses through the sonic outlet condition. The remainder is presumably due to direct total pressure losses occurring through the shock waves which begin to appear at M_2 of about 0.95. These effects are of course not independent, since the pattern of expansion and shock waves which form at the trailing edge play an important role in determining the base pressure. Above the sonic condition, the losses briefly level off (or perhaps even decrease in the case of the design incidence). This leveling off has also been observed before. It is evidently due to the rising base pressure and the increasing obliqueness of the shock wave which impinges on the suction surface. As the exit Mach number increases further, the shocks become stronger and the loss coefficient begins to rise again.

At low exit Mach numbers, the loss coefficient would be expected to approach asymptotically a limiting, low-speed value. This asymptotic behavior is not evident here, particularly for the data for +10 deg of incidence. This may be partly due to the effect of the AVDR. The calculations of Saroch [8] (Fig. 6) suggested that at low Mach numbers the observed losses would be increased by values of the AVDR greater than 1.0, which applies for the +10 deg measurements. However, the main explanation probably lies in the effect of low Reynolds numbers. For the low Mach number data points shown in Fig. 11(*a*), the Reynolds number was the order of 500 000. The influence of the Reynolds number on the losses is confirmed later in this section.

Figure 11(*b*) shows the variation of Y_t with incidence for fixed values of M_2. These curves are a essentially a cross plotting of the data from Fig. 11(*a*), using interpolated values of Y_t at the desired values of M_2. Data for +14.5 deg of incidence have also been included to demonstrate the likely influence of the AVDR.

For subsonic exit Mach numbers, the present blade has fairly constant losses for about ±10 deg about the design incidence. The small rise in losses as +10 deg is approached is most likely due to increased loss production in the suction-side boundary layer on the forward part of the blade. As discussed by Denton [25], the loss production in a boundary layer varies as the cube of the edge velocity. A velocity overshoot near the leading edge similar to that shown in Fig. 8 also occurs for lower Mach numbers, and this probably explains the increase in losses. At its design-point Mach number of 1.05, the blade is more sensitive to incidence, as would be expected. On the other hand, the drop in losses at +14.5 deg is unexpected. However, this drop is consistent with the influence of the AVDR on losses predicted by Saroch's calculations: at supersonic conditions, the high AVDR of 1.25 for the +14.5 deg measurements is predicted to reduce the losses noticeably compared with two-dimensional conditions. It is for this reason that limited loss results are presented for +14.5 deg.

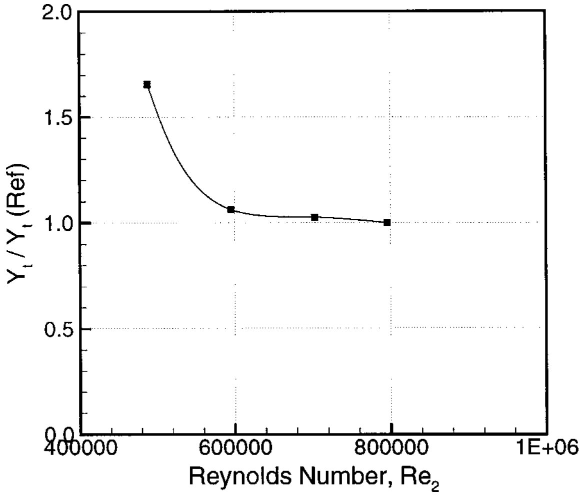

Fig. 12 Reynold's numbers effects on losses at M_2=0.56, $i_{effective}$=4.5 deg

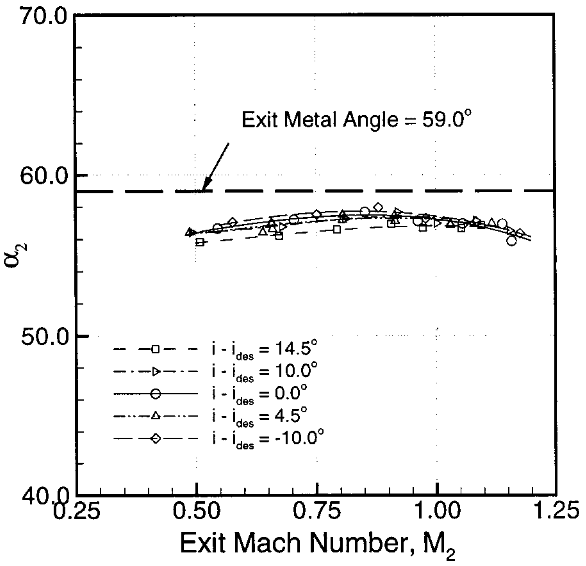

Fig. 13 Effects of incidence and the Mach number on the exit flow angle

The higher than expected losses at very low Mach numbers prompted a brief investigation of the influence of Reynolds number. Measurements were made for a range of Reynolds numbers at a fixed exit Mach number of about 0.56 and an incidence of +4.5 deg. The Reynolds number was varied by partially blocking the wind tunnel exhaust, and thus forcing up the cascade outlet pressure. The results for the losses are shown in Fig. 12. The loss coefficient measured at a Reynolds number of 800 000 was used as the reference value. As seen from the figure, the loss coefficient remained almost constant with decreasing Reynolds number down to about Re=600 000, and then began to rise strongly. For design incidence and a different turbine cascade Ladwig and Fottner [29] found a similar strong rise in losses below a Reynolds number of about 500 000. Assuming the results in Fig. 12 are representative of the behavior of the present cascade at other values of incidence, Reynolds number effects seem to account for the unexpectedly high values of loss coefficient seen in Fig. 11(*a*) for low values of exit Mach number.

Outlet Flow Angle. Finally, Fig. 13 shows the effects of both incidence and the Mach number on the exit flow angle. As is generally found, the maximum exit flow angle occurs at an exit Mach near 1.0. As the downstream flow becomes supersonic, the flow vector must swing back towards the axial to provide the increase in flow area, and this is shown by the measurements. Throughout the Mach number range, +14.5 deg of incidence produced the lowest outlet flow angles by about 0.5 deg. This is probably an indication of the effects of a high AVDR on the outlet flow angle.

Conclusions

Detailed measurements have been presented for the midspan aerodynamic performance of a transonic turbine cascade at off-design conditions. The blade tested is of recent design and incorporates modern design philosophies for high pressure turbine blades.

The data cover a broad range of both incidence and exit Mach numbers. They provide a substantial addition to the data available in the open literature on the behavior of transonic turbine blades at off-design incidence. As such they could be used in the development of improved correlations for profile losses, base pressure behavior, and outlet flow angle. A limited investigation of the effects of the Reynolds number indicated that the present blade experiences increased losses at subsonic exit Mach numbers for Reynolds numbers below about 600 000.

Sieverding recommended a minimum aspect ratio H/C of about 1.6 for two-dimensional, transonic testing of linear turbine cascades. This recommendation appears to be satisfactory for testing near the design incidence. However, for large values of off-design incidence the axial velocity density ratio in the present cascade deviated significantly from 1.0. For +14.5 deg in particular the AVDR reached about 1.25 and this apparently reduced the losses substantially below what they would have been for more nearly two-dimensional conditions. Based on the present results, an aspect ratio considerably larger than 1.6 is recommended for testing at off-design incidence.

Acknowledgments

Financial support for this study provided by the Natural Sciences and Engineering Research Council of Canada and Pratt & Whitney Canada Inc. is gratefully acknowledged.

Nomenclature

AVDR = axial velocity density ratio

$$\left(=\frac{\int_0^1 (\rho_2 C_{(ax)_2})_{MS} d(y/s)}{\int_0^1 (\rho_1 C_{(ax)_1})_{MS} d(y/s)}\right)$$

AVR = axial velocity ratio

$$\left(=\frac{\int_0^1 (C_{(ax)_2})_{MS} d(y/s)}{\int_0^1 (C_{(ax)_1})_{MS} d(y/s)}\right)$$

C = blade chord length or flow velocity
C_b = base pressure coefficient

$$\left(=\frac{P_b-P_{s2}}{q_2}\right)$$

C_{P0} = total pressure coefficient,

$$\left(=\frac{(P_{02}-P_{01}}{q_2}\right)$$

C_x = axial chord length
H = blade span
M = Mach number
P_0 = total pressure
P_b = base pressure
P_{s2} = downstream static pressure
Re = Reynolds number

$$\left(=\frac{(\rho C C_2)}{\mu}\right)$$

T_{o1} = inlet test section total temperature
ΔT_{o1} = drop in inlet test section total temperature
We = wedge angle
Y_t = total pressure loss coefficient $(=(P_{01}-P_{02})/q_2)$
$i_{\text{effective}}$ = effective incidence, in degrees, $(=\alpha_1-(\alpha_1)_{des}=i-i_{des})$
o = throat opening
q = dynamic pressure $(=1/2\rho C^2)$
x = axial distance
y = pitchwise location
s = pitch distance
t = trailing edge thickness
α = flow angle measured from the axial direction, in degrees
β = blade metal angle measured from the axial direction, in degrees
δ = deviation angle, in degrees $(=\beta_2-\alpha_2)$
ζ = stagger angle measured from the axial direction, in degrees
μ = air dynamic viscosity
ρ = air density
θ_u = uncovered turning, in degrees

Subscripts

1 = cascade inlet
2 = cascade outlet
ax = axial
des = design
is = isentropic
MS = mid-span
te = trailing edge
le = leading edge

References

[1] Goobie, S. M., Moustapha, S. H., and Sjolander, S. A., 1989, ''An Experimental Investigation of the Effect of Incidence on the Two-Dimensional Flow,'' Proceedings, IX International Symposium on Air Breathing Engines (ISABE), September 1989, pp. 197–204.
[2] Rodger, P., Sjolander, S. A., and Moustapha, S. H., 1992, ''Establishing Two-Dimensional Flow in a Large-Scale Planar Turbine Cascade,'' AIAA Paper 92-3066.
[3] Whitehouse, D. R., Moustapha, S. H., and Sjolander, S. A., 1993, ''The Effects of Axial Velocity Ratio, Turbulence Intensity, Incidence, and Leading Edge Geometry on the Mid-Span Performance of a Turbine Cascade,'' Can. Aeronautics Space J., **39**, pp. 150–156.
[4] Benner, M. W., Sjolander, S. A., and Moustapha, S. H., 1997, ''Influence of Leading-Edge Geometry on Profile Losses in Turbines at Off-Design Incidence: Experimental Results and an Improved Correlation,'' ASME J. Turbomach., **119**, April pp. 193–200.
[5] Moustapha, S. H., Kacker, S. C., and Tremblay, B., 1990, ''An Improved Incidence Losses Prediction Method for Turbine Airfoils,'' ASME J. Turbomach., **112**, pp. 267–276.
[6] Martelli, F., and Boretti, A., 1987, ''Development of an Experimental Correlation for Transonic Turbine Flow,'' ASME J. Turbomach., **109**, pp. 246–250.
[7] Kacker, S. C., and Okapuu, U., 1982, ''A Mean Line Prediction Method for Axial Flow Turbine Efficiency,'' ASME J. Turbomach., **104**, pp. 111–119.
[8] Saroch, M. F., 1996, ''Contributions to the Study of Turbomachinery: Part I: Design of a Fish-Tail Diffuser Test Section. Part II: Computations of the Effects of AVDR on Transonic Turbine Cascades,'' M. Eng. Thesis, Department of Mechanical and Aerospace Engineering, Carleton University, Ottawa, Ontario, Canada, January 1996.
[9] Graham, C. G., and Kost, F. H., 1979, ''Shock Boundary Layer Interaction on High Turning Transonic Turbine Cascade,'' ASME Paper 79-GT-37.
[10] Perdichizzi, A., 1990, ''Mach Number Effects on Secondary Flow Development of a Turbine Cascade,'' ASME J. Turbomach., **112**, pp. 643–651.
[11] Detemple-Laake, E., 1991, ''Detailed Measurements of the Flow Field in a Transonic Turbine Cascade,'' ASME Paper 91-GT-29.
[12] Moustapha, S. H., Carscallen, W. E., and McGeachy, J. D., 1993, ''Aerodynamic Performance of a Transonic Low Aspect Ratio Turbine Nozzle,'' ASME J. Turbomach., **115**, pp. 400–408.
[13] Krieger, M. W., Lavoie, J. P., Vlasic, E. P., and Moustapha, S. H., 1999, ''Off-Design Performance of a Single-Stage Transonic Turbine,'' ASME J. Turbomach., **121**, pp. 177–183.
[14] Jeffries, M. S., Jouini, D., and Sjolander, S. A., 1997, ''Determining the Sampling Rates and Times in a High Speed Wind Tunnel,'' Proceedings, CASI 6th Symposium on Aerodynamics, Toronto, Canada, April, 1997.
[15] Corriveau, D., 1999, Private Communication, Carleton University, Ottawa, Canada.
[16] Jeffries, M. S., 2001, ''Initial Investigations of Transonic Turbine Aerodynamics using the Carleton University High-Speed Wind Tunnel,'' Ph.D. Thesis, Department of Mechanical and Aerospace Engineering, Carleton University, Ottawa, Ontario, Canada, January, 2001.
[17] Islam. A. M. T., 1999, ''An Experimental and Computational Study of the Aerodynamics of Turbine Blades With Damage,'' Ph.D. Thesis, Department of Mechanical and Aerospace Engineering, Carleton University, Ottawa, Ontario, Canada, September, 1999.
[18] Amecke, J., and Safařik P., 1995, ''Data Reduction of Wake Flow Measurements 2000 Injection of Other Gas,'' DLR-FB 95-32, DLR, Köln, Germany.
[19] Jouini, D. B. M., 2000, ''Effects of Leading-Edge Geometry on the Off-Design Performance of Transonic Axial Turbine Blades,'' Ph.D. Thesis, Department of Mechanical and Aerospace Engineering, Carleton University, Ottawa, Ontario, Canada, July, 2000.
[20] Sieverding, C. H., 1993, ''Advanced Methods for Cascade Testing,'' AGARDograph 328, AGARD-AG-328, August 1993, pp. 22–34.
[21] Kiock, R., Lehthaus, F., Baines, N. C., and Sieverding, C. H., 1986, ''The Transonic Flow Through a Plane Turbine Cascade as Measured in Four European Wind Tunnels,'' ASME J. Eng. Gas Turbines Power, **108**, pp. 277–284.
[22] Dawes, W. N., 1988, ''Development of a 3D Navier Stokes Solver for Appli-

cation to All Types of Turbomachinery,'' ASME Paper 88-GT-70.

[23] Walraevens, R. E., and Cumpsty, N. A., 1995, ''Leading Edge Separation Bubbles on Turbomachinery Blades,'' ASME J. Turbomach., **117**, pp. 115–125.

[24] Mee, D. J., Baines, N. C., Oldfield, M. L. G., and Dickens, T. E., 1992, ''An Examination of the Contributions to Loss on a Transonic Turbine Blade in Cascade,'' ASME J. Turbomach., **114**, pp. 155–162.

[25] Denton, J. D., 1993, ''Loss Mechanisms in Turbomachines,'' ASME J. Turbomach., **115**, pp. 621–656.

[26] Sieverding, C. H., Stanislas, M., and Snoeck, J., 1980, ''The Base Pressure Problem in Transonic Turbine Cascades,'' ASME J. Eng. Power, **102**, pp. 711–714.

[27] Xu, L., and Denton, J. D., 1980, ''The Base Pressure and Loss of a Family of Four Turbine Blades,'' ASME J. Turbomach., **110**, pp. 9–17.

[28] Denton, J. D., and Xu, L., 1990, ''The Trailing Edge Loss of Transonic Turbine Blades,'' ASME J. Turbomach., **112**, pp. 277–285.

[29] Ladwig, M., and Fottner, L., 1993, ''Experimental Investigations of the Influence of Incoming Wakes on the Losses of a Linear Turbine Cascade,'' ASME Paper No. 93-GT-394.

O. J. R. Queune

L. He

School of Engineering,
University of Durham,
Durham, DH1 3LE, United Kingdom

Experimental Study of 3D Unsteady Flow Around Oscillating Blade With Part-Span Separation

This paper documents an investigation conducted on the aerodynamic response of a turbine blade oscillating in a three-dimensional bending mode under massive tip separation. Flow separation near the tip of the blade was realized by use of a step placed upstream of the blade's leading edge. Extensive blade surface steady and unsteady pressure measurements were obtained from a test facility with clearly defined boundary conditions for a range of reduced frequency. The experiment is designed to produce detailed and reliable 3D test cases for aeroelastic applications. A complete set of steady and unsteady blade surface pressure measurements is provided for five spanwise sections at 10, 30, 50, 70, and 90 percent of span. In addition, the issue of linearity is addressed. Experimental results demonstrate a predominant linear behavior of the unsteady pressure response. [DOI: 10.1115/1.1370164]

Introduction

The development of modern steam turbine generators is strongly influenced by the capabilities in predicting blading aerodynamic/aeroelasticity performances at design, as well as off-design, conditions. The development of improved design guidelines for low-pressure turbine flutter is an active research area as there have been several recent occurrences of instability in this kind of blades (Schmidt and Riess, 1999 [1]). Of particular interest is the understanding and prediction of the blade aeroelasticity at low load operation, such as start up. Under such conditions the flow near the tip of the rotor is massively separated due to the formation of the typical back-flow with strong vortices coming from the hub of the previous stator (Fig. 1). The adverse pressure gradient breaks down and there is a region of de-energized flow. For the last stage of a steam turbine with high aspect ratio and unshrouded tip section, blade aeroelasticity then becomes a major concern. Separation-related blade aeroelasticity instabilities, similar to the stall flutter in compressor blade rows, are likely to occur. Furthermore, the large-scale separation patterns may themselves become aerodynamically unstable, resulting in rotating stall. In the latter case, the forced vibration associated with the rotating pattern could become a serious problem. In addition, strong flow-structure coupling may lead to a lock-in of a rotating stall pattern to a blade vibration mode.

Although some test measurements have been obtained from real instrumented turbomachines, e.g., Barton and Halliwell (1987) [2], most of the experimental test cases for the prediction of unsteady flow around oscillating blades are carried out using linear or annular cascade with driven blades. For instance Carta and St. Hilaire (1978 [3], 1980 [4]), Bölcs and Fransson (1986) [5], or He (1998) [6]. Unfortunately, due to the nature of the experiment, or through the measurements taken, only 2D experimental data has been published to date. Bell and He (1997) [7] published 3D test data for unsteady flow around oscillating blades. His results show a marked three-dimensional behavior of the unsteady flow. Using the same test rig, detailed and reliable 3D test data for a turbine blade oscillating in bending mode with massively separated flow are presented. The measurements include steady results as well as unsteady results with a range of reduced frequency. The linearity of the test configuration is subsequently examined.

The purpose of this work is to investigate the three-dimensional unsteady aerodynamic response of a turbine blade oscillating in a bending mode with massive tip separation to enhance our understanding of the three-dimensional nature of such unsteady flows. It is also intended to provide three-dimensional data, in order to validate a 3D numerical method.

Low Speed Test Facility

In this section of the paper the low speed flutter test facility is described. A more detailed description is provided by Bell and He (1997) [8].

Test Rig. Test data were provided by a test facility using a large-scale single prismatic turbine blade (chord: 0.2 m). The working section was a self-contained unit located within the exhaust of a low speed wind tunnel. The sidewalls of the working section were profiled in an attempt to simulate the adjacent blades in cascade, while providing a clear definition of boundary conditions. These profiled regions of the sidewalls met plane sections, which were extended two and a half chords up, and one chord downstream of the blade. A three-dimensional mode of blade vibration was obtained by hinging the blade at root and harmonically driving the tip section at a sinusoidal rate with a single bar crank type mechanism connected with a rod protruding from the blade tip (Fig. 2). Table 1 describes the basic operating conditions of the experimental work performed in the low speed flutter test facility.

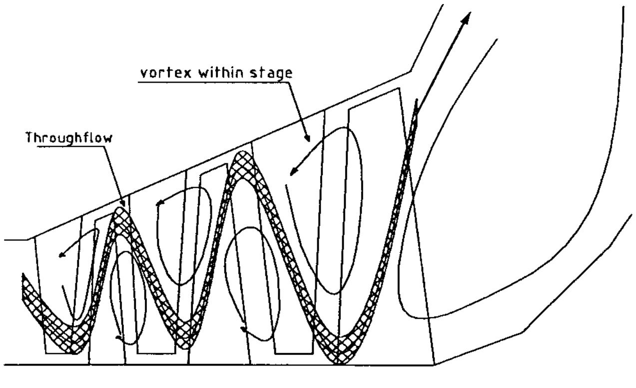

Fig. 1 Schematic representation of separated flow inside the last stage of a steam turbine at low flow conditions

---

Contributed by the International Gas Turbine Institute and presented at the 45th International Gas Turbine and Aeroengine Congress and Exhibition, Munich, Germany, May 8-11, 2000. Manuscript received by the International Gas Turbine Institute February 2000. Paper No. 2000-GT-562. Review Chair: D. Ballal.

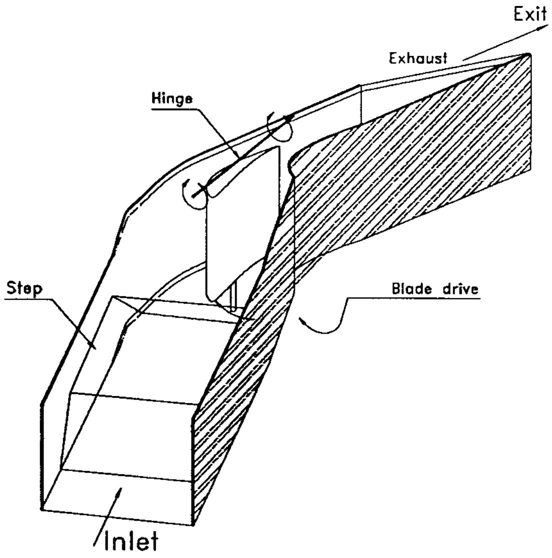

Fig. 2 The test facility working section with step upstream of the blade

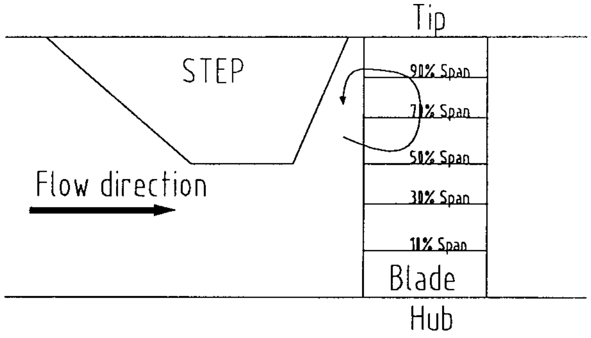

Fig. 3 Working section in side view with the step used to create flow separation

Instrumentation, Data Acquisition and Reduction. The blade surface was instrumented with 110 static tappings, evenly distributed over five spanwise sections (10 percent (near hub), 30, 50, 70, and 90 percent (near the tip) span). At each spanwise section ten tappings were positioned on both the pressure and suction surface, with an extra tapping at the leading and the trailing edge. These tappings were used for both steady and unsteady pressure measurements. Five externally mounted pressure transducers (type: Sensym 142C01D, 0–1 psi range) were employed for unsteady pressure measurements. The unsteady pressure signals from the five pressure transducers were discretized and logged on a personal computer using an Amplicon PC-74 data logging card. The acquisition of measurements was triggered at a fixed phase in the blade motion by use of an optical Schmitt trigger. In an effort to improve the signal to noise ratio and to remove the contribution from turbulent fluctuations, the unsteady pressure signals from each tapping were ensemble averaged over 40 periods. The ensemble-averaged signals were reduced into their harmonic components using a Fourier transform. The final harmonic components were then corrected for phase shift and attenuation along the tube lengths, which separated the blade surface tapping points and the transducer.

Separated Flow. Separated flow upstream of the leading edge near the tip of the blade was produced by the use of a step placed upstream of the blade's leading edge (Fig. 3). When passing the sudden enlargement, the flow separated with consequent pressure loss. The distance of the step from the blade had to be far enough to allow bending mode flutter. Different steps have been modeled and tested for different distances from the leading edge of the blade. The experimental results for this paper were obtained with a step height of 50 percent span height, two axial chords long and placed 15 mm upstream of the leading edge. The noticeable height of the step is a consequence of the test facility's low speed, which allows the flow to recover very shortly after the step. Flow visualization using cotton wire was carried out all around the blade, and showed the flow was reattached at around 30 percent chord both surfaces.

Table 1 Operational conditions

Experiment Conditions	
Nominal deflection	40.3 deg
Typical reference velocity, V_{ref}	33.4 m/s
Bending mode direction	35.5 deg *(to axial)*
Bending amplitude at tip, B_C	0.055 chord (case 1) 0.0275 chord (case 2)
Bending amplitude at hub	0.006 chord (case 1) 0.005 chord (case 2)
Reynolds number, Re	4.5×10^5
Reduced frequency, k	0.15, 0.25, 0.50

Experimental Results

Steady Flow Results. Steady flow results are presented for the test facility operating at a Reynolds number of 4.5×10^5, with a typical exit reference velocity of 33.4 ms^{-1}. Blade pressure measurements were recorded with a tilted manometer bank. Figures 4(*a*) and 4(*b*) show the comparison at steady state of the static pressure coefficient with, and without step, for 10, 50, 70, and 90 percent span. Major differences can be observed. From 10 percent span to 90 percent span the pressure surface and the suction surface present different static pressure coefficients. From 10 percent span to 50 percent span, the static pressure coefficients are lower on both the pressure and the suction surfaces. As the flow passes by the step, it accelerates, increasing the velocity but reducing the pressure. Up to 50 percent chord, at 70 and 90 percent span, the flow is fully separated and the blade is now very negatively loaded.

Unsteady Pressure Measurements. The results presented here are in the form of the first harmonic pressure. Figures 5 and 6 present the phase angle and the amplitude of the first harmonic pressure response with no step, for a reduced frequency of 0.25. Figures 7 and 8 show the phase angle and the amplitude of the first harmonic pressure response with step for a reduced frequency of 0.25. Figure 9 presents the aerodynamic damping with step and without step at the same reduced frequency. In order to preserve clarity they are provided for just four spanwise sections: 10 percent span (near hub), midspan, 70 percent (separated flow), and 90 percent (near tip, separated flow). When comparing Figs. 5 and 7, it is observed that the separated flow clearly modifies the phase angle of the first harmonic pressure. On the suction surface, the measured phase angle of the first harmonic pressure still indicates a stable aeroelastic condition, with a phase lead with respect to the blade motion. Nevertheless, the phase angle closer to 0 degrees at 70 percent span indicates a decrease in blade aeroelastic stability (Fig. 7(*i*)). This decrease in aeroelastic stability at 70 percent span can be observed in Fig. 9. At 70 percent span the phase angle increases with the chord, which means that the unsteady pressure response over the suction surface is now led by the training edge, with a pressure wave propagating upstream. Apart from 70 percent span, there is a consistent shape in the phase angle of the first harmonic pressure. The measured phase angle of the first harmonic pressure on the pressure surface is seemingly unaffected by the separated flow, except at 70 percent span (Fig. 7(*ii*)). At 70 percent span the phase angle decreases after 50 percent chord.

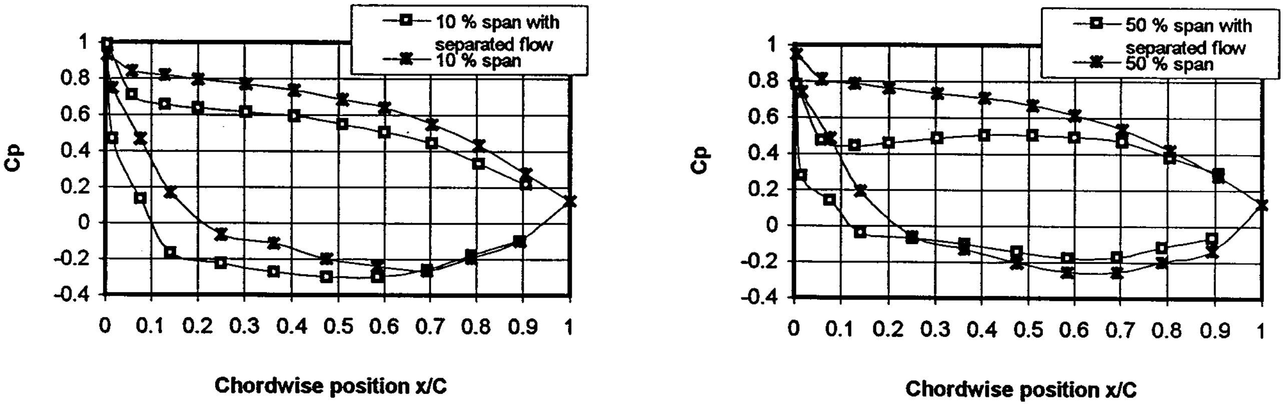

(i). Pressure coefficient at 10 % Span

(ii). Pressure coefficient at 50 % Span

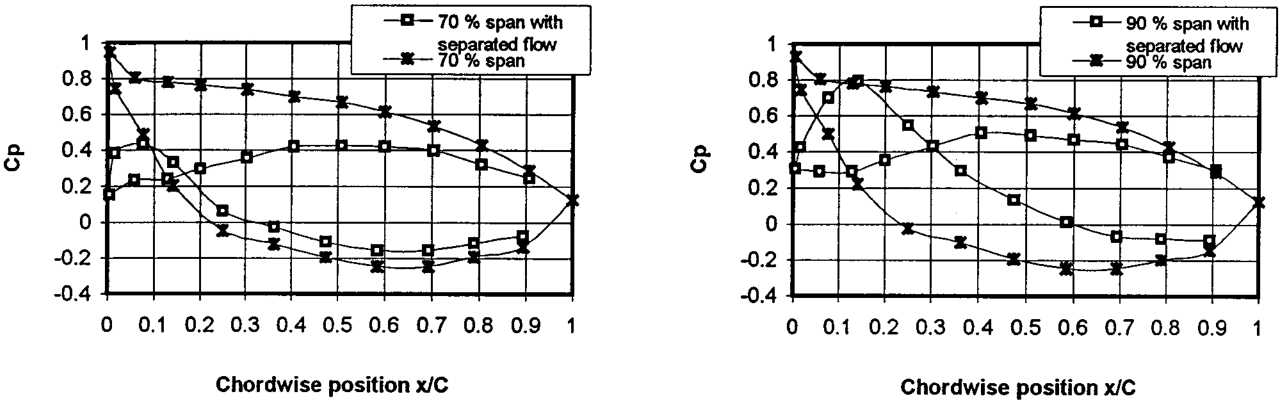

(iii). Pressure coefficient at 70 % Span

(iv). Pressure coefficient at 90 % Span

Fig. 4 (*a*) **Steady flow blade pressure measurements with and without step at 10 and 50 percent span. (*b*) Steady flow blade pressure measurements with and without step at 70 and 90 percent span.**

This variation indicates that the unsteady pressure response near the trailing edge now lags that directly upstream of the pressure surface. The amplitude of the first harmonic response over the suction surface is unchanged except for 70 and 90 percent span. The high amplitude at 70 percent is due to an increase of the flow angle inside the working section. The low inertia of the flow induced by the flow separation increases the effect of the pressure gradient from pressure to suction surface and changes the flow angle. The amplitude of the first harmonic response for the pressure surface follows a uniform trend similar to that without flow separation.

Linearity. Linearity will now be examined through comparison of the amplitude and the phase angle of the first harmonic pressure coefficients for two different bending amplitudes. This is of general interest in terms of the behavior of the unsteady flow. It

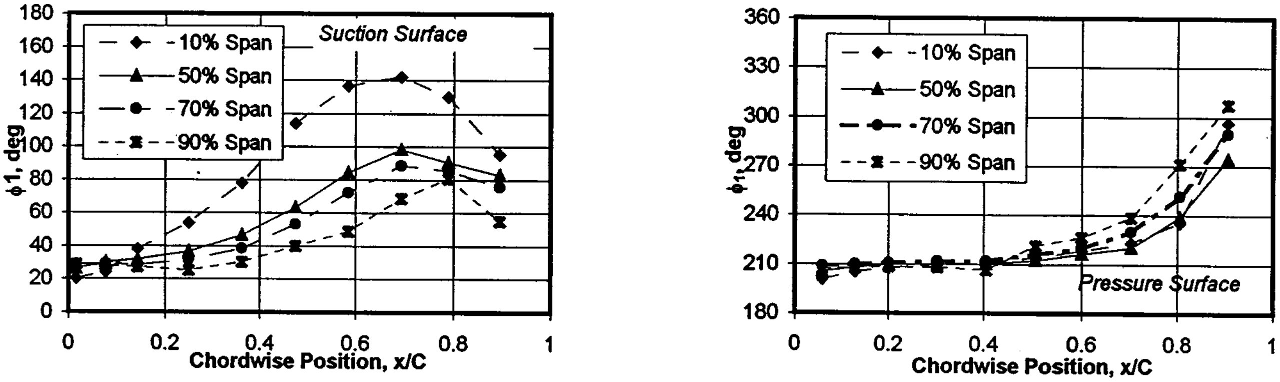

(i). Suction surface

(ii). Pressure surface

Fig. 5 Phase angle of first harmonic pressure with NO STEP (Bc: 0.055 C at k: 0.25)

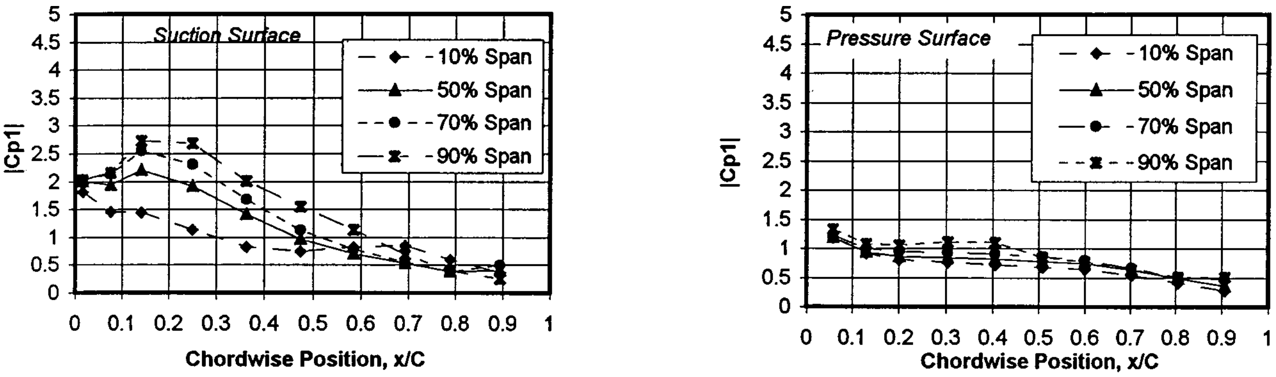

(i). Suction surface

(ii). Pressure surface

Fig. 6 Amplitude of first harmonic pressure with NO STEP (Bc: 0.055 C at k: 0.25)

is also important in order to estimate the suitability of the time-linearized assumption for the general computation and modeling of oscillating blade flows. Figure 10 shows the spanwise distribution in the aerodynamic damping for two different bending amplitudes. Figures 11 and 12 present, respectively, the amplitudes and the phase angles of the first harmonic pressure coefficients for both blade surface and two different bending amplitudes. Figure 13 shows the relative amplitudes of the second harmonic pressure response. The test facility demonstrated predominantly linear behavior of the unsteady aerodynamics when the flow was not separated, Bell and He (1998) [9]. It is therefore to be expected that linearity will be sustained for both amplitude and phase angle at 10 and 50 percent span (Figs. 11 and 12). More surprising is a linear behavior in a region of high unsteady pressure activity until 70 percent chord at 70 percent span (Fig. 11(*ii*)). Downstream of 70 percent chord, nonlinear behavior is indicated by the presence of a predominant second harmonic pressure response (Fig. 13). The measured phase angle at 90 percent span proved to also be

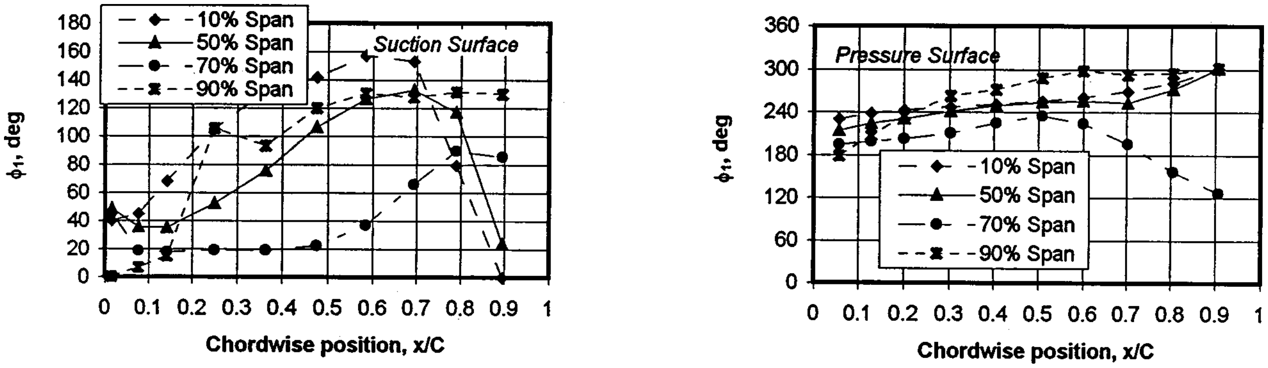

(i). Suction Surface

(ii). Pressure surface

Fig. 7 Phase angle of first harmonic pressure WITH STEP (Bc: 0.055 C at k: 0.25)

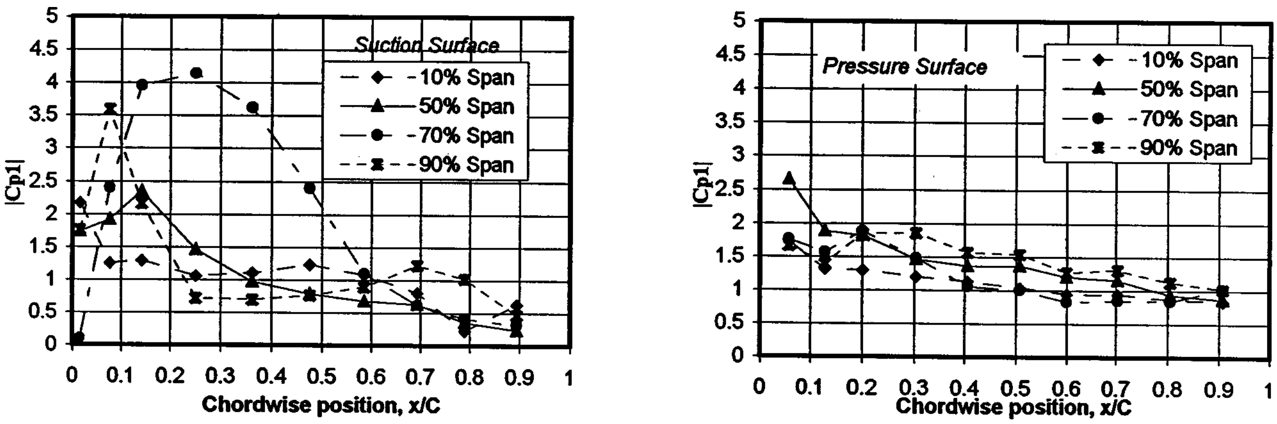

(i). Suction surface

(ii). Pressure surface

Fig. 8 Amplitude of first harmonic pressure WITH STEP (Bc: 0.055 C at k: 0.25)

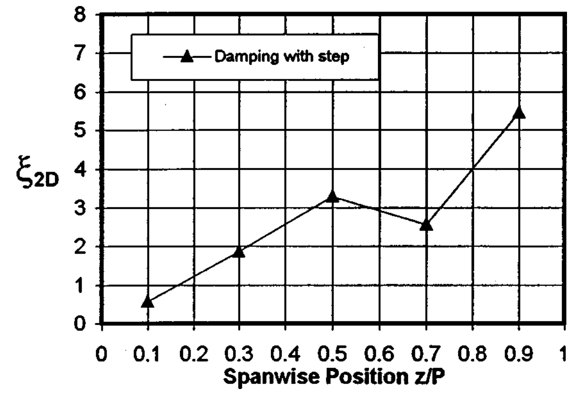

Fig. 9 Aerodynamic damping with step (Bc: 0.055 C at k: 0.25)

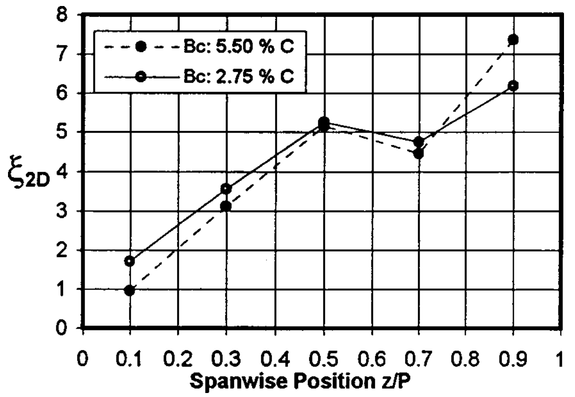

Fig. 10 Spanwise distribution in the 2D damping coefficient for two different bending amplitudes (k: 0.5)

quite linear, apart from the leading and the trailing edge of the pressure surface. The relative amplitude at 90 percent span exhibits a nonlinear behavior over the blade. This nonlinear behavior can also be observed in Fig. 10. Figure 13 shows a prevailing nonlinear behavior at 10 percent span near the trailing edge and at 70 percent span hear the leading edge suction surface. This nonlinear behavior coincides with a region of low unsteady pressure activity and therefore cannot be regarded as an indicator of nonlinearity.

Concluding Remarks

The results and interpretation of an aerodynamic response from a turbine blade oscillating in a three-dimensional bending mode under massive tip separation were presented. Steady and unsteady pressure measurements were also provided. Finally, linearity was checked. The conclusions for this study are as follows:

- Steady results: Blade static pressure coefficients show that the step separated the flow near the blade's tip. Due to the in-

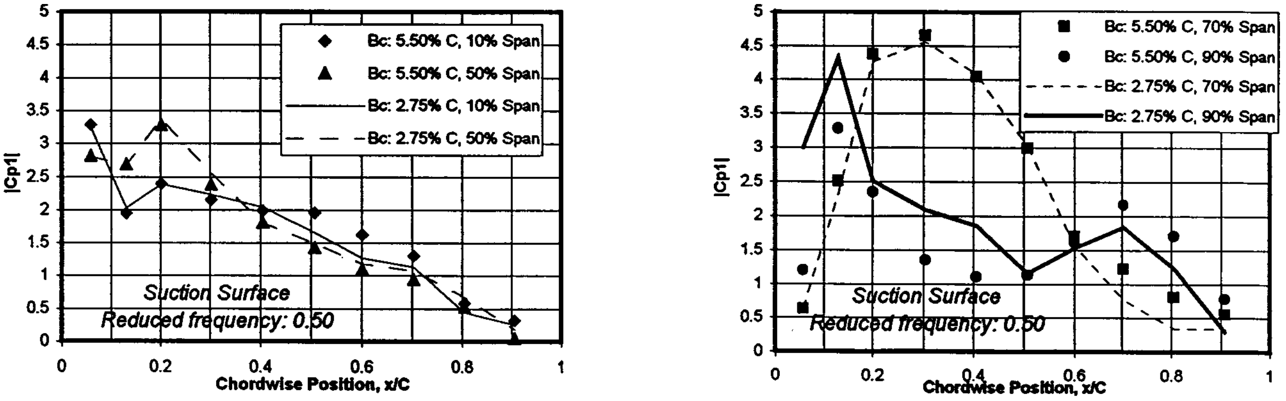

(i). Suction surface 10% and 50% span

(ii). Suction surface 70% and 90% span

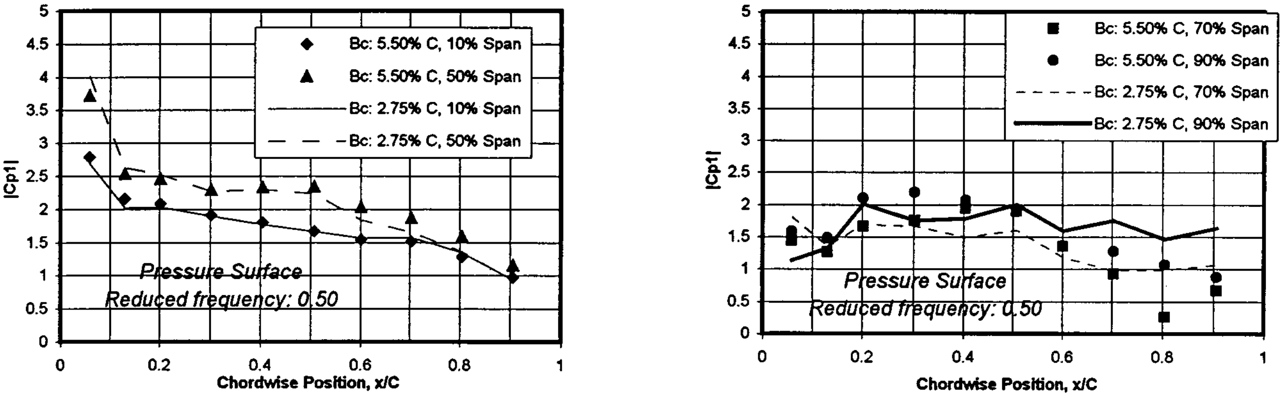

(iii). Pressure surface at 10% and 50% span

(iv). Pressure surface at 70% and 90% span

Fig. 11 Amplitude of the first harmonic pressure response

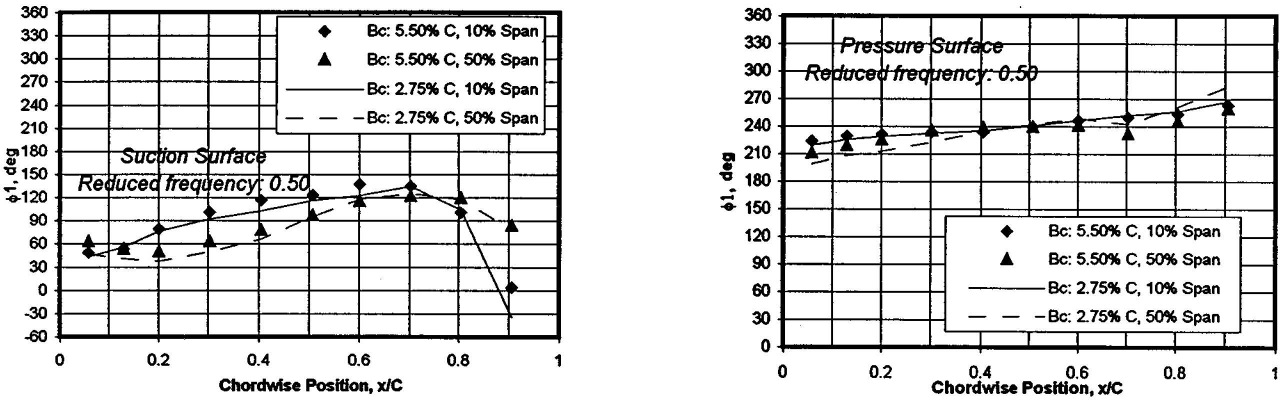

(i). Suction surface at 10% and 50% span

(iii). Pressure surface at 10% and 50%

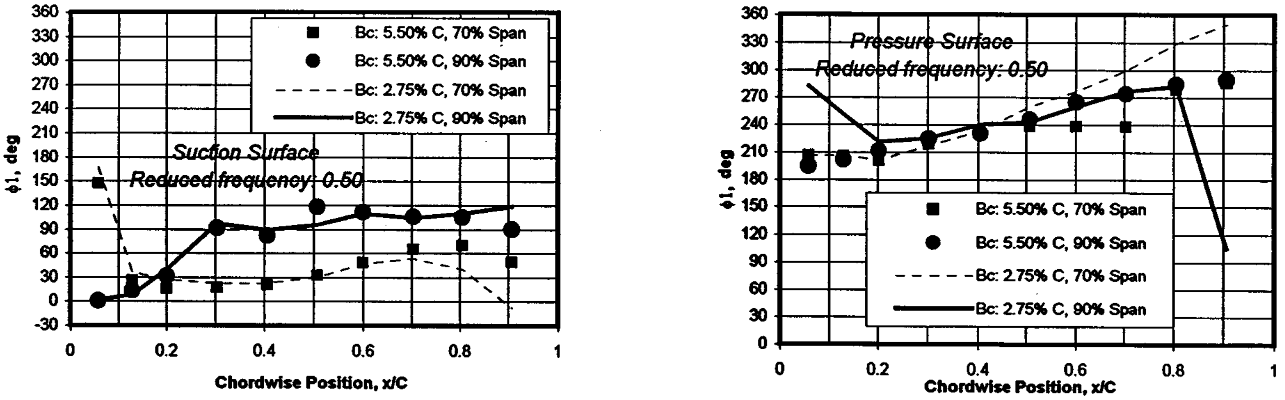

(ii). Suction surface at 70% and 90% span

(iv). Pressure surface at 70% and 90%

Fig. 12 Phase of the first harmonic pressure response

creased velocity and the lower pressure of the flow when passing by the step, 10, 30, and 50 percent span revealed a decrease in static pressure coefficient on both surfaces.

- Unsteady results: In the separated flow region the unsteady pressure had a destabilizing effect on the blade aeroelasticity.
- Linearity: Experimental testing for linearity demonstrated predominantly linear behavior of the unsteady aerodynamics.

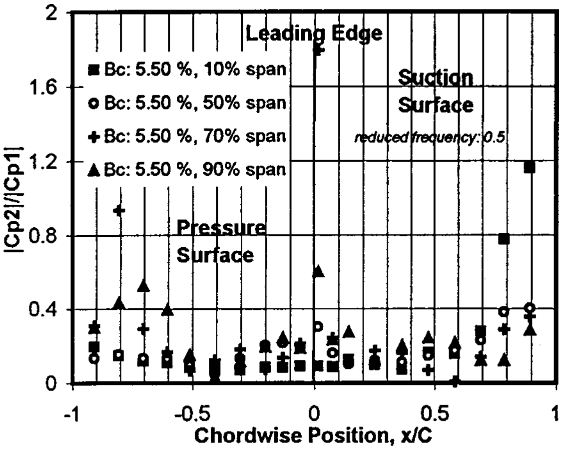

Fig. 13 Relative amplitude of the second harmonic pressure response

Acknowledgments

The research was funded by ABB-ALSTOM Power, and the authors would like to thank Dr. P. Walker and Dr. D. Bell of ABB-ALSTOM for their technical support.

Nomenclature

Ap_n = amplitude of the *n*th harmonic pressure response (Pa)
B_C = bending amplitude at tip, nondimensionalized with chord
B_L = local bending amplitude, nondimensionalized with chord
C = blade chord (m)
Cp = steady pressure coefficient, $Cp=(P-\overline{P_2})/(\overline{P_{01}}-\overline{P_2})$
$|Cp_n|$ = amplitude of the *n*th harmonic pressure coefficient, $|Cp_n|=|\widetilde{P}_n|/(\overline{P_{01}}-\overline{P_2})B_C$
dA = projected blade surface area (unit span), normal to the direction of bending (m^2)
h = blade span (m)
k = reduced frequency, based on chord and reference velocity
S = pitch (m)
V_{ref} = reference velocity (ms^{-1}), $V_{ref}=\sqrt{2(\overline{P_{01}}-\overline{P_2})/\rho}$
x = chordwise position (m)
z = radial position (m)
ϕ_n = phase angle of the *n*th harmonic pressure response, deg
ξ = coefficient of aerodynamic damping, $\xi=(1/h)\times\int_h\int_C[(-\pi B_L|Cp_1|\mathrm{Sin}\phi_1)/CB_C]\cdot dA\cdot dz$

Subscripts

1 = inlet parameter, 1st harmonic
2 = outlet parameter, 2nd harmonic

References

[1] Schmidt, D., and Riess, W., 1999, ''Steady and Unsteady Flow Measurements in the Last Stages of LP Steam Turbines,'' presented at the 3rd European Turbomachinery Conference, London, IMechE C557/023/99.

[2] Barton, H. A., and Halliwell, D. G., 1997, ''Detailed On-Blade Measurements on a Transonic Fan in Unstalled Supersonic Flutter,'' Proceedings of the 4th International Symposium on Unsteady Aerodynamics and Aeroelasticity of Turbomachines (ISUAAT), Aachen, Germany.

[3] Carta, F. O., and St. Hilaire, A. O., 1978, ''Experimentally Determined Stability Parameters of a Subsonic Cascade Oscillating Near Stall,'' ASME J. Eng. Power, **100**, pp. 111–120.

[4] Carta, F. O., and St. Hilaire, A. O., 1980, ''Effects of Interblade Phase Angle on Cascade Pitching Stability,'' ASME J. Eng. Power, **102**, pp. 391–396.

[5] Bölcs, A., and Fransson, T. H., 1986, ''Aeroelasticity in Turbomachines: Comparison of Theoretical and Experimental Cascade Results,'' Communication du Laboratoire de Thermique Apliquée et de Turbomachines, No. 13, Lausanne, EPFL.

[6] He, L., 1998, ''Unsteady Flows in Oscillating Turbine Cascade, Part 1. Linear Cascade Experiment,'' ASME J. Turbomach., **120**, pp. 262–268.

[7] Bell, D. L., and He, L., 1997, ''Three Dimensional Unsteady Pressure Measurements for an Oscillating Turbine Blade,'' ASME Paper No. 97-GT-105.

[8] Bell, D. L., and He, L., 1997, ''Three Dimensional Unsteady Flow Around a Turbine Blade Oscillating in Bending Mode—An Experimental and Computational Study,'' presented at the 8th ISUAAT, Stockholm, Sweden.

[9] Bell, D. L., and He, L., 1998, ''Three Dimensional Unsteady Flow for an Oscillating Turbine Blade and the Influence of Tip Leakage,'' ASME Paper No. 98-GT-571.

Some Aspects of Wake-Wake Interactions Regarding Turbine Stator Clocking

Maik Tiedemann

Friedrich Kost

Institute of Propulsion Technology,
German Aerospace Center (DLR),
Göttingen, Germany

This investigation is aimed at an experimental determination of the unsteady flowfield downstream of a transonic high pressure turbine stage. The single stage measurements, which were part of a joined European project, were conducted in the windtunnel for rotating cascades of the DLR Göttingen. Laser-2-focus (L2F) measurements were carried out in order to determine the Mach number, flow angle, and turbulence distributions. Furthermore, a fast response pitot probe was utilized to determine the total pressure distribution. The measurement position for both systems was 0.5 axial rotor chord downstream of the rotor trailing edge at midspan. While the measurement position remained fixed, the nozzle guide vane (NGV) was ''clocked'' to 12 positions covering one NGV pitch. The periodic fluctuations of the total pressure downstream of the turbine stage indicate that the NGV wake damps the total pressure fluctuations caused by the rotor wakes. Furthermore, the random fluctuations are significantly lower in the NGV wake affected region. Similar conclusions were drawn from the L2F turbulence data. Since the location of the interaction between NGV wake and rotor wake is determined by the NGV position, the described effects are potential causes for the benefits of ''stator clocking'' which have been observed by many researchers. [DOI: 10.1115/1.1370158]

1 Introduction

The continuing challenge to improve the durability and performance of turbomachinery has motivated designers to put more and more effort into the investigation of unsteady effects caused by the relative motion of neighboring blade rows. According to Arndt [1], the interaction of an upstream stator wake (which convects through the rotor) and the rotor wake (stator-rotor wake interaction) may have a significant impact on both the aerodynamic and the structural performance of downstream blade rows. Indexing (clocking) of a turbine nozzle guide vane (NGV) changes the circumferential location of the NGV wake-rotor wake interaction in the inlet plane of a downstream stator.

Investigations of clocking effects both in compressors and turbines have revealed a certain potential for an increase in efficiency. While Barankiewicz and Hathaway [2] found only a 0.2 percent increase in overall efficiency in an experimental investigation of a four-stage compressor, Saren et al. [3] measured a remarkable increase of up to 1.4 percent in a 1.5 stage compressor. Measurements in a 1.5 stage compressor by Dorney et al. [4] indicated a possible efficiency increase of 1.0 percent point. Numerical investigations of Gundy-Burlet and Dorney [5] in a 2.5 stage compressor and Dorney et al. [6] in a 1.5-stage compressor showed stage efficiency increases in the order of 0.6–0.7 percent.

In 1994 Sharma et al. [7] reported an experimentally determined ±0.5 percent variation in the overall efficiency of the two-stage turbine of a space shuttle high-pressure fuel turbopump. Further measurements in the same rig by Huber et al. [8] indicated efficiency variations due to clocking of ±0.4 percent, while a numerical simulation by Griffin et al. [9] revealed only a variation of ±0.15 percent.

In experiments conducted by Halstead et al. [10] in a two-stage low-pressure turbine (LPT), clocking resulted in a 25 percent variation in the profile losses of the second stator. A numerical simulation of the flow in a 1.5-stage LPT by Eulitz et al. [11] showed an efficiency variation of 0.4 percent. The largest benefit due to clocking is reported by Dorney and Sharma [12]. In the numerical investigation of a 1.5-stage turbine, they observed overall efficiency variations of approximately 2 percent.

While Blair et al. [13] observed in a 1.5-stage turbine that the effect of NGV clocking on the second stator heat transfer was negligible, Johnston and Fleeter [14] found, in a two-stage turbine, significant clocking effects on the unsteady heat transfer coefficient of that blade row. Hsu and Wo [15] reported on the beneficial use of clocking for the reduction of unsteady blade loading in a compressor.

Most of the above studies indicated maximum efficiency when the first-stage stator wake impinges on the downstream stator leading edge and minimum efficiency when it passes in between two vanes. Dorney et al. [6,4] and Gundy-Burlet and Dorney [5] observed that in compressors maximum efficiency occurs when the wakes impinge slightly offset toward the pressure side rather than directly on the leading edge. Note that most of these investigations were conducted for identical blade counts of the blade rows, i.e., clocking affected all downstream vanes in the same way. In real engines the benefits of clocking may be substantially smaller, due to different blade counts. Although there seems to be a broad agreement about the potential of clocking for turbomachinery performance and about the optimum relative blade row position, very little and sometimes contrasting information has been published about the assumed reasons. Among the suspected causes is the changed flow unsteadiness in the second stator inlet plane (see, e.g., Dorney and Sharma [12]) which could be responsible for changes in its unsteady transition pattern (Walker et al. [16]). Another possible reason are variations in the downstream stator surface velocities (Griffin et al. [9]).

The current study is aimed at an identification of the variations in the unsteady flow pattern downstream of a transonic high pressure turbine stage at 12 NGV clocking positions. Since the utilized model is only a single stage, no information on the actual performance variation of a downstream stator can be given. Furthermore, possible upstream potential flow effects of the second stator are neglected. This paper presents results of laser-2-focus (L2F) and fast response pitot probe measurements that were car-

---

Contributed by the International Gas Turbine Institute and presented at the 45th International Gas Turbine and Aeroengine Congress and Exhibition, Munich, Germany, May 8–11, 2000. Manuscript received by the International Gas Turbine Institute February 2000. Paper No. 2000-GT-487. Review Chair: D. Ballal.

ried out in order to determine the mid-span distributions of Mach number, flow angle, turbulence, and total pressure 0.5 axial rotor chord downstream of the rotor trailing edge.

2 Experimental Apparatus

2.1 The ''Windtunnel for Rotating Cascades''(RGG). The RGG is a closed circuit, continuously running windtunnel, Fig. 1. A four stage radial compressor (maximum pressure ratio 6) driven by a speed-controlled 1-MW dc motor provides a volume flow rate of up to 15.5 m^3/s. All components of the facility are accurately controlled by means of a ''Simatic S5'' industrial control system.

Possible rotor speeds are up to 10,000 rpm in both directions. The rotor is coupled to a speed-controlled 500-kW dc motor/generator, which can drive or brake the rotor in either direction. The conditions in the test section are adiabatic. An auxiliary compressor provides air for the simulation of NGV coolant ejection. A second auxiliary compressor can be utilized to provide simulated coolant air for the rotor.

For a choked NGV [typical for high-pressure turbines (HPTs)], the stage inlet Mach number is determined by the vane geometry. The static pressure downstream of the NGV throat (and thus the stage pressure ratio and the NGV exit Mach number) is coupled to the rotational speed of the main compressor. Since the Reynolds number depends mainly on the adjustable settling chamber pressure and temperature levels, Mach and Reynolds number can be varied independently within certain limits.

A NGV inlet turbulence level of approximately 1.5 percent is very small for a HPT flowfield. However, Blair et al. [13] observed that, even though the effect of changes in inlet turbulence is dramatic on the NGV heat transfer, it is almost negligible on the rotor heat transfer. This observation was attributed to the fact that the rotor flowfield disturbances are due to the unsteadiness (wakes and shocks) generated by the NGV, rather than to the inlet turbulence. Therefore, this shortcoming of the facility does not necessarily decrease the applicability of the results obtained downstream of the stage. Since the probe carriage systems and the laser-2-focus velocimeter are mounted in fixed circumferential positions, the NGV can be rotated by approximately 18 deg in order to enable circumferential traverses.

2.2 Turbine Stage. The investigated turbine stage was designed by Alfa Romeo Avio in the course of a European turbine project. It comprises a state-of-the-art, full size, transonic, aeroengine HPT. The geometry at midspan where this investigation was conducted is given in Table 1. Figure 2 shows the stage and the measurement position (50 percent of axial rotor chord downstream of the rotor trailing edge). The line labeled ''Trigger'' corresponds to the relative position of the rotor and the measurement location at which the data acquisition was started (i.e., a rotor pitch of 0). Furthermore, the NGV is shown in the position ''NGV pitch is 0.''

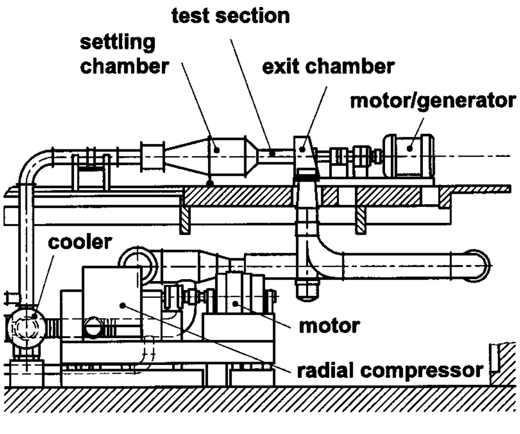

Fig. 1 Sketch of the ''windtunnel for rotating cascades'' (RGG)

Table 1 Geometrical parameters of the turbine blade rows

	NGV	Rotor
Axial chord c_{ax}	29.86 mm	27.45 mm
Tip radius	274.00 mm	274.00 mm
Hub radius (inlet)	238.84 mm	238.84 mm
Aspect ratio (inlet)	0.71	1.07
Stagger angle	51.90°	32.71°
Number of blades	43	64

2.3 Measurement Technique, Data Acquisltion and Data Evaluation

2.3.1 Laser-2-Focus (L2F) System. The measurement principle of L2F, depicted in Fig. 3, is rather simple. The L2F measuring device generates two highly focused light beams in the probe volume which act as a ''light gate'' for tiny particles in the flow. The scattered light from the particles provides two successive pulses, from the time interval between the pulses the velocity perpendicular to the laser beams can be derived. The system has been described in more detail by Kost and Kapteijn [17].

The fact that the measurement volume consists of two very small focuses (diameter roughly 10 μm) determines the general features of the L2F system: (1) The light intensity in a focus is rather high, accordingly small submicron particles which reliably follow the flow are detectable. (2) The small L2F measurement volumes enable measurements close to walls—both features are particularly useful in high speed turbomachine flows. (3) The main disadvantage of the small focuses is that the stop focus has to be rotated around the start focus into the (a priori unknown) direction of the mean flow, to enable the particles to pass both focuses.

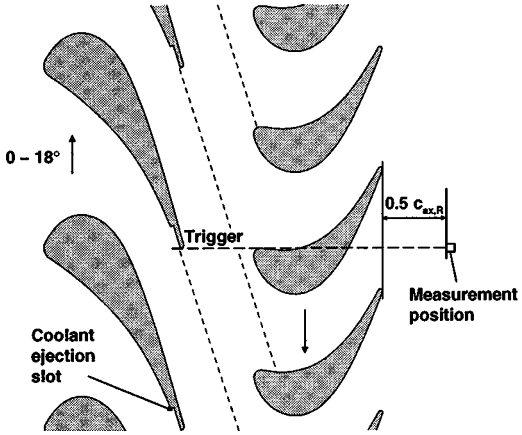

Fig. 2 Stage configuration at midspan and measurement position. ''Trigger'' marks the rotor position at which the data acquisition was started, i.e., ''rotor pitch 0.''

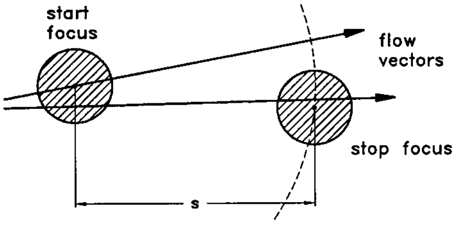

Fig. 3 The L2F measurement volume ($s=207$ μm)

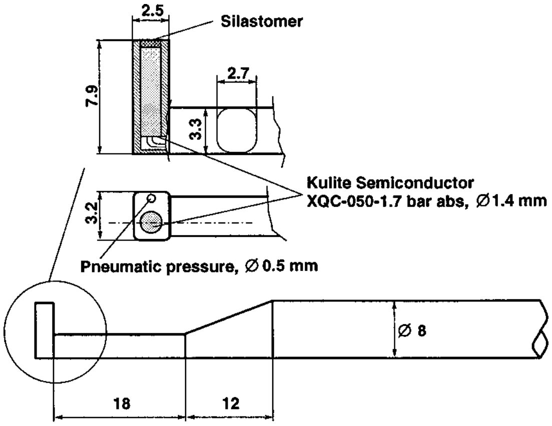

Fig. 4 Fast response total pressure probe with pneumatic reference

The optical parts are all assembled in a rigid casing called the optical head. It contains the laser, the photomultipliers to detect the scattered light, the optical parts to produce the two focuses and to transmit them to the measurement location, and finally a Bragg cell which serves as a light chopper during measurements inside rotating blade channels.

An electronic encoder triggered by a one per blade impulse from the rotor delivers the actual circumferential measurement position relative to the rotor with a precision of 1/16 of the blade gap. The data evaluation is based on standard statistical methods, and provides the Mach number, the angle and the turbulence intensity of the flow.

2.3.2 Total Pressure Probe. The total pressure probe utilized in this investigation (see Fig. 4) is equipped with a fast response piezoresistive pressure transducer. The cutoff frequency of this Pitot probe is well above 50 kHz. A thin silastomer film protects the fragile diaphragm of the transducer against dust particles. Unfortunately, the resistances of doped silicon are temperature dependent, which results in rather inaccurate mean values of the total pressure readings. In order to have an accurate reference mean value, a pneumatic pressure tube which was connected to a standard pressure transducer (averaging time one second) was added to the probe. Except for a resistor network in the unsteady transducer's supply line, no attempt was made to correct for its temperature drift. As no rapid large-scale temperature variations were expected in the measurement region, this was not considered critical regarding the unsteady results. The probe was turned to face the flow at the mean absolute flow angle.

The signal of the transducer was low-pass filtered at 45 kHz before it was fed into the PC-based 12-bit analog-to-digital (A/D) converters. The A/D conversion was paced by a shaft encoder which triggered exactly one sample for each of the 1024 pulses it delivered per revolution. This technique guarantees, that the samples are taken at the same relative NGV-rotor-probe position in every revolution, which is beneficial for the ensemble-averaging technique described below. For the nominal rotor speed of 7894 rpm the resulting sampling rate is 134.7 kHz. For details on the data acquisition and evaluation system see Tiedemann [18].

In order to separate the periodical and random signal components, the ensemble-averaging (EA) technique was applied. The data of the 448 sampled revolutions was averaged at 1024 fixed NGV-rotor-probe phase angles. Thus the EA pressure signal is obtained from

$$\tilde{p}_{0,i}=\frac{1}{N}\sum_{j=1}^{N} p_{0,ij}\,, \quad i=0\ldots1023,\; N=448 \qquad (1)$$

Table 2 Basic operating parameters of the turbine stage

absolute NGV exit Mach number M_2	0.937
relative rotor exit Mach number M_{w3}	0.938
absolute NGV exit Reynold's number Re_2	$0.866\cdot10^6$
relative rotor exit Reynold's number Re_{w3}	$0.396\cdot10^6$
relative rotor inlet angle β_2	40.9 deg
relative rotor exit angle β_3	−56.1 deg
rotor speed **N** [1/min]	7894
reduced speed N_{red} $[1/(\mathrm{min/K}^{1/2})]$	447.4
reduced mass flow M_{red} $[\mathrm{kg/K}^{1/2}/(\mathrm{s\ kPa})]$	0.665
stage pressure ratio p_{01}/p_{03}	2.64
stage reaction factor r	0.454
stage loading coefficient Ψ	1.519
stage flow factor Φ	0.431

Ideally, the random components are averaged out in the resulting periodic-unsteady signal. The EA random unsteadiness

$$\mathrm{RMS}_i=\sqrt{\frac{1}{N-1}\sum_{j=1}^{N}(p_{0,ij}-\tilde{p}_{0,i})^2} \qquad (2)$$

is a measure of nonperiodic effects. Since the characteristic turbulence frequency in the investigated stage of approximately 300 kHz is much higher than the low-pass filter frequency of the system (45 kHz), RMS does not include turbulence effects.

By means of time averaging, the 1024 values per NGV position were further reduced a single value per position. The time-averaged periodic fluctuations

$$\overline{\mathrm{RMS}_p}=\sqrt{\frac{1}{T}\int_0^T(\tilde{p}_0(t)-\tilde{p}_0)^2dt} \qquad (3)$$

are an integral measure for the overall periodic unsteadiness of the signal during the period T (e.g., wake and shock induced unsteadiness).

3 Test Parameters

The operating parameters of the investigated HPT stage are given in Table 2. The error margins in the determination of pneumatic pressures are of the order of 0.1 percent of the measured value, temperatures are determined within ±0.3 K, and the error in the mass flow is less than 1 percent of the measured value. A 6000 marks encoder is used to control N to within ±1 rpm. The Mach number values in Table 2 have accuracies of approximately ±0.004. The Reynolds number Re_2 is based on NGV exit conditions and NGV chord, while Re_{w3} is based on rotor exit conditions in the relative frame of reference and rotor chord. The presented parameters characterize the investigated stage as representative of a small to midsize aircraft engine HPT.

The NGV vanes are equipped with coolant ejection slots at the pressure side, close to the trailing edge (see Fig. 2). Tests were conducted with no coolant ejection and with the design ejection of 3 percent of the main mass flow. In addition, two interblade row gaps ($0.5\,c_{ax,NGV}$ and $0.38c_{ax,NGV}$) were investigated. Even though the flowfield inside the rotor passage shows supersonic portions and a passage shock, no effects of rotor trailing edge shocks were detected at the measurement location.

4 Results and Discussion

4.1 Time-Averaged Results. The time-averaged Mach numbers and total pressures measured downstream of the rotor, are presented in Fig. 5 for the test case of NGV/rotor gap of $0.5c_{ax,NGV}$, where $c_m=3$ percent for the investigated NGV pitch. Around a NGV pitch of 0.8, both traces show distinct minima caused by the low speed, low total pressure flow of the NGV

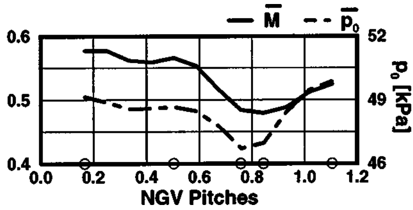

Fig. 5 Time-averaged Mach number and total pressure data for NGV/rotor gap of 0.5 $c_{ax,NGV}$, where $c_m=3$ percent. The circles mark NGV positions of time-resolved plots in Fig. 13.

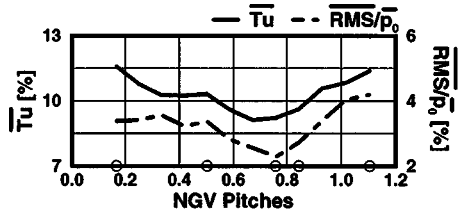

Fig. 6 Time-averaged turbulence and total pressure fluctuations for a NGV/rotor gap of 0.5 $c_{ax,NGV}$, where $c_m=3$ percent. The circles mark NGV positions of time-resolved plots in Fig. 14.

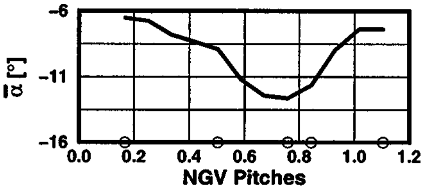

Fig. 7 Time-averaged absolute flow angle data for a NGV/rotor gap of $0.5c_{ax,NGV}$, where $c_m=3$ percent. The circles mark NGV positions of time-resolved plots in Fig. 15.

wake. NGV suction side effects are plotted to the left of this wake. The circles on the x axis mark the origin of the time-resolved data presented in the next section.

Figure 6 shows the turbulence intensity and the total pressure random fluctuations for the same test case. The turbulence is based on the constant circumferential velocity, and is thus a measure for velocity fluctuations which is independent of the local mean velocity. Due to the lack of a similar value for the total pressure, the RMS values are normalized by the local time-averaged total pressure. Note that both values decrease when the flow is affected by the NGV wake (around a NGV pitch of 0.8). Due to the high degree of unsteadiness in the wakes, it could be expected that these measures of unsteadiness increase rather than decrease. It is well known that stator clocking is most effective when the (time-averaged) NGV wake impinges on the leading edge of the downstream stator (maximum efficiency). A couple of researchers arrived at the conclusion that unsteadiness variations due to clocking are the cause of changes in downstream blade row efficiencies, their results are, however, contradictory. While Dorney and Sharma [12] reported maximum efficiencies at maximum unsteadiness, Griffin et al. [9], e.g., observed maximum efficiency at the lowest flow unsteadiness. Since the measurement location in the current study represents a typical position of a second stage stator inlet plane, maximum efficiency (NGV wake impinging on the vane leading edge) in this case would be accompanied by minimum flow unsteadiness. An additional effect that might have a severe impact on the flowfield of a downstream stator is the considerable flow angle variation of about 6 deg shown in Fig. 7.

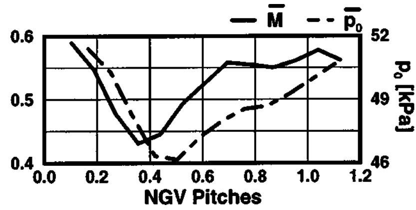

Fig. 8 Time-averaged Mach number and total pressure data for a NGV/rotor gap of 0.38 $c_{ax,NGV}$, where $c_m=3$ percent

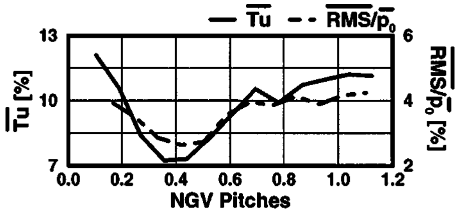

Fig. 9 Time-averaged turbulence and total pressure fluctuation data for a NGV/rotor gap of 0.38 $c_{ax,NGV}$, where $c_m=3$ percent

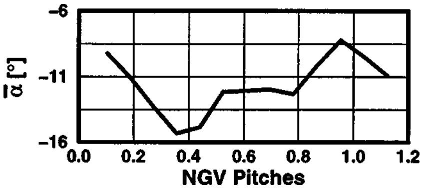

Fig. 10 Time-averaged absolute flow angle data for a NGV/rotor gap of $0.38c_{ax,NGV}$, where $c_m=3$ percent

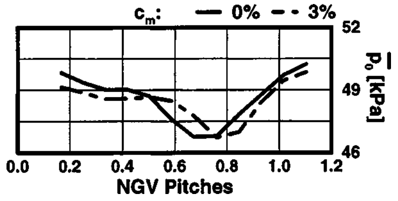

Fig. 11 Comparison of time-averaged total pressure data for 0 percent and 3 percent NGV coolant ejection, the NGV/rotor gap is 0.5 $c_{ax,NGV}$

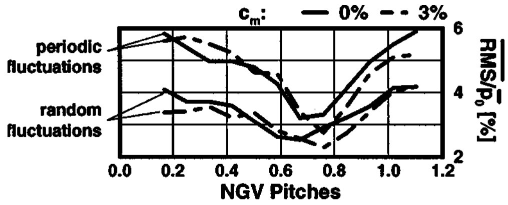

Fig. 12 Comparison of time-averaged total pressure fluctuation data for 0 percent and 3 percent NGV coolant ejection, the NGV/rotor gap is 0.5 $c_{ax,NGV}$

Figures 8–10 show the same type of time-averaged results for the smaller NGV/rotor gap $(0.38c_{ax,NGV})$. Since the axial distance between the NGV and the measurement location is reduced in this case, it is not surprising that the variations in the fluctuations are increased with respect to the larger gap case. Saren et al. [3] found an increase in maximum stage efficiency from 1.0 percent to 1.4 percent when they reduced the inter blade row gap from 0.66 axial rotor chords to 0.23 axial chord lengths. This is a further indication for a relation between the unsteadiness variation

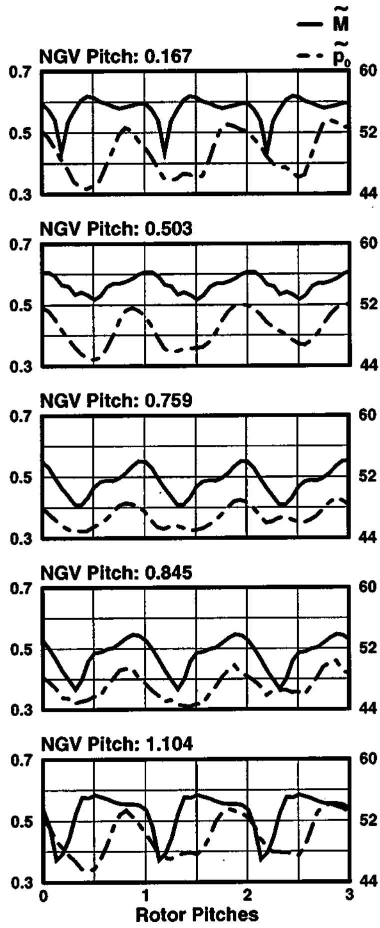

Fig. 13 Ensemble-averaged Mach number and total pressure traces for five different NGV clocking positions; $C_m=3$ percent, and the axial gap is $0.5C_{ax,NGV}$

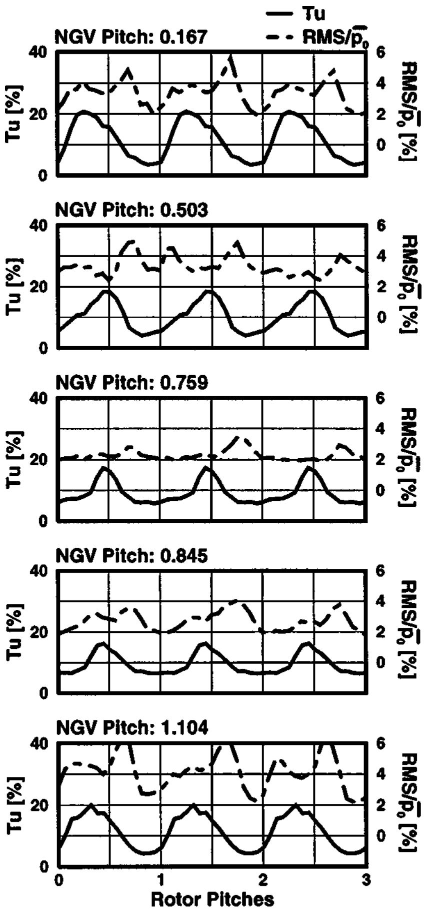

Fig. 14 Turbulence and total pressure fluctuation (normalized by the time-averaged total pressure) traces for five different NGV clocking positions; $C_m=3$ percent, and the axial gap is $0.5C_{ax,NGV}$

and clocking benefits. Since the qualitative features are quite similar in the two test cases and the time-resolved total pressure probe data for the smaller gap suffered from noise problems, the discussion in the next section will be based on the large gap data.

The time-averaged probe data for the two investigated NGV coolant ejection rates are presented in Figs. 11 and 12. Even though the coolant ''fills up'' the NGV wake, there is no indication of significant differences between these cases (the slight phase shift is due to the coolant induced change in NGV exit flow angle), i.e., no differences in the effects on downstream rows are to be expected. The time-averaged periodic fluctuations (periodic with respect to rotor wake occurrences) given in Fig. 12 indicate that the periodic features of the flow decrease as well under the influence of the NGV wake, i.e., the (ensemble-averaged) amplitude of the total pressure decreases. This in turn, means that the rotor wake depth is reduced in the NGV wake affected region. Note that both fluctuation values decrease by roughly 50 percent!

Summing up, the time-averaged data gathered downstream of the rotor indicates a significant reduction of random as well as periodic fluctuations in the region affected by the NGV wake. While the variation of the NGV coolant ejection did not alter the flow pattern in the measurement plane, the reduction of the NGV/rotor gap from $0.5c_{ax,NGV}$ to $0.38c_{ax,NGV}$ led to an increase in the observed fluctuation variations.

4.2 Time-Resolved Results. As the effect of NGV coolant ejection was negligible, only the time-resolved (ensemble-averaged) data of the $0.5c_{ax,NGV}$ NGV/rotor gap, 3 percent coolant ejection test case is presented in this section. Data traces of five of the investigated 12 NGV positions are shown in Figs. 13–15. The L2F results (left ordinates) were determined for only one pitch, and were copied twice to form one trace while the pitot probe data (right ordinates) was determined for all 64 rotor pitches. Due to the rotor motion, the pitch values along the abscissa are a time scale. The respective NGV positions are given in the plot title, and the relation to the pitch position in the time-averaged data plots is indicated by circles in Figs. 5–7.

The rotor wakes are clearly visible in the Mach number and total pressure traces in Fig. 13. In the top plot, where the measurement position is not affected by the NGV wake, both data traces show distinct portions of rotor wake flow (minima) and rotor passage flow (maxima). When the NGV is moved and its wake starts to affect the investigated location (second plot, NGV, pitch 0.503) the amplitude of the fluctuations is decreasing. For the total pressure this reduction in periodic fluctuations was already observed in the discussion of the time-averaged periodic fluctuations presented in Fig. 12. When the NGV is moved further, the amplitude (indicating the rotor wake depth) keeps decreasing until the center of the NGV wake effect is reached at NGV, pitch 0.759. From there on, the amplitudes of both traces recover until their original level is re-established when the measurement position is no longer affected by the NGV wake (the bottom plot of Fig. 13). Note that the total pressure base level (value of the minima) remains more or less constant, i.e., only the maxima are affected by the NGV wake. Apparently, the reduced total pressure in the chopped portions of the NGV wake decreases the total pressure of the rotor passage flow, and thus the difference (i.e., the amplitude) between rotor core flow and rotor wake flow, which results in the observed reduction in periodic fluctuations.

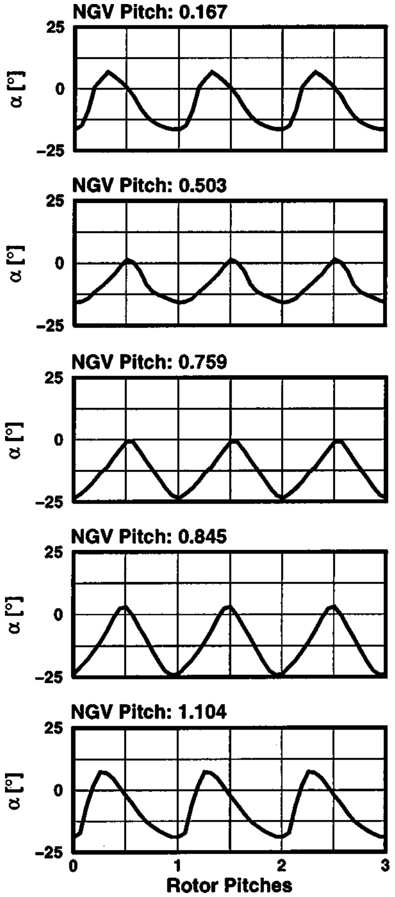

Fig. 15 Absolute flow angle traces for five different NGV clocking positions; $C_m=3$ percent, and the axial gap is $0.5C_{ax,NGV}$

The turbulence and total pressure fluctuation data shown in Fig. 14 indicates not only a significant reduction in the mean level (as seen in the time-averaged data in Fig. 6), but also a change in the time-resolved pattern when the measurement position is affected by the NGV wake. The width of the maxima (representing the rotor wake flow) reduces from the top plot (data not affected by the NGV wake) to the center plot (core of the NGV wake) and increases again when the NGV is moved further. Apparently, the rotor wake fluctuations are narrower in the NGV wake affected positions, while the data in Fig. 13 indicate that the rotor wake itself broadens. In addition, the structure of the data traces changes, particularly in the RMS values. Figure 16 shows a comparison of total pressure and RMS data for the NGV pitch position 1.104, where the mentioned structure is most pronounced and the measurement position is not affected by the NGV wake. In between the rotor passage flow and the wake core region the RMS trace shows two distinct maxima (labeled the ‘‘suction side’’ the and ‘‘pressure side’’). Since the RMS data do not resolve turbulence, these maxima probably result (among other randomly unsteady features, such as changes in the vortex street) from mixing effects at the wake rims. In the turbulence data not only the fluctuations at the wake rims but also the high turbulence intensity inside the wake is resolved. Therefore, the double-peak pattern observed in the RMS data may be hidden in the turbulence data.

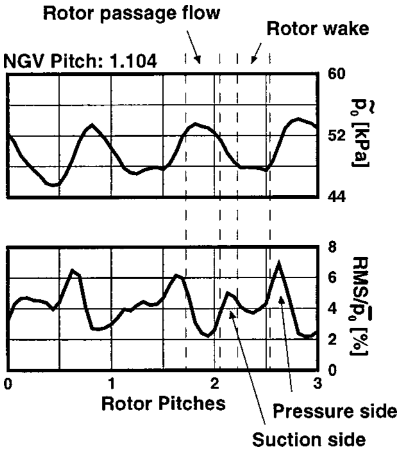

Fig. 16 Comparison of total pressure and RMS values; $C_m=3$ percent, the axial gap is $0.5C_{ax,NGV}$ and the NGV pitch is 1.104

The center plot of Fig. 14 shows that the observed pattern almost vanishes when the measurement position is affected by the NGV wake. Since the discussion of the Mach number and total pressure data led to the conclusion that the differences between rotor core flow and rotor wake flow are reduced in this configuration, it appears reasonable that the wake mixing effects are reduced as well. This hypothesis would explain the vanishing of the two peaks in the RMS traces (which were mainly attributed to the wake mixing effects) and the narrowing of the turbulence maxima (which may be a combination of wake mixing unsteadiness at the rims and turbulence in the core).

Apart from wake mixing differences, the unsteady boundary layer transition on the rotor surfaces may contribute to the observed fluctuation variations. An earlier investigation in the same rig (Tiedemann and Kost [19]) showed that the rotor suction side boundary layer experienced bypass transition when affected by the NGV wake and a combination of bypass transition and shock-induced separated flow transition in between two NGV wakes. These differences in the boundary layer development certainly introduced variations of the rotor wake structure.

As the base level of the plots remains relatively constant, the NGV wake induced decrease in the time-averaged data (see Fig. 6) appears to be solely a result of the reduced maxima in this configuration. The higher turbulence level inside the NGV wake should significantly increase the turbulence in between rotor wakes when it passes through the rotor passage and over the measurement location. A possible reason for the fact that this increase is almost negligible may be the considerable acceleration inside the rotor passage.

The absolute flow angle data given in Fig. 15 indicate that a downstream stator would experience a significant decrease in mean incidence (also see Fig. 7) and a slight decrease in the incidence variation (approximately 3 deg with respect to the unaffected configuration) when the NGV wake core affects its leading edge the NGV (pitch is 0.759). However, a much larger decrease (approximately 10 deg) occurs when the NGV wake approaches the pressure side of a virtual downstream stator (NGV pitch=0.674; $\alpha=-3.5$ deg$--19$ deg, not presented). The decrease in angle variation that results from the reduction in wake mixing intensity may possibly be shifted pitchwise by a secondary effect.

All in all, the presented data indicate a considerable decrease in both the periodic and random fluctuations of velocity and total pressure, when the NGV wake affects the measurement position. Large potions of this decrease may be attributed to the NGV wake induced reduction of the ‘‘step’’ in the flow parameter levels between the rotor passage flow and the rotor wake flow. This reduced step results in a decrease of the wake mixing intensity and thus in random fluctuations. Furthermore, a considerable variation of the second stator incidence angle occurs under the influence of the NGV wake. This incidence variation is slightly out of phase with the random fluctuation variation.

Walker et al. [16] measured downstream of a 1.5-stage low-speed compressor significant variations in the stator wake momentum thicknesses when the IGV was clocked. This phenomenon was attributed to changes in the stator boundary layer transition which are caused by changes in the stator inlet fluctuations. As in the current study, the lowest fluctuation level occurred when the IGV wake impinged directly on the stator leading edge, which was assumed to be the configuration producing the lowest overall losses. The stator boundary layers are likely to be more resistant to separation at the lower inlet fluctuation condition. These observations may be the explanation for the benefits of clocking in compressors. However, since the current measurements revealed similar fluctuation variations, the same physical phenomena may be responsible for efficiency increases in transonic turbines.

Griffin et al. [9] stated that considerable portions of the NGV wake-induced efficiency increase may be attributed to the reduced surface velocities on the downstream blade row. A second suspected reason was the reduced turbulence due to a reduction in the stator inlet fluctuation level. Both phenomena were also detected in the current measurements (assuming that the reduced inlet Mach number would result in reduced surface velocities). However, the total pressure ratio in the two tests (approximately 1.46 for two stages in the first case, [8]; approximately 2.6 in the present case) differed significantly, which reduces the comparability of the two results. Dorney et al. [4] observed reduced skin friction values in the maximum efficiency configuration, which may also be an indication for boundary layer transition variations due to clocking.

At off-design incidence, leading edge separations may occur which would as well change the transition pattern of a blade row. As the decreased incidence range results in a reduced leading edge separation risk, the observed reduction in stator incidence variation under the influence of the NGV wake (maximum efficiency) is an additional candidate phenomenon for the explanation of NGV clocking benefits.

5 Conclusions

The variation in Mach number and total pressure downstream of a transonic HPT stage were investigated for different NGV clocking positions, and time-averaged as well as time-resolved results were presented. As the utilized rig is only a single stage model, no information on the actual performance variation of a downstream stator could be given. While the variation of the stator coolant ejection had no influence on the conditions downstream of the stage, a reduction of the interblade row gap resulted in an intensification of the observed patterns.

The data reveal a significant variation of both periodic and random fluctuations of velocity and total pressure when the NGV was clocked with respect to the fixed measurement location. While the rotor wake decreases in depth and increases in width when it interacts with chopped portions of the NGV wake, the maxima of the random components (i.e., turbulence and the RMS of the total pressure) decrease in height and width. The assumed reason for these observations is the reduction in the velocity and total pressure ''step'' between the rotor passage flow and the rotor wake flow when portions of the NGV wake (consisting of low energy fluid like the rotor wake) are present in the passage. This reduction results in a lowered wake mixing intensity, which in turn results in lower random fluctuations.

The impingement of NGV wakes on the downstream stator leading edge would cause decreased fluctuations, which might result in changes in the stator's boundary layer development and thus losses. Furthermore, the observed considerable NGV wake-induced reduction in stator incidence variation may also contribute to the benefits of clocking.

Acknowledgments

Parts of the above research were carried out in the course of the European IMT Area 3 Turbine Project No. AER2-CT-92-0044. The authors gratefully acknowledge the financial support by the CEC. Furthermore, we would like to thank E. Schüpferling, A. Tappe, and A. Uhl for their technical support during the tests and the data acquisition.

Nomenclature

c_{ax} = [m] axial chord
c_m = [percent] NGV coolant ejection rate
c_p = [J/kg K] specific heat
$\dot{m}$ = [kg/s] mass flow rate
$\dot{m}_{red}$ = $[\mathrm{kg}\sqrt{\mathrm{K}}/(s\,kPa)]$ reduced mass flow $=\dot{m}\sqrt{T_{01}}/p_{01}$
M = Mach number
N = [RPM] number of evaluated rev., rotor speed
N_{red} = $[1/(\min\sqrt{\mathrm{K}})]$ reduced speed $=N/\sqrt{T_{01}}$
p = [kPa] pressure
r = reaction factor $=\dfrac{(p_2/p_{01})^{\gamma-1/\gamma}-(p_3/p_{01})^{\gamma-1/\gamma}}{1-(p_3/p_{01})^{\gamma-1/\gamma}}$
Re = Reynolds number
s = [μm] distance between the two L2F focuses
T = [K], [s] temperature, period
Tu = [percent] turbulence intensity
u = [m/s] circumferential velocity
α, β = [deg] absolute, relative flow angle (vs. axial direction)
Φ = flow factor, equal to the axial velocity/circumfer. velocity
Ψ = loading factor $c_p(T_{03}-T_{01})/u_2^2$

Subscripts

0 = total condition
1, 2, 3 = NGV inlet, NGV exit/rotor inlet, and rotor exit
i, j = index along circumference, and index along revolutions
p = periodic

Superscripts

$\sim$ = ensemble-averaged value
$-$ = time-averaged value

References

[1] Arndt, N., 1993, ''Blade Row Interaction in a Multistage Low-Pressure Turbine,'' ASME J Turbomach., **115**, pp. 137–146.
[2] Barankiewicz, W. S., and Hathaway, M. D., 1997, ''Effects of Stator Indexing on Performance in a Low Speed Multistage Axial Compressor,'' ASME Paper No. 97-GT-496.
[3] Saren, V. E., Savin, N. M., Dorney, D. J., and Sondak, D. L., 1998, ''Experimental and Numerical Investigation of Airfoil Clocking and Inter-Blade-Row Gap Effects on Axial Compressor Performance,'' AIAA Paper No. 98-3413.
[4] Dorney, D. J., Sondak, D. L., Cizmas P. G. A., Saren, V. E., and Savin, N. M., 1999, ''Full-Annulus Simulations of Airfoil Clocking in a 1-1/2 Stage Axial Compressor,'' ASME Paper No. 99-GT-23.
[5] Gundy-Burlet, Karen L., and Dorney, Daniel, J., 1997, ''Physics of Airfoil Clocking in Axial Compressors,'' ASME Paper No. 97-GT-444.
[6] Dorney, D. J., Sharma, O. P., and Gundy-Burlet, K. L., 1998, ''Physics of Airfoil Clocking in a High Speed Axial Compressor,'' ASME Paper No. 98-GT-82.
[7] Sharma, O. P., Ni, R. H., and Tanrikut, S., 1994, ''Unsteady Flows in Turbines-Impact on Design Procedure,'' AGARD-LS-195.
[8] Huber, F. W., Johnson, P. D., Sharma, O. P., Staubach, J. B., and Gaddis, S. W., 1996, ''Performance Improvement Through Indexing of Turbine Airfoils: Part 1—Experimental Investigation,'' ASME J. Turbomach., **118**, pp. 630–635.
[9] Griffin, L. W., Huber, F. W., and Sharma, O. P., 1996, ''Performance Improvement Through Indexing of Turbine Airfoils: Part 2—Numerical Simulation,'' ASME J. Turbomach., **118**, pp. 636–642.
[10] Halstead, D. E., Wisler, D. C., Okiishi, T. H., Walker, G. J., Hodson, H. P., and Shin, H.-W., 1997, ''Boundary Layer Development in Axial Compressors and Turbines,'' Part 1 of 4—Composite Picture, ASME J. Turbomach., **119**, pp. 114–127, Part 2 of 4—Compressors, ASME J. Turbomach., **119**, pp. 426–444. Part 3 of 4—LP Turbines, ASME J. Turbomach, **119**, pp. 225–237. Part 4 of 4—Computations and Analyses, ASME J. Turbomach., **119**, pp. 128–139.
[11] Eulitz, F., Engel, K., and Gebing, H., 1996, ''Numerical Investigations of the Clocking Effects in a Multistage Turbine,'' ASME Paper No. 96-GT-26.
[12] Dorney, D. J., and Sharma, O. P., 1996, ''A Study of Turbine Performance Increases Through Airfoil Clocking,'' AIAA Paper No. 96-2816.

[13] Blair, M. F., Dring, R. P., and Joslyn, H. D., 1988, ‘‘The Effects of Turbulence and Stator/Rotor Interactions on Turbine Heat Transfer, Part I—Design Operating Conditions,’’ ASME J. Turbomach., **111**, pp. 97–103.
[14] Johnston, D. A., and Fleeter, S., 1999, ‘‘Turbine Blade Unsteady Heat Transfer Change Due to Stator Indexing,’’ ASME Paper No. 99-GT-376.
[15] Hsu, S. T., and Wo, A. M., 1997, ‘‘Reduction of Unsteady Blade Loading by Beneficial Use of Vortical and Potential Disturbances in an Axial Compressor With Rotor Clocking,’’ ASME J. Turbomach., **120**, pp. 705–713.
[16] Walker, G. J., Hughes, J. D., Köhler, I., and Solomon, W. J., 1998, ‘‘The Influence of Wake-Wake Interactions on Loss Fluctuations of a Downstream Axial Compressor Blade Row,’’ ASME J. Turbomach., **120**, pp. 695–704.
[17] Kost, F., and Kapteijn, C., 1997, ‘‘Application of Laser-Two-Focus Velocimetry to Transonic Turbine Flows,’’ 7th Int. Conference on ‘‘Laser Anemometry—Advances and Applications,’’ Univ. of Karlsruhe, Germany, September 8–11.
[18] Tiedemann, M., 1998, ‘‘Stator Wake Effects on the Total Pressure Distribution Downstream of a Transonic Turbine Rotor,’’ Transactions of the Institute of Fluid-Flow Machinery of the Polish Academy of Science, No. 104, pp 3–18.
[19] Tiedemann, M., and Kost, F., 1999, ‘‘Unsteady Boundary Layer Transition on a High Pressure Turbine Rotor Blade,’’ ASME Paper No. 99-GT-194.

A Computational Study of a Novel Turbine Rotor Partial Shroud

Neil W. Harvey
Turbine Engineering,
Rolls-Royce Plc,
Derby, United Kingdom

Ken Ramsden
School of Mechanical Engineering,
Cranfield University,
Cranfield, United Kingdom

The over tip leakage (OTL) flow that exists between the stationary casing and the rotor tip of a shroudless HP turbine remains a major source of loss of performance for modern aero gas turbines. To date the principal approaches to reducing OTL loss have been to minimize the clearance gap and/or apply a rotating shroud to the rotor. Tip clearance control systems continue to improve, but a practical limit on tip gap remains. A rotating shroud is highly effective but increases the rotor weight, forcing it to run more slowly and thus increasing other aerodynamic losses. Additional means of reducing OTL loss are still needed. Partial shrouds (winglets) have been tried but none have entered commercial service to date. This paper presents a novel design of partial shroud derived from a review of past research. The (arbitrary) objectives were to halve the OTL loss of a shroudless rotor, at less than half the size of a full shroud. This design has been analyzed using a steady flow RANS CFD code to qualitatively determine its benefits. Attention has been paid to its validation and a realistic determination of its capabilities. The winglet is predicted to significantly improve the efficiency of a highly loaded HP turbine, by 1.2 percent–1.8 percent at 2 percent tip gap/span. A detailed understanding of the flow field shows this to be credible. [DOI: 10.1115/1.1370166]

Introduction

Over tip leakage in axial flow turbomachinery has been the subject of extensive research since the advent of the gas turbine. An analysis of OTL loss is given in Denton [1], while [2] provides a thorough review of OTL flow in shroudless turbines.

The basic form of over tip leakage in a shroudless axial flow turbine is illustrated in Fig. 1. The pressure difference between the two surfaces of the aerofoil drives a leakage flow through the rotor tip/casing clearance gap. Typically this flow is ejected as a strong jet which mixes with the main stream on the suction side, usually rolling up to form a vortex. This interacts in some way with the ''classical'' outer passage secondary flow vortex, described in Sieverding [3]. Detailed measurements of OTL flow have been made by Bindon [4], Moore and Tilton [5], Heyes and Hodson [6], and Yaras et al. [7,8]. All of them studied rotor profiles, with a tip gap, in large scale, low speed, linear cascade. Yaras et al. modeled the relative motion between the casing and rotor with a moving end wall.

A summary of this research is given in the next sections.

Tip Gap Flow Field. Figure 2 (taken from Denton [1]) illustrates the two typical regimes for flow through the tip gap, depending on the thickness of the aerofoil locally. These are sections through the blade, roughly normal to the camberline. The flow entering the gap from the pressure side of the blade separates from the blade tip and contracts to a jet, which is largely lossless up to the minimum flow area. Figure 2 shows the flow for a sharp corner between the pressure surface and rotor tip.

If the blade thickness is large enough (Fig. 2(*a*)) the jet mixes out above the blade tip, increasing the loss and static pressure. Denton [1] states this occurs for a gap height/local blade thickness of 4, while Heyes and Hodson [6] give a ratio of 6. The static pressure after this mixing is depressed by the blockage of the tip leakage vortex; see [7–9].

If the blade tip is thin enough, the jet will not reattach within the gap (Fig. 2(*b*)). This means that there is no pressure recovery in the gap and so the discharge coefficient (*Cd*) will be lower (Heyes et al. [10]). (This is for sharp corners; radiused ones will generally have higher values of *Cd*). For a typical, cooled, turbine rotor this will only occur near the trailing edge. Denton [1] gives a maximum gap/thickness ratio for this of 2.5; Heyes and Hodson [6] give 1.5.

Effects of Secondary Flows and Relative Casing Motion The interaction between the OTL and outer passage secondary flows, and the effects of the relative motion between the rotor tip and the casing, have been observed to vary considerably.

1 The two vortices reinforce each other. Yamamoto [11] found that in the outer half of the passage the OTL and outer passage vortices are in close proximity and counter-rotate. By the trailing edge, the outer passage vortex has moved to below the OTL vortex and near the aerofoil suction surface. Govardan et al. [12] obtained a similar result, describing the interaction as intense.

2 With relative motion between the casing and the rotor the outer passage vortex is enhanced. Morphis and Bindon [9] and Yaras and Sjolander [7,8] found that this reduced the driving pressure difference and ''throttled'' the OTL flow. They also concluded that pressure forces dominated the flow, rather than viscous ones.

3 Graham [13] obtained the opposite result—relative motion between the casing and rotor reduced the flow in the gap directly. This may have been related to the low values of Re in his experiment.

4 Chan et al. [14], using the same facilities as Yaras and Sjolander, found that with a tip clearance of 5.5 percent of span the OTL vortex occupied almost the whole of the passage width by the trailing edge plane with only a small passage vortex.

5 Bindon and Morphis [15] found uniquely that even by the trailing edge plane most of the OTL leakage flow remained in a flat high energy wall jet rather than rolling into a vortex. The cross passage secondary flow on the casing was weak and there seemed to be no indication of a passage vortex. The presence of the OTL jet, as opposed to the vortex, was confirmed in their testing of a full one and a half stage low speed annular rig [16,17].

6 Yamamoto et al. [18,19] found in a $1\frac{1}{2}$ stage turbine that the rotor hub passage vortex confined the outer secondary flow and OTL vortices to near the casing. These two vortices were never present at the same time. The outer passage one was weak at a tip clearance of 0.5 percent span and disappeared at a clearance of 1.9 percent span.

Contributed by the International Gas Turbine Institute and presented at the 45th International Gas Turbine and Aeroengine Congress and Exhibition, Munich, Germany, May 8–11, 2000. Manuscript received by the International Gas Turbine Institute February 2000. Paper No. 2000-GT-668. Review Chair: D. Ballal.

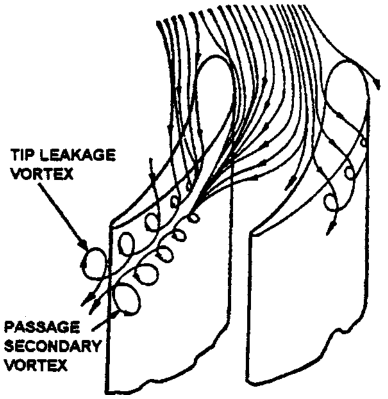

Fig. 1 Illustration of OTL and outer passage secondary flows for a shroudless turbine rotor

Loss Generation. The tip clearance in a typical aero engine varies around its operating cycle and increases during the engine life due to wear and tear; see Stakolich et al. [20]. The sensitivity of the turbine efficiency to changes in tip clearance is very important to the designer. It is usually expressed as an exchange rate: change of efficiency with change in clearance-to-span ratio, $\Delta\eta/\Delta(g/h)$. Hourmouziadis and Albrecht [21] investigated a number of shroudless turbine rig and engine tests at MTU as well as other published studies, and found the OTL exchange rate is in the range 1.5 to 3.0, with a mean of about 2.0.

For shrouded turbines, Hartley [22] shows that for a geometry with two fins and two fences (see Fig. 3) the exchange rate is reduced by a factor of 4 relative to a shroudless turbine, and by a factor of 2 with just two fins present.

An explanation of the generality of the $2.0\Delta\eta/\Delta(g/h)$ exchange rate for shroudless rotors may be found by considering the control volume analysis of Denton [1] for the mixing of the gap flow with the passage flow. Denton presents an (incompressible flow) equation for the row kinetic energy loss coefficient ζ due to OTL:

$$\zeta=\frac{2Cd}{\cos\beta_2}\left(\frac{g}{h}\right)\left(\frac{c}{s}\right)\int_0^1\left(\frac{V_s}{V_2}\right)^3\left(1-\frac{V_p}{V_s}\right)\left[1-\left(\frac{V_p}{V_s}\right)\right]^{1/2}\frac{dz}{c} \qquad (1)$$

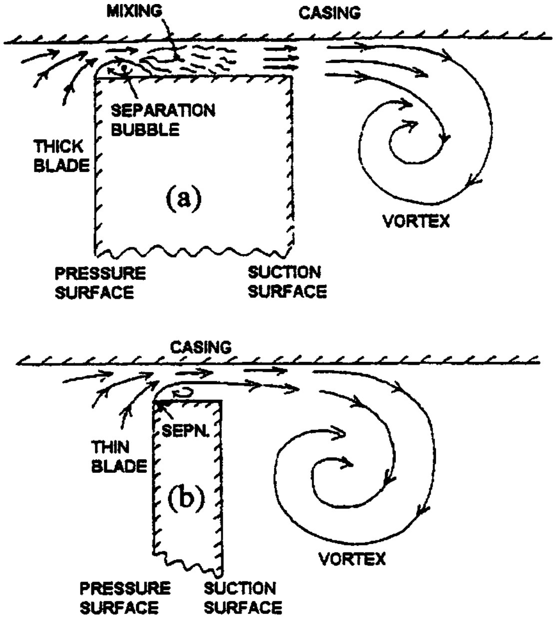

Fig. 2 Tip gap flow for an unshrouded blade [1]

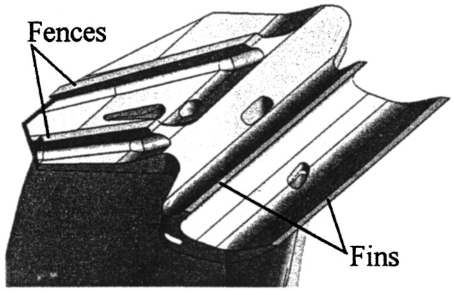

Fig. 3 Perspective view of a typical shroud top geometry for a Rolls-Royce civil HP turbine rotor

Making some further simplifying assumptions (constant lift along the rotor chord, linear variation of tan β through the rotor passage, and small blade thickness) Denton produced contours of rotor ζ at 1 percent g/h with varying inlet and exit angles. Most of the turbines considered by Hourmouziadis and Albrecht [21] have tip exit angles of 60 deg or above. For these Denton calculated values of ζ of 4 percent or more for 1 percent g/h. The percent change in stage efficiency is typically half that in the row loss (depending on reaction), giving a $\Delta\eta/\Delta(g/h)$ value of 2.0 or above.

Other researchers have further simplified the calculation of OTL loss by effectively assuming that the kinetic energy of the OTL flow *normal* to the blade surface at exit is lost in the subsequent mixing with the main stream. It is supported by Dishart and Moore [23], Yaras and Sjolander [24], and Peters and Moore [25].

Conclusions from OTL Research.

(*a*) Apart from Morphis and Bindon, researchers agree that the OTL and passage secondary flows (when present) roll up into vortices soon after the blade trailing edge. There is then little scope for recovering the energy subsequently and it will be dissipated as loss.

(*b*) The effects of relative motion between the casing and the rotor are significant and must be included in any analysis.

(*c*) The loss is largely due to the mixing of the OTL flow with the suction side free stream; a smaller amount is from mixing in the gap.

Over Tip Leakage Loss Reduction

The objective of the work presented here was to define an alternative means of controlling the OTL loss of a shroudless HP turbine rotor, other than applying a full shroud. Examination of Eq. (1) revealed a number of possible means of reducing the OTL loss at a given relative gap height g/h.

1 Reduce the discharge coefficient *Cd*.
2 Increase the pressure side velocity V_p or reduce the suction side velocity V_s—possible using a partial shroud.
3 Modify the rotor aerodynamics to reduce β_2 or increase V_2.
4 Modify the pitch/chord ratio s/c.

These options are considered in the following sections, together with the additional possibility of casing trenching.

Reduced Discharge Coefficient. This is the option most often pursued by researchers. Booth et al. [26] carried out an extensive investigation into rotor tip geometries aimed at reducing *Cd*. They found that a knife edge tip squealer had a *Cd* 25 percent lower than that for a plain tip, although the results were strongly dependent on tip gap Re and the details of the configurations. Heyes et al. [10] showed that a single suction side squealer gave the best reduction in *Cd*. Morphis and Bindon [9] gained a similar result with a contoured tip, which approximated to a suction side squealer. While these results offer the possibility of reducing loss by directly reducing the OTL flow, there are a number of problems.

(*a*) Heyes et al. showed that for any geometry to achieve a low *Cd*, the entry corner radius had to be kept below 0.5 percent chord. For a typical chord of 30 mm the radius must be less than 0.15 mm. This dimension could not be maintained for an in-service engine.

(*b*) The vena contracta in the tip gap is a loss source. The lower the *Cd*, the larger the contraction and thus the mixing loss after it. In addition, if the exit Mn is high enough, shocks will form over the contraction possibly adding to the loss; see Moore et al. [27].

(*c*) The presence of the vena contracta significantly increases the local heat transfer rates, especially at the reattachment point, as shown by Moore et al. [28] and Metzger et al. [29].

Rather than try to reduce the *Cd*, it is suggested the tip pressure surface geometry should be sufficiently radiused to remove the vena contracta thereby reducing potential in-service problems—in particular burnout at the blade tip pressure side; see Bindon [30].

Partial Shrouds (Winglets). Partial shrouds offer the possibility of modifying the local surface velocities at the rotor tip, in particular increasing V_p.

The best result for a winglet has been that of Patel [31], who obtained a stage efficiency improvement of 1.2 percent (at 3 percent tip clearance). The tip loss exchange rate, however, was surprisingly unchanged from 2.0. Booth et al. [26] investigated a number of winglet designs in a water rig. Applying one of these (it is not clear which) to a low aspect ratio transonic turbine they achieved a 0.6 percent improvement in rotor efficiency at a tip clearance of 3 percent g/h. Yaras and Sjolander [7,8] investigated winglets on the suction and pressure sides (individually and together) of a low turning aerofoil in linear cascade at 2.4 percent g/h. They obtained a reduction of 10 percent of OTL loss for each design.

Staubach et al. [32] obtained a negative result with a winglet. They were primarily studying the effect of rotor lean on OTL, but found the winglet reduced stage efficiency by 0.35 percent at 1.7 percent g/h.

No partial shroud is known to have entered commercial service.

Modified Turbine Aerodynamics. A standard approach to reducing OTL loss is to reduce the rotor tip reaction (by reducing the exit angle). Farokhi [33] shows for one turbine that reducing the tip reaction from 89 to 0 percent halved the tip loss exchange rate. This seems to contradict Denton's equation, since V_2 is reduced, which should have increased ζ. However, the lower turning results in lower V_s and in addition lower local V_2 reduces the contribution of the tip loss to the total rotor row loss.

DeCecco et al. [34] and Yamamoto et al. [18,19] also agree that off-loading the tip should reduce OTL flow. Staubach et al. [32] achieved this by bowing their rotor and thus applying a radial body force toward the casing, moving passage mass flow away from the tip. Their best result is with a tangentially bowed aerofoil only. The tip loss exchange rate was reduced by 40 percent. This is not yet, however, a mechanically acceptable option for cooled turbine rotors.

Changing Pitch/Chord Ratio. Equation (1) can be used to estimate the effect of changing the pitch/chord ratio s/c on the OTL loss.

The MT2 turbine studied in this paper (see later for details) has a tip s/c of 1.14. Loss coefficients have been compared at this s/c and at 0.57. For exit angles (β_2) of 60 deg and above, and inlet angles (β_1) of 0 deg (axial) and less, the OTL loss reduced by at least 44 percent. Equation (1) predicts that reducing s/c alone should increase ζ. However, reducing the pitch reduces both the velocity of the OTL flow and the free stream velocity V_s—which have the dominant effects on ζ.

Doubling rotor numbers (increasing the cost, weight, and cooling air requirement) is not an acceptable design solution. However, there is the possibility of having two ''aerofoils'' (or aerofoil sections) at the rotor tip, mounted on a reduced size shroud.

Table 1 Summary of parameters for validation turbines

Parameter	B22	MT2
$\Delta H/U^2$	1.79	1.68
$c_p\Delta T_0/T_{0.\mathrm{in}}$, J/Kg K	218.9	223.2
Total pressure ratio	2.62	2.72
Hub-to-tip ratio	0.83	0.83
Reaction %	42.8	49.4
Nominal tip gap, mm	0.38	0.44
Tip s/c_{ax}	1.28	1.14
Rotor mid-height conditions		
Inlet angle (deg)	46	51.5
Exit angle (deg)	−62.8	61.8
Exit Reynolds number	980,000	783,000

Casing Treatments. Offenburg [35] presents the only detailed investigation into casing ''trenching'' using a cold flow turbine. The tip loss exchange rate with a smooth casing was found to be the standard value of 2.0. He found that the usefulness of tip trenching was a function of the tip gap. At the nominal clearance level, a smooth casing was best. As the clearance increased, a backward facing step upstream of the rotor leading edge proved beneficial for clearances above 2.4 percent g/h—the initial efficiency was lower, but it had a better OTL loss exchange rate.

Conclusions for OTL Loss Reduction. From this research review it was concluded that the best opportunity for reducing OTL loss was to pursue a design of winglet that effectively doubled the number of rotor tips. This should also be combined with aerodynamically off-loading the rotor tip, but not by tangential lean of the rotor—its mechanical design was not practicable.

Reducing the tip discharge coefficient by minimizing the pressure side corner radius was rejected because of the risk of exacerbating in-service overheating problems. Reducing tip reaction is an established means of reducing OTL loss—but applying a tip ''end bend'' to a rotor was also limited by mechanical design considerations. Casing trenching seems only of use at relatively large tip clearances.

Design Methodology

A numerical investigation of different rotor tip winglet designs was undertaken with a standard turbomachinery CFD code used within Rolls-Royce [36]. The exercise was conducted on a single stage HP turbine with highly loaded aerofoils, designated ''MT2,'' the operating conditions for which are given in Table 1. Before presenting the CFD results for the final winglet design the code is described, together with a summary of its validation for turbine rotor OTL flow.

Calculation Method

The CFD code used in this study is a steady flow solver with a pressure correction method based on the algorithm of Moore [37]. A key feature is the use of upwinded control volumes for the momentum and rothalpy equations, thus allowing the equations to be discretized with second order accuracy without the need to introduce smoothing to achieve numerical stability. The iterative method used is based on the SIMPLER pressure correction scheme. Stability in transonic regions is achieved using an upwinded pressure in the calculation of density. The calculations are based on a structured ''letter-box'' type of body fitted H grid, which enables accurate representation of the full blade shape, which is then refined using mesh embedding. Previous work has shown the capa-

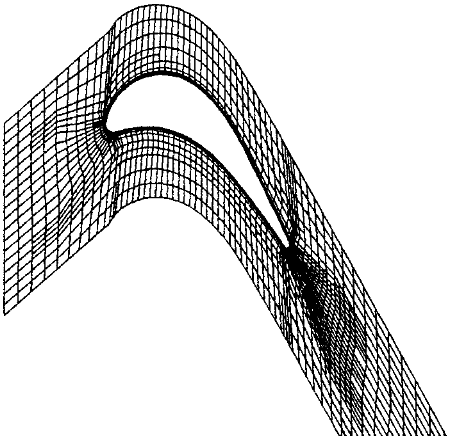

Fig. 4 Calculation grid for MT2. Blade-to-blade view 50 percent span.

bility of this method for the prediction of turbomachinery aerodynamics, e.g., Moore and Gregory-Smith [38] and Robinson and Northall [39].

Grid Details. The calculation grids were first created as a coarse definition on the blade-to-blade plane, stacked in the spanwise direction to produce three-dimensional grids, and then refined using mesh embedding, see Lapworth [40]. The maximum grid size available was about 120,000. The grid for the datum (shroudless) MT2 rotor case with 2 percent g/h is shown in Figs. 4 and 5, while the blade-to-blade grid for the winglet is shown in Fig. 6. Generally the grid definition in the free stream is coarse, with refinement only in the boundary layer, the wake regions and at the tip. Grid details are given in Table 2. The validation analyses of the two turbine rotors used a finer grid in the flow field than the winglet calculation did (which had grid lines concentrated around the winglet). As a check one calculation was repeated for the plain tip MT2 case with a similar (coarse) grid definition. All the geometries were modeled with sharp corners at the tip.

Boundary Conditions and Convergence Criteria. All the turbine rotor calculations for the validation exercises have used inlet boundary conditions (circumferentially averaged) based on measured NGV exit traverses. The MT2 winglet design studies were carried out using idealized, smoothed boundary conditions and at a slightly different reaction. The inlet relative stagnation conditions and relative angle were fixed together with the exit static pressure profile.

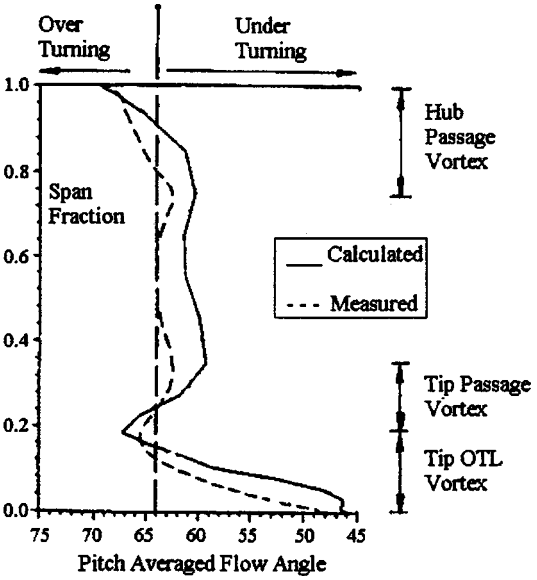

Fig. 6 Rotor cascade exit whirl angle profiles (40 percent c_{ax} downstream of trailing edge), from [45]

For the calculations for the turbine rig rotors, the boundary layers were set to zero at the inlet to the grid. Thus the skewing of the hub end wall boundary layer, as it moves from the NGV exit onto the moving rotor end wall, was not modeled. Bindon [41] showed this increases rotor hub secondary flow, which as a result is underestimated.

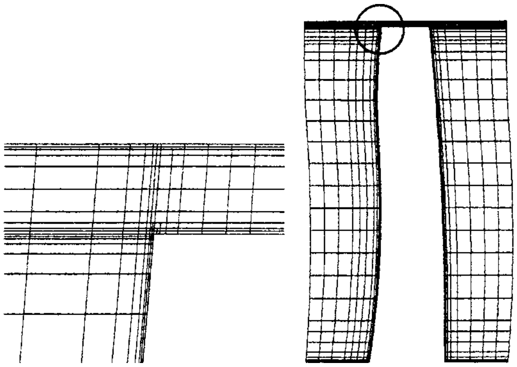

Fig. 5 Calculation grid for MT2. Axial view+pressure side tip detail, 50 percent c_{ax}.

All the boundary layers were set to be adiabatic and turbulent.

Acceptable convergence was achieved when the residuals in all three velocity components and the static pressure had fallen by at least two orders of magnitude from their initial values. Usually this should be achieved after 100 iterations. However, the complexity of the grids used here meant that up to 400 were required for some calculations.

The maximum error in mass flow conservation through the passage in any solution was 0.1 percent, and generally was within ±0.05 percent.

Turbulence Model and Wall Functions. An algebraic mixing length model was used based on Prandtl's formulation for the length scale within a shear layer. Wall functions, described in more detail in Harvey et al. [42], were adopted to represent the near wall variation of the boundary layer based on a generalized expression for the law of the wall; see also White [43] or Spalding et al. [44]. They are valid for values of y^+ up to the edge of the logarithmic region, say 100 to 200 depending on the magnitude of the local pressure gradient. Of particular importance is the ability to apply the wall function model in the buffer layer region, around $y^+=20$, and to give good results irrespective of the y^+ value which inevitably varies significantly over the aerofoil surface.

CFD Validation

Despite the extensive use of CFD, users must be realistic in their expectations of it. CFD does not calculate with equal accuracy all features of turbomachinery flow fields. The following ranking for these features is suggested (in order of decreasing calculation accuracy): static pressure; mass flow and exit angle distributions; secondary flows; overall entropy rise (in subsonic, attached flow); shocks and separations; local surface skin friction and/or heat transfer rates.

The CFD code used here is a general turbomachinery flow solver—validated for the calculation of the bulk flow field and secondary flow deviations, rather than loss. Three test cases are presented that illustrate its capability, with particular emphasis on OTL flow.

Flow Field and Exit Angle Distribution. Moore and Moore [45] present a very detailed comparison of the measured and cal-

Table 2 Summary of calculation grids

	Grid nodes					Tip gap			Near wall y^+			
Reference	Axial	Tangential	Radial	Total* (1000s)	Minimum spacing mm	g mm	g/h %	Points in gap	Average	Minimum	Maximum	Iterations to converge
Moore & Moore [45]	45	28	26	33	$(0.001)c_{\mathrm{ax}}$	5	2.1	6				
B22 Fine1	97	52	48	108	0.032	0.38	0.82	8	14	1	43	200
B22 Fine2	97	52	51	117	0.032	0.92	2.0	11	13	0.4	49	400
MT2 Rig	99	52	41	124	0.032	0.44	0.90	7	19	1.5	61	200
MT2 Fine1	97	52	44	104	0.032	0.40	0.82	8	20	2	93	400
MT2 Fine2	98	54	46	107	0.032	0.98	2.0	9	25	1	75	250
MT2 Coarse2	90	44	44	88	0.125	0.98	2.0	8	91	5	294	350
Winglet	89	65	51	115	0.125	0.98	2.0	8	83	4	281	250

*Solid nodes removed for embedded grids

culated flow fields for a rotor in linear cascade with fixed end wall. The rotor was a typical high turning blade with 45 deg inlet and −66 deg exit angles. Calculation details are given in Table 2.

The tip leakage and outer passage vortices were well modeled, as can be seen in the whirl angle distributions of Fig. 6. However, the OTL loss was underestimated by 16 percent.

Tip Loss Exchange Rate. The single stage research HP turbine ''B22'' has been the subject of extensive previous study—see [46–48]. Its operating conditions are given in Table 1. Its stage efficiency has been measured for two tip clearances, 0.82 and 1.7 percent g/h. Calculation details are given in Table 2. They were carried out at 0.82 and 2 percent g/h (referred to as ''B22 Fine1'' and ''B22 Fine2''). Figure 7 plots the measured and calculated changes in mixed-out rotor loss expressed as a loss of stage efficiency. The measured tip loss exchange rate of 2.3, close to the ''standard'' value of 2.0 identified earlier, is underestimated by 40 percent, at 1.2—this is discussed below. At the design tip clearance of 0.82 percent g/h, the code underestimated the measured loss by 32 percent. This is not surprising since unsteady effects and the correct inlet boundary layers have not been modeled.

Rotor Pressure Field. The MT2 turbine was tested only at 0.9 percent g/h. In addition to the turbine performance, on-blade surface static pressures were measured.

Static pressures measured on an aerofoil section at 93.5 percent span are presented in Fig. 8, normalized by the rig inlet total pressure, and compared with calculation on a grid plane at 96.4 percent span. There is a very good match between the two. The strong depression in the static pressure at about 70 percent chord is due to the presence of the OTL vortex. Yamamoto and Nouse [49] found in their linear cascade experiment that for any ''strong'' vortex (passage, not just OTL) there is a static pressure minimum which nearly coincides with the vortex center. This confirms that that for MT2 the OTL does roll up into a vortex (whose kinetic energy would probably not be recovered in a downstream row).

Details of the calculation are given in Table 2 (referred to as ''MT2 rig''). The code underestimates the measured rotor loss by 36 percent—a similar result to that for B22 (Fig. 7).

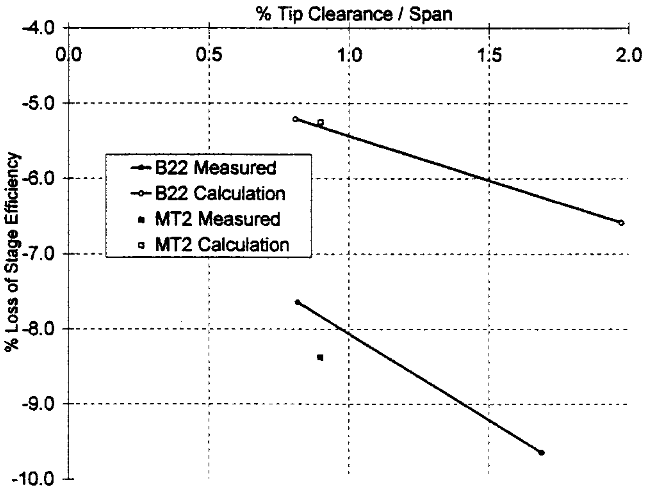

Fig. 7 Comparison of measured and calculated rotor losses (as percent stage efficiency) for Rolls-Royce model rig turbines

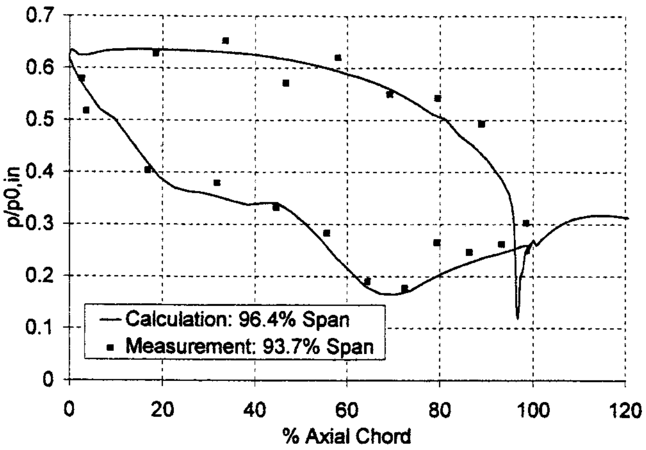

Fig. 8 Comparison of tip static pressure for the MT2 rotor

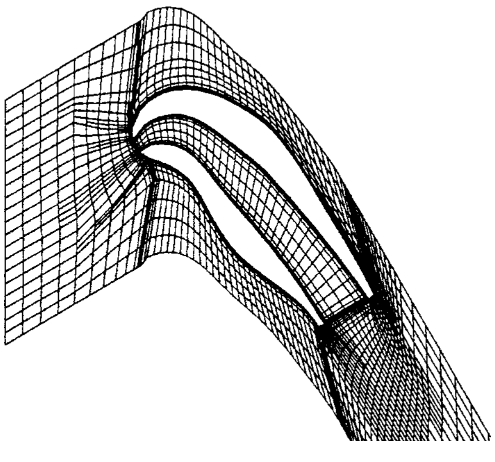

Fig. 9 Calculation grid for MT2 winglet. Blade-to-blade view.

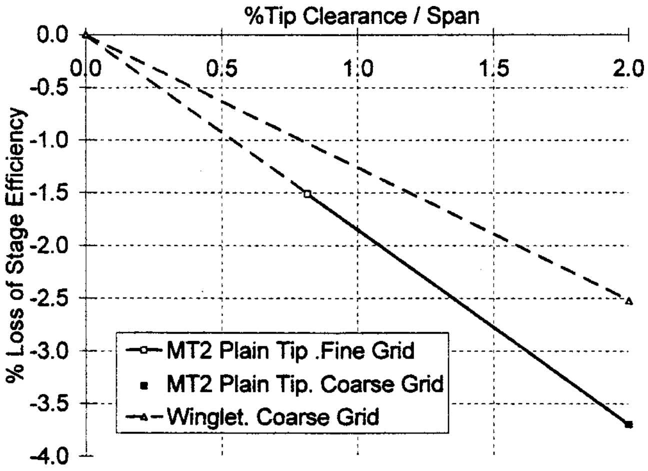

Fig. 10 MT2 rotor: Calculated OTL loss for plain tip and winglet

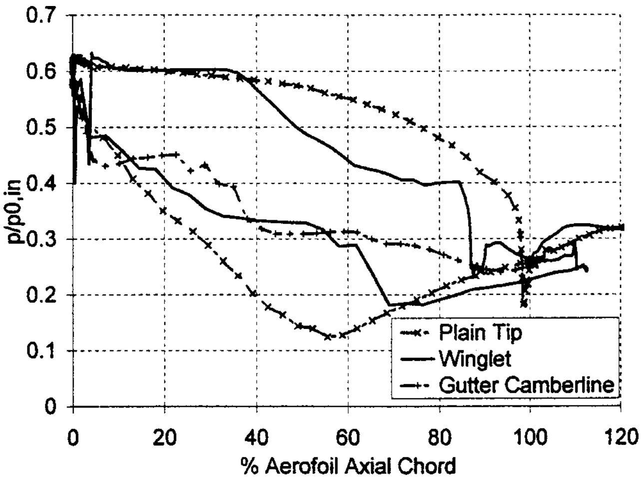

Fig. 11 Calculated static pressure distributions for MT2 rotor at 97.1 percent span, + "gutter" camberline at tip gap mid-height

Conclusions From Validation. The code can be used to calculate the static pressure field and exit whirl angle distributions in the presence of OTL. At best, it can make qualitative comparisons of the losses of different rotors, but not absolute levels. Rotor loss is underestimated by 32 percent–36 percent and the tip loss exchange rate by 40 percent. The large error in the tip loss exchange rate is disappointing. As noted before, the CFD code has previously been used for the prediction of passage flow fields, not loss. The code does not appear to resolve the mixing of the OTL jet with the free stream well; in particular the turbulent viscosity appears to be underestimated resulting in low levels of loss. This is clearly an area for future development of the code, although the detailed data required (such as measured Reynolds stresses in the OTL vortex) are in short supply. The validation presented here is limited, and to make any conclusions about the effect of the winglet on the OTL loss it has had to be assumed that the code is at least consistent in underestimating it.

New Winglet Design

From the research review it was judged that the best opportunity for reducing OTL loss was to pursue a design of partial should that effectively doubled the number of rotor tips, with the aim of

(*a*) reducing velocity of the OTL flow and of the free stream (on the suction side of the tip) that it mixes with;
(*b*) reducing the OTL mass flow by off loading the aerofoil tip, but not by significantly changing the tip gap *Cd*.

The (arbitrary) targets for the design were to halve the shroudless OTL exchange rate and to be less than half the size of a full shroud.

Figures 13 and 14 show the winglet in perspective views, while Fig. 9 shows it in plan view with the embedded calculation grid. The basic elements of the geometry are as follows.

1 There are two ''aerofoil'' shapes at the rotor tip, which form a channel or ''gutter,'' along which there is an *additional*, chordwise leakage flow from the leading edge. They are not equally spaced (pitchwise), and thus are not equally loaded aerodynamically.

2 The pressure and suction side overhangs of the winglet almost halve the passage throat width at the tip.

3 The pressure surface shape is intended to increase blockage, and thus lower the local static pressure driving the OTL flow.

The vehicle used for this study has been the single stage HP turbine MT2. A larger tip gap, 2 percent g/h, was chosen to resolve the effects of the winglet better. The turbine parameters are given in Table 1, and details of the CFD calculations in Table 2. There were three analyses of the plain tip rotor, with smoothed inlet conditions: fine grid at 0.82 percent g/h (referred to as ''MT2 Fine1'' in Table 2), 2.0 percent g/h (''MT2 Fine2''), and ''coarse'' grid at 2.0 percent g/h (''MT2 Coarse2''). The latter was for comparison with the coarse grid winglet analysis (''Winglet'').

Loss Results. Although the validation exercise concluded that the CFD code under estimates OTL and total rotor loss, these results are presented first to make some conclusions about the overall effect of the winglet.

Figure 10 shows the calculated OTL loss for the datum MT2 rotor with plain tip and with the winglet. The value of the rotor loss at zero tip clearance value was found by extrapolating from the 0.82 percent and 2.0 percent g/h (fine grid) results. This datum has been *assumed* to be the same for all the results of Fig. 10 (with and without winglet).

At 2.0 percent g/h the rotor loss is the same with coarse and fine grids, reassuringly, even though the average near wall y^+ values of 91 and 25, respectively, are opposite sides of the optimum range for the boundary layer wall functions. Although not shown here, the two flow fields are similar, but with some details lost with the coarse grid.

The calculated OTL exchange rate for MT2 is 1.85 $\Delta\eta/\Delta(g/h)$, above that calculated for the B22 turbine rotor, but not unexpected as the MT2 rotor aerofoils are more highly loaded. From the validation the ratio of measured to calculated loss is 1.5 (based on total rotor loss for B22 and MT2) Applying this factor gives an OTL exchange rate of 2.7 $\Delta\eta/\Delta(g/h)$. This is high, but is plausible for a highly loaded turbine and within the range observed by Hourmouziadis and Albrecht [21].

The striking result for the winglet is that it is calculated to improve stage efficiency by between 1.2 percent (unfactored) and 1.8 percent (factored). Figure 12 shows contours of relative total pressure ($p_{0,\mathrm{ref}}$) in the trailing edge *grid* planes (which are not wholly axial, as can be seen in Figs. 4 and 9). The reduction in the depth of the OTL vortex loss core is clear, although there is extra loss in the ''gutter.'' Equally as importantly as this, the region of loss below the OTL vortex has almost completely gone. The flow field in the plain tip case exhibits a strong interaction between the OTL and passage vortices, as seen by Yamamoto [11]. The calculation of its elimination is significant.

The winglet reduces the (unfactored) OTL loss exchange rate $\Delta\eta/\Delta(g/h)$ from 1.85 to 1.28, a reduction of 31 percent. This is short of the arbitrary target of 50 percent. However, it compares

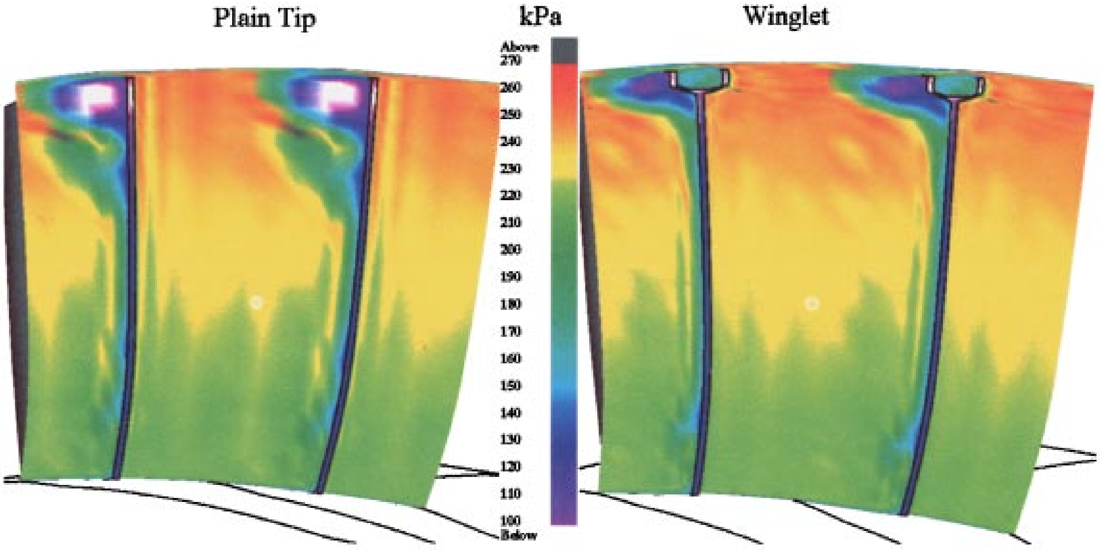

Fig. 12 Contours of calculated relative total pressure at the trailing edge grid planes for MT2 plain tip and winglet

favorably with the result of Staubach et al. [32] who achieved a reduction of 40 percent with their leant rotor, and the reduction of 44 percent predicted from Eq. (1).

The plausibility of these results is discussed in the next sections, but some comment can be made from Fig. 12 on the quality of the calculations. Total pressure oscillations in the flow field are visible in the figure; in particular there are radial striations in the contours which correlate with grid lines (not shown). This confirms grid dependency in the solutions. This is also indicated by the (unexpected) differences in detail between the $p_{0,\mathrm{ref}}$ contours in the inner half of the passage. These concerns should not be overstated, however. The effects of the winglet are still large relative to the effects of grid dependency.

Description of Flow Fields. The tip static pressure distributions give an insight into the operation of the winglet. Figure 11 compares the static pressures (normalized by stage inlet total pressure and plotted against aerofoil c_{ex}) at 97.1 percent span for the two cases. Most authors take the driving static pressures to be at about 90 percent height. A comparison plane close to the tip has had to used here to capture the effect of the winglet.

For the plain tip the difference between these pressures drives the OTL flow. In the case of the winglet the situation is more complicated. Figure 11 includes the static pressure along the gutter camberline at 99 percent span (tip gap mid-height). This is the intermediate pressure between the two halves of the winglet. Figure 11 shows that the pressure difference driving the OTL is largely across the pressure side half. There is little additional acceleration of the OTL flow across the suction side ''aerofoil'' section of the winglet. The pressure drop across its early part is negligible, and the OTL rolls up into a vortex in the gutter. Toward the trailing edge a pressure drop develops, largest between 65 percent and 85 percent c_{ex}—since to satisfy mass flow continuity some OTL flow must exit the tip gap on the suction side of the winglet.

On the pressure side the blockage of the winglet significantly lowers the driving pressure, reducing the tip leakage velocity and

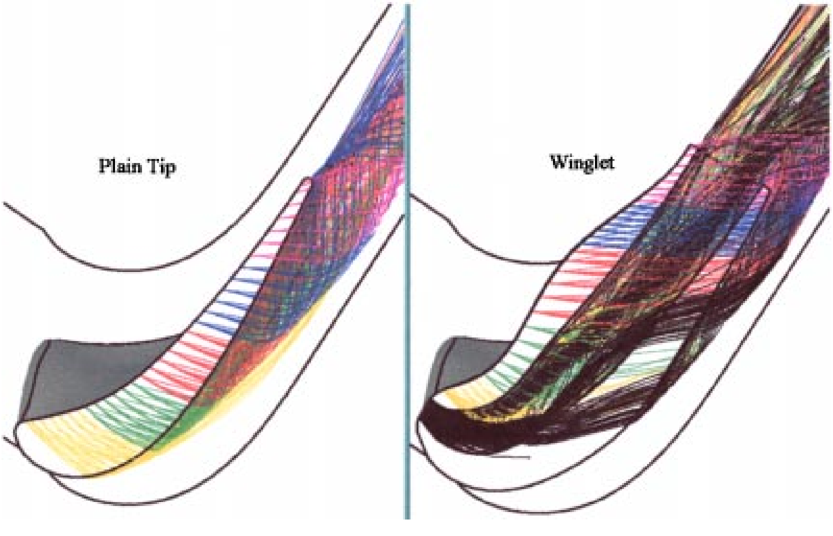

Fig. 13 Visualization of calculated OTL flow for MT2 plain tip and winglet: plan view on tip

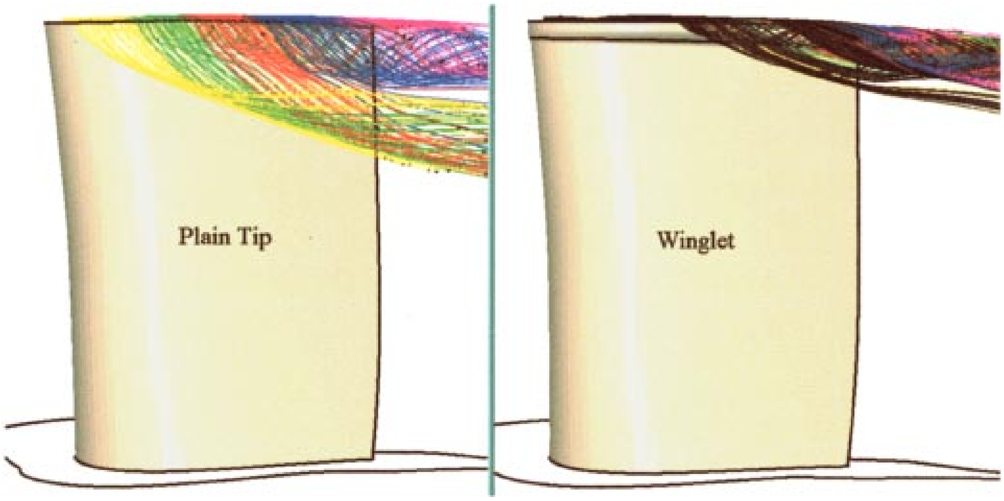

Fig. 14 Visualization of calculated OTL flow for MT2 plain tip and winglet: view on suction side

flow. Normally, this blockage would have an effect on the suction side, raising local velocities there also. However, these are reduced for the winglet. This is because the winglet aerofoil section is off-loaded relative to the plain tip—due, as noted previously, to the winglet overhang effectively halving the passage throat width at the tip.

(The pressure distributions with plain tip in Figs. 8 and 11 are not expected to be the same as they are respectively at rig test and nominal design conditions, and the tip gaps are also slightly different.)

The effect of off-loading the tip pressure distribution can be seen in Figs. 13 and 14 which show the MT2 rotor, with and without winglet, in plan view (onto the tip) and side elevation (onto the suction surface). The OTL flow has been visualized by injecting particles at every grid point in the plane at the entrance to the tip gap. The particle paths are in blocks of the same color, changed every 20 percent of chord. The same convention has been used for plain tip and winglet, with additional black particle paths injected at the entry to the ''gutter.''

For the plain tip, Figs. 13 and 14 show that the early OTL flow feeds into the outer passage vortex. This would not be expected as the two vortices are of opposite sign. The mechanism appears to be that, although there is significant OTL flow over the early suction surface, shear effects due to the relative casing motion are significant. The resulting relative velocity profile increases from near the casing to a maximum almost at the tip, and thus largely has the same vorticity as the passage vortex. After about 50 percent chord the OTL flow velocities are higher, pressure forces dominate, and the shear effect is much less. The OTL flow then rolls up into a vortex with the conventional vorticity—interacting strongly with the passage vortex subsequently.

Figures 13 and 14 also show that for the winglet the tip gap flow over the first 50 percent chord remains in the gutter or carries on into the OTL vortex—no appreciable flow enters the passage vortex. The flow angles over the tip are closer to the streamwise direction, reducing the mixing between the two streams.

The reduction in the strength of the vortices can be seen in Fig. 15 which compares the circumferentially averaged whirl angle profiles at 60 percent c_{ax} downstream of the rotor trailing edge. The whirl angles for the plain tip case have a similar form to those seen by Moore and Moore [45], see Fig. 6. Both distributions exhibit underturning in the three vortices (OTL and inner and outer passages), with overturning at the hub end wall and between the OTL and outer passage vortices. The winglet substantially reduces these angle deviations in the outer half of the passage. This would be expected to be beneficial for any downstream blade row. In the inner half of the passage the whirl angle profiles, which should be the same, are slightly different. This again highlights the issue of grid dependency. The differences between the calculations give an indication of the minimum uncertainty.

Although the winglet reduces the OTL flow velocities it does not change the flow contraction at the pressure side inlet to the gap. Velocity vectors (not shown here) confirm that this part of the flow behavior is much like that shown in Fig. 2, although the calculation grids used do not resolve the reverse flow in the separation bubble of the vena contracta well. The important result is that the winglet does not operate by significantly changing the tip gap *Cd*.

The capacity of the rotor with the winglet is only reduced by 0.3 percent, despite the off-loading of the winglet section. Examination of the aerofoil lift distributions shows that this has not been achieved by increased profile loading below the tip. It appears that the extra area of the gutter and the reduced loss compensates to maintain the capacity.

Loss Reduction Mechanisms. The off-loading of the winglet section generally reduces the OTL velocities. The OTL flow partly mixes in the gutter and on the aerofoil suction side. The main flow velocities in these locations are both reduced, relative to the suction side of the plain tip rotor, and thus the mixing losses

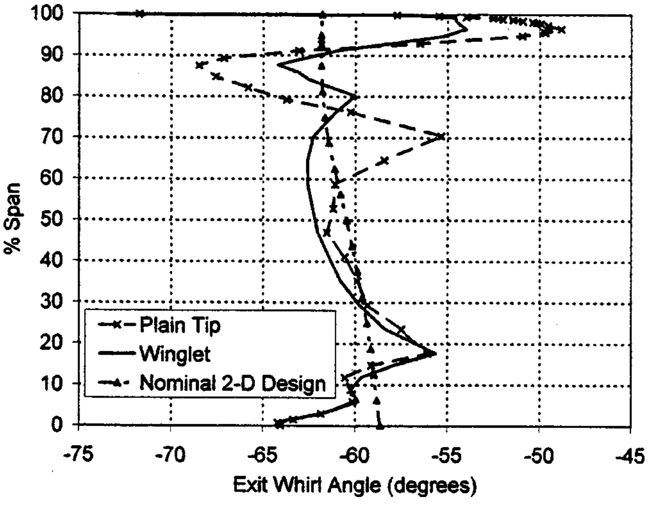

Fig. 15 Calculated exit whirl angle profiles for MT2 rotor, plain tip, and winglet, 60 percent c_{ax} downstream of trailing edge

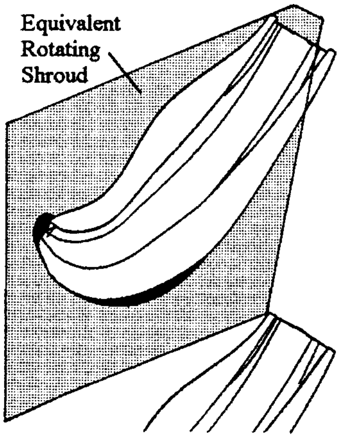

Fig. 16 Comparison of outlines of winglet and typical Rolls-Royce HP turbine (plain-sided) rotor shroud, scaled to the same c_{ax}

are reduced. Equation (1) showed that the loss depends on the cube of these velocities, and thus a significant loss reduction would be expected. The reduction in pressure loading of the tip is about 80 percent of the reduction seen by Staubach [32] for their leant rotor, and they achieved a reduction in OTL loss of 40 percent.

The reduced OTL velocities, more streamwise OTL flow angles, and thus reduced mixing losses, are a direct result of the changes to the tip pressure distribution. As discussed in the CFD validation, this should be the most accurate part of the calculated flow field. Thus the calculated reduction in OTL loss is a wholly plausible result of the operation of the winglet. The open entry to the gutter does add to the total leakage area, but this flow continues on in a largely streamwise direction. The total OTL mass flow has not significantly increased—the reduced OTL velocities at the pressure side entry to the gap outweighing the extra leakage area of the ''gutter'' entry.

Cooling and Mechanical Issues. Figure 16 compares the external shape of the winglet with that of a typical rotating shroud (scaled to the same chord), taken from Hartley [22]. The winglet extent is everywhere within that of the shroud, and thus should be mechanically feasible, except at the suction side trailing edge. This additional overhang may not be mechanically acceptable—if so a cut back version should be investigated.

Compared to a full shroud, the much smaller surface area of the winglet should mean that the total heat load would be reduced. The lower tip gap velocities should result in lower net heat transfer rates at the rotor tip relative to a shroudless rotor. However, it is still expected that positive cooling of the winglet would be necessary.

In a typical aero engine there are large radial and circumferential temperature distortions in the flow entering the rotor, with the hottest gas emerging from the upstream NGV near mid-height and mid-pitch and the coldest gas near the end walls. The ''hot streak'' from the NGV is periodically convected toward the rotor pressure surface and radially outward up it. (Doorney et al. [50] showed that the hottest gas can still enter the tip gap, near the trailing edge, by this mechanism.) Thus cooling of the pressure side ''aerofoil'' section of the winglet would be crucial to ensure its success in service—possibly using small internal convective cooling passages such as those currently applied in HP turbine rotor shrouds; see Hartley [22]. These might also eject cooling air onto the winglet surface (especially onto the pressure side) to provide an additional external barrier to the hot gas. The tip pressure side corner should be radiused to eliminate the separation bubble and prevent the high heat transfer its reattachment would cause; see Bindon [30]. This would increase the OTL mass flow but minimize the loss in the tip gap.

The open leading edge entry to the winglet should help cool it. The flow into the gutter here will be cooler gas from near the end walls (migration of the hottest gas occurs *within* the rotor passage, not before it), helping to reduce the heat load; see Lee [51].

For cooled rotors, air is ejected at the tip from ''dust holes'' at the ends of the main internal cooling passages. The visualization of Fig. 13 shows some OTL flow does remain in the gutter to the trailing edge. This could then entrain some of the ejected air which would help cool the winglet further. This might also have an aerodynamic benefit. It is thought that the fences on a full shroud (see Fig. 3) extract useful work from this ejected air; see Hartley [22]. The trailing edge geometry of the winglet is very similar to these fences and could act in the same way, providing some of this air does stay in the gutter.

Conclusions

A novel design of winglet (partial shroud) for application to an HP turbine rotor, as an alternative to a full shroud, has been derived from a study of the existing, extensive work on OTL.

The winglet has been analyzed using a steady flow CFD code, using mesh embedding to generate the complex grid.

The turbine rotor studied is highly loaded aerodynamically and, with simply a plain tip, exhibits a strong interaction between the OTL and outer passage secondary flow vortices.

The winglet is calculated to significantly reduce OTL flow and loss. A limited validation indicates it would improve the turbine stage efficiency by 1.2–1.8 percent, at a tip clearance of 2 percent g/h, and reduce the tip loss exchange rate by 31 percent (the original target was 50 percent).

A detailed examination of the calculated flow fields indicates that the basis for these predicted improvements is plausible.

The winglet is significantly smaller than a full shroud (less than half the size—the original target). It would remove the limitations of a full shroud on rotor pitch, and should require less cooling overall—but cooling the pressure side section will be critical.

Although this is only a theoretical study the winglet shows sufficient potential to warrant further experimental investigation, both to verify the concept and to provide further data for CFD validation.

Although there is some grid dependency in the CFD solutions obtained, the predicted effects of the winglet are large compared to the resulting uncertainties in the flow fields. Further development of the code is needed to improve its loss prediction capability.

A patent application has been made for the winglet ''gutter'' concept conceived during this work; see Harvey [52].

Acknowledgments

The authors would like to thank the Defense Research Agency (MoD, DTI, and CARAD), Pyestock, and Rolls-Royce plc for their permission to publish this paper. Thanks also go to Mr. G Dailey and Dr. L Lapworth for all their help and encouragement.

Nomenclature

c = Chord
Cd = Discharge coefficient, ratio of actual to ideal mass flow
c_p = Specific heat capacity (constant pressure)
CFD = Computational fluid dynamics
$\Delta H/U^2$ = Stage loading
g = Tip clearance gap
h = Blade span
HP = High pressure
Mn = Mach number
NGV = Nozzle guide vane

OTL = Over tip leakage
p = Pressure (static unless subscript denotes otherwise)
RANS = Reynolds averaged Navier-Stokes
Re = Reynolds number ($=\rho Vc/\mu$)
s = Pitch
V = Velocity
V_τ = Skin friction velocity
y = Distance normal to the surface in a boundary layer
y^+ = Nondimensional distance from the surface$=yV_\tau\rho/\mu$
z = Chordwise distance
β = Relative angle
η = Stage efficiency
μ = Viscosity
ρ = Density
ζ = Row kinetic energy loss coefficient

Subscripts

ax = Axial
in = Stage inlet
p = Pressure side
rel = Relative
s = Suction side
0 = Total/stagnation
1 = Inlet
2 = Exit

References

[1] Denton, J. D., 1993, ‘‘Loss Mechanisms in Turbomachines,’’ ASME 93-GT-435.
[2] VKI Lecture Series, 1997, ‘‘Secondary and Tip-Clearance Flows in Axial Turbines,’’ VKI LS 1997-01.
[3] Sieverding, C. H., 1985, ‘‘Secondary Flows in Straight and Annular Turbine Cascades,’’ *Thermodynamics and Fluids of Turbomachinery*, A. S. Ucer, P. Stowe, and Ch. Hirsch, eds., Nato Series, Vol. II, pp. 621–624.
[4] Bindon, J. P., 1988, ‘‘The Measurement and Formation of Tip Clearance Loss,’’ ASME 88-GT-203.
[5] Moore, J., and Tilton, J. S., 1988, ‘‘Tip Leakage Flow in a Linear Turbine Cascade,’’ ASME J. Turbomach., **100**, pp. 18–26.
[6] Heyes, F. J., and Hodson, H. P., 1992, ‘‘The Measurement and Prediction of Tip Clearance Flow in Linear Turbine Cascades,’’ ASME 92-GT-214.
[7] Yaras, M. L., and Sjolander, S. A., 1991, ‘‘Effects of Simulated Rotation on Tip Leakage in a Planar Cascade of Turbine Blades. Part I: Tip Gan Flow,’’ ASME 91-GT-127.
[8] Yaras, M. I., and Sjolander, S. A., 1991, ‘‘Effects of Simulated Rotation on Tip Leakage in a Planar Cascade of Turbine Blades. Part II: Downstream Flow Field and Blade Loading,’’ ASME 91-GT-128.
[9] Morphis, G., and Bindon, J. P., 1988, ‘‘The Effects of Relative Motion, Blade Edge Radius and Gap Size on Blade Tip Pressure Distribution in an Annular Cascade with Clearance,’’ ASME 88-GT-256
[10] Heyes, F. J. G., Hodson, H. P., and Dailey, G. M., 1991, ‘‘The Effect of Blade Tip Geometry on the Tip Leakage Flow in Axial Turbine Cascades,’’ ASME 91-GT-135.
[11] Yamamoto, A., 1989, ‘‘Endwall Flow/Loss Mechanisms in a Linear Turbine Cascade with Tip Clearance,’’ ASME J. Turbomach., **111**, pp. 264–275.
[12] Govardan, M., Venktrayulu, N., Vishnubhotla, and V. S., 1993, ‘‘Tip Clearance Effects on the Flow Field of an Axial Turbine Rotor Blade Cascade,’’ ISABE 93-7057.
[13] Graham, J. A. H., 1985, ‘‘Investigation of a Tip Clearance Cascade in a Water Analogy Rig,’’ ASME 85-IGT-65.
[14] Chan, J. K. K., Yaras, M. I., and Sjolander, S. A., 1994, ‘‘Interaction Between Inlet Boundary Layer, Tip-Leakage and Secondary Flows in a Low-Speed Turbine Cascade,’’ ASME 94-GT-250.
[15] Bindon, J. P., and Morphis, G., 1990, ‘‘The Development of Axial Turbine Leakage Loss for Two Profiled Tip Geometries Using Linear Cascade Data,’’ ASME 90-GT-152.
[16] Morphis, G., and Bindon, J. P., 1994, ‘‘The Flow in a Second Stage Nozzle of a Low Speed Axial Turbine and its Effect on Tip Clearance Loss Development,’’ ASME 94-GT-145.
[17] Morphis, G., and Bindon, J. P., 1994, ‘‘The Performance of a Low Speed One and a Half Stage Axial Turbine with Varying Rotor Tip Clearance and Tip Gap Geometry,’’ ASME 94-GT-481.
[18] Yamamoto, A., Tominga, J., and Matsunuma, T., 1994, ‘‘Detailed Measurements of Three-Dimensional Flows and Losses Inside an Axial Flow Turbine Rotor,’’ ASME 94-GT-348.
[19] Yamamoto, A., Matsunuma, T., and Ikeuchi, K., 1994, ‘‘Unsteady Endwall/Tip-Clearance Flows and Losses Due to Turbine Rotor-Stator Interaction,’’ ASME 94-GT-461.
[20] Stakolich, E. G., and Stromberg, W. J., 1983, ‘‘JT9D Performance Deterioration Results From a Simulated Aerodynamic Load Test,’’ AIAA J. Aircraft, **20**, No. 8, pp. 650–658.
[21] Hourmouziadis, J., and Albrecht, G., 1987, ‘‘An Integrated Aero/Mechanical Performance Approach to High Technology Turbine Design,’’ AGARD-CP-421, ‘‘Advanced Technology for Aero Gas Turbine Components.’’
[22] Hartley, R., 1996, ‘‘High Pressure Turbine Tip Clearance Performance Investigation,’’ M.Sc. thesis, Cranfield University.
[23] Dishart, P. T., and Moore, J., 1989, ‘‘Tip Leakage Losses in a Linear Turbine Cascade,’’ ASME 89-GT-56.
[24] Yaras, M. I., and Sjolander, S. A., 1990, ‘‘Prediction of Tip-Leakage Losses in Axial Turbines,’’ ASME 90-GT-154.
[25] Peters, D. W., and Moore, J., 1996, ‘‘Tip Leakage Loss Development in a Linear Turbine Cascade,’’ AGARD CP 571-12.
[26] Booth T. C., Dodge, P. R., and Hepworth, H. K., 1981, ‘‘Rotor-Tip Leakage Part I—Basic Methodology,’’ ASME 81-GT-71.
[27] Moore, J., and Elward, K. M., 1992, ‘‘Shock Formation in Overexpanded Tip Leakage Flow,’’ ASME 92-GT-1.
[28] Moore, J., Moore, J. G., and Henry, G. S., 1989, ‘‘Flow and Heat Transfer in Turbine Tip Gaps,’’ ASME J. Turbomach., **111**, pp. 73–79.
[29] Metzger, D., Rued, K., and Chyu, M., (1989), ‘‘Influence of Clearance leakage on Turbine Heat Transfer at and near Blade Tips. Summary of Recent Results,’’ AIAA 89-0327.
[30] Bindon, J. P., 1987, ‘‘Pressure Distributions in the Tip Clearance Region of an Unshrouded Axial Turbine as Affecting the Problem of Tip Burnout,’’ ASME 87-GT-230.
[31] Patel, K. V., 1980, ‘‘Research on a High Work Axial Gas Generator Turbine,’’ SAE 800618.
[32] Staubach, J. B., Sharma, O. P., and Stetson, G. M., 1996, ‘‘Reduction of Tip Clearance Losses Through 3-D Airfoil Designs,’’ ASME 96-TA-13.
[33] Farokhi, S., 1988, ‘‘Analysis of Rotor Tip Clearance Loss in Axial-Flow Turbines,’’ J. Propulsion, **4**, No. 5, pp. 452–457.
[34] De Cecco, S., Yaras, M. L., and Sjolander, S. A., 1995, ‘‘Measurements of the Tip-Leakage Flow in a Turbine Cascade With Large Clearances,’’ ASME 95-GT-77.
[35] Offenburg, L. S., Fischer, J. D., and Hoek, T. J., 1987, ‘‘An Experimental Investigation of Turbine Case Treatments,’’ AIAA-87-1919.
[36] Harvey, N. W., 1997, ‘‘Over Tip Leakage Control in Axial Flow Turbines,’’ M.Sc. thesis, Cranfield University.
[37] Moore J. G., 1985, ‘‘Calculation of 3D Flow Without Numerical Mixing,’’ AGARD-LS-140 on 3D Computation Techniques Applied to Internal Flows in Propulsion Systems, pp. 8.1–8.15.
[38] Moore H., and Gregory-Smith D. G., 1996, ‘‘Transition Effects on Secondary Flows in a Turbine Cascade,’’ ASME 96-GT-100.
[39] Robinson C. J., Northall J. D., and McFarlane C., 1989, ‘‘Measurement and Calculation of the Three-Dimensional Flow in Axial Compressor Stators, With and Without End Bends,’’ ASME 89-GT-6.
[40] Lapworth, B. L., 1993, ‘‘Three-Dimensional Mesh Embedding for the Navier-Stokes Equations Using Upwind Control Volumes,’’ Int. J. Numer. Methods Fluids, **17**, pp. 195–220.
[41] Bindon, J. P., 1980, ‘‘Exit Plane and Suction Surface Flows in an Annular Turbine Cascade With a Skewed Inlet Boundary Layer,’’ Int. J. Heat Fluid Flow, **2**, No. 2, pp. 57–66.
[42] Harvey, N. W., Rose, M. G., Coupland, J., and Jones, T. V., 1998, ‘‘Measurement and Calculation of Nozzle Guide Vane End Wall Heat Transfer,’’ ASME 98-GT-66.
[43] White F. M., 1991, *Viscous Fluid Flow*, McGraw-Hill, New York.
[44] Spalding D. B., and Patankar S. V., 1967, ‘‘Heat and Mass Transfer in Boundary Layers,’’ *Morgan-Grampian*.
[45] Moore, J., and Moore, J. G., 1991, ‘‘A Computational Study of Tip Leakage Flow and Losses in a Linear Turbine Cascade,’’ AGARD Conference Proceedings No. 510 on CFD Techniques for Propulsion Applications, San Antonio, Texas.
[46] Sheard, A. G., 1989, ‘‘Aerodynamic and Mechanical Performance of a High Pressure Turbine Stage in a Transient Wind Tunnel,’’ D.Phil. thesis, University of Oxford.
[47] Dietz, A. J., 1990, ‘‘Blade Surface Pressure Measurements on the Rotor of a Model Turbine Stage in a Transient Flow Facility,’’ D. Phil. thesis, University of Oxford.
[48] Garside, T., 1995, ‘‘The Heat Transfer and Aerodynamic Performance of a Rotating Turbine in the Absence of Upstream Nozzle Guide Vanes,’’ D. Phil. thesis, Oxford University.
[49] Yamamoto, A., and Nouse, H., 1988, ‘‘Effects of Incidence on Three-Dimensional Flows in a Linear Turbine Cascade,’’ ASME 88-GT-110.
[50] Doorney, D. J., Davis, R. L., Edwards, D. E., and Madavan, N. K., 1990, ‘‘Unsteady Analysis of Hot Streak Migration in a Turbine Stage,’’ AIAA-90-2354.
[51] Lee, Ching-Pang, Pietraszkiewicz, E. F., Prakash, C., and Zerkle, R. D., 1994, ‘‘Turbine Blade Having Tip Slot,’’ U.S. patent 5503527.
[52] Harvey, N. W., 1996, ‘‘Turbine Rotor Blades,’’ Patent GB 9607578.

F110-GE-132: Enhanced Power Through Low-Risk Derivative Technology

A. R. Wadia

F. D. James

Large Military Engine Systems Design
and Integration,
GE Aircraft Engines,
Cincinnati, OH 45215

The F110-GE-132, originally referred to as the F110-GE-129 EFE (Enhanced Fighter Engine), presently undergoing qualification testing, is being offered at two different thrust/inspection levels with a maximum augmented thrust of 34,000 pounds. The EFE has been developed using low-risk derivative engine technology. It features a new increased airflow, high efficiency, three-stage long chord blisk fan, and an advanced radial augmentor that reduces complexity, improves maintainability, and provides increased parts life. The paper first provides a historical background of the F110 engines to relate the heritage of the F110-GE-132. The F110 engine model development roadmap is shown to illustrate the incremental low-risk approach used to provide thrust growth with improved product reliability. A detailed description of the unique power management features of the EFE engine to meet individual customer thrust and life requirements is outlined. The long chord blisk fan design, development, and test results are presented, followed by a description of the radial augmentor and the exhaust nozzle. The EFE engine has successfully completed sea level static and altitude development testing and fan aero mechanical qualification at the AEDC in Tullahoma, Tennessee. [DOI: 10.1115/1.1378301]

Historical Background

The development of the F110 engine family has paralleled the dynamic growth of Lockheed Martin's F-16 fighter aircraft. The F110 engine product development roadmap is presented in Fig. 1. The increase in thrust (pounds) with improvement in life (TACs), shown in Fig. 2, illustrates the deliberate path taken by GE Aircraft Engines to use a low-risk derivative engine approach to grow the F110 engine model over the last fifteen years without sacrificing reliability. Figures 1 and 2 are valuable for establishing the current industry standards and state-of-the-art and for identifying future priorities.

The F110-GE-100, rated at 28,000 pound thrust, was deployed on the first United States Air Force F110 powered F16-C/D in October 1986. The F110-GE-100 was introduced to the Air National Guard in June 1991 and to the USAF Reserve in August 1992 and has accumulated nearly 2 million engine flight hours with an unscheduled, engine-caused shop visit rate of 3.45 visits per 1000 flight hours. It currently powers the U.S. Air Force's F-16C/Ds throughout Europe and the Pacific; and has served as the ''Fighting Falcon'' adversary aircraft for the United States Navy's Top Gun program. Since its inception in 1986, the governments of Bahrain, Egypt, Greece, Israel, and Turkey have also chosen the F110-GE-100 to power their front-line fighters. In follow-on purchases, these governments have continued to select the F110 as the engine of choice for the F-16 due to its performance characterized by unrestricted throttle operation throughout the flight envelope and an improved rate of climb. The F110-GE-400, a derivative of the F110-GE-100, powers the U.S. Navy's F-14B and F-14D Tomcat.

The focus on reliability of the F110 fighter engine has continued into the current production F110-GE-129 Increased Performance Engine (IPE). The IPE is a 29,000 pound thrust class engine that has extended a strong fundamental heritage of stall free operability and unrestricted throttle movement which allows the pilots to concentrate on the mission instead of the machine. The IPE's high cycle durability, mature reliability—because of extensive parts commonality (81 percent) with the F110-GE-100—and full thrust retention, has translated into highly desirable in-commission rates and safety records for single engine applications. A good match between the aircraft inlet airflow and engine combination has provided pilots with better penetration performance for strike missions. Engine maintenance was designed to be conducted at the base level to provide maximum self-sufficiency and significant cost savings for the military. Since its deployment in the field in 1992, the IPE has logged over a quarter of a million engine flight hours with an unscheduled engine-caused shop visit rate of less than one visit per 1000 flight hours.

Other F110 engine developments [1] include a highly successful demonstration in the AVEN® thrust vectoring initiative, a rigorous flight test demonstration program utilizing the U.S. Air Force NF-16D VISTA platform. During this effort, the F110 en-

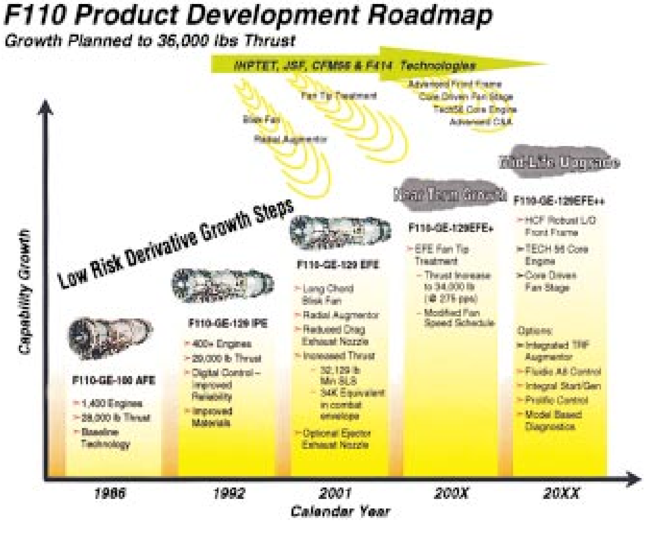

Fig. 1 F110 engine model product development roadmap

Contributed by the International Gas Turbine Institute and presented at the 45th International Gas Turbine and Aeroengine Congress and Exhibition, Munich, Germany, May 8–11, 2000. Manuscript received by the International Gas Turbine Institute February 2000. Paper No. 2000-GT-578. Review Chair: D. Ballal.

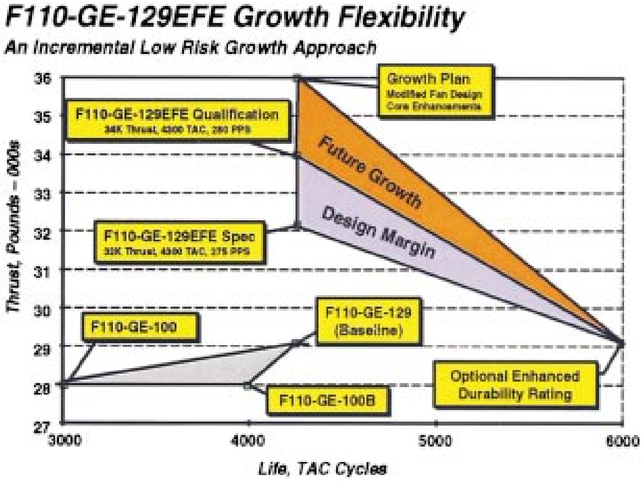

Fig. 2 Reliability and thrust growth provide flexibility to satisfy a wide range of future customer requirements

dured extreme levels of airflow distortion and operated flawlessly in performing super-maneuvers such as the Cobra and the J-Turn.

In 1999, the F110-GE-129 successfully completed flight testing on the McDonnell Douglas F-15E Strike Eagle and is now qualified for new installations or re-engining of the F-15E fleet. The robust F110-GE-129's 275 lbs/sec inlet airflow capability is another good match with the F-15 inlet, paying off in significant range advantages on low-altitude strike scenarios and other combat missions.

Other applications of the F110-GE-129 IPE include powering Japan Air Self Defense Force's (JASDF) F-2, and a derivative of the F110, the F118, powers the B-2 bomber and the U-2 reconnaissance aircraft.

F110-GE-129 EFE New Features and Thrust Requirements

Based on the F110 product growth plan (see Figs. 1 and 2) that utilizes a low-risk derivative approach, GE Aircraft Engines has developed the F110-GE-132 to meet future operational requirements and market opportunities. Technological advances in the

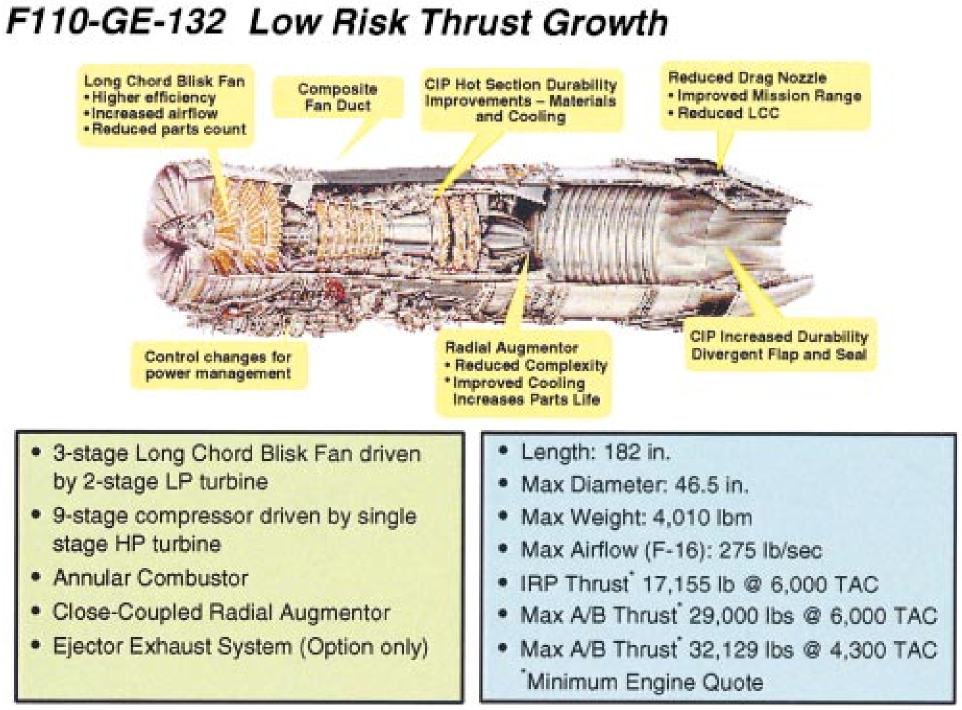

- 3-stage Long Chord Blisk Fan driven by 2-stage LP turbine
- 9-stage compressor driven by single stage HP turbine
- Annular Combustor
- Close-Coupled Radial Augmentor
- Ejector Exhaust System (Option only)

- Length: 182 in.
- Max Diameter: 46.5 in.
- Max Weight: 4,010 lbm
- Max Airflow (F-16): 275 lb/sec
- IRP Thrust* 17,155 lb @ 6,000 TAC
- Max A/B Thrust* 29,000 lbs @ 6,000 TAC
- Max A/B Thrust* 32,129 lbs @ 4,300 TAC

*Minimum Engine Quote

Fig. 3 F110-GE EFE new features

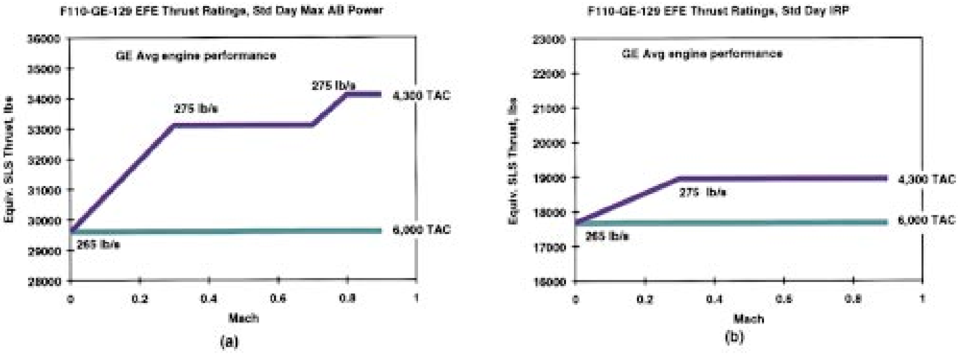

Fig. 4 F110-GE-132 average thrust ratings on a standard day: (*a*) max A/B power; (*b*) intermediate rated power (dry)

EFE, as illustrated in Fig. 3, include a three-stage long chord blisk fan and an advanced radial augmentor. Other changes include a lightweight filament wound composite fan duct, and control system enhancements to power manage the engine up to 34,000 pounds thrust. Durability improvements from current production engine component improvement programs (CIP) for the turbine hot section and exhaust nozzle divergent flaps and seals, form an integral part of the F110-GE-132. The F110-GE-132 has an option to use an ejector nozzle, which results in a significant improvement in exhaust nozzle parts life while at the same time lowering exhaust system weight.

The F110-GE-132 is being offered at two different thrust/inspection levels, as shown in Fig. 4. On a standard day with full afterburner augmentation, these two power ratings are 29,600 pounds of thrust (average, statically) with a 6000 TAC ENSIP overhaul inspection interval [2] or the 33,000 pounds thrust (average) with 4300 TAC ENSIP overhaul inspection interval.

The EFE control system currently provides 34,000 pounds maximum augmented thrust on an average engine basis with a 0.9 Mach number signal when operating in the higher thrust mode. An increasing Mach number signal into the engine control raises fan operating line schedules to increase airflow and available thrust automatically. This increased performance is delivered in the heart of the operational flight envelope where it is tactically useful. As the 34,000 pound thrust option is already automated within the control schedules, no interaction by the pilot is required to achieve this performance and the EFE operating in this mode has the full 4300 TAC durability without any time limitations. At Intermediate Rated Power (IRP), the EFE in the higher thrust mode is capable of producing 19,000 pounds average SLS equivalent thrust. This performance is also achieved at the full 4,300 TAC rating without any time limitations or pilot interaction.

The F110-GE-132 offers the user flexibility in trading performance for life, as shown in Figs. 2–4. However, applying these options requires consideration of all components within the engine. A balance between the advantages gained from the thermodynamic cycle and the mechanical structure's ability to sustain these benefits is required. In selecting the increased performance option, the turbine is the area within the engine that shoulders the maximum life penalty due to increased temperatures. The current production F110-GE-129 has demonstrated more than adequate temperature margin in field service as seen by the absence of hot section failures, no related in-flight shutdowns or power losses, and zero performance-related removals. An additional method of evaluating the mechanical robustness of an engine is through weight growth required for the other components to adapt to the increase in thrust with the new fan. In the case of the F110-GE-132, the small weight increase is associated with the new fan module. This weight increase is a direct consequence of applying long chord fan aerodynamics technology to achieve thermodynamic improvements.

EFE Fan Design and Test Results

The cornerstone of the EFE is a higher airflow long chord blisk fan, adapted from the F118-GE-100 engine used on the B-2 bomber. The blisk design used technology leveraged off the F118 and other IHPTET fans, and incorporated practical lessons learned from F110 field experience to obtain high fan efficiency and improve durability, performance, and thrust. Figure 5 shows the technology trends in fan efficiency between the current production F110-GE-129 fan and some highly loaded, advanced technology IHPTET fans. In engine tests, the F110-GE-132 blisk fan exceeded these IHPTET goals while providing significant improvements in maintainability, reliability, and safety.

A comparison of the fan aerodynamic design point parameters between the current production F110-GE-129 IPE and the F110-GE-132 is shown in Table 1. The significant improvement in fan efficiency at cruise relative to the current production fan translates into lower turbine temperatures that results in increased hot parts life.

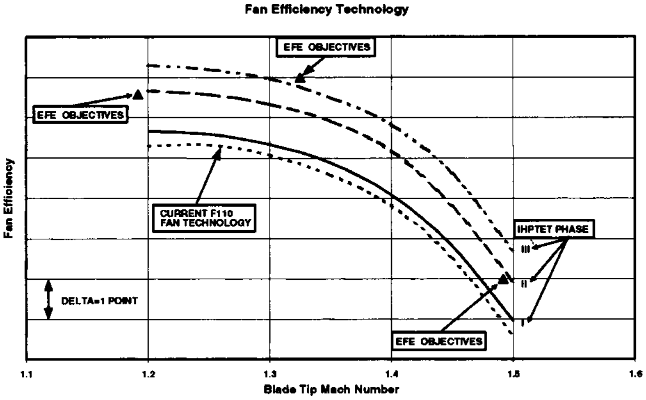

Fig. 5 Fan efficiency technology comparison

Figure 6 shows the comparison of the F110-GE-129 current production fan with the EFE blisk. Significant design, development, repair, and field experience has been accumulated with blisks on the T700 helicopter engines, the LM2500+ Marine and Industrial engines, the F120 ATF/JSF engines and the F414 engines for the Navy F-18E/F. All three stages of the F110-GE-132 fan are of blisk construction. The assembled fan rotor is shown in Fig. 7. The blisk configuration produces a reliability improvement over the current system by eliminating potential sources of high stress regions such as blade dovetails and midspan shrouds [2]. This simplified configuration also reduced the fan module part count by over 65 percent.

The first stage of the F110-GE-132 fan incorporates long chord fan aerodynamic technology while eliminating the midspan shroud and dovetails using blisk technology. The airfoils are robust and have thicker blade leading edges relative to its IPE predecessor (shown in Fig. 8) with on-wing blend limits increased twofold. Recently developed laser shock peen (LSP) technology is also applied to the stage 1 fan blade, reducing crack propagation and further enhancing FOD tolerance capabilities. In engine tests, intentionally damaged LSP fan blades have passed full AMT endurance testing without cracking and the LSP process has been qualified for the current production F110-GE-129.

The F110-GE-132 fan airfoil aerodynamic design uses the latest three-dimensional viscous design codes to increase efficiency [2] and minimize the performance impact of the above-mentioned thickness increases. Blade mean camber line shapes were custom tailored [3] to reduce the shock losses associated with the larger blade wedge angle as a result of an increase in the leading edge thickness. The EFE fan hub end wall contours were also customized to reduce the impact of airfoil maximum thickness increase required to eliminate the midspan shroud. Fan stage 1 vane was leaned, similar to that in the F118-GE-100, to reduce hub inlet Mach numbers and have shock free diffusion along the stator surface for increased performance.

An example of aerodynamic development for the EFE unique closely coupled fan frame and outlet guide vanes is described below. In cutting the engine length to make the long chord blisk

Table 1 Fan aerodynamic design point comparison

Parameters	F110-GE-129	F110-GE-129 EFE
Inlet Corrected Flow (lbs/sec)	269	294
Inlet Corrected Tip Speed (ft/sec)	1400	1483
Pressure Ratio	3.4	4.2

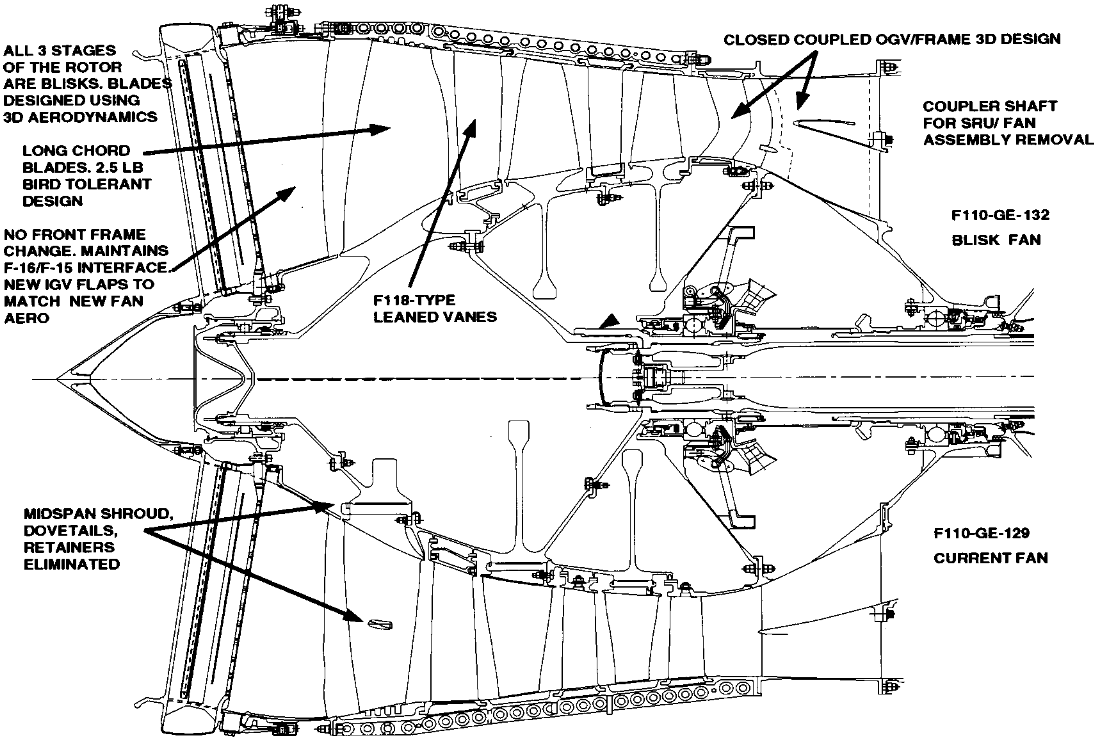

Fig. 6 F110-GE-132 fan design features: EFE fan is physically interchangeable with current production EFE fan. No change in airframe/engine interface is required as the inlet diameter is identical between the two fans.

fan adaptable for the F-16, the outlet guide vanes were packaged closer to the fan frame, as illustrated in Fig. 6. Although only 1.4 inches shorter in length to the fan frame struts, this reduction could not only create an undesired back pressure, with potential to hurt performance and aerodynamic stability, but it could also adversely impact the fan distortion transfer to the compressor. The three-dimensional design of the closely coupled OGV-Fan Frame system described below eliminated this risk. The length and inlet diameter constraints applied to the long chord blisk fan design are significant as they provide the customer with the flexibility to either use the EFE in new aircraft purchases or to retrofit the current production F110-GE-129 IPE fleet with the more efficient blisk fan during the IPE engine's 8000 TAC depot inspection visit.

Commercial aircraft engine applications have for a long time relied on the principle of using non-axisymmetric stator configurations ahead of pylons/struts to achieve a uniform flow field upstream of the stators. This approach is described in the papers by Hemsworth [4] for the General Electric TF-39 engine and by Rubbert et al. [5] for an alternative engine installation on the Boeing 747 aircraft. As a practical alternative to building stator cascades with different camber angles, the F110-GE-132 design started by first considering a slightly more attractive option that lowered the cost of implementation by using circumferentially re-staggered stator vanes to guide the exit flow aerodynamically from the stator trailing edge smoothly around the strut leading edge. To reduce maintenance costs even further, the design evolved into a unique

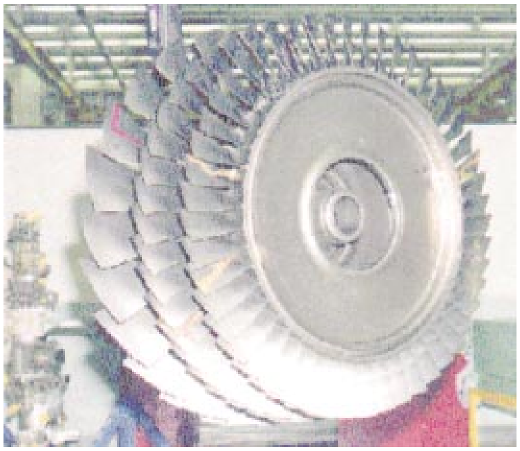

Fig. 7 F110-GE-132 assembled blisk fan rotor. The blisk fan produces reliability improvements over the current system by eliminating potential sources of high stress regions such as blade dovetails and midspan shrouds.

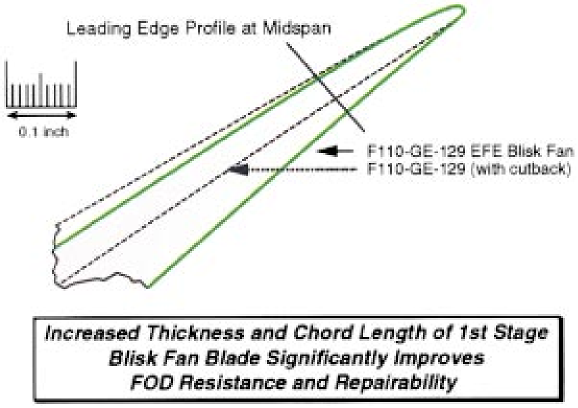

Fig. 8 EFE stage 1 fan blade with thicker blade leading edge

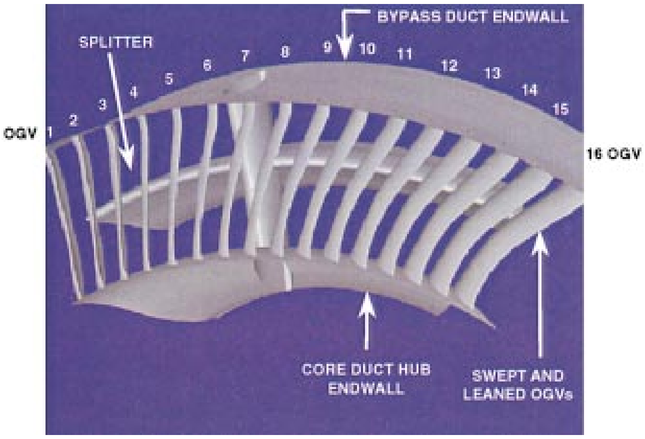

Fig. 9 Three-dimensional pictorial view of the closely coupled fan frame and exit guide vane system

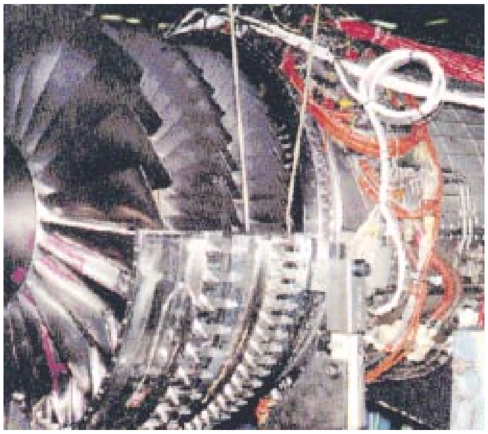

Fig. 11 Instrumented EFE blisk installed in the F110 engine for aeromechanical qualification

set of swept and leaned fan outlet guide vanes that eliminate the complexity of local tailoring (i.e., the need to use different ''vane-types'' or ''vane re-stagger''). Figure 9 shows a three-dimensional pictorial view of the closely coupled fan frame/outlet guide vane system.

Both configurations (i.e., the ''vane constant-stagger'' and ''vane re-stagger'') were analyzed and tested in the full engine environment, including inlet distortion. The tests demonstrated that no reduction in the fan's performance and stability resulted from this reduced length design. Test results showed that the more expensive ''re-stagger'' option with the swept and leaned fan exit guide vanes was not required. The aerodynamic design of the closely coupled fan frame system, highly complex three-dimensional analyses, and engine test results have been reported by Wadia et al. [6]. Figure 10 illustrates an example of the calculated entropy (loss) contours showing the stator wake streaks along both the upper and lower splitter surfaces and also along the inner and outer flowpath surfaces. The splitter, which has to accommodate a significant swing in its leading edge incidence with changes in bypass ratio, is well behaved as represented by the very low loss level shown in ''blue.'' The highest loss levels near the outer wall of the bypass stream are shown in ''red.'' The exit guide vane wakes show up as distinct ''dark blue'' and ''red'' entropy contours along the splitter and endwall surfaces.

General Electric's company-wide quality initiatives [7] entitled Design for Six Sigma (DFSS) and Design for Reliability (DFR) were used to produce the fan blisks. These processes established six sigma capable tolerance levels for a new size range of production titanium blisk airfoils, particularly stage 1, for the critical to quality (CTQ) characteristics such as leading edge thickness, leading edge profile, and blade twist angle. The long chord blisk fan demonstrated excellent structural capabilities in two aero-mechanical design and test iterations. The instrumented blisk to qualify the fan to meet the U.S. Air Force requirements is shown in Fig. 11.

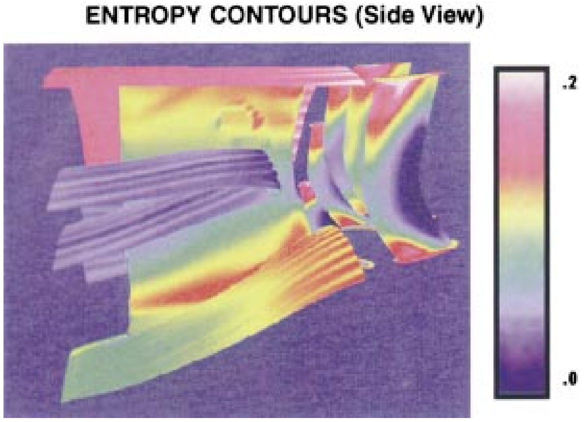

Fig. 10 Entropy contours along the fan frame strut, splitter, and exit guide vanes showing stator wake streaks along the splitter surfaces and outer and inner endwall surfaces

The long chord blisk fan accumulated over 700 hours of test time including over 500 hours of testing at altitude conditions. Testing covered a wide range of flight conditions and power settings from sea level to 40,000 feet/Mach 2.0, idle to 34,000 pounds thrust at standard and hot day operations. Aero-mechanical test data acquired in General Electric's test facilities in Evendale and in the altitude test facilities at Arnold Engineering Development Center (AEDC) in Tullahoma, Tennessee, resulted in resonant responses for all the blades and vanes below GE's design practices and the U.S. Air Force HCF criterion. In addition to the optimized aero-mechanical design, the fan exceeded the EFE efficiency objectives shown in Fig. 5 by an additional 1.5 percent while meeting all its operability requirements.

Radial Augmentor Design and Test Results

The F110-GE-132 features a radial augmentor derived from concepts embodied in the F120 and F414 programs. It provides reduced complexity, improved maintainability, and reliability with over 50 percent improvement in parts life due to advanced cooling of the augmentor parts. Figure 12 shows the comparison between the current production IPE and the EFE augmentor. Some of the unique features of the EFE augmentor are also summarized in the attached table in Fig. 12. The centerbody in the F110-GE-132 is truncated for heatshield (LRU) removals, resulting in a significant (90 percent) reduction in maintenance man hours. The radial augmentor not only lowers LRU removal and shop visit rates, but also reduces the augmentor weight by about 3 percent relative to the current production augmentor. The radial augmentor also has a 50 percent reduction in part numbers and a 15 percent reduction in parts count relative to the current production augmentor.

Like the blisk fan, the radial augmentor was also developed using highly complex three-dimensional CFD analyses. Each element contained in the augmentor shown in Fig. 12 was modeled in the analysis. The model started at the turbine rear frame exit and ended at a predetermined distance aft of the exhaust duct liner. The model spanned 22.5 deg from a fan chute centerline to the adjacent fan chute centerline with periodic boundary conditions imposed on the sidewalls. The model included mixer chutes, wall flameholders, radial heatshield/flameholder, centerbody, spraybars, liners, and blockages due to struts and hangers. Liner

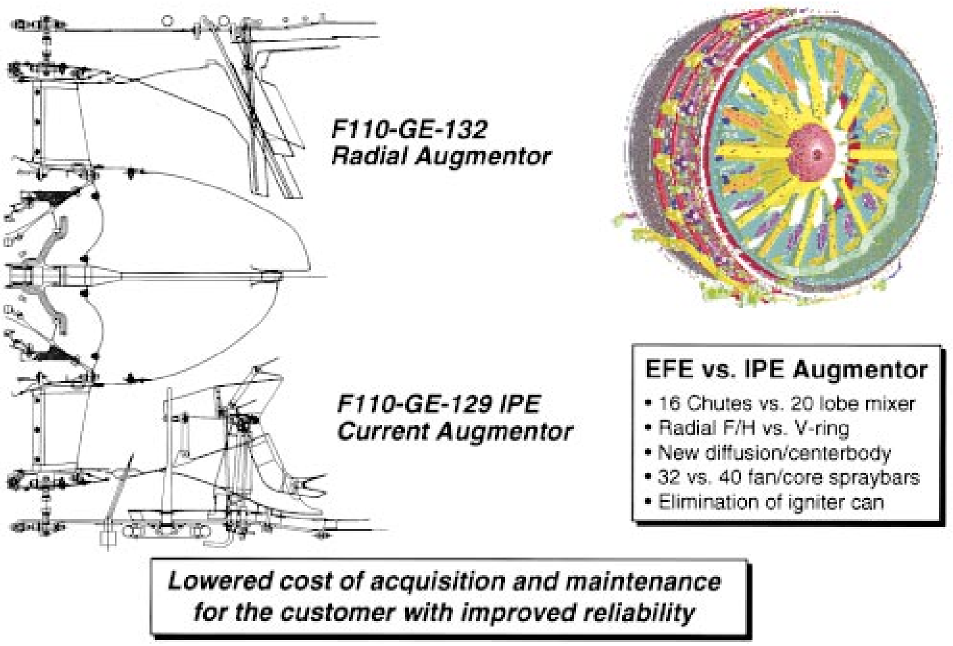

Fig. 12 F110-GE-132 radial augmentor features

screech and cooling holes were treated as porous media flow cells in the analysis. The geometric complexity of the augmentor was accurately modeled with a grid system that exceeded two million grid points.

The analysis was first validated with extensive on-line gas analysis (OLGA) data from the current production augmentor to develop a sound understanding of the inner workings of the three-dimensional computer code. The radial augmentor design was analyzed using the calibrated three-dimensional analyses. The analytical results were used to improve the radial augmentor design. The analyses provided a significant reduction in the time spent on developing the augmentor on the engine. Figures 13 and 14 show a typical example of the large body of data generated by the three-dimensional analyses. Shown here are the velocity vectors in a cross section of the current production (IPE) and the EFE radial augmentors, respectively. The large flow re-circulation (vortex) downstream of the flameholder, shown in Fig. 14, provides more useful mixing in the case of the radial augmentor. The temperature contours for the EFE radial augmentor calculated by the complex three-dimensional analyses at a prescribed after burner flight condition is shown in Fig. 15.

The radial augmentor, developed using the three-dimensional CFD analyses, demonstrated good efficiency and light-off characteristics (quick and stable lights) in 450 hours of total test time on

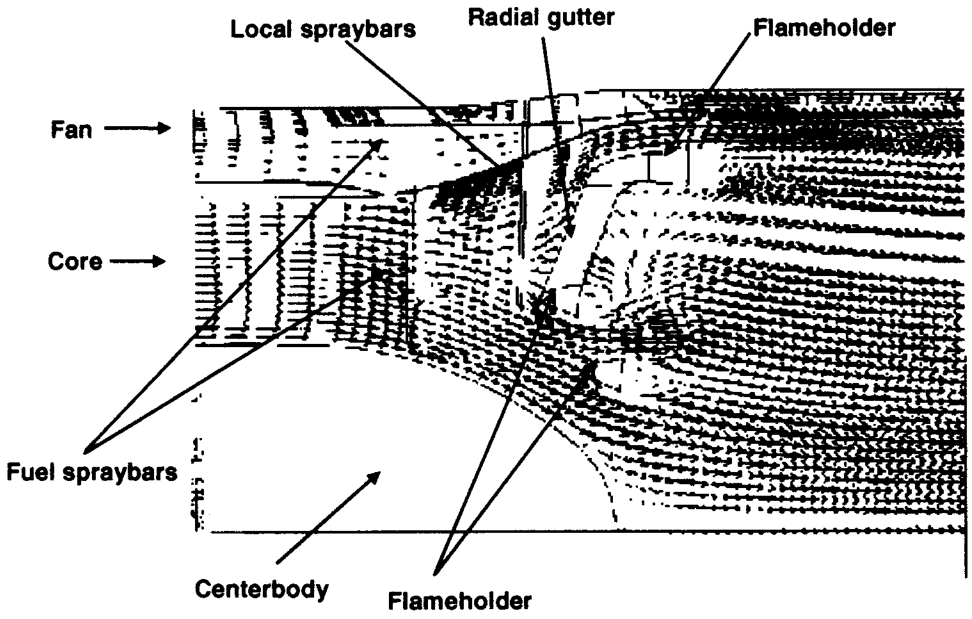

Calculated velocity vectors in current production core-chute cross section

Fig. 13 Calculated velocity vectors for the current production F110-GE-129 augmentor

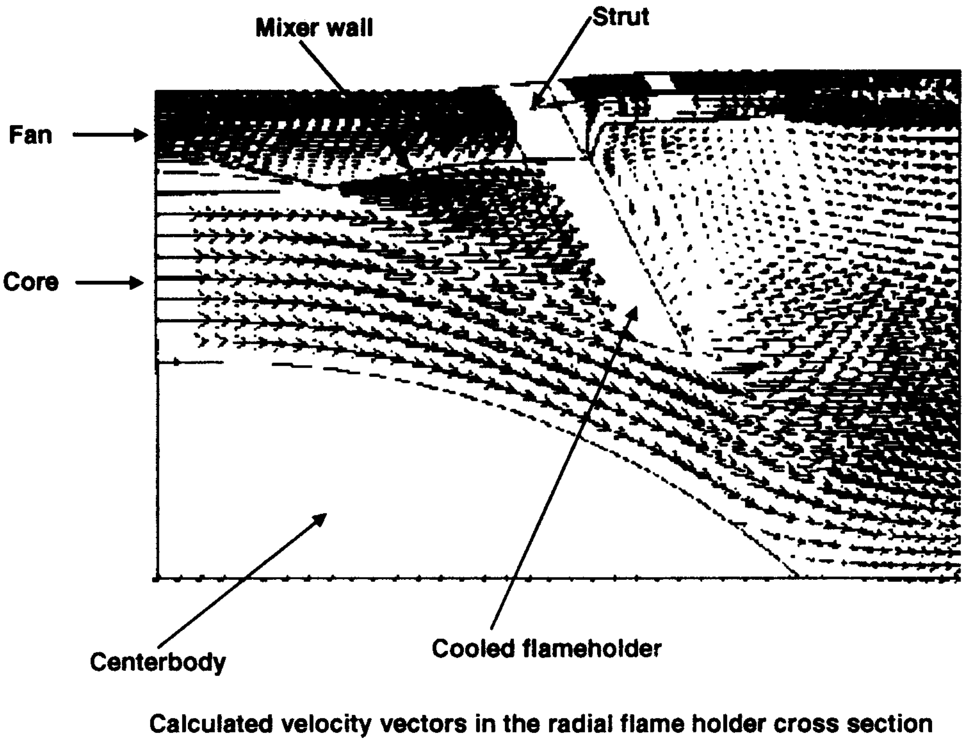

Fig. 14 Calculated velocity vectors for the F110-GE-132 radial augmentor

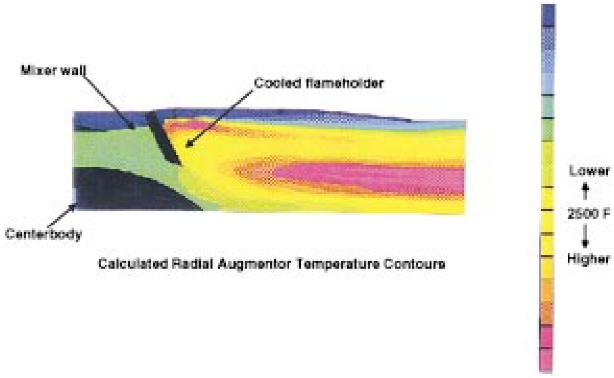

Fig. 15 Calculated temperature contours for the F110-GE-132 radial augmentor at a prescribed flight condition

the engine. The augmentor accumulated 99 hours of testing at sea level and 351 hours at altitude conditions. 85 test hours were spent in combination of maximum A/B and part power A/B operation, which is significantly more than required for 2000 EOH life. The radial augmentor components demonstrated excellent reliability in rigorous testing across the entire flight envelope. The radial augmentor permitted operations at higher cycle temperatures without flameholder burning and demonstrated low screech.

F110-GE-129 EFE Exhaust Nozzle Options

The current production F110-GE-129 IPE exhaust nozzle assembly provides high reliability and smooth thrust modulation throughout the flight envelope. The F110-GE-132 nozzle design is nearly identical to the proven F110-GE-132 engine with years of successful service, but with significant life and maintainability benefits.

The F110 exhaust nozzle, shown in Fig. 16, utilizes a converging-diverging exhaust nozzle design having variable throat area and variable exhaust expansion ratio. This concept provides high cruise performance and low drag, and aids in smooth thrust modulation. The full authority digital electronic control continually schedules the exhaust nozzle throat area to maximize engine thrust while maintaining sufficient fan stall margin for excellent engine operability throughout the flight envelope.

The exhaust duct liner directs film cooling air back to the nozzle flaps and seals, and also provides effective augmentor screech suppression. The nozzle convergent section is comprised of primary flaps and seals while the divergent nozzle section is comprised of divergent flaps and seals. Thermal barrier coatings have been introduced on the divergent flaps and seals to reduce thermal fatigue, extend nozzle life and reduce maintenance.

The F110-GE-132, like its IPE predecessor, is structurally capable of accepting the Multi Axis Thrust Vectoring (MATV) with the modifications to the exhaust nozzle as shown in Fig. 16.

The ejector nozzle, shown in Fig. 17, is another potential option

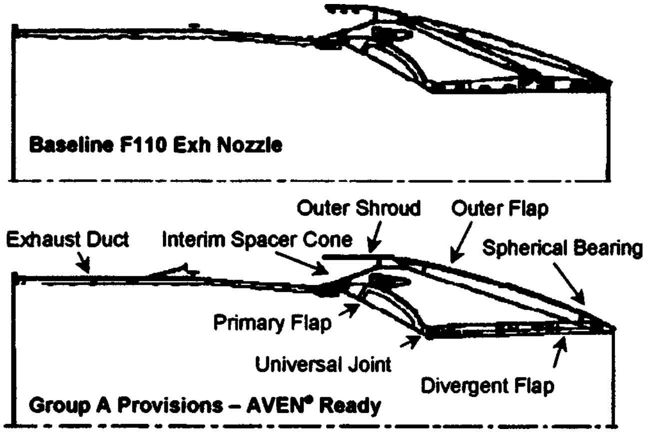

Fig. 16 Comparison of the F110-GE baseline exhaust nozzle feature with the AVEN ready exhaust nozzle features

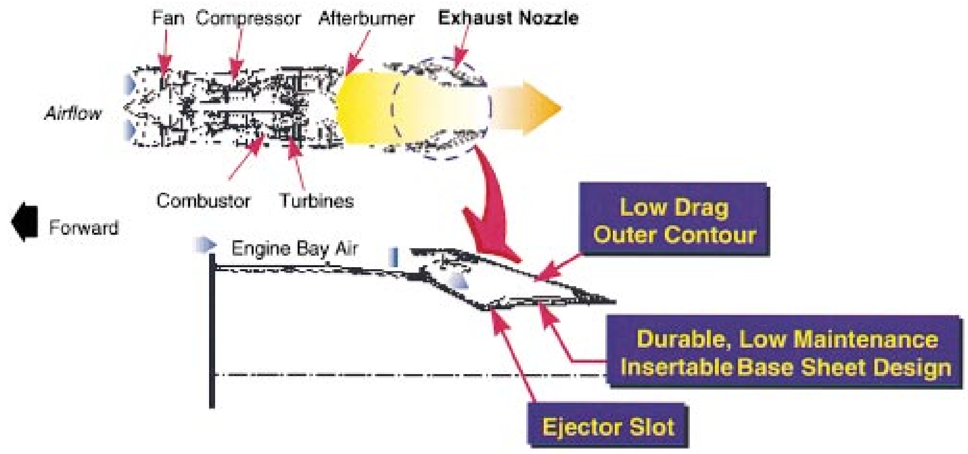

Fig. 17 F110-GE-132 optional ejector nozzle features

available on F110-GE-132. The fundamental idea behind this concept is to use air from the engine bay to cool the nozzle parts. This results in a significant improvement in exhaust nozzle parts life (4×) and a large (50–90 percent) reduction in LRU replacement times. Other benefits of the ejector nozzle are a reduction in parts count, reduced spare parts cost, reduced inspection time, and lower exhaust system weight.

Summary

The F110-GE-132, developed using General Electric's low-risk derivative engine technology, is being offered at two different thrust/inspection levels. The engine can be operated by the customer at either of the two thrust/life ratings. In engine tests the EFE has demonstrated over 34,000 pounds of maximum augmented thrust, and will be qualified at 34,000 pounds thrust rating. Two key new features on the engine include an increased airflow, high efficiency, three-stage long chord blisk fan and an advanced radial augmentor that reduces complexity, improves maintainability, and provides increased parts life. A detailed description of the new features of the F110-GE-132 have been presented. The engine has completed final component validation and is being prepared for qualification testing.

The engine utilizes leading edge technology with new features that provide excellent reliability for new and derivative F-15, F-16, and F-2 aircraft. Building on the success of the F110-GE-100 program and leveraging low-risk derivative engine technology have produced a very high efficiency robust blisk fan for the F110-GE-132. This fan is capable of providing increased thrust or improved engine life to new aircraft and is also available as a retrofit kit for the current United States Air Force and foreign military customer fleets without any airframe mount location modifications. Similarly, the radial augmentor provides significant durability improvements and can be retrofitted to existing engines as well. The improved durability and maintainability features of the F110-GE-132 result in reduced operational cost, with production availability in 2002.

In October 1999, the United States Air Force officially informed GE Aircraft Engines that it had designated the EFE 32,000 pound (minimum) thrust/4300 TAC inspection interval engine option as the F110-GE-132. The EFE's 29,000 pound (minimum) thrust/6000 TAC inspection interval option has been designated as the F110-GE-132A and the 34,000 pound thrust version of the EFE has been entitled as the F110-GE-134.

Acknowledgments

The authors would like to acknowledge Robert Griswold, General Manager, Large Military Engine Programs, Thomas Maxwell, F110 Program Manager, Ron Hutter, Military Marketing and Sales Manager, and Alan Ewing, Jeffery Reno, and Bjorn Gidner, F110 Marketing and Sales, for their support of the EFE development and qualification program. The authors would also like to acknowledge the support provided by several branches of the United States Air Force (AFRL, ATTD, JTDE, CIP, and ASC/LPP) to develop the long chord blisk fan and other key components for the F110-GE-132. The authors are grateful to GE Aircraft Engines for permission to publish this paper.

Nomenclature

A/B = afterburner
AEDC = Arnold Engineering Development Center
CIP = component improvement program
EFE = enhanced fighter engine
ENSIP = engine structural integrity program
F/H = flame holder
FOD = foreign object damage
IHPTET = integrated high-performance turbine engine technology
IPE = improved performance engine
IRP = intermediate rated power (dry thrust)
LRU = line replaceable unit
LSP = laser shock peen
M = Mach number
Max A/B = maximum augmentation
OLGA = on-line gas analysis
TAC = total accumulated cycles

References

[1] Andersen, R. H., 1990, ''F110: Power for the 90's and Beyond,'' ASME Paper No. 90-GT-SSS.
[2] Kandebo, S. W., 1996, ''GE Developing Longer-Life F110,'' Aviat. Week Space Technol., Feb., pp. 42–43.
[3] Wadia, A. R., and Law, C. H., 1993, ''Low Aspect Ratio Transonic Rotors: Part 2—Influence of Location of Maximum Thickness on Transonic Compressor Performance,'' ASME J. Turbomach., **115**, pp. 226–239.
[4] Hemsworth, M. C., 1969, ''Development and Experiences of the First High-Bypass Ratio Engine, TF-39,'' Paper No. 21, presented at the 11th Anglo-American Aeronautical Conference, London.
[5] Rubbert, P. E., Boctor, M. L., Cowan, S. J., and Laprete, R. D., 1972, ''Concept and Design of Stators Tailored to Shield a Fan From Pressure Disturbances Arising in the Downstream Fan Ducts,'' AIAA Paper No. 72–84.
[6] Wadia, A. R., Szucs, P. N., and Gundy-Burlet, K. L., 1999, ''Design and Testing of Swept and Leaned Outlet Guide Vanes to Reduce Stator-Strut-Splitter Aerodynamic Flow Interactions,'' ASME J. Turbomach., **121**, pp. 416–427.
[7] Velocci, A. L., 1998, ''Pursuit of Six Sigma Emerges as Industry Trend,'' Aviat. Week Space Technol., Nov. 16, p. 57.

W. N. Dawes
e-mail: wnd@eng.cam.ac.uk

P. C. Dhanasekaran

A. A. J. Demargne

W. P. Kellar

A. M. Savill

CFD Laboratory and Whittle Laboratory,
Department of Engineering,
University of Cambridge,
Cambridge, UK

Reducing Bottlenecks in the CAD-to-Mesh-to-Solution Cycle Time to Allow CFD to Participate in Design

As CFD has matured to the point that it is capable of reliable and accurate flow simulation, attention is now firmly fixed on how best to deploy that CFD as part of a process to improve actual products. This ''process'' consists of capturing and controlling the geometry of a suitable portion of an aeroengine (e.g., a blade row, or an internal cooling system or a fan-plus-nacelle), building a mesh system, solving the flow and responding to an appropriately visualized flow field by changing or accepting the geometry. This paper looks at that process from the point of view of identifying any bottlenecks and argues that current research should be directed at the CAD-to-mesh-to-solution cycle time rather than, as has been traditional, just looking at the solver itself and in isolation. Work aimed at eliminating some of these bottlenecks is described, with a number of practical examples. [DOI: 10.1115/1.1370162]

Introduction

The modern trend in aeroengines is try to produce more aggressive designs (for example, higher stage loadings) and in reduced design cycle time. The overall imperative is to reduce the cost of the engine and reduce the associated development risk. This trend is in turn causing a rather different focus to be placed on design tools like CFD. The question is no longer simply whether CFD can reproduce experiments sufficiently accurately (which has led to rather excessive activity based narrowly on turbulence modeling) but whether CFD can participate in the design process with sufficient speed to drive down the design cycle time. This emphasis on whether CFD can actually be used to help ''halve the cost of an engine'' has revealed that one of the key bottlenecks is getting access to complex geometry held in a CAD system and converting that into suitable mesh systems for CFD. The concept of ''badly meshable geometry'' was formally recognized only recently by Samareh (1999) [1] who describes CAD features unsuitable for a CFD mesh procedure. This group of geometry features essentially breaks down into two parts—areas where the unsuitability arises from basic geometric errors, i.e., edge mismatches; and areas where the unsuitability is due to the actual information which is represented. The latter commonly arises in, for example, the use of mechanical-type CAD for CFD analysis, where the CAD definition is rendered unusable for a CFD analysis by the presence of extraneous mechanical features.

This principle of the actual level of representation also applies to CAD which is generated specifically for CFD; a CAD definition of a complete turbine stage would contain a large amount of information ranging from the number of blades to the individual spline control points. All of this information can be relevant for the purposes of overall aerodynamic analysis, but the choice of what information is relevant in a particular type of CFD analysis is dependent on the tools being used. For example, an empirical through flow correlation for a turbomachine may require gross parameters such as the number of blades in a stage, whereas a detailed Navier-Stokes analysis of the flow in a blade passage would require access to the actual surfaces of the blades. In general, a CFD engineer could expect to receive a highly complex CAD for aerodynamic analysis, which would often contain many features of very little aerodynamic interest that might nonetheless give problems in grid generation and flow solving procedures. These features might be, for example, rivets on an aeroplane fuselage, or bolt holes in a racing car body.

In a CFD analysis, the most common surface representation used is one of a variety of types of spline, either uni- or bi-variate, depending on the nature of the analysis. Typical geometry representation methods for optimization concentrate to a certain extent on the access given by the parameters to the design space. A parameter set is commonly chosen on the basis of being able to represent most existing designs for a given component. These spline methods of surface representation, by virtue of being an inherently efficient and practical way to represent a surface, tend to be widely available in commercial CAD packages. The NURBS method is not often used currently in CFD-based optimization as the extra flexibility offered, compared with a basic cubic B-spline, is not seen to add much to the design process.

In this paper, recent work relating to a number of issues associated with the CAD-to-mesh-to-solution problem is described, including realistic ''dirty'' geometry acquisition and repair, surface discretization and viscous volume mesh generation, and fast 3D RANS flow solution. The focus is on identifying *bottlenecks* and describing work which overcomes them. A number of practical examples are described as illustrations. Although geometry parameterization itself is not covered in this paper, there is much research starting up in that area. In our group this research is driven by the view that it is the ability to parameterize geometry which determines the absolute ability to optimize design. We believe that the freedom to parameterize requires complete control of the entire CAD-to-mesh-to-solution process—hence this paper.

Desirable Attributes

The desirable attributes in a useful CAD-mesh-CFD system are summarized in Fig. 1; the geometry to be manufactured is assumed held in a CAD (or CAD-like) database. For CFD to be *useful* (i.e., to participate in the design cycle) a number of apparently simple operations must take place. The core requirements are:

- the geometry must be imported from the CAD system;
- fully 3D viscous mesh generation must take place automatically—and for arbitrary domains;

Contributed by the International Gas Turbine Institute and presented at the 45th International Gas Turbine and Aeroengine Congress and Exhibition, Munich, Germany, May 8–11, 2000. Manuscript received by the International Gas Turbine Institute February 2000. Paper No. 2000-GT-517. Review Chair: D. Ballal.

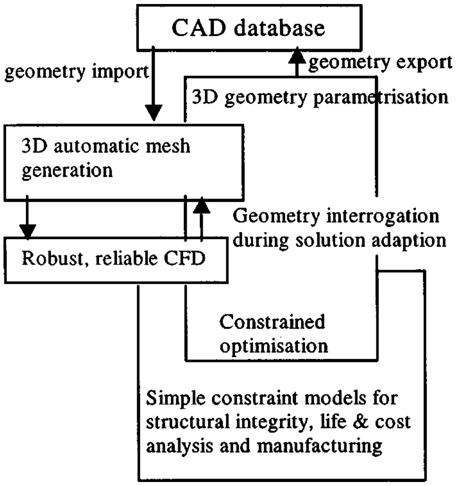

Fig. 1 Desirable attributes in a useful CAD-mesh-CFD system

- a reliable, robust 3D RANS flow solver must run as quickly as possible.

In addition, it would be very desirable for the flow solver and mesh generator to be coupled to permit geometry interrogation during solution adaption (which might take place in both time and space) and for both geometry and flow to sit within a geometry parameterization and constrained optimization harness. Each of these operations is nontrivial, raising issues which are, in many cases, quite novel to the CFD community—both developers and users.

Bottlenecks

Our work on a range of very practical geometries against real deadlines, has brought into sharp focus four bottlenecks:

- importing and fixing ''dirty'' CAD;
- guaranteeing surface integrity during mesh generation;
- avoiding/eliminating ''slivers'' (i.e., tetrahedrons of vanishing volume);
- computer memory/time for useful simulations.

This paper describes our responses to these bottlenecks.

Geometry Import

In many ways the biggest and most time-consuming (and most surprising) bottleneck is simply getting access to the geometry in the first place.

The process of geometry access is limited by the need for CFD to interface with common commercial CAD systems and geometry transfer formats (typically IGES). The nature of this interface is defined from two viewpoints; first that of the CAD draughtsman, who should expect to set the original level of geometry information to be as CFD friendly as possible; and second that of the CFD package, which should expect to automatically interrogate and repair a full range of typical CAD formats and entities. The quality of this interface is crucial to the CFD analysis as a whole; for example, small geometry degeneracies which are extremely hard to repair automatically at the front end of a CFD package can be easily removable by the original CAD draughtsman when familiar with the requirements of CFD.

Surface data are often handled using spline surface definitions. Intersystem transfer of such surfaces with existing formats leads unavoidably to variable degrees of surface degeneracy, for example, gaps in the solid surface due to tolerance mismatches, and crucial topology and component intersection information is generally not supported at all. To deal with such problems a CFD package must interrogate the geometry data at the very lowest and most rigorous level, i.e., at the level of the individual spline surface control points, and topology information must be generated from scratch. Typical CFD procedures incorporate this geometry repair with the mesh generation procedure, where topology and intersections are defined manually in the mesh. This constitutes a major bottleneck in the CFD procedure as a whole, but is not strictly necessary if the geometry definition can be raised to the required standard.

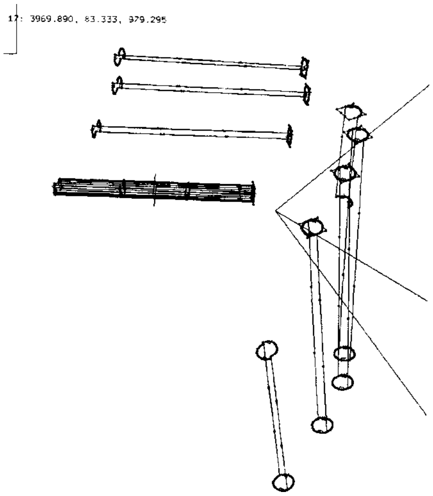

Fig. 2 Fuel injector holes from typical combustor geometry

A limitation of typical intersystem data transfer is shown in Fig. 2. Here, a series of combustor injector holes have been reduced from complex trimmed cylinders to simple geometrically rectangular spline patches by the CAD/CFD geometry transfer formal. To manually repair such intersection information for such realistically complex geometry in a useful design process is not feasible, and the CFD system must then be prepared to automatically calculate intersection and topology information. Discussion with the original draughtsman, in this instance on the length and detail of the injector geometry, can minimize the effort required from the CFD repair.

A typical aerofoil section geometry from a gas turbine combustor inlet is shown in Fig. 3. Degeneracies here fall into two categories. First, the actual spline surface definition is not particularly suitable on the suction surface of the blade; too many patches are used to describe the relatively flat surface, and these may well limit the quality of the surface mesh. A competent automated CFD procedure could be expected to repair this error. Second, a CAD fillet is given at the root of the section. This geometry information is derived from manufacturing data and would not in general be required for the CFD analysis; but respon-

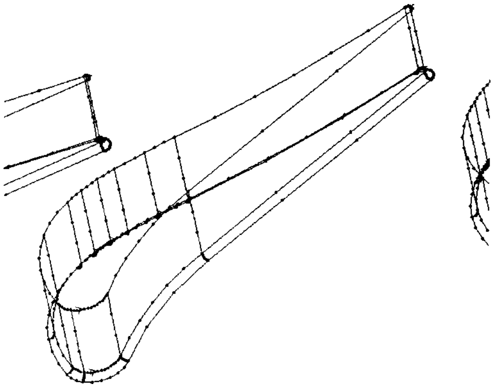

Fig. 3 Inlet aerofoil section from typical combustor geometry

sibility for controlling this level of data falls to the CAD draughtsman, and repair of this type of error must currently be carried out in commercial CAD rather than in a CFD package. However, the fillet information may be required in the CFD for certain levels of analysis, and ideally a geometry-adaptive mesh procedure should have access to the information which can be maintained in the background of the CFD.

Our goal is to produce a CAD-like input file to the mesh generation system, which we call a ‘‘.geo’’ file, containing patches, edges, and topological bindings (Dawes, 1996 [2]); this goal is generic to all mesh generation systems. To achieve this a number of automatic, or semiautomatic tools have been developed in response to much practical experience (Dawes, Dhanaskeran, and Demargne, 1999 [3]):

- read, interpret and assemble skeleton .geo file from raw IGES, trimming the patches and matching trimmed surface to trimmed edge boundaries;
- convert patch geometry data into .geo format, including generating automatic topological information. (The boundaries should have trimmed edges, i.e., all the surface boundary edges should take part in the surface topological information);
- remove duplicate nodes (within certain minimum tolerance) and rebuild the .geo file;
- remove duplicate edges (based on end nodes and checking the gap distances between the middle nodes) and rebuild the .geo file;
- determine any ‘‘dangling’’ nodes or edges and delete from the list;
- check the validity of the .geo file by checking all the vertices, edges, surfaces information with the edge and surface topological information;
- respline any given patch;
- merge patches which have matched trimmed edge along the common edge boundary and rewrite the .geo file;
- split patches (along a particular parametric u/v line) and rewrite the .geo file;
- merge two or more .geo files into a single file with topological information;
- split a single .geo file into many fragments, with topological information;
- skip u/v lines in the given .geo file based on distance tolerance. Large u,v spacing variation on any patch causes problems in curvature calculations in the surface mesh.

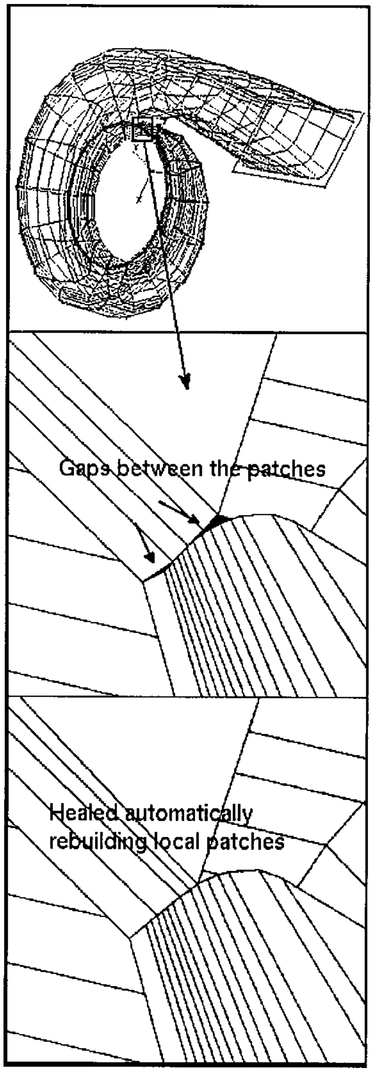

Fig. 4 Typical CAD surface representation errors together with ‘‘healed’’ result

Figure 4 shows typical CAD surface representation errors, with ‘‘healed’’ results near the complex, highly three-dimensional tongue of a radial inflow turbine housing.

3D Automatic Mesh Generation for Arbitrary Domains

While an enormous literature exists describing structured multiblock meshes, chimera meshes, hybrid unstructured meshes, and unstructured meshes, only purely unstructured meshes seem capable of truly automatic generation (Löhner, 1994 [4]). In addition, only unstructured meshes seem infinitely scalable on parallel computer architectures. In principle, the entire meshing process is automatic. However, another major potential bottleneck, which must be under control for the CFD to participate in design, is guaranteeing surface integrity at the mesh generation phase.

Once the mesh generator receives the .geo generic edges/patches/bindings file, the first operation is to triangulate the domain surface. This is performed using an edge-swapping Delaunay algorithm as described by Dawes (1996) [1]. The surface triangulation is both curvature and proximity sensitive and, if appropriate, highly stretched triangles are generated near patch edges to support viscous layers.

The next operation is to insert all the boundary nodes iteratively into a tetrahedralized mesh structure. Node insertion is performed using an edge-swapping Delaunay algorithm (Dawes (1996) [1], Fergusson (1987) [5]). If this is ‘‘unconstrained’’ then the surface integrity of the domain boundary cannot be guaranteed, i.e., surface triangles are not guaranteed to match faces of tetrahedrons and edges of tetrahedrons may pass through surface triangles. This problem is particularly severe when dealing with real, practical geometries where it is not always possible to guarantee ‘‘perfect’’ surface triangulations. The traditional response to this problem (e.g., Peraire et al. (1988) [6]) is to devise elaborate post-processing operations to swap tetrahedron edges to force boundary recovery. Our response is to build surface integrity into the heart of the algorithm: ‘‘march and grab.’’ This approach, illustrated in Fig. 5, is based on the idea of ‘‘marching’’ the domain boundary triangles into the iteratively evolving tetrahedral mesh proceeding from neighbor to neighbor. Once a tetrahedron face coincides with a boundary triangle then that face is marked ‘‘grabbed’’ and no subsequent edge swapping is allowed to disturb that match. The ability to introduce constraints on the fly is a significant advantage of the edge-swapping algorithm (as opposed to the more usual insertion polyhedron methods (Jameson et al. (1986) [7]). The next node to be inserted is then chosen from neighbors of existing ‘‘grabbed’’ faces. Even over complex domains, experience has shown that after all boundary nodes are inserted all but a very small handful (10–20, say) of boundary triangles are matched to tetrahedron faces. The remaining matches can almost always be made using integer arithmetic and simple,

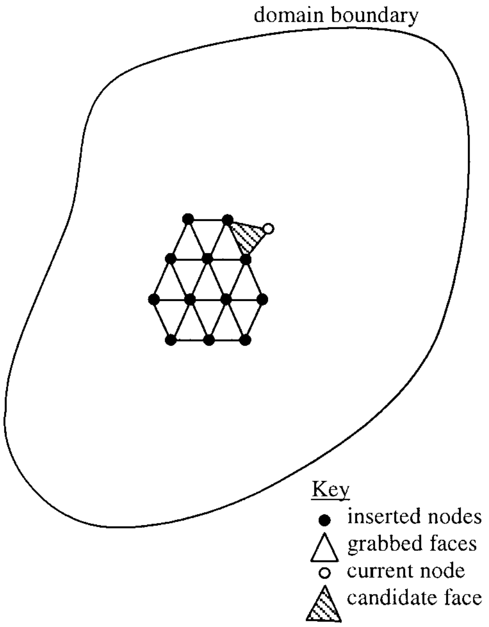

Fig. 5 "March and grab": iterative insertion of surface triangles to guarantee surface integrity

very localized edge swapping. Overall, this strategy eliminates the bottleneck associated with the need to guarantee surface integrity.

The final mesh generation bottleneck is avoiding and/or eliminating ''sliver cells.'' Slivers are one of the most irritating by-products of the Delaunay methodology. A sliver tetrahedron is formed from four nearly co-planar nodes, Fig. 6, and has vanishing volume but satisfies the basic Delaunay criterion of a very compact circumsphere. However, although ''valid,'' slivers cause the flow solver severe accuracy problems and must be removed. Slivers within the body of the mesh can be prevented from forming by adding additional tests in the heart of the meshing algorithm; this can be readily done in an edge swapping approach since ''Delaunay-ness'' is seen simply as a test. Slivers associated with four nodes lying in the same boundary surface are more difficult but can nearly always be removed by locally targeted, semiautomated local edge swaps.

Fast, 3D RANS Flow Solution

The final bottleneck to be confronted is computer memory and time. The only guaranteed way to make a flow solver run faster is to get more computer power; the only scalable way to do this is to exploit parallel architectures. Our work is based on the NEWT family of 3D RANS unstructured mesh flow solvent (Dawes (1992) [8], (1993) [9]) and we have adopted (Rycroft et al. (1999) [10]) a domain decomposition parallelization strategy suitable for both shared-memory and distributed-memory architectures. We routinely use a variety of platforms including a 64 processor Silicon Graphics Origin 2000, 4-processor SGI workstation, and an 8-processor Bœuwulf-type cluster of 450 MHz Pentium PC's. Figure 7 shows typical speedups obtained on real problems.

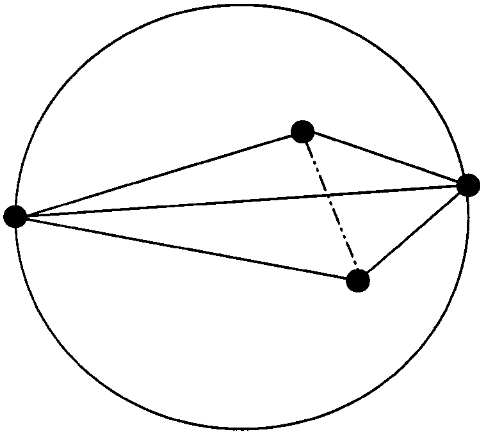

Fig. 6 A "sliver" formed from nearly co-planar nodes with compact circumsphere

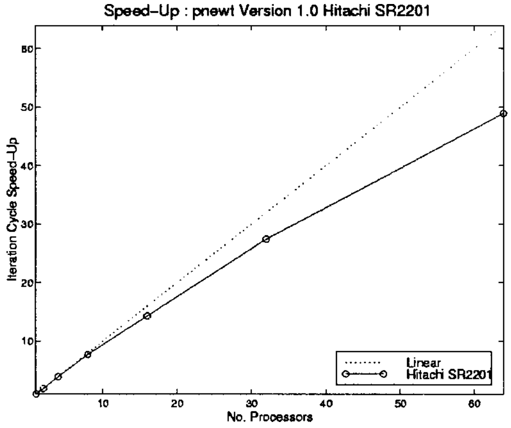

Fig. 7 Parallel speedup of unstructured flow solver on a Hitachi MPP

Examples

- *Axial compressor and underhub leakage*

The first example, taken from Longley and Demargne (2000) [11] and using the present CAD-to-mesh-to-CFD system, is the classical problem of an axial compressor with underhub leakage flow. Figure 8 shows a zoom view of the mesh near the leading edge of an axial compressor cascade with the leakage path upstream of the platform. This gap discharges air pushed into the corresponding gap just downstream of the blade row and driven by the compressor's own pressure rise. Figure 9 shows a comparison of predicted and measured total pressures downstream of the blade row for a case with underhub leakage and a reference case with no leakage cavity. For this case, and this design of leakage path, the effect of the leakage is to substantially increase the size

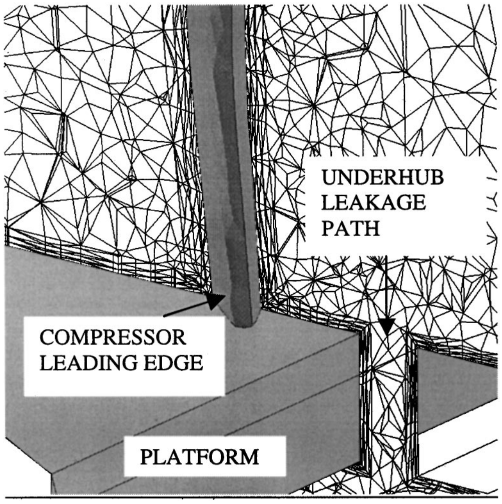

Fig. 8 Zoom view near the LE of a compressor with underhub leakage

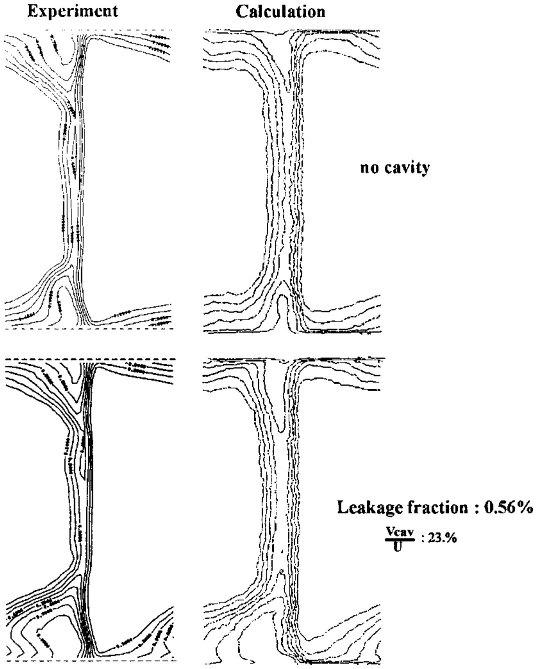

Fig. 9 Predicted and measured total pressures at exit from a compressor with and without underhub leakage

of the corner stall (with corresponding increase in loss coefficient). The agreement with experiment is considered satisfactory; more details and discussion are given in Longley and Demargne (2000) [11].

- *Combustion chamber*

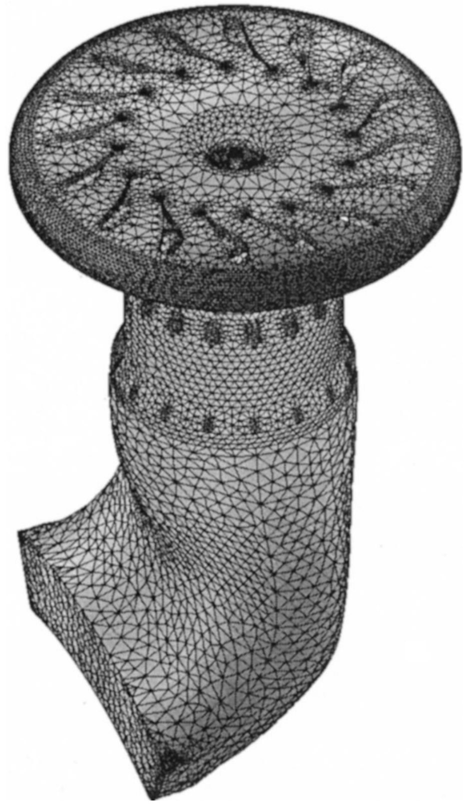

Fig. 10 Surface mesh for the complete combustion chamber

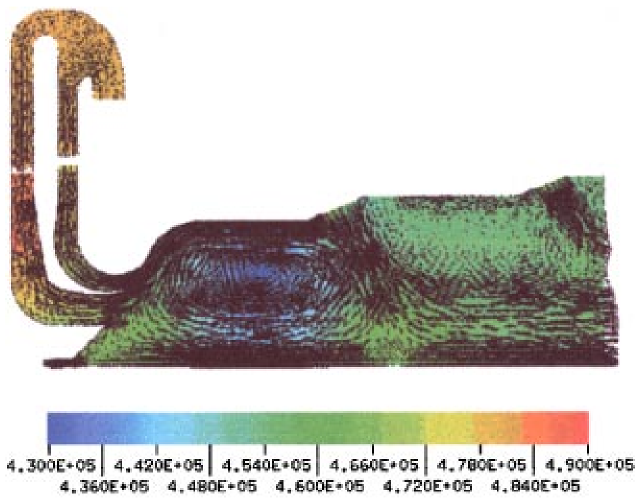

Fig. 11 Cold flow solution showing velocity vectors and pressure contours, subsynchronous idle operating point

The second example, taken from Birkby et al. (2000) [12] and using the present CAD-to-mesh-to-CFD system, is the topical problem of combustion instabilities in an industrial aeroderivative gas turbine. Figure 10 shows the surface mesh for the complete geometry of the Rolls-Royce ''Trent'' aeroderivative combustion chamber. This geometry, imported via IGES from the Rolls-Royce ''CADS'' CAD system, included all the geometry from inlet, past two layers of swirl blades, with four fuel injection pipes per blade pitch, into the main body of the chamber, past secondary and tertiary injection ports to the turbine inlet. The scale of resolved features ranges from 0.7 mm for the fuel pipe diameters to of order 1 m for the overall system length. The geometry definition consisted of 847 separate patches and could only be handled in a realistic time scale because of the almost completely automated nature of our system. With experience, a fully 3D unstructured mesh system can be generated for this type and scale of geometry in a matter of days. A wide variety of cold flow and steady and unsteady fully combusting solution were generated, illustrated here by a single plot, Fig. 11; extensive details and description can be found in Birkby et al. (2000) [12], Kellar et al. (1999) [13], and Kellar (1999) [14].

Concluding Remarks

For CFD to fulfill its full potential research is urgently needed, not on the modeling in the flow solver itself but on reducing the CAD-to-mesh-to-CFD cycle time. This will give CFD access to the design process. Several bottlenecks were identified of which by far the largest is the CAD-to-mesh conversion. Other bottlenecks discussed were forcing surface integrity in mesh generation and flow solver speed for large problems. Our responses to these bottlenecks were described and a range of examples showed how much progress has been possible. Real, practical geometries can now be turned around in days rather than weeks. Soon, we will achieve turn around in hours and be able to improve design.

References

[1] Samareh, J. H., 1999, ''Status & Future of Geometry Modelling and Grid Generation of Design and Optimisation,'' J. Aircr., **36**, No. 1.
[2] Dawes, W. N., 1996, ''The Generation of 3D Stretched, Viscous Unstructured Meshes for Arbitrary Domains'' ASME Paper 96-GT-55.
[3] Dawes, W. N., Dhanasekaran, P. C., and Demargne, A. A. J., 1999, ''NEWT_mesh mesh generation system'' http://www2.eng.cam.ac.uk/~mea/fluid/dawes/newt_mesh2/newt_mesh2.htm.
[4] Löhner R., 1994, ''CFD via Unstructured Grids: Trends & Applications'' Frontiers of CFD, edited by Caughey, D. A., and Hafez, M. M. CMAS: Computational Methods in Applied Science.
[5] Fergusson, N., 1987, ''Delaunay Edge Swapping in Three Dimensions,'' Ph.D.

thesis, Institute for Numerical & Computational Analysis, Dublin.

[6] Peraire, J., Peiro, J., Formaggia, J., Morgan, K., and Zienkiewicz, Q. C., 1988, ''Finite Element Euler Computations in Three Dimensions,'' Int. J. Numer. Methods Eng., **26**, pp. 2135–2159.

[7] Jameson, A., Baker T. J., and Weatherhill, N. P., 1986, ''Calculation of Inviscid Transonic Flow over a Complete Aircraft,'' AIAA Paper 86-0103.

[8] Dawes, W. N., 1992, ''The Practical Application of Solution Adaption to the Numerical Simulation of Complex Turbomachinery Problems,'' *Progress in Aerospace Sciences*, Vol. 29, pp. 221–269.

[9] Dawes, W. N., 1993, ''Simulating Unsteady Turbomachinery Flows on Unstructured Meshes which Adapt both in Time and Space,'' ASME Paper 93-GT-104.

[10] Rycroft, N., Savill, A. M., and Dawes, W. N., 1999, ''The Parallelisation of an Unstructured Mesh CFD Code, CUED Report, Cambridge University Engineering Department.

[11] Longley, J. P., and Demargne, A. A. J., 2000, ''The Aerodynamic Interaction of Stator Shroud Leakage and Mainstream Flows in Compressors,'' ASME Paper No. 2000-GT-570.

[12] Birkby, P., Cant, R. S., Dawes, W. N., Demargne, A. A. J., Dhanasekaran, P. C., Kellar, W. P., Rycroft, N. C., Savill, A. M., Eggels, R. L. G. M., and Jennions, I. K., 2000, ''CFD Analysis of a Complete Industrial Lean Premixed Gas Turbine Combustor,'' ASME Paper No. 2000-GT-131.

[13] Kellar, W. P., Savill, A. M., and Dawes, W. N., 1999, ''Integrated CAD/CFD Visualisation of a Generic F1 Car Front Wheel Flowfield,'' Lecture Notes in Computer Science, Vol. 1593.

[14] Kellar, W. P., ''Geometry Modelling in CFD,'' CUED/CFD Lab Report, 1999.

Viscous-Flow Two-Dimensional Analysis Including Secondary Flow Effects

Reinhard Mönig

Frank Mildner

Siemens AG Power Generation KWU
Mülheim a. d. Ruhr, Germany

Ralf Röper
B&B-AGEMA GmbH
Aachen, Germany

During the last few decades extremely powerful Quasi-three-dimensional (3D) codes and fully 3D Navier-Stokes solvers have been developed and successfully utilized in the design process and optimization of multistage axial-flow compressors. However, most of these methods proved to be difficult in handling and extremely time consuming. Due to these disadvantages, the primary stage design and stage matching as well as the off-design analysis is nowadays still based on fast 2D methods incorporating loss-, deviation- and end wall modeling. Only the detailed 3D optimization is normally performed by means of advanced 3D methods. In this paper a fast and efficient 2D calculation method is presented, which already in the initial design phase of multistage axial flow compressors, considers the influence of hub leakage flows, tip clearance effects, and other end wall flow phenomena. The method is generally based on the fundamental approach by Howard and Gallimore (1992). In order to allow a more accurate prediction of skewed and nondeveloped boundary layers in turbomachines, an improved theoretical approach was implemented. Particularly the splitting of the boundary layers into an axial and tangential component proved to be necessary in order to account for the change between rotating and stationary end walls. Additionally, a new approach is used for the prediction of the viscous end wall zones including hub leakage effects and strongly skewed boundary layers. As a result, empirical correlations for secondary flow effects are no longer required. The results of the improved method are compared with conventional 2D results including 3D loss- and deviation-models, with experimental data of a three-stage research compressor of the Institute for Jet Propulsion and Turbomachinery of the Technical University of Aachen and with 3D Navier-Stokes solutions of the V84.3A compressor and of a multistage Siemens research compressor. The results obtained using the new method show a remarkable improvement in comparison with conventional 2D methods. Due to the high quality and the extremely short computation time, the new method allows an overall viscous design of multistage compressors for heavy duty gas turbines and aeroengine applications. [DOI: 10.1115/1.1370167]

Introduction

Two-dimensional (2D) streamline curvature methods are still the most important tools in the design and performance prediction of axial-flow compressors. Due to the general assumption of axisymmetric and inviscid flow, these methods are principally not able to predict viscous and 3D effects, which predominantly characterize the flow properties within the end wall zones of axial-flow compressors. This deficiency may be acceptable for the front end compressor stages but will lead to significant inaccuracies in the medium- and high-pressure section of multistage compressors. This leads to unacceptable errors in performance prediction for design and especially for off-design operation.

In order to improve the accuracy of these methods, many semi-empirical correlations for 3D loss and deviation were developed. With the introduction of these models a better prediction of the 3D loss generation and the effect on the subsequent compressor stages became possible. However, in most cases, the models were only valid for certain configurations and close to design operation. Furthermore, the spanwise distribution of the 3D effects had to be specified according to limited experimental data, which in most cases only was available for design point operation.

A dramatic improvement was made by the development of two important models to predict the effects of spanwise mixing in axial-flow compressors. The model of Adkins and Smith [1] requires the knowledge of secondary flows and attributes the spanwise mixing to convectional transport phenomena. This method is only attainable for quasi-3D methods where the secondary flow effects are determined during the calculation process. The second important model was developed by Gallimore [2]. This approach explains spanwise mixing by diffusion effects only and therefore does not require the detailed knowledge of 3D flow properties. Both of these models are generally able to improve the radial distribution of the flow properties in a multistage environment and avoid unrealistically high end wall temperatures in rear stages. With the implementation of radial mixing, the 3D losses can be specified locally and the spanwise distribution for downstream blade rows is performed by the mixing models. However, the prediction of flow velocities and flow angles in the end wall regions still remained unsatisfactory due to the lack of any viscous effects in these models.

This deficiency was remarkably reduced by a further important improvement which was developed by Howard and Gallimore in 1992 [3]. For the first time, the viscous effects of the end wall regions were directly implemented into the mixing model developed by Gallimore [2]. The mixing coefficient was reduced in the end wall zones according to a mixing length model. This approach proved to be able to more accurately predict the flow properties within the viscous end wall zones and therefore allowed a better stage matching including end wall bending of airfoils. This method also yields improved boundary conditions for 3D Navier-Stokes calculations of isolated compressor stages. However, the model still requires additional correlations for 3D loss and deviation in order to match the experimental data, especially in the rear

---

Contributed by the International Gas Turbine Institute and presented at the 45th International Gas Turbine and Aeroengine Congress and Exhibition, Munich, Germany, May 8–11, 2000. Manuscript received by the International Gas Turbine Institute February 2000. Paper No. 2000-GT-628. Review Chair: D. Ballal.

part of multistage compressors. Due to this requirement, an inaccuracy for new compressor designs and for off-design performance is still present.

In order to improve compressor efficiency by a reduction of 3D losses, the necessity of a further improvement of the viscous-flow model becomes obvious. The goals of the efforts described in this paper can be summarized as follows:

- remove the necessity of 3D loss and deviation models,
- allow a satisfactory prediction of hub and casing boundary layers including secondary flow effects for multistage axial-flow compressors.

As a result, the present method allows a more precise prediction of the radial flow field and enables the designer to improve the efficiency by a better control of the 3D flow effects.

Main Features of Axial-Flow Compressors

The flow field within axial-flow compressors is dominated by

- airfoil boundary layers,
- hub and casing boundary layers at rotating and stationary end walls,
- tip clearance and hub leakage effects,
- inner and outer bleeds,
- unsteady effects, and
- other 3D viscous flow effects.

For 2D axial-symmetric flow modeling, the airfoil boundary layers and the related effects such as total pressure losses and 2D underturning have to be incorporated by empirical correlations. For NACA airfoils these correlations were determined by extensive measurements in the 1950's and are included in the NACA-SP36 report by Johnson and Bullock [4] (editors). This fundamental analysis still is the basis of most 2D flow calculations and has been improved to also predict the performance of other airfoil families such as the British C4 series or supercritical, transonic and controlled diffusion airfoils. These effects mainly determine the compressor mass flow, the loading distribution, stage matching, and surge margin at high and low-speed operation. Thus, a large amount of effort has been invested to predict these effects as accurately as possible in order to avoid problems in compressor operating behavior and reduce the risk involved in new compressor developing.

Hub and casing boundary layers caused by stationary and rotating end walls together with the tip clearance and hub leakage effects mainly control the 3D-loss generation of multistage compressors. Therefore, these effects have a major influence on compressor efficiency and flow stability. To accurately model these viscous end wall zones is extremely challenging because of the 3D dominance and the changes from absolute to relative frame of reference (and vice versa) which lead to strongly skewed boundary layers. Furthermore, the changes between stationary and rotating blades and end walls and the axial gaps lead to undeveloped boundary layers that have to be addressed by the model in order to correctly simulate the real flow behavior.

Inner and outer bleeds are required for sealing and cooling air in the hot gas section. Therefore, they are characteristic for modern aeroengines and heavy duty gas turbines as well. These extractions also significantly change the radial flow properties and therefore have to be included in 2D computations to consider the impact on subsequent blade rows.

Unsteady effects can of course not be modeled by 2D steady-state calculations. Therefore, only time-averaged properties are calculated by these codes. However, it has to be ensured that the steady-state solution represents the time-averaged properties from measurements and unsteady calculations as close as possible.

The 3D flow effects can also not be directly predicted by 2D methods. By implementing appropriate radial mixing models it is possible however, to take into account the main overall effects that are introduced by 3D features. The use of mixing models allows a more accurate prediction of the radial temperature and pressure distribution and additionally leads to a significant improvement of velocities and flow angles.

Governing Equations and Numerical Model

Two-Dimensional Boundary Layer Model. The viscous end wall model presented in this paper is generally based on the fundamental approach of Gallimore [2] and Howard and Gallimore [3]. However, some features representing the fundamental phenomena of axial-flow compressors had to be introduced in order to more precisely predict the end wall properties in the multistage environment.

As in the original approach, the sublayers close to the end walls are not modeled. The streamlines adjacent to the end walls therefore represent the flow conditions at a certain wall distance, which generally is extremely small (between 0.01 percent and 0.2 percent of the flowpath width).

As is well known from the boundary layer theory (e.g, Schlichting [5]), the velocity profiles strongly depend on the velocity gradient in streamwise direction. The principal velocity distributions are shown in Fig. 1. For accelerated boundary layers the normalized velocity for a given sublayer thickness is higher than for a decelerated flow (Fig. 1(b) and 1(c)). In order to take into account different normalized velocities at the boundary of the sublayer for the mixing length model, the numerical sublayer thick-

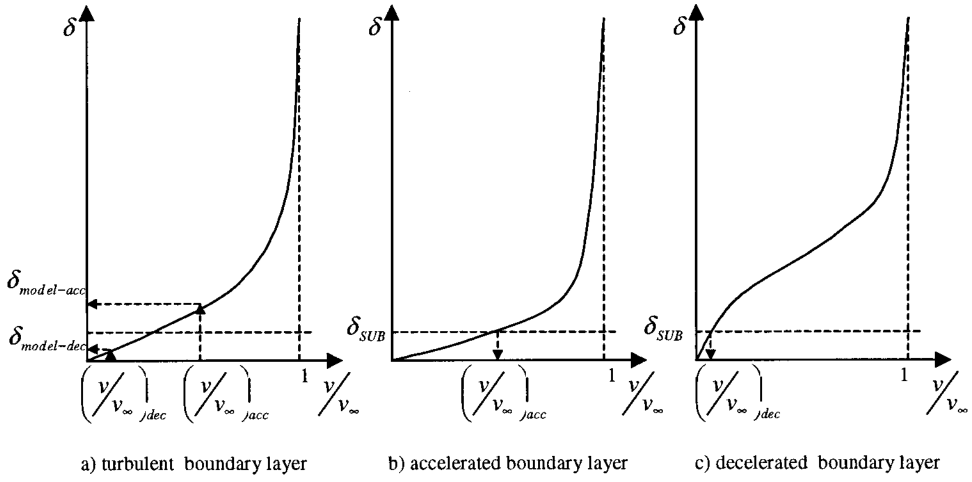

a) turbulent boundary layer b) accelerated boundary layer c) decelerated boundary layer

Fig. 1 Velocity distributions in boundary layers

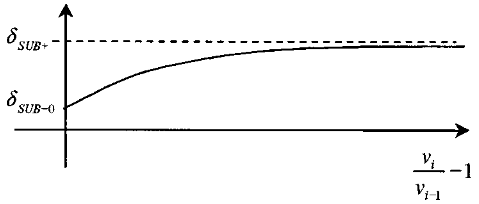

Fig. 2 Numerical sublayer thickness for accelerated flows

ness has to be modified accordingly (Fig. 1(a)). For accelerated flows (Fig. 2), the numerical sublayer thickness has to be larger than for a constant flow field. In this case the nondimensional sublayer thickness is calculated according to the empirical equation

$$\delta_{\mathrm{SUB}}=\delta_{\mathrm{SUB}-0}+\frac{\delta_{\mathrm{SUB}+}-\delta_{\mathrm{SUB}-0}}{\pi/2}\arctan\left(\frac{v_i}{v_{i-1}}-1\right) \tag{1}$$

For decelerated flows (Fig. 3), however, the numerical sublayer thickness has to decrease in order to predict a decreasing end wall velocity by the standard mixing length model (Fig. 1(a)). Therefore, the nondimensional sublayer thickness is determined by

$$\delta_{\mathrm{SUB}}=\delta_{\mathrm{SUB}-0}-\frac{\delta_{\mathrm{SUB}-0}-\delta_{\mathrm{SUB}-}}{\pi/2}\arctan\left(\frac{v_i-1}{v_i}-1\right) \tag{2}$$

Furthermore, in the original model, the end wall boundary layers are treated purely one dimensionally. If a change from steady to rotating end walls occurs, this model therefore also predicts a change of the meridional component due to a change in total velocity. This behavior does not concur with measurements and 3D Navier-Stokes calculations. Due to the complex structures in turbomachines, it is very common that the axial velocity gradient is completely different compared to the circumferential gradient. This behavior will lead to different velocity distributions within the boundary layer with respect to axial and circumferential direction. These differences however are essential for the flow vector close to the end walls. In order to predict this change in relative and absolute flow angles more accurately than before, the original model has been split into a meridional and circumferential part, where especially the eddy viscosity μ_{t} within the boundary layers may have different values for meridional ($\mu_{\mathrm{t-m}}$) and circumferential ($\mu_{\mathrm{t-w}}$) velocities and their derivatives:

$$\frac{\delta s}{\delta m}=\frac{1}{r\rho T v_m}\left[\frac{\delta}{\delta r}\left(rk_s\frac{\delta T}{\delta r}\right)+r\phi\right]+\frac{\delta s_e}{\delta m} \tag{3}$$

with

$$\phi=\mu_{t-m}\left(\frac{\delta v_z}{\delta r}\right)^2+\mu_{t-w}\left[\frac{\delta w}{\delta r}-\frac{v_w}{r}\right]^2 \tag{4}$$

$$\frac{1}{2r^2}\frac{\delta}{\delta m}(r^2v_w^2)=\frac{v_w}{\rho v_m}(E_w+F_w) \tag{5}$$

with

$$E_w=\frac{\delta}{\delta r}\left[\mu_{t-w}\left(\frac{\delta v_w}{\delta r}-\frac{v_w}{r}\right)+\frac{2\mu_{t-w}}{r}\left(\frac{\delta v_w}{\delta r}-\frac{v_w}{r}\right)\right]$$

$$F_w=\text{body force} \tag{6}$$

$$\frac{\delta H_t}{\delta m}=T\frac{\delta s}{\delta m}+\frac{1}{2r^2}\frac{\delta}{\delta m}(r^2v_w^2)+\frac{E_z}{\rho}\cos\phi+\frac{F_m}{\rho} \tag{7}$$

with

$$E_z=\frac{1}{r}\frac{\delta}{\delta r}\left(\mu_{t-m}r\frac{\delta v_z}{\delta r}\right)$$

$$F_m=\text{meridional blade force} \tag{8}$$

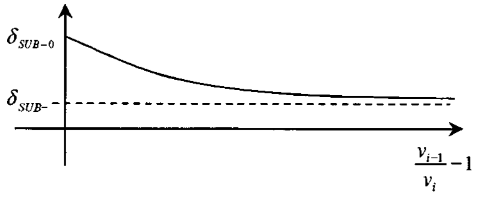

Fig. 3 Numerical sublayer thickness for decelerated flows

In order to determine the eddy viscosity μ_t at a particular grid location, the thickness of the sublayer has to be determined as mentioned above. The turbulent viscosity v_t can be computed according to the mixing length model

$$v_t=l^2\frac{\delta v}{\delta y} \tag{9}$$

with

$$l=ky \tag{10}$$

In this equation k is the Von-Karman constant and y is the wall distance. This calculation has to be performed for both, meridional and circumferential direction. The local derivatives of meridional and circumferential velocity are determined by a second-order accurate discretization:

$$\left.\frac{\delta v_m}{\delta r}\right|_j=\frac{r_j-r_{j-1}}{r_{j+1}-r_{j-1}}\,\frac{v_{m_{j+1}}-v_{m_j}}{r_{j+1}-r_j}+\frac{r_{j+1}-r_j}{r_{j+1}-r_{j-1}}\,\frac{v_{m_j}-v_{m_{j-1}}}{r_j-r_{j-1}} \tag{11}$$

$$\left.\frac{\delta v_w}{\delta r}\right|_j=\frac{r_j-r_{j-1}}{r_{j+1}-r_{j-1}}\,\frac{v_{w_{j+1}}-v_{w_j}}{r_{j+1}-r_j}+\frac{r_{j+1}-r_j}{r_{j+1}-r_{j-1}}\,\frac{v_{w_j}-v_{w_{j-1}}}{r_j-r_{j-1}} \tag{12}$$

Due to the large differences in radial grid spacing close to the end walls (sublayer thickness and spacing between two adjacent streamlines) the velocity derivatives and therefore also the turbulent viscosity may become extremely large. This might produce unrealistic high losses and can also lead to stability problems of the 2D solver. Therefore, the eddy viscosity is limited to a certain value. For most of the calculated compressors, values in the order of 2.0×10^{-4} proved to be satisfactory.

Stationary and Rotating End Walls. In order to account for the shear forces of stationary and rotating end walls, appropriate boundary conditions have to be specified. Due to the change from stationary to rotating end walls and vice versa, the boundary layer profiles in the circumferential direction are generally skewed. To account for this effect, the calculations are carried out in two steps:

1 The first step of computation takes into account the ''upstream history'' of the flow field in order to predict the flow properties of inner streamlines.
2 In a second step the wall streamlines are calculated with the appropriate boundary conditions of the current location.

This modeling method is chosen in order to introduce the near wall shear effects into the calculation and at the same time avoids the prediction of an unrealistic influence of these effects on the interior flow field. The information of different boundary conditions is therefore only transmitted to the interior flow field of subsequent calculation planes by radial mixing.

Considering a compressor design with stators consisting of inner shrouds, the boundary conditions are specified as follows:

Rotor Inlet	Hub	Casing
First pass (inner streamlines)	stationary	stationary
Second pass (wall streamlines)	rotating	stationary

These specifications take into account that the interior flow field at the rotor inlet is predominantly controlled by the stationary boundaries of the upstream stator. Due to the rotating hub, the rotating boundary condition is introduced for the second pass in order to consider the local shear effects for the hub streamline.

Rotor exit	Hub	Casing
First pass (inner streamlines)	rotating	rotating
Second pass (wall streamlines)	stationary	stationary

The inner streamlines at the rotor exit are mainly influenced by the rotating flow field in the relative frame of reference. Therefore, rotating boundaries are specified for the first pass. For the second pass, the underturning near the hub caused by secondary flow effects is considered by the specification of a stationary hub contour. The radial tip clearance and the stationary casing contour is considered by stationary boundaries during the second pass.

Stator inlet	Hub	Casing
First pass (inner streamlines)	rotating	rotating
Second pass (wall streamlines)	stationary	stationary

The interior flow field at the stator inlet section is affected by the rotating flow field of the upstream rotor. Therefore, the boundary conditions in the first pass are set to ''rotating.'' The walls however are stationary. This effect is introduced by specifying stationary boundaries during the second pass for both hub and casing streamline.

Stator exit	Hub	Casing
First pass (inner streamlines)	stationary	stationary
Second pass (wall streamlines)	stationary	stationary

The stator exit flow field is very easy to calculate. The inner flow field is affected by the stationary blade row and the boundary conditions at hub and casing are also stationary.

Stator Leakage Effects and Bleed Flows. For gas turbine and aero engine compressors consisting of stators with inner shrouds, hub leakage flows have to be considered instead of gap flows for cantilevered stators. The amount of these leakage's depends on

- Sealing geometry (number of seal strips and gap width), and
- Pressure difference across the stator.

Therefore, the leakage flow for each of the stators can be determined by a simple equation:

$$m=\alpha A p_2 \sqrt{\frac{1-p_1^2/p_2^2}{zRT_{t2}}} \tag{13}$$

In this equation the constant α is a function of sealing geometry and has to be determined experimentally. Once the leakage flow for each stator is computed, this mass flow has to be extracted behind the stators from the stream tube adjacent to the hub (Fig. 4).

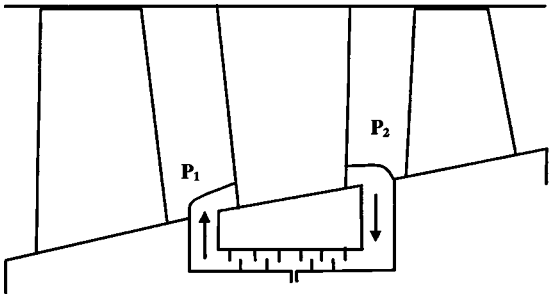

Fig. 4 Model of axial compressor stage with shrouded hub and seal strips

The average value of total temperature is calculated and stored. The streamlines in this location are redistributed in order to obtain the same fractions of the total mass flow for each stream tube as in the other calculation planes. All other flow properties are redistributed in the same manner in order to ensure conservation of mass, momentum, and energy.

For the next overall iteration, the leakage mass flow for each stator is introduced upstream of the stator blade row into the stream tube at the hub. Regarding the leakage flow, it is assumed that

- the radial velocity is negligible (≈ 0),
- the axial velocity is zero,
- the static pressure is equal to the local static pressure at the hub, and
- the circumferential velocity is half of the rotational speed at the hub (due to the shear forces of rotating and stationary seal strips).

Continuity gives

$$m_2=m_L+m_1 \tag{14}$$

The total temperature after mixing is obtained by conservation of energy:

$$T_{t2}=(m_1T_{t1}+m_LT_{tL})/m_2 \tag{15}$$

The velocities downstream of the mixing plane are obtained from conservation of meridional and circumferential momentum:

$$v_{m2}=\frac{m_1}{m_2}v_{m1} \tag{16}$$

$$v_{u2}=\frac{(m_1v_{u1}+m_Lv_{uL})}{m_2} \tag{17}$$

It is assumed that the second streamline is not affected by the introduction of the leakage flow. It is however considered, that the radial shift of the streamlines due to the additional mass flow leads to a change of the circumferential velocity according to the conservation of momentum.

Conservation of mass, energy, and momentum is achieved by assuming that all flow properties vary linearly from second streamline to hub streamline and the properties of the hub streamline are modified accordingly. The streamline locations of all other streamlines are redistributed in order to achieve the specified fractions of the local mass flow for each of the stream tubes. Again, the impact on the interior flow field is computed for subsequent calculation planes by the mixing model only.

In order to account for the proper modeling of inner and outer bleeds, the modeling is very similar to the extraction of leakage flows downstream of the stators. Due to the higher mass flow required for turbine cooling and sealing purposes, the bleed flows might be higher than the mass flow contained by the stream tube adjacent to the bleed location. Therefore, also the second stream tube might have to be modified in order to obtain a correct mod-

Table 1 Main design parameters three-stage research compressor

Rotational speed	17.000	rpm
Total pressure ratio	2	
Corrected mass flow	13.4	kg/s
Power input	920	KW
Outer diameter	0.387	m
Max. relative inlet Mach number	0.89	
Max. circumferential speed	345	m/s
Stage pressure ratios	1.3/1.28/ 1.22	

Table 2 Performance data of the three-stage research compressor

		Experiment	Calculation (new approach)
Pressure ratio		2.03	2.03
Mass flow	Kg/s	13.65	13.63
Adiabatic efficiency		91.16	91.91

eling. The redistribution of the streamlines and the computation of all relevant properties is equivalent to the simulation of leakage flows.

Results I: Three-Stage Research Compressor

To verify the new approach, results of test calculations were compared to measurement data of a three-stage research compressor of the Institute for Jet Propulsion and Turbomachinery of the Technical University of Aachen. This compressor has been analyzed using different measurement techniques, which offer an excellent data resolution especially in the end wall regions (Hoynacki, [6]).

The main design parameters of the research compressor are listed in Table 1:

Figure 5 shows the longitudinal section of the flow path of the research compressor. Characteristic features of the compressor are the fully inverse designed controlled diffusion airfoils, and the high rotational speed combined with high Mach-and Reynolds number levels. These flow parameters are similar to those of industrial application. Therefore the transferability of the obtained results is ensured.

The axial gaps between the blade rows were enlarged to allow detailed probe traverse measurement. The tip clearance of the rotors during operation is less than 0.6/0.8/1.0 percent chord with the rotor blades having no squealer tip. The inlet guide vanes and stator blades consist of inner shrouds.

The steady flow field was investigated in detail, upstream and downstream of each blade row. Combined radial and pitchwise traversing of pneumatic probes has been carried out to measure the distribution of the time-averaged velocity vector and the time-averaged pressure and temperature profiles of the flow field. While five-hole probes were used to measure the distribution over approximately 85 percent blade heights, a miniaturized three-hole probe was developed for measurements inside the end wall boundary layers.

The results for the research compressor presented in this paper are discussed for the design point. Table 2 lists the overall performance data for the design point.

As the improvement of fast 2D streamline curvature methods is the main issue in this paper, in the following discussion, the experimental data are compared to two different releases of the 2D method. The ''new'' results represent the approach presented in this paper. The ''old'' results are gained from a former version, which includes the original mixing model of Howard and Gallimore [3] and conventional empirical correlations for 3D losses and correlations for secondary flow effects based on investigations of Roberts et al., [7]. These ''old'' results are included to point out the main differences between the two approaches and thereby clarify the improvements of the new one.

Both, the old and the current 2D method are based on a duct flow approach. For numerical stability, the number of radial streamlines, and therefore the mesh refinement in radial direction in the end wall regions, is limited. Typical radial numbers of streamlines used for the presented calculations are 17. The application of the presented method within a throughflow code will increase the resolution within the viscous end wall and therefore the accuracy of the method.

In Fig. 6–11 the distribution of the circumferentially averaged values of yaw angle and total pressure at different measurements planes are plotted versus span. All angles are plotted with respect to the axial direction.

Relative Whirl Angle. One of the most important demands in compressor design is the correct prediction of the stagnation enthalpy rise, which requires an accurate representation of the flow turning angles in rotors. Moreover the whole stage matching depends on correctly predicted inlet and exit flow angles of the blade rows. Especially in modern compressor design, where end wall bending of airfoils is a necessity to improve the high level performance, the correct prediction of the flow angles in the end wall regions becomes very important.

The comparison of the values of the relative outlet flow angles behind the rotors shows a good agreement between measurement and both calculations models in the core region. Only the new approach however is capable of predicting the underturning of the

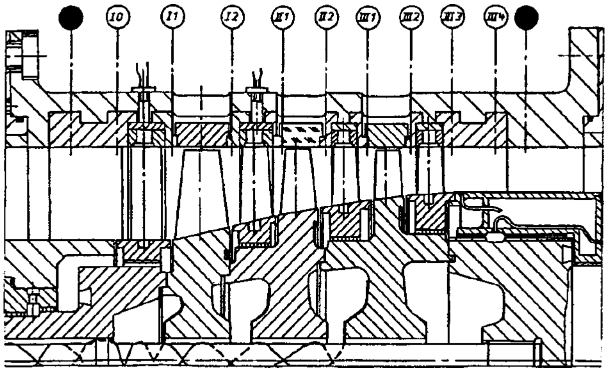

Fig. 5 Compressor cross section three-stage research compressor (Institute for Jet Propulsion and Turbomachinery, Technical University of Aachen)

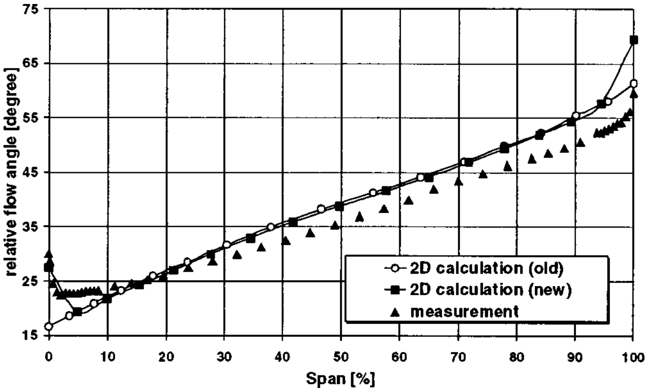

Fig. 6 Relative whirl angle downstream Rotor 1

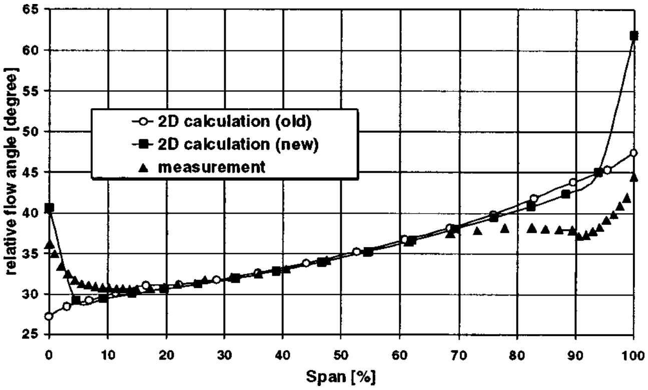

Fig. 7 Relative whirl angle downstream Rotor 3

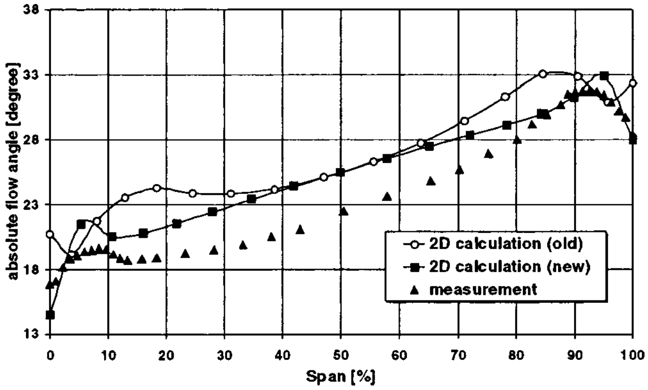

Fig. 10 Exit absolute whirl angle (three-stage research compressor)

flow in the hub region due to secondary flow effects and shear forces produced by the change from a rotating to a stationary wall. In the tip region, the flow field is strongly influenced by the tip clearance vortex. While this three-dimensional effect is not very distinct behind Rotor 1, the vortex covers up to 20 percent span in the rear part of the compressor. This leads to a significant overturning of the flow between 80 percent and 95 percent span and an underturning in the casing boundary layer behind Rotor 3. While the conventional 2D method does not predict this three-dimensional flow phenomena at all, the new approach predicts the underturning in the outer wall boundary layer but still underestimates the influence of the tip vortex between 80 percent and 95 percent span.

Absolute Whirl Angle. The correct prediction of the inlet flow angles influences the quality of the end wall bending in modern compressor design. Moreover detailed analysis of multistage compressors are performed using 3D Navier-Stokes solvers, which investigate single blade rows or portions of a compressor embedded in the multistage regime. Providing these calculation tools with physically correct boundary conditions is essential for the quality of their results.

Figures 8 and 9 show the absolute whirl angle in front of stator 1 and stator 2. Especially in the end wall regions, the analysis with the new approach better represents the experimental data. While a significant improvement of the gradients in the end wall zones is achieved, there is still a discrepancy with respect to the absolute values.

Compared to the new model the spanwise distribution of the absolute inlet flow angle calculated by the conventional approach (''old'') show regions of underturning at 15 percent and 90 percent span upstream Stator 2 and downstream Stator 3 (Fig. 10). These buckles are a result of the correlation for secondary flow effects. These distributions do not agree with the experimental data as the 3D loss and deviation mechanisms are overpredicted and placed too far away from the end walls.

A comparison of the radial flow distribution shows that the new approach is able to predict the physical phenomena fairly well at the front end of the compressor, where the influence of secondary flow mechanisms are small but also at the compressor exit, where secondary flow phenomena dominate the flow field. The whirl angle at the compressor exit (Fig. 10) reveals, that the new approach predicts the location and the magnitude of the over- and underturning at hub and casing with a sufficient accuracy. These effects are caused by a system of channel vortices in the lower- and upper-half of the flow channel at the compressor exit.

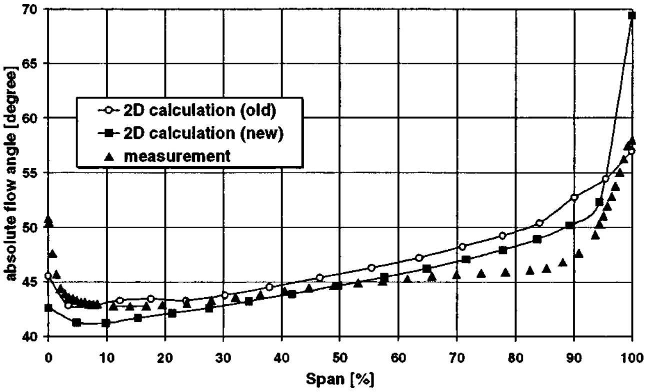

Fig. 8 Absolute whirl angle upstream Stator 1

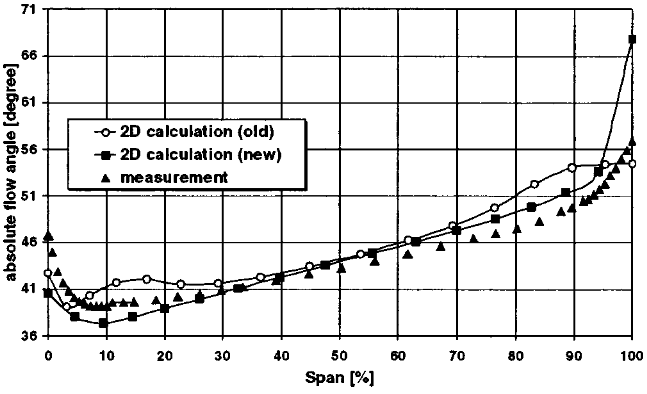

Fig. 9 Absolute whirl angle upstream Stator 2

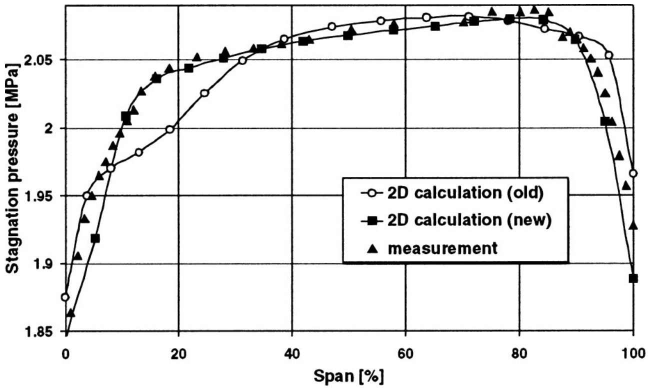

Fig. 11 Stagnation pressure at compressor exit (three-stage research compressor)

In the midspan region between 15 percent and 85 percent span, both 2D calculations miss predict the whirl angles by 3 to 4 deg. In this range, the whirl angles were measured with five hole probes, while the end wall regions were measured with three hole probes. Due to the fact, that the head of the five hole probe is four times larger than the head of the three hole probe, the authors assume, that the five hole probe causes a non-negligible blockage effect. This effect occurs significantly in the back end of the compressor, where the probe size is in the magnitude of 3 percent of the channel heights. This effect can also be seen in the meridional velocity distribution. While in the end wall regions, the measurements coincide with the 2D calculation (new model), a significant increase in the measured meridional velocity occurs between 15 percent and 85 percent span.

Stagnation Pressure. Figure 11 shows the total pressure distribution at the compressor exit. The comparison of total pressure distribution calculated by the new approach with the experimental data points out a remarkable agreement behind stator 3. Both the radial gradients and the absolute values match the experimental data very well.

Due to an overprediction of secondary loss and deviation by the conventional secondary loss and deviation model, a drop in stagnation pressure between 10 percent and 30 percent span can be seen for the ''old'' model. This drop starts in the mid region of the compressor and is strongly related to the above described buckles in the inlet and outlet flow angle distribution.

Results II. V84.3A Compressor

The advanced Model V84.3A was designed by United Technology Corporation and Siemens Power Generation. Advanced features derived from aeroengine technology such as controlled diffusion airfoils and custom tailored blading are included for loss minimization and to account for end wall and 3D flow effects (Hobbs and Weingold, [8], Janssen et al., [9]).

The aerodynamic design point of the compressor is as follows:

Corrected speed 3600 rpm
Corrected mass flow rate 430 kg/s
Pressure ratio 16

The 15-stage V84.3A compressor was analyzed by Elmendorf et al. [10] using the 3D Navier-Stokes code TASCflow™ (TASCflow3D Documentation [11]), which is widely used in sophisticated turbomachinery applications. Successive computations by coupled two-blade-row calculations yield a data base of the whole compressor flow field at design conditions.

Figures 12 and 13 show the computed relative whirl angles (from axial direction) of a typical rotor in the middle and in the rear part of the compressor. The 2D data are compared to the results of the 3D Navier-Stokes analysis. The rotor inlet flow in the mid and rear section of the compressor, is characterized by increased whirl angles at hub and tip due to the incoming boundary layers, which are strongly skewed while changing from the stationary to the rotating frame of reference. The agreement in both the absolute values and the gradients between the new 2D method and the 3D analysis is very good.

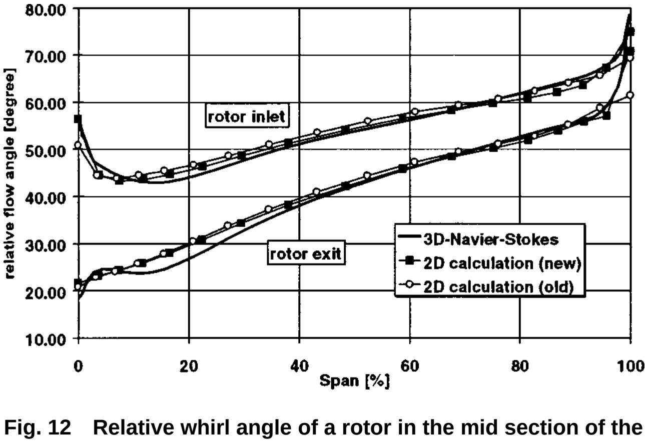

Fig. 12 Relative whirl angle of a rotor in the mid section of the V84.3A compressor

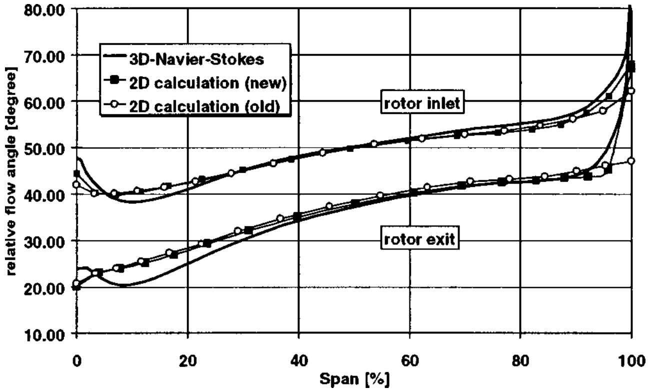

Fig. 13 Relative whirl angle of a rotor at the back end of the V84.3A compressor

At rotor outlet above 90 percent span the flow is dominated by the tip clearance. The underturning, which is mainly caused by shear force influence of the stationary casing wall in combination with the pressure gradient from pressure to suction side over the tip gap, is predicted in both calculation methods with a good agreement. The 3D results for the mid part of the compressor (Fig. 12) at rotor outlet near hub, show the occurrence of a channel vortex that causes an underturning at 5 percent span and an overturning at the hub end wall. In the rear part of the compressor (Fig. 13) underturning in the hub region becomes more significant. In comparison to the detailed 3D results, the 2D methods underpredict these effects near hub in the back end of the compressor. Nevertheless the calculated distributions of relative flow angles demonstrate the reliability of the new advanced 2D calculation method.

Rotor calculations with the 3D code were performed specifying a rotating frame of reference taking into account a rotating hub. For comparability with the 3D results the same boundary conditions were set up for the 2D calculations of the Siemens compressor. This is quite different to the 2D computation of the research compressor. According to the comparison with stationary measurements at a nonrotating hub downstream of the rotor, rotating boundaries are specified only for the first pass (inner streamlines) and for the second pass a stationary hub contour is defined (wall streamlines).

Figure 14 shows the development of total pressure by plotting the dimensionless radial distributions in the axial gaps located in front of stator 5, stator 7, and stator 14. The experimental data are derived from instrumented vanes at 9 radial positions.

The comparison between the 3D Navier-Stokes results and the measurements shows the best agreement. Both radial gradients and absolute levels are predicted with good accuracy.

However, also the radial distributions of the 2D calculations show a good agreement to the experimental data and the 3D results. Besides a minor overestimation of total pressure in the front and middle part of the compressor between 50 percent and 85 percent span, the total pressure rise is well predicted. Considering radial mixing and stator leakage flow yields realistic values at the hub. Due to an accurate prediction of the flow turning angles in rotors the stage matching is calculated with good accuracy.

The main deficiencies are detected for stator 14 in the hub region below 10 percent span. In comparison to the measurements the total pressure is overpredicted. Analyzing the 3D Navier-

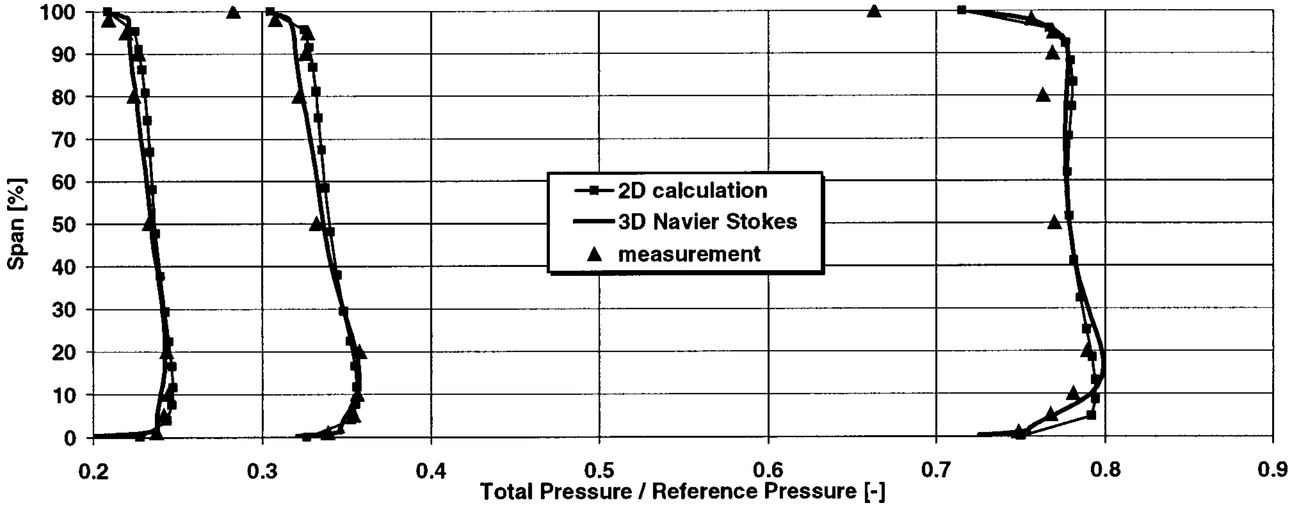

Fig. 14 Development of radial total pressure distribution of the V84.3A compressor

Stokes results, which fit the experimental data better at that location, an overprediction of flow turning within the hub region of rotor 14 becomes obvious.

Results III: Multistage Siemens Research Compressor

In the previous two examples, the quality of the numerical results obtained by the streamline curvature method not only depend on the different modeling of the end wall regions but also on the quality of the loss and deviation correlations for the 2D profile sections. The uncertainty, whether the disagreement between measurement or 3D Navier-Stokes solution and the results of the streamline curvature method is an effect of the 2D correlations or of the end wall model, is eliminated in the third test case.

In this example, the mid part of a multistage Siemens research

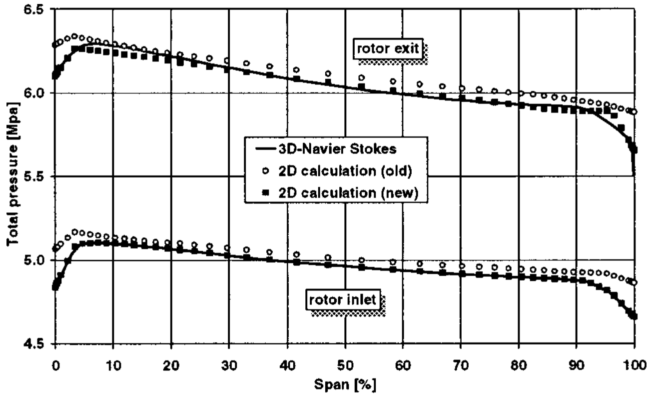

Fig. 15 Total pressure rotor 7

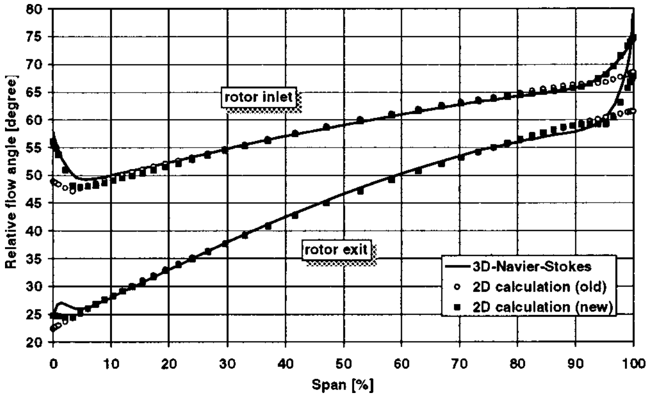

Fig. 17 Relative whirl angle rotor 7

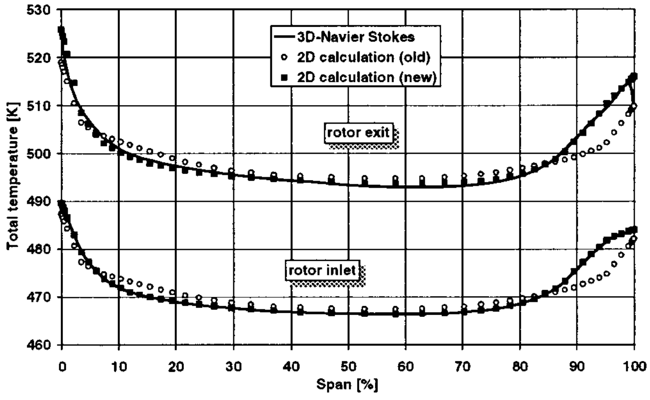

Fig. 16 Total temperature rotor 7

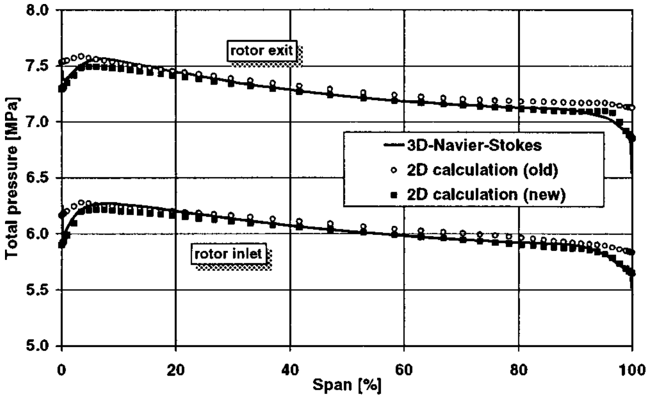

Fig. 18 Total pressure rotor 8

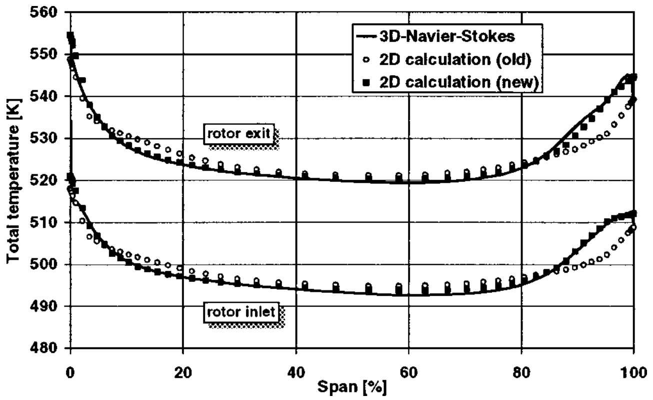

Fig. 19 Total temperature rotor 8

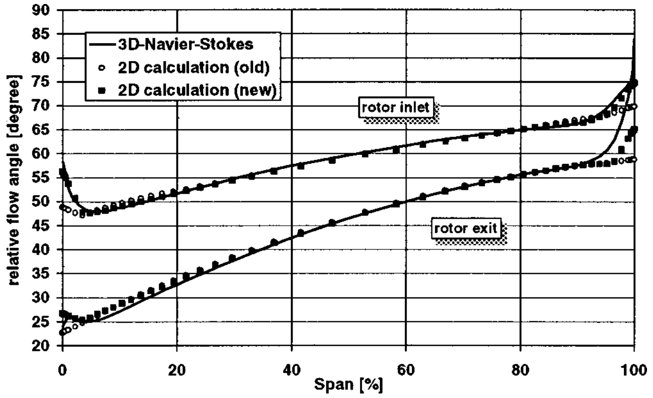

Fig. 20 Relative whirl angle rotor 8

compressor is analyzed with the 3D Navier-Stokes code CFX-TASC flow™ and compared with the ''old'' and ''new'' version of the streamline curvature method. The basis for the design is the new Siemens high performance airfoil (HPA) family, described by Köller et al. [12]. The profile losses and deviation for design and off-design conditions for all airfoils of the profile family are calculated with a blade-to-blade code and stored in a comprehensive database. Within the streamline curvature method, the 2D flow turning and profile losses are no longer calculated by correlations, but extracted out of this database.

Figures 15–20 show some characteristic calculation results of the multistage Siemens research compressor. Due to the above described method, the agreement between the 3D Navier-Stokes solution and the streamline curvature method is very good in all regions, where 2D effects dominate the flow field. In regions where 3D effects influence the flow field, significant differences between the old and new model can be seen. The differences mainly occur below 5 percent span and above 95 percent span. In these regions, differences in inlet and outlet flow angles up to 5 deg can be noticed between the models. This influences the total pressure and temperature rise across the blades and vanes.

The agreement between the new approach and the results of the 3D Navier-Stokes solutions is impressively accurate. Only the flow turning at tip of rotor 8 is calculated too small compared to the 3D solution due to underpredicting the tip leakage effects in the presented model.

Conclusions

A fast and efficient 2D calculation method is presented, which allows an overall viscous design of advanced multistage compressors. In order to improve the accuracy of loss- and deviation prediction, the strongly skewed and nondeveloped end wall boundary layers are split into an axial and tangential component, where especially the eddy viscosity within the boundary layers has different values for the meridional and circumferential direction.

To consider the shear forces due to the change from stationary to rotating end walls and vice versa, appropriate boundary conditions have to be specified. Within the new model, a two-step calculation procedure is described.

Moreover, the prediction of the viscous end wall zones is improved by taking into account the different behavior of accelerated and decelerated endwall boundary flow conditions in the sublayer region. As a result, empirical loss- and deviation correlations for secondary flow effects are no longer required.

For compressors consisting of stators with inner shrouds, bub leakage flows have to be considered instead of gap flows for cantilevered stators. In order to account for these effects, a new model for hub leakage flow effects is described.

The results of the improved method show a good agreement with experimental data of a three-stage research compressor and an improvement in comparisons with a conventional 2D method, which includes correlations for empirical 3D loss- and deviation effects.

The comparison with 3D Navier-Stokes results and measurements from the Siemens full load gas turbine facility of the Siemens V84.3A compressor, demonstrates the reliability of the improved 2D method for advanced industrial compressor designs and enables the designer to improve the efficiency by a better control of the 3D flow effects.

The very encouraging agreement between 3D Navier-Stokes results of a multistage Siemens research compressor and results of the presented method shows, that for future design tasks, a combination of the presented method and a database oriented approach for predicting the 2D loss and deviation effects is highly desirable.

Due to the high accuracy and the short computation time, the new method is a powerful tool in the viscous design and performance prediction of multistage axial compressors for heavy duty gas turbines and aeroengine applications.

Acknowledgments

The authors would like to express their sincerest thanks to the Institute of Jet Propulsion and Turbomachinery of the Technical University of Aachen (Germany) and the Forschungsvereinigung Verbrennungskraftmaschinen (FVV) for providing the experimental data of the three-stage research compressor and for allowing the results to be published.

Nomenclature

A = area
E = axial and tangential shear forces
H = enthalpy
k = von Karman constant
l = mixing length
m = mass flow
p = pressure
r = radius
R = gas constant
s = entropy
T = temperature
v = velocity
y = wall distance
z = number of seal strips
δ = boundary layer thickness
ε = mixing coefficient
k_t = eddy thermal conductivity
μ_t = eddy viscosity
ϕ = dissipation function

ρ = density

subscripts

1 = before mixing
2 = after mixing
L = leakage
SUB = sub layer
acc = accelerated
dec = decelerated
t = stagnation
i = in streamline direction
j = in radial direction
z = axial direction
m = meridional direction
w = circumferential direction

References

[1] Adkins, G. G., and Smith, L. H., ''Spanwise Mixing in Axial-Flow Turbomachines,'' ASME-Paper 81-GT-57.

[2] Gallimore, S. J., 1986, ''Spanwise Mixing in Multistage Axial Flow Compressors: Part II—Throughflow Calculations Including Mixing,'' ASME J. Turbomach., **108**, No. 1, pp. 10–16.

[3] Howard, M. A., and Gallimore S. J., 1992, ''Viscous Throughflow Modelling for Multi-stage Compressor Design,'' ASME-Paper 92-GT-302, Cologne, Germany.

[4] Edited by Johnsen, I. A., and Bullock, R. O., ''Aerodynamic Design of Axial Flow Compressors'', NASA Report SP-36, 1965.

[5] Schlichting, H., 1997, ''Grenzschicht-Theorie,'' 9th Ed. Springer-Verlag.

[6] Hoynacki, A., 1999, ''Einfluß von instationärer Strömung und Turbulenz auf die Grenzschichten und auf die Druckverteilungen von Beschaufelungen moderner mehrstufiger Axialverdichter,'' Forschungsvereinigung Verbrennungskraftmaschinen (FVV) Abschlußbericht, Heft 679.

[7] Roberts, W. B., Serovy, G. K., and Sandercock, D. M., 1988, ''Design Point Variation of Three-Dimensional Loss and Deviation for Axial Compressor Middle Stage,'' ASME J. Turbomach., **110**, pp. 426–433.

[8] Hobbs, D. E., and Weingold, H. D., 1984, ''Development of Controlled Diffusion Airfoils for Multistage Compressor Application,'' ASME J. Eng. Gas Turbines Power, **106**, pp. 271–278.

[9] Janssen, M., Zimmermann, H., Kopper, F., and Richardson, J., 1995, ''Application of Aero-Engine Technology to Heavy Duty Gas Turbines,'' ASME-Paper 95-GT-133, Houston, Texas.

[10] Elmendorf, W., Mildner, F., Röper, R., Krüger, U., and Kluck, M., 1998, ''Three-Dimensional Analysis of a Multistage Compressor Flow Field,'' ASME-Paper 98-GT-249, Stockholm, Sweden.

[11] Tascflow 3D Documentation, 1995–1997, Advanced Scientific Computing Ltd., Waterloo, Ontario, Canada.

[12] Köller, U., Mönig, R., Schreiber, H. A., and Küsters, B., 1999, ''Development of Advanced Compressor Airfoils for HeavyDuty Gas Turbines; Part I: Design and Optimization,'' ASME-Paper 99-GT-95, Indianapolis.

Linearized Unsteady Viscous Turbomachinery Flows Using Hybrid Grids

L. Sbardella

M. Imregun
e-mail: m.imregun@ic.ac.uk

Imperial College of Science,
Technology, & Medicine,
Mechanical Engineering Department,
Exhibition Road,
London SW7 2BX, United Kingdom

The paper describes the theory and the numerical implementation of a three-dimensional finite volume scheme for the solution of the linearized, unsteady Favre-averaged Navier–Stokes equations for turbomachinery applications. A further feature is the use of mixed element grids, consisting of triangles and quadrilaterals in two dimensions, and of tetrahedra, triangular prisms, and hexahedra in three dimensions. The linearized unsteady viscous flow equations are derived by assuming small harmonic perturbations from a steady-state flow and the resulting equations are solved using a pseudo-time marching technique. Such an approach enables the same numerical algorithm to be used for both the nonlinear steady and the linearized unsteady flow computations. The important features of the work are the discretization of the flow domain via a single, unified edge-data structure for mixed element meshes, the use of a Laplacian operator, which results in a nearest neighbor stencil, and the full linearization of the Spalart–Allmaras turbulence model. Four different test cases are presented for the validation of the proposed method. The first one is a comparison against the classical subsonic flat plate cascade theory, the so-called LINSUB benchmark. The aim of the second test case is to check the computational results against the asymptotic analytical solution derived by Lighthill for an unsteady laminar flow. The third test case examines the implications of using inviscid, frozen-turbulence, and fully turbulent models when linearizing the unsteady flow over a transonic turbine blade, the so-called 11th International Standard Configuration. The final test case is a rotor/stator interaction, which not only checks the validity of the formulation for a three-dimensional example, but also highlights other issues, such as the need to linearize the wall functions. Detailed comparisons were carried out against measured steady and unsteady flow data for the last two cases and good overall agreement was obtained. [DOI: 10.1115/1.1371777]

1 Introduction

Over the last three decades, considerable effort has been devoted to developing computational methods for modeling unsteady turbomachinery flows, especially for the prediction of aeroelasticity phenomena such as flutter and forced response. Review articles are given by Whitehead [1], Verdon [2], and Marshall and Imregun [3]. Due to computational limitations, early efforts were focused on semi-analytical formulations, and simplifying assumptions such as inviscid, incompressible, irrotational flows were the norm. In the main, such methods dealt with cascades of flat plates operating at zero incidence [4]. However, most modern computational techniques are based on either inviscid Euler or viscous Navier–Stokes equations and, broadly speaking, they can be divided into: (*i*) nonlinear time-marching methods and (*ii*) linearized frequency domain methods.

Erdos et al. [5] are among the pioneers for tackling nonlinear unsteady flows by time-marching methods. They predicted the two dimentional unsteady flow in a fan stage, including the use of an algorithm to treat unequal pitches. Such methods were further developed during the late 1980's and extended to three dimensions: Rai [6], Giles [7], He and Denton [8]. With currently available computational power, it is possible to undertake unsteady viscous flow predictions with large models. For instance, the forced response calculations for a whole-annulus, three-blade row model of a small fan are described by Sayma et al. [9]. Such computations include the effects of the blade flexibility through moving meshes. Although such investigations are very useful for gaining increased physical understanding of important unsteady flow and aeroelasticity phenomena associated with finite amplitude excitation, boundary layer displacement and separation, and large shock excursion, they can become prohibitively expensive for large models. Therefore, generally speaking, methods based on nonlinear aerodynamics do not meet the immediate needs of turbomachinery designers who require computationally efficient procedures for routine parametric calculations.

A good compromise between computational efficiency and flow accuracy can, in principle, be offered by linearized frequency domain methods. As mentioned earlier, early attempts to predict flow unsteadiness for turbomachinery applications were based on linear cascade theories. Verdon and Caspar [10] were among the first to develop linearized potential solvers. A two-dimensional steady-state flow was obtained from the nonlinear potential equation and three-dimensional effects were introduced by adding stream-tube thickness and radius changes. The complexities of extending the potential analysis to three-dimensional flows, the computational cost of the standard matrix solution methods, and the need to capture the flow details more accurately led to the development of linearized Euler methods. Following earlier work by Ni and Sisto [11], Hall and Crawley [12] developed a finite element method for solving the linearized Euler equations. They investigated flows in subsonic cascades and transonic ducts and used ''shock fitting.'' Further work in the area of linearized Euler equations is reported by Lindquist and Giles [13], Hall and Clark [14], Montgomery and Verdon [15,16]. Lindquist and Giles [13] proved that, if correctly formulated, shock capturing schemes can produce the same answers as shock-fitting schemes. This is an important finding because shock-capturing schemes are very much simpler to implement, particularly in three dimensions.

In any case, the analyses given above are based on an inviscid flow representation and thus they cannot deal with cases where

---

Contributed by the International Gas Turbine Institute for publication in the ASME JOURNAL OF TURBOMACHINERY. Manuscript received at ASME Headquarters February 2001. Associate Editor: T. H. Okiishi.

viscous effects are important: shock-boundary layer interaction, flow separation, and recirculation. Such features are particularly important for turbomachinery unsteady flows because most investigations are conducted at off-design conditions. For instance, generally speaking, fan blades do not encounter flutter problems at the design speed but part-speeds, where the flow behavior is dominated by viscous effects, may cause some concern. One of the first time-linearized Navier–Stokes analyses of a cascade unsteady flow was reported by Cizmas and Hall [17]. The computational domain was divided into two parts: a viscous flow near the airfoil and in the wake region, and an inviscid flow in the rest of the domain. The viscous flow was modeled using a finite difference discretization of the boundary layer equations while the inviscid flow was modeled using a finite element discretization of the full potential equation. However the analysis was limited to incompressible flows and to prescribed boundary layer assumption. Ning and He [18] presented a novel quasi-three dimensional nonlinear harmonic Euler/Navier–Stokes method, which combines the computational efficiency of linearized techniques and some of the accuracy of nonlinear formulations. Holmes et al. [19] are among the first researchers to present a three-dimensional time-linearized Navier–Stokes analysis with a $k-\omega$ turbulence model. Their results were limited to flows with a thin attached boundary layer and whether or not the turbulence model itself needed to be linearized was discussed in detail. Although this issue will be dealt with later in this paper, an overview will be given here. Avoiding the linearization of the turbulence model and using the mean-flow values for the eddy viscosity, the so-called frozen turbulence model is relatively straightforward. On the other hand, the linearization of the turbulence model may require significant algebra and coding effort. The mathematical formulation of a specific turbulence model and its mesh density requirement near the blade surface are further important considerations. For instance, a very fine mesh requirement may well negate some of the computational advantages. In any case, an important contribution is made by Clark and Hall [20] who reported a two-dimensional linearized Navier–Stokes analysis using the one-equation Spalart–Allmaras [21] turbulence model. They predicted the aeroelasticity behavior of a fan blade at some off-design condition that involved high incidence and flow separation over much of the suction surface. Their results showed good overall agreement with the available experimental data.

The present paper describes a three-dimensional finite-volume (FV) scheme for a full discretization of the time-linearized Navier–Stokes equations. The one-equation turbulence model of Spalart–Allmaras [21], which has the form of a sixth conservation equation, was linearized for a consistent formulation. The unified approach described in this paper allows the use of two-dimensional and three-dimensional structured, unstructured or block-structured grids with mixed elements under the same numerical scheme.

2 Time-Linearized Navier–Stokes Equations

2.1 Navier–Stokes Equations on a Moving Grid. For a three dimensional blade row, the unsteady, compressible, Favre-averaged Navier–Stokes equations can be cast in terms of absolute velocity $\vec{v}$ but solved in a relative non-Newtonian reference frame rotating along with the blade about the x_1 axis with angular velocity $\vec{\Omega}$. Using Cartesian coordinates $\vec{x}=(x_1,x_2,x_3)$, such equations can be written in an ALE integral conservative form for a control volume $\mathcal{V}(t)$ with moving boundary $\mathcal{S}(t)$:

$$\frac{\partial}{\partial t}\int_{\mathcal{V}(t)}\mathbf{U}\,d\mathcal{V}+\oint_{\mathcal{S}(t)}\left[\vec{\mathbf{F}}(\mathbf{U},\vec{u})-\frac{1}{\mathrm{Re}}\vec{\mathbf{G}}(\mathbf{U},\nabla\mathbf{U})\right]\cdot\vec{n}\,d\mathcal{S}=\int_{\mathcal{V}(t)}\mathbf{S}\,d\mathcal{V} \tag{1}$$

The viscous term $\vec{\mathbf{G}}$ on the left-hand side of Eq. (1) is scaled by the reference Reynolds number so that flow variables are nondimensionalized consistently. $\vec{n}$ represents the outward unit vector of the control volume boundary $\mathcal{S}(t)$. The vector $\vec{u}$, which represents the velocity in the relative frame of reference minus the velocity $d\vec{x}/dt$ of the boundary $\mathcal{S}(t)$, can be written as:

$$\vec{u}=\vec{v}-\vec{\Omega}\times\vec{x}-\frac{d\vec{x}}{dt} \tag{2}$$

The solution vector of conservative variables $\mathbf{U}$ is given by:

$$\mathbf{U}=[\rho\ \ \rho v_1\ \ \rho v_2\ \ \rho v_3\ \ \rho e]^T \tag{3}$$

The inviscid flux vector $\vec{\mathbf{F}}(\mathbf{U},\vec{u})$ has the following components:

$$\mathbf{F}^j=\mathbf{U}u_j+\mathbf{P}^j \tag{4}$$

$$\mathbf{P}^j=[0\ \ p\delta_{1j}\ \ p\delta_{2j}\ \ p\delta_{3j}\ \ v_jp]^T \tag{5}$$

where δ_{ij} is the Kronecker delta function. The pressure p and the total enthalpy h are related to the density ρ, absolute velocity $\vec{u}$ and internal energy e by the following two perfect gas equations with a constant ratio of specific heat γ:

$$p=(\gamma-1)\rho\left[e-\frac{|\vec{v}|^2}{2}\right],\quad h=e+\frac{p}{\rho} \tag{6}$$

Following the approach of Sbardella and Imregun [22], the viscous part of the governing equations is split into two distinct components, namely:

$$\vec{\mathbf{G}}=\vec{\mathbf{G}}_l+\vec{\mathbf{G}}_m \tag{7}$$

where

$$\vec{\mathbf{G}}_l=\begin{bmatrix}0\\ \mu\vec{\nabla}v_1\\ \mu\vec{\nabla}v_2\\ \mu\vec{\nabla}v_3\\ \mu\Sigma v_j\vec{\nabla}v_j+\dfrac{\gamma}{\gamma-1}\left(\dfrac{\mu_l}{Pr_l}+\dfrac{\mu_t}{Pr_t}\right)\vec{\nabla}T\end{bmatrix} \tag{8}$$

and the jth component of $\vec{\mathbf{G}}_m$ is given by:

$$\mathbf{G}_m^j=\begin{bmatrix}0\\ \mu\dfrac{\partial v_j}{\partial x_1}+(\lambda\vec{\nabla}\cdot\vec{v})\delta_{1j}\\ \mu\dfrac{\partial v_j}{\partial x_2}+(\lambda\vec{\nabla}\cdot\vec{v})\delta_{2j}\\ \mu\dfrac{\partial v_j}{\partial x_3}+(\lambda\vec{\nabla}\cdot\vec{v})\delta_{3j}\\ \mu(\vec{v}\cdot\vec{\nabla}v_j)+\lambda v_j(\vec{\nabla}\cdot\vec{v})\end{bmatrix} \tag{9}$$

In Eqs. (8) and (9), μ represents the total dynamic viscosity of the fluid and is given by the summation of the laminar (physical) dynamic viscosity μ_1 and the turbulent dynamic viscosity μ_t. The linearization of the latter, which needs to be evaluated using a suitable turbulence model, will later be discussed in some detail. The value of λ is given by the Stokes relation $\lambda=-(2/3)\mu$. It is easily seen that the component $\vec{\mathbf{G}}_1$ in Eq. (8) includes the Laplacian operators of the three velocity components and temperature only. The second component, $\vec{\mathbf{G}}_m$, contains the mixed derivative terms, the discretization of which is discussed in Sbardella and Imregun [22]. The vector of source terms $\mathbf{S}$ on the right-hand side of Eq. (1) takes into account for the Coriolis forces per unit mass

$$\mathbf{S}=[0\ \ 0\ \ \rho\Omega v_3\ \ -\rho\Omega v_2\ \ 0]^T \tag{10}$$

2.2 Linearization. The linearization of the governing equations around a steady-state solution starts by expressing the conservation variables and the coordinates as a sum of a mean steady-state value and a small perturbation:

$$\vec{x}(\overline{\vec{x}},t)=\overline{\vec{x}}+\tilde{\vec{x}}(\overline{\vec{x}},t) \tag{11}$$

$$\mathbf{U}(\overline{\vec{x}},t)=\overline{\mathbf{U}}(\overline{\vec{x}})+\tilde{\mathbf{U}}(\overline{\vec{x}},t) \tag{12}$$

It is then possible to express the unsteady flux vector $\vec{\mathbf{F}}$ in Eq. (4) as a summation of three different terms:

$$\vec{\mathbf{F}}=\overline{\vec{\mathbf{F}}}+\tilde{\vec{\mathbf{F}}}-\tilde{\vec{\mathbf{F}}}_{\vec{x}} \tag{13}$$

where $\overline{\vec{\mathbf{F}}}$ represents the mean steady value of the inviscid fluxes, $\tilde{\vec{\mathbf{F}}}$ is the unsteady part of the inviscid fluxes, which does not include the grid motion, while $\tilde{\vec{\mathbf{F}}}_{\vec{x}}$ includes the unsteady terms due to the grid motion only. To first order, using Eqs. (4) and (5), these terms can be expressed as:

$$\overline{\vec{\mathbf{F}}}=\overline{\mathbf{U}}(\overline{\vec{v}}-\vec{\Omega}\times\overline{\vec{x}})+\overline{\vec{\mathbf{P}}} \tag{14}$$

$$\tilde{\vec{\mathbf{F}}}=\tilde{\mathbf{U}}(\overline{\vec{v}}-\vec{\Omega}\times\overline{\vec{x}})+\overline{\mathbf{U}}\tilde{\vec{v}}+\tilde{\vec{\mathbf{P}}} \tag{15}$$

$$\tilde{\vec{\mathbf{F}}}_{\vec{x}}=\overline{\mathbf{U}}\left(\vec{\Omega}\times\tilde{\vec{x}}+\frac{d\tilde{\vec{x}}}{dt}\right) \tag{16}$$

Substituting into Eq. (1), one obtains:

$$\begin{aligned}&\frac{\partial}{\partial t}\int_{\mathcal{V}}(\overline{\mathbf{U}}+\tilde{\mathbf{U}})(d\overline{\mathcal{V}}+d\tilde{\mathcal{V}})+\oint_{\mathcal{S}}(\overline{\vec{\mathbf{F}}}+\tilde{\vec{\mathbf{F}}}-\tilde{\vec{\mathbf{F}}}_{\vec{x}})\cdot(\overline{\vec{n}\,d\mathcal{S}}+\widetilde{\vec{n}\,d\mathcal{S}})\\&\quad-\frac{1}{\mathrm{Re}}\oint_{\mathcal{S}}(\overline{\vec{\mathbf{G}}}+\tilde{\vec{\mathbf{G}}})\cdot(\overline{\vec{n}\,d\mathcal{S}}+\widetilde{\vec{n}\,d\mathcal{S}})-\int_{\mathcal{V}}(\overline{\mathbf{S}}+\tilde{\mathbf{S}})(d\overline{\mathcal{V}}+d\tilde{\mathcal{V}})=0\end{aligned} \tag{17}$$

By dropping the steady-state terms that must always satisfy Eq. (1) and by neglecting second-order terms like $\tilde{\mathbf{U}}\,d\tilde{\mathcal{V}}$, Eq. (17) becomes:

$$\begin{aligned}&\frac{\partial}{\partial t}\int_{\overline{\mathcal{V}}}\tilde{U}\,d\overline{\mathcal{V}}+\oint_{\overline{\mathcal{S}}}\left(\tilde{\vec{\mathbf{F}}}-\frac{1}{\mathrm{Re}}\tilde{\vec{\mathbf{G}}}\right)\cdot\overline{\vec{n}\,d\mathcal{S}}-\int_{\overline{\mathcal{V}}}\tilde{\mathbf{S}}\,d\overline{\mathcal{V}}\\&\quad=\int_{\overline{\mathcal{V}}}\overline{\mathbf{S}}\,d\tilde{\mathcal{V}}-\frac{\partial}{\partial t}\int_{\overline{\mathcal{V}}}\overline{\mathbf{U}}\,d\tilde{\mathcal{V}}-\oint_{\overline{\mathcal{S}}}\left(\overline{\vec{\mathbf{F}}}-\frac{1}{\mathrm{Re}}\overline{\vec{\mathbf{G}}}\right)\cdot\widetilde{\vec{n}\,d\mathcal{S}}\\&\qquad+\oint_{\overline{\mathcal{S}}}\tilde{\vec{\mathbf{F}}}_{\vec{x}}\cdot\overline{\vec{n}\,d\mathcal{S}}\end{aligned} \tag{18}$$

The system of equations in Eq. (18) is linear in the sense that all the coefficients multiplying the unsteady flow term $\tilde{\mathbf{U}}$ depend upon the steady-state flow term $\overline{\mathbf{U}}$ and geometric properties but not on time. In other words, a general solution of Eq. (18) can be represented via the following summations:

$$\tilde{\vec{x}}(\overline{\vec{x}},t)=\mathrm{Re}\sum_{\omega}\hat{\vec{x}}(\overline{\vec{x}},\omega)e^{-i\omega t} \tag{19}$$

$$\tilde{\mathbf{U}}(\overline{\vec{x}},t)=\mathrm{Re}\sum_{\omega}\hat{\mathbf{U}}(\overline{\vec{x}},\omega)e^{-i\omega t} \tag{20}$$

where $\hat{\vec{x}}$ represents the first-order complex amplitude of grid motion about the mean position, $\overline{\vec{x}}$ and $\hat{\mathbf{U}}$ represent the complex amplitude of the small unsteady perturbation of the conservation variables. By substituting the assumed solutions (19) and (20) for a single circular frequency ω into the linearized system of Eq. (18), one obtains:

$$\begin{aligned}&\oint_{\overline{\mathcal{S}}}\left(\hat{\vec{\mathbf{F}}}-\frac{1}{\mathrm{Re}}\hat{\vec{\mathbf{G}}}\right)\cdot\overline{\vec{n}\,d\mathcal{S}}-\int_{\overline{\mathcal{V}}}(i\omega\hat{\mathbf{U}}+\hat{\mathbf{S}})d\overline{\mathcal{V}}\\&\quad=\int_{\overline{\mathcal{V}}}(i\omega\overline{\mathbf{U}}+\overline{\mathbf{S}})d\hat{\mathcal{V}}-\oint_{\overline{\mathcal{S}}}\left(\overline{\vec{F}}-\frac{1}{\mathrm{Re}}\overline{\vec{G}}\right)\cdot\widehat{\vec{n}\,d\mathcal{S}}\\&\qquad+\oint_{\overline{\mathcal{S}}}\overline{\mathbf{U}}(\vec{\Omega}\times\hat{\vec{x}}-i\omega\hat{\vec{x}})\cdot\overline{\vec{n}\,d\mathcal{S}}\end{aligned} \tag{21}$$

In Eq. (21) the left-hand side contains homogeneous terms only, while the right-hand side contains nonhomogeneous terms that depend on the (known) steady-state flow and the prescribed grid motion. The nonhomogeneous terms are identically zero if there is no grid motion ($\hat{\vec{x}}=0$), as is the case for forced response problems. Since the Jacobians with respect to the steady-state flow variables are real quantities, the homogeneous terms of the form $i\omega\int_{\overline{\mathcal{V}}}\hat{\mathbf{U}}\,d\overline{\mathcal{V}}$, which represent the time rate of change of the perturbed conservation variables, couple the real and imaginary parts of the perturbed flow equations.

Indicating with $\hat{\mathbf{H}}(\overline{U},\hat{\mathbf{x}})$ the summation of the nonhomogeneous terms on the right-hand side of Eq. (21) and introducing a pseudo-time derivative so that standard time-marching algorithms can be used, Eq. (21) becomes:

$$\frac{\partial}{\partial\tau}\int_{\overline{\mathcal{V}}}\hat{\mathbf{U}}\,d\overline{\mathcal{V}}+\oint_{\overline{\mathcal{S}}}\left(\hat{\vec{\mathbf{F}}}-\frac{1}{\mathrm{Re}}\hat{\vec{\mathbf{G}}}\right)\cdot\overline{\vec{n}\,d\mathcal{S}}-\int_{\overline{\mathcal{V}}}(i\omega\hat{\mathbf{U}}+\hat{\mathbf{S}})d\overline{\mathcal{V}}=\hat{\mathbf{H}}(\overline{\mathbf{U}},\hat{\vec{x}}) \tag{22}$$

3 Boundary Conditions

There are five different sets of boundary conditions: flow tangency for inviscid flow calculations, no-slip condition for viscous flow calculations, periodic boundaries, inflow, and outflow.

3.1 Flow Tangency. The flow tangency condition at the solid walls is expressed by the requirement that there is no flow through the surface of the moving wall. Therefore, the local fluid velocity relative to the moving wall has no component normal to the wall. Mathematically this can be expressed as:

$$\vec{u}\cdot\vec{n}=\left(\vec{v}-\vec{\Omega}\times\vec{x}-\frac{d\vec{x}}{dt}\right)\cdot\vec{n}=0 \tag{23}$$

Linearizing and keeping zeroth- and first-order terms gives the mean flow and the linearized tangency conditions, respectively:

$$(\overline{\vec{v}}-\vec{\Omega}\times\overline{\vec{x}})\cdot\overline{\vec{n}}=0 \tag{24}$$

$$(\hat{\vec{v}}-\vec{\Omega}\times\hat{\vec{x}}+i\omega\hat{\vec{x}})\cdot\overline{\vec{n}}+(\overline{\vec{v}}-\vec{\Omega}\times\overline{\vec{x}})\cdot\hat{\vec{n}}=0 \tag{25}$$

Applying condition (25) to the evaluation of the flux term for a solid wall surface yields:

$$\begin{aligned}&\oint_{\mathrm{wall}}[\hat{\vec{F}}-\overline{U}(\vec{\Omega}\times\hat{\vec{x}}-i\omega\hat{\vec{x}})]\cdot\overline{\vec{n}\,d\mathcal{S}}+\oint_{\mathrm{wall}}\overline{\vec{F}}\cdot\widehat{\vec{n}\,d\mathcal{S}}\\&=\left[\begin{array}{c}0\\ \hat{p}\,\overline{n_x\,d\mathcal{S}}+\overline{p}\,\widehat{n_x\,d\mathcal{S}}\\ \hat{p}\,\overline{n_y\,d\mathcal{S}}+\overline{p}\,\widehat{n_y\,d\mathcal{S}}\\ \hat{p}\,\overline{n_x\,dS}+\overline{p}\,\widehat{n_x\,d\mathcal{S}}\\ \hat{p}(\vec{\Omega}\times\overline{\vec{x}})\cdot\overline{\vec{n}\,d\mathcal{S}}+\overline{p}[(\vec{\Omega}\times\overline{\vec{x}})\cdot\widehat{\vec{n}\,d\mathcal{S}}+(\vec{\Omega}\times\hat{\vec{x}}-i\omega\hat{\vec{x}})\cdot\overline{\vec{n}\,d\mathcal{S}}]\end{array}\right]\end{aligned} \tag{26}$$

3.2. No-Slip Condition. The no-slip condition at the solid walls is expressed by the requirement that the local fluid velocity relative to the moving wall must be zero. Mathematically this can be expressed as:

$$\vec{u}=\vec{v}-\vec{\Omega}\times\vec{x}-\frac{d\vec{x}}{dt}=0 \tag{27}$$

As before, linearizing and keeping zeroth- and first-order terms gives the mean flow and the linearized no-slip conditions, respectively:

$$\overline{\vec{v}} - \vec{\Omega} \times \overline{\vec{x}} = 0 \tag{28}$$

$$\hat{\vec{v}} - \hat{\Omega} \times \hat{\vec{x}} + i\omega \hat{\vec{x}} = 0 \tag{29}$$

3.3 Periodic Boundaries. The periodic boundary conditions are somewhat more complicated than those for the steady-state flow equations. In a flutter application, the blade may oscillate with a nonzero phase shift with respect to its neighbors. Similarly, in a wake/rotor interaction, there will be a phase difference in the unsteady pressure distributions experienced by neighboring rotor blades if there is no one-to-one correspondence between the wakes and the rotor blades. Such phase differences are represented by the interblade phase angle σ. Using an axisymmetric coordinate system, the periodic boundary condition can be written as:

$$\hat{U}_{\theta_0+\Delta\theta} = \exp(-i\sigma)\hat{U}_{\theta_0} \tag{30}$$

where $\hat{U}$ is the state variable at position θ_0, $\Delta\theta$ representing the angular pitch of the blade-to-blade passage. The same equation can be used for two dimensional cascade, by replacing θ_0 and $\Delta\theta$ by y_0 and P in a Cartesian coordinate system.

3.4 Inflow and Outflow Boundaries. Unsteady flow computations require nonreflecting boundary conditions at the far-field boundaries to prevent spurious inwards reflections of outgoing waves. The single-frequency nonreflecting boundary conditions of Giles [23] will be used here. These boundary conditions are constructed with the aid of the one-dimensional characteristic variables. The equations relating the harmonic primitive variables and the harmonic characteristic variables can be written as:

$$\begin{bmatrix} \hat{w}_1 \\ \hat{w}_2 \\ \hat{w}_3 \\ \hat{w}_4 \\ \hat{w}_5 \end{bmatrix} = \begin{bmatrix} -\overline{c}^2 & 0 & 0 & 0 & 1 \\ 0 & 0 & \overline{\rho c} & 0 & 0 \\ 0 & 0 & 0 & \overline{\rho c} & 0 \\ 0 & \overline{\rho c} & 0 & 0 & 1 \\ 0 & -\overline{\rho c} & 0 & 0 & 1 \end{bmatrix} \begin{bmatrix} \hat{\rho} \\ \widehat{v_x} \\ \widehat{v_\theta} \\ \widehat{v_r} \\ \hat{p} \end{bmatrix} \tag{31}$$

The first characteristic variable represents the one-dimensional entropy wave, the second and third represent the two one dimensional vorticity waves, while the fourth and the fifth characteristic variables represent the forward and backward one-dimensional pressure waves. These one dimensional characteristic variables can be expressed as a sum of spatial harmonics satisfying the periodicity condition with the correct interblade phase angle.

$$\hat{w}_n = \sum_m \hat{w}_n^m \exp\left[i\theta \frac{2\pi m - \sigma}{\Delta\theta}\right] \tag{32}$$

Following the work of Giles [23], it is possible to express the mth harmonic of the incoming one-dimensional characteristic variables as a function of the mth harmonic of the outgoing ones. At the inflow, the boundary condition is:

$$\begin{bmatrix} \hat{w}_1^m \\ \hat{w}_2^m \\ \hat{w}_3^m \\ \hat{w}_4^m \end{bmatrix} = \begin{bmatrix} 0 \\ \dfrac{(1-\mathrm{M}_x)\beta_m}{1-\mathrm{M}_\theta\beta_m + T_m} \\ 0 \\ \dfrac{(1-\mathrm{M}_x)^2\beta_m^2}{(1-\mathrm{M}_\theta\beta_m + T_m)^2} \end{bmatrix} \hat{w}_5^m \tag{33}$$

while at the outflow it becomes:

$$\hat{w}_5^m = \frac{2-\mathrm{M}_x\beta_m}{1-\mathrm{M}_\theta\beta_m + T_m}\hat{w}_2^m + \frac{1-\mathrm{M}_\theta\beta_m - T_m}{1-\mathrm{M}_\theta\beta_m + T_m}\hat{w}_4^m \tag{34}$$

In both cases β_m is an inverse reduced frequency defined by:

$$\beta_m = \frac{2\pi m - \sigma}{r\Delta\theta\omega}\overline{c} \tag{35}$$

where $\overline{c}$ is the average speed of sound and $r\Delta\theta$ is the product of radius and angular pitch. T_m in Eq. (34) is defined by:

$$T_m^2 = (1-\mathrm{M}_\theta\beta_m)^2 - (1-\mathrm{M}_x^2)\beta_m^2 \tag{36}$$

$$T_m = \begin{cases} \operatorname{sign}(1-\mathrm{M}_\theta\beta_m)\sqrt{T_m^2} & T_m^2 > 0 \\ \operatorname{sign}(\omega)\, i\sqrt{-T_m^2} & T_m^2 < 0 \end{cases} \tag{37}$$

Giles [23] suggested that the periodic boundary conditions should be lagged when using pseudo time marching, though this was not found necessary with the particular solver used here. Equations (33) and (34) are the exact two-dimensional analytical boundary conditions. These can be extended to three-dimensional problems by imposing them in a strip-theory fashion at each spanwise radial station at the domain boundary, the so-called quasi-three-dimensional nonreflecting boundary conditions [24]. One limitation of such an approach is the inherent assumption that the radial variation in the mean and unsteady flow fields is considerably smaller than that in the tangential direction. This is not necessarily the case in aeroacoustic applications. A more general three-dimensional approach, developed by Hall et al. [25], is a mixed analytical/numerical boundary condition treatment. The assumption is that the mean flow field is axisymmetric and uniform in the axial direction, but may have significant radial variation. The unsteady flow-field is decomposed into Fourier modes in the circumferential direction, and a radial eigenvalue problem is solved to determine the wave numbers and the radial mode shapes of the unsteady flow modes. The modal information is then used to construct highly nonreflective boundary conditions. However, in some special cases, the identification of the incoming and outgoing modes may be difficult and truncation errors may affect the scheme adversely. Nevertheless, the approach is probably the most general boundary condition treatment currently available.

4 Numerical Implementation

From the outset, it should be noted that the linearization must be done in a consistent fashion, for both the inviscid and viscous fluxes. The former requires the linearization of the artificial dissipation and the latter that of the turbulence model. These issues will now be addressed in more detail. The linearization of the wall function is discussed in the appendix.

As shown for the two dimensional mesh of Fig. 1, using a node-centered approach and choosing the median dual mesh as control volume, a FV discretization of Eq. (1) can be written in the following semi-discrete form:

$$\frac{\partial(\mathcal{V}_1\hat{U}_1)}{\partial t} + \sum_{s=1}^{m_I} [|\vec{\eta}_{IJs}|(\hat{\mathcal{F}}_{IJs} - \hat{\mathcal{G}}_{m_{IJs}}) - \tau_{IJs}\hat{\mathcal{G}}l_{IJs}] = \mathcal{V}_I(i\omega\hat{U}_I + \hat{S}_I + \hat{H}_I) \tag{38}$$

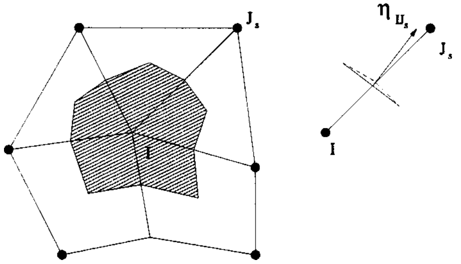

Fig. 1 Median dual control volume for edge *Ijs*, showing nodes *I* and *Js*, and metric vector $\vec{\eta}_{IJs}$

As shown in Fig. 1, node I is connected by edges to m_I nodes, J_a, $\mathcal{V}_I$ representing the control volume associated with it. The metric vector $\vec{\eta}_{IJs}$, associated with edge IJs, is obtained by the summation of the two dual median lengths around the edges, multiplied by their normals. For example, the metric vector of the edge connecting nodes I and Js is shown in Fig. 1 for a two-dimensional mesh. As proposed by Sbardella and Imregun [22], the Laplacian weight τ_{IJs}, associated with edge IJs, is calculated using a finite element approximation.

4.1 Inviscid Fluxes. The discretization of the inviscid flow terms in Eq. (38) is given by:

$$\sum_{s=1}^{m_I} |\vec{\eta}_{IJs}|\hat{\mathcal{F}}_{IJs} \tag{39}$$

where $\hat{\mathcal{F}}_{IJs}$ represents the inviscid flux function along edge IJ_s, which is obtained using a central difference scheme with added matrix artificial dissipation. This artificial dissipation is a blend of second and fourth-order differences. The fourth-order terms ensure the stability of the scheme in smooth regions of the flow, while the second-order terms are required to damp numerical oscillations in the vicinity of discontinuities. The inviscid flux function is expressed as:

$$\hat{\mathcal{F}}_{IJs}=\frac{\hat{\vec{\mathbf{F}}}_I+\hat{\vec{\mathbf{F}}}_{Js}}{2}\cdot\frac{\vec{\eta}_{IJs}}{|\vec{\eta}_{IJs}|}-\hat{\mathcal{D}}_{IJs} \tag{40}$$

where the linearized artificial dissipation $\hat{\mathcal{D}}_{IJs}$ along the edge IJ_s is given by:

$$\hat{D}_{IJs}=\frac{1}{2}|\overline{\mathbf{A}}_{IJs}|[\overline{\phi}\Delta\hat{\mathbf{U}}-\epsilon_4(1-\overline{\phi})\Delta\hat{\mathcal{L}}] \tag{41}$$

Here Δ represents the difference operator along edge IJs:

$$\Delta(\cdot)=(\cdot)_{Js}-(\cdot)_I \tag{42}$$

$|\overline{\mathbf{A}}_{IJs}|$ is the standard Roe matrix [26] between the two stages $\overline{\mathbf{U}}_1$ and $\mathbf{U}_{Js}$; $\epsilon_4\approx 1/16$ is the fourth-order artificial dissipation coefficient. $\hat{\mathcal{L}}$ is a pseudo-Laplacian operator given by:

$$\hat{\mathcal{L}}(\hat{U}_I)=\left(\sum_{s=1}^{m_I}\frac{\hat{\mathbf{U}}_{Js}-\hat{\mathbf{U}}_I}{|\overline{\vec{x}}_{Js}-\overline{\vec{x}}_I|}\right)\left(\sum_{s=1}^{m_I}\frac{1}{|\overline{\vec{x}}_{Js}-\overline{\vec{x}}_I|}\right)^{-1} \tag{43}$$

$\overline{\phi}$ represents the limiting function, which varies between 0 and 1, and it is required in order to switch the scheme to first order ($\overline{\phi}=1$) in the vicinity of discontinuities. This limiter is computed for the steady-state flow using a multidimensional extension of that presented by Jorgenson and Turkel [27].

4.2 Viscous Terms. The viscous fluxes associated with the mixed derivatives in $\vec{\mathbf{G}}_m$ in Eq. (9) are treated in the same way as their inviscid counterparts and their contribution to Eq. (38) is given by:

$$\hat{\mathcal{G}}_{m_{IJs}}=\frac{1}{\text{Re}}(\hat{\vec{\mathbf{G}}}_{m_I}+\hat{\vec{\mathbf{G}}}_{m_{Js}})\cdot\frac{\vec{\eta}_{IJs}}{|\vec{\eta}_{IJs}|} \tag{44}$$

where

$$\hat{\vec{\mathbf{G}}}_m=\hat{\vec{\mathbf{G}}}|_{\overline{\mu}}+\hat{\vec{\mathbf{G}}}_m|_{\Delta\overline{U}} \tag{45}$$

The first term on the left-hand side of Eq. (45) contains the contribution due to the gradients of the unsteady flow velocity and temperature at constant viscosity μ. The second term takes into account the variation of the unsteady viscosity only. The Laplacian terms are treated in a different way in order to improve both the accuracy and the robustness of the numerical scheme. In Eq. (38), these terms take the form:

$$\hat{\mathcal{G}}_{l_{IJs}}=\hat{\mathcal{G}}_{l_{IJs}}|_{\hat{\mu}}+\overline{\mathcal{G}}_{l_{IJs}}|_{\Delta\overline{U}} \tag{46}$$

where

$$\hat{\mathcal{G}}_{l_{IJs}}|_{\overline{\mu}}=\frac{1}{\text{Re}}\begin{bmatrix}0\\ \overline{\mu}_{IJs}\Delta\hat{v}_1\\ \overline{\mu}_{IJs}\Delta\hat{v}_2\\ \overline{\mu}_{IJs}\Delta\hat{v}_3\\ (\overline{\mu\vec{v}})_{IJs}\cdot\Delta\hat{\vec{v}}+\dfrac{\gamma}{\gamma-1}\left(\dfrac{\overline{\mu}_l}{\text{Pr}_l}+\dfrac{\overline{\mu}_t}{\text{Pr}_t}\right)_{IJs}\Delta\hat{T}\end{bmatrix} \tag{47}$$

$$\hat{\mathcal{G}}_{l_{IJs}}|_{\Delta\overline{U}}=\frac{1}{\text{Re}}\begin{bmatrix}0\\ \hat{\mu}_{IJs}\Delta\overline{v}_1\\ \hat{\mu}_{IJs}\Delta\overline{v}_2\\ \hat{\mu}_{IJs}\Delta\overline{v}_3\\ (\overline{\mu}\hat{\vec{v}}+\hat{\mu}\overline{\vec{v}})_{IJs}\cdot\Delta\overline{\vec{v}}+\dfrac{\gamma}{\gamma-1}\left(\dfrac{\hat{\mu}_l}{\text{Pr}_l}+\dfrac{\hat{\mu}_t}{\text{Pr}_t}\right)_{IJs}\Delta\overline{T}\end{bmatrix} \tag{48}$$

The subscript IJs indicates an arithmetic mean over nodes I and Js:

$$(\cdot)_{IJs}=\frac{(\cdot)_I+(\cdot)_{Js}}{2} \tag{49}$$

The evaluation of terms $\overline{\vec{\mathbf{G}}}_m|_{\Delta\overline{\mathbf{U}}}$ and $\vec{\mathcal{G}}_{l_{IJs}}|_{\Delta\overline{\mathbf{U}}}$ requires the linearization of the turbulence model used in the steady flow solver. If this term is neglected, the linearized viscous terms can still be represented by simply using the mean-flow values for the eddy viscosity, the so-called frozen turbulence approach. Such a scheme is relatively simple to implement for any turbulence model, while a full linearization will depend on the particular type of the turbulence model used. A linearized version of the Spalart–Allmaras turbulence model is given in the appendix. The linearized turbulence model was checked against the measured unsteady turbulent boundary layer data compiled in Cebeci [28] for a flat plate. Good agreement was obtained between the computed results and the measured unsteady velocity profiles along the boundary layer.

4.3 Time Integration. The pseudo-time derivative introduced in Eq. (22) allows the use of standard time-marching algorithms when solving the linearized equations. Many different approaches are possible. For instance, Hall and Clark [29] use an explicit Lax–Wendroff technique together with local time-stepping and multigrid in order to accelerate convergence to a steady-state. Marshall and Giles [30] use an explicit multistage Runge–Kutta technique with local time stepping. Here, it is proposed to follow the approach of Montgomery and Verdon [15]. The technique consists of a two-point backward implicit difference and the expansion of the residual about the nth time level. Indicating with $\Delta_r\hat{\mathbf{U}}_I=\hat{\mathbf{U}}_I^{n+1}-\hat{\mathbf{U}}_I^n$ a two-point backward implicit difference, Eq. (38) can be written as:

$$(\overline{\mathbf{J}}_D-i\omega\mathcal{V}_I I)\Delta_r\hat{\mathbf{U}}_I+\sum_{s=1}^{m_I}\overline{\mathbf{J}}_{OD_s}\Delta_r\hat{\mathbf{U}}_{Js}=\hat{\mathbf{R}}_I^n \tag{50}$$

where the block diagonal contribution, $\overline{\mathbf{J}}_D$, to the Jacobian matrix is given by:

$$\overline{\mathbf{J}}_D=\mathcal{V}_I\left(\frac{1}{\delta\tau}\mathbf{I}-\frac{\partial\overline{\mathbf{S}}_I}{\partial\overline{\mathbf{U}}_I}\right)+\sum_{s=1}^{m_I}\left(|\vec{\eta}_{IJs}||\overline{\mathbf{A}}_{IJs}|+\tau_{IJs}\left.\frac{\partial\overline{\mathcal{G}}_{l_{IJs}}}{\partial\overline{\mathbf{U}}_I}\right|_{\overline{\mu}}\right) \tag{51}$$

where $\delta\tau$ represents the local pseudo-time step which is evaluated using a CFL-like condition. The off-diagonal contribution of node Js is:

$$\overline{\mathbf{J}}_{OD_s}=\frac{1}{2}\,\frac{\partial\overline{\vec{\mathbf{F}}}_{Js}}{\partial\overline{U}_{Js}}\cdot\vec{\eta}_{IJs}-|\vec{\eta}_{IJs}||\overline{\mathbf{A}}_{IJs}|-\tau_{IJs}\,\frac{\partial\overline{\mathcal{G}}_{l_{IJs}}}{\partial\overline{\mathbf{U}}_{Js}}\bigg|_{\overline{\mu}} \tag{52}$$

The term $(1/2)\Sigma(\partial\overline{\vec{\mathbf{F}}}_I/\partial\overline{\mathbf{U}}_{\mathbf{I}})\cdot\vec{\eta}_{IJs}$ has been omitted from Eq. (51) because its contribution is null due to the conservation property. The right-hand side term, represented by vector $\hat{\mathbf{R}}_I^n$ and evaluated at time level n, is given by

$$\hat{\mathbf{R}}_I^n=\mathcal{V}_I(i\omega\hat{\mathbf{U}}_I^n+\hat{\mathbf{S}}_I^n+\hat{\mathbf{H}}_I)-\sum_{s=1}^{m_I}\,[|\vec{\eta}_{IJs}|(\hat{\mathcal{F}}_{IJs}^n-\hat{\mathcal{G}}^n m_{IJs})-\tau_{IJs}\hat{\mathcal{G}}^n l_{IJs}] \tag{53}$$

Equation (50) represents a sparse linear system, which needs to be solved at each time level n. It is worth to note that a *defect-correction procedure* is used in the evaluation of this system. This procedure discretizes the left-hand side sparse matrix using a lower-order approximation, which is first-order in space. Such a route is chosen not only because of efficient storage and coding simplicity, but also because the resulting matrix is better conditioned than that obtained from higher-order approximations [31]. Furthermore, the mixed-derivative term of the viscous fluxes $\vec{\mathbf{G}}_m$ is treated explicitly only.

The sparse linear system (50) is solved using a point Jacobi iteration. Indicating with $\hat{\mathbf{\Phi}}_I^l$ the lth approximation to $\Delta_\tau\hat{\mathbf{U}}_I$, the iterative method can be outlined as:

$$(\overline{\mathbf{J}}_D-i\omega\mathcal{V}_I\mathbf{I})\hat{\mathbf{\Phi}}_I^{l+1}=\hat{\mathbf{Q}}_I^l \tag{54}$$

$$\hat{\mathbf{Q}}_I^l=\hat{\mathbf{R}}_I^n-\sum_{s=1}^{m_I}\overline{\mathbf{J}}_{OD_s}\hat{\mathbf{\Phi}}_{Js}^l \tag{55}$$

$$\lim_{l\to\infty}\Phi^l=\Delta_r\hat{\mathbf{U}}_I \tag{56}$$

By splitting the equations above into their real and imaginary parts, one obtains:

$$\mathrm{Re}(\hat{\mathbf{\Phi}}_I^{l+1})=(\overline{\mathbf{J}}_D+\omega^2\mathcal{V}_I^2\overline{\mathbf{J}}_D^{-1})^{-1}[\mathrm{Re}(\hat{\mathbf{Q}}_J^l)-\omega\mathcal{V}_I\overline{\mathbf{J}}_D^{-1}\,\mathrm{Im}(\hat{\mathbf{Q}}_I^l)] \tag{57}$$

$$\mathrm{Im}(\hat{\mathbf{\Phi}}_I^{l+1})=(\overline{\mathbf{J}}_D+\omega^2\mathcal{V}_I^2\overline{\mathbf{J}}_D^{-1})^{-1}[\mathrm{Im}(\hat{\mathbf{Q}}_I^1)+\omega\mathcal{V}_I\overline{\mathbf{J}}_D^{-1}\,\mathrm{Re}(\hat{\mathbf{Q}}_I^l)] \tag{58}$$

This formulation requires the storage of only two 5×5 block matrices, which are computed only once at the beginning of the numerical integration. Local time stepping is employed in order to speed up convergence. Numerical experiments suggest that a good convergence to steady state can be obtained by performing around 10 Jacobi iterations using a CFL number of around 15.

5 Test Cases

5.1 Linear Flat-Plate Cascade. Small-amplitude perturbations of a uniform, inviscid steady-state flow past an unloaded flat-plate cascade were studied first. In order to handle the leading and trailing edge discontinuities, a fine mesh resolution was used in these regions.[1] A case with a pitch-to-chord ratio of 0.5, a stagger angle of 30 deg and a mean-flow Mach number of 0.7 was used to simulate a wake/blade interaction, an incoming sinusoidal wake with a reduced frequency of π being specified at the inflow boundary. The interblade phase angle is −90 deg. The results of the unsteady flow computations were checked against the benchmark LINSUB code by plotting the real and imaginary parts of the (complex) unsteady pressure difference across the plate. As can be seen from Fig. 2, there is excellent agreement between the present method and the benchmark LINSUB code. Very similar results, not reported here, were obtained for two further disturbances: potential/blade interaction and unsteadiness due to the bending motion of the plate.

5.2 Unsteady Laminar Boundary Layer on a Flat Plate. This test case studies an unsteady laminar boundary layer with fluctuations in external velocity. The computational mesh is shown in Fig. 3. The boundary layer region is discretized using 15 layers of quadrilateral elements, while the rest of the domain consists of triangles. The pitch-to-chord ratio of this cascade is unity so that the flow is as close as possible to that over an isolated flat plate. The steady-state flow over an unstaggered flat plate cascade was obtained for a Mach number of 0.2. The free-stream Reynolds number is 60,000. Such a case is well within the incompressible flow regime, thus enabling a meaningful comparison with the Blasius solution. Indeed, the computed steady-state velocity profile and the skin friction coefficient are found to be in very good agreement with the incompressible laminar boundary layer theory of Blasius (Fig. 4). Once the steady-state flow has been validated, the next stage is to study a velocity perturbation of the form:

$$u=\varepsilon u_0 e^{-i\omega t} \tag{59}$$

where u_0 is the free-stream velocity and ω is the circular frequency. The disturbance is along the plate, in the free-stream di-

---

[1] Mesh convergence studies were conducted for all results presented in this paper.

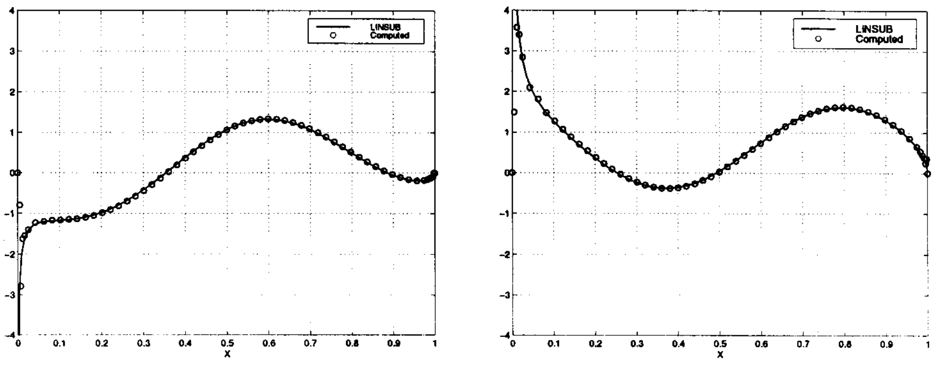

(a) Real part

(b) Imaginary part

Fig. 2 Pressure jump on flat plate due to wake/rotor interaction

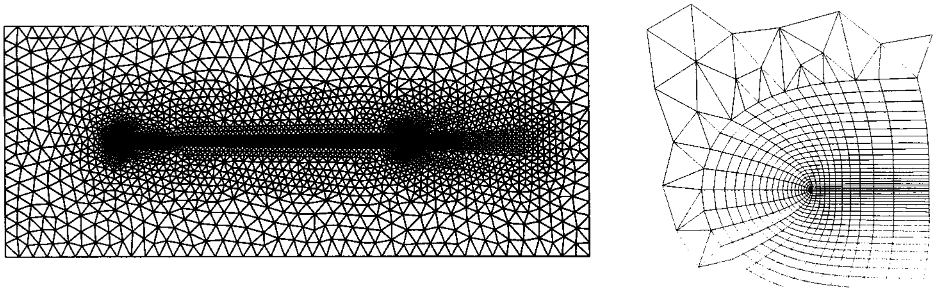

(a) Computational mesh (5954 points) (b) trailing edge

Fig. 3 Computational domain for laminar flow over a flat plate cascade: (*a*) computational mesh (5954 points); (*b*) trailing edge

rection, denoted by coordinate x. Lighthill's [32] theory provides two asymptotic values for the unsteady skin friction coefficient, one for very small and the other for very large reduced frequency values. Figure 5(*a*) shows the wall shear stress amplitude variation with reduced frequency $\omega x/u_0$ while Fig. 5(*b*) shows the computed phase angle between shear stress and external velocity. As expected, the computed results become asymptotic for the limiting cases of very small and very large reduced frequency. Similar comparisons between numerical results and Lighthill's theory are also reported by Cebeci [28].

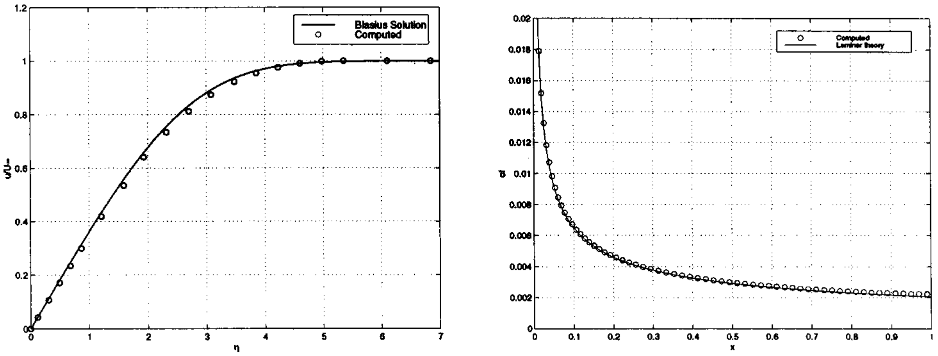

(a) Velocity profile (b) Skin friction coefficient

Fig. 4 Steady laminar flow over a cascade of flat plates: (*a*) velocity profile; (*b*) skin friction coefficient

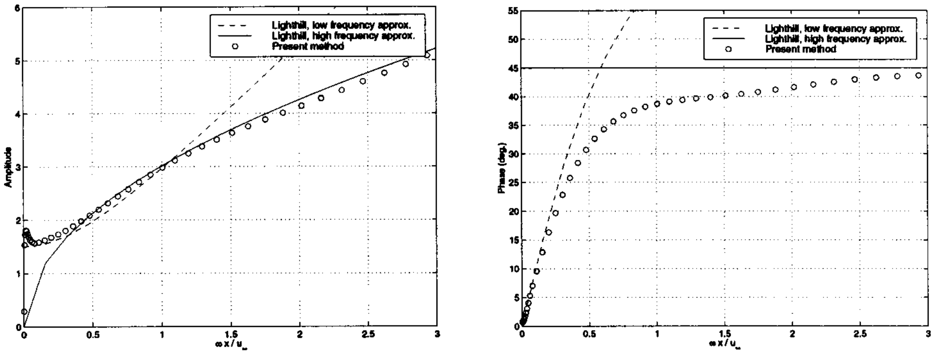

(a) Amplitude (b) Phase angle with respect to external velocity fluctuation

Fig. 5 Unsteady wall shear stresses for an oscillating laminar boundary layer: (*a*) amplitude; (*b*) phase angle with respect to external velocity fluctuation

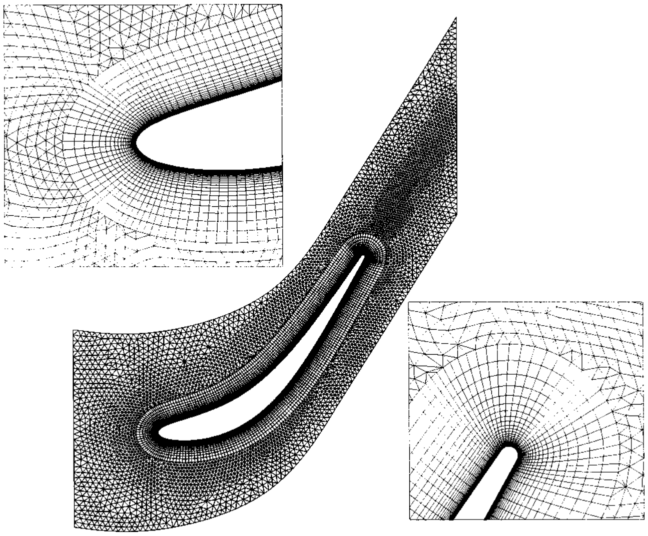

Fig. 6 11th Standard configuration: viscous mesh

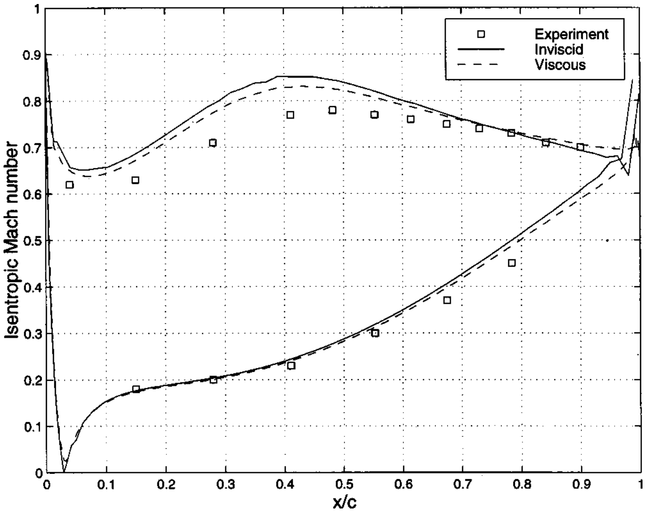

Fig. 8 11th Standard configuration: isentropic Mach number distribution along chord, subsonic case

5.3 11th International Standard Configuration: Turbine Cascade. The 11th International Standard Configuration is focused on a turbine blade geometry and several flow regimes have been studied by Fransson et al. [33].[2] Two particular flows will be considered here: a subsonic attached flow and a transonic flow showing a separation bubble on the suction surface. Figure 6 shows the computational mesh used for all viscous calculations. There are 9312 quadrilaterals in the boundary layer region and 7751 triangles in the rest of the domain, the total number of grid points being 13,481. A second mesh, used for the inviscid calculations, was obtained from the viscous mesh of Fig. 6 by simply removing the quadrilateral elements in the boundary layer.

Steady-State Flow Results. For the subsonic flow case, the inlet flow angle is −15.2 deg, the outlet isentropic Mach number

---

[2] The data for the International Standard Configurations can be found at http://www.egi.kth.se/ekv/stcf/.

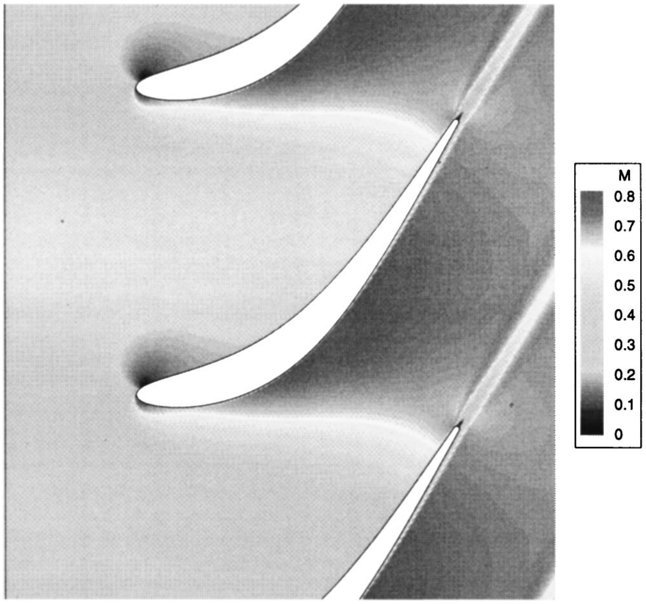

Fig. 7 11th Standard configuration: steady-state Mach contours, subsonic case

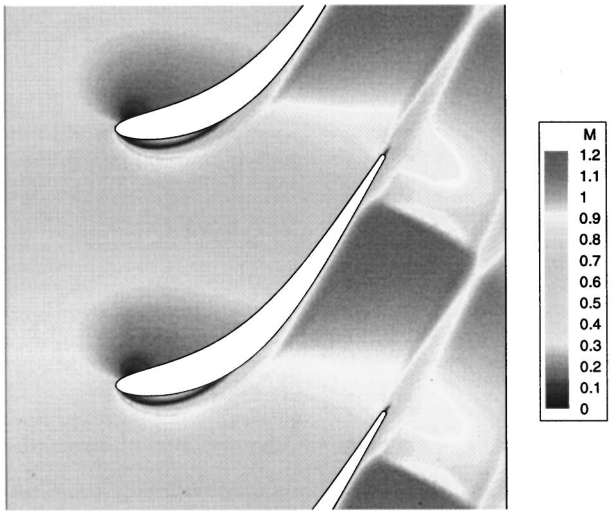

(a) Mach contours

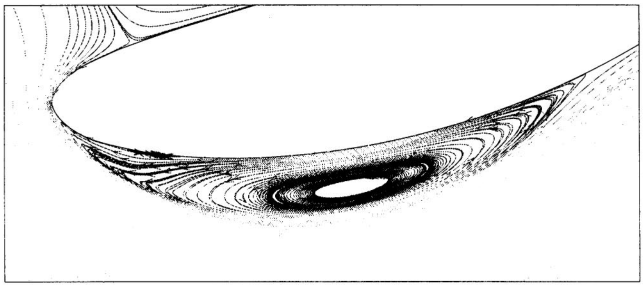

(b) Particle traces in the separation bubble

Fig. 9 11th Standard configuration: steady-state Mach contours, transonic case: (*a*) Mach contours; (*b*) particle traces in the separation bubble

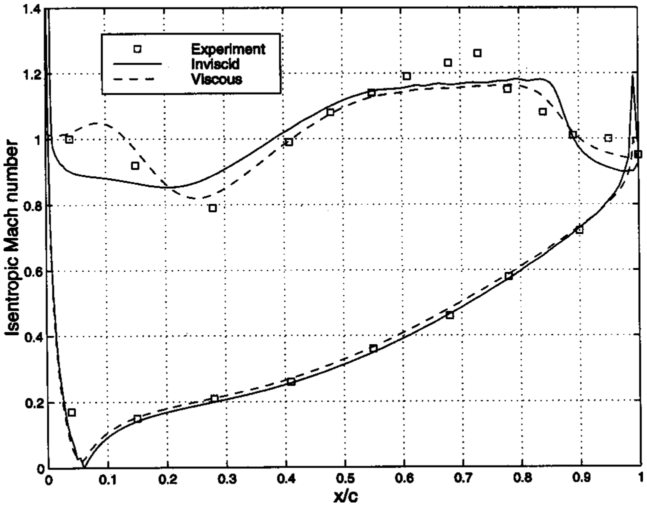

Fig. 10 11th Standard configuration: isentropic Mach number distribution along blade, transonic case

is 0.69, and the inlet Reynolds number, based on the blade's chord, is 650,000. The maximum value of $y+$ is around 4, which guarantees a good resolution of the viscous sublayer using the Spalart–Allmaras turbulence model. The predicted Mach number contours are shown in Fig. 7, while a comparison of the inviscid and viscous analyses with measured data is given in Fig. 8. For the suction surface, both the viscous and inviscid computations somewhat overpredict the Mach number distribution at around midchord. However, a similar solution was obtained by Fransson et al. [33], and the reasons for the discrepancy are discussed in some detail. Here, we will consider that the steady-state flow has been captured adequately for the purposes of providing a starting point for the linearized unsteady flow.

For the transonic off-design case the inlet flow angle is 34 deg, the outlet isentropic Mach number is 0.99, and the inlet Reynolds number, based on the blade's chord, is 860,000. The maximum $y+$ value is around 5. The predicted Mach number contours are plotted in Fig. 9(*a*). A particular feature of the flow, the recirculation bubble on the suction surface, is shown in Fig. 9(*b*). Because of the significant viscous features, the Navier–Stokes analysis shows a much better agreement with the measured data, with perhaps the exception of the trailing edge behavior (Fig. 10). However, as discussed by Fransson et al. [33], the preshock Mach number is very sensitive to the experimental inlet conditions. In any case, as expected, a viscous analysis is required to predict the separation bubble of the suction side, which occurs between 10–30 percent blade chord, a feature that can be seen from the flow deceleration in Fig. 10. As will be discussed in the next section, such differences in the steady-state flow will lead to major discrepancies for unsteady flow predictions.

Linearized Unsteady Flow Results. The unsteadiness due to bending motion of the blade in the direction normal to its chord was computed using the linearized flow solver. The reduced fre-

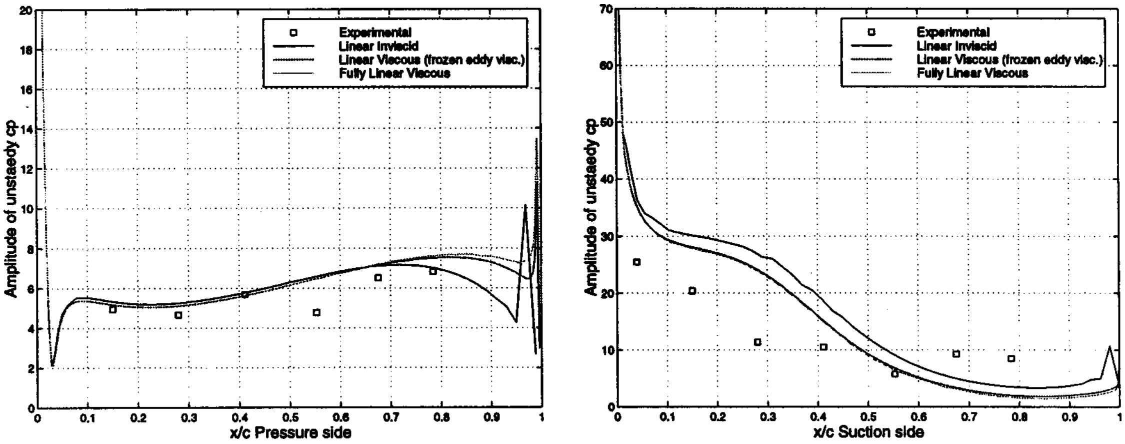

Fig. 11 11th Standard configuration: amplitude of $\tilde{c}_p$ ($\sigma=180$), subsonic case

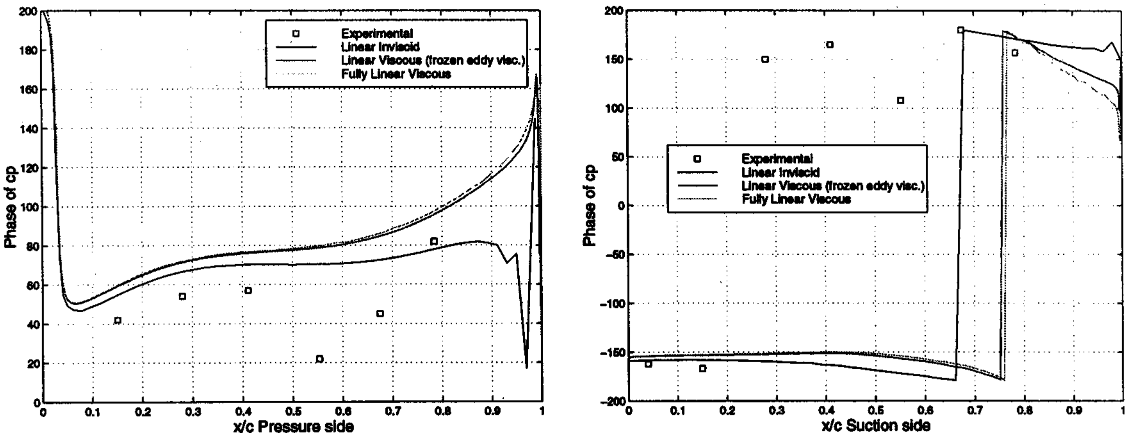

Fig. 12 11th Standard configuration: phase of $\tilde{c}_p$ ($\sigma=180$), subsonic case

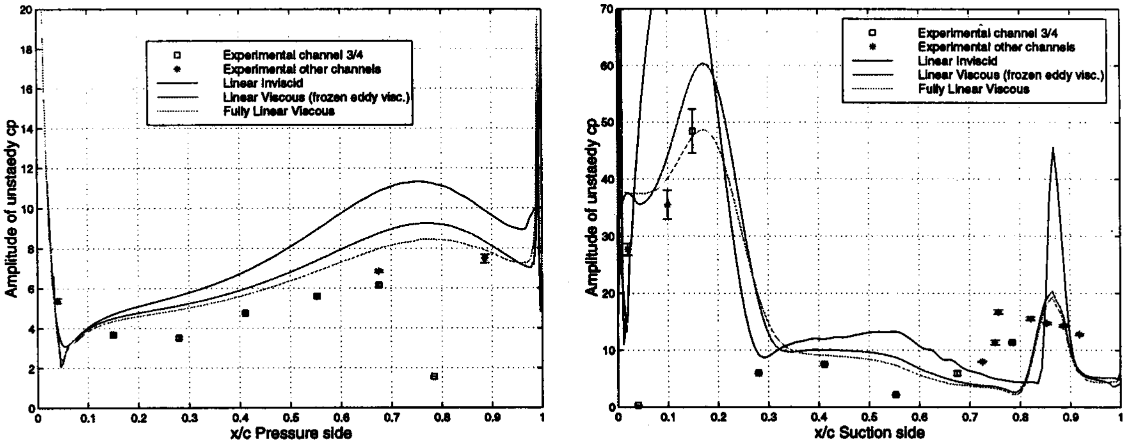

Fig. 13 11th Standard configuration: amplitude of $\tilde{c}_p$ (σ=180), transonic case

quency is 0.21 for the subsonic case and 0.15 for the transonic case. Three different sets of flow calculations were performed for each case: (*i*) inviscid linearized using an inviscid base steady-state flow, (*ii*) viscous linearized with frozen turbulence using viscous fully turbulent base flow, and (*iii*) viscous fully linearized using the same viscous base flow as in (*ii*). In calculations (*ii*), neither the laminar nor the turbulent viscosities were linearized and their values were kept fixed at their steady-state values. Calculations (*iii*) were performed with a fully linearized Spalart–Allmaras turbulence model.

The amplitude and phase of the predicted unsteady pressure distribution are compared to measured data in Figs. 11 and 12 for the subsonic case. The first noticeable feature is the similarity of the amplitude predictions for the three modeling levels, though some deviations can be observed for the phase plots. This result is somewhat expected because of the similarity of the inviscid and viscous steady-state solutions. There is reasonable overall agreement with the measured data, though the undershoot at around 50 percent chord is not captured in any of the computations. An inspection of the phase plots reveals that the negative to positive (or stable to unstable) phase jump is predicted much farther downstream than the measured position. However, the fully nonlinear viscous unsteady calculations of Fransson et al. [33] exhibit the same trend, and hence the cause of the discrepancy is not due to linearization.

The amplitude and phase of the predicted unsteady pressure distribution is compared to measured data in Figs. 13 and 14 for the transonic case. The linearized inviscid approach is seen to overpredict the unsteady pressure coefficient on the suction side of the blade, both in the recirculation region (0–30 percent of chord) and around the trailing edge. This is probably due to the fact that the inviscid approximation is not good enough to capture the viscous-effect-dominated features of the flow in these regions.

In any case, the discrepancies between the different three modeling levels are now more pronounced. In the recirculation region, the full linearization of the viscous terms yields better results than freezing the turbulence model and the two approaches are seen to be equivalent elsewhere. Finally, it is worth noting that there is very good overall agreement between the current linearized results and the nonlinear time-marching viscous predictions of Fransson et al. [33], the maximum discrepancy being under 2 percent.

5.4 Three Dimensional Transonic Rotor/Stator Interaction. The last study is a three dimensional coupled rotor/stator interaction case for which steady and unsteady flow data were obtained at the Osney Laboratory's turbine rotating rig facility [34]. A nonlinear insteady flow analysis of the same geometry and comparison with measured data are reported by Sayma et al. [35]. The rig is representative of a typical modern HP turbine stage and there are 36 stator blades and 60 rotor blades. The design speed, at which the measurements were taken, is 8834 rpm and the rotor blade's tip diameter is 554 mm.

Following the method of Sbardella et al. [36], semi-structured single blade passages were generated for the nozzle guide vanes

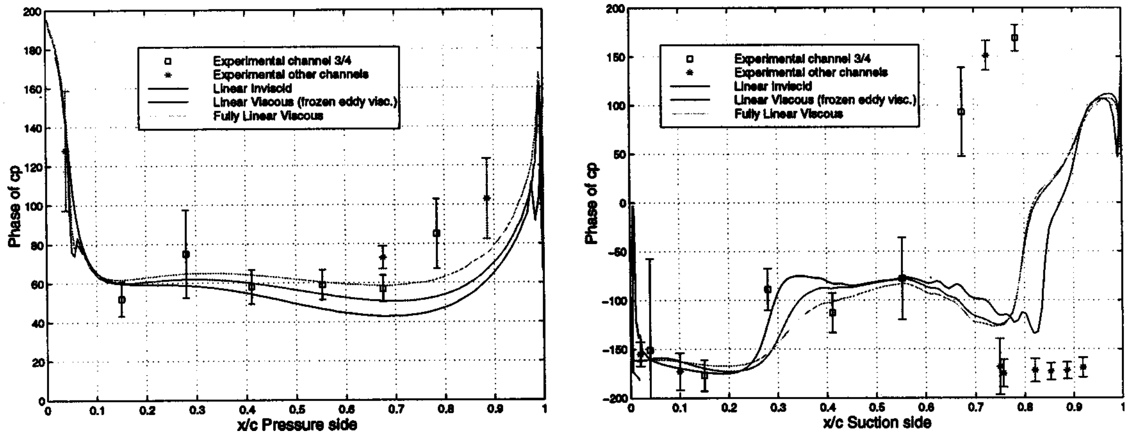

Fig. 14 11th Standard configuration: phase of $\tilde{c}_p$ (σ=180), transonic case

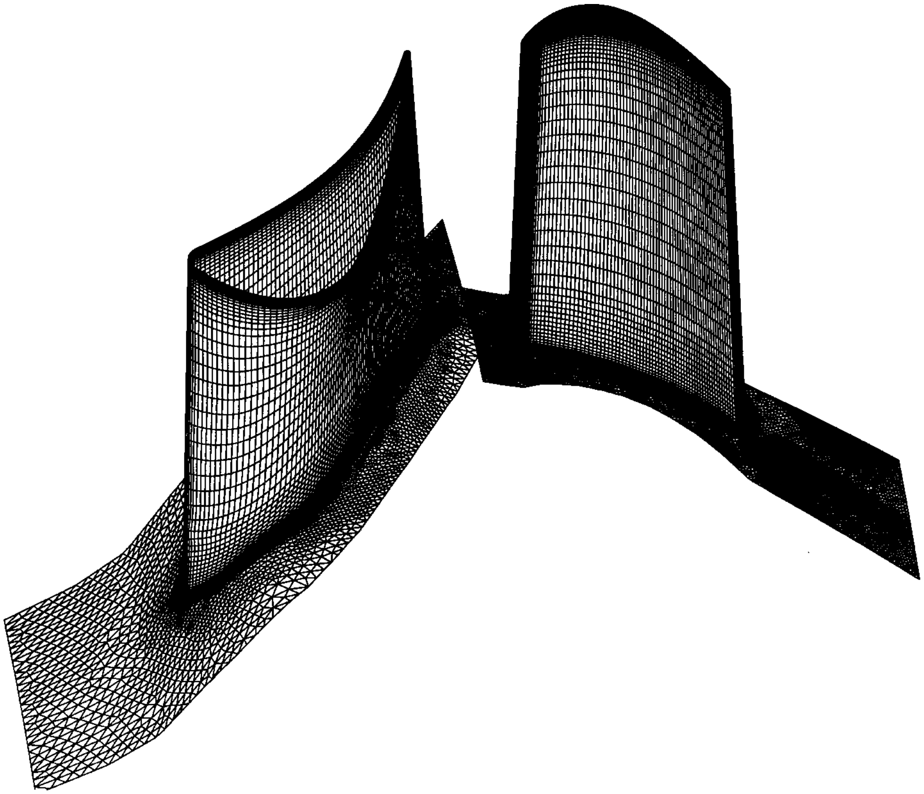

(a) 3D view

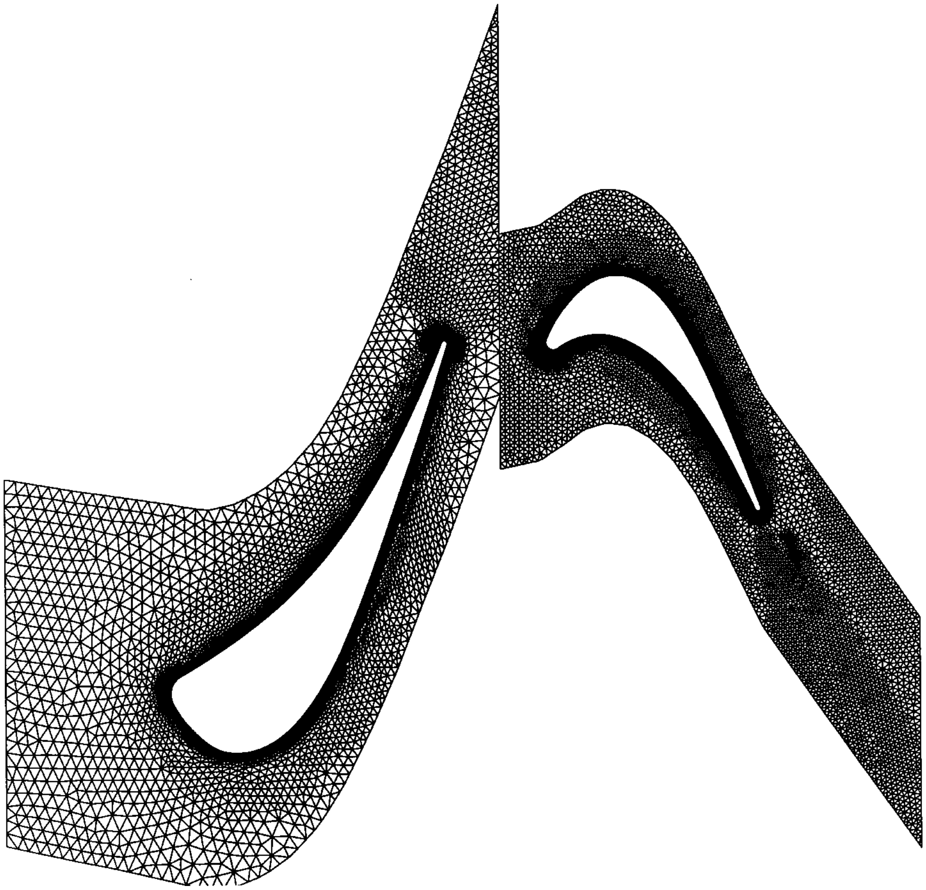

Fig. 15 Computational mesh for three dimensional rotor/stator interaction: (*a*) three-dimensional view; (*b*) midheight section

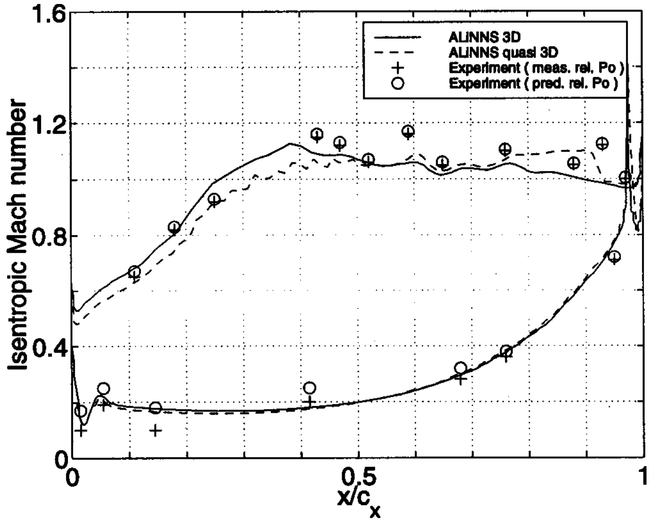

Fig. 16 Isentropic steady-state Mach number distribution at midheight section

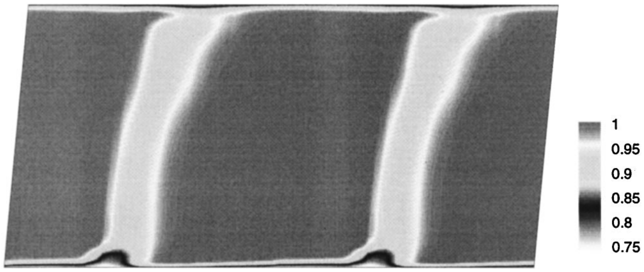

Fig. 17 Nondimensional total pressure at NGV outlet

(NGVs) and the rotor blades. Both the NGV and the rotor blade boundary layer regions were discretized via 12 layers of hexahedral elements arranged in an **O**-type grid. Tetrahedral elements were used for the rest of the computational domain. The mesh layers in the radial direction were clustered toward the end walls to capture the secondary flow effects (Fig. 15). The tip gap of 0.5 mm was modeled by direct meshing.

Steady-State Nonlinear Flow Results. The steady-state computations were conducted for a single passage NGV and rotor domains, containing about 230,000 and 340,000 grid points, respectively. The NGV outflow and the rotor inflow were treated as

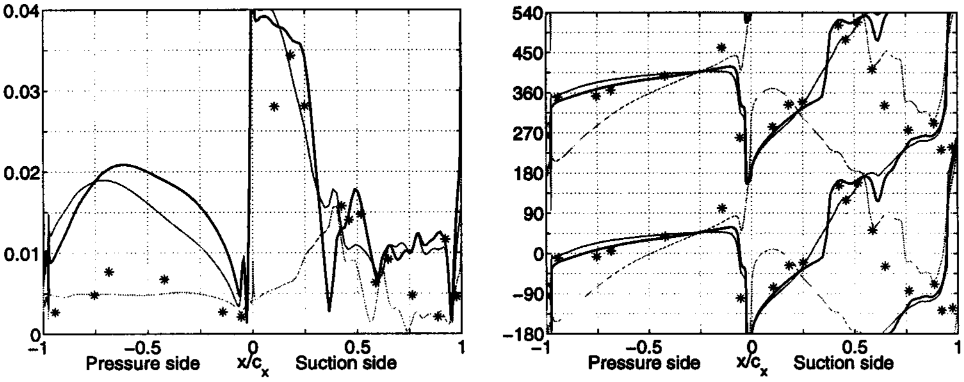

(a) First Fourier harmonic

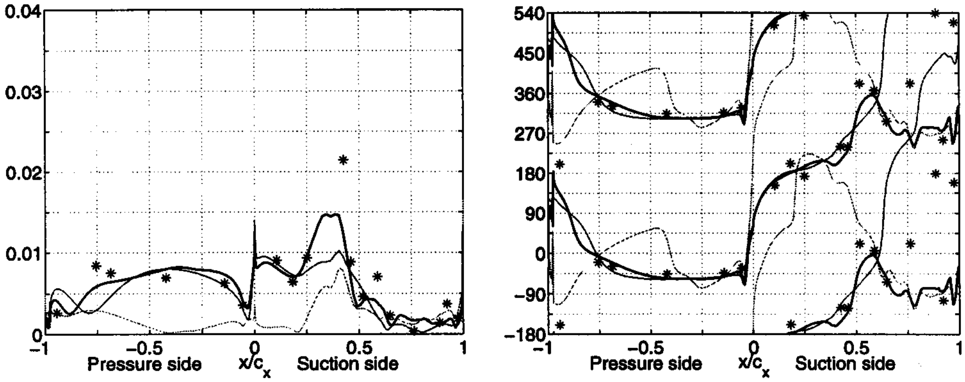

(b) Second Fourier harmonic

Fig. 18 Amplitude (left) and phase (right) of the first two Fourier components of the unsteady pressure p/p_0 at midheight section (50 percent span); potential/rotor interaction (thin solid/blue), wake/rotor interaction (thin dotted/red), superimposed (darkest/black), measured (*): (*a*) first Fourier harmonic; (*b*) second Fourier harmonic

two separate boundaries, and the mixing plane approach of Denton [37] was used to obtain a steady-state solution for the combined domain. Constant stagnation pressure, constant stagnation temperature and flow angle were specified at the NGV inlet. A static pressure distribution condition was applied at the rotor outlet.

Figure 16 shows a comparison of the predicted and measured isentropic Mach number distributions at blade midheight. It should be noted that two sets of measured data are plotted in Fig. 16. These are calculated from the time-averaged unsteady static pressures but using two different values of the rotor relative total pressures at the leading edge, namely the measured and computed values. Also plotted in Fig. 16 is the result of a quasi-three-dimensional calculation and it is immediately seen that the true three-dimensional calculation agrees better with the measurements in the forward part of the suction surface, while it overpredicts the exit pressure.

Linearized Unsteady Flow Results. The steady-state total pressure at the NGV outlet is plotted in Fig. 17 for two blade passages. The rotor blades move through the flowfield of Fig. 17 from left to right and they see the spatial nonuniformities as unsteady perturbations. Such nonuniformities at the NGV outlet must be transformed into elementary waves so that a linearized frequency-domain analysis becomes possible for unsteady aerodynamics. Such an approach, made possible by Goldstein's wave splitting theorem [38] and discussed in detail in Sbardella [39], considers the steady-state flow at the NGV outlet to be a summation of three different waves: vortical, potential, and entropic. The summation of the vortical and entropic waves is then used to evaluate wake/rotor interaction, while the potential wave can be used for potential/rotor interaction.

The unsteady flow computations were conducted for the frozen viscosity model. The fully turbulent base flow was perturbed by applying the potential/rotor and the wake/rotor interaction terms. The results are compared in Fig. 18 with the experimental data of Moss et al. [34] for the rotor blade midheight position. The unsteadiness resulting from the first and second Fourier harmonics of each disturbance is reported in magnitude and phase format. For the first harmonic, the amplitude is overpredicted for the pressure surface, though the phase is in reasonable agreement. The suction surface predictions agree well with the measured data, both in terms of amplitude and phase angle. The agreement is seen to be much better for the second Fourier harmonic.

Computational Effort. The steady-state computations took about 10 hours to converge on a single 400 MHz Alpha EV5 CPU. Each unsteady flow calculation with a single Fourier harmonic required about 3 hours on the same machine. Therefore, $3\times3=9$ hours were needed to consider the first three harmonics of the combined potential/rotor and wake wake/rotor interactions. The same geometry was studied by Sayma et al. [35] using a nonlinear time-accurate viscous unsteady flow model but using a significantly coarser (unstructured) mesh than that used here. Their unsteady analysis took about 30 times longer than their steady flow analysis, suggesting that the current mesh would require $30\times10=300$ CPU hours for a time-accurate nonlinear unsteady flow analysis. Therefore, the current linearized analysis can be expected to be about $300/9=33.3$ times faster than the equivalent nonlinear analysis.

6 Concluding Remarks

(*i*) A finite-volume scheme has been presented for the solution of the linearized viscous flows for turbomachinery applications. The method employs an edge-based data structure and uses a nearest neighbor stencil for the discretization of the Laplacian operator. Both two-dimensional and three-dimensional structured, unstructured, or block structured grids with mixed elements can be used without any modification of the numerical scheme.

(*ii*) The proposed time-linearized Navier–Stokes analysis is applicable to off-design conditions where viscous effects are not limited to the boundary layer.

(*iii*) The method is computationally very efficient, making it a useful tool for routine aeroelasticity design calculations. For a given harmonic, the unsteady flow computation time is slightly less than that needed for the steady-state base flow computation, though several such harmonics may need to be taken into account. On the other hand, for an equivalent time-accurate calculation, the ratio between unsteady and steady flow analysis times is around 30. However, the issue whether linearized methods are applicable to all flow regimes is not one that is addressed here.

(*iv*) The two-dimensional transonic turbine flow results show that the linearization of the turbulence model plays an important role wherever the viscous effects are important, exemplified in this case by the recirculation bubble. When there are no such effects, the frozen turbulence approach should produce very similar results. In other words, an inspection of the steady-state solution should provide guidance as to which modeling level would be appropriate.

(*v*) The steady-state flow analysis of the three-dimensional rotor/stator interaction case was performed with a wall function. Consequently, the wall stresses were set to zero during the unsteady computations and a linearized frozen turbulence model was used. A better and more consistent alternative is the lineariztion of the wall function itself, though such an approach may not be necessary for most applications. This issue will be addressed in a forthcoming paper.

Acknowledgments

The authors gratefully acknowledge the financial support from the European Commission under the TMR scheme. They also thank Prof. R. Ainsworth and Dr. R. Moss of Osney Laboratory (Oxford University) where the turbine rig measurements were conducted with funding from Defense Research Agency (Pyestock), the Ministry of Defense and the Department of Trade and Industry.

Appendix

Linearized Version of the Spalart–Allmaras Turbulence Model. Using the same notation as for the mean flow equations, the one-equation Spalart–Allmaras turbulence model can be written in an ALE integral conservative form as:

$$\frac{\partial}{\partial t}\int_{\mathcal{V}(t)}\rho \nu_t\,d\mathcal{V}+\oint_{\mathcal{S}(t)}\left(\vec{F}_t-\frac{1}{\mathrm{Re}}\vec{G}_t\right)\cdot\vec{n}\,d\mathcal{S}=\int_{\mathcal{V}(t)}S_t\,d\mathcal{V} \tag{A1}$$

where the flux vectors $\vec{F}_t$ and $\vec{G}_t$ and the source term S_t are given by:

$$\vec{F}_t=\rho\nu_t\vec{u} \tag{A2}$$

$$\vec{G}_t=\frac{1}{\sigma}(\mu_1+\rho\nu_t)\vec{\nabla}\nu_t \tag{A3}$$

$$S_t=c_{b1}P\rho\nu_t+\frac{\rho}{\mathrm{Re}}\left[\frac{c_{b2}}{\sigma}(\vec{\nabla}\nu_t)^2-c_{w1}f_w\left(\frac{\nu_t}{d}\right)^2\right] \tag{A4}$$

The quantity P represents the production term given by:

$$P=|\vec{\nabla}\times\vec{u}|+\frac{1}{\mathrm{Re}}\frac{\nu_t}{\kappa^2d^2}f_{\nu2} \tag{A5}$$

where d is the distance from the wall. The turbulent viscosity μ_t is related to the turbulent unknown $\rho\nu_t$ through the relation:

$$\mu_t=\rho\nu_tf_{\nu1} \tag{A6}$$

The functions and constants appearing in Eqs. ($A3$), ($A4$), ($A5$), and ($A6$) are those reported by Spalart and Allmaras [21].

Following the same procedure as for the mean flow equations, the frequency domain linearization of the Spalart–Allmaras turbulence model yields:

$$\frac{\partial}{\partial t}\int_{\overline{\mathcal{V}}}\widehat{\rho v}_t d\overline{\mathcal{V}}+\oint_{\overline{S}}\left(\hat{\vec{F}}_t-\frac{1}{\mathrm{Re}}\hat{\vec{G}}_t\right)\cdot\overline{\vec{n}\,dS}-\int_{\overline{\mathcal{V}}}(i\omega\widehat{\rho v}_t+\hat{S}_t)d\overline{\mathcal{V}}$$

$$=\hat{H}_t(\overline{\rho v_t},\overline{U},\hat{\vec{x}}) \qquad (A7)$$

The linearized inviscid and viscous fluxes are given by:

$$\hat{\vec{F}}_t=\widehat{\rho v}_t(\overline{\vec{v}}-\vec{\Omega}\times\overline{\vec{x}})+\overline{\rho v}_t\hat{\vec{v}} \qquad (A8)$$

$$\hat{\vec{G}}_t=\frac{1}{\sigma}(\overline{\mu_l}+\overline{\rho v_t})\vec{\nabla}\hat{v}_t+\frac{1}{\sigma}(\hat{\mu}_l+\widehat{\rho v}_t)\vec{\nabla}\overline{v_t} \qquad (A9)$$

The term $\hat{H}_t$ at the right-hand side of Eq. ($A7$) denotes the inhomogeneous terms arising from the grid motion:

$$\hat{H}_t(\overline{\rho v_t},\overline{\mathbf{U}},\hat{\vec{x}})=\int_{\overline{\mathcal{V}}}(i\omega\overline{\rho v}_t+\overline{S}_t)d\hat{\mathcal{V}}-\oint_{\overline{S}}\left(\overline{\vec{F}}_t-\frac{1}{\mathrm{Re}}\overline{\vec{G}}_t\right)\cdot\widehat{\vec{n}\,d\mathcal{S}}$$

$$+\oint_{\overline{S}}\overline{\rho v}_t(\vec{\Omega}\times\hat{\vec{x}}-i\omega\hat{\vec{x}})\cdot\overline{\vec{n}\,d\mathcal{S}} \qquad (A10)$$

The linearized source term $\hat{S}_t$ is given by:

$$\hat{S}_t=c_{b1}(\overline{P}\widehat{\rho v}_t+\hat{P}\overline{\rho v}_t)+\frac{2\overline{\rho}}{\mathrm{Re}}\left[\frac{c_{b2}}{\sigma}(\vec{\nabla}\overline{v_t})(\vec{\nabla}\hat{v}_t)-c_{w1}f_w\frac{\overline{\rho v}_t\widehat{\rho v}_t}{d^2}\right] \qquad (A11)$$

The numerical implementation of Eq. ($A7$) is very similar to that employed for the mean flow Eq. (38).

Linearization of the Wall Function. When performing linearized turbulent-flow calculations with a slip condition at the solid walls, an additional problem, namely that of evaluating the linearized sheer stresses $\tilde{\tau}_w$, arises. The linearization of the wall function yields an equation of the form:

$$\tilde{\tau}_w=\overline{A}\tilde{\rho}+\overline{B}\tilde{u}_{\parallel} \qquad (A12)$$

where $\overline{A}$ and $\overline{B}$ are two constants that depend on the steady-state quantities and the particular type of the wall function used. $\tilde{u}_{\parallel}$ is the linearized velocity parallel to the wall.

In the Spalart–Allmaras formulation, the eddy viscosity at a slip wall is proportional to the shear stresses, a feature that allows the unsteady perturbations of $\tilde{\mu}_t$ at the solid wall to be expressed by a linear relationship:

$$\tilde{\mu}_t=\overline{C}\tilde{\tau}_w \qquad (A13)$$

If the frozen eddy viscosity approach is used, $\tilde{\mu}_t=0$ throughout the computational domain. In this case, it is seen from Eq. ($A13$) that $\tilde{\tau}_w=0$, indicating that the wall unsteady shear stresses are ignored in the frozen eddy viscosity model. On the other hand, they need to be evaluated from Eq. ($A12$) for a full linearization.

Nomenclature

$|\overline{\mathbf{A}}_{IJs}|$ = Roe matrix
c = speed of sound
$\mathcal{C}$ = airfoil chord
$\mathcal{D}$ = artificial dissipation column vector
e = dimensionless total energy per unit mass
$\vec{\mathbf{F}}$ = vector of inviscid fluxes with Cartesian column vector components $(\mathbf{F}_1,\mathbf{F}_2,\mathbf{F}_3)$
$\mathcal{F}$ = numerical inviscid flux function
$\vec{\mathbf{G}}$ = vector of viscous fluxes with Cartesian column vector components $(\mathbf{G}_1,\mathbf{G}_2,\mathbf{G}_3)$
$\mathcal{G}$ = numerical viscous flux function
h = dimensionless total enthalpy per unit mass
i = $\sqrt{-1}$
$\overline{\mathbf{J}}_D$ = block diagonal contribution to Jacobian matrix
$\mathcal{L}$ = pseudo-Laplacian operator for 4th-order artificial dissipation
M = Mach number
p = static pressure
P = production term in Spalart–Allmaras turbulence model
Pr = Prandtl number
r = radial coordinate in cylindrical coordinate system x,r,θ
$\mathbf{R}$ = right-hand-side residual vector
Re = reference Reynolds number
$\mathbf{S}$ = column vector of source terms
St = Stroudhal number
$S(t)$ = moving boundary of control volume $\mathcal{V}$
t = physical time
T = static temperature
$\vec{u}$ = fluid velocity vector in relative frame of reference
U = column vector of conservative variables
$\vec{v}$ = dimensionless fluid velocity vector in absolute frame of reference
$\vec{x}$ = Cartesian coordinate vector, usually associated with grid motion
β_m = inverse reduced frequency
Δ = difference operator along edge IJs
δ_{ij} = Kronecker delta function
γ = specific heat ratio
$\vec{\eta}_{IJs}$ = metric vector associated with edge IJs
λ = defined by Stokes relation
μ = dynamic viscosity
μ_l = laminar viscosity
μ_t = turbulent viscosity
$\vec{n}$ = outward unit vector of control volume
$\mathcal{V}(t)$ = control volume
ω = reduced frequency
Ω = angular velocity
ν = kinematic viscosity
ρ = static density
σ = interblade phase angle
θ = tangential coordinate (cylindrical coordinate system x,r,θ)
$\tilde{\tau}_w$ = unsteady wall shear stress
ϕ = limiter function for inviscid fluxes
σ = Courant–Friedrichs–Lewy (CFL) number
τ_{IJs} = Laplacian weight associated with edge IJs
I = arbitrary mesh node
Js = mesh node connected to typical node I via an edge
IJs = belongs to edge between nodes I and Js
$\overline{}$ = steady part
$\sim$ = unsteady part
$\hat{}$ = complex amplitude for small perturbation
^{j} = j th flux component
^{l} = first component of viscous flux
^{m} = mixed derivative component of viscous flux

References

[1] Whitehead, D. S., 1987, ''Classical 2D methods,'' in: *AGARD Manual on Aeroelasticity in Axial-Flow Turbomachines, Unsteady Turbomachinery Aerodynamics*, Vol. 1, pp. 3.1–3.30. AGARD-AG-297.

[2] Verdon, J. M., 1993, ''Review of Unsteady Aerodynamics Methods for Turbomachinery Aeroelastic and Aeroacoustic Applications,'' AIAA J., **31**, pp. 235–250.

[3] Marshall, J. G., and Imregun, M., 1996, ''A Review of Aeroelasticity Methods With Emphasis on Turbomachinery Applications,'' J. Fluids Struct., **10**, pp. 237–267.

[4] Smith, S. N., 1972, ''Discrete Frequency Sound Generation in Axial Flow Turbomachines,'' Technical Report 3709, Cambridge University Engineering Department, Cambridge, UK.

[5] Erdos, J. I., Alzner, E., and McNally, W., 1977, ''Numerical Solution of Periodic Transonic Flow Through a Fan Stage,'' AIAA J., **15**, pp. 1559–1568.

[6] Rai, M. M., 1987, ''Navier–Stokes Simulations of Rotor/Stator Interaction Using Patched and Overlaid Grids,'' J. Propul. Power, **3**, No. 5, pp. 387–396.

[7] Giles, M. B., 1990, ''Stator/Rotor Interaction in a Transonic Turbine,'' J. Propul. Power, **6**, No. 5, pp. 621–627.

[8] He, L., and Denton, J. D., 1993, ''Inviscid–Viscous Coupled Solution for Unsteady Flows Through Vibrating Blades: Part 1—Description of the Method,'' ASME J. Turbomach., **115**, pp. 94–100.

[9] Sayma, A. I., Vahdati, M., and Imregun, M., 1999, ''Fan Forced Response Predictions Due to Inlet Distortions and Excitation From Inlet Guide Vanes at High Deflection,'' in: *Proc. 4th National Turbine Engine High Cycle Fatigue (HCF) Conference*, San Antonio, TX.

[10] Verdon, J. M., and Caspar, J. R., 1984, ''A Linearized Unsteady Aerodynamic Analysis for Transonic Cascades,'' J. Fluid Mech., **149**, pp. 403–429.

[11] Ni, R. H., and Sisto F., 1975, ''Numerical Computation of Non-stationary Aerodynamics of Flat Plate Cascades in Compressible Flows,'' ASME Paper No. 75-GT-5.

[12] Hall, K. C., and Crawley, E. F., 1989, ''Calculation of Unsteady Flows in Turbomachinery Using the Linearized Euler Equations,'' AIAA J., **27**, pp. 777–787.

[13] Lindquist, D. R., and Giles, M. B., 1991, ''On the Validity of Linearized Unsteady Euler Equations With Shock Capturing,'' AIAA Paper No. 91-1598-CP.

[14] Hall, K. C., and Clark, W. S., 1993, ''Linearized Euler Predictions of Unsteady Aerodynamic Loads in Cascades,'' AIAA J., **31**, No. 3, pp. 540–550.

[15] Montgomery, M. D., and Verdon, J. M., 1997, ''A 3D Linearized Euler Analysis for Bladerows. Part 1: Aerodynamic and Numerical Formulations,'' in: *Proc. 8th Int. Symposium on Unsteady Aerodynamics and Aeroelasticity of Turbomachines (ISUAAT)*, pp. 427–444, Stockholm.

[16] Montgomery, M. D., and Verdon, J. M., 1997, ''A 3D Linearized Euler Analysis for Bladerows. Part 2: Unsteady Aerodynamic Response,'' in: *Proc. 8th International Symposium on Unsteady Aerodynamics and Aeroelasticity of Turbomachines (ISUAAT)*, pp. 445–464, Stockholm.

[17] Cizmas, P. G. A., and Hall, K. C., 1995, ''A Viscous–Inviscid Model of Unsteady Small-Disturbance Flows in Cascades,'' AIAA Paper No. 95-2655.

[18] Ning, W., and He, L., 1998, ''Computation of Unsteady Flows Around Oscillating Blades Using Linear and Nonlinear Harmonic Euler Methods,'' ASME J. Turbomach., **120**, pp. 714–722.

[19] Holmes, D. G., Mitchell, B. E., and Lorence C. B., 1997, ''3D Linearized Navier–Stokes Calculations for Flutter and Forced Response,'' in: *Proc. 8th Int. Symposium on Unsteady Aerodynamics and Aeroelasticity of Turbomachines (ISUAAT)*, pp. 211–224, Stockholm.

[20] Clark, W. S., and Hall, K. C., 2000, ''A Time-Linearized Navier–Stokes Analysis of Stall Flutter,'' ASME J. Turbomach., **122**, pp. 467–476.

[21] Spalart, P. R., and Allmaras, S. R., 1992, ''A One-Equation Turbulence Model for Aerodynamic Flows,'' AIAA Paper No. 92-0439.

[22] Sbardella, L., and Imregun, M., 2000, ''An Efficient Discretisation of Viscous Fluxes on Unstructured Mixed-Element Grids,'' Commun. Num. Methods Eng., **16**, pp. 839–849.

[23] Giles, M. B., 1990, ''Non-reflecting Boundary Conditions for the Euler Equation Calculations,'' AIAA J., **28**, No. 12, pp. 2050–2058.

[24] Saxer, A. P., and Giles, M. B., 1993, ''Quasi-3D Non-reflecting Boundary Conditions for Euler Equation Calculations,'' J. Propul. Power, **9**, No. 2, pp. 263–271.

[25] Hall, K. C., Lorence, C. B., and Clark, W. S., 1993, ''Non-reflecting Boundary Conditions for Linearized Unsteady Aerodynamic Calculations,'' AIAA Paper No. 93-0882.

[26] Roe, P., 1981, ''Approximate Riemann Solvers, Parameter Vectors and Difference Schemes,'' J. Comput. Phys., **43**, pp. 357–372.

[27] Jorgenson, P. C., and Turkel, E., 1993, ''Central Difference TVD Schemes for Time Dependent and Steady State Problems,'' J. Comput. Phys., **107**, pp. 297–308.

[28] Cebeci, T., 1977, ''Calculation of Unsteady 2D Laminar and Turbulent Boundary Layers With Fluctuations in External Velocity,'' Proc. R. Soc. London, Ser. A, **355**, pp. 225–238.

[29] Hall, K. C., and Clark, W. S., 1991, ''Prediction of Unsteady Aerodynamic Loads in Cascades Using the Linearized Euler Equations on Deforming Grids,'' AIAA Paper No. 91-3378.

[30] Marshall, J. G., and Giles, M. B., 1997, ''Some Applications of a Time-Linearized Euler Method to Flutter and Forced Response in Turbomachinery,'' in: *Proc. 8th Int. Symposium on Unsteady Aerodynamics and Aeroelasticity of Turbomachines (ISUAAT)*, pp. 225–240, Stockholm.

[31] Tidriri, M. D., 1995, ''Krylov Methods for Compressible Flows,'' Technical Report 95-48, ICASE.

[32] Lighthill, M. J., 1954, ''The Response of Laminar Skin Friction and Heat Transfer to Fluctuations in the Stream Velocity,'' Proc. R. Soc. London, Ser. A, **224**, pp. 1–23.

[33] Fransson, T. H., Jöcker, M., Bölcs, A., and Ott, P., 1999, ''Viscous and Inviscid Linear/Nonlinear Calculations Versus Quasi-Three-Dimensional Experimental Cascade Data for a New Aeroelastic Turbine Standard Configuration,'' ASME J. Turbomach., **121**, pp. 717–725.

[34] Moss, R. W., Ainsworth, R. W., Sheldrake, C. D., and Miller, R., 1997, ''The Unsteady Pressure Field Over a Turbine Blade Surface: Visualization and Interpretation of Experimental Data,'' ASME Paper No. 97-GT-474.

[35] Sayma, A. I., Vahdati, M., Sbardella, L., and Imregun, M., 2000, ''Modelling of 3D Viscous Compressible Turbomachinery Flows Using Unstructured Hybrid Grids,'' AIAA J., **38**, No. 6, pp. 945–954.

[36] Sbardella, L., Sayma, A. I., and Imregun, M., 2000, ''Semi-structured Meshes for Axial Turbomachinery Blades,'' Int. J. Numer. Methods Fluids, **32**, pp. 569–584.

[37] Denton, J. D., 1992, ''The Calculation of Three-Dimensional Viscous Flow Through Multistage Turbomachines,'' ASME J. Turbomach., **114**, pp. 18–26.

[38] Goldstein, M. E., 1978, ''Unsteady Vortical and Entropic Distortions of Potential Flows Round Arbitrary Obstacles,'' J. Fluid Mech., **89**, pp. 433–468.

[39] Sbardella, L., 2000, ''Simulation of Unsteady Turbomachinery Flows for Forced Response Predictions,'' PhD thesis, Imperial College, MED, Dynamics Section, London.

The Basic Thermodynamics of Turbine Cooling

J. H. Horlock
Whittle Laboratory,
Engineering Department,
Cambridge University, United Kingdom

Analyses of gas turbine plant performance, including the effects of turbine cooling, are presented. The thermal efficiencies are determined theoretically, assuming air standard (a/s) cycles, and the reductions in efficiency due to cooling are established; it is shown that these are small, unless large cooling flows are required. The theoretical estimates of efficiency reduction are compared with calculations, assuming that real gases form the working fluid in the gas turbine cycles. It is shown from a/s analysis that there are diminishing returns on efficiency as combustion temperature is increased; for real gases there appears to be a limit on this maximum temperature for maximum thermal efficiency. [DOI: 10.1115/1.1370156]

I Introduction

The emphasis on raising the maximum temperature $T_{\max}$ in a gas turbine plant is essentially based on attempting to emulate the Carnot cycle, in which the efficiency increases with $T_{\max}$, and this point is reinforced by the use of complex codes for calculating open cycle efficiency, when no account is taken of turbine cooling. However, cycle calculations, made with realistic estimates of the probable turbine cooling air requirements (based on heat transfer correlations), suggest that for modern gas turbines there may be a limit on the combustion temperature for maximum thermal efficiency (Elmasri [2], Chiesa, Consonni, Lozza, and Macchi [3], MacArthur [4], and Horlock, Watson, and Jones [5]). This paper takes a more fundamental approach in examining the basic thermodynamics associated with the introduction of turbine cooling, in order to ascertain whether or not it is always likely to be advantageous in terms of thermal efficiency.

The main analysis is presented by reference to a closed ''air standard'' (a/s) cycle using a perfect gas as a working fluid in an externally heated plant. But it is argued subsequently that many of the conclusions reached in this way will remain substantially valid for an open cycle with combustion, i.e., for one involving real gases with variable composition and specific heat varying with temperature.

The arguments are developed sequentially, starting (briefly) with reversible cycles and then considering irreversibilities. We adopt the nomenclature introduced by Hawthorne and Davis [1], as indicated in the notation.

II Internally Reversible Cycles

A Reversible Uncooled Cycle $[\mathbf{CHT}]_{RU}$. The original Joule-Brayton cycle is used as a standard, i.e., an internally reversible uncooled closed gas turbine cycle 1, 2, 3, and 4 [Fig. 1(*a*)], with a maximum temperature T_3 and a pressure ratio r. However, irreversibility is involved in the heat supply from an external reservoir at temperature T_A, and the heat rejection to a reservoir at temperature T_B. The internal thermal efficiency $(\eta)_{RU}$ of this cycle is well known to be independent of the maximum temperature and is simply a function of the isentropic temperature ratio $x=r^{(\gamma-1)/\gamma}$:

$$(\eta)_{RU}=1-(1/x) \tag{1}$$

However, the nondimensional specific work

$$w=(w_t-w_c)/c_pT_1=[(\theta/x)-1](x-1) \tag{2}$$

does increase with $\theta=T_3/T_1$.

Such a consideration of the internal thermal efficiency alone does not provide a full discussion of the thermodynamic performance of a plant when supplied with heat from the external reservoir at T_A. If the reservoirs for heat supply and rejection are of infinite capacity, then it may be shown that the irreversibilities in the heat supply and the heat rejection (Q_A and Q_B respectively, both positive) are

$$\begin{aligned} I_A&=T_B\int (dQ_A/T)-Q_AT_B/T_A \\ &=Q_A[c_pT_B\ln(T_A/T_2)/Q_A-T_B/T_A] \end{aligned} \tag{3}$$

and

$$I_B=Q_B-T_B\int (dQ_B/T)=Q_A[Q_BQ_A-T_Bc_p\ln[T_4/T_B]/Q_A] \tag{4}$$

But, since $T_A=T_3=xT_4$ and $T_2=xT_1=xT_B$, so that $(T_A/T_2)=(T_4/T_B)$, it follows that

$$\Sigma I=I_A+I_B=Q_A[(Q_B/Q_A)-(T_B/T_A)] \tag{5}$$

The maximum possible work is then

$$\begin{aligned} W_{\max}&=W+\Sigma I \\ &=Q_A-Q_B+Q_B-Q_AT_B/T_A \\ &=Q_A[1-(T_B/T_A)] \\ &=\eta_{\mathrm{CAR}}Q_A \end{aligned} \tag{6}$$

where η_{CAR} is the Carnot efficiency.

As a numerical example, for a reversible cycle with $T_A=1800\,\mathrm{K}$, $T_B=300\,\mathrm{K}$ and $x=2.79$ $(r=36.27)$, it follows that

$$(\eta)_{RU}=0.642,\quad I_A/Q_A=0.072,\quad I_B/Q_A=0.120,$$

$$\eta_{\mathrm{CAR}}=(\eta)_{RU}+\Sigma I/Q_A=0.833.$$

We shall compare below the performance of cooled reversible and irreversible cycles with the performance of the reversible uncooled Joule-Brayton cycle, as outlined above. In each of the cycles considered below, the heat supplied (Q_A) is unchanged, as is the (unit) mass flow through the heater and its temperature rise (T_A-T_2). The irreversibility I_A is therefore also unaltered.

B Reversible Cooled Cycle $[\mathbf{CHT}]_{RC}$

1 Single Step Cooling. We first study a cycle with reversible compression and expansion, but one in which, after unit flow of the compressed gas has been heated externally, it is cooled by mixing with ''extra'' compressor delivery air before entering the turbine in the internal cycle, which is otherwise reversible (Fig.

Contributed by the International Gas Turbine Institute for publication in the JOURNAL OF TURBOMACHINERY. Manuscript received at ASME Headquarters March 2000. Associate Editor: T. H. Okiishi.

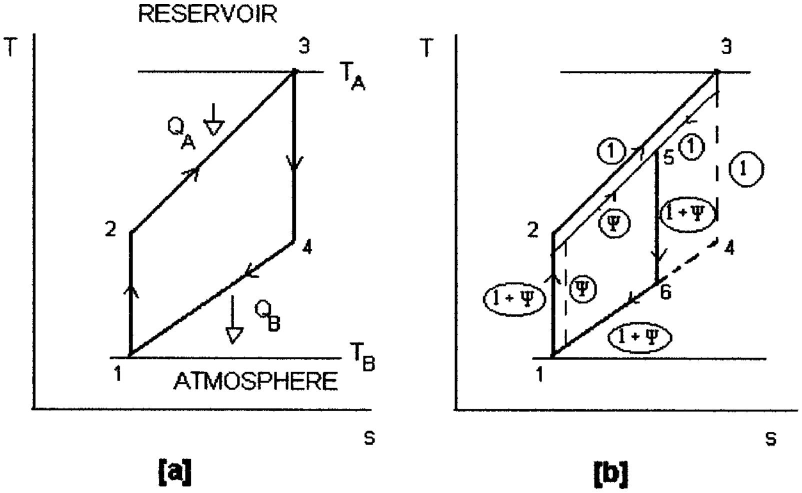

Fig. 1 (*a*) Basic Joule-Brayton cycle, $[\mathrm{CHT}]_{RU}$; (*b*) reversible cycle with single-step cooling, $[\mathrm{CHT}]_{RC1}$

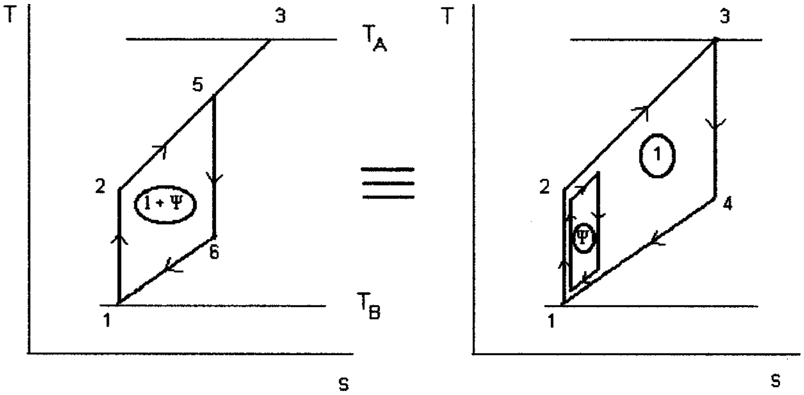

Fig. 2 Breakdown of $[\mathrm{CHT}]_{RC1}$ cycle

1(*b*)). This single step of cooling is representative of cooling the nozzle guide vanes (NGVs) in a real gas turbine plant, reducing the rotor inlet temperature.

Consider the case of low velocity (constant pressure) mixing of the ''extra'' cooling gas mass flow (ψ) at temperature T_2 with the gas stream (unit mass flow) which has been heated to the maximum temperature $T_3 = T_A$. From the steady flow energy equation, if both streams have the same specific heat c_p, it follows that

$$\psi T_2 + T_3 = (1+\psi) T_5 \tag{7}$$

where T_5 is the resulting temperature in the mixed stream, before it is expanded through the turbine. The turbine work output is now $W_t = (1+\psi) c_p T_5 [1-(1/x)]$, and the compressor work is $W_c = (1+\psi) c_p T_1 (x-1)$. But the heat supplied, before the mixing process, to the stream of unit mass flow is still $Q_A = c_p (T_A - T_2)$, which from Eq. (7) may be written

$$Q_A = (1+\psi) c_p (T_5 - T_2) \tag{8}$$

Thus the internal thermal efficiency is

$$\begin{aligned}(\eta)_{RC1} &= (W_t - W_c)/Q_A \\ &= \frac{(1+\psi) c_p T_5 [(1-(1/x)] - (1+\psi) c_p T_1 (x-1)}{(1+\psi) c_p (T_5 - T_2)} \\ &= [(\theta'/x) - 1](x-1)/[(\theta'-1)-(x-1)] \end{aligned} \tag{9}$$

where $\theta' = T_5/T_1$. But this expression simplifies to

$$(\eta)_{RC1} = [1-(1/x)] = (\eta)_{RU} \tag{10}$$

which is independent of θ'.

Thus the cooled ''reversible'' cycle $[\mathrm{CHT}]_{RC}$ with a first rotor inlet temperature, T_5, will have an internal thermal efficiency exactly the same as that of the uncooled cycle $[\mathrm{CHT}]_{RU}$ with a higher turbine entry temperature $T_3 = T_A$, and the same pressure ratio. There is no penalty on efficiency in cooling the turbine gases at entry[1] [although the specific work output, $w = (w_t - w_c)/c_p T_1 = [(\theta'/x) - 1](x-1)$ is reduced, since $\theta' < \theta$].

This result requires some explanation and we turn first to an argument given by Denton [6], who pointed out that the expansion of the mixed gas $(1+\psi)$ from T_5 to T_6 may be thought of as a combination of unit flow through the turbine from T_3 to T_4, and an expansion of a flow ψ from T_2 to T_1, through a ''reversed'' compressor. The cycle (1,2,3,5,6,1,) is equivalent to two parallel cycles as indicated in Fig. 2: a cycle (1,2,3,4) with unit circulation; plus another cycle passing through the state points (1,2,2,1) with a circulation ψ. The second cycle has the same efficiency as the first (but a vanishingly small work output), so the combined

---

[1] Although this conclusion is valid for the simple gas turbine cycles $[\mathrm{CHT}]_{RU}$ and $[\mathrm{CHT}]_{RC}$, it is not true for regenerative cycles; the introduction of turbine cooling leads to a lower thermal efficiency for cycle $[\mathrm{CHTX}]_{RC}$, compared with cycle $[\mathrm{CHTX}]_{RU}$.

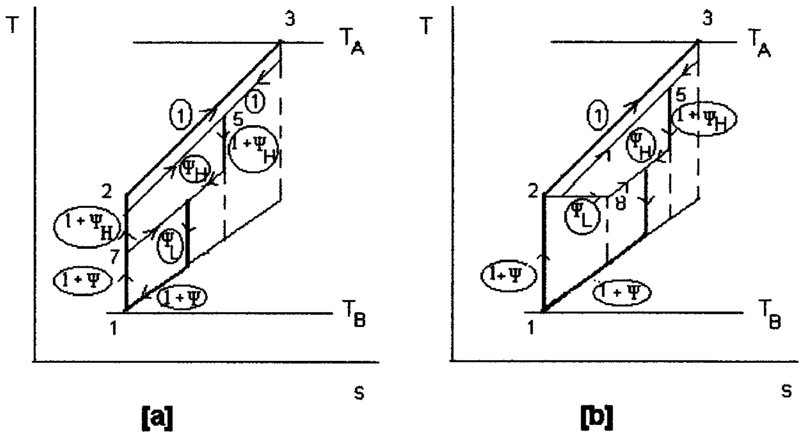

Fig. 3 (*a*) Reversible cycle with two-step cooling, $[\mathrm{CHT}]_{RC2}$; (*b*) reversible cycle with two step cooling, low pressure air throttled, $[\mathrm{CHT}]_{RC2T}$

cooled cycle has the same efficiency as each of the two component cycles. (This interpretation will also be useful when we come to consider internally irreversible cycles below.)

An apparent paradox is that since the cooled cycle contains an irreversible process (constant pressure mixing), its efficiency might be expected to be lower than the original uncooled cycle. The answer to this paradox follows from a consideration of all the irreversibilities in the cycle. The irreversibility associated with the heat supply is unchanged, but the sum of the irreversibility associated with the heat rejection Q_B (now between temperatures T_6 and $T_1=T_B$) and the irreversibility in the adiabatic constant pressure mixing may be shown to be the same as the irreversibility associated with heat rejection in the uncooled cycle [Eq. (5)]. Thus the maximum work and the thermal efficiency are unchanged. A fuller discussion of this point, with numerical examples, is given by Young and Wilcock [7].

2 Two-Step Cooling. Figure 3(a) shows the (T,s) diagram for a reversible cycle with the turbine expansion split into high pressure (HP) and low pressure (LP). The mass flow through the heater is still unity and the temperature rises from T_2 to $T_3=T_A$; so the heat supplied, Q_A, unchanged, as is the overall isentropic temperature ratio (x). Cooling air of mass flow ψ_H is used at entry to the HP turbine (of isentropic temperature ratio x_H); now, however, additional cooling of the mass flow ψ_L is drawn from the compressor at state 7, and mixed at constant pressure with the HP exhaust. Expansion of the mixed flow then takes place through the LP turbine (of isentropic temperature ratio x_L). The total cooling flow is $\psi=\psi_H+\psi_L$. An analysis similar to that described above for single-step cooling may then be developed to show that the thermal efficiency, for this two-step cooling is also the same as that of the uncooled cycle. However, it is important to note that this conclusion becomes invalid if the air for cooling the LP turbine is taken from compressor delivery and then throttled at constant temperature ($T_2=T_8$) to the lower pressure before being mixed with the gas leaving the HP turbine (as in Fig. 3(b)). As another internal irreversibility has been introduced the thermal efficiency drops; it may be shown to be

$$(\eta)_{RC2T}=(\eta)_{RU}-\psi_L(x_H-1)/(\theta-x) \tag{11}$$

where the subscript T indicates throttling of the compressor delivery air.

The drop in thermal efficiency due to throttling the LP cooling air is very small. For $\psi_L=0.05$, $x_H=1.22$, $\theta=6$, and $x=2.79$, the second term in Eq. (11) is only 0.003, i.e., the thermal efficiency drops from $(\eta)_{RU}=0.642$ to $(\eta)_{RC2T}=0.639$.

3 Multistep Cooling. The arguments developed above can be extended for three or more steps of cooling, to give the same efficiency as the uncooled cycle. Indeed, the efficiency will be the same for multistep cooling, with infinitesimal amounts of air abstracted at an infinite number of points along the compressor to cool each infinitesimal turbine stage at the required pressure. This may be a more realistic approach to cooling of real turbines, in which cooling air is introduced continuously through the flow path, and not only through the blade surfaces.

An analysis of such multistep cooling (after Traupel [8], Hawthorne [9], and Elmasri [10]) involves dealing with the turbine expansion in a fashion similar to that of analysing a polytropic expansion. Figure 4 shows gas flow $(1+\psi)$ at (p,T) entering an elementary process made up of a mixing process at constant pressure p, in which the specific temperature drops from temperature T to temperature T', followed by an isentropic expansion in which the pressure changes to $p+dp$ and the temperature changes from T' to $T+dT$.

In the first mixing process, the entry mainstream flow $(1+\psi)$ mixes with cooling flow $d\psi$ drawn from the compressor at temperature T_{comp}. Thus

$$c_p(1+\psi+d\psi)T'=c_p(1+\psi)T+d\psi c_pT_{\mathrm{comp}}$$

and

$$c_p(T-T')=c_p(T'-T_{\mathrm{comp}})d\psi/(1+\psi) \tag{12}$$

In the second process of isentropic expansion,

$$c_p[(T+dT)-T']=v\,dp, \tag{13}$$

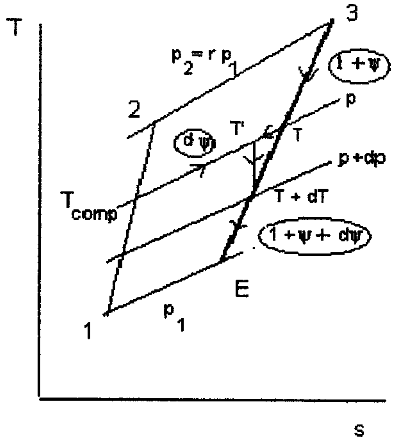

Fig. 4 Multistep reversible cooling

where v is the specific volume. Subtracting Eq. (12) from Eq. (13), it then follows that in the overall elementary process, $(p,T,1+\psi)$ to $(p+dp,T+dT,1+\psi+d\psi)$,

$$c_p dT + c_p(T' - T_{\text{comp}})d\psi/(1+\psi) = v\,dp \tag{14}$$

or

$$c_p dT/T = R\,dp/p - c_p(T' - T_{\text{comp}})d\psi/[T(1+\psi)]. \tag{15}$$

There are two approaches to integrating this equation: (a) the three terms can be integrated separately to give a p,T,ψ relation; and (b) two of the three terms can be brought together if an expression for $d\psi/dT$ is known; a more familiar polytropic (p,T) type of relation can then be obtained.

Solution (a). For a process which does not deviate too far from the original (uncooled) isentropic expansion, the term $[T' - T_{\text{comp}}]/T$ in Eq. (15) may be written approximately as $\delta \approx 1-(T_2/T_3) \approx 1-(x/\theta)$, so this equation may be integrated to give

$$c_p \ln T = R \ln p - c_p \delta \ln[1+\psi] + [\text{const}, C]$$

$$T/p^{[\gamma-1]/\gamma} = C/[1+\psi]^{\delta} \tag{16}$$

If the cooling is carried out over the full turbine expansion, the boundary conditions on this expansion process are at the entry state 3, $p = rp_1$, $T = T_3 = T_A$, and $\psi = 0$, and, at the exit state E, $p = p_1$, $T = T_E$, and $\psi = \psi_E$. These then yield

$$\theta_E = T_E/T_1 = (\theta/x)/[1+\psi_E]^{\delta} < (\theta/x) \tag{17}$$

Solution (b). In the second method of solution a value for ψ_E is not assumed but a relationship for $d\psi/dT$ is determined from semi-empirical expressions for the amount of cooling air required in an (elementary) turbine blade row. For example, a value for $\lambda = -[T/(1+\psi)](d\psi/dT)$ is derived in the Appendix, following an approach similar to that outlined by Elmasri [10].

Equation (15) can then be written

$$c_p(1-\lambda)dT/T = R\,dp/p \tag{18}$$

which may be integrated to give

$$T/p^{\sigma} = \text{const} \tag{19}$$

where $\sigma = (\gamma-1)/\gamma(1-\lambda)$.

For a fully cooled expansion, again applying the boundary conditions at 3 ($p = rp_1$, $T = T_3$, $\psi = 0$) and at the exit state E ($p = p_1$, $T = T_3$, $\psi = \psi_E$), it follows that

$$\theta_E = T_E/T_1 = \theta/r^{\sigma}. \tag{20}$$

If $\psi = \lambda = 0$, then from Eq. (17) or (19) the normal isentropic relation holds, $\theta_E = (\theta/x)$.

C Turbine Exit Condition (for Reversible Cooled Cycles). There is a final point to be made about the reversible cooled cycles: there is a link between the thermal efficiency and the turbine exit temperature T_E. It results from expressing the thermal efficiency of the cycle in the form

$$\eta = [1-(Q_B/Q_A)] = 1-(1/x),$$

which is valid for all the cycles considered above (except that with second step cooling by throttled compressor delivery air).

If the total amount of cooling air supplied from the compressor is $\psi = \psi_E$, then the heat rejected will be $Q_B = c_p(1+\psi_E)(T_E - T_1)$. Thus the efficiency is given by

$$\eta = [1-(Q_B/Q_A)] = 1-[(1+\psi_E)(T_E-T_1)/(T_3-T_2)]$$

$$= 1-(1/x) \tag{21}$$

The exhaust temperature T_E is therefore a function of $\psi = \psi_E$, and is always given by

$$\theta_E = T_E/T_1 = 1 + [(\theta - x)/x(1+\psi_E)]. \tag{22}$$

III Irreversible Cycles

Irreversible cycles are next considered, with compressor and turbine isentropic efficiencies η_c and η_t, respectively.

A Irreversible Uncooled Cycle $[\mathbf{CHT}]_{IU}$. The "air standard" (a/s) efficiency of the irreversible uncooled turbine is given by

$$(\eta)_{IU} = \frac{(\alpha - x)(x-1)}{x(\beta - x)} \tag{23}$$

where $\alpha = \eta_c \eta_t \theta$ and $\beta = 1 + \eta_c(\theta - 1)$, with $\theta = T_3/T_1$ (see Horlock and Woods [11]).

As a numerical illustration, for the a/s cycles studied by Horlock and Woods, with $T_3 = 1800$ K, $T_1 = 300$ K, $(\theta = 6.0)$, $\eta_t = 0.9$, $\eta_c = 0.8$, $\alpha = 4.32$, and $\beta = 5$, $(\eta)_{IU}$ attains a maximum of 0.4442, at $x = 2.79$ [$r = 36.27$], cf. $(\eta)_{RU} = 0.642$. We wish to see how the expression for $[\eta]_{IU}$ is modified when turbine cooling takes place.

B Irreversible Cooled Cycles $[\mathbf{CHT}]_{IC}$

1 Single Step Cooling $[CHT]_{IC1}$. First consider the simplest case of compressor delivery air (mass flow ψ, at T_2) mixed at constant pressure with unit mass flow of combustion products (at T_3) to give a mass flow $(1+\psi)$ at T_5 (see Fig. 5(*a*)). Again, following Denton, the turbine expansion from T_5 to T_6 may be interpreted as being equivalent to an expansion of unit flow from T_3 to T_4 together with an expansion of flow ψ from T_2 to T_9.

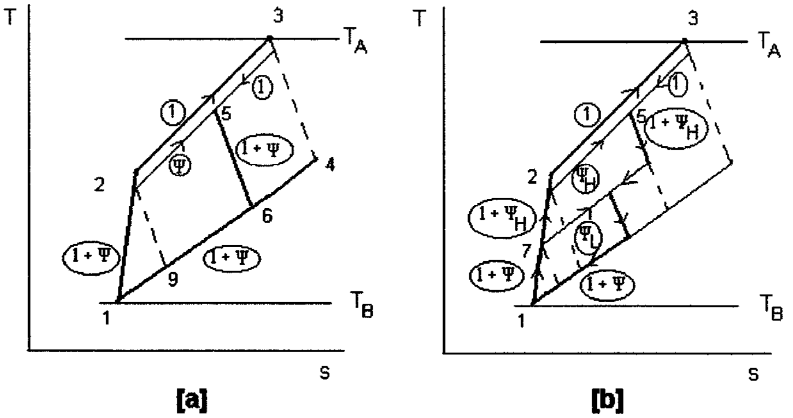

Fig. 5 (*a*) Irreversible cycle with single-step cooling, $[\mathbf{CHT}]_{IC1}$; (*b*) irreversible cycle with two step cooling, low pressure air throttled, $[\mathbf{CHT}]_{IC2T}$

However, the work input to compress ψ of the mainstream compressor flow is not now effectively cancelled by the latter expansion. We are faced with combining two cycles: one of unit mass flow following the original uncooled cycle state points 1, 2, 3, and 4 [and with the same efficiency $(\eta)_{IU}$]; and another of mass flow ψ following the state points 1, 2, 2, and 9. The second effectively has negative work output and a heat supply which in the limit is zero.

Analytically this combination of the two cycles may be expressed as

$$(\eta)_{ICI}=\frac{(T_3-T_4)+\psi(T_2-T_9)-(1+\psi)(T_2-T_1)}{(T_3-T_2)}$$

$$=(\eta)_{IU}-\psi\varepsilon(x-1)/(\beta-x) \tag{24}$$

where $\varepsilon=[1-(\eta_t\eta_c/x)-\eta_t+(\eta_t/x)]$.

Thus the efficiency of the cooled cycle is now less than that of the uncooled cycle by an amount directly proportional to the cooling air used (ψ). This deficit—the second term in Eq. (24)—not only becomes zero if $\psi=0$, but also if ψ is nonzero and $\eta_t=\eta_c=1$. It is therefore likely to be small for a cycle with compressors and turbines of high isentropic efficiency. For a cooled version of the example of Sec. III A, with $\psi=0.15$ and $x=2.79$, the second term in Eq. (24) is 0.0200, the cooled efficiency $(\eta)_{IC1}$ dropping to 0.4242 from $(\eta)_{IU}=0.4442$. The deficit term also decreases as the combustion temperature T_3 is increased; the denominator $(\beta-x)$ increases more rapidly than the numerator. So the uncooled and cooled efficiencies come together at the higher values of top temperature.

The above analysis, limited to a single step of turbine cooling (the first stage nozzle row), suggests that the reduction in cycle efficiency is small (two percentage points in the numerical example, and decreasing at higher temperatures). However even such a reduction may be significant in some applications, especially if η_t falls because of the introduction of cooling.

2 Two-Step Cooling $[CHT]_{IC2}$. Figure 5(*b*) shows the case of two-step cooling but now with irreversible compression and expansion. The turbine entry temperature is reduced from T_3 to T_5 by mixing with cooling air ψ_H taken from compressor exit (at state 2, pressure p_2, and temperature T_2). After expansion to pressure p_7 the HP turbine gas flow $(1+\psi_H)$ is mixed with compressor air (mass flow ψ_L) abstracted at the same pressure p_7 to give cooled gas flow $(1+\psi_H+\psi_L)$ at entry to the LP turbine.

An analysis similar to that given previously leads to an expression for the two stage cooled efficiency of

$$\eta_{IC2}=(\eta)_{IU}-[\psi_H\varepsilon(x-1)+\psi_L\varepsilon_L[(x_L-1)]/(\beta-x)] \tag{25}$$

where $\varepsilon_L=[1-(\eta_t\eta_c/x_L)-\eta_t+(\eta_t/x_L)]$. It has been implied here that $x\gg x_H$, so that the efficiencies η_c and η_t are the same over the isentropic temperature ratios x and x_L (alternatively unchanged polytropic efficiencies could have been assumed). As $x_L\rightarrow x$, and $\varepsilon_L\rightarrow\varepsilon$, Eq. (25) becomes Eq. (24).

For the a/s example quoted above, with this form of two stage cooling (and $x=2.79$, $x_H=1.22$, $\psi_H=0.1$, and $\psi_L=0.05$), the thermal efficiency is reduced from 0.4442 (uncooled) to 0.4257, i.e., by 0.0185. If the second step of cooling operates using compressor delivery air rather than air taken at the appropriate pressure along the compressor, as in Fig. 5(*b*), it may then be shown that the thermal efficiency is

$$(\eta)_{IC2T}=(\eta)_{IU}-[\psi\varepsilon(x-1)/(\beta-x)]-\psi_L[(\varepsilon-\varepsilon_L)/(\beta-x)]$$
$$-\eta_t\psi_L[(x_H-1)/(\beta-x)] \tag{26}$$

The first two terms on the right-hand side represent the efficiency for the irreversible cycle with single stage cooling, the third term on the right is very small indeed, and the last term represents the LP throttling loss in this cycle.

For the numerical example, Eq. (26) gives the cooled efficiency $(\eta)_{IC2T}$ as 0.4205. The small extra loss in efficiency for throttling the LP cooling air is therefore $(\eta)_{IC2}-(\eta)_{IC2T}=0.4257-0.4205=0.0052$.

3 Multistep Cooling. The two step cooling analysis can be extended to multistep cooling of the turbine, but it becomes complex. It is now more convenient to treat the turbine expansion as a modification of the normal polytropic expansion; the analysis is essentially an adaptation of that given in Sec. II B 3 for the multistep cooled turbine cycle.

If the polytropic efficiency with no cooling is η_p, then Eq. (15) becomes

$$c_p dT/T=\eta_p R dp/p-c_p\delta d\psi/(1+\psi) \tag{27}$$

This equation may again be integrated following the solutions of Sec. II B 3 for solution (a),

$$T/p^{(\gamma-1)\eta p/\gamma}=C/(1+\psi)^{\delta} \tag{28}$$

$$T_E/T_1=\theta[x^{\eta p}(1+\psi_E)^{\delta}] \tag{29}$$

and, for solution (b),

$$T/p^{\sigma'}=\text{const} \tag{30}$$

$$T_E/T_1=\theta/x^{\eta p'} \tag{31}$$

where $\sigma'=\eta_p(\gamma-1)/\gamma(1-\lambda)$, $\eta_p'=\eta_p/(1-\lambda)$ is a modified polytropic efficiency, and λ may again be obtained from an equation such as (*A*4) given in the Appendix. A point of interest is that if $\eta_p=(1-\lambda)$ then $\eta_p'=1$ and the expansion becomes isentropic (but not reversible adiabatic), a vertical line on the (T,s) chart. The example in the Appendix gives $\lambda\approx0.34$, for $\eta_p=0.85$ and $\eta_p'=1.29$ and $\sigma'=0.36$ for $\gamma=1.4$, so that the expansion line ''heels over'' beyond the vertical on the (T,s) chart. With T_E known from Eq. (29) or (31), the thermal efficiency may be determined as

$$(\eta)_{\mathrm{ICM}}=1-(Q_B/Q_A)=1-\{[\eta_c(1+\psi_E)(T_E/T_1-1)]/(\beta-x)\} \tag{32}$$

IV Performance as a Function of Maximum Turbine Temperature

For modern practical gas turbine systems which are cooled, the definition of the maximum temperature $T_{\max}$ is somewhat arbitrary. Mukherjee [12] suggested three possible definitions. The first is the combustion outlet temperature (T_3 in the notation of this paper) which is based on the averaged temperature at exit from the combustion chamber. The second definition, the rotor inlet temperature (T_5 here), has tended to be used more widely within the gas turbine industry (e.g., Walsh and Fletcher [13]). T_5 is based on the averaged temperature taken at entry to the first rotor section (i.e., the exit of the first nozzle guide vanes), and can be calculated if it is assumed that the NGV cooling air has mixed completely with the mainstream, as we have assumed. Mukherjee's third definition, the so-called firing temperature T_F, can be calculated from the combustion equations and a known fuel-air ratio, but this definition is not often used. In this section we explain how the efficiency of the cooled gas turbine varies with both T_3 and T_5 but we do not use T_F.

The major variables to be considered in the assessment of gas turbine thermal efficiency are the maximum temperature and the pressure ratio ($\eta=f(T_{\max},r)$). Initially it is convenient to express this relationship in the form of the variation of η with maximum temperature (T_3) for selected values of r (and x). We can then consider the maximum temperature being increased (at a constant x) together with the required increase in cooling air ψ; analytically we wish to determine $[\partial(\eta)_{IC1}/\partial\theta]_x$ with $\theta=\theta_3=T_3/T_1$.

Consider a single step of cooling (as in Sec. III B 1). Figure 6(*a*) diagrammatically shows both $(\eta)_{IU}$ and $(\eta)_{IC1}$ plotted

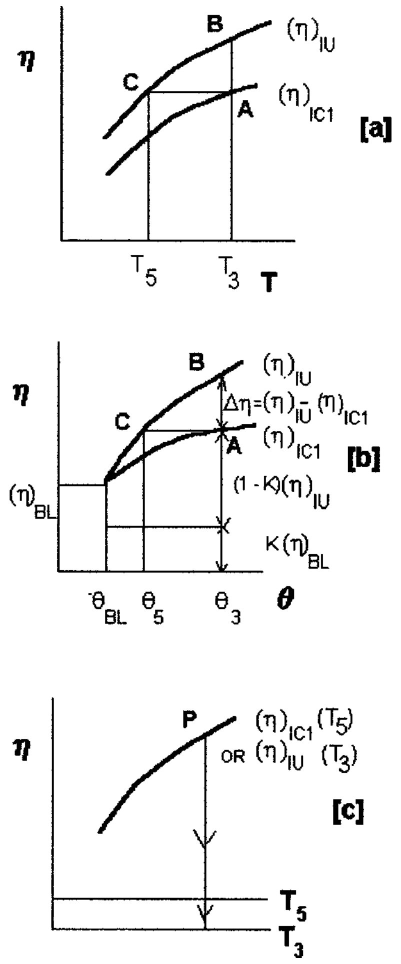

Fig. 6 Diagrams showing variations in thermal efficiency with maximum temperatures

against the combustion temperature T_3. The efficiency of the cooled gas turbine $(\eta)_{IC1}$ (point A) is less than the efficiency of the uncooled turbine $(\eta)_{IU}$ at the same T_3 (point B), as Eq. (24) illustrated. But it is the same as the efficiency of the uncooled turbine $(\eta)_{IU}$ at point C—at maximum temperature T_5 (the rotor inlet temperature of the cooled turbine). The analysis of Sec. III B 1 for air standard cycles with constant specific heats, is used to find the slopes of the curves $(\partial\eta/\partial\theta)_x$ at all three points A, B, and C; the slopes are then used to determine relations between the expressions for $(\eta)_{IC1}$ and $(\eta)_{IU}$.

The expression for thermal efficiency was

$$(\eta)_{IC1}=(\eta)_{IU}-\psi\varepsilon(x-1)/(\beta-x)$$

and, using an approximate relation

$$\psi=K[T_3-T_{BL}]/[T_{BL}-T_2], \tag{33}$$

where T_{BL} is the allowable [constant] blade temperature [see Eq. (*A*3) of the Appendix], it may be shown that

$$[\partial(\eta)_{IC1}/\partial\theta]_x=\varepsilon\eta_c(x-1)/(\beta-x)^2+\varepsilon\psi(x-1)\times\eta_c\{1-[(\beta-x)/\tau\eta_c]\}/(\beta-x)^2 \tag{34}$$

where $\tau=[\theta_3-\theta_{BL}]$, with $\theta_{BL}=T_{BL}/T_1$. The first term on the right-hand side gives the rate of increase of thermal efficiency in the absence of cooling.

After some algebra, it follows that

$$\{[\partial(\eta)_{IC1}/\partial\theta]_x\}_A=(1-K)\{[\partial(\eta)_{IU}/\partial\theta]_x\}_B \tag{35}$$

So in Fig. 6(*a*), the slope of the $(\eta)_{IC1}$ curve at point A is $(1-K)$ times the slope of the $(\eta)_{IU}$ at point B. $(\eta)_{IC1}$ thus increases a smaller rate than $(\eta)_{IU}$ with T_3, but neither $[\partial(\eta)_{IC1}/\partial\theta]_x$ nor $[\partial(\eta)_{IU}/\partial\theta]_x$ become zero.

Equation (35) may then be integrated to temperature θ from the point BL, where $\theta=\theta_{BL}$ and $\psi_{BL}=0$, and the uncooled and cooled efficiencies are the same, $[(\eta)_{IU}]_{BL}=[(\eta)_{IC1}]_{BL}=(\eta)_{BL}$. Thus

$$(\eta)_{IC1}-(\eta)_{BL}=(1-K)[(\eta)_{IU}-(\eta)_{BL}] \tag{36}$$

or

$$(\eta)_{IC1}=(1-K)(\eta)_{IU}+K(\eta)_{BL} \tag{36a}$$

and

$$\Delta\eta=(\eta)_{IU}-(\eta)_{IC1}=K[(\eta)_{IU}-(\eta)_{BL}] \tag{37}$$

These relationships are illustrated in Fig. 6(*b*).

An alternative approach is illustrated in Fig. 6(*c*). Here the cooled efficiency $(\eta)_{IC1}$ is presented initially as a unique function of the rotor inlet temperature (T_5), for a given x and component efficiencies. But from the Elmasri expression, [Eq. (33)] the cooling air quantity ψ is a function of the combustion temperature T_3, for a given x (and T_2) and a selected blade temperature T_{BL}, so there is a value of T_3 corresponding to the rotor inlet temperature T_5; analytically we may therefore state that $(\eta)_{IC1}=f(T_5)$ or $(\eta)_{IC1}=f(T_3)$, and the cooled efficiency may be plotted against two horizontal scales, T_3 and T_5, as indicated in Fig. 6(*c*).

However, note that it is the thermodynamic effects of single stage cooling only that have been considered above, and Young and Wilcock [7] have emphasised that in practice there are other irreversibilities involved in turbine cooling; for example, those associated with the total pressure loss, the change in species concentration due to mixing, and coolant pumping work. Mixing pressure losses for the single-stage cooling can be taken into account by a simple extension of the air standard analysis, using the work of Horlock and Woods [11]. Equation (24) then becomes

$$(\eta)_{IC1}=(\eta)_{IU}-\{\psi(x-1)\varepsilon+[k\alpha\psi(\gamma-1)/\gamma x]\}/(\beta-x) \tag{38}$$

where it has been assumed that the extra pressure loss due to coolant mixing is $[\Delta p_0/p_0]=k\psi$ (following Hartsel [14]) and k is a small constant (of the order of 0.1). Now $[\partial(\eta)_{IC1}/\partial\theta]_x$ becomes even less as T_3 (and ψ) is increased, and the thermal efficiency curve tends to flatten out more. However $(\eta)_{IC1}$ does not reach a maximum (although in theory it could do so if k took a large value, very much greater than those encountered in practice). The overall conclusions from this discussion are as follows. (a) The cooled efficiency $(\eta)_{IC1}$ is less than the uncooled efficiency $(\eta)_{IU}$ at a given combustion temperature T_3, but it also increases less rapidly with T_3. (b) $(\eta)_{IC1}$ at T_3 is the same as $(\eta)_{IU}$ at T_5, the ''mixed out'' rotor inlet temperature that is obtained by mixing the cooling air ψ with the combustion products.

Figures such as Figs. 6(*a*)–6(*c*) give the complete picture. But *from air standard analysis* there is no evidence that $(\eta)_{IC1}$ can attain a maximum, even at very high values of T_3.

V Real Gas Effects

There are obviously limitations in the analysis developed on the basis of air standard cycles so the influence of real gas effects was next considered. In the course of this investigation a code developed by Young [15] was used.

A Reductions in Thermal Efficiency. First it can be argued that the reductions in thermal efficiency due to turbine cooling will be of comparably small order of magnitude for cycle calculations with real gases, with $c_p(T)$. Referring to Fig. 5(*a*) for single-step cooling, we again invoke Denton's concept of two equivalent parallel turbine expansions, through the same overall pressure ratio, one from combustion temperature T_3 and one from

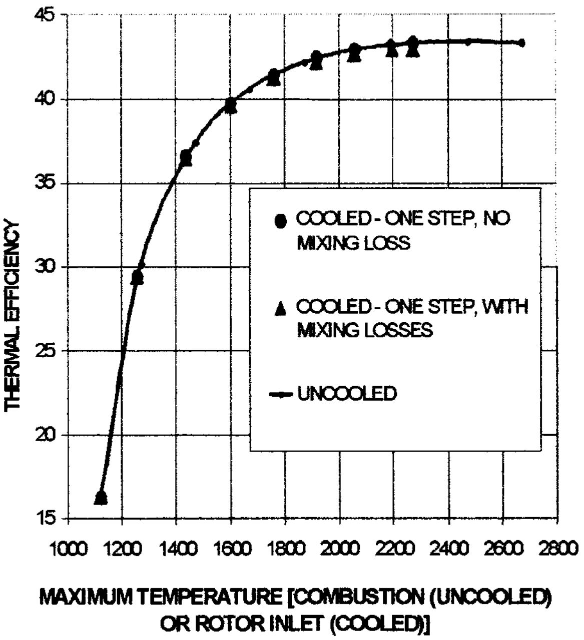

Fig. 7 Real gas thermal efficiency calculations, $[\mathrm{CHT}]_{IU}$ and $[\mathrm{CHT}]_{IC1}$. For $r=30$, $\eta_c=0.8$, $\eta_t=0.9$, $T_{\mathrm{BL}}=1123$ K, convective cooling (using the Elmasri expression for cooling fraction, with $K=0.05$, no mixing losses). Maximum temperatures absolute (K).

compressor outlet temperature T_2. But for real gases, the first expansion will take place with a higher mean c_{pg} and lower mean γ_g (for high-temperature combustion gas, subscript g), compared with the second with c_{pa} and γ_a (for air, subscript a). The mixture of gases in the actual turbine has a mean specific heat given by $c_{pm}=(c_{pg}+\psi c_{pa})/(1+\psi)$ and a gas constant $R_m=(R_g+\psi R_a)/(1+\psi)$. The work from the two equivalent turbine is $(c_{pg}T_3\xi_g+\psi c_{pa}T_2\xi_a)$, with $\xi=[1-(1/r^{\phi})]$ and $\phi=(\gamma-1)\eta_p/\gamma$. But the work from the actual turbine is $(1+\psi)c_{pm}T_5\xi_m$, where $T_5=(c_{pg}T_3+\psi c_{pa}T_2)/c_{pm}(1+\psi)$, which is not the same. (Wilcock and Young [7] derived the difference formally). However for small cooling quantities ψ, the differences between R_m and R_g, and between c_{pm} and c_{pg} (and hence between γ_m and γ_g) will not be large, so the a/s analysis should still give guidance for the (small) changes in efficiency with cooling.

Using the real gas code, the change in efficiency due to cooling was initially computed using similar assumptions to those made for the numerical a/s examples given earlier, i.e., $T_3=1800$ K, and for the optimum pressure ratio of 36.27. (This value of r gives the maximum thermal efficiency for the a/s cycle example, but it is less than the optimum for real gases.) The ''real gas'' thermal efficiency at this pressure ratio was calculated as 0.4402. For a total cooling air fraction $\psi=0.15$, the changes in efficiency given by the real gas calculation were from 0.4442 to 0.4298 for single-step cooling; and from 0.4402 to 0.4273 for two-step cooling. These drops in efficiency are about half those estimated in the air standard analyses. To illustrate the arguments of Sec. IV (and Fig. 6) further, two sets of parametric real gas calculations (varying maximum temperature and pressure ratio) were then made using the Young code.

The first set of results, for single-step cooling, is illustrated in Fig. 7, showing that with a given pressure ratio of 30, $\eta_c=0.8$ and $\eta_t=0.9$, the uncooled thermal efficiency $(\eta)_{IU}$ increases steadily with T_3. The Elmasri expression for the cooling quantity ψ (Eq. (A2) with $K=0.05$, but with no extra pressure losses due to mixing) was then used to obtain the single step cooled efficiencies. As anticipated, these dropped slightly, but when plotted against the rotor inlet temperature (T_5) they fell on the uncooled efficiency line, as Fig. 7 shows [also note that $(\eta)_{ICI}$ is exactly equal to $(\eta)_{IU}$ at $T_3=T_{\mathrm{BL}}=1123$ K]. The figure also shows the effect of including mixing pressure losses, $[\Delta p_0/p_0]=k\psi$ with $k=0.07$]; the reduction in thermal efficiency is small for single step cooling. Similar results were obtained with $r=40$ and 50 for single step cooling.

A second set of more realistic calculations using the Young real gas code were reported earlier by Horlock et al. [5]. The assumptions made were (i) a constant polytropic efficiency of 0.9 for both compressor and turbine; (ii) a cooling flow fraction of

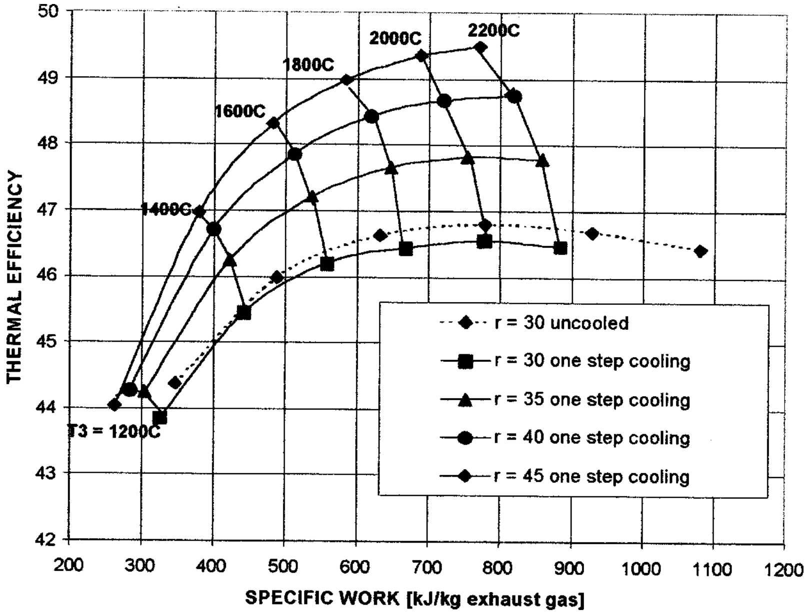

Fig. 8 Real gas calculations of thermal efficiency and specific work, for single step cooling cycle $[\mathrm{CHT}]_{IC1}$. $\eta_{pc}=\eta_{pt}=0.9$, $T_{\mathrm{BL}}=1073$ K, film cooling with combustion and mixing stagnation pressure losses, after Horlock et al. [5].

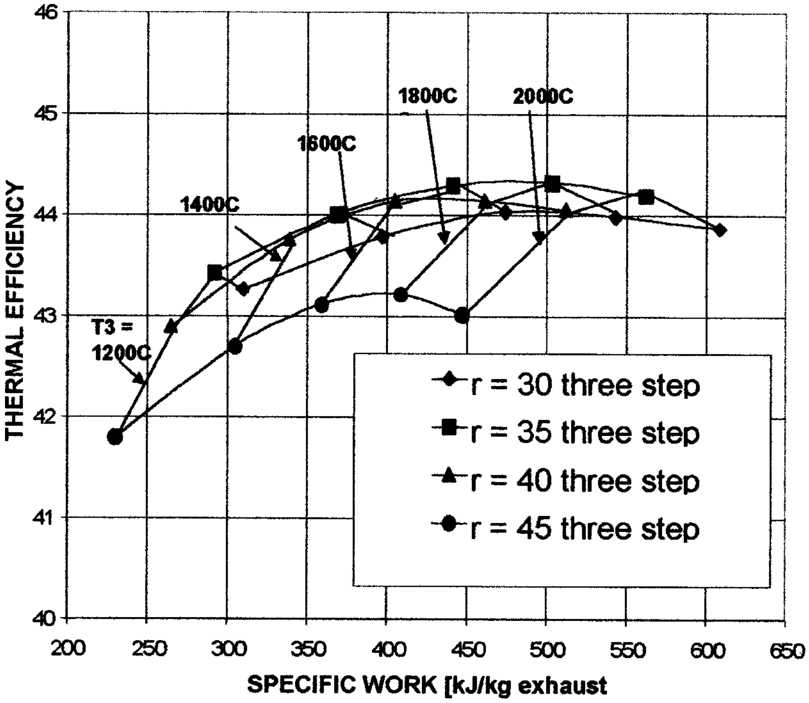

Fig. 9 Real gas calculations of thermal efficiency and specific work, for three-step cooling cycle $[\mathrm{CHT}]_{IC3T}$. $\eta_{pc}=\eta_{pt}=0.9$, $T_{\mathrm{BL}}=1073$ K, film cooling, with combustion and mixing stagnation pressure losses, after Horlock, Watson, and Jones [5].

the form $\psi=0.045W^*$, where the parameter W^* now included the effects of film cooling in each cooling step; and (iii) total pressure losses due to combustion mixing of $\Delta p_0/p_0=0.03$ and cooling mixing losses of $\Delta p_0/p_0=0.07\psi$.

Figure 8 shows a carpet plot of $(\eta)_{ICI}$ against specific work. For given pressure ratios these single-step efficiencies appear to reach maxima with a combustion temperature T_3, the optimum points increasing with pressure ratio in a similar fashion to uncooled efficiency behavior ($(\eta)_{IU}$ for $r=30$ is also shown in Fig. 8 for comparison).

Figure 9 shows a similar carpet plot for three step cooling. However, now the picture is different, with the efficiencies $(\eta)_{ICT3}$ collapsing into a narrow band around 44 percent, for temperatures T_3 between 1600 and 2000°C and for pressure ratios at 30, 35, and 40. The advantages on thermal efficiency of higher pressure ratio at high T_3, for both uncooled and single step cooling, are now negated, because of the higher cooling flows required. However the higher combustion temperature continues to give advantage in larger specific work.

By way of illustration, at $T_3=1800°\mathrm{C}$, the required cooling flows for the three steps (as fractions of compressor air flow), were calculated as

$$0.133, 0.115, \text{ and } 0.082 \text{ for } r=35$$

$$0.162, 0.157, \text{ and } 0.117 \text{ for } r=45$$

These numbers illustrate that for the second step (first rotor) the cooling air required is less that that for the first step (first nozzle row) because of the reduction in stagnation temperature relative to the blading; and that for the third step (second nozzle row) the requirement is much less because of the drop in stagnation temperature through the first stage. Further, for a larger pressure ratio, with the higher compressor delivery temperature, more cooling air is required, and this also causes higher mixing losses. Such cooling flows were used in the calculations of Fig. 9.

B Maximum Thermal Efficiency. Both these sets of real gas calculations give indications of maxima in the plots of thermal efficiency against T_3 for a given pressure ratio. These did not appear in the a/s analysis, but now occur not only for cooled but also, surprisingly, for uncooled calculations. The graphs are very flat; but there is clearly a real gas effect independent of cooling at high T_3. Recent detailed investigations of these real gas effects by Wilcock and Young [16] have revealed that this ''turnover effect'' on thermal efficiency at high values of T_3 is related to the changes in real gas properties (c_{pg} and γ_g) with both temperature and composition.

However in practice the attainment of the maximum thermal efficiency will depend on a complex mix of factors—the real gas property effect, the number of cooling steps, the quantities of cooling air required (dependent on entry stagnation temperature at entry to each step, the permissible blade temperature and the temperature of the available cooling air), and the associated mixing losses.

VI Conclusions

It has been shown that from *air standard* cycle analysis that (a) plant thermal efficiency drops relatively little due to turbine cooling; (b) the difference between uncooled and cooled efficiencies decreases at high combustion temperature; and (c) the rate of increase of thermal efficiency of the cooled cycle falls with increasing T_3, but there is no prediction of a maximum efficiency being attained at high T_3.

These conclusions are broadly confirmed by *real gas* calculations for single step cooling. But it appears that thermal efficiency does tend toward a maximum level for realistic calculations of more highly cooled turbines.

Acknowledgment

The author is indebted to Professors J. D. Denton and J. B. Young and R. C. Wilcock for their assistance.

Nomenclature

(specific quantities in lower case)

c_p = specific heat at constant pressure, also used with subscripts a or g
C = blade cooling parameter
h, H = enthalpy
I = irreversibility
k, K = constants
m = total cooling mass flow in a blade row
M_u = blade Mach number
p = pressure
q, Q = heat supplied
r = pressure ratio
s, S = entropy
R = characteristic gas constant
T = temperature (absolute)
w, W = work
w^*, W^* = blade cooling parameters
x = isentropic temperature ratio
α = $\eta_c \eta_t \theta$
β = $1+\eta_c(\theta-1)$
δ = $1-(x/\theta)$
ε = $[1-(\eta_t \eta_c/x)-\eta_t+(\eta_t/x)]$
γ = c_p/c_v
θ = temperature ratio, T_3/T_1
θ' = temperature ratio, T_5/T_1
ψ = cooling mass flow in a ''step'' (per unit mass flow through heater)
η = plant thermal efficiency
η_c = isentropic efficiency of compressor
η_t = isentropic efficiency of turbine
η_p = polytropic efficiency [uncooled turbine]
η'_p = ''polytropic'' efficiency [cooled turbine]
λ = $-[T(1+\psi)](\partial\psi/\partial T)$, defined as in Sec. II B C
Φ = turbine stage loading coefficient
σ = $(\gamma-1)/\gamma(1-\lambda)$, defined as in Sec. II B 3
σ' = $\eta_p(\gamma-1)/\gamma(1-\lambda)$ defined as in Sec. III B 3
ξ = $[1-(1/r^{\phi})]$
ϕ = $\eta_p(\gamma-1)/\gamma$

Subscripts

a = air
A = supply reservoir
B = atmosphere
BL = blade (temperature)
CAR = Carnot
$C1$ = single step cooling
$C2$ = two step cooling comp compressor
E = exit (from turbine)
F = firing
g = gas [products of combustion]
H = high pressure
I = irreversible
L = low pressure
m = mixture
R = reversible
S = surface
U = uncooled
t = turbine
T = throttled
1, 2, 3, 4,... = locations in plant (see figures)

Gas turbine cycles are referred to as (after Hawthorne and Davis [1]). CHT, CBT, CHTX, and CBTX, where C denotes a compressor, H a heater; B a burner (combustion); T a turbine, and X a heat exchanger. R and I indicate reversible and irreversible, subscripts U and C refer to uncooled and cooled turbines in a cycle, and subscripts 1 and 2 indicate the number of cooling steps. Thus, for example, $[\mathrm{CHTX}]_{IC2}$ indicates an irreversible cooled regenerative cycle with two steps of turbine cooling.

Appendix: Cooling Flow Requirements

Horlock et al. [5] showed that the total cooling mass flow m required in a convectively cooled blade with unit entry mass flow is given by

$$m=Cw^* \tag{A1}$$

Here $w^*=\varepsilon_0/\eta_{\mathrm{cool}}(1-\varepsilon_0)$, in which ε_0 is the blade cooling effectiveness, $\varepsilon_0=(T_3-T_{\mathrm{BL}})/(T_3-T_2)$, with T_{BL} the allowable blade temperature and T_2 the cooling air entry temperature; η_{cool} is the cooling efficiency; $\eta_{\mathrm{cool}}=(T_{2'}-T_2)/(T_{\mathrm{BL}}-T_2)$, in which $T_{2'}$ is the cooling air outlet temperature before mixing; and $C=\mathrm{St}_g(A_{sg}/A_g)(c_{pg}/c_{pc})$, in which St_g is the external Stanton number, A_{sg} and A_g are the gas surface and cross-sectional areas, respectively, and c_{pg} and c_{pc} are the gas and coolant specific heats.

C and η_{cool} do not vary greatly, and, if they are amalgamated into a single constant $K=C/\eta_{\mathrm{cool}}$, then

$$m=K\varepsilon_0/(1-\varepsilon_0) \tag{A2}$$

or

$$m=K(T_3-T_{\mathrm{BL}})/(T_{\mathrm{BL}}-T_2)=K(\theta-\theta_{\mathrm{BL}})/[\theta_{\mathrm{BL}}-(T_2/T_1)] \tag{A3}$$

in the notation used in this paper. With $\eta_{\mathrm{cool}}=0.7$ and $C=0.035$ and say, $K=0.05$, Eq. (A2) then correlates well with values used by Elmasri [2,17].

If the cooling flow is added in a blade row of a 50 percent reaction stage (of stage loading coefficient $\Phi=c_p\Delta T/U^2$ where ΔT is the temperature drop, and U is the blade speed), then the gradient of (fractional) mass addition with temperature across the blade row is approximately

$$\begin{aligned}\lambda&=-[T/(1+\Psi)](d\Psi/dT)=2m/(\Delta T/T)=2mc_pT/\Phi U^2\\&=2C^*w/\Phi(\gamma-1)M_u^2\end{aligned} \tag{A4}$$

where M_u is the blade Mach number. Equation (A4) may then be used in the expressions derived in the main part of the paper for multistep cooling. For the conditions of the example in the text, with $T_{\mathrm{BL}}=1123\,\mathrm{K}$, $m=Cw^*=0.05$, $\Phi=1.5$, $M_u=0.7$, and $\lambda=0.1/1.5.0.4.0.49=0.34$.

References

[1] Hawthorne, W. R., and Davis, G. de V., 1956, ''Calculating Gas Turbine Performance,'' Engineering, **181**, p. 361.
[2] Elmasri, M. A., 1987, ''Energy Analysis of Combined Cycles: Part 1—Air-Cooled Brayton-Cycle Gas Turbines,'' ASME J. Eng. Gas Turbines Power, **109**, pp. 228–235.
[3] Chiesa, P., Consonni, S., Lozza, G., and Macchi, E., 1993, ''Predicting the Ultimate Performance of Advanced Power Cycles Based on Very High Temperatures,'' ASME Paper No. 93-GT-223.
[4] MacArthur, C. D., 1999, ''Advanced Aero-engine Turbine Technologies and Their Application to Industrial Gas Turbines,'' ISABE Paper No. 99-7151, 14th International Symposium on Air-Breathing Engines, Florence, Italy.
[5] Horlock, J. H., Watson, D. E., and Jones, T. V., 2000, ''Limitations on Gas Turbine Performance Imposed by Large Turbine Cooling Flows,'' ASME Paper No. 2000-GT-0635.
[6] Denton, J. D., 1993, ''Loss Mechanisms in Turbomachines,'' ASME Paper No. 93-GT-435.
[7] Young, J. B., and Wilcock, R. C., 2001, ''Modelling the Air-Cooled Gas Turbine, Part 1,'' ASME paper, to be published.
[8] Traupel, W., 1966, *Thermische Turbomaschinen*, Springer-Verlag, Berlin.
[9] Hawthorne, W. R., 1956, ''The Thermodynamics of Cooled Turbines, Parts I and II,'' Proc. ASME, **78**, pp. 1765, 1781.
[10] Elmasri, M. A., 1986, ''On Thermodynamics of Gas Turbine Cycles: Part II Model for Expansion in Cooled Turbines,'' ASME J. Eng. Gas Turbines Power, **108**, pp. 151–159.

[11] Horlock, J. H., and Woods, W. A., 2000, ''Determination of the Optimum Performance of Gas Turbines,'' Proc. Instn. Mech. Eng., **214C**, pp. 243–255.
[12] Mukherjee, D. K., 1976, ''Design of Turbines, Using Distributed or Average Losses; Effect of Blading,'' AGARD 195, 8-1.
[13] Walsh, P. P., and Fletcher, P., 1998, *Gas Turbine Performance*, Blackwell Science, Oxford.
[14] Hartsel, J. E., 1972, ''Prediction of Effects of Mass-Transfer Cooling on the Blade-Row Efficiency of Turbine Airfoils,'' AIAA Paper No. 72-11..-8-13.
[15] Young, J. B., 1998, ''Computer-Based Project on Combined-Cycle Power Generation,'' Cambridge University Engineering Department Report.
[16] Wilcock, R. C., and Young, J. B., 2001b, *Real Gas Effects on Gas Turbine Plant Efficiency* (to be published).
[17] Elmasri, M. A., 1988, ''GASCAN—An Interactive Code for Thermal Analysis of Gas Turbine Systems,'' ASME J. Eng. Gas Turbines Power, **110**, pp. 201–209.

Large-Scale Testing to Validate the Influence of External Crossflow on the Discharge Coefficients of Film Cooling Holes

D. A. Rowbury
Rolls-Royce plc,
Bristol, United Kingdom

M. L. G. Oldfield
Department of Engineering Science,
University of Oxford,
Oxford, United Kingdom

G. D. Lock
Department of Mechanical Engineering,
University of Bath,
Bath, United Kingdom

This paper discusses large-scale, low-speed experiments that explain unexpected flow-interaction phenomena witnessed during annular cascade studies into the influence of external crossflow on film cooling hole discharge coefficients. More specifically, the experiments throw light on the crossover phenomenon, where the presence of the external crossflow can, under certain circumstances, increase the discharge coefficient. This is contrary to most situations, where the external flow results in a decrease in discharge coefficient. The large-scale testing reported helps to explain this phenomenon through an increased understanding of the interaction between the emerging coolant jet and the free-stream flow. The crossover phenomenon came to light during an investigation into the influence of external crossflow on the discharge coefficients of nozzle guide vane film cooling holes. These experiments were performed in the Cold Heat Transfer Tunnel (CHTT), an annular blowdown cascade of film cooled vanes that models the three-dimensional external flow patterns found in modern aero-engines. (Rowbury et al., 1997, 1998). The variation in static pressure around the exit of film cooling holes under different flow conditions was investigated in the large-scale tests. The study centered on three holes whose geometries were based on those found in the leading edge region of the CHTT vanes, as the crossover phenomenon was witnessed for these rows during the initial testing. The experiments were carried out in a low-speed wind tunnel, with the tunnel free-stream flow velocity set to match the free-stream Reynolds number (based on the local radius of curvature) and the ''coolant'' flow velocity set to replicate the engine coolant-to-free-stream momentum flux ratio. It was found that the apparent enhancement of film cooling hole discharge coefficients with external crossflow was caused by a reduction in the static pressure around the hole exit, associated with the local acceleration of the free-stream around the emerging coolant jet. When these measured static pressures (rather than the free-stream static pressure) were used to calculate the discharge coefficient, the crossover effect was absent. The improved understanding of the crossover phenomenon and coolant-to-free-stream interactions that has been gained will be valuable in aiding the formulation of predictive discharge coefficient schemes.

[DOI: 10.1115/1.1375171]

Introduction

The successful implementation of a turbine cooling system requires careful design to achieve effective cooling (leading to maximum permissible turbine entry temperature) without a dramatic performance penalty.

A film cooling system is designed to supply the mass flow rate of coolant needed to produce a near-uniform vane temperature. Failing to do so will result in thermal stresses within the vane and, consequently, a reduced vane life. For a first-stage nozzle guide vane (NGV), the coolant-to-mainstream pressure ratio is usually set by the compressor exit pressure and the combustion pressure drop, so the design problem hinges on correct hole sizing in order to provide the requisite coolant flow. This requires reliable discharge coefficient, C_d, data covering the particular geometry and flow.

The C_d of a cooling hole depends on both the local geometry and the flow conditions upstream and downstream of the hole. The work discussed in this paper provides an improved understanding of these dependencies, specifically through the interaction between the coolant and mainstream flows, thereby helping to explain the Crossover Phenomenon [1]. Furthermore, the knowledge gained has been invaluable in aiding the formulation of predictive discharge coefficient schemes [2].

Discharge Coefficient Studies at Oxford

The experimental work reported in this paper continues the studies on the Cold Heat Transfer Tunnel (CHTT; [3]) at the University of Oxford. The CHTT consists of an annular cascade of 36 NGVs that is representative of the first-stage high-pressure (HP1) section of a modern aero-engine. The vanes are 1.4 times larger than engine size, resulting in good spatial resolution on all measurements taken. The CHTT is a short duration, transonic test facility, which not only provides engine representative Reynolds and Mach numbers, but also, being an annular cascade of NGVs, models the three-dimensional flow patterns found in modern aeroengines, including all secondary flow phenomena. Moreover, the coolant system design, employing a ''foreign gas'' coolant [4], allows the engine coolant-to-mainstream density ratio, ρ_{0c}/ρ_{0m}, blowing parameter, $B=\rho_c u_c/\rho_m u_m$, and momentum flux ratio, $I=\rho_h u_h^2/\rho_m u_m^2$, to be matched to and varied about actual engine design values.

The NGV cooling geometry consists of 14 rows of holes, fed from one of two internal cavities (Fig. 1). The six rows of cooling

---

Contributed by the International Gas Turbine Institute and presented at the 45th International Gas Turbine and Aeroengine Congress and Exhibition, Munich, Germany, May 8–11, 2000. Manuscript received by the International Gas Turbine Institute February 2000. Paper No. 2000-GT-293. Review Chair: D. Ballal.

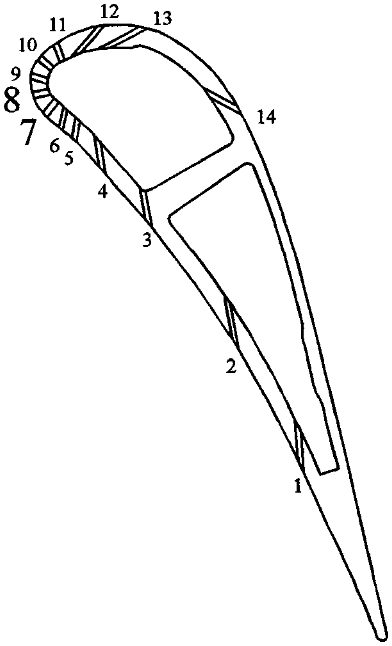

Fig. 1 Cross section through a CHTT vane, illustrating the locations of film cooling rows 7 and 8

holes around the leading edge (Rows 5–10) are cylindrical, while each of the remaining rows (except one) have been investigated with both a cylindrical and a fan-shaped (see, for example, [5]) geometry. Data were collected both with and without the presence of external crossflow, with the rows blown singularly. Although the external crossflow generally resulted in a decrease in C_d, the data highlighted how, in the leading edge region, the presence of external crossflow can lead to an enhancement in the hole C_d at a given coolant total-to-freestream static pressure ratio, PR [1]. This behavior was termed the ''Crossover Phenomenon,'' and was witnessed on all six of the leading edge film cooling rows. In an attempt to explain the phenomenon, an investigation on large-scale models of the leading holes was undertaken, as reported herein.

Flow Mechanics and Flow Interaction

Thole et al. [6] investigated the influence of internal cashflow on the velocity profile at exit from a 30 deg inclined hole (i.e., $\theta=30$ deg and $\alpha=0$ deg, see Fig. 2). They concluded that the velocity profile was strongly dependent on the internal crossflow Mach number. With no crossflow at the hole inlet, there is separation on the downstream side of the hole entrance (relative to the direction of the free-stream flow), causing the jet to exit from the upstream portion of the hole. This is illustrated in Fig. 3, which reproduces a CFD prediction reported by McGovern and Leylek [7]. Conversely, a high internal crossflow velocity (in the same direction as the mainstream) leads to separation on the upstream side of the hole inlet and the flow exits from the downstream portion of the hole. Common sense dictates that this is to be expected, and, furthermore, that the effect abates as the hole length increases and the inlet separation is mixed out. It should also be appreciated that the existence of nonuniform exit velocity profiles is long established: Bergeles et al. [8] reported on the velocity profile at exit from a normal (90 deg) hole with external crossflow. The authors concluded that ''the velocity of ejection is substantially nonuniform . . . for $M_m=0.24$ only 25% of the injectant leaves from the leading half of the hole.''

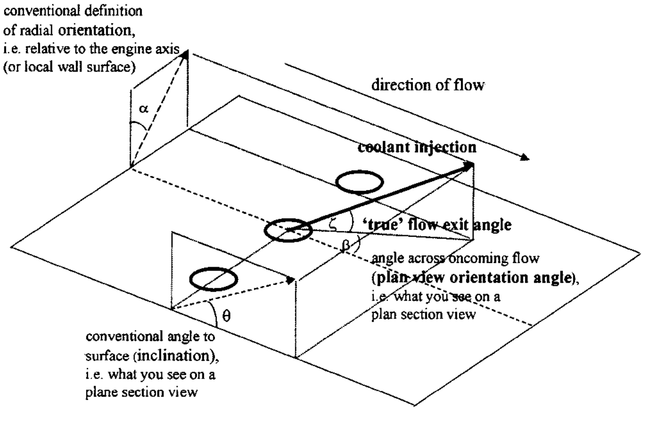

Fig. 2 Definition of film cooling hole flow angles

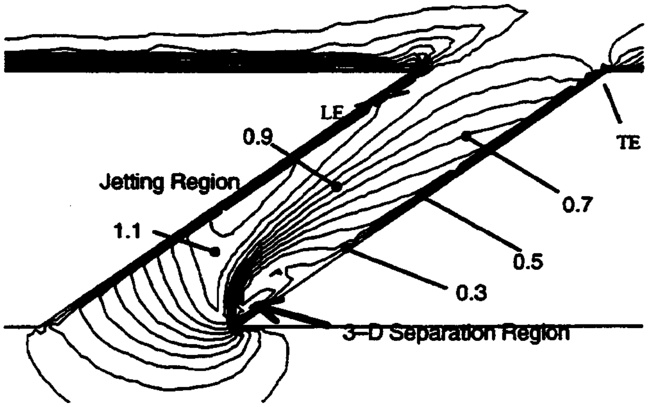

Fig. 3 Illustration of inlet separation and coolant "jetting," as highlighted by the velocity ration, u_h/u_m, contours for flow through a 35 deg inclined hole, at zero orientation and a blowing ratio of 1.25 [7]

Burd and Simon [9] conducted a similar study, relating exit plane velocity distributions to the supply plenum geometry (i.e., orientation of the crossflow on the coolant side) and hole l/d ratios. They report how short holes exhibit a prominent ''jetting'' of the coolant, characterized by higher effective velocities in the upstream portion of the hole, as well as concluding that ''the free stream significantly induces the flow.'' This work is further reported in their paper of the following year ([10]; see below).

Walters and Leylek [11] present the results of a computational simulation of the flowfield associated with streamwise injection through a cylindrical film cooling hole. They state how the jetting region, highlighted by Thole et al. [6] and Burd and Simon [9], and counterrotating flow within the film hole are a consequence of separation and flow turning near the hole inlet (Fig. 3). They proceed to discuss how the velocity distribution at hole exit is influenced by two competing mechanisms. Although the jetting/counterrotating flow leads to higher momentum coolant fluid in the portion of the hole opposite the separation, the impingement of the oncoming (free-stream) crossflow on the emerging jet leads to a high-pressure zone upstream of the jet leading edge and a low-pressure region downstream of the jet trailing edge, with the effect of increasing the jet momentum in the downstream portion of the hole. This alteration of the static pressure distribution around the hole (Fig. 4) is important, and will be revisited. Walters and Leylek [11] conclude that the relative influence of the two mechanisms depends on the blowing ratio, density ratio, and hole geometry, or, in the case of their study, l/d and B. They consider the influence of blowing ratio for the case of separation at inlet on the downstream side of the hole, stating that at low blowing ratios, the jet–crossflow interaction dominates, so flow exits from the downstream portion of the hole (Fig. 4(b)), while at high blowing ratios the flow structure within the hole dominates

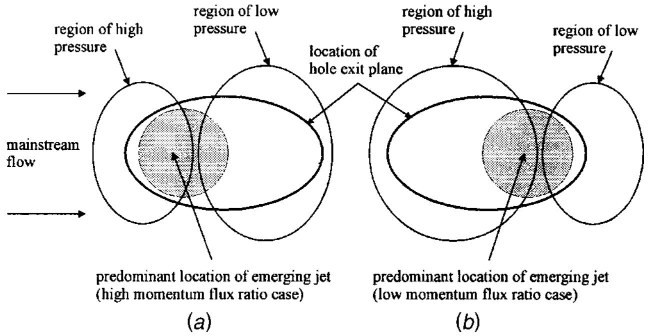

Fig. 4 Illustration of how the location of the emerging jet influences the magnitude of the local pressure: (*a*) coolant emerging from the upstream portion of the hole; (*b*) coolant emerging from downstream portion of the hole

and the flow is more likely to exit from the upstream portion (Fig. 4(a)). As the length-to-diameter ratio, l/d, decreases, the effects of the separation region have less time to attenuate, and therefore exert a greater influence on the exit conditions, so the flow exits from the upstream portion of the hole.

This analysis has been supported by measurements reported by Burd and Simon [10], who emphasize the strong influence that the coolant distribution at the exit plane has over the hole C_d. They present C_d measurement in terms of the external or outlet additive loss coefficient, δ_{out}, defined as:

$$\delta_{\text{out}}=\frac{[(p_{0c}-p_m)^{\text{with}}_{\text{crossflow}}-(p_{0c}-p_m)^{\text{without}}_{\text{crossflow}}]_{\rho_h u_h}}{0.5\rho_h u_h^2} \tag{1}$$

They conclude that the supply plenum geometry (i.e., orientation of the crossflow on the coolant side) and hole l/d have a significant impact on δ_{out} values. Furthermore, negative δ_{out} values (i.e., flow enhancement with external crossflow) are obtained. Burd and Simon [10] explained this in terms of the static pressure distribution around the emerging jet. Outlet loss coefficients are reduced in situations where more coolant is distributed in the upstream portion of the hole exit plane (e.g., short holes). As already mentioned, static pressures upstream of the jet–mainstream boundary are higher than in the absence of the jet, while those downstream of the emerging jet are lower, as illustrated in Fig. 4. As Burd and Simon [10] point out, this situation is analogous to a cylinder in crossflow, for which high pressures are found in the stagnation region and low pressures are encountered downstream, in the cylinder wake. The low-pressure region is responsible for the increase in coolant mass flow from that portion of the hole. As the balance of the coolant distribution shifts towards the downstream portion of the hole (Fig. 4(b)), the high-pressure region also shifts downstream, reducing the size of the low-pressure region covering the hole exit plane, and resulting in a higher effective static pressure at the hole exit. Consequently, configurations with more coolant exiting from the downstream portion of the hole (e.g., long holes) have higher δ_{out} values and lower discharge coefficients.

The work of Thole et al. [6], Walters and Leylek [11], and Burd and Simon [9,10] supports the hypothesis of Rowbury et al. [1]. Their speculation that the enhancement in C_d by the presence of external flow results from a reduction in static pressure at the hole exit, due to a local acceleration of the mainstream flow, is largely substantiated. This acceleration is caused by blockage of the mainstream path by the exiting coolant flow, and results, effectively, in additional ''suction'' on the coolant. This model would imply that the extent of the crossover would be greater for steeper inclination angles (i.e., $\theta\sim 90$ deg) and larger angles of orientation ($\alpha\sim 60$ deg), as discovered by Burd and Simon [9] for lateral injection as compared to streamwise injection. Furthermore, the hypothesis that the extent of the enhancement, or otherwise, is dependent on the external crossflow Mach number (in effect, the blowing ratio) is also validated.

Large-Scale Test Facility

In an attempt to understand the physical basis for the enhancement in C_d with external crossflow, a series of experiments were devised that investigated the variation in static pressure around the exit of ''large-scale'' film cooling holes under different flow conditions. The study centered on holes whose geometries were based on those found in the leading edge region of a present day High-Pressure Nozzle Guide Vane, as reproduced and investigated in the CHTT. Holes in this region of the vane were modeled because the crossover phenomenon is witnessed for these rows.

The investigation involved the measurement of two (interlinked) flow parameters. First, the static pressure distribution around the exits of ''normal'' (i.e., 9 deg angle of inclination, θ, and 0 deg angle of orientation, α; see Fig. 2) and ''leading edge'' holes (i.e., modeled on engine vane leading edge holes) was measured and compared to the static pressures measured at the same locations for the solid body (i.e., in the absence of coolant flow). At the same time, the discharge coefficients of the film cooling holes were measured, using the static pressure measured both with and without coolant flow present to calculate the ideal mass flow rate of coolant. The working hypothesis is that the apparent discharge coefficients would increase as the static pressure at hole exit fell relative to the assumed value.

Design Details: Rig Parameters. The leading edge region of a NGV can be modeled as a cylindrical test section, since, at any location, the vane exterior can be considered as a curved surface with a particular radius of curvature. As the cylinder successfully models this, the choice of cooling hole geometries is free to be matched to engine values. If a method of accurately controlling the coolant flow can be achieved, chosen CHTT coolant flow parameters can then also be reproduced.

The flow over the cylinder exterior, equivalent to the CHTT mainstream flow, was produced by placing the cylinder in a low-speed wind tunnel. The wind tunnel chosen to house these experiments can provide air speeds in the range $\sim 5-25\ \text{m s}^{-1}$, and is approximately 480×510 mm in cross section. It was decided to manufacture the working section (i.e., containing the holes) from four 50-mm-thick Perspex disks, the length of the cylinder being made up by aluminum tubing. The availability of aluminum tubing of outer diameter 140 mm (giving a blockage ratio of 0.28, which is reasonable) set the cylinder diameter, which, in turn, sets the tunnel velocity for matching to CHTT conditions; matching Re (based on the vane showerhead diameter, *D*) gives:

$$\left(\frac{\rho u D}{\mu}\right)_{\text{cylinder}}=\left(\frac{\rho u D}{\mu}\right)_{\text{CHTT}} \tag{2}$$

As ambient temperature air is the mainstream gas for both cases, $\mu\sim$const and $\rho_{\text{CHTT}}/\rho_{\text{cylinder}}\sim 2$ (the CHTT total pressure is roughly twice that in the wind tunnel), giving:

$$(uD)_{\text{cylinder}}=2(uD)_{\text{CHTT}} \tag{3}$$

The radius of curvature of the CHTT vane showerhead is $\sim$6.5 mm and the mean mainstream velocity at the leading edge plane is $\sim 35\ \text{m s}^{-1}$, so the design tunnel velocity for matching is:

$$u_{\text{tunnel}}\sim 2(35)(13/140)=6.5\ \ \text{ms}^{-1}$$

The crossover phenomenon has been witnessed on Rows 5–10 of the CHTT vanes (Fig. 1). It was decided to model Rows 7 and 8, as these provide very clear examples of the phenomenon.

Design Details: Hole Geometries. Since the CHTT vanes are scale replicas of those currently operating in a modern aero-engine, the geometries of Rows 7 and 8 are complex, as illustrated in Table 1.

Table 1 Geometries of rows 7 and 8 on the CHTT aerofoil (i.e., 1.4 × engine scale)

Row No.	Diameter of holes, d (mm)	Hole pitch, s (mm)	Angle of Inclination θ	Angle of Orientation α	Length-to-Diameter Ratio (l/d)	Design MFR, I_{design}
7	1.035	2.491	89.99°	60°	6.09	20.5
8	1.035	2.491	88.79°	60°	6.09	5.40

It is worth discussing the scaling of the CHTT vane parameters to the cylindrical model. The inclination, θ, and orientation, α, angles (Fig. 2) for the model were chosen to be 90 and 60 deg, respectively. Matching the ratio of wall thickness-to-showerhead diameter, t/D, gives:

$$t_{\text{cylinder}}=(140/13)3.150\sim 34.0 \text{ mm} \tag{5}$$

Matching the hole length-to-diameter ratio, l/d, is then equivalent to matching t/D, t/d, or d/D, giving:

$$d_{\text{cylinder}}=(140/13)1.035\sim 11.1 \text{ mm} \tag{6}$$

and matching the hole pitch-to-diameter ratio, s/d, is equivalent to matching s/D, giving:

$$s_{\text{cylinder}}=(140/13)2.491\sim 26.8 \text{ mm} \tag{7}$$

Alternatively, a hole diameter d mm would result in a pitch of $(2.491/1.035)d\sim 2.41d$ mm, and a surface spacing of $\sim 4.82d$ mm, due to the holes being orientated at 60 deg to the cylinder surface. Hence, taking a cylinder wall thickness of 35 mm, the maximum hole diameter that allowed three holes to fit into the Perspex section was 11.3 mm. For ease of manufacture, it was decided to set $d=10.5$ mm (model $d/D\sim 0.075$; engine $d/D\sim 0.080$), $t=35$ mm (model $l/d\sim 6.67$; engine $l/d\sim 6.09$), and surface spacing at 50 mm (model $s/d\sim 2.38$; engine $s/d\sim 2.41$). Given the close match on hole angles (model $\theta=90$ deg and $\alpha=60$ deg, engine $\theta=90$ deg and $\alpha=60$ deg), it can be seen that the model geometry closely represents that of the holes in the leading edge region of an engine vane.

In addition to those engine representative, ''leading edge'' (i.e., ''angled'') holes, a set of three ''normal'' holes (i.e., 90 deg inclination, θ, and 0 deg orientation, α; see Fig. 2) were drilled through the Perspex in order to provide a comparison data set. Eight static pressure tappings were located, at 45 deg intervals, 2 mm from the edge of the center hole of each set of three. It was assumed that these tappings would give a good indication of how the emerging coolant jet, and its interaction with the free-stream flow, would influence the static pressure around the cooling hole, compared to the pressure expected from the distribution around the noncooled cylinder. The tapping positions, relative to the hole outlets, are illustrated in Fig. 5, while Fig. 6 shows a close-up view of the exit from a leading edge hole.

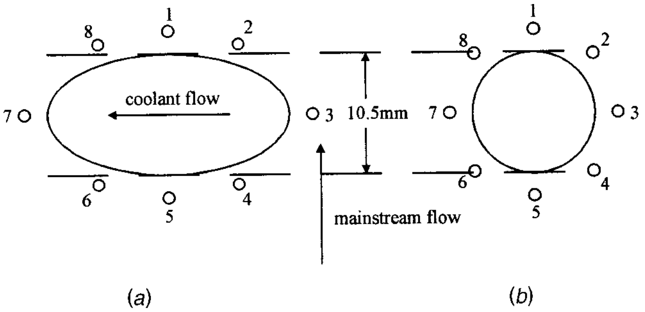

(*a*) (*b*)

Fig. 5 Pressure tapping locations around: (*a*) "leading edge," and (*b*) "normal" film cooling hole outlets. Numbering is to aid presentation of results.

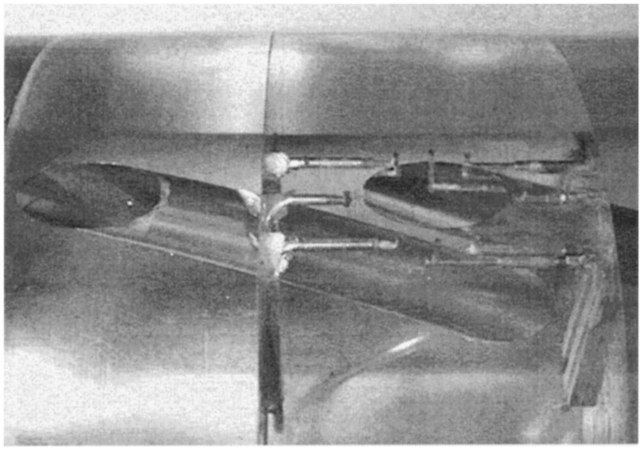

Fig. 6 Close-up view of large-scale leading edge holes, illustrating the static pressure tapping locations

Experimental Technique: Flow Measurement. The discharge coefficient of a film cooling hole is defined as the ratio of the measured (i.e., actual) to the ideal mass flow rate of coolant, $\dot{m}_{\text{actual}}/\dot{m}_{\text{ideal}}$. The actual mass flow rate was measured using British Standard orifice plates [12]. Furthermore, if the static pressure at the exit from the holes, p_m, and the cavity (upstream) total pressure and temperature, p_{0c} and T_{0c}, are known, then the isentropic flow equations can be used to determine the ideal mass flow rate, namely:

$$\dot{m}_{\text{ideal}}=A\left(\frac{p_m}{p_{0c}}\right)^{1/\gamma}\cdot\frac{p_{oc}}{\sqrt{RT_{oc}}}\cdot\sqrt{\frac{2\gamma}{\gamma-1}\cdot\left[1-\left(\frac{p_m}{p_{0c}}\right)^{(\gamma-1)/\gamma}\right]} \tag{8}$$

for unchocked flow [13], which was always the case in these experiments.

In this way, the cooling hole C_d could be measured without external crossflow, for both the leading-edge and normal holes, and compared to the C_d with external crossflow present. With external crossflow present, the C_d was measured for various angular positions of the holes (measured relative to the cylinder leading edge) and different momentum flux ratios.

In addition to the cooling hole C_d, the static pressures around the hole exit were also measured during each test. It was hypothesized that the C_d would increase as the static pressure measured on the solid cylinder surface at the pressure tapping location.

Static Pressure Measurement. All required pressures were measured on Sensor Technics pressure transducers, and voltage outputs transferred directly to computer. Due to the low-speed nature of the work, pressure changes were generally quite small, the exception being in the pressures associated with the British Standard orifice plate. The transducers used for the low-pressure measurements were 0–50 mbar transducers from the HCXM range (HCXM050D6V), while the larger pressures were measured using either 0–5 or 0–15 psi transducers from the PTE5000 range (either PTE5005D1A or PTE5015D1A). Pressures were measured differentially, where possible, to improve accuracy.

The static pressure around the solid cylinder (i.e., with no coolant flow) was measured and converted to a pressure coefficient. Consequently, by measuring the tunnel total pressure and tunnel velocity, the pressure coefficient could then be used to determine the ''expected'' static pressure variation around the cylinder. Comparison with the measured values at each of the tapping locations (Fig. 5) around the film cooling holes would then provide some indication of whether the static pressure at the outlet from the cooling hole was decreased by the presence of the coolant. The results from these experiments are reported in the next section.

Experimental Results

Pressure Distribution Around a Cylinder. The variation in static pressure around the noncooled, ‘‘solid’’ cylinder was measured by means of a single static pressure tapping, by rotating the cylinder. The pressures were converted to a nondimensional pressure coefficient,

$$C_p=\frac{p_s-p_m}{p_{0m}-p_m}=\frac{p_s-p_m}{0.5\rho u^2},$$

where p_s is the static pressure on the cylinder surface, and u, p_{0m}, and p_m, are the free-stream velocity and total and static pressures upstream of the cylinder. This provides a means of obtaining the expected static pressure at any location on the cylinder surface from the tunnel total and static pressures (or total pressure and velocity). In turn, this provides a comparison to the static pressures measured around the film cooling hole exits. The pressure distribution around the cylinder was measured for two tunnel velocities: 5.25 m s^{-1} and 24.7 m s^{-1}. These tunnel velocities result in momentum flux ratios of 67.5 and 2.5, respectively, for the ‘‘leading edge’’ hole, which, although high, bound typical I values of leading edge rows (Table 1). The corresponding pressure coefficients are presented in Fig. 7. As expected [14], the viscous action causes the flow to separate from the downstream surface of the cylinder and form a wake in which the pressure variation differs from the inviscid prediction. The good agreement with the ‘‘experimental’’ case illustrated in Massey (p. 331)—both in terms of the point of deviation from the theoretical and in the magnitude of C_p—provides evidence that the tunnel is working well and is suitable for this series of experiments (hole positions up to 70 deg from the stagnation point). In order to minimize pressure fluctuations around the cylinder due to the instability of the wake region, a tailboard was attached on the downstream portion of the cylinder. Measurements demonstrated that its presence did not affect C_d in the region of interest (i.e., hole positions up to 70 deg from the stagnation point; see Fig. 7).

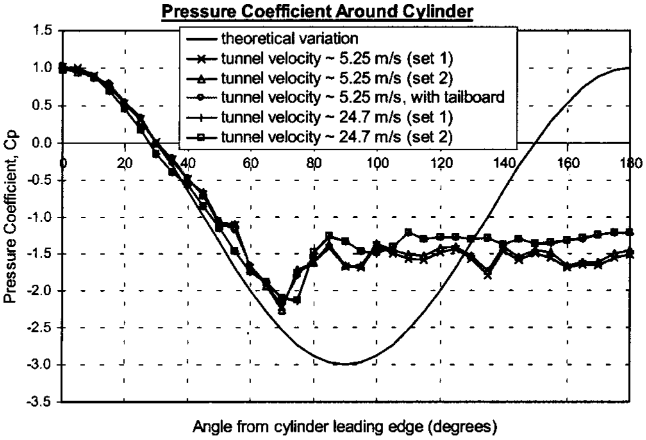

Fig. 7 Pressure coefficient, $C_p=(p_s-p_m)/(p_{0m}-p_m)=(p_s-p_m)/0.5\rho\mu^2$, around the cylinder surface for two different tunnel velocities (or Reynolds numbers). The inviscid prediction is shown for comparison.

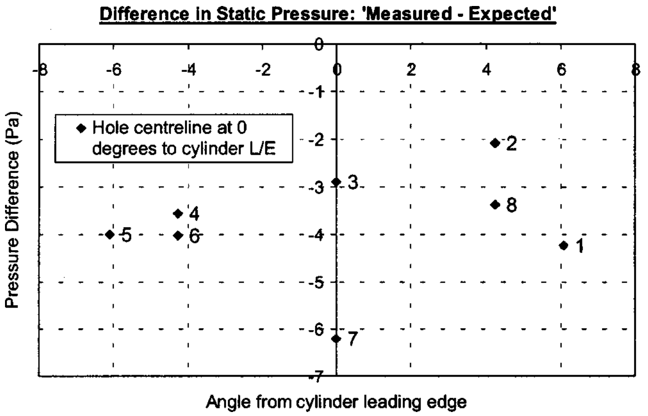

Fig. 8 Static pressure around a normal hole, with no external crossflow, measured relative to atmospheric pressure. As in all subsequent figures, numbering refers to Fig. 5.

Pressure Distribution Around Film Cooling Holes. The static pressure was measured at eight locations (Fig. 5) around the exit of both ‘‘normal’’ and ‘‘leading edge’’ film cooling holes. Measurements were made both with and without external crossflow, and, for the with-crossflow case, for different momentum flux ratios,

$$I=\frac{\rho_h u_h^2}{\rho_m u_m^2}$$

as opposed to blowing rates,

$$B=\frac{\rho_h u_h}{\rho_m u_m}$$

Results presented in this section illustrate the difference between the measured static pressure and the expected static pressure. The expected static pressure was atmospheric pressure for the non-crossflow tests, and the pressure calculated from the pressure coefficient (see ‘‘Static Pressure Measurement’’ section and Fig. 7) for the with-crossflow tests. Figure 8 shows the pressure distribution around the exit of a ‘‘normal’’ film cooling hole without external crossflow present (i.e., $I=\infty$). All measured pressures are slightly lower (2–6.5 Pa) than atmospheric pressure (the expected pressure), as the emerging coolant jet disturbs the flow around the hole exit, increasing dynamic pressure and reducing static pressure.

Figure 9 gives an example of the relative pressures recorded with external crossflow present ($I=65.9$: the ‘‘high momentum flux ratio’’ case). In this case, note the relatively large discrepancy (260–430 Pa) between the measured and expected pressures (calculated from the pressure coefficient at the location of the tappings). It should be noted that the pressures on the ‘‘upstream’’ side of the hole are reduced less than those on the ‘‘downstream’’

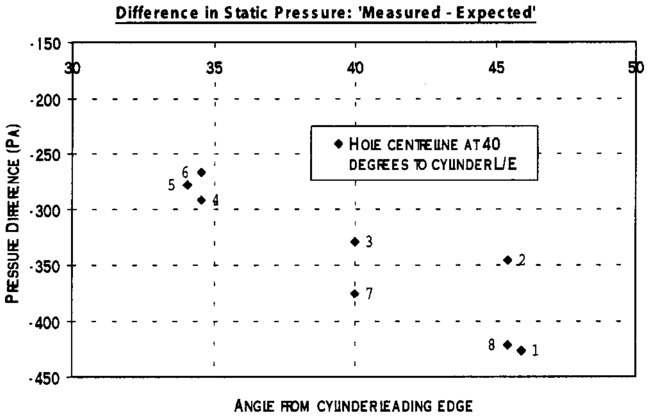

Fig. 9 Static presssure around a leading edge film cooling hole, with external crossflow ($I=65.9$), measured relative to the static pressure calculated from the pressure coefficient

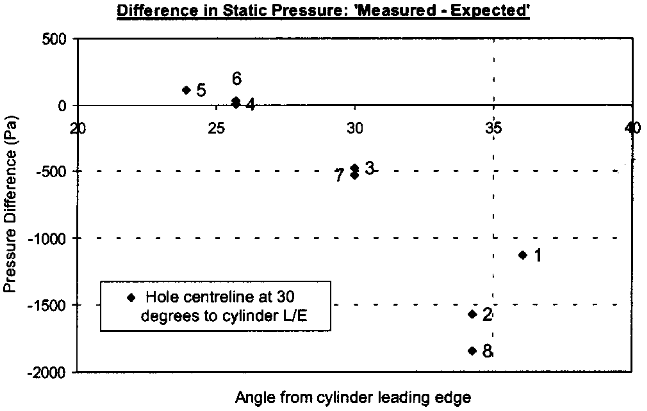

Fig. 10 Static pressure around a normal hole, with external crossflow ($I=2.78$), measured relative to the static pressure calculated from C_p

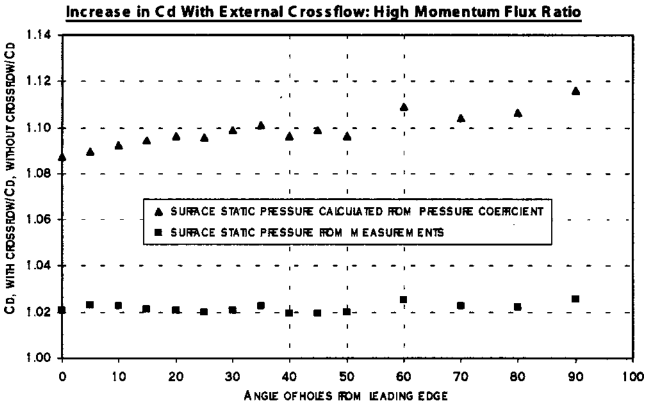

Fig. 12 $C_{d,\text{crossflow}}/C_{d,\text{no crossflow}}$ for leading edge hole, with $I\sim 67.5$, calculated using the external static pressure as either expected or "measured"

side. This can be explained by the structure of the flow around the jet emerging from a ''leading edge'' hole: The coolant jet emerge in the plane perpendicular to the free-stream flow direction, and can be regarded close to the surface as cylindrical obstacles to the main flow. The free-stream flow will, generally, be accelerated by the blockage of the jet, even on the upstream side of the hole (tappings 4, 5, and 6), and will be accelerated more as it passes between the jets (tappings 3 and 7). The lowest pressures will be in the wake region, on the downstream side of the hole (tappings 8, 1, and 2).

The static pressure at the exit of the film cooling holes is only seen to increase in two of the situations investigated in this study, both times for the tappings on the upstream side of the hole (tappings 4, 5, and 6), those being:

(*a*) the ''leading edge'' hole when positioned 60 deg from the cylinder leading edge, for the ''very low momentum flux ratio'' case (the only case of its type investigated, achieved by reducing the coolant feed pressure), and

(*b*) the ''normal'' hole when positioned 30 deg from the leading edge of the cylinder, for the ''low momentum flux ratio'' case, as presented in Fig. 10.

The average pressure ''reduction'' for the eight tappings around the ''leading edge'' hole, for the ''high momentum flux ratio'' case, is presented in Fig. 11 against angular position of the hole from the cylinder leading edge.

As part of the study, the discharge coefficients of the cooling holes were also measured. In order to calculate the discharge coefficient, C_d, of a hole, a value for the static pressure at the hole outlet is required (Eq. (8)). The C_d could therefore be calculated using either:

(*a*) the static pressure calculated from the pressure coefficient derived in the absence of film cooling (Fig. 7), which is equivalent to assuming the presence of the cooling does not affect the local static pressure, or

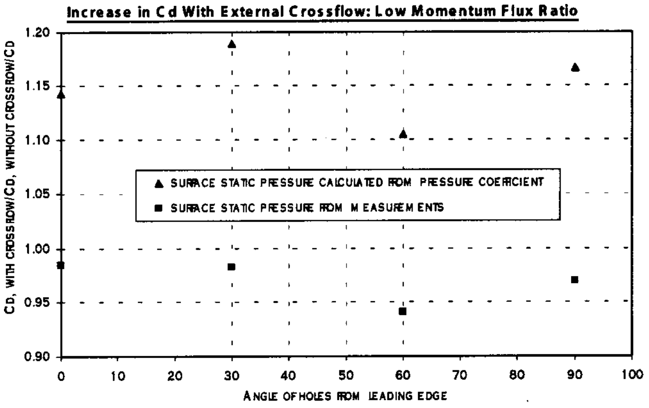

Fig. 13 $C_{d,\text{crossflow}}/C_{d,\text{no crossflow}}$ for leading edge hole, with $I\sim 2.50$, calculated using the external static pressure as either expected or "measured"

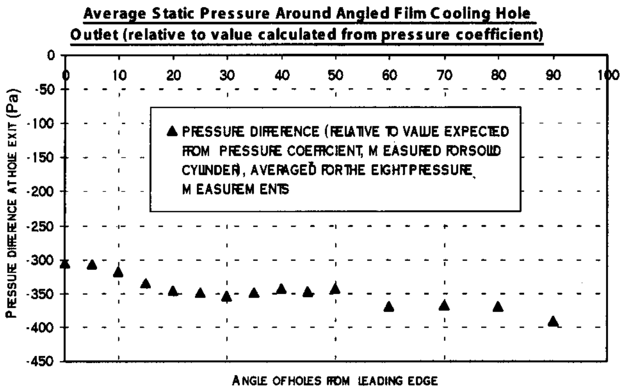

Fig. 11 Average difference in static pressure around leading edge hole, with external crossflow ($I=67.5$) versus angle from the cylinder leading edge

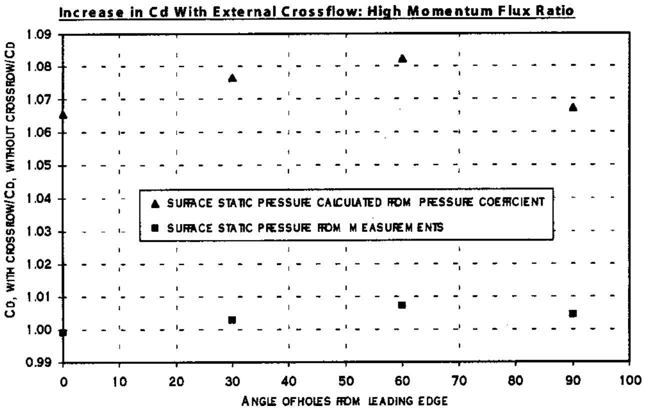

Fig. 14 $C_{d,\text{crossflow}}/C_{d,\text{no crossflow}}$ for normal hole, with $I\sim 82.0$, calculated using the external static pressure as either expected or measured

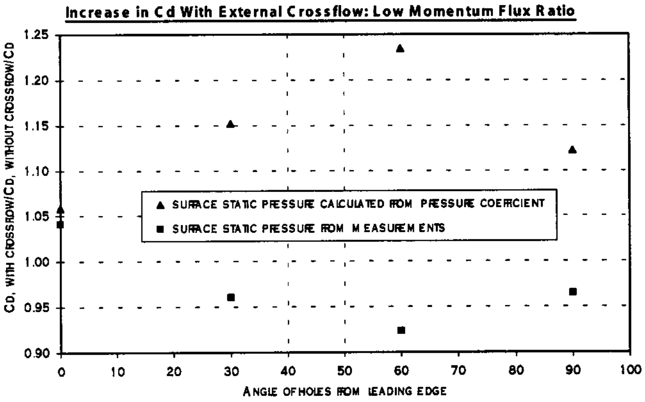

Fig. 15 $C_{d,\mathrm{crossflow}}/C_{d,\mathrm{no\ crossflow}}$ **for normal hole, with $I \sim 2.80$, calculated using the external static pressure as either expected or measured**

(*b*) the average pressure measured from the eight tappings (Fig. 11).

Consequently, the data presented in the next section consist of two data points for each specific test.

Discharge Coefficients of Film Cooling Holes. It has already been stated that this study was undertaken ''in an attempt to understand the physical basis for [the] enhancement in C_d with external crossflow.'' This was followed by the hypothesis that ''the apparent discharge coefficients would increase as the static pressure at hole exit fell relative to the assumed value.'' It has been shown that the static pressure at the hole exit falls relative to the assumed value, so is the C_d enhanced? The answer is yes. Figures 12–15 show how, when using the static pressure calculated from the pressure coefficient for the solid cylinder, the C_d is always enhanced, for both the ''leading edge'' and the ''normal'' holes. This is hardly surprising, as the leading edge region of the vane has been modeled, where an enhancement in C_d is expected. But how and why does this happen? It is important to realize that there are two opposing effects that determine whether the C_d is increased or decreased by the presence of external crossflow. First, there is the widely acknowledged ''pinching'' or ''capping'' of the emerging coolant jet by the free-stream flow, which results in a reduction in C_d. This is a well-documented effect to which Rogers and Hersh [15] proposed the ''lid model.'' However, at the same time, the emerging jet presents a blockage to the oncoming free-stream flow, causing it to accelerate (by continuity), as identified by Crabb et al. [16]. The accelerated flow has increased dynamic pressure and, consequently, *lower static pressure*, resulting in a larger pressure drop across the hole. It is therefore seen that the presence of the external crossflow increases the mass flow of coolant by increasing the pressure drop across the hole, rather than by increasing the actual discharge coefficient of the hole. In effect, the increase in C_d arises due to the incorrect value of external static pressure being used in the calculation of the ideal mass flow rate. For the data presented here, the C_d values calculated from the average of the eight static pressure tapping measurements provide a more accurate prediction of the *true* C_d.

However, it can be seen that, for the high momentum flux ratio cases (Figs. 12 and 14), the use of the measured static pressures at the hole exit does not completely eliminate the enhancement in Cd with external crossflow. This may be due to the fact that the pressure tappings are located 2 mm from the hole edge, so will not provide the exact values of static pressure at the hole exit. Furthermore, the approximation to the exit static pressure obtained by averaging just eight readings is rather crude. However, the ''reduced static pressure effect'' does not account for the majority of the apparent enhancement.

Naturally, the net effect of the free-stream flow will depend on the exact flow conditions. If the above-described theories hold true, the C_d would be expected to decrease with decreasing momentum flux ratio (as the ''capping'' effect dominates) but increase with increasing blockage presented by the jet to the oncoming flow (i.e., with increasing inclination and orientation angles). This is certainly born out by the data collected here and on the CHTT vanes.

Uncertainty Analysis. Within the study, the main source of uncertainty is the inaccurate measurement of the recorded pressures. The uncertainty on the free-stream pressure is greatest at low tunnel speeds (Fig. 7), while the largest error in coolant total pressure occurs for low momentum flux ratios, especially with the cooling holes near the leading edge (where the feed pressure is reduced in order to maintain the same I). Overall, the uncertainty in C_d due to uncertainties in measured pressure is expected to be ± 1–2 percent. The overall uncertainty in C_d is expected to be in the range ± 1.5–2.5 percent.

Conclusions

This paper has discussed an experimental program carried out to investigate the variation in static pressure around the exit of film cooling holes under different flow conditions, and the association between this pressure and the discharge coefficient of the hole. Measurements were made on large-scale ''leading edge'' and ''normal'' film cooling holes, and the results reported. The ''leading edge'' holes were modeled on those found in Rows 7 and 8 (Fig. 1) of a current aero-engine NGV. The reason for modeling these particular rows was that the crossover phenomenon is witnessed for these rows on the CHTT vanes. The investigation aimed to throw light on the physical reasons behind this enhancement in C_d with external crossflow.

The investigation involved the measurement of two (interrelated) flow parameters, namely the surface static pressures around the hole exits and the discharge coefficients of the holes. The influence of momentum flux ratio and the position of the holes on the cylinder surface relative to the cylinder leading edge were investigated. The hypothesis was that the discharge coefficients would increase as the static pressure at hole exit fell relative to the assumed value. This hypothesis has been born out by the experimental data collected and presented.

The work has highlighted the fact that the C_d of film cooling holes can be increased by the presence of external crossflow, due to a reduction in the static pressure in the vicinity of the hole exit. This is a result of the local acceleration of the oncoming free-stream flow as it diverts around the blockage caused by the emerging coolant jet.

The improved understanding of the crossover phenomenon and coolant-to-free-stream interactions will be valuable in aiding and validating the formulation of predictive discharge coefficient schemes. Consequently, this work will be of interest to aero-engine designers as it provides a mean of modifying their cooling hole C_d predictions.

Acknowledgments

This work has been carried out with support of Rolls-Royce plc, DERA, MoD, and DTI. The authors would also like to thank Professor T. V. Jones and Dr. C. R. B. Day for their help and guidance, and Mr. K. Walton and Mr. T. Godfrey for their practical assistance.

Nomenclature

A = flow area
B = coolant-to-mainstream blowing ratio $= \rho_h u_h / \rho_m u_m$
C_d = discharge coefficient $= \dot{m}_{\mathrm{actual}} / \dot{m}_{\mathrm{ideal}}$
C_p = pressure coefficient
d = hole diameter
D = cylinder (i.e., ''leading edge'') diameter
I = momentum flux ratio $= \rho_h \cdot u_h^2 / \rho_m \cdot u_m^2$

l = hole length
$\dot{m}$ = mass flow rate
M = Mach number
p = pressure
PR = pressure ratio across hole$=p_{0c}/p_m$
R = gas constant
Re = Reynolds number $=\rho u d/\mu = 4\dot{m}/\pi d\mu$
s = hole pitch
t = wall thickness
T = temperature
u = velocity
α = angle of orientation (see Fig. 2)
β = plan view orientation angle (see Fig. 2)
δ_{out} = outlet additive loss coefficient
ζ = ''true'' flow exit angle (see Fig. 2)
θ = angle of inclination (see Fig. 2)
μ = dynamic viscosity
ρ = density

Subscripts

c = coolant
h = inside the hole
m = mainstream (=free-stream)
s = cylinder surface static
0 = total

References

[1] Rowbury, D. A., Oldfield, M. L. G., and Lock, G. D., 1997, ''Engine-Representative Discharge Coefficients Measured in an Annular Nozzle Guide Vane Cascade,'' ASME Paper No. 97-GT-99.

[2] Rowbury, D. A., Oldfield, M. L. G., and Lock, G. D., 2001, ''A Method for Correlating the Influence of External Crossflow on the Discharge Coefficients of Film Cooling Holes,'' ASME J. Turbomach., **123**, pp. 258–265.

[3] Martinez-Botas, R. F., Main, A. J., Lock, G. D., and Jones, T. V., 1993, ''A Cold Heat Transfer Tunnel for Gas Turbine Research on an Annular Cascade,'' ASME Paper No. 93-GT-248.

[4] Rowbury, D. A., Oldfield, M. L. G., Lock, G. D., and Dancer, S. N., 1998, ''Scaling of Film Cooling Discharge Coefficient Measurements to Engine Conditions,'' ASME Paper No. 98-GT-79.

[5] Gritsch, M., Schulz, A., and Wittig, S., 1998, ''Discharge Coefficient Measurements of Film-Cooling Holes With Expanded Exits,'' ASME J. Turbomach., **120**, pp. 560–567.

[6] Thole, K. A., Gritsch, M., Schulz, A., and Wittig, S., 1997, ''Effect of a Crossflow at the Entrance to a Film-Cooling Hole,'' ASME J. Fluids Eng., **119**, pp. 553–541.

[7] McGovern, K. T., and Leylek, J. H., 2000, ''A Detailed Analysis of Film-Cooling Physics, Part 2: Compound-Angel Injection With Cylindrical Holes,'' ASME J. Turbomach., **122**, pp. 113–121.

[8] Bergeles, G., Gosman, A. D., and Launder, B. E., 1976, ''The Near-Field Character of a Jet Discharged Through a Wall at 90 deg to a Main Stream,'' ASME J. Heat Transfer., **98**, No. 3.

[9] Burd, S. W., and Simon, T. W., 1997, ''The Influence of Coolant Supply Geometry an Film Coolant Exit Flow and Surface Adiabatic Effectiveness,'' ASME Paper No. 97-GT-25.

[10] Burd, S. W., and Simon, T. W., 1999, ''Measurements of Discharge Coefficients in Film Cooling,'' ASME J. Turbomach., **121**, pp. 243–248.

[11] Walters, D. K., and Leylek, J. H., 2000, ''A Detailed Analysis of Film-Cooling Physics: Part 1—Streamwise Injection With Cylindrical Holes,'' ASME J. Turbomach., **122**, pp. 102–112.

[12] British Standards Institution—BS1042, 1981.

[13] Rowbury, D. A., Oldfield, M. L. G., and Lock, G. D., 1996, ''Discharge Coefficients of Nozzle Guide Vane Film Cooling Holes With Engine-Representative External Flow,'' *Proc. 1996 Symposium on Measuring Techniques for Transonic aand Supersonic Flow in Cascades and Turbomachines*, Zurich.

[14] Massey, B. S., 1989, *Mechanics of Fluids*, Van Nostrand Reinhold, United Kingdom.

[15] Rogers, T., and Hersh, A. S., 1975, ''The Effect of Grazing Flow on the Steady State Resistance of Square-Edged Orifices ,'' AIAA Paper No. 75-493.

[16] Crabb, D., Durao, D. F. G., and Whitelaw, J. H., 1981, ''A Round Hole Normal to a Crossflow,'' Trans. ASME, **103**, pp. 142–153.

Local Heat/Mass Transfer Measurement on the Effusion Plate in Impingement/Effusion Cooling Systems

Hyung Hee Cho
e-mail : hhcho@yonsei.ac.kr

Dong Ho Rhee

Yonsei University,
Department of Mechanical Engineering,
134, Shinchon-dong, Seodaemoon-gu,
Seoul 120-749, Korea

The present study is conducted to investigate the local heat/mass transfer characteristics for flow through perforated plates. A naphthalene sublimation method is employed to determine the local heat/mass transfer coefficients on the effusion plate. Two parallel perforated plates are arranged in two different configurations: staggered and shifted in one direction. The experiments are conducted for hole pitch-to-diameter ratios of 6.0, for gap distance between the perforated plates of 0.33 to 10 hole diameters, and for Reynolds numbers of 5000 to 12,000. The result shows that the high transfer region is formed at stagnation region and at the midline of the adjacent impinging jets due to secondary vortices and flow acceleration to the effusion hole. For flows through the perforated plates, the mass transfer rates on the surface of the effusion plate are about six to ten times higher than for effusion cooling alone (single perforated plate). In general, higher heat/mass transfer is obtained with smaller gap distance between two perforated plates.

[DOI: 10.1115/1.1344904]

Introduction

The thermal efficiency and specific power of gas turbine systems depend strongly on turbine inlet temperature. Inlet temperature is limited by the potential structural failure of the engine components mainly attributable to high thermal stresses and reductions in material strength due to high wall temperature. Wall temperature can be reduced by various cooling techniques including transpiration and film cooling. Transpiration materials produce uniform heat/mass transfer rates on their surface with flow through the plate. However, transpiration materials usually have weak structures and clogging problems. To reduce these problems, cooling methods with two perforated plates (impingement/effusion cooling) have been developed. In this cooling scheme, inner surfaces of hot components, such as combustor wall or blade surface, are cooled by the impingement of cooling air and outer surface contacts with hot gases are protected by effusion film cooling. This includes two flow situations: jet impingement on a plate, and effusion flow through the holes of the target plate.

The previous studies are mainly concerned with impinging jets on the solid plate without effusion. Downs and James [1], Jambunathan et al. [2], and Viskanta [3] reviewed the previous studies of jet impinging heat transfer extensively.

However, there are a few investigations of the heat transfer characteristics for effusion cooling and impingement/effusion cooling. Cho and Goldstein [4] investigated the effect of crossflow on the heat/mass transfer characteristics near an effusion hole and inside the hole, and they reported that heat/mass transfer is essentially the same with and without crossflow. Huber and Viskanta [5] examined the effect of spent air exit in the orifice plate on the local and average heat transfer for array of impinging jets. Their result shows that the interaction of adjacent impinged jets is reduced by spent air, and then the heat transfer on target plate is more enhanced.

Cho and Goldstein [6] investigated the effect of hole arrangements on local heat/mass transfer characteristics inside the effusion plate. They found that the high transfer rate is induced by strong secondary vortices and flow acceleration, and the overall transfer rate is approximately 45∼55 percent higher than that for impingement cooling alone. Hollworth and Dagan [7] and Hollworth et al. [8] measured the average and local heat transfer coefficients of arrays of turbulent air jets impinging on perforated target surfaces, and reported that arrays with staggered vents consistently yield higher heat transfer rates than do the impinging jets on the solid plates.

In the present study, two parallel perforated plates with circular holes in a square array are used to simulate the impingement/effusion cooling, and the local heat/mass transfer characteristics on the inner surface of effusion plate are investigated with the variations of gap distance, Reynolds number, and hole arrangement. To prevent hot spots and obtain better cooling performance, not only information of overall heat transfer coefficient but also its local variation is required [9]. Therefore, a naphthalene sublimation method is used to measure local heat/mass transfer coefficients around the effusion hole. This technique eliminates the conduction error inherent in heat transfer experiments. The surface boundary condition is analogous to an isothermal surface in a corresponding heat transfer problem.

The flow characteristics should be considered to understand local heat/mass transfer characteristics on the surface of effusion plate. Therefore, the present computational simulations using a commercial program (FLUENT) are accomplished to understand the flow patterns in impingement/effusion cooling.

Experimental Apparatus and Procedure

1 Experimental Apparatus

Duct and Test Plate. A schematic view of experimental apparatus is shown in Fig. 1. Cho and Goldstein [4] reported that heat/mass transfer coefficients on the inside surface of the effusion plate are the same with and without crossflow; therefore, the effect of crossflow is not considered in the present study. Room air drawn into a settling baffle passes through the perforated test plate into the plenum chamber, through an orifice plate (flow rate measuring device) and a blower, and then is discharged outside

---

Contributed by the International Gas Turbine Institute and presented at the 45th International Gas Turbine and Aeroengine Congress and Exhibition, Munich, Germany, May 8–11, 2000. Manuscript received by the International Gas Turbine Institute February 2000. Paper No. 2000-GT-252. Review Chair: D. Ballal.

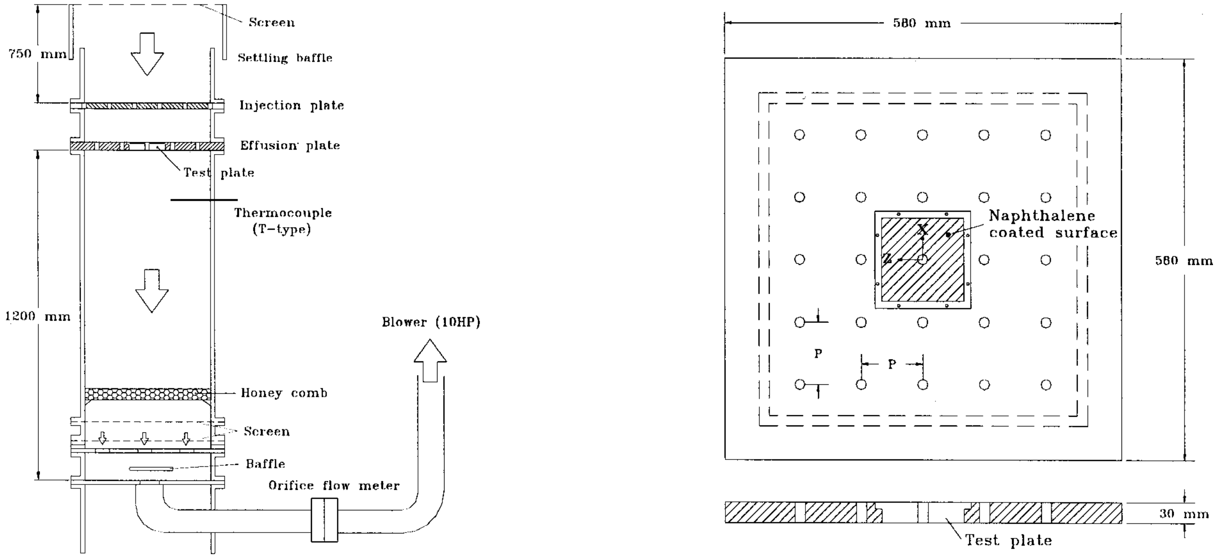

(a) Test apparatus

(b) Effusion plate

Fig. 1 Schematic diagrams of experimental apparatus and effusion plate

the building. Plenum chamber is 450 by 450 by 1200 mm, and screens and honeycombs are installed in plenum chamber for uniform suction of the flow.

Two parallel and perforated plates, which have the same hole size and square array hole pattern, are positioned with various gap distances. The gap distance between the two plates varies from $H/d=0.33$ to $H/d=10.0$, and Reynolds number of injected jet varies from $\mathrm{Re}_d=5000$ to $\mathrm{Re}_d=12{,}000$. The array of holes maintains a ratio of hole pitch-to-diameter (P/d) of 6:1 with a hole diameter of 15 mm, and the thicknesses of injection plate (t_1/d) and effusion plate (t_2/d) are 1.33 and 2.0, respectively. The effusion plate has 25 (5×5) holes and the injection plate has 25 (5×5) holes and an additional 11 holes to change hole arrangement by shifting injection plate. For local mass transfer measurements on the target surface of the second plate, a naphthalene-coated test plate is positioned at the center of the effusion plate as shown in Fig. 1(*b*). The naphthalene casting area of test plate is $8.3d\times8.3d$, and an effusion hole is located in the center of test plate.

Hole Arrangement. Two different arrangements are investigated with the two perforated plates; (1) staggered and (2) shifted in one direction. Schematic views of the hole arrangement and coordinate are presented in Fig. 2. For each arrangement, the origin of the coordinate is the center of effusion hole of the test plate. For staggered arrangement, the impinging jets from the first plate are centered among four effusion holes on the second plate. For the shifted hole arrangement, the first plate is offset a half pitch $(3d)$ in one direction, and impinging jets are positioned between two effusion holes.

2 Data Acquisition. In order to obtain local mass transfer coefficients, the profile of the naphthalene surface coated on the test plate is scanned by an automated surface measuring system before and after exposure to air flow. Sublimation depth during the run is calculated from the difference of the surface profiles. The measuring system consists of a depth gage, a linear signal conditioner (LUCAS ATA-101), a digital multimeter (Keithley model 2001), two stepping-motor driven positioners, a motor controller, and a personal computer with GPIB (IEEE-488) board. The depth gage is a Linear Variable Differential Transformer (LVDT) made by Schaevitz Engineering (LBB-375TA-020), which has a resolution of 0.025 μm. Error of the LVDT measurements on a flat plate is within 1 percent of averaged sublimation depth of 40 μm during the run. The automated system typically obtains more than 2000 data points in an hour.

3 Heat/Mass Transfer Coefficient. The local mass transfer coefficient is defined as:

$$h_m=\frac{\dot{m}}{\rho_{v,w}-\rho_{v,\infty}}=\frac{\rho_s(dy/d\tau)}{\rho_{v,w}} \tag{1}$$

Since the impinging jet flow contains no naphthalene, $\rho_{v,\infty}=0$ in

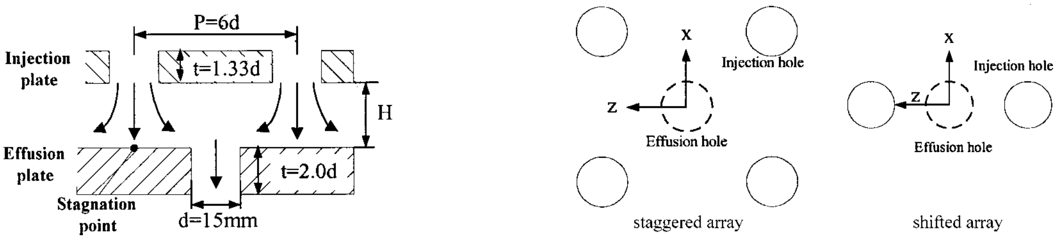

(a) Side view

(b) Top View

Fig. 2 Schematic views of hole arrangements and coordinate (hole size not to scale) the present study. Therefore, the mass transfer coefficient is calculated from the local sublimation depth of naphthalene (dy), run time $(d\tau)$, density of solid naphthalene (ρ_s), and naphthalene vapor density $(\rho_{v,w})$. The naphthalene vapor pressure is obtained from a correlation of Ambrose et al. [10]. Then the naphthalene vapor density, $\rho_{v,w}$, is calculated from the perfect gas law.

The Sherwood number can be expressed as:

$$\mathrm{Sh}=\frac{h_m d}{D_{\mathrm{saph}}} \tag{2}$$

D_{naph} is based on the discussion of naphthalene properties given by Goldstein and Cho [11].

The mass transfer coefficients can be converted to the heat transfer coefficients using the heat and mass transfer analogy [12]:

$$\frac{\mathrm{Nu}}{\mathrm{Sh}}=\left(\frac{\mathrm{Pr}}{\mathrm{Sc}}\right)^{0.4} \tag{3}$$

Uncertainty of the Sherwood numbers using Kline and McClintock's [13] method for single-sample experiments, considering the measured temperature, depth, position, and correlation equations, is within 7.1 percent in the entire operating range of the measurement, based on a 95 percent confidence interval. This uncertainty is attributed mainly to the uncertainty of properties of naphthalene, such as the naphthalene saturated vapor pressure (3.8 percent), and diffusion coefficient of naphthalene vapor in the air (5.1 percent). However, uncertainty due to the sublimation depth measurement is only 0.7 percent. The other uncertainties are 0.2, 1.1, and 4.9 percent for T_w, ρ_s, and h_m, respectively.

4 Flow Visualization. Smoke-wire flow visualization is conducted to study the flow patterns of injected jet. Two fine Nichrome wires (0.1 mm in diameter) are installed at the centerline of injection holes near the surface of injection and effusion plates. Before each test the wire is painted with gear oil resulting in small droplets of oil distributed evenly on the wire. White smoke filament lines (streaklines) are produced by evaporation of droplets with a proper electric power supply (about 60 V). The visualized flow patterns are obtained by using a video camera connected to image processing board (MIL-Lite Matrox II board) in the PC. The injected jet has a very low Reynolds number of 300 for the smoke visualization to obtain clear flow patterns between two plates.

Numerical Analysis

The numerical simulations using a commercial program (FLUENT) are accomplished to understand the flow patterns in impingement/effusion cooling. Figure 3 shows the computation domain, which is modeled by the geometry used in the experimental study. The symmetry boundary conditions for one cell of impingement/effusion cooling are imposed to reduce grid size and calculation time. The computation domain grids are created using the GAMBIT solid modeling, and the number of grids is about 40×60×70. Different grids are used to verify the grid independence of the solution at Reynolds number of 10,000. The steady solutions for turbulent flow field in an impingement/effusion cooling system are calculated using a Reynolds Stress Model with a standard wall function for a near-wall region. The flow characteristics with the variations of gap height and hole arrangement are investigated in the present numerical simulation.

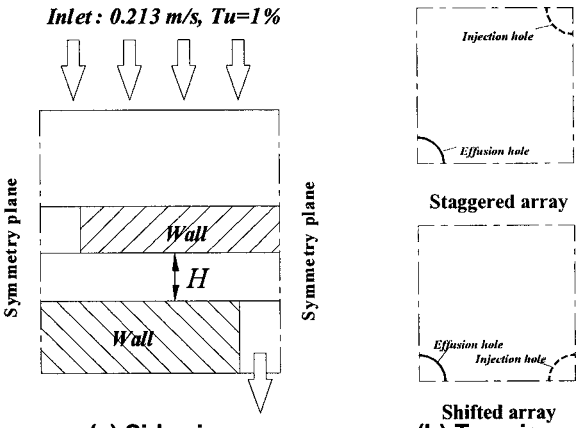

(a) Side view (b) Top view

Fig. 3 Geometry and boundary conditions in numerical calculation

Results and Discussion

In this study, flow patterns and heat/mass transfer characteristics are investigated with the variations of gap distance, Reynolds number, and hole arrangement. Test parameters are described in Table 1.

Figure 4 shows the contour and local plots of the Sherwood number for a single layer, which means that only the effusion plate is installed. The small half circle in the contour plot is the effusion hole with the aluminum rim between two circles. As flow approaches the effusion hole, flow is accelerated, and a high transfer region is formed symmetrically near the effusion hole. This high transfer region has a diamond shape due to the effect of adjacent effusion holes.

1 Effect of Gap Distance Variation

Numerical Simulation. The velocity fields at selected planes $(z/d=-3.0,\ -1.5$ and $0.0)$ for $H/d=0.33$ and 1.0 are shown in Fig. 5. The coordinates used in numerical computation are the same as those used in the experiment.

The incoming flow separates at the sharp edge of the injection hole, and reattaches at about 0.6d from the hole inlet. These results are consistent with the experimental results by Cho and Goldstein [4]. Reattachment length is independent of gap distance, and the size of a separation bubble is small because of the low incoming flow velocity. Therefore, the uniform flow is injected on the target surface for each case.

Table 1 Test parameters

Hole arrangement		H/d	Re_d
Single layer		-	10,000
Double layer	Staggered array	0.33*, 1.0*, 2.0, 6.0*, 10.0	5,000 10,000* 12,000
	Shifted array	1.0*	10,000*

(* : numerical simulation)

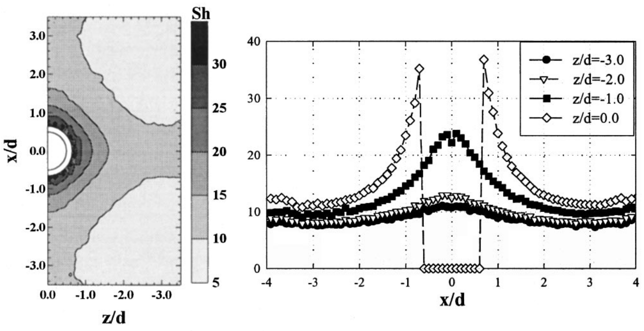

(a) Contour plot (b) Local distribution

Fig. 4 Sherwood number for single layer at Re_d=10,000

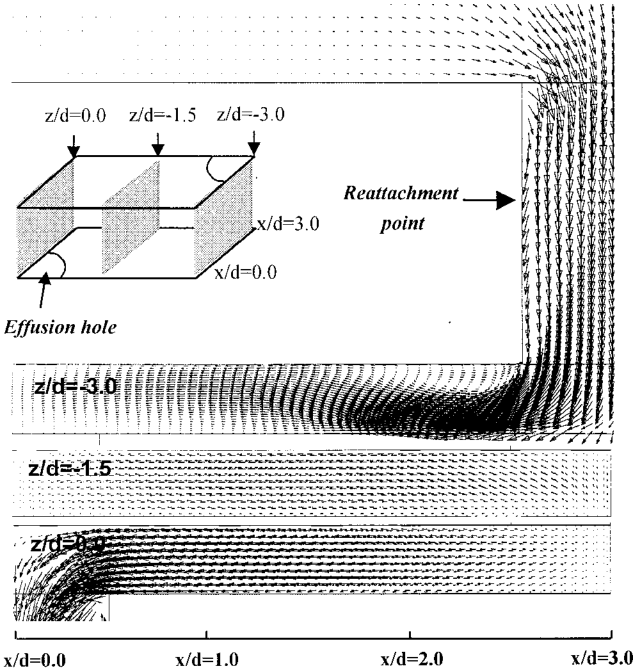

(a) H/d=0.33

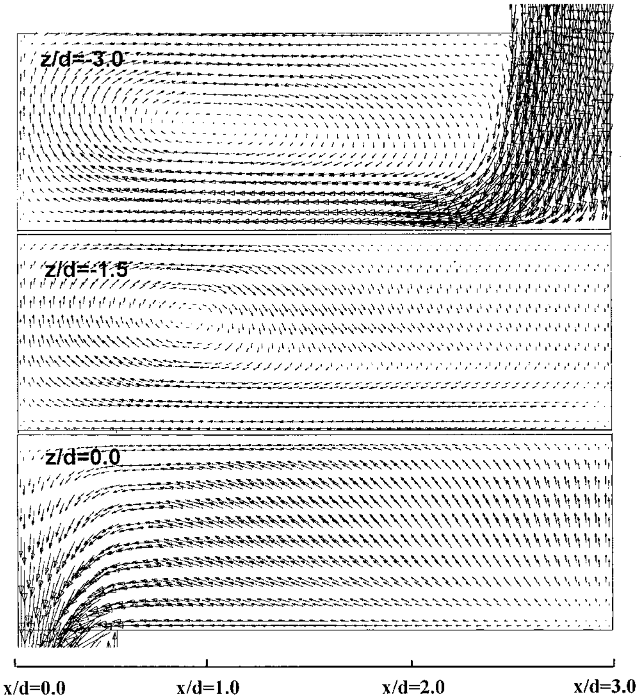

(b) H/d=1.0

Fig. 5 Velocity vectors at selected planes for staggered array at Re_d=10,000

For $H/d=0.33$, a small recirculation region is observed near the exit of injection hole at the inlet plane ($z/d=-3.0$) due to the entrainment of ambient fluid. As flow goes, most of the space between two plates is filled up with wall jets and the flow pattern is similar to a duct flow because of the extremely small gap distance. Therefore, uniform velocity distributions are obtained at the midplane ($z/d=-1.5$) and the exit plane ($z/d=0.0$), and the interaction between the adjacent wall jets is expected to be very weak due to the confined space.

For $H/d=1.0$, a large scale vortex (primary vortex) is formed at the inlet plane due to the interaction between adjacent wall jets and entrainment, and consequently a strong upward flow pattern is shown at $x/d=0.0$. It can be inferred from these results that the secondary counter vortices are generated between the upward flow; however, it is difficult to observe the existence of the secondary vortices in Fig. 5(b) due to the limitation of grid size. The existence of secondary vortex is shown apparently in experimental results, which is presented later.

Although the results are not shown in this paper, the flow patterns for $H/d=6.0$ are nearly the same as those for $H/d=1.0$. However, the center of primary vortex moves upward from the surface for $H/d=6.0$ due to large gap distance.

Local Heat/Mass Transfer Measurement. Figure 6 shows the contour plots of Sh for different gap distances ($H/d=0.33\sim10.0$) with staggered array. The white dotted circles represent the injection holes projected on the target plate. The pattern of local Sh is similar for all cases and shows good symmetry at $z/d=0.0$, and the distributions of Sh around the impinging jets have the same trend as those of single impinging jet due to the large hole-to-hole pitch ($P/d=6$). The Sh values are high around the stagnation points ($z/d=-3.0$ and $x/d=\pm3.0$) and decrease as the wall jet boundary layer is developed after impingement.

With small H/d (0.33 and 1.0), there are two peaks in the Sherwood number near the stagnation region. The inner peak, which is $0.5d$ apart from stagnation point, is caused by the effect of stagnation flow acceleration, which makes the boundary layer thin. The mass transfer decreases after this peak due to developing of the boundary layer from decelerating flow. Beyond this region, the boundary layer is transition to turbulence and the local heat/mass transfer coefficient reaches a secondary maximum value at the region that is $1.5d$ apart from the stagnation point. This phenomenon is also referred as the rolling vortex and the secondary vortex induced by unsteady flow separation, which is initiated by the unsteady adverse pressure gradient produced by the main rolling vortex [14]. The vortices on the wall disturb the boundary layer flow and entrain the ambient fluid into the boundary layer. These two peak values increase with small gap distance.

However, with large H/d ($\geqslant 2$), turbulence intensity of the jet core increases. Therefore, the heat/mass transfer in the stagnation region is higher than the previous case, but the secondary peak value decreases. It is thought that the strength of the secondary vortex is weakened due to the large nozzle-to-plate distance and the decelerating velocity effect is much stronger than the flow transition. At $H/d=6.0$, the heat/mass transfer coefficient of the stagnation region reaches a maximum value because the jet potential core remains until this distance with a maximum turbulence intensity. However, the secondary peak disappears and the heat/mass transfer decreases monotonically. This might be because the wall jet is already transitioning to a turbulent flow from the stagnation region.

For moderate gap distances ($H/d=1.0\sim6.0$), additional peak values of Sh are observed along the midline ($z/d=0.0$ and $x/d=0.0$) because the secondary vortices impinge on the midline, and then accelerate to the effusion hole [6]. For $H/d=0.33$, the overall heat/mass transfer rate is higher than that for other cases; however, as expected in the numerical results, the peak Sh values at the middle region by the secondary vortices is not clearly observed.

Local Sh distributions at $z/d=-3.0$ (along the stagnation line) and at $z/d=0.0$ are shown in Fig. 7. The solid black circle represents Sh values for the single layer. In Fig. 7(a), as mentioned before, there are two peak values at $x/d=\pm3.0$ and $x/d\cong\pm1.5$ with small gap distance, and these peak values show the maximum for $H/d=0.33$. Sh values show uniform distributions along the midway (Fig. 7(*b*)), and these values are almost the same for moderate gap distances due to the interaction and flow accelera-

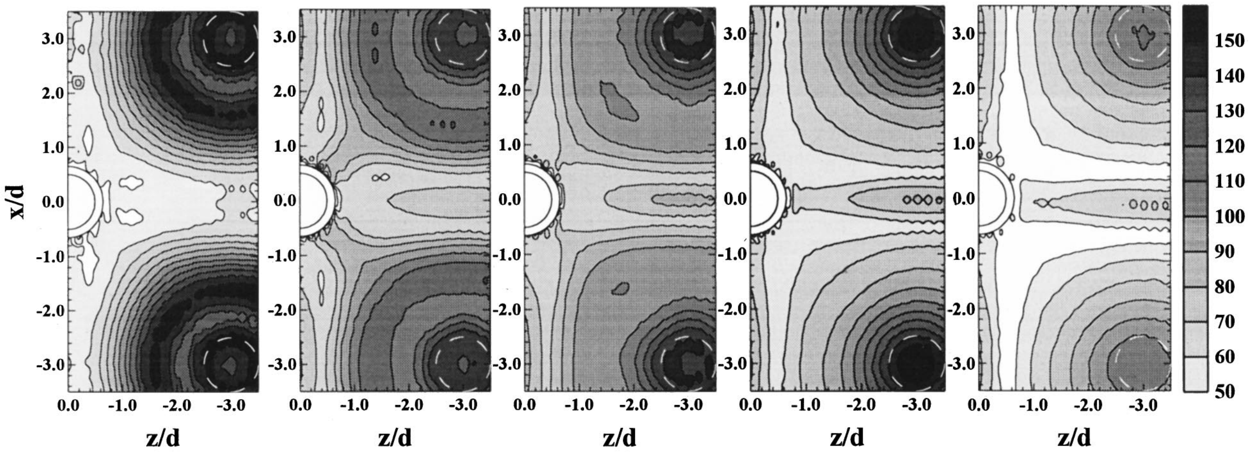

(a) H/d=0.33 (b) H/d=1.0 (c) H/d=2.0 (d) H/d=6.0 (e) H/d=10.0

Fig. 6 Contour plots of Sh for various gap distances with staggered array

tion. However, mass transfer rates for $H/d=0.33$ are about 25 percent lower than those for other cases due to the weak interaction between wall jets.

Figure 8 shows the local Nu distributions obtained by a heat/mass transfer analogy of the present study and other single jet result [15] for $H/d=2.0$ and $\mathrm{Re}_d=10{,}000$. In spite of some differences in experimental conditions, there is a favorable agreement on the results. However, the result in the present study, in contrast with the single jet results, shows the lower values at $x/d \cong -0.5$ and the additional peak at $x/d=0.0$ due to the interaction of the adjacent wall jets. The expected flow pattern is drawn schematically in Fig. 9. This interaction is shown clearly in smoke-wire flow visualization (Fig. 15).

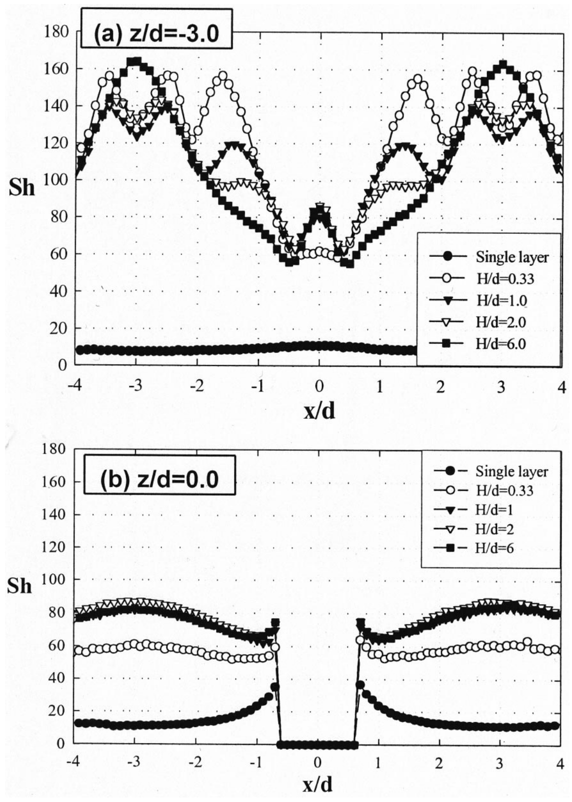

Fig. 7 Local Sh for various gap distances with staggered array

Table 2 shows the average Sherwood numbers for different gap distances. The averaged values are obtained by numerical integration in the region of $-3.0 \leqslant x/d \leqslant 3.0$ and $-3.0 \leqslant z/d \leqslant 0.0$. As expected in Figs. 4 and 6, the averaged values are 6~10 times higher than that for the single layer. $\overline{\mathrm{Sh}}$ shows the maximum value at $H/d=0.33$ and decreases with increasing gap distance. Although $\overline{\mathrm{Sh}}$ shows the highest value for $H/d=0.33$, the slope of local Sh distribution is very steep. Therefore, impingement/effusion cooling with extremely small gap distance is not recommended from a view point of thermal stresses.

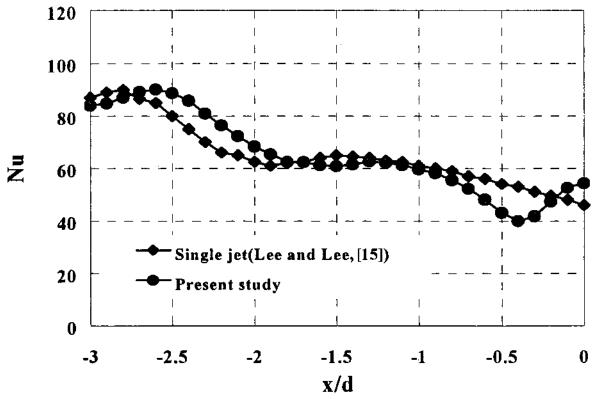

Fig. 8 Comparison of local Nu for impinging jet with other results for *H/d*=2.0 and Re$_d$=10,000 along *z/d*=0.0

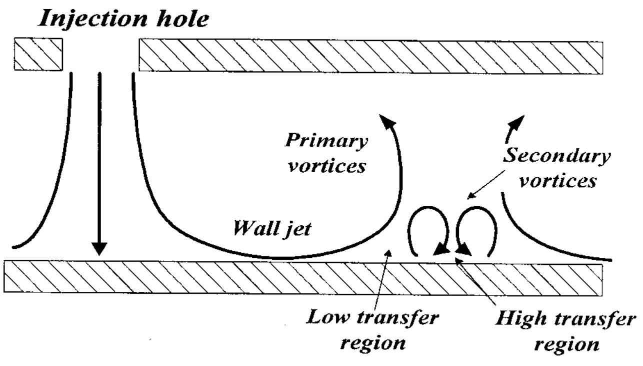

Fig. 9 Expected flow pattern of array impinging jets

Table 2 Average Sherwood number for different gap distances at Re_d=10,000 and staggered array

H/d	Single layer	0.33	1.0	2.0	6.0	10.0
$\overline{\mathrm{Sh}}$	11.0	100.8	96.0	92.8	82.9	68.2

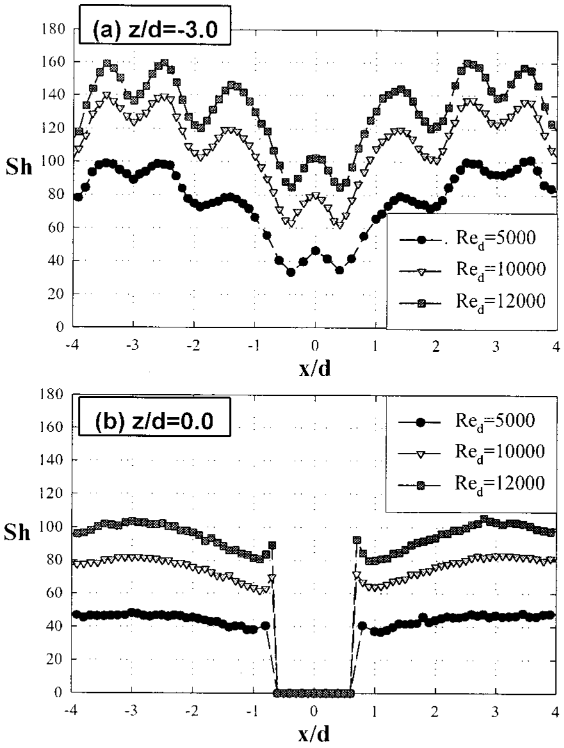

Fig. 10 Local plots of Sh for different Re_d at H/d=1.0 with staggered array

2 Effect of Reynolds Number. Figure 10 shows the local distributions of Sherwood number for various Reynolds numbers at $H/d=1.0$. The patterns of Sh distribution are similar for all Reynolds numbers, but the levels of Sh and the secondary peak values increase continuously with Reynolds numbers.

For Re_d=5000 to 12,000, an overall averaged Sh at the effusion plate is fitted in a line for $H/d=1.0$:

$$\overline{\mathrm{Sh}}=0.562\,\mathrm{Re}_d^{0.558} \tag{4}$$

3 Effect of Hole Arrangement

Numerical Simulation. Flow patterns for the shifted array at $H/d=1.0$ and Re_d=10,000 are shown in Fig. 11. At $z/d=-3.0$, the flow pattern is similar to that for the staggered array. However, as z/d increases, the center of primary vortex moves toward the effusion hole, and a low-momentum region is formed near $x/d=3.0$ at $z/d=0.0$ plane. The reason is that most of the injected fluid flows into the effusion hole due to the short distance between the injection and effusion holes, and the heat/mass transfer is expected to be very low on this low momentum region.

Figure 12 shows the contour plots of turbulence intensity near the surface of the effusion plate for $H/d=1.0$ and Re_d=10,000. Dotted arcs in Fig. 12 represent the projected position of a quarter of injection holes. High turbulence intensity is observed at the stagnation region and near effusion hole in each case. However, in the shifted array, the region with low turbulence intensity is observed with low flow velocity.

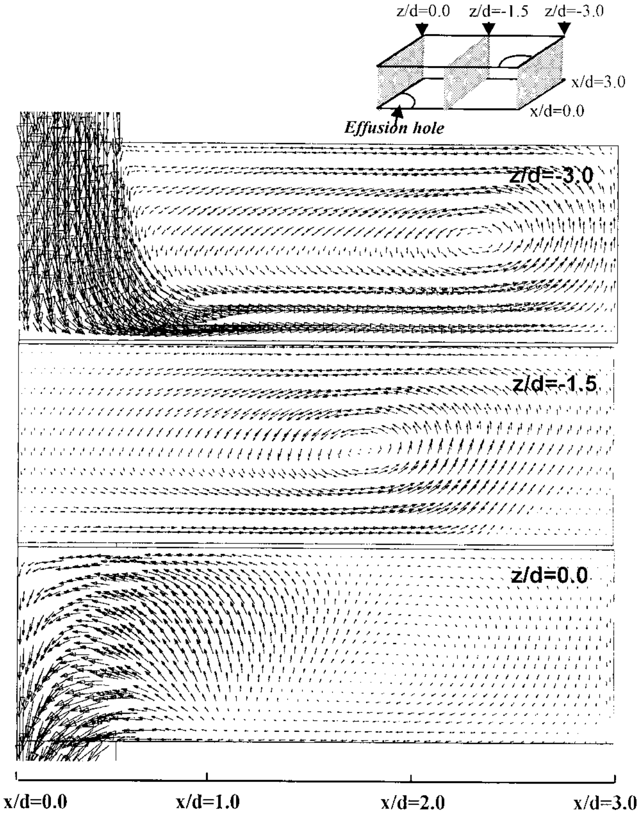

Fig. 11 Velocity vectors for shifted array at H/d=1.0 and Re_d=10,000

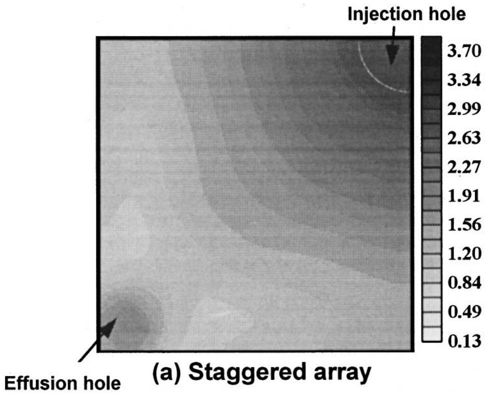

(a) Staggered array

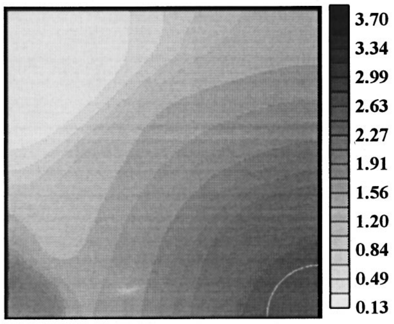

(b) Shifted array

Fig. 12 Contour plots of turbulence intensity (percent) at the plane of 0.067d apart from the surface of the effusion plate for H/d=1.0 and Re_d=10,000

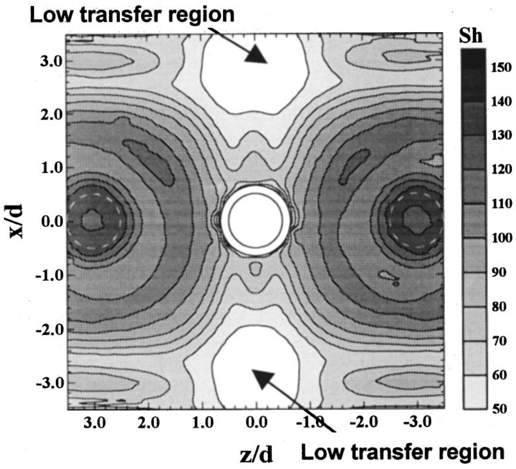

Fig. 13 Contour plots of Sh for $H/d=1.0$ and $Re_d=10{,}000$ with shifted array

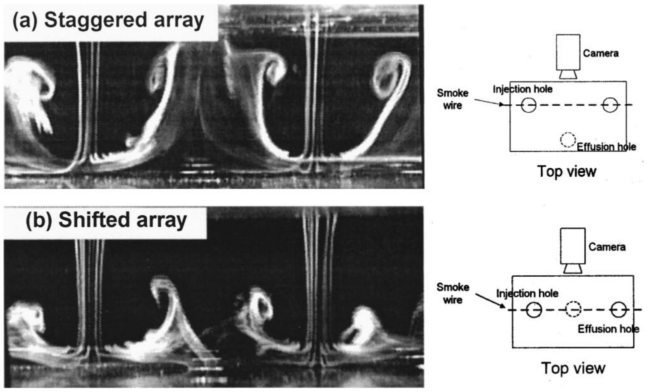

Fig. 15 Smoke-wire flow visualization for different hole arrangements at $H/d=4.0$

Local Heat/Mass Transfer Measurement. Figure 13 shows the contour plot of Sherwood number for the shifted hole arrangement at $Re_d=10{,}000$ and $H/d=1.0$. In the shifted array, the centers of injection holes (white dotted circle) and effusion hole are on the same line as shown in Fig. 2. High heat/mass transfer around the impingement region is observed and Sh pattern along the line of $x/d=\pm 3.0$ is similar to that of the staggered array (Fig. 6(*b*)). However, the high heat/mass transfer region is limited, and the low heat/mass transfer region exists along the line at $z/d=0.0$, except for the region near the effusion hole ($-0.6<x/d<0.6$) as expected in the numerical results.

Figure 14 shows the local distributions of Sh for different hole arrangements at selected positions; $z/d=-3.0$ and $z/d=0.0$. The heat/mass transfer distributions for each hole arrangement show the similar patterns near the stagnation region, as shown in Fig. 14(*a*). At $z/d=0.0$ (Fig. 14(*b*)). Sh values near the effusion hole for the shifted array are higher than those for the staggered array due to the interaction of wall jets and flow acceleration. However, in the region of $z/d<-2.5$ and $z/d>2.5$, Sh for the shifted array are 25~50 percent lower than that for the staggered array, as presented in the contour plot (Fig. 13). Therefore, this low transfer region will produce a hot spot including large thermal stress due to nonuniformity of the heat transfer rates. In overall transfer rate, the average value of Sh for the shifted array is $\overline{\mathrm{Sh}}=86.8$, and this is about 10 percent lower than that for the staggered array. Thus, the hole arrangement is very important to obtain a high and uniform transfer on the effusion plate.

4 Flow Visualization. Figure 15 shows the smoke-wire flow visualization results for the different hole arrangements at $H/d=4$. For the staggered array, the strong upward flow patterns are clearly shown due to the interaction of adjacent wall jets. Hence, the secondary vortices may be formed between the strong upward primary vortices. However, for the shifted array, the strength of primary vortices is weaker than that for the staggered array because of the suction of approaching wall jets by the effusion hole.

Figure 16 shows the oil-lampblack surface flow visualizations for the two hole arrangements at $H/d=2.0$ and $Re_d=10{,}000$. A thin mixture of oil and carbon powder is used to observe the shear flow pattern on the wall. In the case of staggered array, square cells are formed as expected in the contour plots. Two black lines (accumulation of carbon powder) exist between the adjacent effusion holes, and these lines represent the low transfer region as mentioned in Fig. 9. A bright region (high transfer region) exists along the centerline of effusion holes (between the black lines). This reveals that the formation and flow of secondary vortices affect the heat/mass transfer enhancement. For the shifted array, a dead zone indicated by black region is observed between the ef-

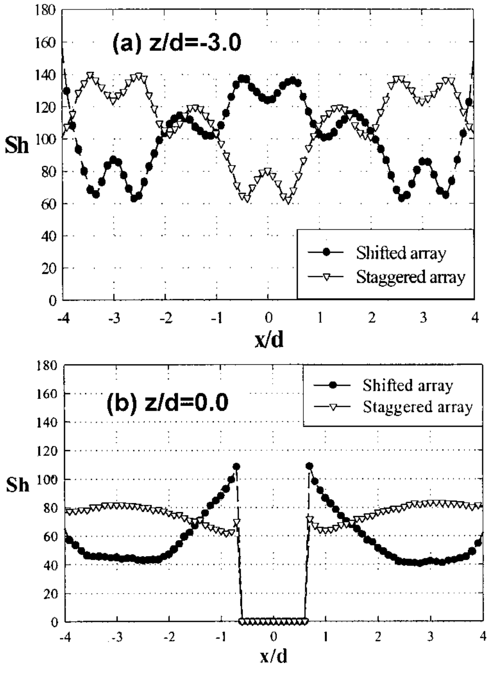

Fig. 14 Local plots of Sh for different hole arrangements at $H/d=1.0$ and $Re_d=10{,}000$

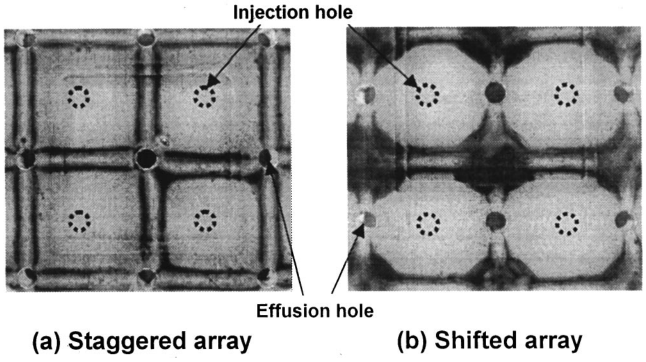

Fig. 16 Oil-lampblack surface flow visualization for $H/d=2.0$ and $Re_d=10{,}000$

fusion holes presenting low heat/mass transfer. These results are in good agreement with the numerical and mass transfer experimental results.

Conclusions

The effects of gap distance, Reynolds number, and hole arrangement in an impingement/effusion cooling system are studied; the flow patterns are investigated by numerical calculation and flow visualization, and heat/mass transfer characteristics by naphthalene sublimation method. The results are summarized as follows:

Variation of Gap Distance

- For the small gap distance, interaction between adjacent impinging jets is very weak, and the flow pattern in gap spacing is similar to a duct flow.
- The averaged Sh for the staggered hole arrangements are approximately 6～10 times higher than that for the single layer flow (effusion only). The heat/mass transfer at the stagnation point is the highest at $H/d=6.0$ without secondary peaks, and the overall heat/mass transfer rate increases as H/d decreases.

Variation of Reynolds Number

- Levels of Sh increase monotonically with Reynolds numbers showing that the patterns of heat/mass transfer are similar for all tested Reynolds numbers.

Variation of Hole Arrangement

- With the shifted array, the low momentum flow region is observed between the effusion holes due to the sink flow of injected jet into the effusion hole.
- The secondary vortices are strengthened strongly and accelerated to the effusion holes for the staggered hole arrangement, resulting in heat/mass transfer enhancement. Therefore, the cooling of effusion plate with the staggered hole arrangement shows better performance than the cooling with the shifted hole arrangement. Thus, the hole arrangement is very important to obtain a high and uniform transfer on the effusion plate.

Acknowledgments

The authors wish to acknowledge support for this study by the KOSEF under grant No. 98-0200-13-01-3 and by the Ministry of Science and Technology through their National Research Laboratory program.

Nomenclature

d = injection and effusion hole diameter
dy = local sublimation depth of naphthalene
$d\tau$ = test duration
D_{naph} = mass diffusion coefficient of naphthalene vapor in air
H = gap distance between injection and effusion plates
h_m = local mass transfer coefficient
$\dot{m}$ = local naphthalene mass transfer per unit area and time
Nu = Nusselt number based on the hole diameter$=hd/k$
Pr = Prandtl number
P = pitch of array holes
Re_d = Reynolds number based on hole diameter and the average velocity in the hole
Sc = Schmidt number
Sh = Sherwood number based on the hole diameter $=h_m d/D_{\mathrm{naph}}$
$\overline{\mathrm{Sh}}$ = average Sherwood number
t_1 = thickness of injection plate
t_2 = thickness of effusion plate
x, z = distance from the center of a hole (Fig. 2)
ρ_s = density of solid naphthalene
$\rho_{v,w}$ = naphthalene vapor density on the surface
$\rho_{v,\infty}$ = naphthalene vapor density of the injected jet.

References

[1] Downs, S. J., and James, E. H., 1987, ''Jet Impingement Heat Transfer—A Literature Survey,'' ASME Paper No. 87-HT-35.
[2] Jambunathan, K., Lai, E., Moss, M. A., and Button, B. L., 1992, ''A Review of Heat Transfer Data for Single Circular Jet Impingement,'' Int. J. Heat Fluid Flow, **13**, pp. 106–115.
[3] Viskanta, R., 1993, ''Heat Transfer to Impinging Isothermal Gas and Flame Jets,'' Exp. Therm. Fluid Sci., **6**, pp. 111–134.
[4] Cho, H. H., and Goldstein, R. J., 1995, ''Heat (Mass) Transfer and Film Cooling Effectiveness With Injection through Discrete Holes—Part I : Within Holes and on the Back Surface,'' ASME J. Turbomach., **117**, pp. 440–450.
[5] Huber, A. M., and Viskanta, R., 1994, ''Effect of Jet–Jet Spacing on Convective Heat Transfer to Confined, Impinging Arrays of Axisymmetric Air Jets,'' Int. J. Heat Mass Transf., **37**, No. 18, pp. 2859–2869.
[6] Cho, H. H., and Goldstein, R. J., 1996, ''Effect of Hole Arrangements on Impingement/Effusion Cooling,'' *Proc. 3rd KSME–JSME Thermal Engineering Conf.* pp. 71–76.
[7] Hollwarth, B. R., and Dagan, L., 1980, ''Arrays of Impinging Jets With Spent Fluid Removal Through Vent Holes on the Target Surface. Part 1: Average Heat Transfer,'' ASME J. Eng. Power, **102**, pp. 994–999.
[8] Hollwarth, B. R., Lehmann, G., and Rosiczkowski, J., 1983, ''Arrays of Impinging Jets With Spent Fluid Removal Through Vent Holes on the Target Surface, Part 2: Local Heat Transfer,'' ASME J. Eng. Power, **105**, pp. 393–402.
[9] Cho, H. H., and Goldstein, R. J., 1997, ''Total Coverage Discrete Hole Wall Cooling,'' ASME J. Turbomach., **119**, pp. 320–329.
[10] Ambrose, D., Lawrenson, I. J., and Sparke, C. H. S., 1975, ''The Vapor Pressure of Naphthalene,'' J. Chem. Thermodyn., **7**, pp. 1173–1176.
[11] Goldstein, R. J., and Cho, H. H., 1995, ''A Review of Mass Transfer Measurement Using Naphthalene Sublimation,'' Exp. Therm. Fluid Sci., **10**, pp. 416–434.
[12] Eckert, E. R. G., 1976, ''Analogies to Heat Transfer Processes,'' in: *Measurements in Heat Transfer*, E. R. G. Eckert and R. J. Goldstein, eds., Hemisphere, New York, pp. 397–423.
[13] Kline, S. J., and McClintock, F., 1953, ''Describing Uncertainty in Single Sample Experiments,'' Mech. Eng. (Am. Soc. Mech. Eng.), **75**, Jan., pp. 3–8.
[14] Cho, H. H., Lee, C. H., and Kim, Y. S., 1998, ''Characteristics of Heat Transfer in Impinging Jets by Control of Vortex Pairing,'' ASME Paper No. 98-GT-276.
[15] Lee, J. H., and Lee, S. J., 1998, ''Turbulent Heat Transfer Characteristics in a Stagnation Region of Axi-Symmetric Jet Impingement,'' *Proc. 11th IHTC*, Vol. 5, pp. 433–438.

N. Syred

A. Khalatov

Department of Mechanical Engineering and
Energy Studies,
School of Engineering,
Cardiff University,
P.O. Box 685,
The Parade, Cardiff CF23 3TA, United Kingdom

A. Kozlov

Department of Power Engineering,
Kazan Scientific Centre,
Russian Academy of Sciences,
P.O. Box 190,
City of Kazan, 420503, Russia

A. Shchukin

R. Agachev

Department of Aeroengines,
Chair of Turbomachinery,
Kazan State Technical University (KAI),
10 K. Marx St.,
City of Kazan, 420111, Russia

Effect of Surface Curvature on Heat Transfer and Hydrodynamics Within a Single Hemispherical Dimple

Turbulent heat transfer and hydrodynamics have been studied in concavely and convexly curved dimples with Reynolds numbers ranging from 1.3×10^5 to 3.1×10^5. The large-scale single hemispherical dimple 50 mm in diameter and 25 mm in depth was arranged on the smooth concave or convex wall of a curved rectangular-shaped passage. The fluid flow and heat transfer measurements, and surface streamline observations were performed within the flow curvature parameter δ^{**}/R ranged from 0.002 to 0.007. The ''tornado-like'' oscillating vortex bursting periodically out of the dimple was registered in the experiments with a ''curved'' dimple. This vortex structure is similar to that earlier observed in a ''flat'' dimple. The surface curvature considerably influences the dimple heat transfer rate in both cases. It enhances heat transfer in a ''concave'' dimple and reduces it in a ''convex'' one; however, the more remarkable effect occurred in a concavely curved dimple. The correction factors describing the effect of curvature on average heat transfer in a ''curved'' dimple have been obtained as a result of experimental study.

[DOI: 10.1115/1.1348020]

Introduction

It is well known that increases in the thermal efficiency of gas turbine can effectively be achieved through a higher turbine inlet gas temperature. In prototype aeroengine gas turbines, the entry temperature has already reached 1750–1800 K, while the air pressure ratio has gradually approached factor of 35.0, with projections to 40.0 being made. Since modern gas turbines operate at inlet temperature levels above the blade melting point, both internal and external cooling systems are employed to meet blade service life requirements. Some 30 heat transfer enhancement techniques are in use now; however, due to design and technological restrictions, designers of blade internal cooling systems still apply very few of these techniques. Among the basic technologies are: impingement cooling, pin fins (pedestals), plain and broken ribs and their combinations.

Despite remarkable progress in design of cooling systems, some specific blade zones, such as leading and trailing edge areas, still remain very difficult to cool adequately with conventional cooling techniques. Since the potential of currently used internal cooling techniques is nearly exhausted, further cooling efficiency improvements can only be achieved through increases in the air flow rate extracted from the compressor; that, however, leads to reductions in the thermal efficiency of working cycle. Recent effort in the former USSR, USA, UK, Germany, and other countries has focused on studies of novel cooling techniques with improved thermal-hydraulic performance. A few research programs have been launched to explore some novel concepts. The leading technologies are often based on the vortex and swirl flow concepts, including the ''Hemispherical Surface Dimple Technique,'' based on generation of small, but powerful oscillating vortices.

The unstable ''self-organized'' vortex structure has been observed in the early experiments of Wighart and Tillman [1] over two-dimensional surface extensions. Afterward, the detailed data of Bearnlan and Harvey [2] and Mehta [3], based on golf-ball experiments, have confirmed the *nontrivial nature of the vortex*, existing over three-dimensional surface concavity (dimple). Based on the experiments of Wighart and Tillman, Lavrent'ev and Shabat [4] have predicted a generation of unstable ''self-organized'' ring vortices over a dimple with round shape contour. The unique heat transfer properties in three-dimensional surface dimples were reported over ten years ago in the comprehensive Russian publications [5,6]. It was demonstrated that implementation of regular dimples on a flat plate enhances heat transfer and mitigates accompanying pressure losses (water and air flow). Over the limited range of Reynolds number, the increase in heat transfer and pressure losses is nearly equivalent; they change virtually ''in synch.'' This remarkable feature makes this concept especially attractive for industrial applications.

Kuethe [7] was the first one to suggest to using surface dimples for heat transfer enhancement. Since that time fairly limited contributions were made to the heat transfer subject. Kesarev and Kozlov [8] have studied local heat transfer within a single dimple and found that heat flux up to a factor of 1.5 compared with plane circle of an identical diameter can be achieved. Shchukin et al. [9] have considered heat transfer downstream of a single dimple under pressure gradient and free-stream turbulence influences. Terekhov et al. [10] have performed detailed heat transfer measurements within a single dimple and reported the dimple depth magnitude, giving the maximum heat transfer effect. Afanasyev et al. [11] have studied heat transfer and pressure drop in passage with one side dimpled wall; the authors revealed the limited Reynolds number range where a heat transfer enhancement rate up to a factor of 1.4 can be achieved without additional pressure losses.

Detailed experimental heat transfer studies have been performed by Gachechiladze et al. [12] and Nagoga [13]. Nagoga has

---

Contributed by the International Gas Turbine Institute and presented at the 45th International Gas Turbine and Aeroengine Congress and Exhibition, Munich, Germany, May 8–11, 2000. Manuscript received by the International Gas Turbine Institute February 2000. Paper No. 2000-GT-236. Review Chair: D. Ballal.

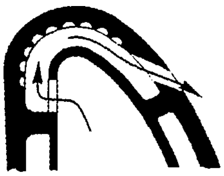

Fig. 1 Turbine blade cooling passage with hemispherical surface dimples in a leading edge area (concave wall; possible design)

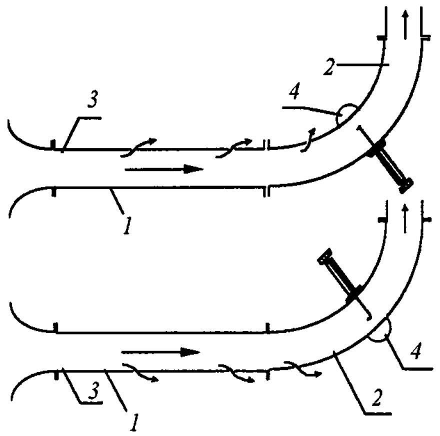

Fig. 2 Test section: (1) straight rectangular passage; (2) curved passage; (3) flow turbulator; (4) dimple

reported a heat transfer enhancement rate up to a factor of 2.7, achieved within a narrow passage with one side dimpled wall ($H/d=0.17$; $\Delta/d=0.13$). The experimental study of Moon et al. [14] was limited by the passage height ratio $H/d=0.37$; for this reason the authors could not achieve a heat transfer ratio over a factor of 2.1. Actually, identical heat transfer levels have been obtained by Nagoga at identical fluid flow conditions. Chyu et al. [15] have studied local heat transfer in one side dimpled passage (two dimple shapes). The heat transfer rate factor of 2.1 reported in this paper is comparable with the data of Nagoga and Glezer et al. Both Chyu and Glezer have confirmed the excellent thermal-hydraulic performance of the dimple technology earlier reported by Gachechiladze et al. [12]. Recent investigations of Gortyshev et al. [16] have shown that the additional heat transfer effect (1.2–1.8) is achieved if a row of dimples exist on both passage sides, or due to a mutual displacement of two dimpled walls (1.2–1.3). Reviews of recent achievements in the field have been reported by Khalatov and Izgoreva [17] and Shchukin et al. [18]. Some specific aspects of the surface dimple technology (dimpled tube bundle; water boiling) have been studied by Belen'ky et al. [19] and Khalatov et al. [20]. The asymmetric surface dimple design was proposed by Khalatov et al. [21].

The effect of surface curvature on heat transfer and fluid flow over a smooth surface is quite remarkable [22], and should be taken into account if the hemispherical surface dimple technique is used to cool ''curved'' surfaces (Fig. 1). However, despite the obvious importance, this factor still has not been reported in the existing ''dimple'' publications. The broad experimental program was jointly undertaken by the UK and Russian teams to study the curvature effect. This paper presents heat transfer and fluid flow measurements within a single hemispherical dimple located on a convex or concave wall.

Experimental Facility and Procedure

The experimental program was performed in a wind tunnel of an open type; Fig. 2 presents a schematic view of the test section. A single large-scale dimple was arranged on a concave or convex wall of a rectangular-sectioned curved passage ($140\times 100\,\text{mm}^2$) with the curvature radius 400 mm and 500 mm ($H=100\,\text{mm}$). The dimple diameter d is 50 nm, its depth Δ is 25 mm ($\Delta/D=0.5$), and the circular rim of both dimples has a sharp edge. Air flows from an in-house compressor into a large volume (plenum) and then through the contracting unit and the intermediate straight rectangular passage and enters the test section. Flow tubulator 3 was installed 10 mm downstream of the contracting unit to ''activate'' a turbulent flow structure and to identify the boundary layer starting point. The inlet air velocity $\langle u_0\rangle$ ranged from 17.7 to 42.3 m/s. The velocity fluctuations $\langle u_0'^2\rangle^{1/2}$ ranged from 3.5 to 4.5 percent. Reynolds number Re, based on the inlet velocity $\langle u_0\rangle$ and the equivalent passage diameter, ranged from 1.3×10^5 to 3.1×10^5. The inlet air temperature $T_0=T_\infty$ was about 23°C. When the heat transfer experiments were carried out, the dimple made of the stainless steel was heated by means of an electrical heater installed just under the dimple itself. The wall surface temperature T_w was within 83–93°C, so the range of the temperature difference T_w-T_∞ was 60–70°C. Altogether 62 K-type thermocouples were flush-mounted on the internal and external surfaces of each dimple to register the local wall temperature T_w. Each thermocouple solder was embedded into a specially cut groove; the groove depth has the same size (0.1 mm) as the diameter of thermocouple wires; its length is 1 mm. The finite quantity of the thermocouple wires and heat losses in the thermocouple lead was taken into account when uncertainty analysis was made. The wall temperature measurements were used as the temperature boundary conditions to solve numerically the two-dimensional inverse conductivity problem to determine both the stationary temperature field inside of a dimple wall and the local surface heat flow. Calculations have shown that in this particular case the two-dimensional approach is quite justified. According to this approach, the local heat fluxes were found from the basic equation $q_w=-k(\partial T/\partial n)_{n=0}$. The local heat transfer coefficient and local Stanton number were calculated as $h=q_w/(T_w-T_\infty)$ and $\text{St}=h/(c\rho u_0)$, respectively. Both the average heat transfer coefficient $\langle h\rangle$ and average Stanton number $\langle \text{St}\rangle$ were calculated from the local heat flux and local wall temperature measurements.

The local wall static pressures were measured by means of 0.4-mm-dia tap-holes using the liquid manometer with a multiplying factor of 1 mm. Altogether 25 holes were drilled in a dimple body normal to the surface tangent. The pressure coefficient c_p was calculated as $c_p=(p-p_0)/(\rho\langle u_0\rangle^2/2)$, where p_0 is the static pressure on a smooth curved surface just in front of the dimple. A hot-wire anemometer DISA 55M and a miniature velocity probe with a tungsten wire were used to measure local flow velocity and its fluctuations. The probe wire diameter is 5 μm, its length is 1.2 mm. Surface flow visualizations were also performed in the experimental program. For this purpose the dimple was made of transparent acrylic, silk treads were pasted onto the dimple surface to detect the surface streamlines (traces).

The flow curvature parameter δ^{**}/R defines the curved flows similarity, it was used to identify the curvature effect on heat transfer [22]. The magnitude of momentum thickness δ^{**} was changed by means of a partial flow suction in front of a dimple. For this purpose three transverse slots were made on both passage walls, and a combination of partially or fully open slots was used providing variations in the boundary layer momentum thickness. The flow curvature parameter δ^{**}/R ranged from 5×10^{-4} to 7×10^{-3} on the convex wall and from 2.1×10^{-4} to 2.2×10^{-3} on the concave one.

The maximum experimental uncertainty for the local heat transfer coefficient was within ±16 percent, and the uncertainties in measurements of velocity and turbulent fluctuations were estimated to be within ±5 and ±12 percent, respectively, at the confidence probability of 0.95.

Results and Discussion

The flow visualization observations and velocity measurements have confirmed that, as in a ''flat'' dimple [8] the flow pattern in a ''curved'' dimple contains the ''tornado-like'' oscillating vortex bursting periodically out of the dimple. Thus, the surface curvature does not radically change the dimple flow pattern, which has a ''self-organized'' nature. The frequency of the vortex angular oscillations is approximately the same as in a ''flat'' dimple ($\delta^{**}/R=0$). There is no Reynolds number effect on the average flow parameters (c_p, $\langle u\rangle$, etc.). In the nondimensional representation, the maximum nondimensional reverse flow ($u_\delta/\langle u_0\rangle$) does not depend on the surface curvature type (concave or convex); as in a ''flat'' dimple, this ratio is 0.4. The surface curvature promotes changes in the wall static pressure distributions, which are more remarkable in a ''concave'' dimple (Fig. 3). The velocity fluctuations in a ''concave'' dimple exceed those in a ''convex'' dimple. This result agrees well with the general character of radial pressure gradient influence over smooth curved surfaces [22].

The character of the local Stanton number distributions is identical to that in a ''flat'' dimple (Fig. 4). The concavely curved dimple enhances heat transfer comparatively in a ''flat'' dimple, while the ''convex'' dimple promotes reductions in the heat transfer rate. Again, this effect is in agreement with heat transfer over a smooth concave or convex wall. The heat transfer measurements over a ''flat'' dimple (reference data) were performed in the same test section (Fig. 2), in this case the straight passage containing a single dimple was installed instead of the curved passage. Approximately the same character of heat transfer distribution was found for the average Stanton number over the whole range of Reynolds number (Fig. 5). Again, the experimental data for the ''concave'' dimple are located over the solid line, describing the ''flat'' dimple data, while results of the ''convex'' dimple lie below that curve. The curvature effect is considerable and should be taken into account in heat transfer predictions.

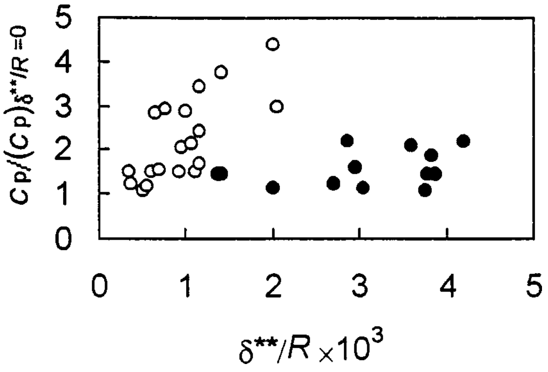

Fig. 3 Average static pressure coefficient in a dimple "pole" versus curvature parameter: open symbols-dimple on a concave wall; close symbols-dimple on a convex wall

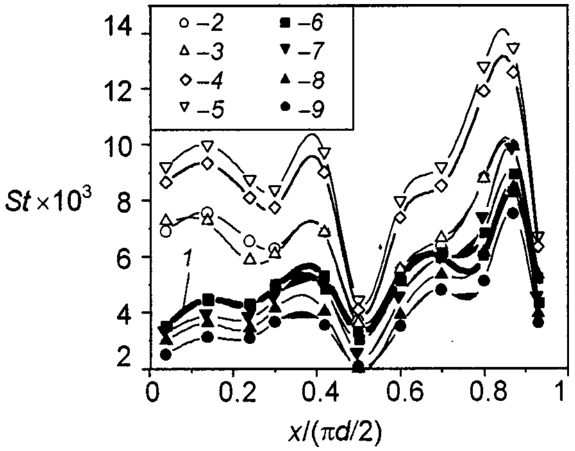

Fig. 4 Local Stanton number distributions: lengthwise meridian cross section of a dimple. Re=2.2×10^5: open symbols =dimple on a concave wall; closed symbols=dimple on a convex wall. (1) dimple on a flat plate; (2) δ''/R=0.2×10^{-3}; (3) 0.44×10^{-3}; (4) 1.1×10^{-3}; (5)=1.7×10^{-3}; (6) 2.2×10^{-3}; (7)=3.5×10^{-3}; (8) 5.2×10^{-3}; (9) 6.9×10^{-3};1 *x*=distance in streamwise direction.

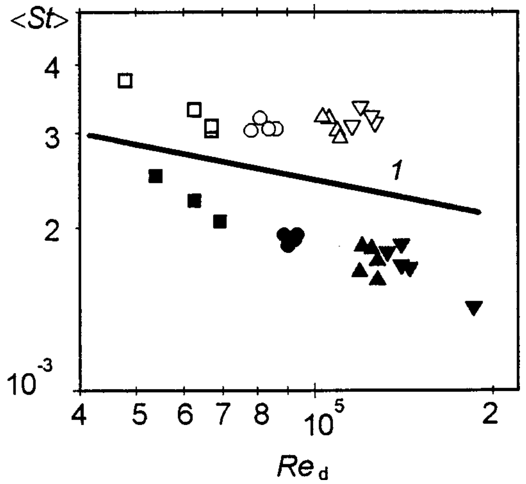

Fig. 5 Average Stanton number in a "curved" dimple; Re$_d$ =$u_0 d/\nu$; designations: Fig. 4

In order to separate the surface curvature effect the experimental correlations were used to describe the ''pure'' surface curvature effect on heat transfer over a smooth concave or convex wall [23,22]. These correlations summarize the vast experimental data obtained throughout the world in a wide range of the curvature factor:

Concave surface curvature [23]:

$$\Psi_{\mathrm{conc}}=\mathrm{St}_{\mathrm{conc}}/\mathrm{St}_0=[1+1.8\times10^3\times|\delta^{**}/R|]^{0.16} \qquad (1)$$

Convex surface curvature [22]:

$$\Psi_{\mathrm{conv}}=\mathrm{St}_{\mathrm{conv}}/\mathrm{St}_0=[1+1000(\delta^{**}/R)]^{-0.12} \qquad (2)$$

where St_0 is Stanton number over a smooth flat plate at the same Reynolds number.

Correlations (1) and (2) are shown in Fig. 6 along with the experimental data for ''concave'' and ''convex'' dimples. As shown, the additional curvature effect occurs for both ''curved'' dimples, and additional correction factors should be introduced to describe the experimental data properly. Therefore, there is a difference between the curvature effect over a smooth curved surface and over a ''curved'' dimple.

The processing of findings, based on the curvature effect ''isolation'' allowed us to identify the correction factor $(\Psi_d)_{\mathrm{curv}}$ in both cases. This factor is 1.2 and 0.9 for dimples, located on a concave or convex wall, respectively. Both factors are approximately constant over the whole range of Reynolds number and the curvature parameter occurring in the experiments. Taking into account these correction factors, the following experimental correlations have been derived, describing an average heat transfer in a ''curved'' dimple:

Dimple on a concave wall:

$$\langle\mathrm{St}\rangle=1.2\times\Psi_{\mathrm{conc}}\times\langle\mathrm{St}_0\rangle \qquad (3)$$

Dimple on a convex wall:

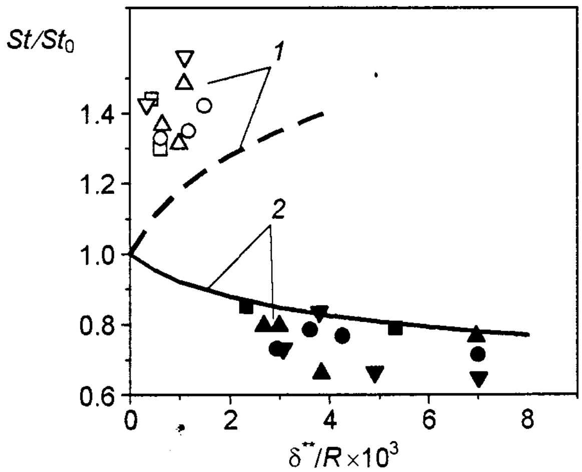

Fig. 6 Relative Stanton number: (1) concave wall; (2) convex wall; curves: smooth curved surface [correlations (1) & (2)]; dots: dimpled curved surface (present experiments)

$$\langle \mathrm{St}\rangle = 0.9\times\Psi_{\mathrm{conv}}\times\langle \mathrm{St}_0\rangle \tag{4}$$

Here $\langle \mathrm{St}_0\rangle$ is the average Stanton number correlation for a ''flat'' dimple (solid line; Fig. 7).

Thus, in order to predict an average heat transfer within a single ''curved'' dimple, the correlations (1)–(4) can be used along with the correlation for a ''flat'' dimple. Figure 7 confirms that the ''multiplication'' of two factors is quite justifiable in this particular case. After elimination of the surface curvature effect and the curvature correction factor, results for both cases agree pretty well with the basic correlation for a ''flat'' dimple.

Figure 8 gives the pictorial representation of an average heat transfer for different configurations. Among these are the smooth flat plate, smooth concave and convex surface, dimple arranged on a flat plate, row of dimples arranged on one side of narrow passage, dimple arranged on concave or convex surfaces. For all situations, the Stanton number $\langle \mathrm{St}_0\rangle$ reflects the smooth flat plate data. Both a ''flat'' dimple and a smooth concave wall provide identical heat transfer enhancement rate with a factor of 1.5. A row of dimples in narrow passage gives approximately the same heat transfer rate (2.5) as a single ''concave'' dimple. Therefore, the higher heat transfer enhancement rate would be expected in a narrow curved passage with a row of dimples arranged on a concave wall. Such a respectable heat transfer level is very attractive in various industrial applications, in particular, in turbine blade cooling.

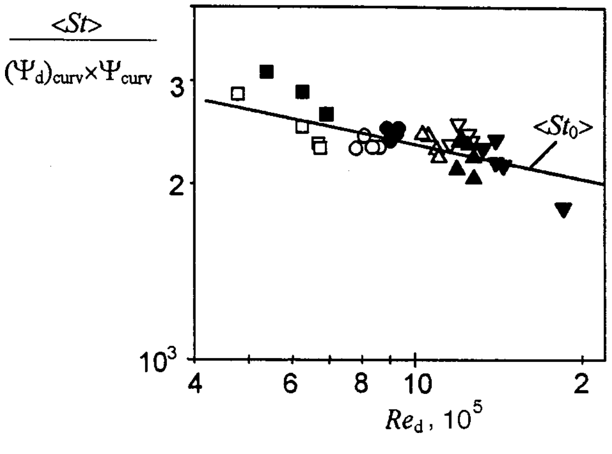

Fig. 7 Summarizing of experimental data: dimple on a concave or convex surface; solid line: single dimple on a flat plate

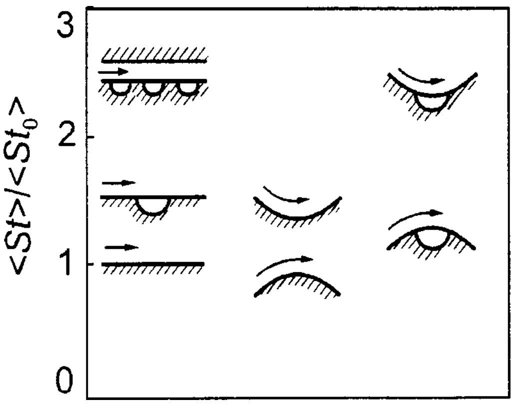

Fig. 8 Average relative heat transfer rate: various configurations; $\delta^{**}/R = 2\times10^{-3}$, $\mathrm{Re}_d = 8\times10^4$

Summary

An experimental program has been undertaken to examine the surface curvature effect on heat transfer and fluid flow within a single hemispherical dimple located on a concave or convex wall. The dimple geometry and passage height were constant, while the range of Reynolds number and the curvature parameter were variable. The surface curvature influences heat transfer and fluid flow parameters, promoting increased rarefaction rate throughout a dimple surface, but the more remarkable effect was found in a ''concave'' dimple. Turbulent fluctuations in a concavely curved dimple exceed those occurring in a ''convex'' dimple. Heat transfer behavior in a ''curved'' dimple is identical to that in a ''flat'' dimple. The concave surface curvature increases the heat transfer rate compared with the ''flat'' dimple data, but the convex curvature reduces it. The fairly respectable heat transfer enhancement rate (about 2.5) has been obtained in a ''concave'' dimple. Such a respectable augmentation is particularly attractive for applications to aircooled gas turbine components (internal blade cooling; combustor line), where various ''curved'' surfaces exist. The effect of surface curvature on an average heat transfer within a ''curved dimple'' is different from that over a smooth concave or convex wall. The correction factors describing the additional curvature effect in both cases have been obtained as a result of the experimental data processing.

Acknowledgments

This work was supported by a NATO Linkage Grant (HTECH. LG 973717), grants of a Russian Foundation (No. 99-02-18191; No. 00-15-96690) and a Federal Russian Program ''Integration'' (project No. 244). The authors are very grateful to Dr. O. Bulanov for assistance in collection and processing of experimental data.

Nomenclature

c = heat capacity, J/kg K
c_p = pressure coefficient $= (p - p_0)/(\rho\langle u_0\rangle^2/2)$
D = equivalent passage diameter = 117 mm
d = dimple diameter = 50 mm
h = local heat transfer coefficient, Wt/m^2 K
H = passage height, m
k = heat conductivity, Wt/m K
n = coordinate normal to dimple surface, m
p = wall static pressure, N/m^2
q_w = specific heat flux, Wt/m^2
u = flow velocity, m/s

R = wall curvature (concave or convex) radius, m
Re = Reynolds number $= \langle u_0 \rangle D/\nu$
St = Stanton number $= h/(c\rho\langle u_0 \rangle)$
T = temperature, K
x = curvilinear distance along dimple wall, m
δ^{**} = boundary layer momentum thickness, m
δ^{**}/R = curvature parameter
ν = kinematic viscosity, m^2/s
ρ = density, kg/m^3
Ψ = relative Stanton number
Δ = dimple depth $= 25$ mm

Subscripts

conc = concave
conv = convex
curv = curved
d = dimple
0 = inlet: curved passage section
w = wall
δ = boundary layer edge
∞ = free-stream parameter over dimple
$\langle\ \rangle$ = average value
$'$ = fluctuations

References

[1] Wighart, K., 1953, ''Erhohung des turbulenten Reibungswiderstandes durch Oberflachenstorugen,'' Forschung. Schiffstech., No. 1, pp. 65–68.
[2] Bearman, P. W., and Harvey, J. K., 1976, ''Golf Ball Aerodynamics,'' Aeronaut. Q., **27**, pp. 112–122.
[3] Mehta, R. D., 1985, ''Aerodynamics of Sports Balls,'' Annu. Rev. Fluid Mech., **17**, pp. 151–189.
[4] Lavrent'ev, M. A., and Shabat, B. V., 1977, *Problems of Hydrodynamics and Its Mathematical Models* [in Russian], Moscow, Russia, Nauka, p. 350.
[5] Kiknadze, G. I., and Krasnov, Yu. K., 1986, ''Evolution of the Tornado-Like Viscous Flows,'' [in Russian], Dokl. Akad. Nauk, SSSR Gidromechanika, **290**, pp. 1315–1319.
[6] Kiknadze, G. I., and Krasnov, Yu. K., 1986, ''Vortex Self-Organizing Over Hemispherical Dimple at Water Overflow,'' [in Russian], Dokl. Akad. Nauk SSSR, Gidromechanika, **291**, pp. 1315–1318.
[7] Kuethe, A. M., 1971, ''Boundary Layer Control of Flow Separation and Heat Exchange,'' US Patent No. 3,578,264.
[8] Kesarev, V. S., and Kozlov, A. P., 1993, ''Flow Pattern and Heat Transfer at Hemispherical Dimple Flowing by Turbulized Air Flow,'' [in Russian], Vestnik MGTU. Ser. Mashinostroenie, No. 1, pp. 131–145.
[9] Shchukin, A. V., Kozlov, A. P., and Agachev, R. S., 1995, ''Study and Application of Hemispheric Cavities for Surface Heat Transfer Augmentation,'' ASME Paper No. 95-GT-59.
[10] Terekhov, V. I., Kalinina, S. V., and Mshvidobadze, Yu. M., 1997, ''Heat Transfer Coefficient and Aerodynamic Resistance on a Surface With a Single Dimple,'' J. Enhanced Heat Transfer, **4**, pp. 131–145.
[11] Afanasyev, V. N., Chudnovsky, Ya. P., Leont'ev, A. I., and Roganov, P. S., 1993, ''Turbulent Flow Friction and Heat Transfer Characteristics for Spherical Cavities on a Flat Plate,'' *Experimental Thermal and Fluid Science*, Elsevier Science, New York, Chap. 7, pp. 1–8.
[12] Gachechiladze, I. A., Kiknadze, G. I., and Krasnov, Yu. K., 1988, ''Heat Transfer at Self-formation of Whirlwind Structure'' [in Russian], *Heat and Mass Transfer, Convective, Radiation and Complex Heat Transfer, Problem Reports*, Minsk, ITMO AN BSSR, pp. 83–125.
[13] Nagoga, G. P., 1996, *Effective Blade Cooling Techniques for High Performance Gas Turbines* [in Russian], Moscow, Russia, Aviation Institute, p. 105.
[14] Moon, H. K., O'Connell, T. O., and Glezer, B., 2000, ''Channel Height Effect on Heat Transfer and Friction in a Dimpled Passage,'' ASME J. Eng. Gas Turbines Power, **122**, pp. 307–313.
[15] Chyu, M. K., Yu. Y., Ding, H., Downs, J. P., and Soechting, F. O., 1997, ''Concavity Enhanced Heat Transfer in an Internal Cooling Passage,'' ASME Paper No. 97-GT-437.
[16] Gortyshev, Yu. F., and Popov, I. A., 1998, ''Studies of Hydrodynamics and Heat Exchange With Various Types of Intensifiers,'' *Proc. 11th International Heat Transfer Conference*, Vol. 6, Aug. 23–28, Kyongju, Korea.
[17] Khalatov, A. A., and Izgoreva, I. A., 1996, ''Heat Transfer Over Dimpled Surfaces'' [in Russian], Report TGD-96-1, Institute of Engineering Thermophysics, Kiev, Ukraine, p. 45.
[18] Shchukin, A. V., Kozlov, A. P., Chudnovsky, Ya. P., and Agachev, R. S., 1998, ''Intensification of Heat Exchange by Spherical Depressions: a Survey,'' Appl. Energy, **36**, No. 3, pp. 45–62.
[19] Belen'ky, M. Ya., et al., 1995, ''Thermal-Hydraulic Characteristics of Transversally Streamlined Dimpled Surfaces,'' [in Russian], Teploenergetika, No. 1, pp. 49–51.
[20] Khalatov, A. A., Kovalenko, G. V., and Geletuha, G. G., 1997, ''Heat Transfer on Horizontal Dimpled Tube at a Water Boiling in a Large Space,'' [in Russian], Promyshlennaya Teplotechnika, **19**, No. 1, pp. 53–57.
[21] Khalatov, A. A., Kovalenko, G. V., and Geletuha, G. G., 1997, ''Heat Exchange Surface,'' Patent of the Ukraine, No. 13888A, Priority of July 12, 1994.
[22] Khalatov, A. A., et al., 1999, *Thermogasdynamics of Complex Flows Over Curved Surfaces* [in Russian], Institute of Engineering Thermophysics, Kiev, Ukraine, p. 300.
[23] Kutateladze, S. S., Volchkov, E. P., and Terekhov, V. I., 1987, *Aerodynamics and Heat and Mass Exchange in Bounded Vortex Flows*, Novosibirsk, Institute of Thermophysics, Siberian Branch of Academy of Sciences USSR.

Arash Saidi

Bengt Sundén
e-mail: bengt.sunden@vok.lth.se

Division of Heat Transfer,
Lund Institute of Technology,
221 00 Lund, Sweden

On Prediction of Thermal-Hydraulic Characteristics of Square-Sectioned Ribbed Cooling Ducts

This paper presents the results of an investigation on prediction of local and mean thermal-hydraulic characteristics in rib-roughened ducts of square cross section. the Navier–Stokes and energy equations together with two low-Re k–ε turbulence models are solved numerically. The Reynolds turbulent stress tensor is calculated by two methods, namely, an eddy viscosity model (EVM) and an explicit algebraic stress model (EASM). The pressure–velocity coupling is handled by the SIMPLEC algorithm and calculations were carried out on a collocated grid. The convection–diffusion terms were calculated using the hybrid scheme (the changes in the results obtained by the other schemes, e.g., QUICK and Van Leer, were not significant). The considered ribbed duct configuration is identical to that in an experimental study and comparisons between the predictions and experimental results are provided. A discussion of the capabilities of the two methods (EVM and EASM) is presented. [DOI: 10.1115/1.1371779]

1 Introduction

It has been shown that one way to increase the performance of gas turbine cycles is to raise the temperature of the gas entering the turbine, but this increase is limited by the mechanical and thermal properties of the materials used in gas turbine blades. To remedy this problem, several cooling methods have been suggested; one method includes internal ducts in the blades. There are various types of such ducts, but the focus in this study is on square ducts with rib-roughened walls for heat transfer enhancement.

Experimental investigations gave some information concerning the influence of rib pitch and height on the overall Nusselt number and friction factor, effects of rib shape, and the importance of model orientation [1–4]. Investigations concerned with local measurements have become available recently, e.g., the studies of [5,6]. Such investigations are useful as various models are evaluated.

There are also previous numerical studies done on this subject. Acharya et al. [7] examined the ability of a nonlinear k–ε turbulence model to predict the flow and heat transfer between two successive two-dimensional ribs in the periodic fully developed region of a rectangular duct with ribs periodically mounted along the uniformly heated bottom wall. They used nonlinear and standard k–ε models and both models performed poorly in the separated region just behind the ribs where the Reynolds stresses were underpredicted and local Nusselt were underpredicted by both models as well. Another study was carried out by Liou et al. [8]. They employed the k–ε–ASM turbulence model. This nonlinear model predicted more realistic Reynolds stresses in the core flow region immediately after the ribs. Prakash and Zerkle [9] analyzed a square duct with ribbed walls. In their investigation they used a turbulence model, together with wall functions, and they achieved together with wall functions, and they achieved good agreement with experimental correlation for the stationary cases, but they had to keep the Reynolds numbers high due to the limitations of wall functions approach. More recently, Iacovides [10] carried out computations of periodic flow and heat transfer through stationary and rotating ducts for square cross section with rib-roughened walls. He considered a zonal model and a low-Re model. The low-Re model produced a more realistic heat transfer variation in the separation zone and reasonable Nusselt number levels. A numerical study was performed by Rigby [11] for flow in a rotating internal square duct with ribbed walls and the k–ω turbulence model was employed. Some modifications were proposed and applied to the original wall boundary condition of ω to achieve reasonable flow topology, and Reynolds numbers were low. Saidi and Sundén [12–14] used a combination of an Explicit Algebraic Stress Model and a low-Re version of the k–ε model to study the flow and heat transfer in a rib-roughened square duct. The results showed that using the EASM improved the prediction of some fluid flow phenomena, although there was no significant difference in its performance compared to the linear eddy viscosity method regarding the mean flow (friction factor) and heat transfer values.

The ribbed duct geometry in this investigation is set identical to that of [6] because local thermal and hydraulic measurements are available. Such measurements appear very rarely in the literature. Two methods to model the turbulent stresses (EVM and EASM) are employed and their results are compared. Thus it is possible to evaluate the methods and their performances as prediction tools of internal blade cooling.

The geometric configuration of the considered problem is depicted in Fig. 1. The figure shows the computational domain of the problem. The duct has a square cross section, with square ribs on two opposite walls. This geometry has a pitch to rib height ratio of 9 ($p/e=9$) and rib height to hydraulic diameter ratio of 0.1 ($e/D_h=0.1$).

2 Mathematical Model

The method is steady-state one and incompressible flow is assumed. The density is thus constant, and further the thermophysical properties are assumed constant. First, the velocities encountered are so low that compressibility are not important. Second, the natural convection effects are omitted. For ribbed ducts, due to existence of many repeated ribs, the fully developed situation is dominating in the major part of the ducts. Rau et al. [6] studied the periodicity in their experiment and found that the flow becomes periodic after a certain entry distance. These evidences

---

Contributed by the International Gas Turbine Institute for publication in the ASME JOURNAL OF TURBOMACHINERY. Manuscript received at ASME Headquarters March 2001. Associate Editor: R. Bunker.

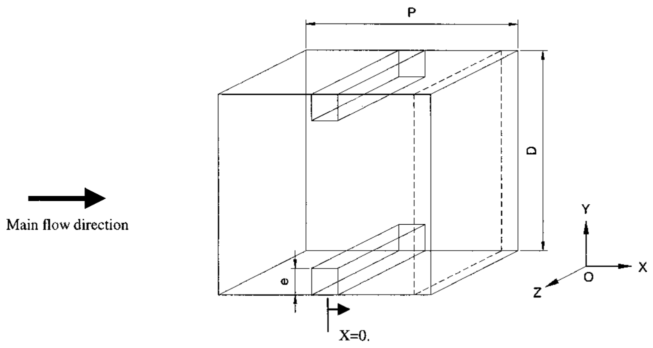

Fig. 1 One module of the two-sided ribbed square duct, aspect ratio is unity (dashed lines show the plane in Fig. 2)

show that periodicity is a reasonable assumption. The fluid is assumed to be Newtonian, and the viscous dissipation is neglected in the energy equation.

The governing equations are the steady-state continuity, the time-averaged Navier–Stokes, and the energy equation for turbulent flow, i.e.,

$$\frac{\partial}{\partial x_j}(\rho U_j)=0 \tag{1}$$

$$\frac{\partial}{\partial x_j}(\rho U_j U_i)=-\frac{\partial P}{\partial x_i}+\frac{\partial}{\partial x_j}\left[\mu\left(\frac{\partial U_i}{\partial x_j}+\frac{\partial U_j}{\partial x_i}\right)\right]+\frac{\partial}{\partial x_j}(-\rho\overline{u_i u_j}) \tag{2}$$

$$\frac{\partial}{\partial x_j}(\rho U_j T)=\frac{\partial}{\partial x_j}\left[\frac{\mu}{Pr}\frac{\partial T}{\partial x_j}-\rho\overline{u_j t}\right] \tag{3}$$

An incompressible flow is considered. The assumption of fully developed periodic conditions is applicable for ribbed ducts in many cases. It has been shown experimentally that after a number of ribs, periodic fully developed flow prevails in which the mean velocity and thermal fields are periodically repeated with a constant shift. Moreover, the periodicity is pointed out and proved by experimental evidence in the considered case [6]. The procedure chosen here to handle periodicity is the same as suggested by Patankar et al. [15] and has then been applied extensively. One introduces,

$$P=-\beta x+p^* \tag{4}$$

where β resembles the nonperiodic pressure gradient and P^* is the periodic part of pressure in the main flow direction. In the energy equation, a constant heat flux boundary condition is applied because this prevailed in the experimental setup.

The periodic thermally developed regime for repeated wall heat transfer can be handled by considering the temperature profiles at positions of $(x,x+p)$ and $(x+p,x+2p)$ to have identical shapes, but they will be shifted up (in the heating case) by a constant value, so that:

$$T(x+p,y,z)-T(x,y,z)=T(x+2p,y,z)-T(x+p,y,z)\ldots=\gamma\cdot p \tag{5}$$

It may easily be proved that:

$$\gamma=\dot{Q}/\dot{m}c_p p \tag{6}$$

where Q is the rate of heat input (over one pitch length) to the fluid. The temperature field can be written as

$$T(x,y,z)=T^*(x,y,z)+\gamma x \tag{7}$$

and T^* is the periodic part of the temperature field. Furthermore, inserting this decomposition in the energy equation will add a source term like $-\rho U\gamma$ to the right-hand side of Eq. (3).

2.1 Turbulence Models.

Several models have been suggested for prediction of turbulent flow and heat transfer problems [16]. Due to their capability and stability, two-equation models accompanied by the eddy viscosity concept have become popular because in engineering computations they provide reasonable overall results at least for simple cases. In this investigation two low-Re versions of the k–ε model by Abe et al. [17] (AKN hereafter) and Chang et al. [18] (CHC hereafter) have been employed. It has been theoretically proved that these models remove the singular point problem accompanied with the friction velocity scale in separated flows. Instead of the friction velocity, these models use the Kolmogorov velocity scale [17], u_ε in Eq. (14), and the $\sqrt{k}$ (k turbulent kinetic energy) in [18], respectively. In addition, these models do not have the problem of the initially guessed values of k and ε, which has been reported with other models, [14]. These two models can be summarized by the equations:

Turbulent kinetic energy

$$\frac{\partial}{\partial x_j}(\rho U_j k)=\frac{\partial}{\partial x_j}\left[\left(\mu+\frac{\mu_t}{\mathrm{Pr}_k}\right)\frac{\partial k}{\partial x_j}\right]-\rho\overline{u_i u_j}\frac{\partial U_i}{\partial x_j}-\rho\varepsilon \tag{8}$$

Turbulent dissipation

$$\frac{\partial}{\partial x_j}(\rho U_j\varepsilon)=\frac{\partial}{\partial x_j}\left[\left(\mu+\frac{\mu_t}{\mathrm{Pr}_\varepsilon}\right)\frac{\partial\varepsilon}{\partial x_j}\right]-C_{\varepsilon 1}\frac{\varepsilon}{k}\rho\overline{u_i u_j}\frac{\partial U_i}{\partial x_j}-C_{\varepsilon 2}f_\varepsilon\rho\frac{\varepsilon^2}{k} \tag{9}$$

Turbulent viscosity

$$\mu_t=C_\mu f_\mu\rho\frac{k^2}{\varepsilon} \tag{10}$$

Turbulence Re number

$$\mathrm{Re}_t=\frac{\rho k^2}{\mu\varepsilon} \tag{11}$$

Nondimensional wall distance

$$y^*=\frac{\rho u_\varepsilon y}{\mu} \tag{12}$$

Reynolds number based on $\sqrt{k}$:

$$\mathrm{Re}_k=\frac{\sqrt{k}y}{\nu} \tag{13}$$

The Kolmogorov velocity scale:

$$u_\varepsilon=(\nu\varepsilon)^{1/4} \tag{14}$$

The damping functions of these models are given in Table 1 and the constants are provided in Table 2.

Table 1 Model damping functions

Model	f_μ	f_ε
AKN	$\left[1-\exp(-\frac{y^*}{14})\right]^2\left[1+\frac{5}{\mathrm{Re}_t^{3/4}}\exp\left\{-(\frac{\mathrm{Re}_t}{200})^2\right\}\right]$	$\left[1-\exp(-\frac{y^*}{3.1})\right]^2\left[1-0.3\exp\left\{-(\frac{\mathrm{Re}_t}{6.5})^2\right\}\right]$
CHC	$[1-\exp(-0.021\mathrm{Re}_k)]^2\left[1+\frac{31.66}{\mathrm{Re}_t^{5/4}}\right]$	$[1-0.01\exp(-\mathrm{Re}_t)]^2[1-\exp\{-0.0631\mathrm{Re}_k\}]$

Table 2 Model constants

Model	C_μ	$C_{\varepsilon 1}$	$C_{\varepsilon 2}$	Pr_k	Pr_ε
AKN	0.09	1.44	1.92	1.0	1.3
CHC	0.09	1.5	1.9	1.4	1.4

Two methods have been employed for calculations of the Reynolds stresses. The first one is the eddy viscosity model (EVM) and the second one is the explicit algebraic stress model (EASM) of Speziale and Xu [19]. In the EVM the ''Reynolds stresses'' are calculated as:

$$\overline{u_i u_j} = \frac{2}{3} k \delta_{ij} - 2 \frac{\mu_t}{\rho} \overline{S_{ij}} \tag{15}$$

$$\overline{u_i u_j} = \frac{2}{3} k \delta_{ij} - \alpha_1^* \frac{k^2}{\varepsilon} \overline{S_{ij}} - \alpha_2^* \frac{k^3}{\varepsilon^2} \overline{(S_{ik}\omega_{kj}} + \overline{S_{jk}\omega_{ki}}$$

$$+ \alpha_3^* \frac{k^3}{\varepsilon^2} \left(S_{ik} S_{kj} - \frac{1}{3} \overline{S_{kl} S_{kl}} \delta_{ij} \right) \tag{16}$$

$\overline{S_{ij}}$ and $\overline{\omega_{ij}}$ are the mean rate of strain tensor and mean vorticity tensor, respectively, i.e.:

$$\overline{S_{ij}} = \frac{1}{2} \left(\frac{\partial U_i}{\partial x_j} + \frac{\partial U_j}{\partial x_i} \right) \tag{17}$$

$$\overline{\omega_{ij}} = \frac{1}{2} \left(\frac{\partial U_i}{\partial x_j} - \frac{\partial U_j}{\partial x_i} \right) \tag{18}$$

and $\alpha_{1,2,3}^*$ are EASM model constants, which are calculated as:

$$\alpha_1^* = \frac{(1+2\xi^2)(1+6\eta^5) + \left(\frac{5}{3}\right)\eta^2}{(1+2\xi^2)(1+2\xi^2+\eta^2+6\beta_1\eta^6)} \alpha_1 \tag{19}$$

$$\alpha_{2,3}^* = \frac{(1+2\xi^2)(1+\eta^4) + \left(\frac{2}{3}\right)\eta^2}{(1+2\xi^2)(1+2\xi^2+\beta_{2,3}\eta^6)} \alpha_{2,3} \tag{20}$$

$$\alpha_1 = \left(\frac{4}{3} - C_3 \right) g \qquad \alpha_2 = \frac{1}{2} \left(\frac{4}{3} - C_3 \right) (2 - C_5) g^2$$

$$\alpha_3 = \left(\frac{4}{3} - C_3 \right) (2 - C_4) g^2 \tag{21}$$

$$g = \left(\frac{1}{2} C_1 + \frac{P_k}{\varepsilon} - 1 \right)^{-1} \tag{22}$$

P_k in Eq. (22) is equal to

$$-\rho \overline{u_i u_j} \frac{\partial U_i}{\partial x_j}$$

and the model constants are:

$$C_1 = 6.80 \quad C_2 = 4.20 \quad C_3 = 0.36 \quad C_4 = 1.25 \quad C_5 = 0.40$$

$$\beta = 7.0 \quad \beta_2 = 6.3 \quad \beta_3 = 4.0$$

In Eqs. (19) and (20), η and ξ are given by:

$$\eta = \frac{1}{2} \frac{\alpha_3}{\alpha_1} \frac{k}{\varepsilon} (\overline{S_{ij}} \overline{S_{ij}})^{1/2} \tag{23}$$

$$\xi = \frac{\alpha_2}{\alpha_1} \frac{k}{\varepsilon} (\overline{\omega_{ij}} \overline{\omega_{ij}})^{1/2} \tag{24}$$

The turbulent heat flux term $\overline{-u_j t}$ has been modeled using the commonly applied Simple Eddy diffusivity model:

$$-\overline{u_j t} = \frac{\mu_t}{\mathrm{Pr}_t} \frac{\partial T}{\partial x_j} \tag{25}$$

The molecular Pr number is set as Pr=0.7 while the turbulent Pr_t number is set as $\mathrm{Pr}_t = 0.89$.

2.2 Boundary Conditions. Periodic boundary conditions are applied at the inlet and outlet of every periodic module (which is equal to one pitch in the ribbed wall duct). This condition is defined as (U,V,W are velocity components, P, k, and ε are pressure, turbulent kinetic energy, and turbulent energy dissipation, respectively):

$$\Phi(x,y,z) = \Phi(x+L,y,z) \tag{26}$$

$$\Phi = U, V, W, P^*, k, \varepsilon \tag{27}$$

The boundary conditions at walls are imposed as:

$$U = V = W = k = 0 \tag{28}$$

and

$$q_w = \mathrm{const} \tag{29}$$

$$\varepsilon_w = 2 \frac{\mu}{\rho} \left(\frac{\partial \sqrt{k}}{\partial n} \right)^2 \tag{30}$$

where n represents the normal wall distance. Due to symmetry, a quarter of the duct cross section has been taken as the computational domain, and the symmetry boundary condition (zero gradients) has been applied there.

2.3 Auxiliary Equations. To calculate the friction factor and Nusselt numbers, some additional equations are needed. These are:

The Reynolds number is defined as

$$\mathrm{Re} = \frac{\rho U_b D}{\mu} \tag{31}$$

The friction factor (mean value) is defined as

$$f = \frac{\beta D/4}{\rho U_b^2 / 2} \tag{32}$$

The local Nusselt number is defined as

$$\mathrm{Nu} = \frac{-\partial T}{\partial n} \frac{D}{T_w - T_b} \tag{33}$$

The mean Nusselt numbers for the walls are calculated by averaging the Nusselt numbers over the wall area, according to,

$$\overline{\mathrm{Nu}} = \frac{1}{A} \int \mathrm{Nu} \, dA \tag{34}$$

The rms values of vertical and streamwise fluctuations have been calculated via the respective values of the components of the Reynolds stress tensor computed in the EASM method. The rms of the streamwise fluctuations is calculated as:

$$u_{\mathrm{rms}} = \sqrt{\overline{uu}} \tag{35}$$

The rms of the vertical fluctuations is calculated as (because V is the transverse velocity component):

$$v_{\mathrm{rms}} = \sqrt{\overline{vv}} \tag{36}$$

3 Numerical Solution Procedure

The employed finite-volume computer code uses a collocated grid arrangement and employs the Rhie and Chow [20] method to interpolate values of velocity at the control volume faces. The SIMPLEC [21] algorithm is employed to handle the coupling between pressure and velocity. The hybrid scheme is used for determination of convective fluxes in all equations. It was found, during the course of this study, that using higher order schemes like QUICK [22] and Van Leer [23] for determination of convective fluxes did not have any significant effects on the final results, the differences were observed to be in order of 1 percent. This small difference between higher order convective flux methods and the hybrid scheme can be explained by the fact that in this investigation the turbulence source terms were more significant than any numerical diffusion caused by the hybrid scheme. A certain method is developed [14] to deal with the de-coupling of the velocity and Reynolds stress fields in the EASM calculations. A nonuniform grid with grid refinement has been applied. The application of a low-Re model made it necessary that the y^+ value of the first grid point adjacent to a wall is close to unity. In this work y^+ is in the range of 0.5–0.8. The calculations were terminated when the absolute residuals of all the variables became less than 10^{-6}. The underrelaxation factors for all calculations were set to values in the range of 0.5–0.6. The nonperiodic pressure gradient β is specified to create a flow field. Through the rate of mass flow, the Reynolds number is coupled to β. Thus various values of β correspond to various Reynolds numbers. Grid influence issues were considered, and grid refinement was applied, in both the normal and the axial directions. The presented results were obtained by $70\times28\times39$ grid points and the results (mean Nu and f values) changed less than on percent as further refinement to $110\times28\times38$ grid points was applied (grid refinement was already applied in the normal to wall directions, namely Y and Z directions). Because the y^+ value is kept so low, the mesh near wall becomes skewed, and the effects of this have been studied by testing a $70\times45\times45$ grid. No changes have been observed using this grid. These conclusions hold for both the AKN and CHC models. The CPU times for calculations with EASM were about 70 percent higher than those of EVM.

4 Results

The case considered in the present investigation has been studied experimentally in [6]. The duct has a square cross section with ribs on two opposite walls. The pitch to rib height ratio is 9 ($p/e=9$), and rib height to hydraulic diameter is equal to 0.1 ($e/D_h=0.1$).

The overall average results are shown in Table 3. This table presents a comparison between predicted Nu numbers and friction factors at Re=30,000. The results for the friction factor show that both methods (EVM and EASM) predict the experimental values of the friction factor within an error band of 3–6 percent, and Nusselt numbers within −5 to 8 percent error. The Nusselt number values are normalized with Nu_0 (see Table 3) which is the same formula used for normalization of the experimental results. However, the comparison shows that the EASM predicts a larger friction factor than the EVM and with greater deviations from the experiment. The difference in results between the AKN and CHC turbulence models is small.

Figure 2 compared the secondary flow pattern predicted by the two methods (EVM and EASM with AKN) in a Y–Z plane, where $X/e=5.5$. As can be seen, the EASM predicts a stronger secondary flow pattern, and the maximum velocities shown in this figure are about 2–3 percent of mean velocity in the main flow direction. This figure shows only a quarter of the duct cross section. Unfortunately, there is no experimental evidence supporting the strength or direction of this secondary flow pattern.

Figure 3 shows the experimental [6] and calculated values for the U (streamwise) velocity component between the ribs at $Y/e=0.1$, i.e., the U values very close to the surface. As shown in the figure, the calculations captured the general trend fairly well, although brief differences occur at positions between $X/e=1.5$ and 4. This region corresponds to the separation bubble in both the experiments and the calculations. All models predict the zero velocity point somewhere around $X/e=2.4$, but the experiments indicates a position closer to $X/e=3.4$. This means that the calculations predict a separation zone in the symmetry plane almost 30 percent smaller than in the experimental measurements.

Table 3 Comparisons of mean thermal-hydraulic predictions, Re=30,000. Deviations from experimental data are given in percent. $f_0=0.046\ \mathrm{Re}^{-0.2}$, $\mathrm{Nu}_0=0.023\ \mathrm{Re}^{0.8}\mathrm{Pr}^{0.4}$ are the values of a corresponding square duct.

Method	f/f_0, error %	$\mathrm{Nu}/\mathrm{Nu}_0$, error % (floor between ribs)	$\mathrm{Nu}/\mathrm{Nu}_0$, error % (side wall)
EVM with AKN	10.31, +3%	2.53, +8%	2.10, -2%
EASM with AKN	11.25, +12.5%	2.40, -5%	2.10, -2%
EVM with CHC	9.86, -1%	2.42, +3%	2.20, +3%
EASM with CHC	11.67, +16.7%	2.43, +4%	2.24, +5%

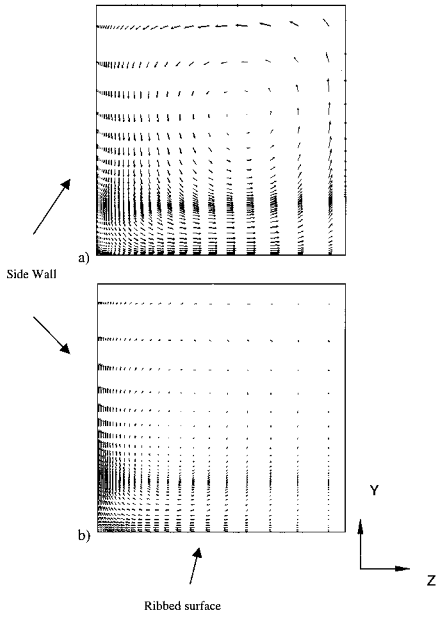

Fig. 2 Secondary flow vectors in a *YZ* cross-sectional plane, at $X/e=5.5$; (*a*) EASM and (*b*) EVM predictions (AKN predictions)

The vertical velocity component (V) is measured at the symmetry line (see Fig. 4). This velocity component (V), which is negative just downstream of the rib, can be related to the flow entrainment from the mainstream to the recirculation zone. This flow brings the cold air from the center in contact with the wall and an increase in heat transfer is expected. As can be seen in the figure, all models give very similar results. However, no model predicts the value and location of the minimum.

The rms values of the vertical velocity component at a distance $Y/e=0.3$ from the wall in the symmetry plane are presented in Fig. 5. The experimental results are compared with the square root of the $\overline{vv}$ component of the Reynolds stress tensor calculated with the EASM. The predictions are qualitatively correct, and the sec-

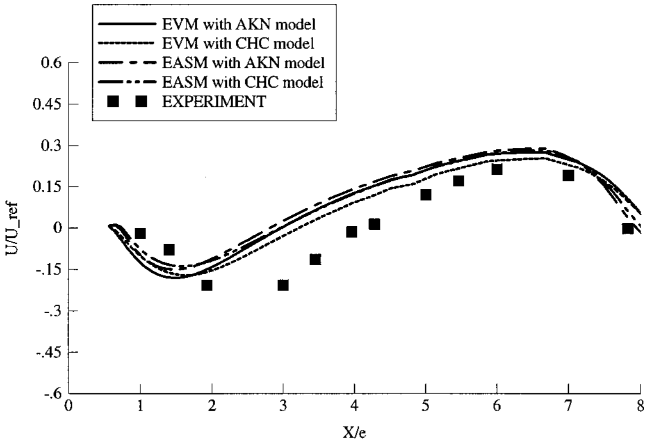

Fig. 3 *U* component between two adjacent ribs at $Y/e=0.1$ in the symmetry plane ($y/D=0.05$)

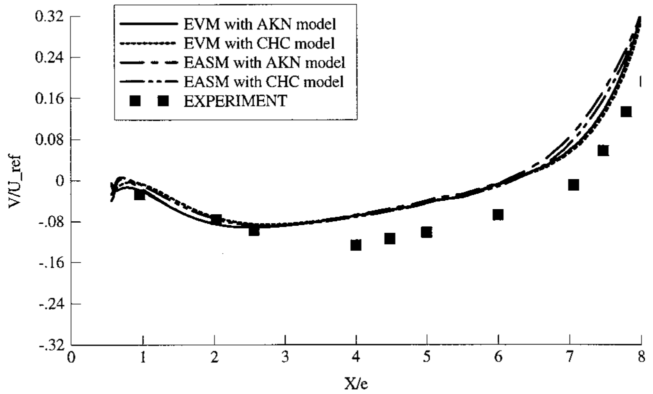

Fig. 4 Flow entrainment between the ribs at $Y/e=1$ in symmetry plane

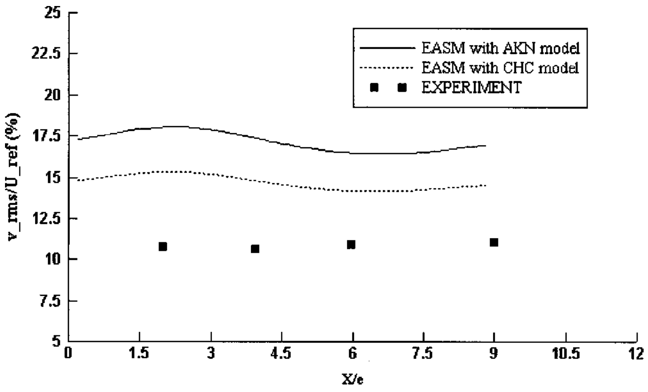

Fig. 7 Vertical fluctuation component in the duct center, $Y/D=0.5$, $Z/D=0.5$

ond rise in the vertical fluctuation component just upstream the second rib is well captured. However, the predicted value at the maximum point is higher than in the experiments and it occurs at a smaller *X/e* value.

Figures 6 and 7 show the measured and calculated rms values on the centerline for the streamwise (Fig. 6) and the vertical (Fig. 7) components. The calculated and experimental results show only modest changes of these components in the *X* direction so the trend is well captured by the simulations. In Fig. 6 showing the streamwise component, it can be seen that both models overpredict the values, but the CHC model presents rms fluctuations closer to the experimental ones. A similar pattern is shown in Fig. 7 for the vertical fluctuating component. Overprediction appears here too, but again the CHC model provides values closest to the experimental values.

The mean Nu for the floor between adjacent ribs and the smooth side walls are also compared in Table 3. As shown, all methods predict the Nusselt numbers in reasonable agreement with experiment. Figure 8 shows a comparison between predicted and experimental local values (normalized with $\mathrm{Nu}_0=0.023\mathrm{Re}^{0.8}\mathrm{Pr}^{0.4}$ for a smooth duct). The prediction methods provide almost the same trend, but the EASM predicts lower values being closest to the experimental results [6] for the AKN case. The trend of the variations in Nu number between adjacent ribs along this symmetry line is not the same for these two low-Re models. As is evident in Fig. 8, the calculations with AKN result in a sharp rise in Nu just downstream of a rib and then Nu increases all the way until the point of maximum Nu is reached. This occurs at around $X/e=7$. On the other hand, the CHC model gives a sharper rise downstream of a rib, but then Nu falls and reaches a local minimum at around $X/e=2.5$, and afterward there is a smooth increase again.

Finally, the Nu enhancement pattern on the smooth side wall for both methods (EASM and EVM) is shown in Fig. 9. A similar diagram has been provided experimentally and reproduced from [6]. The experimental pattern shows somewhat higher values near

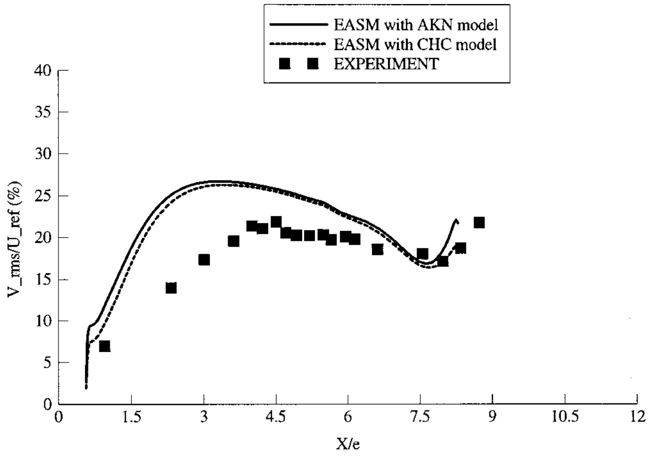

Fig. 5 The rms of vertical fluctuation velocity component between the ribs at $Y/e=0.3$ in symmetry plane

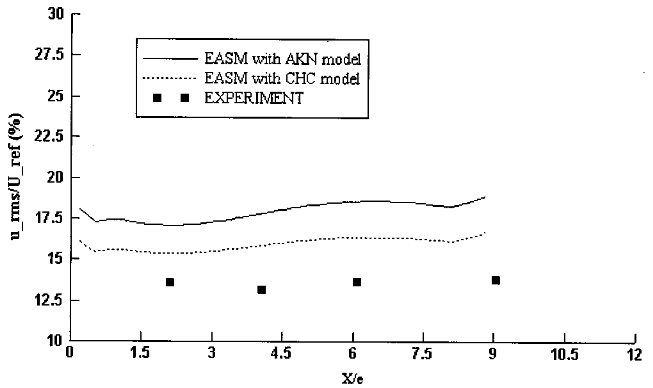

Fig. 6 Streamwise fluctuation component in the duct center, $Y/D=0.5$, $Z/D=0.5$

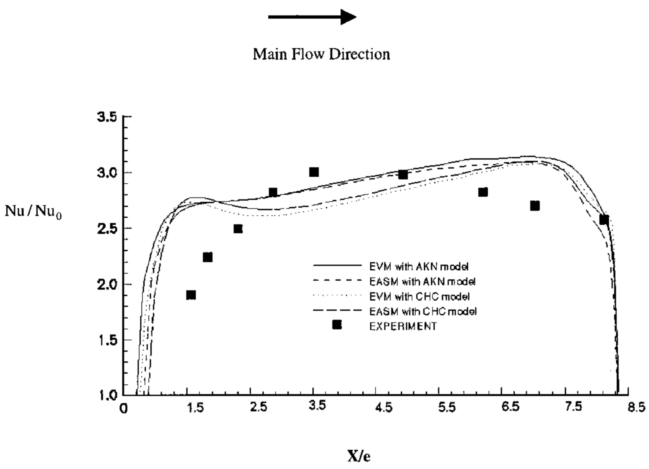

Fig. 8 Nusselt number enhancement predictions compared to experimental results of [6] along the symmetry line of the duct between adjacent ribs

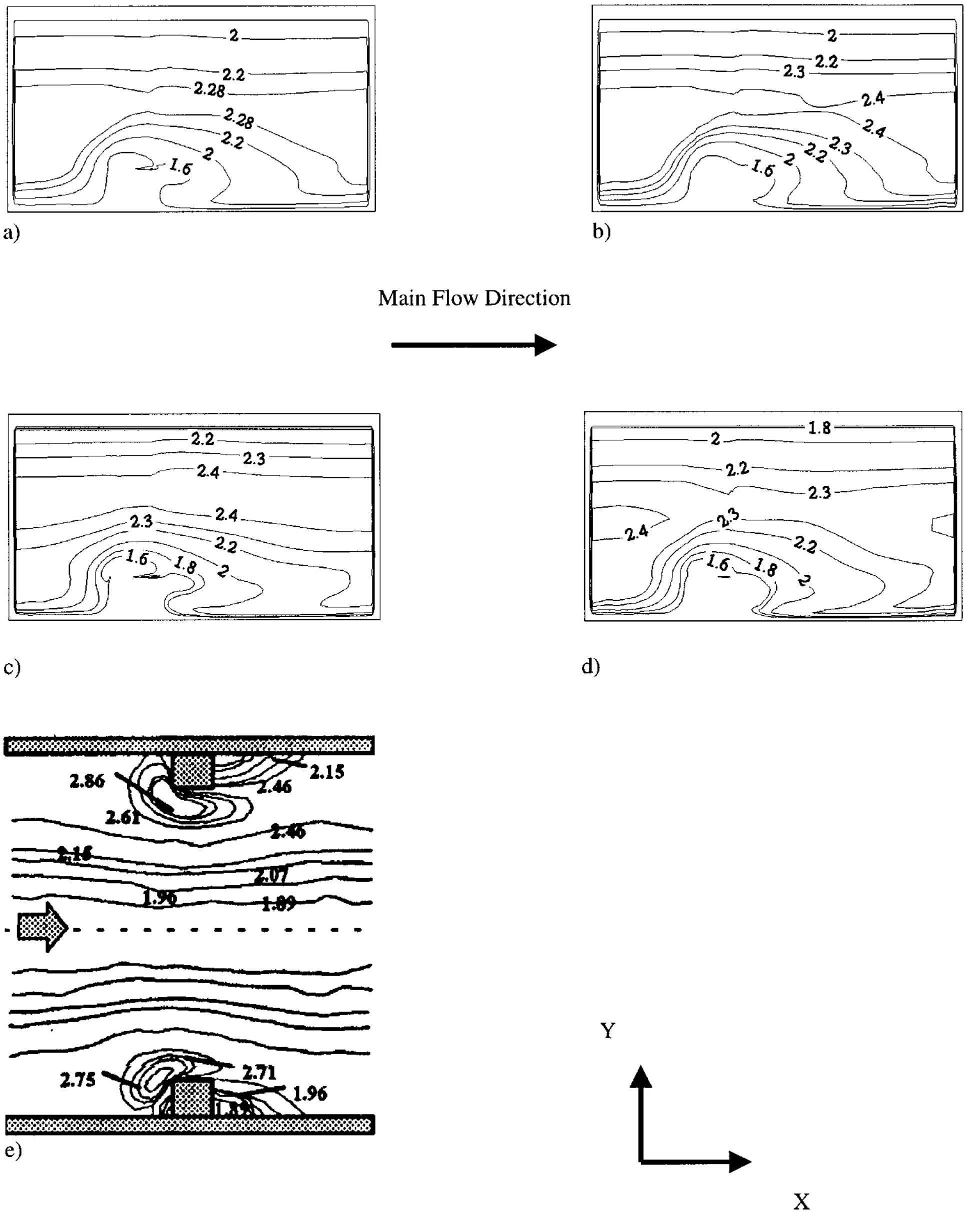

Fig. 9 Nusselt number enhancement pattern over the smooth side wall: (*a*) EVM with AKN model, (*b*) EASM with AKN model, (*c*) EVM with CHC model, and (*d*) EASM with CHC model predictions, (*e*) experimental results from Rau et al. [6]

the edges of the upper upstream side of the rib, but lower values near the symmetry line at $Y/D=0.5$ compared to the calculations.

The EASM predictions downstream of the rib demonstrate a smoother change in Nu than the EVM for the AKN cases, but this difference is not as pronounced in the CHC calculations. This fact may be attributed to the existence of a stronger secondary flow, which in turn enhances the mixing process downstream the rib.

5 Conclusions

A numerical investigation was carried out for prediction of the thermal-hydraulic characteristics in a ribbed duct. Two different methods for determination of the Reynolds stresses were considered. The test case was chosen identical to an experimental run [6]. To investigate the effects of the method for low-Re modeling, two different models, AKN [17] and CHC [18] were used.

The ability to predict the average Nusselt number was similar for EVM and EASM, and also for the low-Re models AKN and CHC. The friction factor predictions showed that the EVM gave friction factors in close agreement with the experimental result, but the EASM gave large errors. The error in the friction factor prediction using EASM was higher as the CHC model was applied. However, the average Nu was predicted with satisfactory accuracy for all models. The EASM predicted stronger secondary flow compared to EVM, but there are no experimental data available to confirm or oppose this fact.

The EASM method requires larger computing times. The convergence behavior of the two low-Re models, AKN and CHC, was found to be similar and they did not have the singular point problem in the recirculation zone.

This study has shown that experimental studies with emphasis on local values of the heat transfer and the flow fields are needed as turbulence models are evaluated. The local values will enable careful examination and judgement of different turbulence models. It is also necessary that the experimental investigations provide the local Reynolds stress fields and preferably turbulent heat fluxes, because the new advanced turbulence models are capable of predicting these fields as well as the mean flow field properties.

As the detailed discussion in the previous section made clear, the models used in the present study could not provide a perfect picture of the velocity and thermal fields. Although all models tested have been able to provide the overall thermal and flow field features reasonably well, further research in turbulence modeling is needed and new or improved models have to be examined in demanding test cases of engineering relevance.

Nomenclature

c_p = specific heat
D = hydraulic diameter
e = rib height
f = friction factor
f_ε, f_μ = damping functions, Table 1
g = auxiliary variable
n = wall normal distance
Nu = Nusselt number
p = rib pitch, distance between ribs
P = pressure
P^* = periodic pressure
P_k = production term in k equation
Pr_k = turbulence Prandtl number for k
Pr_ε = turbulence Prandtl number for ε
Q = total heat added in a modular pitch
Re_k = Reynolds number based on velocity scale $\sqrt{k}, = \frac{\sqrt{k}y}{\nu}$
Re_t = turbulence Reynolds number
S_{ij} = mean rate of strain tensor
T = mean temperature
T^* = periodic part of temperature
t = fluctuating temperature
U,V,W = components of mean velocity
u_ε = Kolmogorov velocity scale
u,v,w = fluctuating velocity components
y^+ = wall distance
$\alpha_{1,2,3}$ = EASM model variables
β = nonperiodic pressure gradient
γ = periodic temperature gradient
μ = dynamic viscosity (molecular)
μ_t = turbulence viscosity
ν = kinematic viscosity
ω_{ij} = mean vorticity tensor

Subscripts

b = bulk
w = wall

References

[1] Han, J. C., 1988, ''Heat Transfer and Friction Characteristics in Rectangular Channels With Rib Turbulators,'' ASME J. Heat Transfer, **110**, pp. 321–328.
[2] Liou, T., and Hwang, J., 1993, ''Effect of Ridge Shapes on Turbulent Heat Transfer and Friction in a Rectangular Channel,'' Int. J. Heat Mass Transf., **36**, pp. 931–940.
[3] Johnson, B. V., Wagner, J. H., Steuber, G. D., and Yeh, F. C., 1994, ''Heat Transfer in Rotating Serpentine Passages With Selected Model Orientations for Smooth or Skewed Trip Walls,'' ASME J. Turbomach., **116**, pp. 738–744.
[4] Parsons, J. A., Han, J. C., and Zhang, Y., 1995, ''Effect of Model Orientation and Wall Heating Condition on Local Heat Transfer in a Rotating Two-Pass Square Channel With Rib Turbulators,'' Int. J. Heat Mass Transf., **38**, pp. 1151–1159.
[5] Hwang, J., and Liou, T., 1997, ''Heat Transfer Augmentation in a Rectangular Channel With Slit Rib-Turbulators on Two Opposite Walls,'' ASME J. Turbomach., **119**, pp. 617–623.
[6] Rau, M., Cakan, M., Moeller, D., and Arts, T., 1998, ''The Effects of Periodic Ribs on the Local Aerodynamics and Heat Transfer Performance of a Straight Cooling Channel,'' ASME J. Turbomach., **120**, pp. 368–375.
[7] Acharya, S., Dutta, S., Myrum, T. A., and Baker, R. S., 1993, ''Periodically Developed Flow and Heat Transfer in a Ribbed Duct,'' Int. J. Heat Mass Transf., **36**, pp. 2069–2082.
[8] Liou, T., Hwang, J., and Chen, S., 1993, ''Simulation and Measurement of Enhanced Turbulent Heat Transfer in a Channel With Periodic Ribs on One Principal Wall,'' Int. J. Heat Mass Transf., **36**, pp. 507–517.
[9] Prakash, C., and Zerkle, R., 1995, ''Prediction of Turbulent Flow and Heat Transfer in a Ribbed Rectangular Duct With and Without Rotation,'' ASME J. Turbomach., **117**, pp. 255–264.
[10] Iacovides, H., 1996, ''Computation of Flow and Heat Transfer Through Rotating Ribbed Passages,'' Biennial Colloquium on Computational Fluid Dynamics, UMIST, pp. 3-19-3-24.
[11] Rigby, D. L., 1998, ''Prediction of Heat and Mass Transfer in a Rotating Ribbed Coolant Passage With a 180 Degree Turn,'' ASME Paper No. 98-GT-329.
[12] Saidi, A., and Sundén, B., 1998, ''Calculation of Convective Heat Transfer in Square-Sectioned Gas Turbine Blade Cooling Channels,'' ASME Paper No. 98-GT-204.
[13] Saidi, A., and Sundén, B., 1999, ''On Prediction of Turbulent Convective Heat Transfer in Rib-Roughened Rectangular Cooling Ducts,'' *Engineering Turbulence Modeling and Experiments—4*, W. Rodi and D. Laurence, eds., Elsevier Science, pp. 763–772.
[14] Saidi, A., and Sundén, B., 2000, ''Numerical Simulation of Turbulent Convective Heat Transfer in Square Ribbed Ducts,'' Numer. Heat Transfer, Part A, **36**, pp. 67–88.
[15] Patankar, S. V., Liu, C. H., and Sparrow, E. M., 1977, ''Fully Developed Flow and Heat Transfer in Ducts Having Streamwise-Periodic Variations of Cross-Sectional Area,'' ASME J. Heat Transfer, **99**, pp. 180–186.
[16] Wilcox, D. C., 1993, *Turbulence Modeling for CFD*, DCW Industries, Inc., USA.
[17] Abe, K., Kondoh, T., and Nagano, Y., 1994, ''A New Turbulence Model for Predicting Fluid Flow and Heat Transfer in Separating and Reattaching Flows—I. Flow Field Calculations,'' Int. J. Heat Mass Transf., **37**, pp. 139–151.
[18] Chang, K. C., Hsieh, W. D., and Chen, S. C., 1995, ''A Modified Low-Reynolds-Number Turbulence Model Applicable to Recirculating Flow in Pipe Expansion,'' ASME J. Fluids Eng., **117**, pp. 417–423.
[19] Speziale, C. G., and Xu, X.-H., 1995, ''Towards the Development of Second-Order Closure Models for Non-Equilibrium Turbulent Flows,'' Proc. 10th Symp. on Turbulent Shear Flows, Penn. State University, pp. 23-7–23-12.
[20] Rhie, C. M., and Chow, W. L., 1983, ''Numerical Study of the Turbulent Flow Past an Airfoil With Trailing Edge Separation,'' AIAA J., **21**, pp. 1525–1532.
[21] Van Doormal, J. P., and Raithby, G. D., 1984, ''Enhancement of the SIMPLE Method for Predicting Incompressible Fluid Flows,'' Numer. Heat Transfer, **7**, pp. 147–163.
[22] Leonard, B. P., 1979, ''A Stable and Accurate Convective Modeling Procedure Based on Quadratic Upstream Interpolation,'' Comput. Methods Appl. Mech. Eng., **19**, pp. 59–98.
[23] Van Leer, B., 1974, ''Towards the Ultimate Conservative Difference Scheme. II. Monotonocity and Conservation Combined in a Second-Order Scheme,'' J. Comput. Phys., **14**, pp. 361–370.

A Study of Convective Heat Transfer in a Model Rotor–Stator Disk Cavity

R. P. Roy

G. Xu

J. Feng

Department of Mechanical and Aerospace Engineering,
Arizona State University,
Tempe, AZ 85287

In this study, the fluid (air) temperature field and the convective heat flux distribution on the rotor disk surface were measured and computed in a model rotor–stator disk cavity. Both mainstream flow and secondary air flow were provided. The radial distribution of convective heat transfer coefficient on the rotor disk surface, which was calculated as the ratio of the local heat flux and the local temperature difference across the thermal boundary layer on the disk, is also reported. In the experiments, the disk rotational Reynolds number, Re_ϕ, ranged from 4.65×10^5 to 8.6×10^5, and the nondimensional secondary air flow rate, c_w, ranged from 1504 to 7520. The secondary air was supplied at the cavity hub. All experiments were carried out at the same mainstream air flow rate, $Re_m=5.0\times10^5$. The cavity fluid temperature distribution was measured by traversing miniature thermocouples, and the rotor disk surface temperature and heat flux were measured by a quasi-steady thermochromic liquid crystal technique in conjunction with resistance temperature detectors embedded in the disk. The measurements are compared with predictions from the commercial CFD code Fluent. The Fluent simulations were performed in the rotationally symmetric mode using a two-zone description of the flow field and the RNG $k-\varepsilon$ model of turbulence. The convective heat transfer coefficient distribution on the rotor disk surface exhibited the influence of the source region and the core region of air flow in the cavity. In the source region, which is radially inboard, the convective heat transfer was dominated by the secondary air flow rate. In the core region, which is radially outboard, the heat transfer was dominated by the rotational motion of the fluid relative to the rotor disk. An empirical correlation for the local Nusselt number on the rotor disk surface is suggested for the core region. [DOI: 10.1115/1.1371776]

1 Introduction

In the first few stages of high-temperature gas turbines, secondary air must be supplied to the rotor–stator cavities to prevent ingestion of hot mainstream gas. Cooler air bled from the compressor is usually used for this purpose. However, this exacts a penalty on turbine cycle performance. Secondary air usage must therefore be reduced to the extent possible while maintaining its sealing and cooling functions. Efficient use of secondary air requires a good understanding of the flow and thermal fields in the cavities and the mainstream gas path.

Heat transfer in rotor–stator cavities has been studied extensively. Kapinos [1] invoked the Reynolds analogy to obtain a relation for the local convective heat transfer coefficient at the rotor disk surface for the case of superposed radial outflow in the cavity. He assumed that the fluid radial velocity remained invariant across the cavity axial gap, the core fluid tangential velocity was zero, and the core fluid temperature was the same as the secondary fluid temperature at cavity inlet. These assumptions may not be appropriate in many situations. Metzger [2] and Owen et al. [3] measured the average convective heat transfer coefficient at the rotor disk surface, based on an average disk surface heat flux and the temperature difference between the surface and the incoming secondary air. The results from these studies show that the average convective heat transfer coefficient on the rotor disk surface increases with the disk rotational speed and secondary air flow rate. Also, the average heat transfer coefficient is smaller than the corresponding free-disk value when c_w is lower than the free disk pumping flow rate. Qureshi et al. [4] measured the local fluid temperature at five radial positions in a disk cavity to obtain radial-segment-averaged convective heat transfer coefficients for $3000<c_w<18{,}600$ and $4\times10^5<\mathrm{Re}_\phi<1.86\times10^6$. However, neither the axial location of the temperature sensor in the cavity gap nor the fluid temperature variation across the gap were reported. Dibelius and Heinen [5] obtained the convective heat transfer coefficient distribution on the rotor disk surface by measuring the heat flux on the disk and the air temperature at the cavity midplane (gap ratio $G=0.0125$, 0.0625, and 0.1375; $b=800$ mm) at six radial positions for $c_w=0$, 6.7×10^4, 13.4×10^4, and $6.0\times10^5<\mathrm{Re}_\phi<1.93\times10^6$.

Metzger et al. [6] employed the transient thermochromic liquid crystal technique to measure the local convective heat transfer rate on a rotor disk in a rotor–stator configuration ($G=0.1$, $b=102$ mm). The secondary air was introduced at the cavity hub and at other radial locations. The experiments were performed at $\mathrm{Re}_\phi=2.71\times10^5$, 4.64×10^5 and $850<c_w<1200$. The local convective heat transfer coefficient, which was based on the secondary air temperature at cavity inlet as the reference temperature, was observed to decrease radially up to the disk rim. The heat transfer coefficient at $r/b=0.8$ was only 15 percent of the value given by the free disk correlations of Kreith et al. [7] and Dorfman [8]. Bunker et al. [9,10] used the transient liquid crystal technique to measure the radial distribution of convective heat transfer coefficient on a rotor disk in a rotor–stator cavity ($G=0.05$, 0.1, 0.15; $b=100$ mm). The ranges of the experiments were: $2.0\times10^5<\mathrm{Re}_\phi<5.0\times10^5$, $835<c_w<1670$. In this study, the fluid mixed-mean temperature radial profile was estimated from a heat balance and then used to determine the convective heat transfer coefficient. However, as the authors pointed out, the calculations did not account for either recirculating flows or rotation of the core fluid in the cavity.

Kim and Kleinman [11] extended the work of Metzger et al. [6] in a study of the convective heat transfer coefficient and cooling effectiveness distributions on the rotor disk of a rotor–stator cav-

---

Contributed by the International Gas Turbine Institute for publication in the ASME JOURNAL OF TURBOMACHINERY. Manuscript received at ASME Headquarters March 2001. Associate Editor: R. S. Bunker.

ity ($G=0.1$, $b=125$ mm) with rim seals. The experimental ranges were: $\mathrm{Re}_\phi=6.56\times10^5$, 6.84×10^5; $2070<c_w<16{,}540$. The results that were obtained may be questioned since the local fluid temperature in the cavity could not be due simply to the mixing of the main and secondary flows at their respective inlet temperatures as was assumed, but would also be affected by the heat transfer between the fluid and the rotor and stator disks.

Influences of the secondary air flow rate, rotor disk speed, and axial gap ratio on the rotor disk heat transfer in a disk cavity with throughflow of secondary air were studied by Long [12]. The secondary air inlet temperature was used to calculate the local convective heat transfer coefficient on the rotor disk. More recently, Chen et al. [13] and Wilson et al. [14] employed the adiabatic rotor disk temperature corresponding to the secondary air inlet temperature to obtain the heat transfer coefficient distribution.

At engine conditions, windage influences the disk cavity air temperature. Depending on the experimental condition in a laboratory rig, this influence may or may not be significant.

As the preceding literature survey demonstrates, most of the studies to date have used either the secondary air inlet temperature or the corresponding adiabatic rotor disk temperature as the reference temperature to obtain the local convective heat transfer coefficient on the rotor disk. The local core fluid temperature would have been more appropriate as the reference temperature [15]. It should also be noted that neither stator vanes nor rotor blades were involved in the experimental apparatus, although they are known to play key roles in mainstream gas ingestion into the cavity and consequently can influence the fluid temperature field in the cavity.

In the present study, the fluid temperature distribution and the local convective heat transfer coefficient distribution on the rotor disk surface were measured in a rotor–stator cavity. The heat transfer coefficient was obtained as the ratio of the local surface heat flux and the local temperature difference across the thermal boundary layer. Key features such as stator vanes, rotor blades, and rim discouragers (seals) were provided in the apparatus. Computations giving the same quantities were carried out using the commercial CFD code Fluent [16].

2 Experimental Apparatus and Procedure

The rotor–stator disk cavity is shown schematically in Fig. 1. Mainstream air is supplied by a centrifugal blower (Hauck) equipped with a variable-frequency motor drive and capable of providing up to 1.42 $\mathrm{m^3/s}$ (≅3000 cfm) air flow rate. This flow rate is measured by a pitot tube rake (with five pitot tubes) located in the suction duct of the blower. The rotor–stator section is located on the suction side of the blower, allowing the section to remain optically accessible from the radial as well as axial (air inlet) directions. The secondary air is supplied through a 38.1 mm I.D. pipe by another centrifugal blower (Hauck) also equipped with a variable-frequency motor drive and capable of providing up to 0.12 $\mathrm{m^3/s}$ (≅250 cfm) air flow rate. The secondary air flow rate is measured by a turbine flowmeter (EG&G Flow Technology).

The 0.403 m (15.875 in.) diameter aluminum rotor disk is equipped with 52 partial height blades (≈ one-third of actual height in engine). This partial blade height allows the axial velocity of the mainstream air to approach or exceed the rotor disk rim speed at specific combinations of the air flow rate and disk speed. A variable-frequency motor drive can rotate the disk up to a speed of 5000 rpm. The plexiglass stator disk, of the same diameter as the rotor disk, is equipped with 59 partial height vanes. The vanes turn the mainstream air by 55 deg, imparting a realistic swirl to the flow. A 2 kW radiant heater unit of annular cross section was constructed and installed adjacent to the aluminum rotor disk on the side away from the cavity. In this unit, the heater is embedded in a ceramic plate and heats the rotor disk to desired temperature levels.

The axial gap, s, between the rotor and stator disks was maintained at 16.5 mm. This corresponds to an axial gap ratio, G, of 0.084.

The method employed to measure the convective heat flux distribution on the rotor disk utilizes a thermochromic liquid crystal (TLC) coating along with video data acquisition and computer-assisted image analysis. A thin layer ($\delta_e=1$ mm) of low-thermal-conductivity epoxy, Hysol RE2039 ($k_e=0.21$ W/m/K), covers the disk surface facing the cavity over the region $r=44.5$–180.2 mm. Black paint is then sprayed on the epoxy layer to serve as background for enhancing the brightness and color contrast of the TLC. Next, TLC is airbrushed onto on the black paint (≈10 μm coating thickness). The TLC used in the present work is R45C1W (Hallcrest, Inc.) for which the nominal temperatures for initiation of red, green, and blue colors are, respectively, 45°C, 45.5°C, and 46°C. The temperature for green color display at 70 percent threshold was found by calibration to be 45.8 ±0.2°C. During experiments, the TLC color information is obtained by analysis of standard chrominance video signals.

Four resistance temperature detectors (RTDs) were embedded in the rotor disk at an axial distance of 7 mm from the disk surface facing the cavity at four radial locations ($r=81$, 110, 144, and 173 mm) to measure the substrate (aluminum) temperature. The RTD signals are transmitted through a slip-ring to a data acquisition system (Analogic 6500). For each experiment, a best-fit quadratic relation was constructed from the four temperatures. The instantaneous substrate temperature, T_s, at any radial position was then obtainable from this relation (see Fig. 8).

To measure the fluid temperature distribution in the cavity, T-type thermocouples (each a mini-hypodermic probe with needle diameter of 0.2 mm, time constant ≈10 ms, Omega) were installed at the five radial locations shown in Fig. 1(*a*) and traversed axially in the cavity gap. The temperature data were acquired by a FLUKE data acquisition system. The stator disk surface temperatures at the same five radial locations were assumed to be equal to the air temperature measured by the corresponding thermocouples at an axial position very close to the stator disk. Additionally, the mainstream air and secondary air inlet temperatures were monitored continuously by two J-type thermocouples.

During the experiments, two separate cooling systems were required—one for the slip-ring assembly, and the other for the rotor shaft and bearing adjacent to the rotor disk, which was prone to overheating due to friction.

Each heat transfer experiment was performed in a quasi-steady state manner with the rotor disk cooling down slowly (<0.3°C/min) from its initial temperature of approximately 60°C (the heat-up being by the radiant heater). Assuming the temperature difference across the aluminum substrate between the RTD location and the aluminum–epoxy interface (=6 mm) to be very small, the heat flux at any position on the rotor disk surface can be calculated as:

$$q''_{w,ro}=k_e\frac{(T_s-T_w)_{ro}}{\delta_e} \tag{1}$$

where k_e is equal to 0.21 W/m/K, δ_e is equal to 1 mm, and T_w is the disk surface temperature corresponding to green color display at 70 percent threshold ($T_w=45.8\pm0.2°\mathrm{C}$). This heat flux, $q''_{w,ro}$, is comprised of the convective heat flux, $q''_{w,ro,\mathrm{conv}}$, from the rotor disk surface to the cavity fluid, and the radiative heat flux, $q''_{w,ro,\mathrm{rad}}$, from the rotor disk surface to the stator disk surface. The radiative heat flux can be estimated as

$$q''_{w,ro,\mathrm{rad}}=\frac{\sigma[(T_{w,ro}+273.15)^4-(T_{w,st}+273.15)^4]}{1/\varepsilon_1+1/\varepsilon_2-1} \tag{2}$$

where σ is the Stefan–Boltzmann constant ($5.67\times10^{-8}\ \mathrm{W/m^2/K^4}$), ε_1 is the emissivity of the rotor surface (≈0.97), and ε_2 is the emissivity of the stator disk surface (≈0.80). $T_{w,st}$ was equated to the average of the stator disk sur-

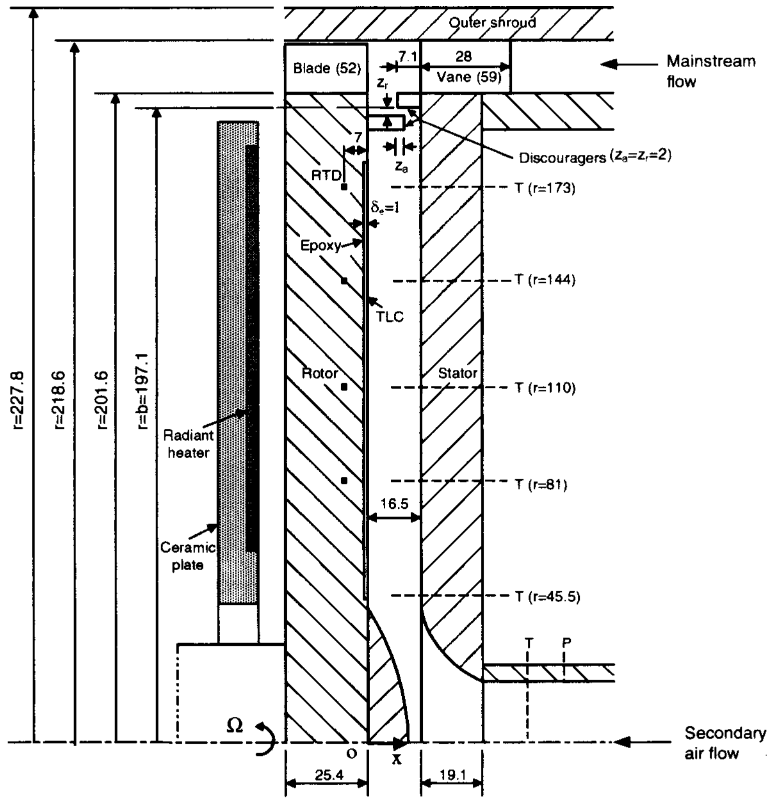

(a) The disks and cavity

All dimensions are in mm

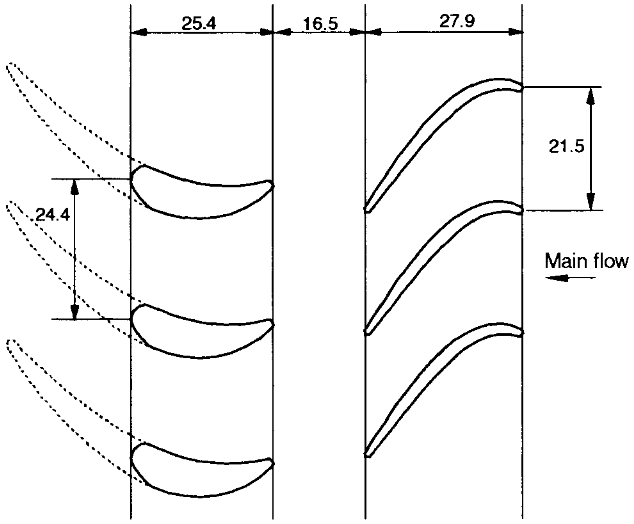

(b) Schematic of guide vanes and blades

Fig. 1 The rotor–stator system

face temperatures at the five thermocouple locations. The local convective heat transfer coefficient may now be calculated as

$$h(r)=\frac{q''_{w,ro,\mathrm{conv}}(r)}{T_{w,ro}-T_{\mathrm{ref}}(r)}=\frac{q''_{w,ro}(r)-q''_{w,ro,\mathrm{rad}}}{T_{w,ro}-T_{\mathrm{ref}}(r)} \tag{3}$$

The fluid temperature at the outer edge of the thermal boundary layer on the rotor disk at any radial location was adopted as the value of T_{ref} at that position. To determine the location of the thermal boundary layer outer edge at each thermocouple position, a separate experiment was performed at each experimental condition. In this experiment, the axial distribution of cavity fluid temperature was measured at each of the five radial positions within 2 minutes of when the rotor disk surface temperature at that position reached 45.8°C (the TLC transition temperature at 70 percent green color intensity). For each experiment, a best-fit curve was constructed on the basis of the five measured T_{ref} values (see Fig.

8). The T_{ref} value at any radial position could then be obtained from this curve.

The adiabatic disk temperature based on the local air temperature and the local velocity difference $(\Omega r - V_\phi)$ may also be used as the reference temperature in Eq. (3) [17]:

$$T_{\text{ref}}(r) = T_{\text{air}}(r) + R\,\frac{(\Omega r - V_\phi)^2}{2C_p} \tag{4}$$

where $R = \text{Pr}^{1/3}$. If $\beta = 0.4$, then at $r = b \approx 0.197$ m,

$$R\,\frac{(\Omega r - V_\phi)^2}{2C_p} \approx 0.6°\text{C}.$$

This was not done in the present work. The use of adiabatic disk temperature in determining h will increase the rotor disk Nusselt number by between about 3 percent (near the hub) and about 10 percent (near the rim).

In calculating Nu_r and Gr_r, air properties at the local film temperature were used, this temperature being the average of the rotor disk surface temperature (45.8°C) and the local thermal boundary layer outer edge temperature.

The effect of natural convection was not considered since $\text{Gr}_r/\text{Re}^2_{\phi,r}$ was less than 0.08 for all experiments.

The experimental conditions are given in Table 1. The nondimensional free disk pumping mass flow rate at each rotational speed is also shown. Uncertainty estimates of the measurements were carried out using standard techniques for single-sample measurements [18]. Table 2 lists the results.

The rise in temperature of the cavity air due to windage was estimated for the conditions of Table 1 and found to be less than 1°C.

3 Free-Disk Experiments and Validation of Disk Surface Heat Flux Measurement

Heat transfer experiments were carried out first with the rotor disk operating as a free disk to validate the experimental method because heat transfer from free disks is well understood [3,7,8]. For these experiments, the stator disk, secondary air inlet pipe, and the outer shroud were removed from the apparatus. The ambient air temperature was equated to the average of the outputs of two J-type thermocouples located at a distance of 600 mm from the rotor disk slightly above and slightly below the disk shaft centerline. This temperature was adopted as T_{ref} in Eq. (3) to determine the local convective heat transfer coefficient on the disk surface.

Table 1 Experimental conditions

Re_m	Re_ϕ	c_w	$c_{w,fd}$	m_s/m_m (%)
5.0×10^5	4.65×10^5	1504	7490	0.51
5.0×10^5	4.65×10^5	3008	7490	1.03
5.0×10^5	4.65×10^5	7520	7490	2.55
5.0×10^5	7.0×10^5	1504	10390	0.51
5.0×10^5	7.0×10^5	3008	10390	1.03
5.0×10^5	7.0×10^5	7520	10390	2.55
5.0×10^5	8.6×10^5	1504	12250	0.51
5.0×10^5	8.6×10^5	3008	12250	1.03
5.0×10^5	8.6×10^5	7520	12250	2.55

Table 2 Estimated uncertainties

	T_s	$T_{w,ro}$	T_f	$q''_{w,ro}$	h	Nu_r	Re_ϕ	c_w	Re_m
Uncertainty	± 0.3°C	± 0.2°C	± 0.3°C	± 8 %	± 10 %	± 10 %	± 2 %	± 5 %	± 3 %

The local Nusselt number versus the local rotational Reynolds number plots for $\text{Re}_\phi = 4.75\times10^5$ (2000 rpm) and 7.14×10^5 (3000 rpm) are shown in Fig. 2. Three distinct regions can be identified in this plot: a laminar boundary layer region, a region of transition from laminar to turbulent boundary layer, and a turbulent boundary layer region. Transition appears to commence at $\text{Re}_{\phi,r} \approx 2\times10^5$ and the boundary layer is fully turbulent when $\text{Re}_{\phi,r} > 3\times10^5$. This is consistent with the results obtained from flow visualization using the china-clay technique by Gregory et al. [19].

In the laminar boundary layer region, $\text{Re}_{\phi,r} \leq 2\times10^5$, the measured values fall consistently below the predictions by a correlation from Kreith et al. [7], the discrepancy decreasing as the local rotational Reynolds number increases (i.e., radially outward). This discrepancy is caused by the alteration of the boundary layer on the rotor disk by the disk hub cap, of 42 mm radius and 12 mm height at its center, Fig. 1(*a*). The influence of the hub cap decreases radially outward. It is noteworthy that while the local Nusselt numbers obtained from experiments at the two rotational speeds essentially overlap for $\text{Re}_{\phi,r} > 1\times10^5$, the local Nusselt numbers for 3000 rpm are smaller than those for 2000 rpm at $\text{Re}_{\phi,r} < 1\times10^5$. This is because the radial position corresponding to any given value of $\text{Re}_{\phi,r}$ is closer to the hubcap at the higher disk speed.

In the turbulent boundary layer region, $\text{Re}_{\phi,r} > 3\times10^5$, the measurements are compared with the predictions by a correlation due to Dorfman [8]. The agreement is reasonably good, the average difference being about 5 percent.

4 Computational Method

The commercial CFD code Fluent, version 5.0, was used to calculate the fluid flow and heat transfer in the rotor–stator disk cavity and the main gas path. The simulations were carried out in the steady rotationally symmetric mode (all variables are assumed to be ϕ-independent). The two-layer model of Wolfstein [20] was used. In this model, the flow domain is divided into two layers (or zones) on the basis of the Reynolds number:

$$\text{Re}_y = \frac{\rho\sqrt{k}\,y}{\mu} \tag{5}$$

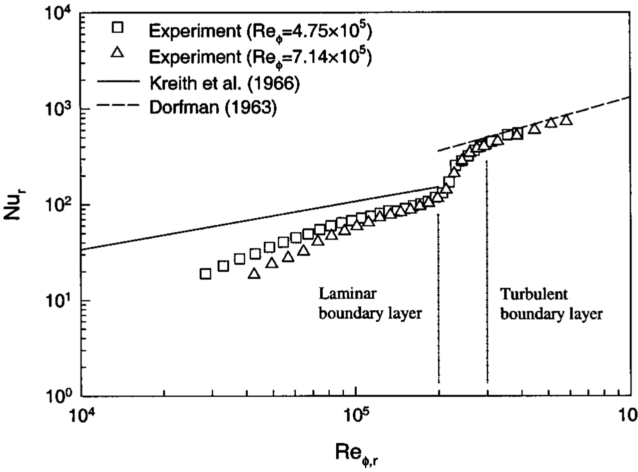

Fig. 2 Radial distribution of Nusselt number for free rotor disk

where y is the normal distance from the wall. When $\mathrm{Re}_y > 200$, the high Reynolds number renormalization group (RNG) model k and ε equations were solved. When $\mathrm{Re}_y < 200$, only the k equation was solved and ε and the turbulent viscosity were calculated from algebraic equations suggested by Chen and Patel [21]. This choice for the present calculations had its basis in a study [22] in which the Daily and Nece [23] experiments were simulated using several models. The best agreement with the experimental data was achieved with the aforementioned model.

A large number of grid points were packed near the walls while the grid away from the wall was relatively coarse. Also, the grid point adjacent to the wall was always at $y^+ < 1$.

Steady three-dimensional simulations in which the near-wall description was replaced by a wall function were also performed.

Figure 3 (to be discussed in detail later) shows the computational domain for the rotationally symmetric simulations. The vane was not included explicitly; instead, the swirl velocity imparted by it was added to the axial velocity of the incoming mainstream air, and this provided the velocity boundary condition at the vane trailing edge plane. The other boundary conditions were: the pressure at the main gas path exit (the rotor blade was not included), the secondary air velocity at the supply pipe entrance, and isothermal rotor and stator disk surfaces. On the rotor disk surface, the temperature was set to 45.8°C (the TLC transition temperature), while the average of the measured temperatures at five radial positions was prescribed at the stator disk surface.

5 Results and Discussion

Experimental and computational results for the fluid temperature distribution in the disk cavity and the convective heat transfer coefficient distribution on the rotor disk surface are presented and compared here. The effects of the significant parameters—for example, secondary air flow rate and rotor disk speed—are described. Additionally, the convective heat transfer coefficients are compared with selected measurements from the literature.

The flow field in the disk cavity was briefly described by Roy et al. [24] on the basis of experiments and simulations. Figure 3 shows the computed flow field for one experimental condition. None of the simulations performed in either the steady rotationally symmetric mode or the steady three-dimensional mode predicted main air ingestion, although tracer gas experiments indicate that ingestion occurred at six of the nine conditions given in Table 1 (all except $c_w = 7520$) [25]. The cavity axial gap was sufficiently large for separate boundary layers to form on the rotor and stator disks at all of the experimental conditions listed in Table 1. A recirculation region developed radially inboard in the cavity, where a strong radial outflow was found close to the rotor disk and a weak inflow near the stator disk. In this, the source region, rotation of the core fluid was minimal. The radial extent of this region increased with the secondary air flow rate, and decreased slightly as the rotor disk speed increased. Radially outboard, in the core region, the flow was dominated by its tangential velocity except when the secondary air flow rate was high (for example, close to the free disk pumping flow rate).

5.1 Fluid Temperature Distribution in the Disk Cavity.

As mentioned earlier, when the rotor disk surface temperature at any of the five thermocouple radial locations reached the TLC transition temperature, the cavity fluid temperature axial distribution was measured quickly (within a 2-minute interval) at that radial location. Figure 4 shows, in a nondimensional form, the axial temperature distribution at the five radial locations for the experiment: $\mathrm{Re}_\phi = 7.0 \times 10^5$, $c_w = 3008$, $\mathrm{Re}_m = 5.0 \times 10^5$. Based on these distributions, the axial positions of 2.5 mm ($x/s = 0.15$), 3 mm ($x/s = 0.18$), 3 mm, 3 mm, and 3 mm from the rotor disk surface were chosen to be the outer edges of the thermal boundary layer on the rotor disk at $r = 45.5$, 81, 110, 144, and 173 mm, respectively, for this experimental condition.

The fluid axial temperature profiles computed by Fluent, also shown in Fig. 4, indicate that, in the source region, the axial temperature gradient at the rotor disk surface becomes steeper radially outward (this is not visible in Fig. 4). This is indicative of an increase in the disk surface heat flux radially outward in the source region, this being aided slightly by the higher thermal conductivity of air as its temperature rises. In the core region, the temperature gradient at the rotor disk decreases radially outward, this contributing to a decrease in the disk surface heat flux in spite of the continued increase in the thermal conductivity of air. These

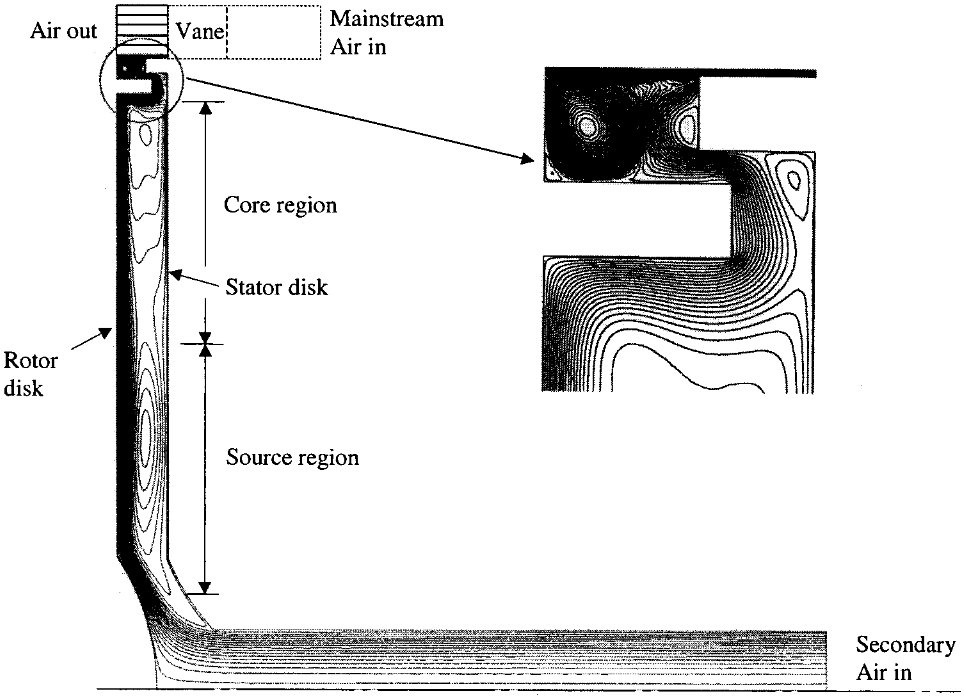

Fig. 3 Computed streamlines for $\mathrm{Re}_\phi = 7.0 \times 10^5$, $c_w = 3008$, $\mathrm{Re}_m = 5.0 \times 10^5$

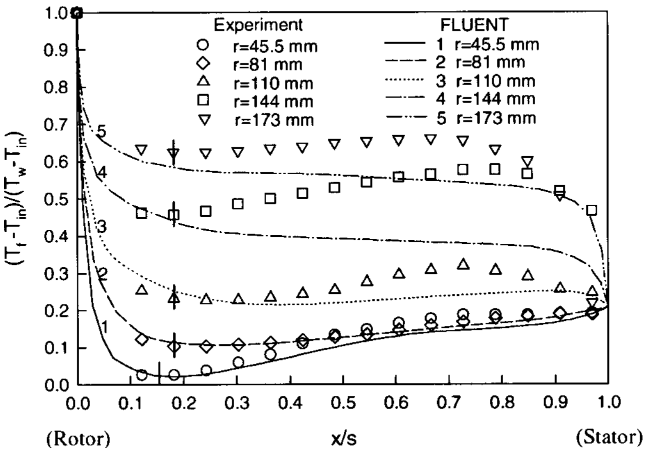

Fig. 4 Fluid temperature distribution in the disk cavity for $Re_\phi=7.0\times10^5$, $c_w=3008$, $Re_m=5.0\times10^5$ ($s=16.5$ mm, $T_w=45.8°C$)

trends will be used in section 5.2 to explain some features of the convective heat transfer coefficient distribution on the rotor disk. Also, radially inboard in the cavity, for example at $r=45.5$ mm, both the measurement and the Fluent calculation indicate a substantial drop in the cavity air temperature axially from the rotor disk. This is mainly due to the strong flow of the incoming secondary air in the region.

In the vicinity of the stator disk, the fluid temperature as measured changed little axially at the two innermost radial locations and decreased as the disk surface was approached at the three radially outboard locations. The measured air temperature near the stator disk was lower at $r=173$ mm compared to that at $r=144$ mm. This is quite possibly due to the combined effects of the ingested cooler mainstream air and heat loss to the stator disk. In the event of ingestion, the cooler mainstream air would mix with the higher temperature cavity air from the vicinity of the rotor disk surface rim and then flow radially inward along the stator disk.

The measured and computed fluid temperatures near the rotor disk surface agree well, Fig. 4, and the measured and computed axial temperature distributions at $r=45.5$ and 81 mm are similar. There are, however, significant differences between the measured and computed distributions away from the rotor disk at the two outermost radial locations. It should be noted that an isothermal boundary condition was prescribed at the stator disk surface in the computations whereas the actual condition at the stator is neither isothermal nor adiabatic. Furthermore, the simulations, which were performed in the rotationally symmetric mode, were unable to predict main gas ingestion in cases where ingestion definitely occurred according to the recent tracer gas experiments performed in this rig. The implication is that the computed flow and thermal fields radially outboard in the disk cavity have some inaccuracies.

5.1.1 Effect of Rotor Disk Speed on the Cavity Fluid Temperature Distribution. Figures 5(*a*, *b*) show, at three disk rotational Reynolds numbers and $c_w=3008$, $Re_m=5.0\times10^5$, the axial distribution of fluid temperature in the disk cavity at $r=81$ and 173 mm, respectively. Both measured and computed distributions are shown. At $r=81$ mm, which is in the source region, the fluid temperature distribution near the rotor disk remained essentially the same at each Re_ϕ, indicating that the heat flux at the disk surface changed little. The fluid temperature near the stator disk increased slightly with Re_ϕ as did the disk surface heat flux. Also, the thermal boundary layer on the rotor disk became thinner as Re_ϕ increased.

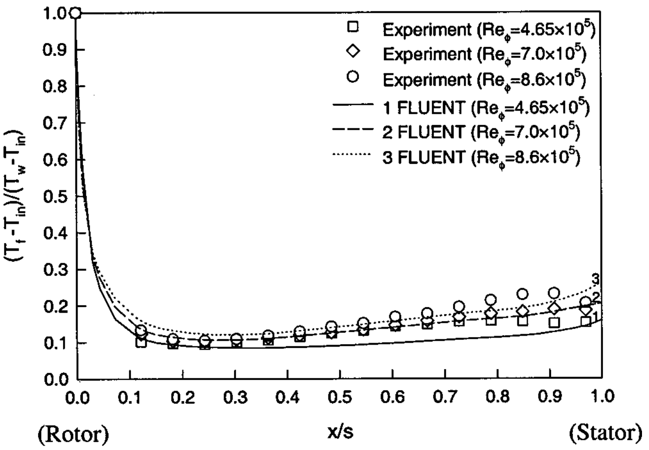

(a) r=81 mm

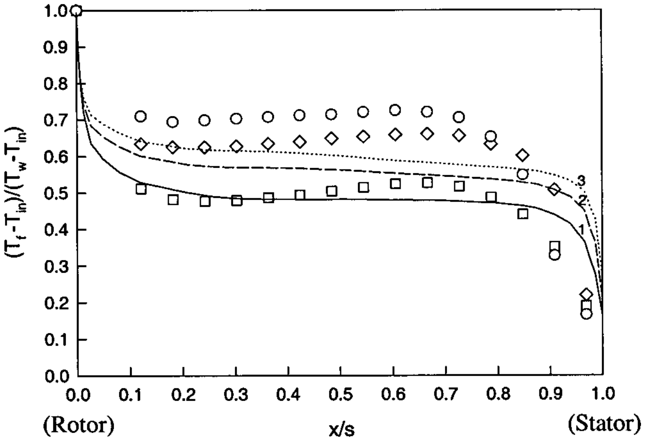

(b) r=173 mm

Fig. 5 Effect of rotor disk speed on the cavity fluid temperature distribution for $c_w=3008$, $Re_m=5.0\times10^5$

5.1.2 Effect of Secondary Air Flow Rate on the Cavity Fluid Temperature Distribution. Figures 6(*a*, *b*) show the measured and computed axial distributions of fluid temperature in the disk cavity at $r=81$ and 173 mm, respectively, at three secondary air flow rates (c_w) and $Re_\phi=7.0\times10^5$, $Re_m=5.0\times10^5$. At both radial locations, the fluid temperature was lower when the secondary air flow rate was higher. The heat flux at the rotor disk surface increased with c_w. At $r=173$ mm, which is in the core region, heat loss to the stator disk increased as c_w decreased. Also, the fluid temperature drop in the axial direction commenced farther from the stator disk as c_w decreased. These trends may be due to ingestion of the cooler main air into the cavity.

5.2 Convection Heat Transfer Coefficient Distribution on the Rotor Disk Surface. During each quasi-steady state experiment, the rotor disk substrate (aluminum) cooled at a rate slightly lower than 0.3°C per minute. The corresponding cooling rate of the air at the rotor disk thermal boundary layer outer edge at the five thermocouple radial locations was substantially lower than 0.3°C per minute. These are shown in Fig. 7 for the experimental condition $Re_\phi=7.0\times10^5$, $c_w=3008$, $Re_m=5.0\times10^5$. In Fig. 8, the radial profiles of the rotor disk substrate temperature and thermal boundary layer outer edge temperature at one time instant ($t=1000$ s) are shown. Each profile could be fitted with a quadratic expression for all time instants. The rotor disk substrate

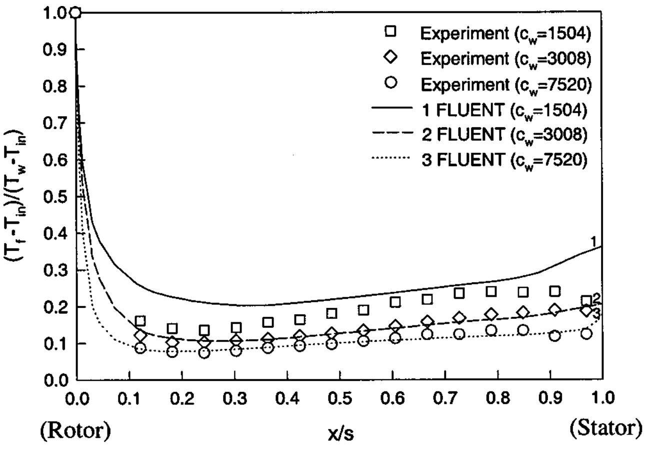

(a) r=81 mm

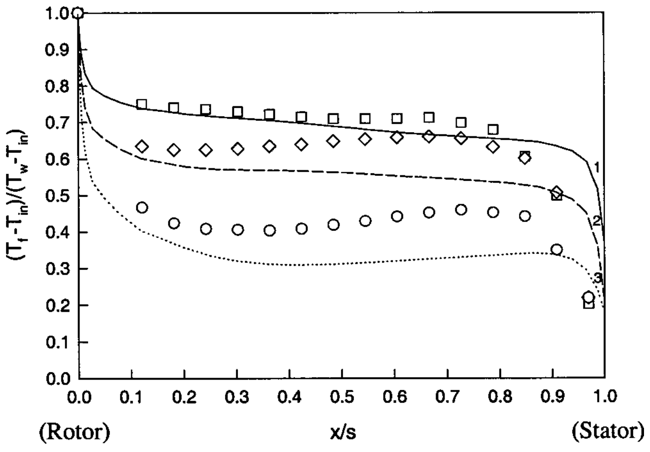

(b) r=173 mm

Fig. 6 Effect of secondary air flow rate on the cavity fluid temperature distribution for $\mathrm{Re}_\phi=7.0\times10^5$, $\mathrm{Re}_m=5.0\times10^5$

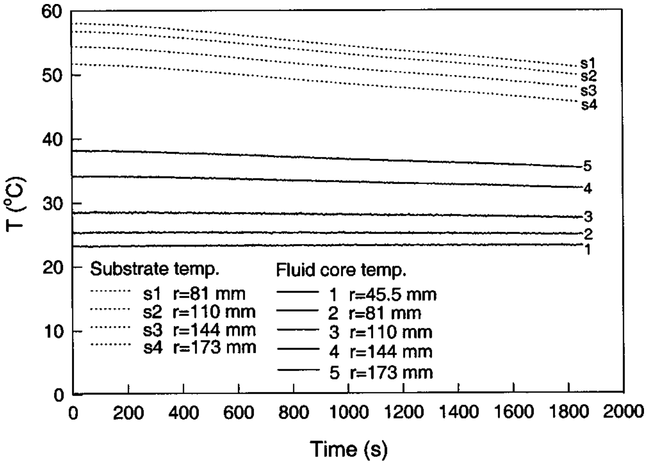

Fig. 7 Measured variation of rotor disk substrate temperature and fluid core temperature with time ($t=0$ s is the beginning of the rotor disk cool-down) for $\mathrm{Re}_\phi=7.0\times10^5$, $c_w=3008$, $\mathrm{Re}_m=5.0\times10^5$

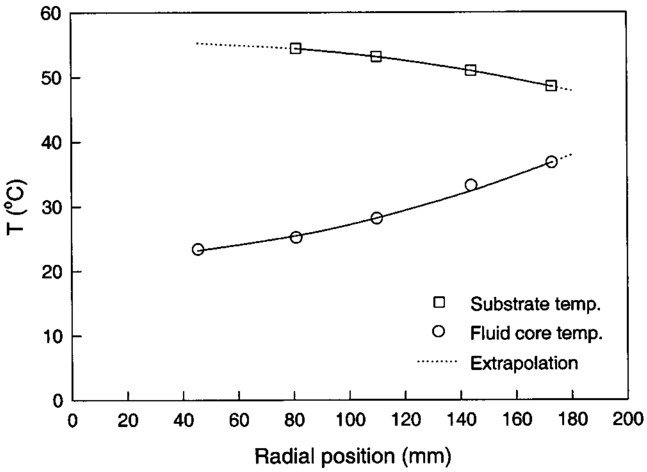

Fig. 8 Measured radial profiles of rotor disk substrate temperature and fluid core temperature at one time instant ($t=1000$ s) for $\mathrm{Re}_\phi=7.0\times10^5$, $c_w=3008$, $\mathrm{Re}_m=5.0\times10^5$

temperature and thermal boundary layer outer edge temperature at the time of TLC color transition at any particular radial position were then obtained from the respective quadratic fits. Figure 9 shows the plot, versus radius, of the measured thermal boundary layer outer edge temperature at the time of TLC color transition on the rotor disk surface. The measured values are slightly higher than those predicted by Fluent.

In Fig. 10, the measured and computed radial distributions of the heat flux at the rotor disk surface are shown for the same experiment. The heat flux is the response to the thermal driving force, (T_w-T_{ref}), and the convective heat transfer coefficient. The measured and computed distributions are similar, although the latter is somewhat higher. An examination of the disk cavity flow field is helpful in understanding the heat flux distribution. The incoming secondary air impinges on the rotor disk at the hub and then flows radially outward. No measurements were made on the hub cap, but the Fluent computation is available. Here, the radial heat flux distribution resembles that due to jet impingement. At the periphery of the hub cap, the calculation shows a sharp decrease in heat flux. A saddle separation point due to a small recirculation bubble is predicted here. This is followed by a sharp increase in heat flux due to reattachment. The TLC measurement began immediately outboard of the hub cap periphery. The heat

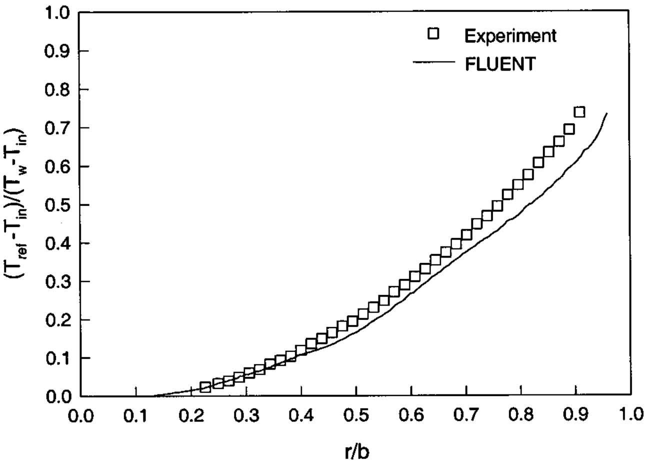

Fig. 9 Thermal boundary layer outer edge temperature at the time of TLC color transition on the rotor disk surface versus radius for $\mathrm{Re}_\phi=7.0\times10^5$, $c_w=3008$, $\mathrm{Re}_m=5.0\times10^5$

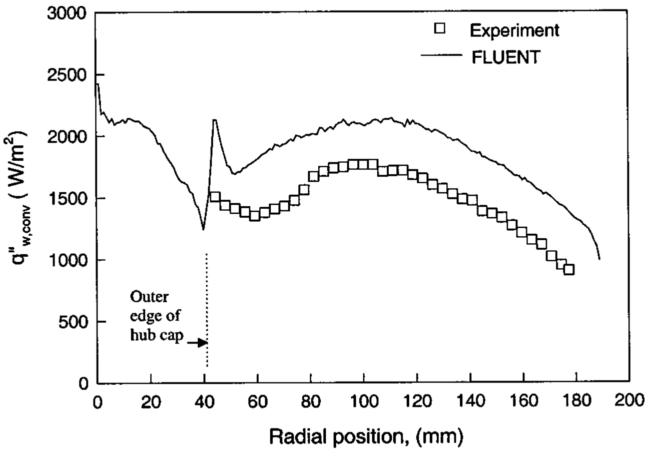

Fig. 10 Radial distribution of heat flux on the rotor disk surface for $Re_\phi=7.0\times10^5$, $c_w=3008$, $Re_m=5.0\times10^5$

flux decreases radially outboard from the high value caused by the reattachment. This is followed by an increase radially outward until the end of the source region is reached. In the core region the heat flux decreases in the radial direction.

Figure 11 shows the radial distribution, based on measurement, of the convective heat transfer coefficient on the rotor disk for the experiment $Re_\phi=7.0\times10^5$, $c_w=3008$, $Re_m=5.0\times10^5$ (the same experiment as Figs. 7–10). In the source region of the cavity where the influence of secondary air flow is strong and the tangential velocity in the fluid core modest, the trend in h is similar to that in the surface heat flux. In the core region, h increases with radius. Referring to Figs. 9 and 10, even though the surface heat flux decreases radially in the core region, the core fluid temperature increases such that the overall effect is an increase in h.

Also shown in Fig. 11 is the radial distribution of h calculated using Fluent. Agreement with the measured distribution is reasonably good, the calculated values being typically 8 percent higher. One factor contributing to this difference may be the isothermal boundary condition at the stator disk surface that was used in the calculations.

The convective heat transfer coefficient distribution at the rotor disk surface predicted by a correlation due to Kapinos [1] is also plotted in Fig. 11. Agreement with the experimental values is good in the core region of the disk cavity. It is less so in the source region where the effect of secondary air impingement is felt.

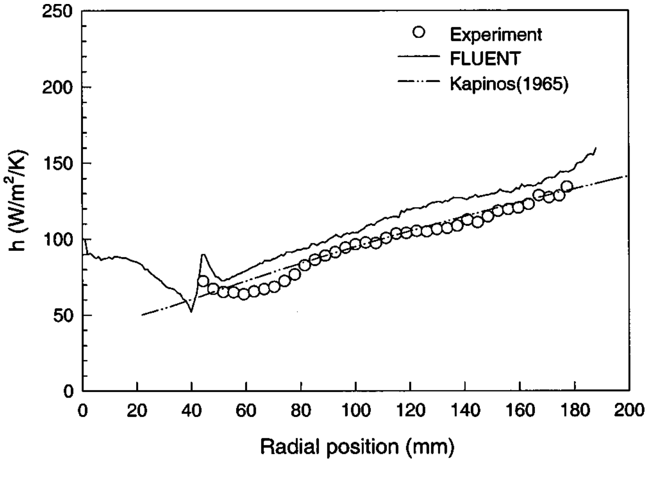

Fig. 11 Convective heat transfer coefficient distribution on the rotor disk surface for $Re_\phi=7.0\times10^5$, $c_w=3008$, $Re_m=5.0\times10^5$

5.2.1 Effect of Rotor Disk Speed on the Convective Heat Transfer Coefficient Distribution. Figures 12(*a–c*) depict the effect of rotor disk speed on the convective heat transfer coefficient distribution on the disk surface at three secondary air flow rates. The influence of rotor disk speed is somewhat different in the source and core regions, and at the different secondary air flow rates.

In the source region, the fluid radial velocity in the rotor disk boundary layer strongly influences the heat transfer at the rotor disk surface. The radial velocity decreases radially outward. The effect of the relative tangential velocity between the rotor disk and the core fluid is substantial especially in the core region where it has a much stronger influence than the flow radial velocity.

At each secondary air flow rate, the relative tangential velocity between the rotor disk and the core fluid increases radially outward in the cavity (see Roy [24] for these results). Also, the relative tangential velocity increases with Re_ϕ. Compounding the complexity of the convective heat transfer at the rotor disk is the ingested cooler mainstream air which probably commences its influence immediately outboard of the source region. The magnitude of ingestion increases as the secondary air flow rate decreases.

The Fluent results for h are also plotted in these figures. Agreement with the measured distribution is good in some regions for certain combinations of Re_ϕ and c_w. In other cases they differ by up to 25 percent.

Some features of the measured h-distributions should be noted. At small radii, $45\,\mathrm{mm}<r<55\,\mathrm{mm}$, the heat transfer coefficients do not differ by much at the three rotor disk speeds. This is especially the case at the two lower secondary air flow rates (c_w). At $r>80\,\mathrm{mm}$, the heat transfer coefficients are significantly affected by the disk speed. The impingement-like peaks at $c_w=1504$ for the two higher disk rotational Reynolds numbers (Re_ϕ) may be due to the ingested mainstream air encountering the rotor disk here.

5.2.2 Effect of Secondary Air Flow Rate on the Convective Heat Transfer Coefficient Distribution. Figures 13(*a–c*) show the influence of secondary air flow rate on the rotor disk convective heat transfer coefficient distribution at three disk rotational speeds. In the source region of the cavity, the heat transfer coefficient increases markedly with the secondary air flow rate. It should be borne in mind that, at a given Re_ϕ, the source region extends radially outward with higher secondary air flow rate. In the core region, the secondary air flow rate influences the heat transfer coefficient at higher Re_ϕ.

5.3 Comparison With Earlier Works. In Fig. 14, the rotor disk convective heat transfer coefficient data from one experiment ($Re_\phi=8.6\times10^5$, $c_w=7520$, $Re_m=5.0\times10^5$) have been compared in the nondimensional format Nu_r versus $Re_{\phi,r}$ with selected data from two earlier works, Dibelius and Heinen [5] and Chen et al. [13], obtained at broadly similar conditions. The latter data were read off the respective figures; as such, some inaccuracy may have been introduced in these.

The present data agree with those of Dibelius and Heinen [5] to within 5 percent. The discrepancy between the present data and those of Chen et al. [13] increases when $Re_{\phi,r}>3\times10^5$. Chen et al. used the secondary air temperature at cavity inlet as T_{ref} to calculate the local convective heat transfer coefficient rather than the corresponding thermal boundary layer outer edge temperature. Since the latter temperature is higher, its use as T_{ref} will provide a higher local h.

The measured h distribution is also compared with the Kapinos correlation [1]. Good agreement is seen for $Re_\phi>3\times10^5$ (the core

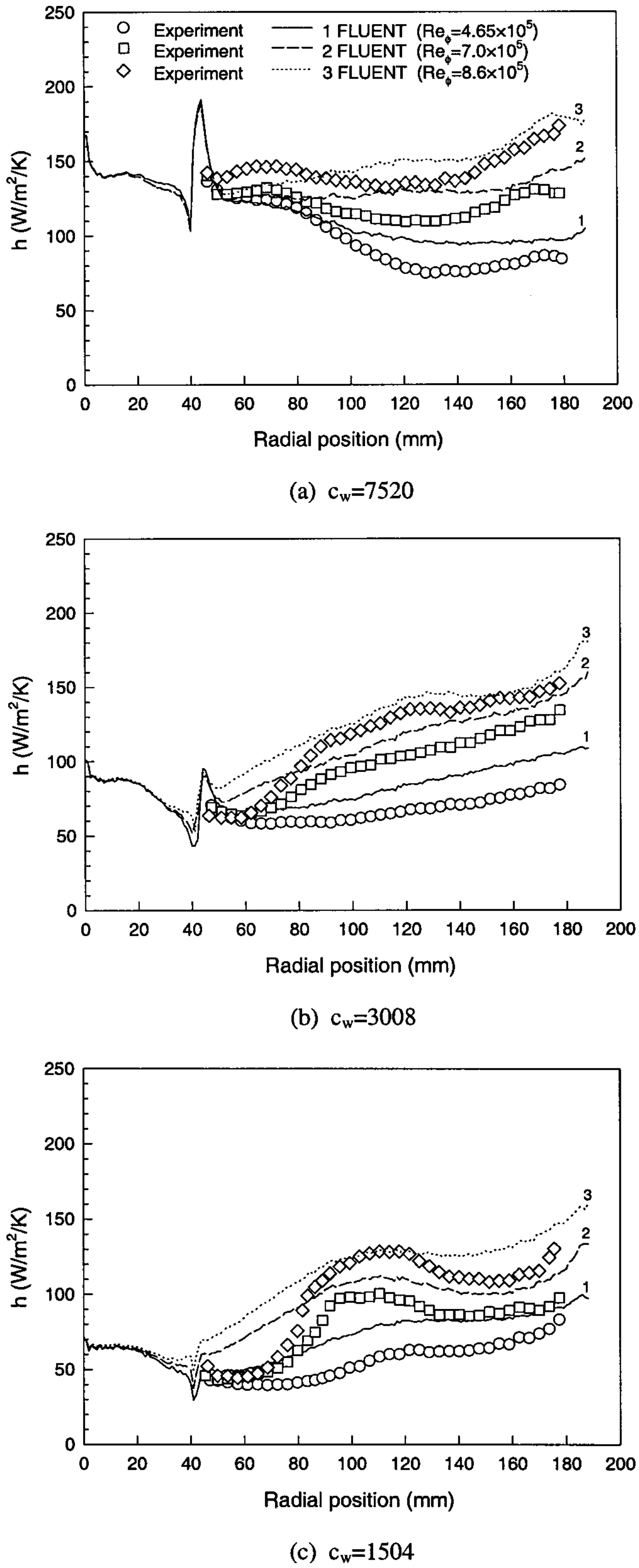

(a) c_w=7520

(b) c_w=3008

(c) c_w=1504

Fig. 12 Effect of rotor disk speed on the convective heat transfer coefficient distribution

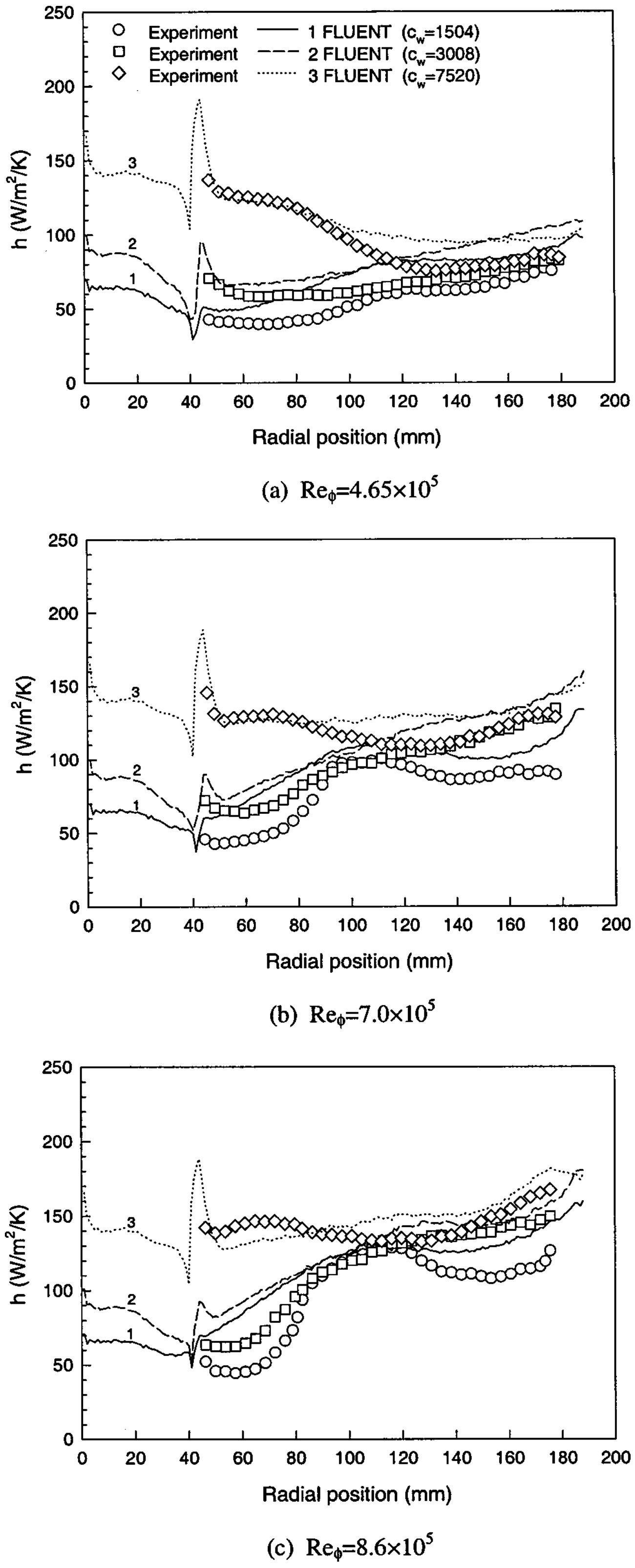

(a) Re$_\phi$=4.65×10^5

(b) Re$_\phi$=7.0×10^5

(c) Re$_\phi$=8.6×10^5

Fig. 13 Effect of secondary air flow rate on the convective heat transfer coefficient distribution

region) while they are higher than the correlation in the source region. The correlation, which is based on a momentum integral approach, considers the radial and tangential velocity components of the cavity air flow but not the axial velocity component, which can be expected to give rise to impingement-like heat transfer in the inner part of the source region. As such, the Kapinos correlation will be unsatisfactory there.

The present data agree reasonably well with Fluent predictions.

5.4 Correlations. The heat transfer data from this study were used to develop an empirical correlation for the local con-

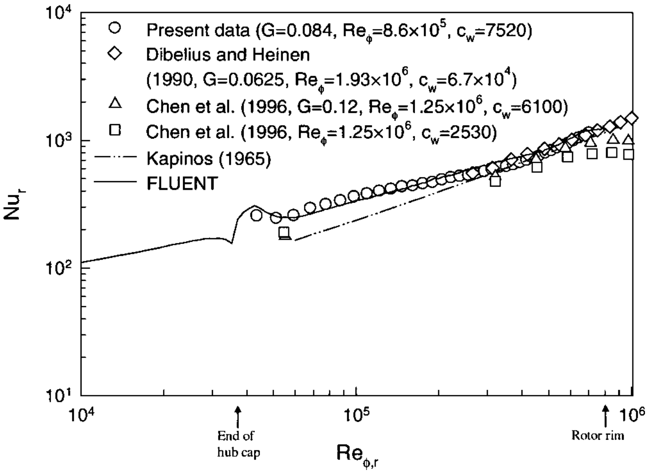

Fig. 14 Comparison of selected results of the present work with some earlier works

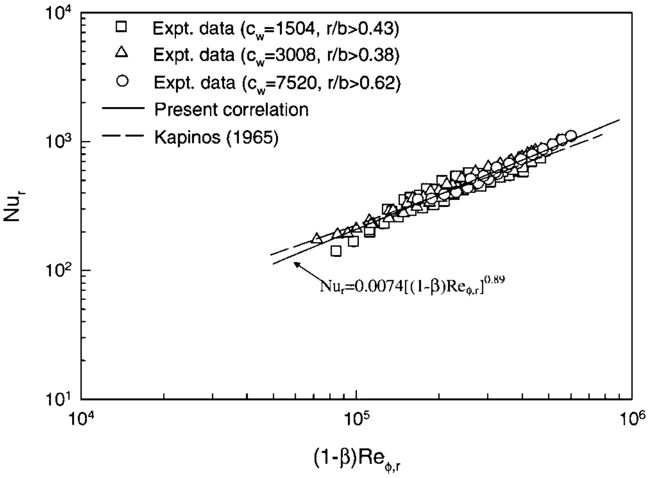

Fig. 16 Local Nusselt number versus local relative rotational Reynolds number (experimental data and correlation are for the core region and radially outermost part of the source region)

vective heat transfer coefficient on the rotor disk. The data radially inboard in the source region were not considered. The local convective heat transfer coefficient on free or enclosed rotor disks may be correlated by a relation of the form:

$$\mathrm{Nu}_r = C\,\mathrm{Re}_{\phi,r}^m \tag{6}$$

Values of $C=0.0195$ and $m=0.80$ provided the best fit for the present data, Fig. 15. The average deviation of the data from the correlation is about 7.3 percent for $c_w=7520$, 7.3 percent for $c_w=3008$, and 16.9 percent for $c_w=1504$.

Equation (6) does not consider the effect of secondary air flow rate on the tangential velocity of the cavity fluid. This effect may be included indirectly in the heat transfer correlation by using the local relative rotational Reynolds number, Re_r, which is based on the relative tangential velocity between the rotor disk and the core fluid. The core fluid tangential velocity varies with the rotor disk speed, secondary air flow rate, and radial location in the cavity. This velocity was measured in the same disk cavity by Particle Image Velocimetry [24], and was found to agree well with the correlation proposed by Daily et al. [26]:

$$\frac{\beta}{\beta^*} = \frac{1}{1+12.74\dfrac{\lambda_{turb}}{(r/b)^{13/5}}} \tag{7}$$

where $\beta^*=0.43$. Equation (7) can therefore be used to obtain the local relative rotational Reynolds number:

$$\mathrm{Re}_r = \rho(\Omega r - V_{\phi,c})r/\mu = (1-\beta)\mathrm{Re}_{\phi,r} \tag{8}$$

The local Nusselt number versus the local relative rotational Reynolds number plot of the present heat transfer data is shown in Fig. 16. The correlation obtained is:

$$\mathrm{Nu}_r = 0.0074\,\mathrm{Re}_r^{0.89} \tag{9}$$

The average deviation of the data from the correlation is approximately 4.1 percent for $c_w=7520$, 6.4 percent for $c_w=3008$ and 12.2 percent for $c_w=1504$.

The derived Nusselt number correlation, Eq. (9), should be applicable in the core region and the radially outermost part of the source region of disk cavities (see Fig. 3). The extents of these regions depend upon where the secondary flow enters the disk cavity. In real gas turbine disk cavities, the secondary flow entrance is usually radially outboard of the hub, and the correlation should hold in the resulting core region and outer part of the source region.

6 Concluding Remarks

An experimental study of the fluid temperature distribution and the convective heat transfer coefficient distribution on the rotor disk surface was carried out in a model rotor–stator disk cavity with both mainstream and secondary air flow present. The ranges of the experiments were $4.6\times10^5<\mathrm{Re}_{\phi,r}<8.6\times10^5$, $1500<c_w<7520$, and $\mathrm{Re}_m=5.0\times10^5$. Numerical simulations were also performed using the commercial CFD code Fluent. The simulation results were compared with the experimental data.

A fluid core was found to exist in the cavity between the boundary layers on the rotor and stator disks. The core fluid temperature, as measured at the outer edge of the thermal boundary layer on the rotor disk, was adopted as the reference fluid temperature in determining the local convective heat transfer coefficient on the rotor disk. The thermal boundary layer on the rotor disk was influenced by both the rotor disk speed and the secondary air flow rate. Ingestion of the cooler mainstream air into the disk cavity and heat loss to the stator disk also played significant roles.

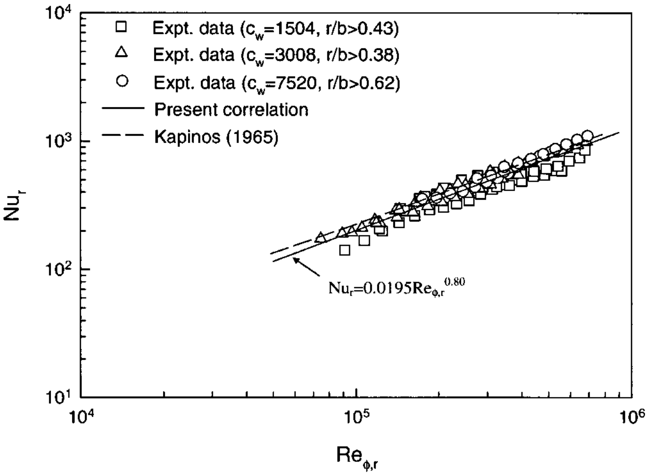

Fig. 15 Local Nusselt number versus local rotational Reynolds number (experimental data and correlation are for the core region and radially outermost part of the source region)

The local convective heat transfer coefficient on the rotor disk varied with the rotor disk speed and secondary air flow rate. In the source region, which is radially inboard in the cavity, the effect of rotor disk speed was weak and that of the secondary air flow rate strong, the heat transfer coefficient increasing with the air flow rate. In the core region, which is radially outboard in the cavity, the convective heat transfer coefficient was dominated by the rotor disk speed, especially at high secondary air flow rates. The influence of secondary air flow rate was important especially at the higher rotor disk speeds. Ingested mainstream air, which can be substantial at low secondary air flow rate and high rotor disk speed, affects the rotor disk convective heat transfer coefficient radially outboard of the source region.

The measured convective heat transfer coefficient distributions were in reasonable agreement with those computed by Fluent in the steady-state rotationally symmetric mode although, clearly, some important trends were not predicted by the computations. A key reason may be that ingestion and therefore the corresponding effects were not predicted. This was also the case when the simulations were steady three dimensional. Recent measurements of the unsteady pressure field in the mainstream gas path and the disk cavity in the same rig at some of the relevant experimental conditions [27] suggest that the computations will need to be unsteady as well as three dimensional to be able to predict ingestion correctly.

Finally, an empirical correlation for the local Nusselt number on the rotor disk in terms of the local relative rotational Reynolds number is proposed. This correlation should be applicable in the core region and radially outer part of the source region in a rotor–stator disk cavity.

Acknowledgments

This research was performed under subcontract No. 95-01-SR033 sponsored by the U.S. Department of Energy–Federal Energy Technology Center through a cooperative agreement with the South Carolina Institute for Energy Studies at Clemson University. A grant from AlliedSignal Engines, Phoenix, AZ, during the initial phase of this work is gratefully acknowledged. Discussions with J. Howe and Y. Kim of AlliedSignal Engines, and B. Glezer and M. Fox of Solar Turbines, during this work were very helpful.

Nomenclature

b = outer radius of disk cavity (Fig. 1); also radius of free disk
C_p = specific heat of air at constant pressure
c_w = nondimensional mass flow rate of secondary air $= \dot{m}_s / \mu b$
$c_{w,fd}$ = nondimensional free disk pumping mass flow rate $= 0.219\,\mathrm{Re}_\phi^{0.8}$
G = axial gap ratio $= s/b$
Gr_r = local Grashof number $= \mathrm{Re}_{\phi,r}^2 \Delta T / T_{\mathrm{ref}}$
h = local convective heat transfer coefficient $= q''_{w,\mathrm{conv}}/(T_w - T_{\mathrm{ref}})$
k = thermal conductivity; also turbulent kinetic energy
$\dot{m}_m$ = mass flow rate of mainstream air
$\dot{m}_s$ = mass flow rate of secondary air
Nu_r = local Nusselt number $= hr/k_{\mathrm{air}}$
q''_w = total heat flux at rotor disk surface
$q''_{w,\mathrm{conv}}$ = convective heat flux at rotor disk surface
$q''_{w,\mathrm{rad}}$ = radiative heat flux at rotor disk surface
r = radial coordinate
Re_m = mainstream flow Reynolds number $= \rho V_m b/\mu$
Re_ϕ = disk rotational Reynolds number $= \rho \Omega b^2/\mu$
$\mathrm{Re}_{\phi,r}$ = local rotational Reynolds number $= \rho \Omega r^2/\mu$
Re_r = local relative rotational Reynolds number $= (1-\beta)\mathrm{Re}_{\phi,r}$
s = axial gap between rotor and stator disks
T = temperature
T_{ref} = reference temperature of cavity fluid
T_w = rotor disk surface temperature
T_∞ = ambient air temperature
ΔT = $T_w - T_{\mathrm{ref}}$
U_τ = friction velocity at surface
V_m = mainstream flow bulk axial velocity
V_r = local radial velocity of cavity fluid
V_ϕ = local tangential velocity of cavity fluid
$V_{\phi,c}$ = tangential velocity of the core fluid
x = axial coordinate
y^+ = normal distance from surface in wall unit $= yU_\tau/\nu$
z_a = rim discourager (seal) axial overlap (Fig. 1(*a*))
z_r = rim discourager radial clearance (Fig. 1(*a*))
β = core fluid rotation ratio $= V_{\phi,c}/\Omega r$
δ_e = thickness of epoxy layer on the rotor disk
ε = dissipation rate of turbulent kinetic energy
λ_{turb} = turbulent flow parameter $= c_w\,\mathrm{Re}_\phi^{-0.8}$
μ = dynamic viscosity
ν = kinematic viscosity
ρ = density
ϕ = azimuthal coordinate
Ω = disk rotational speed

Subscripts

air = air in the disk cavity
c = fluid core
e = epoxy
f = fluid
in = inlet value
ref = reference value
ro = rotor disk
s = substrate
st = stator disk
w = wall (surface)

References

[1] Kapinos, V. M., 1965, ''Heat Transfer From a Disc Rotating in a Housing With a Radial Flow of Coolant,'' J. Eng. Phys., **8**, pp. 35–38.

[2] Metzger, D. E., 1970, ''Heat Transfer and Pumping on a Rotating Disk With Freely Induced and Forced Cooling,'' ASME J. Eng. Power, **92**, pp. 663–667.

[3] Owen, J. M., Haynes, C. M., and Bayley, F. J., 1974, ''Heat Transfer From an Air-Cooled Rotating Disk,'' Proc. R. Soc. London, Ser. A, **336**, pp. 453–473.

[4] Qureshi, G., Nguyen, M. H., Saad, N. R., and Tadros, R. N., 1989, ''Heat Transfer Measurements for Rotating Turbine Discs,'' ASME Paper No. 89-GT-236.

[5] Dibelius, G. H., and Heinen, M., 1990, ''Heat Transfer From a Rotating Disc,'' ASME Paper No. 90-GT-219.

[6] Metzger, D. E., Bunker, R. S., and Bosch, G., 1991, ''Transient Liquid Crystal Measurements of Local Heat Transfer on a Rotating Disk With Jet Impingement,'' ASME J. Turbomach., **113**, pp. 52–59.

[7] Kreith, F., Taylor, J. H., and Chong, J. P., 1959, ''Heat and Mass Transfer From a Rotating Disk,'' ASME J. Heat Transfer, **81**, pp. 95–105.

[8] Dorfman, L. A., 1963, *Hydrodynamic Resistance and the Heat Loss of Rotating Solids*, Oliver and Boyd, Edinburgh and London.

[9] Bunker, R. S., Metzger, D. E., and Wittig, S., 1992, ''Local Heat Transfer in Turbine Disk Cavities. Part I: Rotor and Stator Cooling With Hub Injection of Coolant,'' ASME J. Turbomach., **114**, pp. 211–220.

[10] Bunker, R. S., Metzger, D. E., and Wittig, S., 1992, ''Local Heat Transfer in Turbine Disk Cavities. Part II: Rotor Cooling With Radial Injection of Coolant,'' ASME J. Turbomach., **114**, pp. 221–228.

[11] Kim, Y. W., and Kleinman, D. A., 1994, ''Heat Transfer and Cooling Effectiveness Studies on Rotating Disks,'' *Heat Transfer in Gas Turbines*, ASME HTD-Vol. 300, pp. 101–109.

[12] Long, C. A., 1994, ''Disk Heat Transfer in a Rotating Cavity With an Axial Throughflow of Cooling Air,'' Int. J. Heat Fluid Flow, **15**, No. 4, pp. 307–316.

[13] Chen, J.-X., Gan, X., and Owen, J. M., 1996, ''Heat Transfer in an Air-Cooled Rotor–Stator System,'' ASME J. Turbomach., **118**, pp. 444–451.

[14] Wilson, M., Pilbrow, R., and Owen, J. M., 1997, ''Flow and Heat Transfer in a Preswirl Rotor–Stator System.'' ASME J. Turbomach., **119**, pp. 364–373.

[15] Owen, J. M., and Rogers, R. H., 1989, *Flow and Heat Transfer in Rotating–Disc Systems, 1: Rotor–Stator System*, Research Studies Press, Taunton; Wiley, New York.

[16] Fluent, Inc., 1999, ‘‘Computational Fluid Dynamics Software—FLUENT/UNS,’’ User’s Guide, Release 5.0, Lebanon, NH.

[17] Chen, J.-X., Gan, X., and Owen, J. M., 1997, ‘‘Heat Transfer From Air-Cooled Contrarotating Disks,’’ ASME J. Turbomach., **119**, pp. 61–67.

[18] Kline, S. J., and McClintock, F. A., 1953, ‘‘Describing Uncertainties in Single Sample Experiments,’’ Mech. Eng. (Am. Soc. Mech. Eng.), **74**, pp. 3–8.

[19] Gregory, N., Stuart, J. T., and Walker, W. S., 1955, ‘‘On the Stability of Three-Dimensional Boundary Layers With Application to the Flow Due to a Rotating Disk,’’ Philos. Trans. R. Soc. London, Ser. A, **248**, pp. 155–199.

[20] Wolfstein, H., 1969, ‘‘The Velocity and Temperature Distribution of One-Dimensional Flow With Turbulence Augmentation and Pressure Gradient,’’ Int. J. Heat Mass Transf., **12**, pp. 301–318.

[21] Chen, C. H., and Patel, V. C., 1988, ‘‘Near-Wall Turbulence Models for Complex Flows Including Separation,’’ AIAA J., **26**, No. 6, pp. 641–648.

[22] He, J., 1999, ‘‘Numerical Simulation of Turbulent Flow and Thermal Fields in a Rotor–Stator Cavity With External Flow,’’ M.S. Thesis, Arizona State University.

[23] Daily, J. W., and Nece, R. E., 1960, ‘‘Chamber Dimension Effects on Induced Flow and Frictional Resistance of Enclosed Rotational Disks,’’ ASME J. Basic Eng., **82**, pp. 217–232.

[24] Roy, R. P., Devasenathipathy, S., Xu, G., and Zhao, Y., 1999, ‘‘A Study of the Flow Field in a Model Rotor–Stator Disk Cavity,’’ ASME Paper No. 99-GT-246.

[25] Roy, R. P., Xu, G., and Feng, J., 2000, ‘‘A Study of Main-stream Gas Ingestion in a Model Rotor–Stator Disk Cavity,’’ AIAA Paper No. 2000–3372.

[26] Daily, J. W., Ernst, W. D., and Asbedian, V. V., 1964, ‘‘Enclosed Rotating Discs With Superimposed Throughflow,’’ Report No. 64, Department of Civil Engineering, Hydrodynamics Laboratories, Massachusetts Institute of Technology, Cambridge, MA.

[27] Roy, R. P., Xu, G., Feng, J., and Kang, S., 2001, ‘‘Pressure Field and Main-stream Gas Ingestion in a Rotor–Stator Disk Cavity,’’ ASME Paper No. 2001-GT-564.